Sergey Vasil'yevich Klyuev
Alexander Vasil'yevich Klyuev
Nikolay Ivanovich Vatin
Linar S. Sabitov   *Editors*

Innovations and Technologies in Construction

Selected Papers of BUILDINTECH BIT 2022

Springer

Lecture Notes in Civil Engineering

Volume 307

Lecture Notes in Civil Engineering (LNCE) publishes the latest developments in Civil Engineering—quickly, informally and in top quality. Though original research reported in proceedings and post-proceedings represents the core of LNCE, edited volumes of exceptionally high quality and interest may also be considered for publication. Volumes published in LNCE embrace all aspects and subfields of, as well as new challenges in, Civil Engineering. Topics in the series include:

- Construction and Structural Mechanics
- Building Materials
- Concrete, Steel and Timber Structures
- Geotechnical Engineering
- Earthquake Engineering
- Coastal Engineering
- Ocean and Offshore Engineering; Ships and Floating Structures
- Hydraulics, Hydrology and Water Resources Engineering
- Environmental Engineering and Sustainability
- Structural Health and Monitoring
- Surveying and Geographical Information Systems
- Indoor Environments
- Transportation and Traffic
- Risk Analysis
- Safety and Security

To submit a proposal or request further information, please contact the appropriate Springer Editor:

- Pierpaolo Riva at pierpaolo.riva@springer.com (Europe and Americas);
- Swati Meherishi at swati.meherishi@springer.com (Asia—except China, Australia, and New Zealand);
- Wayne Hu at wayne.hu@springer.com (China).

All books in the series now indexed by Scopus and EI Compendex database!

Sergey Vasil'yevich Klyuev ·
Alexander Vasil'yevich Klyuev ·
Nikolay Ivanovich Vatin · Linar S. Sabitov
Editors

Innovations and Technologies in Construction

Selected Papers of BUILDINTECH BIT 2022

 Springer

Editors
Sergey Vasil'yevich Klyuev
Belgorod State Technological University
Belgorod, Russia

Nikolay Ivanovich Vatin
Peter the Great St. Petersburg Polytechnic
University
St. Petersburg, Russia

Alexander Vasil'yevich Klyuev
Belgorod State Technological University
Belgorod, Russia

Linar S. Sabitov
Kazan Federal University
Kazan, Russia

Preface

The III International Conference "BUILDINTECH BIT 2022. INNOVATIONS AND TECHNOLOGIES IN CONSTRUCTION" was held during March 9–10, 2022, in Belgorod (Russian Federation), on the basis of Belgorod State Technological University named after V. G. Shukhov, Belgorod, Russia.

The III International Scientific Conference "BUILDINGTECH BIT 2022" contains advanced achievements in the field of improving methods for calculating the strength, stiffness, crack resistance of structures, taking into account the features of their structure and optimizing the composition. It is also devoted to strengthening building structures and assessing their suitability for use, monitoring buildings, improving building technologies, energy efficiency of building envelopes, introducing new structures and materials, and economic assessment of construction. It also consists of test data for load-bearing building structures. This volume will prove to be a valuable resource for those in academia and industry.

As a result, there is a real opportunity among a wide range of scientists, teachers, industry representatives, and students in various fields related to material engineering, science, to exchange ideas, share knowledge, and establish close cooperation. The successful organization and holding of the conference are evidenced by the wide geography of the participants, as well as the high level of the reports presented. With its high quality, it provides an exceptional value for students, academics, and industry researchers. It also provides a premier interdisciplinary platform for researchers, practitioners, and educators to present and discuss the most recent innovations, trends, and concerns as well as practical challenges encountered and solutions adopted in the fields of building construction and materials sciences.

The conference has an active participation of more than 150 scientists and experts from different Russian regions (up to 32) and 10 countries (Australia, Armenia, China, Iraq, Morocco, Egypt, Syria, Kazakhstan, Tajikistan, and Uzbekistan).

A major part of theoretical information and experimental data is the results of studies, which were realized within the framework of implementation of state and national programs in the scientific field as a grant, federal targeted programs, decrees of the Government of the Russian Federation, and other programs.

Thanks to the invaluable contribution of a group of highly qualified reviewers, all articles went through high-quality peer review and several stages of editing. The organizing committee expresses its sincere gratitude to everyone who contributed to the conference. In addition, we would like to express our deep gratitude to the authors, reviewers, participants, and the entire organizing team for their support and enthusiasm, which ensured the success of the conference.

Editors

Sergey Vasil'yevich Klyuev, Candidate of Engineering Sciences, Associate Professor, Head of Research Department, Belgorod State Technological University named after V. G. Shukhov
Nikolay Ivanovich Vatin, Doctor of Engineering Sciences, Professor, St. Petersburg Polytechnic University of Peter the Great
Alexander Vasil'yevich Klyuev, Candidate of Engineering Sciences, Associate Professor, Head of Research Department, Belgorod State Technological University named after V. G. Shukhov
Linar S. Sabitov, Deputy Director for Research, Doctor of Engineering Sciences, Associate Professor, Kazan (Volga Region) Federal University

Organizing Conference Committee

Evtushenko E. I., Doctor of Engineering Sciences (Advanced Doctor), Professor, Belgorod State Technological University named after V. G. Shukhov, Belgorod, Russia
Davydenko T. M., Doctor of Pedagogical Sciences (Advanced Doctor), Professor, Belgorod State Technological University named after V. G. Shukhov, Belgorod, Russia
Sergey Vasil'yevich Klyuev, Candidate of Engineering Sciences (Ph.D.), Associate Professor, Belgorod State Technological University named after V. G. Shukhov, Belgorod, Russia
Lesovik V. S., Doctor of Engineering Sciences (Advanced Doctor), Professor, Corresponding Member of RAASN, Belgorod State Technological University named after V. G. Shukhov, Belgorod, Russia
Nikolay Ivanovich Vatin, Doctor of Engineering Sciences (Advanced Doctor), Professor, Peter the Great St. Petersburg Polytechnic University, St. Petersburg, Russia
Fediuk R. S., Candidate of Technical Sciences (Ph.D.), Professor, Far Eastern Federal University, Vladivostok, Russia
Kozhukhova N. I., Candidate of Engineering Sciences (Ph.D.), Associate Professor, Belgorod State Technological University named after V. G. Shukhov

Ayzenshtadt A. M., Doctor of Chemical Sciences (Advanced Doctor), Professor, Northern (Arctic) Federal University named after M. V. Lomonosov

Potapov V. V., Doctor of Engineering Sciences (Advanced Doctor), Professor, Research Geotechnological Center of the Far Eastern Branch of the Russian Academy of Sciences

Mestnikov A. E., Doctor of Technical Sciences (Advanced Doctor), Professor, North-Eastern Federal University named after M. K. Ammosov

Suleymanova L. A., Doctor of Engineering Sciences (Advanced Doctor), Professor, Belgorod State Technological University named after V. G. Shukhov

Alfimova N. I., Candidate of Engineering Sciences (Ph.D.), Associate Professor, Belgorod State Technological University named after V. G. Shukhov

Alexander Vasil'yevich Klyuev, Candidate of Engineering Sciences (Ph.D.), Associate Professor, Belgorod State Technological University named after V. G. Shukhov

Linar S. Sabitov, Doctor of Engineering Sciences (Advanced Doctor), Associate Professor, Kazan Federal University

Scientific Conference Committee

Amir Abdulrahman, Iraq—Doctor of Engineering, Professor, Anbar University

Ali Belloush, Morocco—Ph.D., Professor, Rector, Funtius Institute

Kovtun M. A., Australia—Ph.D.

Kozhukhova M. I., the USA—Ph.D., University of Wisconsin-Milwaukee

Loganina V. I., RF—Doctor of Engineering Sciences (Advanced Doctor), Professor, Penza State University of Architecture and Construction

Lukuttsova N. P., RF—Doctor of Engineering Sciences (Advanced Doctor), Professor, Bryansk State Engineering Technological University

Nevzorov A. L., RF—Doctor of Engineering Sciences (Advanced Doctor), Professor, Northern (Arctic) Federal University named after M. V. Lomonosov

Nenad Stoykovich, Serbia—Ph.D., Nish Higher Technical School of Vocational Education

Naumov A. E., RF—Candidate of Engineering Sciences (Ph.D.), Associate Professor, Belgorod State Technological University named after V. G. Shukhov

Elyan Issa Jamal Issa, Jordan—Ph.D., Amman University

Salyamova K. D. , Uzbekistan—Doctor of Engineering Sciences (Advanced Doctor), Professor, Institute of Mechanics and Seismic Stability of Structures of the Academy of Sciences of the Republic of Uzbekistan

Sovann Chin, Cambodia—Ph.D.

Strokova V. V., RF—Doctor of Engineering Sciences (Advanced Doctor), Professor, Belgorod State Technological University named after V. G. Shukhov

Suleymanova L. A., RF—Doctor of Engineering Sciences (Advanced Doctor), Professor, Belgorod State Technological University named after V. G. Shukhov

Fisher H. B., Germany—Professor, Bauhaus-University of Weimar

Tabet Salem Al-Azab, Yemen—Ph.D.

Eknik Jürgen, Switzerland—Ph.D., Professor, Executive Director of a Swiss Company, Performance Selling Academy Zurich Area GmbH
Hussein Motawi, Egypt—Ph.D., Professor, Vice-Rector, Damanhour University
Shakarna Mahmoud Husni Ibrahim, Palestine—Ph.D.

We would like to acknowledge all of those who supported The III International Conference "BUILDINTECH BIT 2022. INNOVATIONS AND TECHNOLOGIES IN CONSTRUCTION". Each individual and institutional help were very important for the success of this conference. Especially we would like to thank the organizing committee for their valuable advices in the organization and helpful peer review of the papers. We sincerely hope that The III International Conference "BUILDINTECH BIT 2022. INNOVATIONS AND TECHNOLOGIES IN CONSTRUCTION" will be a forum for excellent discussions that will put forward new ideas and promote collaborative researches. We are sure that the proceedings will serve as an important research source of references and the knowledge, which will lead to not only scientific and engineering progress but also other new products and processes. All conference delegates express deep gratitude to the Science team.

Belgorod, Russia	Sergey Vasil'yevich Klyuev
Belgorod, Russia	Alexander Vasil'yevich Klyuev
St. Petersburg, Russia	Nikolay Ivanovich Vatin
Kazan, Russia	Linar S. Sabitov

Contents

High-Efficiency Wall Materials Based on Technogenic Aluminosilicate Raw Materials

A. A. Volodchenko(✉) ⓘ, V. S. Lesovik ⓘ, A. N. Volodchenko ⓘ, and V. V. Voronov

Belgorod State Technological University Named After V.G. Shukhov, Belgorod, Russia
Alex-0904@mail.ru

Abstract. At the present time the development of new generation building composites, distinguished not only by high performance characteristics, but also contributing to the optimization of the system "human-material-living environment" is actual. In construction, sand-lime bricks are widely used as wall material. According to the normative documentation in its production pure quartz sand with a minimum content of clay impurities are used. However, there is a large proportion of quartz sands containing clay impurities. Such rocks do not satisfy the requirements of normative documents to sands for silicate materials. The urgent task is to conduct researches on development of building composites of new generation with the use of this type of raw materials. As a result of this research it is shown that fine sands characterized by the presence of clay impurities, represented by miscible clay minerals can be used as raw materials for the production of silicate materials. The use of such raw materials can optimize the microstructure and accelerate the synthesis of new formations represented by low-base calcium hydrosilicates. Increase of strength characteristics of products is caused by formation of new formations of increased degree of crystallinity, and also at the expense of optimization of granulometric composition. The content of the required percentage of used raw materials in the raw mix of sand-lime bricks contributes to an increase in strength characteristics of raw bricks by 2 times, the finished product by 1.8 times, which simplifies the production of products of complex shape.

Keywords: Construction materials · Wall materials · Silicate materials · Clay rocks

1 Introduction

At the present time the development of new generation building composites, distinguished not only by high performance characteristics, but also contributing to the optimization of the system "human-material-living environment" is actual [1–3]. Development of such composites is possible with the use of theoretical provisions of the new transdisciplinary scientific direction of research of geonics (geomimetics). Also at design of new kinds of building composites it is necessary to use new kinds of raw materials which are not used now [4–6].

In construction, sand-lime bricks are widely used as wall material [7–10]. According to the normative documentation, pure quartz sands with a minimum content of clay

impurities are used in its production. However, there is a large proportion of quartz sands containing clay impurities. Such rocks have a minimum number of plasticity and are characterized as sandy loam.

Such siliceous raw materials, characterized by an increased content of clay impurities, are widespread in Russia, including those that fall into the zone of mining operations in the region of the Kursk Magnetic Anomaly. Such rocks do not meet the requirements of normative documents for sands for silicate materials [9, 10]. The task of research on development of building composites of new generation, in particular silicate materials, with the use of this type of raw materials is actual [11–14].

2 Methods and Materials

In these studies, building lime (see Table 1) produced by JSC "Stroymaterialy" (Russia) and corresponding to the requirements of GOST 22,688-2018 was used as an active binder component.

Table 1 Characteristics of the used construction lime

Name of indicator	Content, wt%
Content of active $CaO + MgO$	70
Content of active MgO	5
Content of CO_2	7
Slake time, min	8

To develop compositions of lime-silica binder, to obtain on its basis wall materials, we used fine-dispersed sand (Russia, Kursk Magnetic Anomaly region) with specific surface area of 80–100 m^2/kg and the content of clay impurities 15–20 wt%. The number of plasticity is 5, which allows us to attribute this rock to sandy loam. Bulk density is 1590 kg/m^3.

Sand (Russia, Kursk Magnetic Anomaly region) with a specific surface area of 30–40 m^2/kg and content of dusty, silty and clayey particles less than 0.05 mm in size, not more than 5 wt% was used as an aggregate.

Raw mix for the production of wall materials is prepared in two stages. In the first stage by grinding construction lime and fine sand together, a lime-silica binder with a specific surface area of 800 m^2/kg is produced. The resulting lime-silica binder is mixed in a laboratory mixer with aggregate sand, followed by moistening with water and holding the mixture to slake the lime in the raw mix. The samples are formed by hydraulic pressing at a pressing pressure of 20 MPa. Curing of specimens is carried out in autoclave at pressure of 6–12 bar. Duration of isothermal soaking was 8 h.

The following performance parameters were determined in the obtained specimens: compressive strength, average density, water resistance. The microstructure of the samples, as well as the composition of the formed neoplasms were studied by X-ray diffraction and differential-thermal analysis and scanning electron microscopy.

3 Results and Discussion

The mineralogical composition of the fine sand was investigated using thermographic (see Fig. 1) and radiographic (see Fig. 2) methods of analysis. The rock was found to contain fine-dispersed quartz, mixed clay minerals, and other minerals.
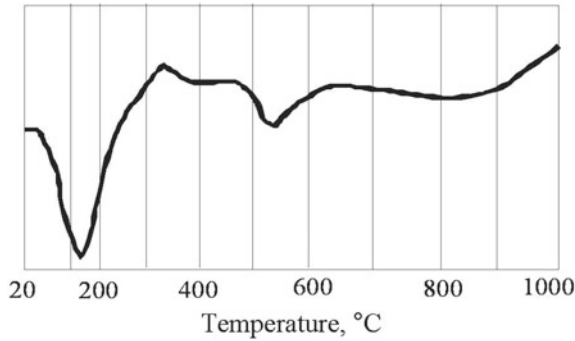
Fig. 1 Differential thermal curve of fine sand with clay impurities
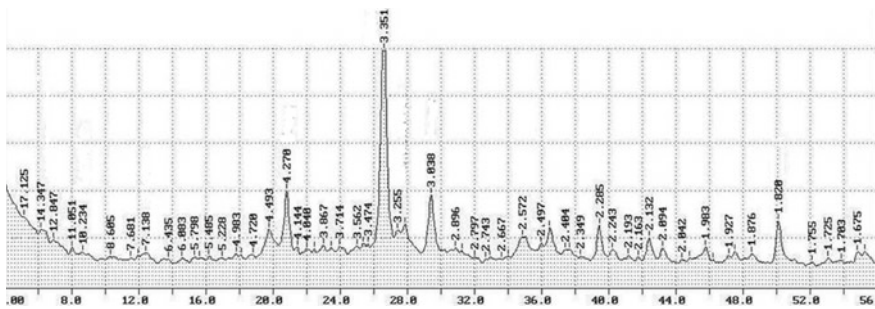
Fig. 2 Radiograph of fine sand containing clay impurities

In the microstructure of fine sand (see Fig. 3a) containing clay impurities, quartz sand particles with a corroded surface and covered with clay mineral particles are identified. The total mass of aggregate sand is dominated by particles of a rounded shape (see Fig. 3b).

In the studies on the production of sand-lime bricks in the first phase was carried out to determine the rational moisture content of the raw mix in order to maximize the strength characteristics of products (see Table 2).

The content of active CaO was 8 wt%. The amount of fine sand with clay impurities varied in the range 20–40 wt%, molding moisture varied in the range 6–16 wt%. Specimens were steamed at $1.5 + 6 + 1.5$ h at a saturated steam pressure of 1.0 bar.

It was found that increasing the content of liquid in the mixture of raw materials increases the strength of the specimens. So the moisture content of the raw mixture in the range of 8–12 wt% is optimum.
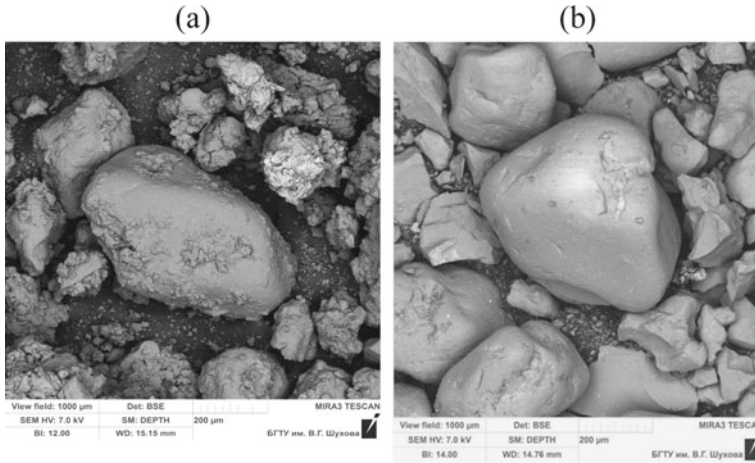
Fig. 3 Microstructure of the used sands: **a** fine sand with clay impurities, **b** aggregate sand

Table 2 Effect of molding moisture on specimen properties

Content of fine sand, wt%	Compressive strength (MPa) at molding moisture, %					
	6	8	10	12	14	16
20	12.4	23.5	27.1	25.1	22.5	13.9
30	12.4	22.8	26.4	23.5	20.86	19.8
40	12.4	24.1	26.1	25.1	19.8	19.5

The important characteristic in the technology of sand-lime bricks is the strength of raw bricks. In the study the effect of fine sand characterized by the content of clay impurities on the strength of raw bricks was determined (see Table 3). It is found that the use of fine sand characterized by the content of clay impurities in the manufacture of sand-lime brick will improve the formability of the raw mixture and increase the strength of the raw brick.

Table 3 Effect of fine sand content on the strength of raw bricks

Compressive strength (MPa) at fine sand content, wt%						
0	5	10	20	30	40	50
0.43	0.47	0.5	0.79	0.93	0.96	1.08

Based on physical and mechanical tests (see Table 4) of the specimens obtained it was found that with increasing the proportion of fine sand in the raw mix strength of specimens increases from 11 to 18 MPa at the content of CaO—4 wt% and from 16

to 20.8 MPa at the content of CaO—6 wt%. An increase in the content of fine sand, along with an increase in the content of building lime, leads to a decrease in strength characteristics.

Table 4 Physical and mechanical characteristics of specimens

Physical and mechanical characteristics	Content of fine sand, wt%			
	0	10	30	60
Content of building lime—4 wt%				
Compressive strength, MPa	11	13	19,1	18
Average density, g/cm^3	1.77	1.78	1.79	1.79
Content of building lime—6 wt%				
Compressive strength, MPa	16	15	22	20,8
Average density, g/cm^3	1.81	1.81	1.85	1.85
Content of building lime—8 wt%				
Compressive strength, MPa	30	22	27	26
Average density, g/cm^3	1.82	1.81	1.82	1.81

In order to determine the rational compositions of raw mixes to obtain the optimal strength characteristics, studies were conducted using the method of mathematical planning of the experiment (see Table 5).

Table 5 Mathematical planning of the experiment

Factors		Levels of variation			Variation interval
Natural view	Coded view	−1	0	+1	
Fine sand, wt%	x_1	10	35	60	25
Isothermal exposure, h	x_2	2	5	8	3
Hydrothermal treatment pressure, bar	x_3	0.6	0.9	1.2	0.3
Building lime, wt%	x_4	4	7	10	3

On the basis of the obtained data the regression Eq. (1) of the compressive strength dependence was obtained and graphical nomograms were plotted (see Fig. 4).

$$R = 21.8 + 1.3 \cdot x_1 + 4.2 \cdot x_2 + 3.7 \cdot x_3 + 4.4 \cdot x_2 - 2.6 \cdot x_1^2 + 2.8 \cdot x_2^2$$
$$--3.5 \cdot x_3^2 - 1.2 \cdot x_4^2 --0.73 \cdot x_1 \cdot x_2 + 0.4 \cdot x_1 \cdot x_3 - 0.4 \cdot x_1 \cdot x_4$$
$$+ 0.22\, x_2 \cdot x_3 + 1.9 \cdot x_2 \cdot x_4 + 1.5 \cdot x_3 \cdot x_4 \tag{1}$$
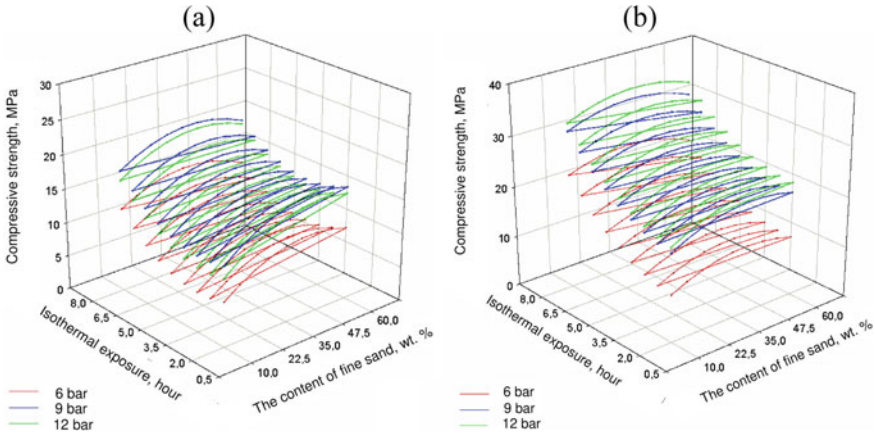
Fig. 4 Dependence of compressive strength on the content of fine sand, isothermal exposure time and building lime: **a** content of building lime—4 wt%; **b** content of building lime—10 wt%

It was found that the increase in the proportion of the studied fine sand up to 42% allows increasing the index of the compressive strength. Such a composition of the raw mix contributes to the formation of the strongest crystalline framework of new formations, which is confirmed by the results of the X-ray method of research (see Fig. 5).
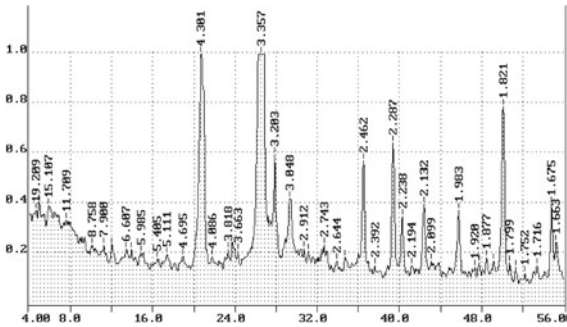
Fig. 5 Radiograph of a specimen with a fine sand content of 40 wt% and CaO—7 wt% (hydrothermal treatment pressure—9 bar;isothermal exposure—5 h)

The results of the analysis show that almost the entire clay component in the fine sand interacted with the building lime. At the same time, low-base hydrosilicates (d = 3.048 Å), two-base hydrosilicates (d = 3.2, 2.28 Å) are formed in the composition of new formations.

If the content of fine sand in the raw mix of more than 42 wt%, it remains in a free form, which deteriorates the strength properties of products.

With the increase in the content of fine sand in the raw mix the increase in the average density of silicate products is noted. Probably, increase of average density of specimens

is connected with introduction of fine-grained sand increasing density of packing of a material. This can also explain the reduction of water absorption of products by 5%. With increasing the input of fine sand up to 30 wt% the softening coefficient of silicate products increases, and over 30 wt% leads to a decrease in the softening coefficient. Increasing the pressure of hydrothermal treatment increases the softening coefficient of silicate products.

4 Conclusion

Thus, as a result of studies it is shown that the fine sands characterized by the presence of clay impurities in the amount of 15–20 wt%, represented by mixed clay minerals can be used as raw materials for the production of silicate materials. The use of such raw materials allows optimizing the microstructure and accelerating the synthesis of new formations represented by low-base calcium hydrosilicates.

Fine sand is introduced into the raw mass as part of the lime-silica binder with a specific surface area of $800 \, m^2/kg$. This provides a uniform distribution of clay impurities in the raw mix.

The increase in the strength characteristics of the products is due to the formation of new formations with an increased degree of crystallinity, as well as due to the optimization of the granulometric composition.

The content of the required percentage of used raw materials in the raw mix of sand-lime bricks contributes to increase in strength characteristics of raw bricks by 2 times, the finished product by 1.8 times, which simplifies the production of products of complex shapes.

References

1. Strokova, V.V., Le Saout, G., Nelubova, V.V., Ogurtsova, Y.N.: Composition and properties of cement system with glutaraldehyde. Mag. Civil Eng. **103**(3), 10307 (2021). https://doi.org/10.34910/MCE.103.7
2. Tolstoy, A.D.: Fine-grained high-strength concrete. Constr. Mater. Prod. **3**(1), 39–43 (2020). https://doi.org/10.34031/2618-7183-2020-3-1-39-43
3. Yadykina, V.V., Gridchin, A.M., Kuznetsova, E.V., Lebedev, M.S.: Increasing the efficiency of mineral powder from technogenic raw materials due to its hydrophobization. Constr. Mater. Prod. **3**(4), 24–30 (2020). https://doi.org/10.34031/2618-7183-2020-3-4-24-30
4. Nelyubova, V.V.: The composition and properties of autoclaved gas concrete with amorphized raw modifiers. Mater. Sci. Forumthis **974**, 142–148 (2020). https://doi.org/10.4028/www.scientific.net/MSF.974.142
5. Tolypina, N.M., Rakhimbayev, S.M., Khakhaleva, E.N.: The materials are resistant hydration hardening the filler concrete scrap. Bulletin of BSTU named after V.G. Shukhov **7**, 6–9 (2017). https://doi.org/10.12737/article_5940f017098708.32121774

6. Ahmed, A.A.A., Lesovik, R.V.: Thermokinetic processes of hydration of binders based on scrap concrete. Lect. Notes Civil Eng **147**, 8–14 (2021). https://doi.org/10.1007/978-3-030-68984-1_2

7. Kostrzewa-Demczuk, P., Stepien, A., Dachowski, R., Krugiełka, A.: The use of basalt powder in autoclaved brick as a method of production waste management. J. Clean. Prod. **320**, 128900 (2021) https://doi.org/10.1016/j.jclepro.2021.128900

8. Nourredine, A., Chelghoum, N., Jauberthie, R., Molez, L.: Formation of C-S-H in calcium hydroxide–blast furnace slag- quartz-water system in autoclaving conditions. Adv. Cem. Res. **27**(3), 153–162 (2015). https://doi.org/10.1680/adcr.13.00069

9. Volodchenko, A.A., Lesovik, V.S., Zagorodnjuk, L.H., Glagolev, E.S.: On the issue of reducing the energy intensity of the silicate composites production with the unconventional aluminosilicate raw materials use. Mater. Sci. Forum **974**, 20–25 (2019). https://doi.org/10.4028/www.scientific.net/MSF.974.20

10. Lesovik, V.S., Volodchenko, A.A., Fediuk, R.S., Mugahed Amran, Y.H., Timokhin, R.: Enhancing performances of clay masonry materials based on nanosize mine waste. Constr. Build. Mater. **269**, 121333 (2021). https://doi.org/10.1016/j.conbuildmat.2020.121333

11. Lesovik, R.V., Klyuev, S.V., Klyuev, A.V., Tolbatov, A.A., Durachenko, A.V.: The development of textile fine-grained fiber concrete using technogenic raw materials. Res. J. Appl. Sci. **10**(10), 696–701 (2015)

12. Klyuev, S.V., Klyuyev, A.V., Lesovik, R.V., Netrebenko, A.V.: High strength fiber concrete for industrial and civil engineering. World Appl. Sci. J. **24**(10), 1280–1285 (2013)

13. Lesovik, R.V., Klyuyev, S.V., Klyuyev, A.V., Netrebenko, A.V., Durachenko, A.V.: High-strength fiber-reinforced concrete containing technogenic raw materials and composite binders with use of nanodispersed powder. Res. J. Appl. Sci. **9**(12), 1153–1157 (2014)

14. Lesovik, R.V., Klyuyev, S.V., Klyuyev, A.V., Netrebenko, A.V., Kalashnikov, N.V.: Fiber concrete on composite knitting and industrial sand KMA for bent designs. World Appl. Sci. J. **30**(8), 964–969 (2014)

Modernization of the Mill's Working Bodies for the Production of Fine Building Materials

A. A. Romanovich[1] , S. A. Dukhanin[1(✉)] , M. A. Romanovich[1] , and Aidin Salamzadeh[2]

[1] Belgorod State Technological University Named After V.G. Shukhov, Belgorod, Russia
duhanin777@yandex.ru

[2] The Innovation & Entrepreneurship Research Lab (IERL), GECC, London, UK

Abstract. The article represents a method for calculating the structural elements of surfacing on the working bodies of an impact-vortex mill. The method enables to calculate the geometric dimensions of the grid cell, taking into account the properties of the crushed materials and the method of applying to the working surface of the beater. It contributes to pressing the crushed material into the cell, and reduces the wear rate of the beater, due to the absence of full contact with the working surface. The dimensions of the cell are selected in such a way that the resulting pushing force is equal to or less than the holding force, but it remains sufficient for surfacing the impact-vortex mill beaters on the working surface. It is proved that the pressing and retention of crushed material particles in the cells is largely determined by its geometric dimensions, as well as the physical and mechanical characteristics of crushed rocks. The design of the beater is proposed, which increases its durability by reducing the contact area of the crushed material with its working surface.

Keywords: Working bodies (beaters) · Wear resistance · Impact-Vortex mills · Wear · Surfacing

1 Introduction

Dry building mixes are widely used in the construction industry, while the consumption of building mixes per year per person can reach up to 30 kg, as for example it is in Germany or Finland [1–4]. Large companies that are engaged in construction and repair use about 75% of the total sales of building mixes.

Various designs of vortex mills have been created for grinding materials, where the material is crushed under the action of rapidly rotating working bodies and turbulent air currents. An aggregate of this class is the RVM-3000 mill of Izhevsk production Enterprise LLC PC ADAMANT, which provides the fine grinding of various materials in the construction, road, chemical, metallurgical and food industries. Industries where the productivity is 3–5 tons per hour, depending on the processed material, the particle size of the source material is no more than 5 mm, while the finished product reaches 100 microns, the rotor rotation speed is 3000 min1, and the power consumption is 90 kW [5].

The design of the VM-3000 rotary vortex mill is made vertically with two-rotor housing with belt drive and two electric motors (see Fig. 1).
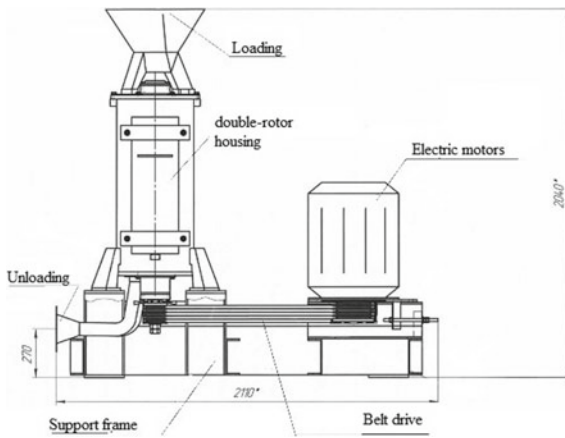
Fig. 1 Rotary-vortex mill

One of the problems of these units is the rapid wear of their working bodies, which currently amounts to 150–250 h depending on the production technology. Many industrial companies are working to create reliable structures of working bodies. Beaters are usually made of high-cost wear-resistant metal.

It is necessary to conduct research aimed at reducing the cost of production of working bodies that maintain operability to the limit state with the necessary breaks for repairs [6, 7].

2 Methods and Materials

The practical use of impact-vortex mills shows that their operation conditions have a significant impact on the durability of working bodies and the rate of their wear. For example, the high temperature of the source material can be a serious danger to drill beaters with a solid work surface, and the use of such a technique leads to a significant consumption of expensive materials.

When manufacturing the working bodies of mills, it is necessary to take into account the physical and mechanical properties of the materials being crushed and the wear factors caused by their destruction. It is also important to make the working bodies of the units from a material that reduces this wear type. However, this is economically impractical or difficult to implement. Therefore, many manufacturers are trying to develop effective methods to increase the durability of the working bodies of mills, taking into account the properties of the material being crushed. Theoretical analysis of the results obtained and formulation of conclusions about the most effective form of GA for its use in the compositions of filling mixtures.

Scientists of the BSTU named after V. G. Shukhov have proposed a method in order to increase the durability of the working bodies of impact-vortex mills. This is a method of applying a special mesh to the working surface in the form of a rectangular cell, which presses the crushed material into the cell, and reduces the rate of their wear, due to the absence of full contact with the working surface [8].

In addition, this method enables to reduce the consumption of expensive material, since it is applied not by continuous surfacing on the working surface of the beaters, but in the form of a grid.

The use of this method of surfacing enables to protect the working surface of the beaters from intense wear by pressing the crushed material in the cells. However, it is worth noting that the geometric dimensions of the cell are essential for retaining the pressed material inside it.

As a rule, the surfacing material is chosen based on the method of application and the chemical composition of the base material, taking into account the method of applying the protective mesh and the properties of the crushed material.

To protect the working bodies from abrasive wear, the following wear-resistant materials are widely used: Powdered Stalinite, used for welding by electric arc of rapidly wearing steel and cast iron parts; Vocar is a granular mixture of crushed tungsten and carbon; Relites are tubular- grain alloys based on tungsten; Vishom is a cheap granular alloy that does not contain tungsten, as well as cast wear-resistant alloys, which are a solid solution of chromium carbides in cobalt (stellites) or in nickel and iron (sormites).

Three standard samples of impact-vortex mill beaters made of 45 steel were selected for experimental tests. Sormite was chosen as a wear-resistant alloy for surfacing on the working top of the impact elements of the mill. The hardness of the surface layer of the sormite surfacing is 73–74 HRA or 48–50 HRC, and the chemical composition is 25% chromium, 2.5% carbon, 3% silicon, 5% nickel, about 2% manganese.

3 Results and Discussion

The dimensions of the cell must be selected in such a way that the resulting pushing force is equal to or less than the holding force, but its dimensions remain sufficient to implement the method of surfacing wear-resistant material on the working surface of the parts.

It follows from the above that the pressing conditions largely depend on the size of the cell and the physical and mechanical properties of the crushed material.

On the surface of the second experimental sample, a continuous surfacing of the working surface with a wear-resistant material is applied, while on the surface of the third sample, the surfacing is in the form of a grid with cells, according to the method of BSTU scientists.

The technical solution of the scientists of the BSTU named after V. G. Shukhov was used on the working surface of the RVM-3000 mill of the Izhevsk production enterprise LLC PC ADAMANT (see Fig. 2). The surfacing on the working top of the beaters has a rectangular shape, with the dimensions of the sides m, n, height c, as well as the radius of rounding in the corners of the cell [9].

Fig. 2 A sample with surfacing on the working surface of the beaters in the form of a grid

It is established that at the moment of collision with a part, the crushed material is pressed into the cell under the force of impact, at the moment of balancing the velocities in the cell, an elastic expansion occurs, which is aimed at pushing the pressed particles out of the cell. If the total pushing forces are less than or equal to the friction forces of the particles against the side surface of the cell of the applied mesh, then the particles of the crushed material will be held inside the cell, otherwise it will fall out of the cell.

Let us consider the scheme of force action in a cell, making assumptions that the elastic expansion force F is distributed over its entire lateral surface sideways (see Fig. 3).
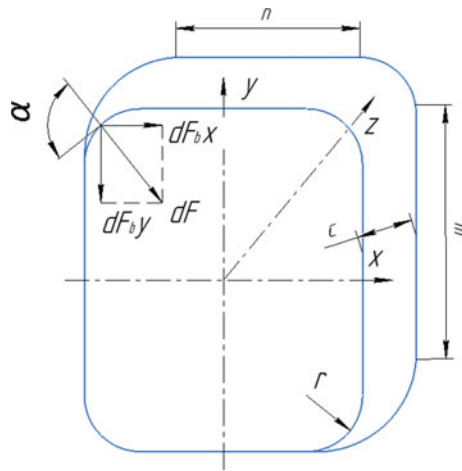
Fig. 3 The scheme of force action in the cell: dF—the magnitude of the force acting on the elementary area of the side surface of the cell of the parts, $dF_0(z)$, $dF_0(x)$ and $dF_0(y)$—elastic expansion forces acting on the side surface on the corresponding axis coordinates

Based on the above assumption and based on the condition that ensures the retention of the volume of particles in the cell $\sum F_{\text{fric.}} \geq \sum F$ we get that:

$$2r^2(n+m) \cdot F \cdot \sin \alpha + F \cdot n \cdot m \cdot r^2 + \pi \cdot r^2 \cdot F \leq f \cdot 2r^2(n+m) \cdot F \cdot \cos \alpha$$
$$+ f \cdot \pi \cdot r^2 \cdot F + f \cdot r \cdot c(n+m) \cdot F \tag{1}$$

where

r—the radius of rounding in the corners of the cell;
α—the average angle of the direction of the resulting pushing force;
F—the elastic expansion force;
n—the width of the mesh cell made of wear-resistant material, mm;
m—the length of the mesh cell made of wear-resistant material, mm;
c—the height of the mesh cell made of wear-resistant material, mm;
f—the coefficient of external friction.

Thus, from the obtained expression (1), it is possible to determine the coefficient of external friction:

$$f \leq \frac{2r \cdot ((n + m) \cdot \sin\alpha + ((n \cdot m)/2)) + \pi/2)}{2r \cdot (n + m) \cdot \cos\alpha + \pi \cdot r + c \cdot (n + m)} \tag{2}$$

As a result of analytical studies, the dimensions of the cell were selected in such a way that the resulting pushing force was equal to or less than the holding force, which in turn is provided by the coefficient of external friction f, which depends on the properties of the material and the surface of the parts.

The coefficient of external friction of the crushed materials to increase the durability of the working surface of the parts and pressing it into the mesh cell should be $f \leq 0.5$. In this case, the following dimensions of the sides of the grid cell will be optimal: $m = 6$ mm, $n = 5$ mm, $c = 3$ mm, $r = 2$ mm, which are interconnected.

Substituting the optimal dimensions in expression (2), we obtain that the coefficient of external friction will be:

$$f \leq \frac{2 \cdot 2 \cdot ((5 + 6) \cdot \sin 43 + ((5 \cdot 6)/2)) + \pi/2)}{2 \cdot 2 \cdot (5 + 6) \cdot \cos 43 + \pi \cdot 2 + 3 \cdot (5 + 6)} = 0.466 \tag{3}$$

At the moment of impact of the rotor-vortex mill, the crushed material is pressed into the cell, and the resulting pushing force is equal to or less than the holding force, the durability of the working surface of the drill increases, which in turn is provided by an external friction coefficient f equal to 0.466 according to the calculation results [10].

In order to confirm the expediency and effectiveness of the proposed technical solution we conducted comparative tests.

As mentioned earlier, three standard samples of impact-vortex mill parts made of 45 steel were selected for experimental tests.

A continuous surfacing with a wear-resistant material was applied to the surface of the second experimental sample, and a surfacing in the form of a grid with cells was applied to the surface of the third sample, according to the methodology of BSTU scientists. Based on the results of the study, a graphical dependence was constructed showing the percentage of wear of each sample from the operating time in hours, which is presented in Table 1 (see Fig. 4).

The analysis of the graphical dependence allowed us to establish that the most rapid wear of the tested samples is subject to a part made of 45 steel, without hardening its working surface, that is, without surfacing. The wear value of the samples where a solid

Table 1 Research results

Wear amount, %	Operating hours		
	Steel 45	Surfacing mesh (sormite)	Solid surfacing (sormite)
5	50	70	100
10	65	120	150
15	75	150	175
20	80	165	195
25	90	170	215
30	100	190	230
35	110	205	240
40	120	215	260
45	130	225	275
50	140	240	285
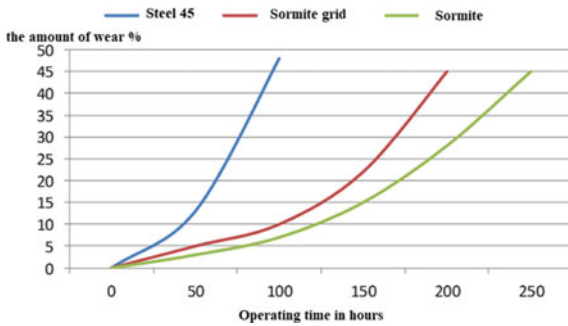
Fig. 4 Influence of the surface protection method on the wear resistance of the parts

surfacing or in the form of a mesh was applied is much smaller compared to the first sample, while a solid surfacing gives a higher percentage of durability, but leads to increased consumption of expensive materials. Therefore, the application of a grid is the most appropriate. This confirmed the effectiveness of the method of hardening the parts by applying a mesh with cells made of wear-resistant material on their working surfaces.

The use of this method helps to increase the durability and reduce the cost of the parts, by reducing the amount of expensive material deposited on their working surface.

After analyzing the obtained results of experimental studies, it was found that the parts with surfacing have a higher durability compared to the working bodies made without surfacing; this is due to the different hardness of their working surfaces.

As a result of an analytical study of the computational scheme of force interaction in a cell, an equation was obtained to determine its coefficient of external friction f, which depends on the properties of the material and the surface of the part.

The differences for wear of the parts made by solid surfacing and mesh with cells are insignificant; this is because the crushed material is held in the mesh cells and thereby prevents the wear of the surface of the part at the bottom of the cell.

4 Conclusion

The developed technical solution for surfacing the working top of the parts in the form of a grid with cells of a certain size increases the durability of the parts, but at the same time reduces their cost by reducing the amount of expensive material deposited on the work surface.

As a result of the analysis of the force interaction in the cell deposited on the surface of the working body, it was found that the coefficient of external friction f to increase the durability and pressing of the crushed material into the mesh cell should be $f \leq 0.5$.

It is established that the pressing conditions largely depend on the size of the cell and the physico-mechanical properties of the crushed material. The cell dimensions are selected in such a way that the resulting pushing forces is equal to or less than the holding force, which in turn is provided by the coefficient of external friction f, which depends on the properties of the material and the surface of the parts.

References

1. Kochkonbaev, M.A.: A review of modern rotary vortex mills for fine grinding. Sci. Innovative Technol. **4**(21), 72–78 (2021). https://doi.org/10.33942/sit2015
2. Kochkonbaev, M.A.: Perspective directions of fine grinding mills. Sci. Innovative Technol. **4**(21), 79–84 (2021). https://doi.org/10.33942/sit2016
3. Yinwei, Y., Kai, F., Jing, X.: A novel control method for roll gap of roller crusher based on Fuzzy-PID with decision factor self-correction. IOP Conf. Ser. Mater. Sci. Eng. **892**, 12–19 (2020)
4. Xuemin, L., Man, Z., Nan, H.: Calculation model of coal comminution energy consumption. Miner. Eng. **92**, 21–27 (2016)
5. Romanovich, A.A., Glagolev, S.N., Babaevskiy, A.N.: Methods to improve efficiency of production technology of the innovative composite cementing materials. IOP Conf. Ser. Mater. Sci. Eng. **327**(3), 2009 (2018)
6. Egorov, S.N., Sirotin, P.V., Tamadaev, V.G.: Analysis of the surface layer of the grinding element of a rotary vortex mill. North Caucasian region. Tech. Sci. 81–85 (2020). https://doi.org/10.17213/1560-3644-2020-1-81-85
7. Zhang, X., et al.: Effect of route on tensile anisotropy in equal channel angular pressing. Mater. Sci. Eng. **676**, 65–72 (2016)
8. Romanovich, A.A., Dukhanin, S.A., Romanovich, M.A., Zakeri, A.: Improving the wear resistance of rotary-vortex mill hammers. Environ. Constr. Eng. Reality Future **1**, 277–284 (2021)

9. Impact crusher [text]: utility model patent 208012 U1 Russian Federation: IPC B02C 13/06. 2021120119

10. Romanovich, A.A., Dukhanin, S.A., Romanovich, M.A.: Methods for increasing the wear resistance of the working bodies of a rotary vortex mill. Bulletin of the Belgorod State Technological University. V. G. Shukhov, **4** 116–123 (2022). https://doi.org/10.34031/2071-7318-2021-7-4-116-123

Using of Citrogypsum in Alkali Activated Systems

N. I. Kozhukhova[1,4][(✉)] , I. M. Shurakov[1] , N. I. Alfimova[1,2] ,
I. V. Zhernovskaya[1] , and M. I. Kozhukhova[1,3]

[1] Belgorod State Technological University Named After V.G. Shukhov, Kostyukov St., 46,
Belgorod 308012, Russia
kozhuhovanata@yandex.ru

[2] National Research Tomsk State University, 36, Lenin Ave, Tomsk 634050, Russia

[3] Department of Civil&Environmental Engineering, University of Wisconsin Milwaukee, P.O.
Box 413, Milwaukee, WI 53201, USA

[4] Laboratory of Advanced Materials and Technologies, Belgorod National Research University,
Pobeda 85, Belgorod 308015, Russia

Abstract. A large amount of research and previously obtained experimental data allows us to conclude with a high degree of confidence that one of the key roles in the synthesis of alkali-activated binders, cement, concretes, etc. plays an alkaline component or activator, which, in fact, is the initiator of all structure-forming processes during the hardening of the system. In this study, we studied the features of the synthesis of alkali-activated binders with different component compositions using a complex of industrial waste "citrogypsum—electrometallurgical slag" as a solid-phase component. Based on the obtained experimental results, it was found that the addition of 10% citrogypsum promotes an increase in strength by 13% (from 4.9 to 5.54 MPa), i.e., a synergistic effect is observed. A similar trend: higher density values are provided with the combined action of the components (compaction up to 3–5%) versus similar values for the components that form a solid structure separately. The study of the effect of the type of alkaline activating agent showed that both activators used in the work (NaOH and Na_2SiO_3) do not have a significant effect on the strength indicators of synthesized alkaline-activated binders with citrogypsum. Moreover, the dosage of the introduced alkaline agent up to 5% reduces the compressive strength from 19% (for NaOH) to 43% (for Na_2SiO_3).

Keywords: Citrogypsum · Electrometallurgical slag · Alkali-Activated binder · Physical and mechanical characteristics

1 Introduction

Currently, quite a wide range of binders and materials for construction purposes is known, distinguished by their high efficiency in use and found their field of practical application. As a rule, a significant proportion of binders is occupied by multicomponent systems or composite binders/materials. It is important to note that the effectiveness of advanced

materials is due not only to their basic performance characteristics. Environmental and economic components are also very important [1–9]. Increasingly widespread use of multicomponent or composite systems is often due to the need to improve the operational characteristics of the resulting composite. In most cases, this is achieved through the mechanical action of the introduction in the form of grinding, mechanical activation, or mechanochemistry, as well as through the introduction of additional additives, modifiers, active fillers, etc. into the binder system [10–14].

Among the promising composite systems for the construction industry, it is necessary to highlight the binding systems of alkaline activation. Also, the literature review confirms that waste from the production of phosphoric acid and phosphoric fertilizers acts as one of the valuable modifiers in these systems [15]. Previously, Rashad [16] studied the possibility of processing calcined phosphogypsum as a partial replacement for fly ash in alkali-activated binders based on it. The results showed that the compressive strength increases with dosages of calcined phosphogypsum up to 10%. At the same time, an increase of this additive in the binder system up to 15% leads to a decrease in strength values. The effect of a complex additive of gypsum and phosphoric acid on the properties of an alkali-activated slag using sodium silicate (water glass) as an activator was studied in earlier works [17]. Phosphoric acid was used as a set time retarder and gypsum was used as a shrink-resistant component when drying the system. Bakharev et al. [18] presented the results of a study of concrete consisting of alkali-activated slag and gypsum additives (6% of the slag mass), which confirmed the shrink-resistant effect of gypsum.

Guo et al. [19] used a complex alkaline activator: sodium hydroxide and sodium silicate solution—for the synthesis of binders based on high-calcium (class C) fly ash and other Ca-containing additives such as Portland cement and gypsum-containing waste obtained during desulfurization of flue gases and water treatment. Due to their high strength values (up to 80.0 MPa), these alkali-activated binders can be used in various fields, in particular, for the production of building materials, as well as for hardening and "conservation" of hazardous waste, which allows us to speak about the environmental friendliness of these materials. Chinese scientists have established the possibility of the production of building materials using semi-aqueous phosphogypsum, the joint use of which provides both an environmental and economic effect. At the same time, a close analog of phosphogypsum, citrogypsum, is formed in the Russian Federation as a waste product. Citrogypsum is a waste product from citric acid production. This work aims to study the behavior of cytogypsum in alkali-activated binders of different component compositions.

2 Materials and Methods

Methods. In the work, electrometallurgical slag (OEMK slag), (Russia) was used as an aluminosilicate component. The chemical composition of the raw solid-phase components: slag and cytogypsum, was determined by X-ray analysis (XRF) using an ARL 9900 X-ray WorkStation diffractometer (Termo Scientific). X-ray diffraction spectra were obtained with an ARL X 'tra diffractometer using CuK 1,2 radiation. Drying of raw materials was carried out in a laboratory oven BINDER FD-53 (Memmert, Germany).

Compressive strength tests were carried out using a PGM 100 hydraulic press machine (SKB Stroypribor, Russia).

Materials. In this study, two types of solid-phase components were used: OEMK slag and citrogypsum waste, the physicochemical characteristics of which are presented in Tables 1, 2 and 3.

Table 1 Chemical composition of OEMK slag and citrogypsum

Oxides content (wt%)

CaO	SiO$_2$	Fe$_2$O$_3$	MgO	Al$_2$O$_3$	MnO	Na$_2$O	Cr$_2$O$_3$	TiO$_2$	P$_2$O$_5$	SO$_3$	K$_2$O
40.78	24.55	15.03	12.51	4.18	0.92	0.49	0.3	0.2	0.18	0.17	0.11
30.6	0.75	–	0.25	–	–	–	–	–	–	44.7	–

Table 2 Mineral composition of OEMK slag

№	Mineral	Concentration, wt%
1	Ca$_2$SiH$_2$O$_5$	20.42
2	γ-C$_2$S	17.65
3	Okermanite 2CaO·MgO·2SiO$_2$	10.13
4	Merwinite 3CaO·MgO·2SiO$_2$	8.26
5	α-quartz	2.4
6	Calcite	4.88
7	Wustite FeO	25.98
8	Magnetite FeO· Fe$_2$O$_3$	10.26

Table 3 Compositions and properties of the «OEMK slag—citrogypsum» system

Compopsition	Components, %			Citrogypsum	
	OEMK slag	Water	Citrogypsum	Yield compressive strength, MPa	Average density, g/cm^3
1	85.7	14.3	–	4.9	2.25
2	–	14.3	85.7	3.1	2.3
3	81.4	14.3	4.3	5.54	2.37

Preliminary treatment by additional drying is required for both wastes: OEMK slag and citrogypsum. This is justified by the fact that waste is, normally, stored in open landfills and, as a result, has excess moisture, which can complicate research, as well as adversely affect the properties of the synthesized compounds.

The drying procedure was carried out until the materials reached a constant mass, after which the materials were stored under laboratory humidity (35%).

3 Results and Discussions

Effect of the component composition on the physical and mechanical properties of the binder. To study the physical and mechanical characteristics of the binding system "OEMK slag—citrogypsum", experimental compositions were molded (Table 3). The experimental mixtures were molded into cubes of $20 \times 20 \times 20$ mm and left for hardening in ambient laboratory conditions (temperature 23 ± 2 °C; relative humidity— $33 \pm 2\%$). Compression strength and average density tests of the hardened specimens were carried out at the age of 9 days.

The results of the compressive strength given in Table 3 showed that the addition of 10% citrogypsum to the "OEMK slag—water" system leads to an increase in strength by 13% (from 4.9 to 5.54 MPa). Thus, there is a manifestation of a synergistic effect in structure formation during the interaction of these two wastes. This is confirmed by the fact that the hardening of slag and citrogypsum components separately demonstrates lower strength characteristics (3.1 MPa—for cement paste containing citrogypsum). Speaking about the average density of the composite system "OEMK slag—citrogypsum", a similar tendency is observed: higher density values are achieved with the combined action of the components (compaction up to 3–5%) compared to the same values for the separately hardened components.

Effect of the type of alkaline activator on the physical and mechanical properties of the binder. Also, various additives, modifiers, fillers contained in the binder matrix are very important (if they have a reactive or chemical activity to the rest of the system). In this regard, at this stage of the work, the effect of two types of alkaline activators, such as liquid glass Na_2SiO_3 and sodium hydroxide NaOH, on the physical and mechanical properties of synthesized binders containing citrogypsum waste was studied (Fig. 1).
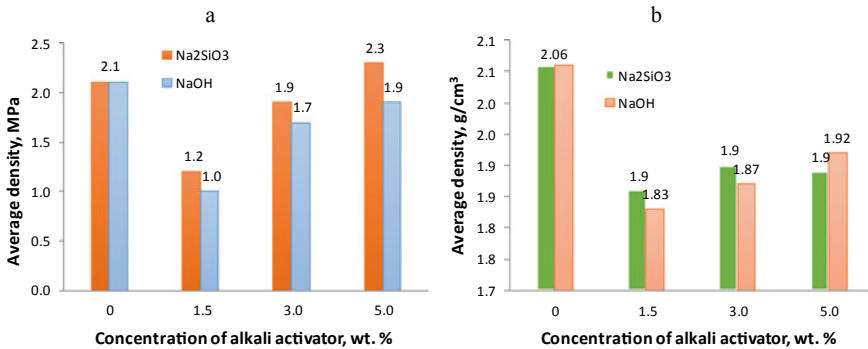
Fig. 1 Effect of the type and concentration of the alkaline activator on the physical and mechanical properties of, citrogypsum-containing binders: **a** compressive strength, **b** average density

The analysis of the results obtained, which are presented in Fig. 1, showed that both used alkaline activators (NaOH and Na_2SiO_3) do not have a significant effect on the strength characteristics of the synthesized alkaline-activated binders containing citrogypsum. Moreover, the dosage of the introduced alkali up to 5% leads to a decrease in the compressive strength from 19% (for NaOH) to 43% (for Na_2SiO_3). On the other

hand, the strength values of the experimental compositions at 5%-concentration of an alkaline activator of both types are comparable (1.9 and 2.3 MPa) with an alkali-free analogue (2.1 MPa). At the same time, for compositions with an alkali concentration of more than 5%, significant leaching is observed at the surface of the samples, and a longer period of hardening of mixtures and their transition to a consolidated state is observed, as well. Thus, a further increase in the alkaline component is technically in-efficient.

4 Conclusion

Based on the research presented in the article, the following conclusions can be formulated:—introduction of 10% citrogypsum additive into the "OEMK slag—water" system increases the strength of the cement paste by 13%, which indicates the manifestation of a synergistic effect when the interaction of these two types of waste. For density values, a similar tendency is observed: compaction is observed up to 3–5%);—Studies of physical and mechanical properties of the "OEMK slag—water—citrogypsum" system with various types and concentrations of alkaline activators showed that the dosage of the introduced alkali up to 5% causes a decrease in compressive strength from 19% (for NaOH) to 43% (for Na_2SiO_3).

References

1. Kirillova, N.K., Alekseeva, A.N., Egorova, A.D.: Application of additive technologies in construction and in the production of ceramic products. Bulletin of BSTU named after V.G. Shukhov **2**, 134–141 (2020). https://doi.org/10.34031/2071-7318-2020-5-2-134-141
2. Antonenko, M.V., Ogurtsova, Y.N., Strokova, V.V., Gubareva, E.N.: Photocatalytic active self-cleaning cementbased materials. Compositions, properties, application. Bulletin of BSTU named after V. G. Shukhov **3**, 16–25 (2020). https://doi.org/10.34031/2071-7318-2020-5-3-16-25
3. Salamanova, M.S., Nakhaev, M.R., Sarsenbaev, B.K.: Development of special recipes of binding compositions with improved properties. Constr. Mater. Prod. **3**(4), 5–12 (2020). https://doi.org/10.34031/2618-7183-2020-3-4-5-12
4. Mirzoeva, A.R.: Organizational and technological features of productions with complex use of raw materials. Chem. Bull. **1**(3), 52–61 (2018)
5. Kozhukhova, N.I., Lebedev, M.S., Vasilenko, M.I., Goncharova, E.N.: Ecology-toxicology study of low-calcium solid wastes from power plants. Int. J. Pharm. Technol. **8**(3), 15349–15360 (2016)

6. Fomina, E.V., Strokova, V.V., Kozhukhova, M.I.: Effect of previously slacked lime on properties of autoclave composite binders. World Appl. Sci. J. **24**(11), 1519–1524 (2013). https://doi.org/10.5829/idosi.wasj.2013.24.11.7018

7. Kozhukhova, N.I., Zhemovsky, I.V., Strokova, V.V., Kalashnikova, V.A.: Influence of mechanical and chemoactivation processes on operational characteristics of geopolymer binder. Res. J. Appl. Sci. **10**(10), 620–623 (2015). https://doi.org/10.3923/rjasci.2015.620.623

8. Cherevatova, A., Kozhukhova, N., Zhernovskaya, I., Osadchaya, M., Klepak, I., Kozhukhova, M.: Efficiency of wet mechanoactivation of granite using different milling units. E3S Web Conf. **126**, 00078 (2019). https://doi.org/10.1051/e3sconf/201912600078

9. Fomina, E.V., Kozhukhova, N.I., Belovodsky, E.A., Klimenko, V.A., Kozhukhova, M.I.: Microstructural analysis of changes in the morphology of quartz raw materials of different genesis at dry milling. Mater. Sci. Forum **1017**, 91–100 (2021). https://doi.org/10.4028/www.scientific.net/MSF.1017.91

10. Muzenski, S., Flores-Vivian, I., Farahi, B., Sobolev, K.: Towards ultrahigh performance concrete produced with aluminum oxide nanofibers and reduced quantities of silica fume. Nanomaterials **10**, 2291 (2020). https://doi.org/10.3390/nano10112291

11. Kozhukhova, N.I., Teslya, A.Y., Kozhukhova, M.I., Zhernovsky, I.V., Yermak, S.N., Ogurtsova, Y.N.: In-service performance of hybrid geopolymer binders based class F fly ash. IOP Conf. Ser. Mater. Sci. Eng. **552**(1), 012035 (2019). https://doi.org/10.1088/1757-899X/552/1/012035

12. Alfimova, N.I., Shurakov, I.M., Ageeva, M.S., Kozhukhova, N.I.: Research on the possibility of using volcanic sand of Kamchatka as a component of a composite binder. Lect. Notes Civil Eng. **95**, 113–117 (2021). https://doi.org/10.1007/978-3-030-54652-6_17

13. Lesovik, V.S., Leshchev, S.I., Ageeva, M.S., Alfimova, N.I.: Zeolite-containing terra-silicea as a component of composite binders. Mater. Sci. Forum **974**, 136–214 (2020). https://doi.org/10.4028/www.scientific.net/MSF.974.136

14. Shen, W., Liu, Y., Yan, B., Wang, J., He, P., Zhou, C., Ding, Q.: Cement industry of China: driving force, environment impact and sustainable development. Renew. Sustain. Energy Rev. **75**, 618–628 (2017). https://doi.org/10.1016/j.rser.2016.11.033

15. Gijbels, K., IonIacobescu, R., Pontikes, Y., Schreurs, S., Schroeyers, W.: Alkali-activated binders based on ground granulated blast furnace slag and phosphogypsum. Constr. Build. Mater. **215**(10), 371–380 (2019). https://doi.org/10.1016/j.conbuildmat.2019.04.194

16. Rashad, A.M.: Potential use of phosphogypsum in alkali-activated fly ash under the effects of elevated temperatures and thermal shock cycles. J. Clean. Prod. **87**, 717–7252 (2015). https://doi.org/10.1016/j.jclepro.2014.09.080

17. Chang, J.J., Yeih, W., Hung, C.C.: Effects of gypsum and phosphoric acid on the properties of sodium silicate-based alkali-activated slag pastes. Cement Concr. Comp. **27**(1), 85–91 (2005). https://doi.org/10.1016/j.cemconcomp.2003.12.001

18. Bakharev, T., Sanjayan, J.G., Cheng, Y.B.: Effect of admixtures on properties of alkali-activated slag concrete. Cement Concr. Res. **30**(9), 1367–1374 (2000). http://doi.org/10.1016/S0008-8846(00)00349-5

19. Guo, X., Shi, H., Chen, L., Dick, W.A.: Alkali-activated complex binders from class C fly ash and Ca-containing admixtures. J Hazard. Mat. **173**(1), 480–486 (2010). https://doi.org/10.1016/j.jhazmat.2009.08.110

Efficiency of Stabilization of Sandy, Coarse-Grained and Technogenic Soils with Polymer Complexes and Surfactants of Structural Layers of Highways

I. Trautvain[✉] [iD]

Department of Roads and Railways, Belgorod State Technological University Named After V G Shukhov, Kostyukov St, 46, Belgorod 308012, Russia
trautvain@bk.ru

Abstract. The study was aimed at evaluating the effectiveness of using polymer-colloidal complexes based on acrylic and styrene as well as traditional ionogenic surfactants based on silicone compounds to stabilize soils in the preparation of materials based on sandy, coarse clastic and technogenic soils for the construction of load-bearing and additional base layers of motor road pavement. It has been established that the use of polymer-colloidal complex based on acrylic acid butyl ester copolymer and styrene has high efficiency in the development of composite material from coarse clastic soils, while the use of stabilizing additives for soils does not provide a significant increase in the physical and mechanical characteristics of samples based on sandy, coarse clastic and technogenic (granulated asphalt concrete) mixtures in complex with cement. The results indicate that the particle size composition of the mineral part has a significant impact on the efficiency of the use of additives for various functional purposes. Polymeric styrene-acrylic dispersions have a more significant effect on the composite material with coarse-grained particle size composition (C-6). It is connected with a more complete polymerization of the film on the surface of internal pores of the composite, which affects the level of structure formation of the whole system. It has been established that the removal of water from polymeric dispersions leads to the formation of its supramolecular structure at the boundary of the mineral binder (cement) and stone material, which contributes, as a rule, to increasing the adhesive interaction between them.

Keywords: Polymer-Colloid complexes · Ionogenic surfactants · Silicone compounds · Sandy · Coarse clastic and technogenic soils · Structural layers of road pavement · Life cycle

1 Introduction

The constant increase in traffic volume and intensity brings new requirements for pavement structures, especially for the strength characteristics of materials and reliability. The constantly expanding network and intensive operation of roads leads to an increase

in the volume of construction, as well as medium and major repairs. In this regard, it is necessary to optimize the construction of structural layers of rigid type pavement in order to extend the life cycle of roads by developing special additives of cumulative action and their adaptation to local materials and technology of cold recycling. At present, there are numerous different modifiers to increase the physical and mechanical characteristics of the base layers of pavement on the basis of crushed rock-gravel and granulated asphalt concrete mixtures [1–6]. Special types of surfactants with hydrophobic effect, designed to stabilize and strengthen soils, are beginning to gain wide popularity for these materials.

According to the manufacturers of stabilizers, their composition includes superplasticizers, water repellent agents, and complex organic compounds, added to the basis of silicone compounds and ionogenic complexes. Their mechanism of action in ground systems is based on the exchange of electric charges between ionized water and ground particles. As a result, natural connections of ground particles with capillary and film water are broken, water is easily separated from ground particles, thereby creating favorable conditions for soil compaction, and a thin hydrophobic film is formed on the capillary walls. However, the effectiveness of their use in order to strengthen the load-bearing and additional layers of the base of the road pavement on the basis of sandy, coarse clastic and technogenic (including granulated asphalt) soils has not been studied. Colloidal systems based on various polymeric compounds can act as an alternative for these types of additives [7–10].

It is known [7] that polymeric additives based on acrylic, styrene, butadiene or their complex compounds can significantly improve the performance properties (strength characteristics, water resistance and corrosion resistance) of traditional building materials such as concrete. However, there are no studies on their use in the field of strengthening sand-gravel and granulated asphalt concrete mixtures using cement-based inorganic binder.

The study was aimed at evaluating the effectiveness of using traditional ionogenic surfactants based on silicone compounds for stabilizing soils and polymer-colloidal complexes based on acrylic and styrene in the preparation of materials based on sandy, coarse clastic and technogenic soils for the construction of load-bearing and additional base layers of motor road pavement.

2 Materials and Methods

In this work, we investigated stabilizing additives for soils, the main component of which are silicone compounds. Stabilizer-1 is an additive based on silicone polymer (siloxane), which is a translucent liquid (pH of aqueous solution: 4–7), contributing to the process of ionic exchange, polarizing the clay particles of the soil. It is used together with inorganic binders to strengthen the soil of the working layer and the structural layers of the base. Stabilizer-2 is a surfactant based on sodium methylsiliconate. It is a colorless liquid with an alkaline reaction, comprising the basis of a wide range of stabilizing additives for soils, and used in combination with mineral binders to strengthen cohesive soils, including technogenic soils.

The following additives were used as polymer-colloid complexes (PCCs), the properties of which are presented in the Table 1: PCC-103 is an aqueous dispersion of acrylic

acid and styrene butyl ester copolymer, and PCC-111 is an aqueous dispersion of acrylic acid butyl ester copolymer, acrylic acid, acrylic acid amide and styrene.

Table 1 Physical and chemical properties of PCC

Additive name	Density, g/cm^3	Solid content, %	pH	Mean particle size, μm
PCC-103	1.04	29–31	7.5–9.0	0.06–0.065
PCC-111	1.05	49–51	7.5–9.0	0.15

The following were used as stone materials for organic-mineral compositions of structural layers of the road base: crushed sand of 0–5 mm fraction per GOST 32,730-2014, C-7 crushed rock-sand mixture (0–10 mm fraction) and C-6 crushed rock-sand mixture (0–20 mm fraction) per GOST 25,607-2009, as well as milled dense fine-grained asphalt concrete mixture with maximum grain size up to 20 mm. The maximum density of sand was 1.49 g/cm^3 at an optimum moisture content of 8.2%; for crushed rock-sand mixture C-7—1.37 g/cm^3 at an optimum moisture content of 5.7%; C-6—1.41 g/cm^3 at an optimum moisture content of 4.5%. Inorganic binder—cement CEM I 42.5 according to GOST 31,108-2016 and bituminous emulsion EBDC M according to GOST R 58,952.1-2020 were used.

The study was conducted in accordance with the following regulatory documents: GOST 23,558-94 "Crushed rock-gravel-sand mixtures and soils treated with inorganic binders for road and airfield construction," the methodological guidelines for the restoration of asphalt concrete pavements and bases of roads (os 568 p).

3   Results and Discussions

The research work consisted of two stages. The task of the first stage was to study the effect of FCC additives and stabilizing additives on the properties of stone (mineral) materials with different particle size composition based on crushed sand of fraction 0–5 mm, and crushed rock-sand mixtures C-7 and C-6 with inorganic binder. The amount of binder was 9%, PCC—0.13%, stabilizing additives—0.007% of the weight of the stone materials. The specified amount of additives provided the minimum value of the water saturation index for samples of all compositions. In order to obtain the maximum density of the composite material, the necessary amount of water was introduced into its composition to obtain the maximum density of the samples. The samples of composites based on sandy and coarse clastic soils were tested for the following physical and mechanical characteristics: compressive strength at the age of 7 and 28 days ($R_{compr.}$ (7 days), $R_{compr.}$ (28 days) respectively), cracking strength at the age of 28 days ($R_{crack.}$), as well as frost resistance. The results are presented in diagrams (Fig. 1) and Table 2.

The results indicate that the particle size composition of the mineral part has a significant impact on the efficiency of the use of additives for various functional purposes. Polymeric styrene-acrylic dispersions have a more significant effect on the composite material with coarse-grained particle size composition (C-6). It is connected with a more
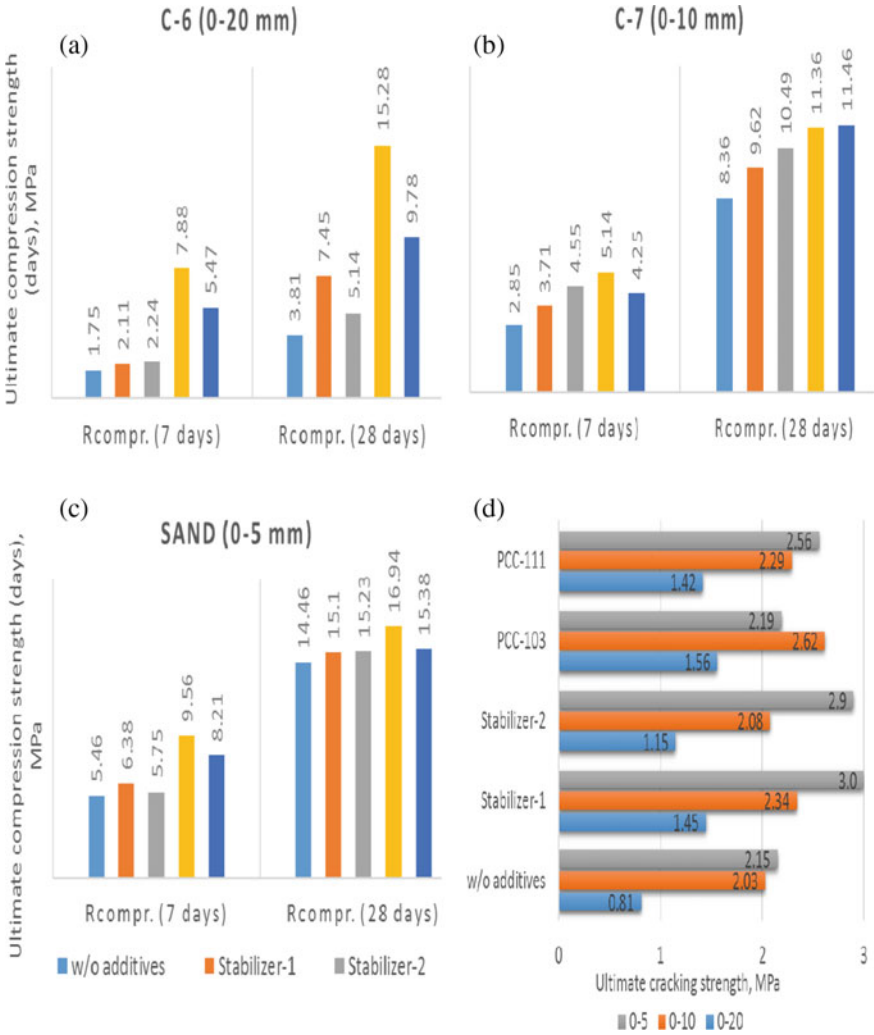
Fig. 1 Strength characteristics of samples of composites based on sandy and coarse clastic soils: crushed rock-sand mix C-6 (**a**), crushed rock-sand mix C-7 (**b**), crushed sand (**c**), ultimate cracking strength (at 28 days), MPa (**d**)

complete polymerization of the film on the surface of internal pores of the composite, which affects the level of structure formation of the whole system. It has been established that the removal of water from polymeric dispersions leads to the formation of its supramolecular structure at the boundary of the mineral binder (cement) and stone material, which contributes, as a rule, to increasing the adhesive interaction between them. If the packing density of grains is high, when using a fine-grained stone material, the dispersed particles of PCC may not coagulate with each other into a thin film, that is, its integrity is violated, which contributes to the penetration of moisture in the system,

Table 2 Frost resistance grade of samples of composites based on sandy and coarse clastic soils

Composite material	Without additives	Stab.-1	Stab.-2	PCC-103	PCC-111
C-6 (fraction 0–20 mm)	F10	F 50	F 50	F 50	F 15
C-7 (fraction 0–10 mm)	F 15	F 50	F 50	F 50	F 25
Sand (fraction 0–5 mm)	F 15	F 50	F 50	F 50	F 25

similar to a composite material without polymeric additives. In this regard, a significant increase in physical and mechanical properties may not be observed. Moreover, the PCC polymerization process in such a system may not occur completely or may be stretched over time, which reduces the hydraulic activity of the cement.

Thus, it was found that the highest effectiveness in coarse-grained (highly porous) systems occurs with the use of the additive PCC-103, and a slightly smaller increase in the physical and mechanical characteristics of the composite samples is observed with the introduction of additive PCC-111. A higher effectiveness of using an additive based on PCC-103 is due to the small size of the polymer particle diameter (up to 0.08 microns) and its content not exceeding 30%. This promotes high adsorption of polymer particles on the surface of the cement, forming a thin elastic film that does not interfere with the hydration of the inorganic binder. Using the additive PCC-103 can increase the ultimate compression strength of C-6 samples by 3 times, and in case of PCC-111—by 2 times; ultimate strength at cracking—by 93 and 75% respectively. However, the use of the additive PCC-111 increases frost resistance only by 5 cycles, which makes this additive not effective for the structural layers of the base of motor road pavement.

When introducing PCC into a finer-grained system (C-7), a decrease in the efficiency of PCC is observed compared to their use for composition materials based on C-6. It should be noted that for this type of mixture the most effective additive is also PCC-103. The increase in the compressive and cracking strength of samples at the age of 28 days with its use is from 36 and 29% respectively, while at the same time high frost resistance of the composition material is observed.

Considering the sand type of composition material, we can note the increase in the effectiveness of the use of stabilizing additives based on silicone compounds developed specifically for fine-grained soil systems (sandy loam, loam and clay). For this type of mixture (fraction 0–5 mm), which has a higher density and small diameter pores, unlike the other two compositions of stone materials, we can note a significant increase in the cracking strength of samples at the age of 28 days (by 40 and 35% respectively when using additives stabilizer-1 and 2). High values of the ultimate cracking strength of samples modified with stabilizer-1 and 2 additives characterize the stable resistance of the material to small plastic deformations typical of the base layers of road pavements, and contribute to an increase in the carrying capacity of the entire road structure. The use of the researched stabilizing additives helps to increase the frost resistance of the materials up to grade F50. However, when using them, the increase in compression strength of the sand mixture samples is insignificant (up to 5%).

At the second stage, we evaluated the effectiveness of additives for restoration of asphalt concrete pavement by cold regeneration based on granulated asphalt concrete

mixture in combination with inorganic and organic binders (cement and bituminous emulsion) in the amount of 3% of each type of binder. The amount of water in the composition of the organomineral composite was 2%. The second stage of the study was conducted using a PCC: PCC-103 and PCC-111. The choice of additives was due to the fact that PCC demonstrated the highest efficacy according to the first phase of the study. At the same time, the amount of additives introduced varied from 1 to 6% of the weight of the granulated asphalt concrete mixture. Granulated asphalt concrete samples were examined in terms of the following physical and mechanical properties: compressive strength at 20 and 50 °C ($R_{compr.}$ (20 °C) and $R_{compr.}$ (50 °C) respectively), water resistance (Kw), water saturation (W), frost resistance (F), and the results are presented in the diagrams (Fig. 2).

Based on the data presented, the optimal amount of additives in the composition of granulated asphalt concrete can be determined. Thus, the highest physical and mechanical properties were obtained by adding PCC-103 in an amount of 3%, or PCC-111—1%, to the granulated asphalt concrete mixture. The effectiveness of additives in the granulated asphalt concrete composition, compared with the control composition, is due only to an increase in the strength characteristics of the samples and a slight decrease in water saturation. Increase in frost resistance by 5 cycles is observed in the case of the additive PCC-103. All this indicates insignificant effectiveness of the use of PCC in granulated asphalt concrete.

It is known [7] that the effectiveness of dispersed polymer solutions is due to emulsion decomposition (water evaporation) and polymer curing. However, when using PCC in granulated asphalt concrete mixtures based on cement in combination with bitumen emulsion (BE), we can note the fact that the presence of an organic binder (BE) hinders the decomposition of PCC and the formation of a polymer film on the surface of inorganic binder and stone particles of granulated asphalt concrete mixture, which also contains bitumen. With the use of PCC additives in question, it is possible to increase the compression strength of granulated asphalt concrete samples at 20 °C up to 10%, at 50 °C—by 4% and 20% respectively for additives PCC-103 and PCC-111, frost resistance—no more than 5 cycles when using additive PCC-103, an increase in water resistance is not observed.

4   Conclusions

The influence of traditional ionogenic surfactants for stabilization of soils based on silicone compounds and polymer-colloidal complexes based on acrylic acid and styrene butyl ether copolymer on physical and mechanical characteristics of sandy, coarse clastic and technogenic soils in combination with inorganic binder for the construction of load-bearing and additional base layers of motor road pavement has been established, the properties of which are presented in the Table 3.

When constructing base layers on the basis of coarse clastic soils (mixtures C-6 and C-7), the additive PCC-103 shows high effectiveness by all the studied criteria, while complex stabilizers of soil systems based on silicone compounds and ionogenic surfactants show effectiveness by cracking strength and frost resistance of the sandy soil-based composite.
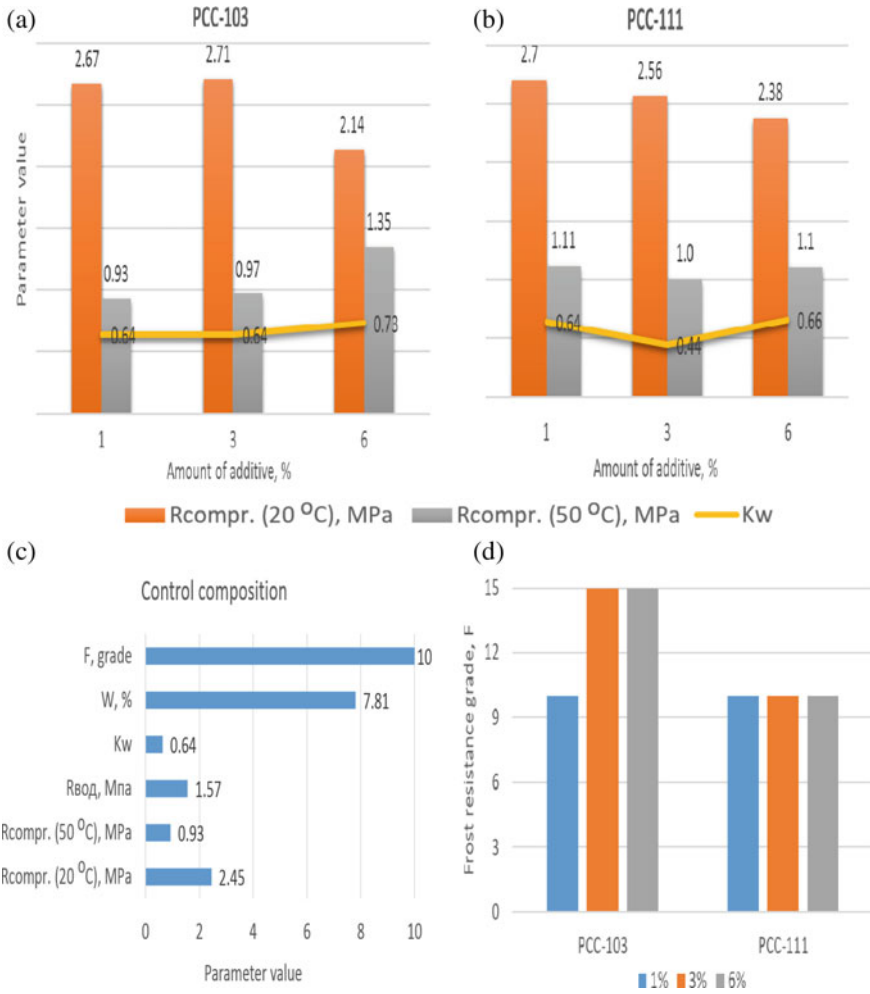
Fig. 2 Physical and mechanical characteristics of granulated asphalt concrete samples: PCC-103 (**a**), PCC-111 (b), physical and mechanical characteristics of the control composition (**c**), frost resistance grade, F (**d**)

Table 3 Physical and mechanical characteristics of samples of composites based on sandy and coarse clastic soils, with maximum efficiency

Physical and mechanical characteristics	Samples of composites based on coarse clastic soils (mixtures C-6)		Samples of composites based on coarse clastic soils (mixtures C-7)		Samples of composites based on sandy soils		
	w/o additives	PCC-103	w/o additives	PCC-103	w/o additives	Stabilizer-1	PCC-103
Ultimate compression strength (7 days), MPa, R_{compr}	1.75	7.88	2.85	5.14	5.46	6,38	9.56
Ultimate compression strength (28 days), MPa, R_{compr}	3.81	15.28	8.36	11.36	14.46	15.1	16.94
Ultimate cracking strength, MPa, Rpac (28 сут)	0.81	1.56	2.03	2.62	2,0.5	3	2.19
Frost resistance grade, F	10	50	15	50	15	50	50

References

1. Sergeeva, A.M., Polyakova, T.A.: Improving the performance of dirt road surfaces by using additives (stabilizers). Economy: yesterday, today, tomorrow **11**(2–1), 179–185 (2021). https://doi.org/10.34670/AR.2021.28.89.022
2. Trautvain, A.I., Akimov, A.E., Grichanikov, V.A.: Stabilization of the clay soil of the increased humidity for road construction. Lect. Notes Civil Eng. **95**, 66–72 (2021). https://doi.org/10.1007/978-3-030-54652-6_10
3. Sabri, M.M., Shashkin, K.G., Zakharin, E., Ulybin, A.V.: Soil stabilization and foundation restoration using an expandable polyurethane resin. Mag. Civil Eng. **6**(82), 68–80 (2018). https://doi.org/10.18720/MCE.82.7
4. Trautvain, A., Akimov, A., Yakovlev, E.: Improvement of properties of the argillaceous soils when using additives "chimston" in combination with inorganic astringent. Mater. Sci. Forum **945**, 136–140 (2019). https://doi.org/10.4028/www.scientific.net/MSF.945.136

5. Gridchin, A.M., Zolotykh, S.N.: PMC Nicoflok research effect as mechanochemical activator on the cement characteristic used in the soil stabilization. Bulletin of BSTU named after V.G. Shukhov **3**(5), 5–10 (2018). https://doi.org/10.12737/article_5af5a72640c9f7.36216170

6. Saha, M.C. et al.: Effect of density microstructure and strain rate on compression behavior of polymeric foams. Mater. Sci. Eng. J. **A406**(1–2), 328–336 (2005). https://doi.org/10.1016/j.msea.2005.07.006

7. Mrdak, I. et al:. Analysis of the influence of dynamic properties of structures on seismic response according to montenegrin and european regulations. Appl. Mech. Mater. **633–634**, 1069–1076 (2014). https://doi.org/10.4028/www.scientific.net/AMM.633-634.1069

8. Usmanov, R., Vatin, N., Murgul, V.: Experimental research of a highly compacted soil beds. Appl. Mech. Mater. **633–634**, 1082–1085 (2014). https://doi.org/10.4028/www.scientific.net/AMM.633-634.1082

9. Usmanov, R., Vatin, N., Murgul, V.: Reinforced soil beds on weak soils. Appl. Mech. Mater. **633–634**, 932–935 (2014). https://doi.org/10.4028/www.scientific.net/AMM.633-634.932

10. Novoskoltseva, O.A. et al.: Polyelectrolytes and polycomplexes for stabilization of sandy soils. High Mol. Weight Compd. **63**(5), 317–325 (2021). https://doi.org/10.31857/S2308113921050090

Investigation of Gas Release Processes in a Polymer Composite Filled with Amorphous Boron Under Thermal and Radiation Exposure

R. N. Yastrebinsky(✉) , E. O. Pilavidou , A. V. Yastrebinskaya ,
and A. V. Akimenko

Belgorod State Technological University Named After V.G. Shukhov, Belgorod, Russia
yrndo@mail.ru

Abstract. The composition and level of outgassing of a protection material based on a polymer composite filled with amorphous boron at temperature and radiation exposure has been studied. An assessment of the danger of gas emissions under conditions of overheating of the material in an emergency situation is given. The sanitary-chemical characteristics of the protection material have been obtained. It has been established that the level of air pollution when the material is overheated to 180 °C for 1–2 days does not exceed the maximum allowable concentration of harmful substances in the air of the working area established for industrial premises. The specified temperature can be tolerated under conditions of overheating of the material in an emergency situation. As a result of overheating of the material in the temperature range of 190–200 °C, a sharp increase in gas emissions was found with an excess of the MPC level provided for by the toxicological and hygienic requirements for protection materials for class V premises. The overheating temperature of the material allowed in an emergency situation should not exceed 180 °C.

Keywords: Polymer composite · Amorphous boron · Temperature effect · Radiation effect · Outgassing · Radiation resistance

1 Introduction

The use of polymer composite materials for protection against ionizing cosmic radiation is currently one of the most important areas due to their increased radiation resistance and the possibility of using biological protection of astronauts and radiation protection of spacecraft under conditions of mass and overall dimensions [1, 2]. At the same time, polymeric materials are able to quite significantly withstand the processes of thermal cycling in space when they are on the shady and sunny side of the spacecraft, respectively, at temperatures from −180 to +180 °C [3, 4]. The search for and implementation of polymeric materials with higher thermal and radiation resistance is of great practical importance for new space projects, including interplanetary flights and the use of nuclear power propulsion systems in space [5–7].

This work is devoted to the study of the composition and level of outgassing of a polymer composite based on polysulfone and amorphous boron under temperature and radiation exposure exceeding operating conditions. An assessment of the danger of gas emissions under conditions of overheating of the material in an emergency situation is given. The use of amorphous boron is technologically justified due to the possible occurrence of neutron radiation inside the spacecraft during the interaction of protons and electrons with structural elements [8–10].

2 Methods and Materials

A thermoplastic composite material based on polysulfone and amorphous boron grade PSF-1.5B is considered as the starting material. The composition of the material includes: binder—polysulfone grade PSF-150 (aromatic polysulfone oxide) in the amount of 98.5 wt%, and filler—amorphous boron in the amount of 1.5 wt%. The sample for research was presented in the form of a plate $200 \times 200 \times 50$ mm.

The composite material was obtained by extrusion mixing of the indicated components at a temperature of 300 °C. The plates are made by direct pressing with the following technological parameters:

- heating at a temperature of 290–295 °C for 4 min/mm plate thickness;
- cooling up to 275–280 °C and pressure supply 120 kgf/cm^2;
- cooling under pressure to ambient temperature.

Qualitative analysis of the composition of gas emissions:

When preparing samples of the required size, their deformation under conditions of overheating of the material and the transition of the polymer to the amorphous state was taken into account. The samples were made in the form of rods $42 \times 10 \times 5$ mm in size. In each experiment, the rod was placed in a glass ampoule, which is part of the installation for the study of gas emissions.

To obtain a gas extract to be analyzed, the sample was placed in an ampoule and kept for 2 h at a saturation 8 times higher than the specified one. The studies were carried out at temperatures of 180 °C, 190 °C and 200 °C and an absorbed radiation dose of 5 MGy.

Samples of the gas extract were analyzed by chromatography using a PE-624 capillary column 60 m long. Identification of gas emission components was carried out on a 3700 series chromatograph.

The list of gas emission components of the PSF-1.5B material is systematized in Table 1.

Table 1 shows that the qualitative composition of gas emissions did not change with increasing temperature from 180 °C to 200 °C. At the same time, a preliminary assessment (according to the peak values of the chromatograms) showed a noticeable increase in gas emissions, especially at a temperature of 200 °C.

Quantitative analysis of gas emissions:

At temperatures of 180, 190 and 200 °C, three tests lasting 1–2 days were carried out. Organic substances released from the material were analyzed by the chromatographic method on a «Tsvet-110» instrument with a flame ionization detector. The components

Table 1 Components of outgassing of material PSF-1.5B

Substances	Presence in gas emissions at temperature (absorbed dose 5 MGy)		
	180 °C	190 °C	200 °C
Hydrocarbons limit and unsaturated	+	+	+
Acetaldehyde	+	+	+
Methanol	+	+	+
Ethanol	+	+	+
Пропаналь	+	+	+
Acetone	+	+	+
Iso-propanol	+	+	+
Oil Aldehyde	+	+	+
2-butanol	+	+	+
Benzene	Traces	+	+
N-butanol	+	+	+
Pentanal	+	+	+
Toluene	+	+	+
Nylon aldehyde	+	+	+
Xylols	+	+	+
Heptanal	+	+	+
Methylfinyl ether	+	+	+
Pseudocumol	+		+
Benzaldehyde	Traces	+	+
Octanal	Traces	+	+
Sulfur dioxide	Traces	+	+
Carbon monoxide	+	+	+

of gas emissions were separated and identified on a column with polyethylene glycol adipate. The length of the column is 3 m, the temperature is 70 °C. To identify and quantify methanol, ethanol, isopropanol, and methyl ethyl ketone, we used the data of chromatographic analysis on a PE-624 capillary column.

Inorganic substances were also controlled during the tests. Instead of indicator tubes, electrochemical gas analyzers MGL-19 for carbon monoxide and ANKAT were used to determine carbon monoxide and sulfur dioxide.

3 Results and Discussion

At a given saturation of 0.45 m^2 per 1 m^3 and selected heating temperatures of material samples, three chamber tests were carried out. The accumulation of harmful substances

in the volume of the chamber was traced at the exposure time of the material for 1–2 days, and for carbon monoxide ~ about 3 days. To assess the growth dynamics of the concentration of gas emission components, a number of measurements were performed in the first hours of the sealing regime.

The heating temperature of the material samples in the first, second, and third tests was maintained at 180 ± 0.6 °C, 190 ± 0.6 °C, and 200 °C ± 0.6 °C, respectively.

The obtained data on the composition of organic substances released from the material and the dynamics of their accumulation in a closed volume are presented in Tables 2, 3 and 4. The dynamics of the accumulation of inorganic substances—carbon monoxide and sulfur dioxide is shown in Tables 5, 6 and 7.

Table 2 Concentration of organic substances, mg/m^3, in the volume of the chamber when testing a sample of material PSF-1.5B. Saturation 0.45 m^2 per 1 m^3. Temperature 180 ± 0.6 °C

Substances	Exposure time, hour	
	24	45
Acetaldehyde	0.45	0.60
Acetone	0.35	0.50
Methylethylketone	0.26	0.28
Methanol	0.38	0.41
Ethanol	0.45	0.48
Iso-propanol	0.30	0.32
The sum of oxygen-containing compounds	2.20	2.06

Table 3 Concentration of organic substances, mg/m^3, in the volume of the chamber when testing a sample of material PSF-1.5B. Saturation 0.45 m^2 per 1 m^3. Temperature 190 ± 0.6 °C

Substances	Exposure time, hour				
	1	2	4	28	46
Acetaldehyde	0.25	0.35	0.40	0.80	1.10
Acetone	0.20	0.34	0.35	0.60	0.90
Methylethylketone	0.11	0.19	0.22	0.56	0.64
Methanol	0.10	0.18	0.20	0.51	0.58
Ethanol	0.07	0.12	0.14	0.35	0.41
Iso-propanol	0.12	0.20	0.20	0.60	0.67
The sum of oxygen-containing compounds	0.90	1.40	1.50	3.40	4.30

Tables 2, 3 and 4 show that oxygen-containing organic compounds were constantly found in the gas emissions. Acetaldehyde, acetone, methanol, ethanol, and isopropanol

Table 4 Concentration of organic substances, mg/m^3, in the volume of the chamber when testing a sample of material PSF-1.5B. Saturation 0.45 m^2 per 1 m^3. Temperature 200 ± 0.6 °C

Substances	Exposure time, hour			
	0.5	1.5	24	45
Acetaldehyde	0.50	0.60	2.00	2.20
Acetone	0.35	0.40	1.80	2.30
Methylethylketone	0.59	1.40	9.70	7.90
Methanol	0.71	1.70	11.60	9.50
Ethanol	0.45	1.10	7.30	5.90
Iso-propanol	0.75	1.80	12.3	10.10
Hexanal	2.50	3.90	9.200	6.40
The sum of oxygen-containing compounds	5.90	10.90	53.90	44.40

Table 5 Concentration of inorganic substances, mg/m^3, in the volume of the chamber when testing a sample of material PSF-1.5B. Saturation 0.45 m^2 per 1 m^3. Temperature 180 ± 0.6 °C

Substances	Exposure time, hour		
	24	45	69
Carbon monoxide	5.0	9.0	11.0
Sulfur dioxide	–	–	–

Table 6 Concentration of inorganic substances, mg/m^3, in the volume of the chamber when testing a sample of material PSF-1.5B. Saturation 0.45 m^2 per 1 m^3. Temperature 190 ± 0.6 °C

Substances	Exposure time, hour				
	1	2	4	28	46
Carbon monoxide	1.0	2.0	3.0	12.0	17.0
Sulfur dioxide	–	–	0.9	1.0	1.9

were isolated from the material. At higher temperatures of 180–200 °C, methyl ethyl ketone was also detected; and at 200 °C—caproic aldehyde. Characteristic for the entire temperature range under study was the release of carbon monoxide, and at temperatures of 190–200 °C, also sulfur dioxide.

The above results of the analysis of the air environment under conditions of overheating of the PSF-1.5B material are summarized in Tables 8 and 9. To characterize the level of air pollution with harmful chemicals, the values of the ratio of the detected concentration to the maximum allowable concentration in the air of the working area of

Table 7 Concentration of inorganic substances, mg/m^3, in the volume of the chamber when testing a sample of material PSF-1.5B. Saturation 0.45 m^2 per 1 m^3. Temperature $200 \pm 0.6\,°C$

Substances	Exposure time, hour			
	0.5	1.5	24	45
Carbon monoxide	2.5	3.0	21.0	29.0
Sulfur dioxide	–	–	3.1	5.2

industrial premises are given. For each temperature, the total indicator of air pollution is calculated.

Table 8 Levels of air pollution after 1 day of testing a sample of material PSF-1.5B

Substances	MPCr.z., mg/m^3	C, mg/m^3			C/MPCr.z		
		180	190	200	180	190	200
Acetaldehyde	5	0.45	0.80	2.00	0.09	0.16	0.40
Acetone	200	0.35	0.60	1.80	$1.8 \cdot 10^{-3}$	$3.0 \cdot 10^{-3}$	$9.0 \cdot 10^{-3}$
Methylethylketone	200	0.26	0.56	9.70	$1.3 \cdot 10^{-3}$	$2.8 \cdot 10^{-3}$	$5.0 \cdot 10^{-2}$
Methanol	5	0.38	0.51	11.60	0.08	0.10	2.30
Ethanol	1000	0.45	0.35	7.30	$4.5 \cdot 10^{-4}$	$3.5 \cdot 10^{-4}$	$7.3 \cdot 10^{-3}$
Iso-propanol	10	0.30	0.60	12.30	0.03	0.06	1.20
Hexanal	10	–	–	9.20	–	–	0.92
Carbon monoxide	20	5.00	12.00	21.0	0.25	0.60	1.10
Sulfur dioxide	10	–	1.00	3.10	–	0.10	0.31
$\sum$(C/ MPCr.z.)					0.45	1.0	6.32

The tables show that the main contribution to air pollution was made by: methanol, isopropanol, caproic aldehyde, carbon monoxide, acetaldehyde, sulfur dioxide.

The total indicator of air pollution at material heating temperatures of 180, 190 and 200 °C reached, respectively, 0.7; 1.4 and 6.3 units. Thus, when the material is overheated to 200 °C, a significant excess of the level provided for by the toxicological and hygienic requirements for class V premises is expected. When the material is overheated to 190 °C, a relatively lower level is expected: 1 and 1.4 units. for 1 and 2 days, respectively. It seems inappropriate to evaluate the PSF-1.5B material at the level of the maximum allowable concentrations for the air of uninhabited premises of group 1-A. Upon overheating to 200 °C, a strong deformation of the sample was observed, caused by the melting of the material and its leakage from the holder. At 190 °C, the shape of the sample was retained, but a noticeable melting of the surface was detected. In this case, the limitation of the superheat temperature should be determined not by the level of outgassing, but by other criteria.

Table 9 Levels of air pollution after 2 days of testing a sample of material PSF-1.5B

Substances	MPCr.z., mg/m^3	C, mg/m^3			C/MPCr.z		
		180	190	200	180	190	200
Acetaldehyde	5	0.60	1.10	2.20	0.12	0.22	0.40
Acetone	200	0.50	0.90	2.30	$2.5 \cdot 10^{-3}$	$4.5 \cdot 10^{-3}$	$9.0 \cdot 10^{-3}$
Methylethylketone	200	0.28	0.64	7.90	$1.4 \cdot 10^{-3}$	$3.2 \cdot 10^{-3}$	$5.0 \cdot 10^{-2}$
Methanol	5	0.41	0.58	9.50	0.08	0.12	2.30
Ethanol	1000	0.48	0.41	5.90	$4.8 \cdot 10^{-4}$	$4.1 \cdot 10^{-4}$	$7.3 \cdot 10^{-3}$
Iso-propanol	10	0.32	0.67	10.0	0.03	0.07	1.20
Hexanal	10	–	–	6.40	–	–	0.92
Carbon monoxide	20	9.0	17.0	29.0	0.45	0.83	1.10
Sulfur dioxide	10	–	1.90	5.25	–	0.19	0.31
$\sum$(C/ MPCr.z.)					0.68	1.44	6.00

At a temperature of 180 °C, no change in the shape of the sample was found, as in previous tests of less heated samples. The level of air pollution when the material was overheated to 180 °C for 1–2 days approached unity. The specified temperature can be tolerated under conditions of overheating of the material in an emergency situation.

4 Conclusion

Thus, as a result of the work, the sanitary-chemical characteristics of the PSF-1.5B protection material were obtained in a wide temperature range—from +180 to +200 °C. It has been established that the level of air pollution when the material is overheated to 180 °C for 1–2 days does not exceed the maximum permissible concentration of harmful substances in the air of the working area of industrial premises. The specified temperature can be tolerated under conditions of overheating of the material in an emergency situation.

As a result of overheating of the material in the temperature range of 190–200 °C, a sharp increase in gas emissions was found with an excess of the MPC level provided for by the toxicological and hygienic requirements for protection materials for class V premises.

The overheating temperature of the PSF-1.5B material allowed in an emergency situation should not exceed 180 °C.

References

1. Pavlenko, V.I., Cherkashina, N.I., Yastrebinsky, R.N.: Synthesis and radiation shielding properties of polyimide/Bi_2O_3 composites. Heliyon **5**, E01703 (2019)
2. Pavlenko, A.V., Cherkashina, N.I., Yastrebinskii, R.N.: Nanodisperse metalloorganosiloxane fillers of polymers. Nanotechnol. Constr. Sci. Internet-J **8**(4), 113–130 (2016)
3. Xie, S., Zhang, Z., Wei, W.: Synthesis and properties of polyimide-based optical materials. J. Korean Phys. Soc. **51**, 1536–1541 (2007)
4. Bloom, P.D., Baikerikar K.G., Otaigbe J.U., Sheares V.V.: Development of novel polymer/quasicrystal composite materials. Mat. Sci. Eng. A-Struct, 156–159 (2000)
5. Sorokin, V.V., Sharapov, O.N., Shunkin, N.M., Kiryushina, N.Y.: New polymeric composites based on epoxy resin with techogenic wastes. Bulletin of BSTU named after V.G. Shukhov **6**, 8–13 (2019)
6. Pavlenko, A.V., Cherkashina, N.I., Yastrebinski, R.N.: Nanodisperse metalloorganosiloxane fillers of polymers. Nanotechnol. Constr. Sci. Internet-J. **8**(4), 113–130 (2016)
7. Sickafus, K.E.: Radiation-induced amorphization resistance and radiation tolerance in structurally related oxides. Nat. Mater. **6**(3), 217–223 (2007)
8. Yastrebinsky, R.N., Karnauhov, A.A., Yastrebinskaya, A.V.: Improving the radiation-thermal stability of titanium hydride. J. Phys. Conf. Ser. 1–6 (2020)
9. Shestakov, I.Y., Veretnova, T.A., Strekalova, T.A.: Investigation of water electrical activator with coaxial arrangement of electrodes. Chem. Bull. **4**(1), 12–18 (2018)
10. Arbuzova, A.A., Votyakov, M.A.: Estimation of the influence of the state of the reinforcing polymer in the structure of polymeric fiber material using mathematical prediction methods. Chem. Bull. **1**(1), 12–17 (2018)

Obtaining Energy Efficient Polymer-Bitumen Binders Using Polymer-Bitumen Concentrate

V. V. Yadykina$^{(\boxtimes)}$, V. P. Denisov , A. E. Akimov , and K. S. Vyrodova

Department of Roads and Railways, Belgorod State Technological University Named After V G Shukhov, Kostyukov St, 46, Belgorod 308012, Russia
vvya@intbel.ru

Abstract. New requirements for the operational reliability of highways lead to the need for the expanded use of polymer-bitumen binders (PBB) in road construction. The traditional technology for the production of polymer-bitumen binder includes very energy-consuming processes: bitumen preparation, polymer grinding in a colloid mill and additional exposure in containers at temperatures above 170 °C. This leads to an increase in the consumption of electricity and fuel (most often it is natural gas or fuel oil) and, as a result, to an increase in the cost of the final product. In addition, the process of binder synthesis for a long time at high temperatures leads to increased aging, which significantly reduces the service life of this material in the pavement. The article presents the results of studies on the effect of polymer-bitumen concentrate (PBC) on the characteristics of bitumen. It has been established that the use of PBC in a bituminous binder leads to an increase in the temperature range of plasticity, elasticity, cohesive strength with a decrease in the viscosity of the modified bitumen and an increase in the softening temperature. Thus, the expediency of using a complex additive containing a polymer and surface-active substances (surfactants) that can be distributed in bitumen without the use of a colloid mill and a plasticizer has been proven to improve the quality of the organic binder. It is shown that the use of the PBC modifier can significantly reduce the energy intensity of the process and reduce emissions of volatile bitumen components.

Keywords: Polymer-Bituminous concentrate · Polymer-Modified bituminous binder · Structure formation · Cohesion strength · Ductile temperature range · Waste gas reduction

1 Introduction

Nowadays, the modification of bituminous binders with polymers is one of the promising methods for the production of high quality asphalt concrete for road and airfield construction [1–12]. Using polymer-bitumen binders is justified for several reasons [3, 4]. First, asphalt concrete pavements for PBB reduce the dependence of physical and mechanical characteristics on temperature vs. with the use of unmodified bitumen. At high operating temperatures during the summer period, the use of PMB provides greater strength and less creep to the material. At low temperatures during the winter period

of operation, the material remains elastic longer, preventing the appearance of thermal and fatigue cracks. Second, the use of PBB makes it possible to obtain a coating that combines high resistance to the accumulation of plastic deformations, achieved due to an increased softening temperature and increased cohesive strength, with significant resistance to fatigue failure due to high elasticity and the ability to relax internal stresses. On the other hand, the use of polymer-bitumen binders in the creation of asphalt concrete pavements is associated with technological and economic difficulties [7] because of the use of complex equipment, including colloidal mills, as well as a large fleet of equipment for the preparation and additional curing of the binder. In addition, the process of binder synthesis for a long time at high temperatures leads to their increased aging, which significantly reduces the service life of such material on the road surface. These difficulties severely limit the production of PBB through the activities of road construction enterprises. The purchase of ready-to-use PBB from specialized manufacturing companies also has a number of negative aspects, which include the high price, the tendency of PBB to delaminate during transportation and storage. This leads to the need for additional preparation of the binder, as well as variable binder quality and complicated input control. Technological processes for the production of PBB are highly resource-consumptive. It is required to provide preheating and maintaining the temperature of the initial bitumen at the preparatory stages; one- or two-stage polymer dispersion in a colloid mill; and maintaining the temperature at the stage of additional curing of the binder. In addition, during the transition from one stage of production to another, it is necessary to ensure multiple pumping of the polymer-bitumen binder and its components through the pipeline system. This leads to an increase in energy costs per unit of output, an increase in the consumption of electricity and natural gas, which, as a result, leads to an increase in the cost of RMB. In addition, as a result of long-term technological processes associated with maintaining a high temperature of the binder, the emission of combustion products, carbon dioxide and evaporation of volatile bitumen compounds into the atmosphere increases, which is not in line with the policy of rational environmental management. These problems can be solved by the development and use of a polymer additive that is effectively dissolved in bitumen by mixing and does not require complex equipment for the preparation of a binder. One of the options for the preparation of PBB by road construction companies is the use of a polymer-bitumen concentrate, in which the polymer is dispersed to the optimal size and stabilized. When preparing PBB with its use, a colloid mill and containers for preparation and additional curing of the binder are excluded from the technological process. The purpose of this work is to analyze the effect of PBB on the properties of the binder.

2 Materials and Methods

As an object of study, a polymer-bitumen concentrate developed by Selena LLC was used, which is a multi-component composition based on SBS-type polymers in combination with surfactants based on a mixture of vegetable oil processing products.

PBC was introduced into bitumen BND 70/100 in the amount of 6, 8 and 10% by wt. of the binder. The characteristics of the studied modifier are shown in Table 1.

Table 1 Characteristics of the studied modifier

Parameter	Actual value
Appearance at 20 °C	Black rubbery substance
Softening temperature, °C	110
Content of styrene–butadiene–styrene rubber, at least, %	40
Content of bound styrene, %	12 ± 1
Estimated increase in the softening point of the binder, according to KiSh, at 8% dosage, at least, %	35
Estimated elasticity of PBB at 8% dosage, at least, %	85

The PBC modifier was introduced into petroleum road bitumen grade BND 70/100 at a concentration of 6, 8 and 10%. Physical and chemical characteristics of the original binder are shown in Table 2.

Table 2 Characteristics of binder

Parameter	Specification Requirements	Actual values
Needle penetration depth, 0.1 mm at 25 °C	71–100	73
Needle penetration depth, 0.1 mm at 0 °C	21 at least	26.0
Extensibility, cm at 25 °C	62 at least	87.0
Extensibility, cm at 0 °C	3.7 at least	4.5
Softening temperature, °C	47 at least	47.3
Brittleness temperature, °C	up to −18	19.0
Elasticity, %	–	–

The dissolution of the polymer-bitumen concentrate occurs with stirring with a paddle mixer. After a short aging to improve uniformity, the binder is ready for further research. Determination of indicators of basic physical and chemical properties was carried out according to standard tests for road bitumen. Cohesion was determined by the value of the torque required to rotate through an angle of 90° of the cylinder in the sample of the studied binder under load.

3   Results and Discussions

The results of determining the physical and mechanical characteristics of the studied samples of bituminous binders, as well as the requirements of the relevant documents for bitumen BND 70/100 and PBB 60 are shown in Table 3.

The data obtained allow us to conclude that the introduction of a minimum amount of PBC into bitumen (6%) leads to an increase in bitumen penetration by 17.8 and

Table 3 Physical and mechanical characteristics of the studied binders

Parameter	GOST 31,133-2014	GOST 52,056-2003	Consecration of PBC in the binder, %			
			0	6	8	10
Needle penetration depth, 0.1 mm at 25 °C	71–100	60 at least	73	86.0	90	92
Needle penetration depth, 0.1 mm at 0 °C	21 at least	32 at least		34.0	38.0	41.0
Extensibility at 25 °C, cm	62 at least	25 at least	87.0	64.0	47.0	43.0
Extensibility at 0 °C, cm	3.7 at least	11 at least	4.5	13.0	14.0	13.5
Softening temperature, °C	47 at least	54 at least	47.3	48.7	53.9	55.2
Brittleness temperature, °C	up to−18	−20 at least	19.0	19.5	20.0	22.0
Elasticity, %	–	80 at least	–	76	81	87

30.8% at 25 °C and 0 °C, respectively, and a slight increase in the softening temperature and a decrease in the brittleness temperature. The appearance of elasticity in the binder indicates that the polymer, when introduced into bitumen, creates a spatial network that provides viscoelasticity at higher temperatures. However, the most important values for softening and brittleness, as well as elasticity, do not meet the requirements for PBB 60 given in the technical specifications.

The results presented in Table 1 indicate that introducing concentrate into bitumen in an amount of 8–10% contributes to a more intensive change in indicators, especially extensibility at a temperature of 25 °C (by 46.1–57.7%), softening point (by 13.9–16.7%) (Fig. 1), and elasticity, which can be considered as one of the indicators of achieving the optimal polymer concentration in the binder, which allows bitumen to be structured to the required degree.
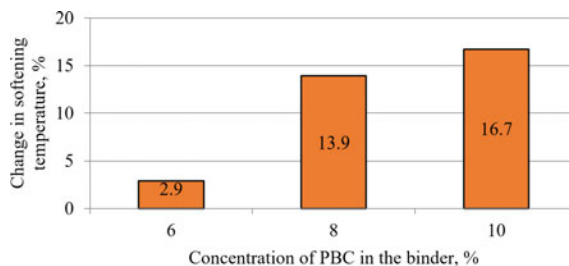
Fig. 1 Softening temperature variation for the studied mixes

At the same time, the bitumen becomes less viscous (Fig. 2). This may be due to the presence of a plasticizer and surfactant in the additive. This will increase the adhesion of the binder to the mineral components of the asphalt mix.
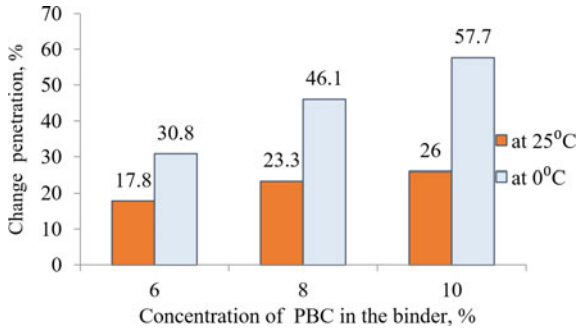
Fig. 2 Variations in the penetration of the studied mixes

It should be noted that the use of PBC in an amount of 8–10% led to the appearance of binder properties that meet the requirements of Russian Standard GOST 52,056-2003 for PBB 60 based on a polymer of the styrene–butadiene–styrene type, which is produced using a colloid mill.

Based on the data obtained, the temperature ranges of plasticity of the studied binders were calculated as follows:

$$T = T_r + \left| T_f \right|$$

where T_r is the softening temperature of the binder; T_f is binder the brittleness temperature.

The data shown in Fig. 3 shows that the use of PBC in a bituminous binder results in an increase in the plasticity temperature range by 3, 11.5 and 16.4% at concentrations of 6, 8 and 10%, respectively.
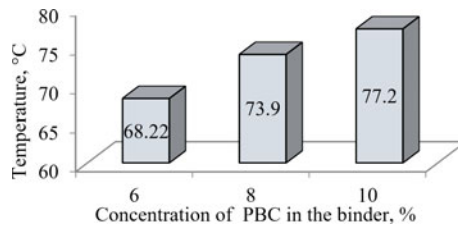
Fig. 3 Temperature range of plasticity for the studied binders

The temperature range of plasticity is considered to be the temperature range in which bitumen is viscoelastic, i.e. it can effectively absorb the load without causing plastic deformations of asphalt concrete, but at the same time it does not become brittle,

which makes it possible to relax the internal stresses arising in asphalt concrete and prevent the appearance of cracks [5].

One of the important characteristics of an organic binder is its cohesive strength. The determination of cohesion is based on the measurement of the shear resistance force of a thin layer of bitumen (10 microns) at a constant rate of load increase. Figure 4 shows that an increase in the concentration of PBC in the binder is accompanied by an increase in cohesion. At an additive concentration of 8–10%, cohesion increases by 10–13% vs. with original bitumen. An increase in cohesion contributes to an increase in the strength of asphalt concrete. Thus, the introduction of the PBC modifier into the original bitumen leads to an increase in the cohesive strength of the resulting binder, which will positively affect the properties of asphalt concrete.
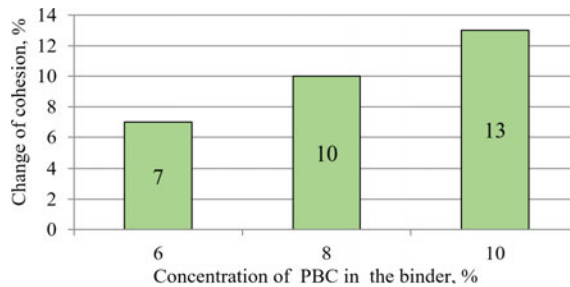
Fig. 4 Effect of polymer content in bitumen on cohesion

The characteristics of the binder obtained using the PBC modifier show that the resulting material fully meets the requirements of the technical specifications for polymer-bitumen binders.

Next, it is necessary to compare the traditional and researched PBB production technology on the environmental impact.

As the first criterion, the emission of components of the base part of bitumen during heating and maintaining the process temperature during the entire time of PBB production will be considered. To evaluate this parameter, the binder was held at temperatures for a time period equal to the technological cycle of the corresponding technology. After exposure, the mass loss of the sample was determined. The results are shown in Table 4.

Table 4 Estimation of the emission of bitumen components during the preparation of PBB according to the traditional technology and with the use of the PBC modifier

Bitumen sample	Binder curing time, min	Binder curing temperature, °C	LOI, %
Bitumen with traditional PBB synthesis technology	240	175	0.21
Bitumen with PBC modifier	60	155	0.04

As noted above, the technology for producing a polymer-bitumen binder using a PBC modifier can significantly reduce the duration of all high-temperature technological preparation processes: preliminary curing of the binder with a plasticizer, two-stage mixing in a colloid mill, and subsequent additional curing. In addition, the mixing of bitumen with PBC occurs at a lower temperature (155 °C vs. 175 °C). These features lead to a significant reduction in the emission of volatile bitumen components during the production process. Weight loss as a result of imitation of technological processes for preparing a modified binder decreased by 4 times. Thus, under the conditions of mass production of PBB, can significantly reduce the negative effect on the environment.

To assess the savings of fossil fuels and carbon dioxide emissions, an enlarged calculation of the energy capacity of PBB production using traditional and proposed technologies was made based on data on the average carbon intensity of obtaining 1 kW of electrical energy [13]. The evaluation results are shown in Table 5.

Table 5 Estimation of energy costs when cooking of PBB according to traditional technology and with the use of the PBC modifier

Technology type	Total amount of energy per 1 ton of product, kW	Emission of carbon dioxide during power generation, kg
Traditional	485	230.38
With the use of the PBC modifier	223	105.93

The results obtained indicate a 2.17-fold decrease in carbon dioxide emissions upon switching to the PBB production technology using the studied modifier. In addition, saving fossil fuels contributes to better environmental management.

4 Conclusion

It has been established that the use of PBC in a bituminous binder leads to an increase in the temperature range of plasticity, elasticity, cohesive strength with a decrease in the viscosity of the modified bitumen and an increase in the softening temperature. At the same time, the use of a colloid mill is not required for preparing a binder. Using PBC in an amount of 8–10% leads to the appearance of binder properties that meet the requirements of Russian Standard GOST for PBB 60 on a styrene–butadiene–styrene type polymer.

The ongoing changes in the physical and mechanical characteristics indicate that the polymer in PBC does not just mix with the modified binder, but forms an effective spatial structure similar to PBB on SBS. At the same time, the production costs of the modified binder using the PBC are much lower.

Introducing a minimum concentration of PBC into bitumen ensures the elasticity of the binder, which increases with an increase in the amount of the modifier. This result should have a positive effect on the fatigue life of asphalt concrete based on such a binder,

because due to the increased elasticity of the binder, fatigue stresses arising under the action of cyclic loads will be effectively extinguished.

An increase in the temperature range of binder plasticity with introducing PBC makes it possible to ensure the resistance of asphalt concrete to the accumulation of plastic deformations in the summer period and the appearance of thermal cracks in the winter period, which will favorably affect the overall service life of the coating.

Reducing the time spent on production and lowering the temperature of PBB preparation using the proposed technology can significantly reduce the emission of bitumen volatile components into the atmosphere, which contain compounds harmful to health and the environment. Using less energy-consumptive technological processes when producing PMB according to the proposed technology makes it possible to achieve a reduction in carbon dioxide emissions and save fossil fuels.

References

1. Gokhman, L.M.: Bitumen, Polymer-Bitumen Binders, Asphalt Concrete, Polymer Asphalt Concrete. ZAO ECON-INFORM, Moscow (2008)
2. Zolotarev, V.A.: Polymer-modified bitumens and asphalt-polymer concretes. Road Eng. 16–23 (2009)
3. Doshlov, O.I., Speshilov, E.G.: Polymer-bitumen binder—a high-tech basis for a new generation of asphalt. Bull. Irkutsk State Tech. Univ. **6**(77), 140–144 (2013)
4. Kotenko, N.P., Shcherba, Y.S., Evforitsky, A.S.: Influence of polymeric and functional additives on the properties of bitumen and asphalt concrete. News of higher educational institutions. North Caucasian region. Eng. Sci. **1**(201), 94–99 (2019). https://doi.org/10.17213/0321-2653-2019-1-94-99
5. Kalgin, Y.I., Strokin, A.S., Tyukov, E.B.: Perspective Technologies for the Construction and Repair of Road Surfaces Using Modified Bitumen, p. 223. Voronezh State University, Voronezh (2014)
6. Yadykina, V.V., Navolokina, S.N., Gridchin, A.M.: Improving the bitumen quality through the comprehensive polymer-based modification. Mater. Sci. Forum **992**, 238–242 (2020). https://doi.org/10.4028/www.scientific.net/MSF.992.238
7. Rybachuk, N.A.: Problems of the production of polymer-bitumen binders in road construction. Bull. Irkutsk State Tech. Univ. **5**(100), 98–105 (2015)
8. Wang, J., Yuan, J., Xiao, F., Li, Z., Wang, J., Zhizhou, X.: Performance investigation and sustainability evaluation of multiple-polymer asphalt mixtures in airfield pavement. J. Clean. Prod. **S0959–6526**(18), 30879–30885 (2018). https://doi.org/10.1016/j.jclepro.2018.03.208
9. Onishchenko, A., Stolyarova, L., Bieliatynskyi, A.: Evaluation of the durability of asphalt concrete on polymer modified bitumen. E3S Web Conf. **157**, 06005 (2020)
10. Khafizov, E.R., Vdovin, E.A., Fomin, A.Y., Ilyina, O.N.: Study of the physical and mechanical properties of multi-crushed asphalt concrete based on polymer-bitumen binders. Izvestiya KGASU **1**, 211–215 (2016)
11. Yadykina, V.V., Navolokina, S.N., Gridchin, A.M.: Increasing the resistance of macadam-mastic asphalt concrete to rut formation due to the use of polymer modifiers. Constr. Mater. Prod. **6**(3), 27–34 (2020). https://doi.org/10.34031/2618-7183-2020-3-6-27-34

12. Polyakova, V.I., Polyakova, S.V.: Features of obtaining and using polymer-bitumen binders in road construction. Roads Bridges **1**, 24–24 (2013)
13. IEA (2019), Global Energy & CO_2 Status Report 2019, IEA, Paris https://www.iea.org/reports/global-energy-co2-status-report-2019

Effect of Cyclic Loading Level on Elastic-Strength Characteristics and Kinetics of Damage Accumulation in Polymers

T. A. Nizina[1,2(✉)] , D. R. Nizin[1,2] , and N. S. Kanaeva[1]

[1] National Research Mordovia State University, Saransk, Russia
nizinata@yandex.ru

[2] Research Institute of Building Physics (NIISF), Moscow, Russia

Abstract. We studied the change in the elastic-strength parameters of the Etal-247 epoxy resin polymer cured by the Etal-45 M hardener depending on the cyclic exposure level. It was established that the increased cyclic loading from 40 to 80% of the sample tensile strength (without cyclic loading) leads to the increased mechanical strength of samples at the failure stage by 12–23%. Cyclic exposure corresponding to the total loading of 96 mJ/m^3 leads to the increased relative elongation under maximum load at the failure stage by 5–7%, and the elastic modulus increase of 12–18%. The relative polymer elongation at break in the initial state is 8.05%, decreasing to 5.74% with an increase in the cyclic stress. We offer an algorithm for estimating the effect of cyclic loads on the kinetics of failure accumulation in polymeric materials. We study the effect of the change in intensity and frequency of cyclic loading on the kinetics, and specific indicator of failure accumulation in Etal-247 epoxy resin samples cured by the Etal-45 M hardener. We found a decrease in specific index determined for the failure stage by 4–17% with an increase in the cyclic loading from 10 to 20 MPa compared with the same indicator obtained for the control series of samples without cyclic exposure.

Keywords: Epoxy polymers · Cyclic loading · Failure accumulation

1 Introduction

Resistance to cyclic influences—both mechanical loading and aggressive factors and environments, is one of the main conditions for ensuring uninterrupted operation of building products and structures. According to [1–3], the strength indicators of polymer composite materials during the dynamic fatigue test differ significantly from similar indicators determined when exposed to static loads. Under variable loads, both hardening and softening processes can occur, associated with the initial structural state of materials, as well as its change exposed to cyclic deformations, formation and redistribution of residual microstresses, as well as the occurrence and development of microfailures.

The influence of cyclic action on the change in bearing capacity and durability of composite materials is characterized by high complexity and laboriousness both in

terms of experimental studies and variety of processes in materials. The reliability of predicting strength and durability of structural polymeric materials exposed to cyclic loading is complicated by various degradation factors, such as climatic effects, aggressive environments, etc. [4–6]. Moreover, the joint effect of factors is often accompanied by the synergistic effects.

Determining the fatigue failure accumulation limit and predicting the residual operating life with an acceptable level of failure are important scientific problems [7]. In [8, 9], the team of authors proposed a technique for assessing the kinetics of failure accumulation in the structure of polymer composites exposed to static loading under tensile loads, based on the use of fractal analysis methods in the study of deformation curves, with a high frequency of readings. The presented approach makes it possible to quantitatively determine the critical level of microdefects accumulation leading to the specimen structure decompaction and appearance of the first cracks, as well as to analyze the subsequent loading stage until the polymer fails. To quantify the change in the kinetics of failure accumulation in polymer material samples exposed to tensile loads, it was proposed [9, 10] to use the index ω. It is the ratio of the number of points with a fractality index less than 0.5, to the total number of the deformation curve points (up to the level of maximum stresses) and the specific index θ—the ratio of the total share of accumulated failure to the ultimate strength of the polymer material sample.

This paper describes the adaptation of this technique for assessing the effect of cyclic loads, as well as the analysis of the influence of intensity and frequency of cyclic exposure. Main provisions of the proposed approach, which makes it possible to calculate gradual failure accumulation exposed to cyclic loading, are given in [11].

2   Methods and Materials

The object of the study was samples of polymeric material made of Etal-247 epoxy resin (TU 2257-200-18,826,195-02 amend. 1) and Etal-45 M hardener (TU 2257-045-18,826,195-01). Eights samples were tested in accordance with GOST R 57,143-2016 "Polymer composites. Fatigue test method under cyclic tension" under soft cyclic amplitude loading; stress is the control parameter. The target cycling levels are 40, 60 and 80% of the samle tensile strength without pre-cycling. Taking into account rounding up to a factor of 5, they correspond to internal stresses of 10, 15 and 20 MPa. The need for this rounding is due to subsequent comparison of the results obtained for the compound under study with the results of other compounds of polymeric materials simultaneously tested, including after exposure to aggressive factors. The number of cycles for internal stress levels of 10 and 15 MPa is calculated based on the value of the total loading action, equivalent to 5 cycles of tensile load for a level of 20 MPa.

Movement speed of the clamps of AGS-X series tensile testing machine with the TRAPEZIUM X software was 2 mm/min, reading frequency was 0.01 s. Test temperature was 23 ± 2 °C and relative air humidity—50 ± 5%. At least 5 samples were tested at each cyclic loading level.

The approach proposed for assessing the kinetics of damage accumulation in polymeric materials exposed to cyclic loads included the following steps:

(1) Determining the number of loading acts recorded with a reading frequency of 0.01 s, both for individual cycles $N_1, N_2, \ldots, N_m$, and for the destruction stage $N_{dest.}$ (up to the maximum tensile load point).

(2) Identifying the number of loading acts, accompanied by the failure of the structural elements of the material under study. The values of the time series fractality index $\mu(\sigma, \varepsilon)$ were used as an indicator characterizing the state of the sample at the point of time, calculated using the least coverage method based on the change in the increase in tensile stresses during loading. Points with a value of $\mu(\sigma, \varepsilon)$ less than 0.5 were taken as acts of failure of structural elements (by analogy with classical methods of time series fractal analysis). The calculation is both for each loading cycle (from 1 to m) and for the failure stage—respectively, $N_{def.1}, N_{def.2}, \ldots, N_{def.m}$ and $N_{def.dest.}$.

(3) Calculation of the total number of loading acts N_0, leading to the limiting level of tensile stresses:

$$N_0 = \sum_{i=1}^{m} N_{def.i} + N_{def.dest.} + N_{dest.}, \tag{1}$$

where $N_{dest.}$ is the number of the failure stage acts (after cyclic impact) with no failures.

(4) Calculation of the total number of failures:

- exposed to cyclic loads separately for each stage of loading:

$$\omega_i = \frac{N_{def.i}}{N_0} \cdot 100, \tag{2}$$

where $i = 1 \div m$ is the loading cycle number;
- when exposed to a destructive load (up to the maximum tensile stress level)

$$\omega = \frac{N_{def.dest.}}{N_0} \cdot 100, \tag{3}$$

(5) Calculation of the number of failures depending on the relative elongation and tensile stress for the cyclic loading stages and the failure stage with graphical dependencies (Fig. 2).

(6) Calculation of the specific index (%/MPa) as the ratio of the total share of accumulated failure to the ultimate strength of a polymer material sample, determined in two versions:

- failure stage analysis

$$\theta_{dest.} = \frac{\omega_{dest.}}{\sigma_{str.}}, \tag{4}$$

where $\omega_{dest.}$ is the number of accumulated failures for the destruction stage, determined as:

$$\omega_{dest.} = \frac{N_{def.dest.}}{N_{def.dest.} + N_{dest.}} \cdot 100; \tag{5}$$

- analysis of the loading history (cyclic impacts and failure stage)

$$\theta = \frac{\omega}{\sigma_{str.}}. \qquad (6)$$

Specific index θ calculated as (6) compares series of samples subjected to various combinations of cyclic loads with subsequent failure, specific index $\theta_{dest.}$ (4) assesses the polymer state before and after cyclic exposure.

A software package based on Python was used for calculations.

3   Results and Discussion

The process of cyclic tensile loading of a polymer sample for a 10 MPa internal stress level is shown in Fig. 1. The complex deformation curve includes the cyclic effect stage (25 cycles; Fig. 1b) and the stage of the final sample loading up to failure.
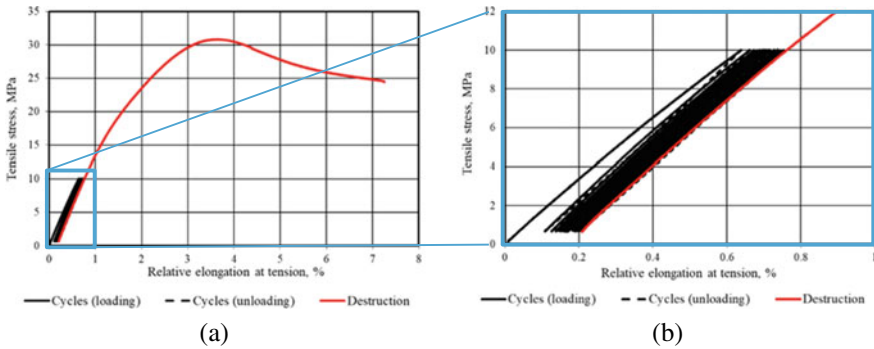
Fig. 1 The deformation curve of epoxy resin Etal-247 polymer cured by Etal-45 M subjected to 25 cycles of loading with a tensile load of 10 MPa, followed by stretching to complete failure (**a** deformation curve (complete); **b** cycles Nos. 1–25)

The elastic modulus, strength, and relative elongation at tension and rupture were determined for the samples under study, before and after cyclic loading (Table 1). It was established that cyclic action in the stress range under study (from 10 to 20 MPa), corresponding to the total loading of 96 MJ/m³, leads to an increase in the mechanical strength of polymer samples in tension and rupture by 12–23%. Cyclic action leads to an increase in relative elongation in tension at the destruction stage by 5–7%. In turn, the dependence of the total cyclic deformations on the applied stresses is directly proportional, with the main contribution being made during the first loading cycle. The elasticity modulus of the polymer under study, determined at the destruction stage increases by 12–18%, which indicates an increase in the sample rigidity during the preliminary cyclic exposure. The polymer elongation at break is 8.05%, decreasing with a level of applied stress increasing to 5.74%. Figure 2 shows failure accumulation curves as a function of elongation and tensile stress, calculated according to the above algorithm, after cycling
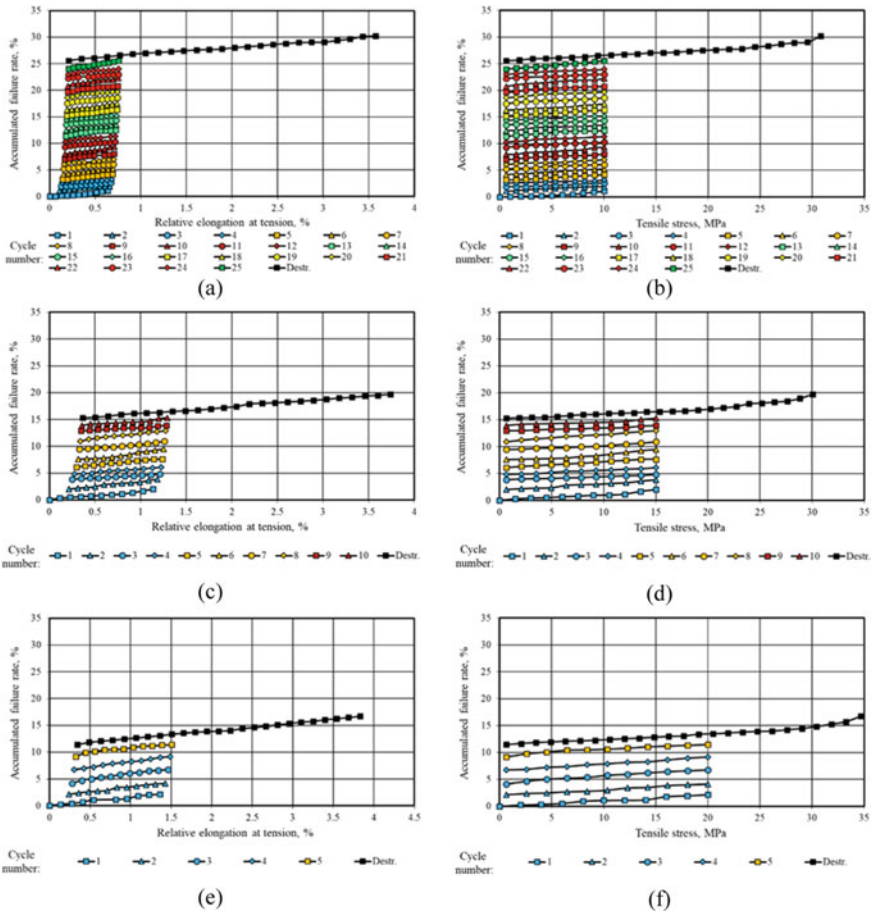
Fig. 2 Plots of failure accumulation in the Etal-247 epoxy resin polymer cured by Etal-45 M subjected to 25 (**a**, **b**), 10 (**c**, **d**), 5 (**e**, **f**) cycles of tensile loading of 10 (**a**, **b**), 15 (**c**, **d**), 20 (**e**, **f**) MPa, followed by stretching until complete failure depending on relative elongation (**a**, **c**, **e**) and tensile stress (**b**, **d**, **f**)

at three different levels (10, 15 and 20 MPa). Plots allow to trace the process of failure accumulation rate during deformation of polymers subjected to cyclic loads of the given intensity as well as the subsequent sample loading up to the tensile strength limit.

Plots of the change in the accumulated failure rate ($\omega_{dest.}$, ω) and specific indices ($\theta_{dest.}$, θ) of a series of polymer samples calculated only for the failure stage, as well as jointly for all loading stages, are shown in Fig. 3. It was established that a decrease in the level of tensile cyclic stresses from 20 to 10 MPa with a simultaneous increase in the number of loading cycles from 5 to 25 (to achieve one level of loading effect) leads to an almost twofold increase in the total failure rate—from 16 to 30.5% (Fig. 3a). Such a high difference can also be explained by the chosen model for describing the processes under study, which does not imply complete or partial restoration of the polymer matrix

Table 1 Change in the elastic-strength characteristics of Etal-247 epoxy resin polymer samples cured by Etal-45 M, subjected to 25, 10 and 5 loading cycles exposed to tensile stresses of 10, 15, 20 MPa, respectively

Level of cyclic stresses, MPa	Number of cycles	Tensile strength, MPa	Breaking strength, MPa	Relative elongation after the cyclic loading stage, %	Relative tensile elongation (destruction stage), %	Relative elongation at break, %	Tensile modulus, MPa
0	0	26.4	22.2	–	3.19	8.05	1672
10	25	31.1	25.3	0.21	3.38	8.04	1969
15	10	30.0	26.0	0.34	3.35	6.64	1892
20	5	33.1	28.8	0.39	3.41	5.74	2051

structure in the unloading areas during cyclic loading. At the same time, the accumulated failure rate for the destruction stage varies within a rather narrow range (from 5.84 to 6.63%). Obviously, this is due to the elimination of some defects when removing cyclic load.
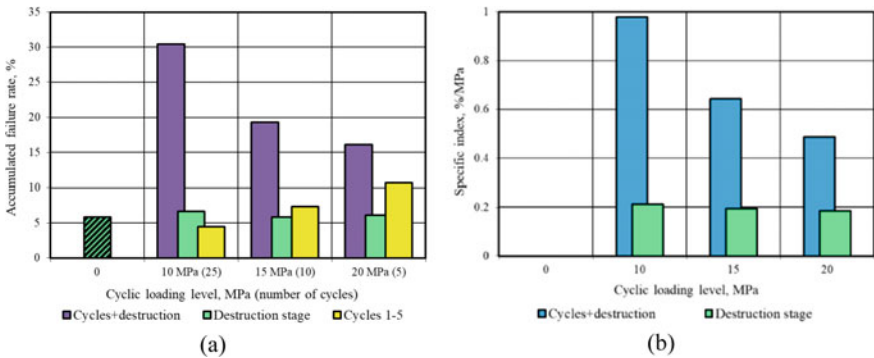
Fig. 3 Change in accumulated failure rate (**a**) and specific index (**b**) of Etal-247 epoxy polymer cured with Etal-45 M versus cyclic loading level

To assess the effect of the tensile load intensity, we compared total failure rate accumulated over the first 5 cycles (Fig. 3a). We found a monotonous increase in this index from 4.5 to 10.6% with an increase in the applied stress from 10 to 20 MPa.

Analysis of Fig. 3b indicates a decrease in specific index $\theta_{dest.}$, determined for the destruction stage, by $3.8 \div 16.8\%$ with an increase in the cyclic loading from 10 to 20 MPa compared with the same index obtained for the control series of samples before cyclic impact. Specific index θ which describes the complete process of loading and failure of polymeric material samples decreases by a factor of two in the range of cyclic impacts under study.

4 Conclusion

Based on the results of the study, it can be concluded that the approach proposed earlier [8, 9] for assessing the kinetics of failure accumulation in the polymer composite structure exposed to static loading under tensile loads can also be used in analyzing the effect of cyclic loads of various intensity. At the same time, in addition to calculating the kinetics of failure accumulation in each individual loading area, it becomes necessary to take into account the total number of deformation acts determining a gradual failure accumulation throughout the tests.

References

1. Bondar, V.S., Danshin, V.V., Makarov, D.A.: Mathematical modelling of deformation and damage accumulation under cyclic loading. PNRPU Mech. Bull. **2**, 125–152 (2014). https://doi.org/10.15593/perm.mech/2014.2.06
2. Gots, A.N., Glinkin, S.A.: Review of models of fatigue fracture under cyclic loading. Fundam. Res. **9**(3), 478–482 (2016)
3. Gorokhov, V.A.: Numerical modeling of the processes of elastic-viscoplastic deformation and destruction of structural elements under quasi-static thermosilic, cyclic and thermoradiative effects. Ph.D. thesis, UNN (2018)
4. Kirillov, V.N., Efimov, V.A., Shvedova, A.K., Nikolaev, E.V.: Investigation of the influence of climatic factors and mechanical loading on the structure and mechanical properties of PCM. Aviat. Mater. Technol. **4**(21), 41–45 (2011)
5. Gladkikh, A.V., Kurs, I.S., Kurs, M.G.: Analysis of the data of full-scale climatic tests combined with the application of operational factors, non-metallic materials (overview). Proc. VIAM **10**(70), 74–82 (2018). https://doi.org/10.18577/2307-6046-2018-0-10-74-82
6. Nesterova, T.A., Nazarov, I.A., Barbotko, S.L., Volny, O.S., Platonov, M.M.: Investigation of the influence of operational and climatic factors on the properties of the material for the balloon of the pneumatic ladder for emergency exit of the helicopter cabin. Proc. VIAM **6**(54), 94–101 (2017). https://doi.org/10.18577/2307-6046-2017-0-6-11-11
7. Yerasov, V.S., Nuzhny, G.A.: Rigid loading cycle during fatigue tests. Aviat. Mater. Technol. **4**(21), 35–40 (2011)
8. Nizina, T.A., Selyaev, V.P., Nizin, D.R., Balykov, A.S., Korovkin, D.I., Kanaeva, N.S.: Application of fractal analysis methods in the study of mechanisms of deformation and fracture of composite building materials. IOP Conf. Ser **456**, 012058 (2018)
9. Nizina, T.A., Nizin, D.R., Kanaeva, N.S., Kuznetsov, N.M., Artamonov, D.A.: Applying the fractal analysis methods for the study of the mechanisms of deformation and destruction of polymeric material samples affected by tensile stresses. Key Eng. Mater. **799**, 217–223 (2019)
10. Nizina, T.A., Nizin, D.R., Kanaeva, N.S.: Statistical analysis of the frequency of damage accumulation in the structure of epoxy composites under tensile loads. Lect. Notes Civil Eng. **95**, 1–8 (2021)
11. Nizin, D.R., Nizina, T.A., Kanaeva, N.S.: Kinetics of failure accumulation in polymers under the cyclic loads. In: AIP Conference Proceedings (2022)

Research Methods for Flame Retardant and Construction and Technological Properties of Protective Coatings

V. A. Absimetov(✉) , E. V. Saltanova , and S. V. Drokin

Belgorod State Technological University Named After V.G. Shukhov, Belgorod, Russia
absimetov57@mail.ru

Abstract. Fire protection of building structures is an integral part of the system of measures to ensure fire safety and fire resistance of buildings and structures. The scope of various methods of fire protection is determined taking into account the required fire and technical characteristics of structures, the type of the protected structure, temperature and humidity conditions of operation and production of fire protection works, aesthetic and other requirements imposed on the structures. Fire protection is designed to increase the actual fire resistance of structures to the required values and to limit the spread of fire through them. This task is performed through the use of heat shields and heat-absorbing screens, special design solutions, flame retardant compositions, technological methods and operations, as well as the use of materials of reduced flammability. The paper presents the results of studies of flame retardant, physical and mechanical, weather-resistant properties of flame retardant foaming coatings. The most effective polymer film-forming catalysts, flame retardants, fillers are given. The selection of components of flame retardant foaming coatings is made. The optimum composition for a thermally resistant foam coating layer with the introduction of mineral fillers: wollastonite (up to 20–30%) and vermiculite (up to 10%) has been determined. Attention is paid to the possibility of reducing the flammability of coatings by physical and chemical methods. It is shown that in the process of shrinkage of the foaming coating layer under the influence of high temperatures, the needle fibers of wollastonite fusing create a barrier to burnout of the remaining part of the film formation. At the same time, as the specific gravity of perchlorvinyl resin increases from 1.0 to 1.4 g/cm^3, the impact strength and adhesion increases. It has been proved, using the capacitance-ohmic method that the protective properties of coatings increase with the introduction of wollastonite and ammonium phosphate into the composition. As a result of studies, the possibility of partial replacement of expensive components of flame retardant materials, with a simultaneous increase in their weathering resistance and durability is shown.

Keywords: Fire protection · Paint coating · Efficiency

1 Introduction

Selection of a suitable method of fire protection of structures, a particular fire-retardant material or composition is made taking into account structural, operational, technological, technical and economic factors [1]. There are the following ones among them: the value of the required limits of fire resistance of structures; types of protected structures and orientation of protected surfaces in space; types of loads acting on the structure; temperature and humidity conditions of operation and work on fire protection; the degree of aggressiveness of the environment in relation to fire protection and the material of structures, as well as the degree of aggressiveness of the fire protection material in relation to steel; increasing the load on the structure due to the mass of fire protection; periods of installation of fire protection; aesthetic requirements for the structure; technical and economic indicators, etc. [2].

Flame retardant paints, varnishes, enamels delay combustion of materials, reduce the spread of flame on the surface of materials and perform the following functions: they are a protective layer on the surface of combustible materials, absorb heat from decomposition, release inhibitor gases, release water, accelerate the formation of coal [3].

Flame retardant paint compositions are divided into two groups: non-foaming and foaming. Non-foaming paints do not increase the thickness of the layer when heated. Foaming paints when heated increase the thickness of the layer by 3–20 times. They are more effective because heat causes the formation of a foamy carbon layer, which is a caked melt of some substances.

Well-known flame retardant compositions have two significant drawbacks: low water resistance, due to the presence of water-soluble components in the compositions, and high material consumption. The need to apply flame retardant compositions in thick layers, in addition to increasing the cost, reduces their physical and mechanical properties (adhesion, bending and impact strength) [4].

The main raw materials for the production of flame retardants are presented in Table 1.

Fire protection compositions are multi-component compositions containing film-forming substances, solvents, flame retardants, pigments. The most promising direction is the partial replacement of expensive components of fire retardant materials, as well as simultaneous improvement of their weathering resistance and reliability [5].

Foaming paints and varnishes are one of the most intensively developing areas in the development of compositions for fire protection of metal and wooden structures [6]. High efficiency, the possibility of using traditional methods of applying compositions to the surface of structures causes increased interest in them. The use of foaming compositions provides an increase in the fire resistance limit of building structures from 0.5 to 2 h and limits the limit of spread of fire on wooden structures [7].

The main characteristics of the proposed fire retardant compositions are presented in Table 2.

According to their functions, the main components of flame retardant foaming coatings are classified as follows: polymeric film formers; carbonizing materials (carbon

Table 1 Main raw materials for the production of flame retardants

№	Name of raw material	Type of flame retardant material	Possibility of application as a component of a flame retardant
1	Liquid glass	Varnishes, coatings	Film—forming, alkaline catalyst
2	P-646, P-647, P-4, P-5	Compositions with polymer film-forming agents	Solvents, diluents
3	Shungite, starch	Foaming coatings	Polyhydrate compounds
4	Orthophosphoric acid, ammonium phosphates, ammonium sulfates	Varnishes, impregnations, foaming coatings	acid catalysts
5	Wollastonite, vermiculite, pyrophyllite, magnesite	Foaming coatings	Fillers, blowing agents
6	Titanium dioxide, zinc white, iron oxide, ochre	Foaming coatings	Pigments

frame sources); carbonization catalysts, effective flame retardants used as acid catalysts; polyhydrate compounds formed by interaction with acid abundant carbon residue (blowing agents); fillers, pigments and other additives [8].

We used polyvinyl chloride resin PSX-L as a polymer film forming agent. In addition to the resin, the following raw materials were used:

Technical polyvinyl chloride (PVC) nCH_2 is an amorphous powder of white color. Good chemical resistance of polyvinyl chloride against many inorganic acids, alkalis and salt solutions allows its wide use for the production of various corrosion-resistant structures and chemical industry.

Pentaerythritol $C(CH_2ON)_4$ is obtained by the interaction of formaldehyde with acetaldehyde in the presence of $Ca(OH)_2$.

Vermiculite $(Mg, Ca) y (Al, Fe, Mg) z (Si, Al, Fe)_4 O10 (OH)_2 (H_2O)$ is a mineral of the hydromica group, capable of swelling when heated. It is a product of low-temperature hydrothermal processes and subsequent weathering of magnesian and magnesian-iron mica, phlogopite and biotite.

Dicyandiamide (dicyanguanidine) $HN = C[NH_2] NHCN$; melting point 209 °C; solubility in water-3.96%, obtained by treatment with $CaCN_2$; cyanamide dimerization in water-alkali solutions.

Starch—the main reserve carbon of plants. It is a mixture of two polysaccharides: linear (amylose), built from α-D-glucopyranose residues with 1–4 bonds, and branched (amylopectin), whose molecule consists of amylose fragments.

Wollastonite (board feldspar), a mineral of the pyroxene class, subclass of chain silicates, $Ca_3[Si_3 O_9]$. Calcium silicate (metasilicate). The chemical composition of wollastonite ore mined by the companies of the main countries producing wollastonite concentrates is shown in Table 3.

Table 2 Characteristics of the proposed flame retardants

№	Name of flame retardant	Construction surface	Fire resistance rating	Consumption per square meter (kg)
1	Varnish "Shield-1"	DK	1 group	0.8
2	OZS-MV	MK	0.75–2.0	13–39
3	OZS-MV	DK	1 group	1.6
4	OGRAKS-V-SK	MK	0.75 h	2.2
5	OZP-1	MK	0.75 h	4
6	OZP-1	DK	1 group	0.7
7	MVPO composition	MK	0.5–0.75	2.0–3.0
8	MVPO composition	DK	1 group	1.0
9	Fiflex-Crylac	MK	0.75	1.25
10	Fiflex-400	MK	0.75	12
11	Fiflex c-200	DK	1 group	1.5
12	Endotherm XT-150	MK	0.5–1.0 h	2.2–4.2
13	S 605	MK	0.75–2.0	1.2–4.2

Table 3 Chemical composition of wollastonite ore

Country of origin of wollastonite	Content of chemical components,%					
	CaO	SiO_2	Fe_2O_3	MgO	Al_2O_3	P.o.i
India	47	52	0.31			0.55
China	44	48	0.2			3.00
Mexico	38.4	49.82	0.96		5.34	4.56
USA	46.9	50.9	0.61	0.1	0.25	0.9
Finland	44.5	51.8	0.3	0.8	0.6	1.7
Japan	46	50	0.3	0.4	0.3	2
Kazakhstan	47	50.5	0.8	0.2	2	1.5

2 Materials and Methods

Next we will focus on methods for determining the physical and mechanical properties of protective coatings: adhesion tests; water resistance tests; method for determining the bending strength; method for determining the impact strength; tests for resistance of

flame retardant coatings in atmospheric conditions; testing of protective properties by capacitance-ohmic method [9].

Determination of fire retardant adhesion to the surface of wood and metal is carried out by the method of lattice incisions GOST 15,140-78.

In the water resistance test fire retardant is considered to have passed the test if in the process of exposure to water there was no destruction of the protective layer while maintaining the fire retardant properties of GOST 16,363-76.

The method for determining the bending strength. When using a fire retardant that forms a film on the protected surface (varnishes, paints), it is recommended to test the elasticity of the film at bending GOST 6806-73.

Method of determination of impact strength GOST 4765-73. The maximum height, falling from which at normal acceleration load of 1 kg does not cause mechanical damage to the film (cracking, crushing, flaking) was taken as the index of strength. Also we determined: drying according to GOST 19,007 to degree 3; viscosity according to GOST 8420; degree of dispersion of "rubbing" according to GOST 6589.

To determine the weather resistance of flame retardants in the laboratory, complex methods were used that simulate various climatic conditions, in which testing in artificial weather chambers is combined with additional exposure to factors such as high humidity (humid climate), chloride deposition and industrial pollution of the atmosphere with sulfates, subzero temperatures and temperature differences. The resistance of fire-resistant coatings in atmospheric conditions is assessed by the decorative and protective properties of GOST 9.407-84.

When using the capacitive-ohmic method, the coating itself is not destroyed. The method under consideration gives an opportunity to study the kinetics of destruction of paintwork on the metal in electrolytes and with its help to obtain information about the mechanism of this process. By changing the capacitance and tangent of the dielectric loss angle, and especially their frequency dependence, it is possible to judge the change in the protective properties of the coatings, their adhesion and durability under operating conditions.

3   Results and Discussions

Based on the study of reducing the flammability of organic coatings with flame retardants-additives, film-forming agents, fillers, pigments, the components of flame-retardant coatings were selected.

Obtaining flame retardant compositions can be achieved by using heat-resistant polymers with a minimum content of organic part, coking when exposed to flame. The effectiveness of flame retardant blowing composition for fire protection of metal structures is shown in accordance with Fig. 1. As evidenced by the results of fire tests of metal structures, fire resistance depends to a large extent on the thickness of the given composition. The use of flame retardant foaming composition provides fire resistance limit of metal structures: 0.5 h at a thickness of 1.0 mm; 0.75 h at a thickness of 1.5 mm; 1 h at a thickness of 2.2 mm. A further increase in coating thickness in accordance with Fig. 1 does not result in an increase in the fire resistance limit.
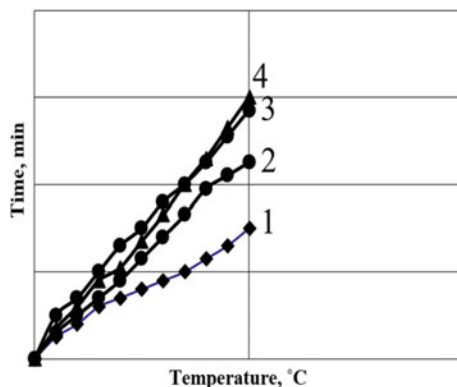
Fig. 1 Dependence of temperature on the unheated surface of the specimen on time for the composition No. 2. 1—1.0 mm thick; 2—1.5 mm thick; 3—2.2 mm thick; 4—3.0 mm thick

Composition No.2—wollastonite was used as filler, performing the role of a structural additive. The developed new composition, including wollastonite, allowed obtaining qualitatively new thermal protection properties of flame retardant foaming composition.

(1) The most promising film-forming agent for the development of flame retardant materials is chlorinated: polyvinyl chloride resin PSX-L, because during the carbonization of the resin the main decomposition product is nonflammable HCI.

(2) Phosphorus-containing flame retardants are almost the only compounds that prevent smoldering and reduce the possibility of secondary combustion of the polymer, due to the fact that the carbonized phosphorus-containing layer is very resistant to prolonged heating. When exposed to heat, phosphorus additives readily convert to phosphoric acid, forming a continuous glassy film of polyphosphoric acid on the surface of the burning polymer, acting as a barrier to the transfer of heat, oxygen and fuel.

(3) Aluminum oxide trihydrate in the composition based on polyvinyl chloride resin behaves as a fairly effective flame retardant, but the effectiveness of this flame retardant appears only when used in large quantities—up to 80% of the weight of the composition, and this causes a significant deterioration in the physical and mechanical properties of coatings.

(4) The thermal resistance of the foamed layer increases with the introduction of mineral fillers: compositions with the content of wollastonite 20–30%, vermiculite 10%. The compositions of the investigated FFC are shown in Table 4.

Laboratory specimens were prepared by applying the test composition on a metal plate with subsequent testing 1—clean plate; 2—composition №2 (with wollastonite); 3—composition №1 (with vermiculite); 4—composition №3 (with asbestos). Temperature change on the unheated surface of the sample from time is shown in Fig. 2.

The mechanism of fire protection can be represented as several simultaneous and mutually influencing processes. The greatest influence on the flame retardant properties

Table 4 Flame retardants based on perchlorovinyl resin

№	Application as	Name of component	Quantity, wt. h
1	Film-forming	12% perchlorovinyl resin PSX-LS in solvent P-4	25
	Polyhydrate compound	Pentaerythritol	10
	Acid catalyst	Ammonium phosphate	20
	Foaming agent	Dicyandiamide	10
	Plasticizer	Tricresyl phosphate	5
	Filler	Vermiculite	30
2	Film-forming	12% perchlorovinyl resin PSX-LS in solvent P-4	25
	Polyhydrate compound	Pentaerythritol	10
	Plasticizer	Tricresyl phosphate	5
	Foaming agent	Dicyandiamide	10
	Filler	Wollastonite	30
3	Film-forming	12% perchlorovinyl resin PSX-LS in solvent P-4	25
	Polyhydrate compound	Pentaerythritol	10
	Acid catalyst	Ammonium phosphate	20
	Plasticizer	Tricresyl phosphate	5
	Foaming agent	Dicyandiamide	10
	Filler	Asbestos	30

Fig. 2 Temperature change on the unheated surface of the specimen from time. 1—clean plate; 2—composition 2 (with wollastonite); 3—composition 1 (with vermiculite); 4—composition 3 (with asbestos)

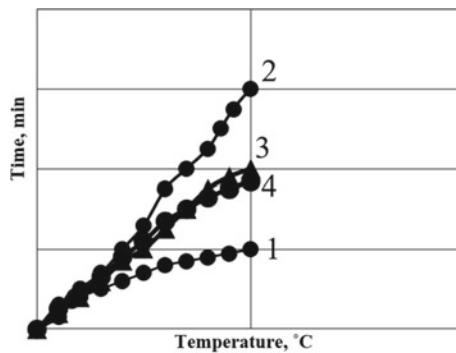is heat transfer and endothermic physical and chemical effects identified by differential thermal analysis in the heating of flame retardant compositions. Based on the above, it should be concluded that it is possible to improve significantly the flame retardant properties by reducing the average density of the coating at the initial stage of heating. This is possible only by introducing lightweight aggregates into the composition: vermiculite (composition 1), wollastonite (composition 2), asbestos (composition 3).

(1) The introduction of pentaerythritol 10% as a polyol in flame retardant compositions increases the crack resistance of the resulting foamcoke.

(2) The most effective foaming agent for flame retardant composition is dicyandiamide, because the fire retardant efficiency in the fire test reaches 45 min, the compositions with melamine—32 min, compositions with urea—28 min.

(3) It should be noted that the stable foaming of coatings is accompanied by the release of gases after the melting of the film mass, but before its solidification, before the formation of the carbonized layer.

(4) The composition of the bloating flame retardant additive was selected with certain melting and degradation temperatures of the polyol, catalyst, and bloating agents so that they reacted in a given sequence.

(5) Detailing the process of polymer combustion, allows us to outline ways to reduce combustibility by physical and chemical measures. Physical measures can include: reduction of heat input to the material by insulating shielding of its surface; cooling of the flame as a result of heat loss for decomposition and evaporation of components, heat entrainment by flowing polymer melt; creating a physical barrier between the coating and the oxidizing environment, slowing down the diffusion of combustible ingredients.

Chemical influences can include purposeful changes in the composition and structure of the polymer, the composition and ratio of the initial components of the coatings, which leads to a change in the kinetics and mechanism of the chemical reaction in the condensed and gas phases, on their interface [10].

(1) Sustainable foaming of coatings must be accompanied by the release of gases after the melting of the film mass, but before its solidification, before the formation of the carbonized layer. Therefore, the composition of the foaming flame retardant additive is selected with certain melting and decomposition temperatures of the polyol, catalyst, and foaming agents.

(2) It is possible to significantly increase the flame retardant properties of compositions based on PVC resin PSX-SL by introducing light fillers into the composition: vermiculite, wollastonite and asbestos.

(3) Tests on fire resistance showed that in the process of shrinkage of the blown coating layer under the influence of high temperatures, only needle fibers of wollostanite fused, create a barrier to the burnout of the remaining part of the film-forming agent.

(4) The study of physical and mechanical properties showed that with an increase in the specific gravity of perchlorvinyl resin from 1.0 to 1.4 g/cm^3, the impact strength and adhesion increases. The introduction of wollastonite filler increases

the hardness and strength of the flame retardant coating. However, the elasticity of the composition deteriorates with increasing amount of fillers.

(5) The results of capacitance-ohmic methods for evaluating the protective properties of flame retardant compositions showed a good insulating ability of compositions with wollastonite and ammonium phosphate. The increase in capacitance corresponds to the moment when the coating begins to break down.

4 Conclusions

Currently, the effectiveness of flame-retardant coatings for metal structures is increased by the use of lightweight materials and light fillers, foaming perlite and vermiculite, mineral fiber. But flame-retardant foaming compounds are especially effective.

Ways to improve the fire protection of structures should be aimed primarily at the reliability, durability, moisture and weather resistance of fire-resistant materials.

The choice of each method of fire protection must be made specifically for the particular conditions, taking into account:

- values of the required fire-resistance limits of structures;
- the type of load acting on the structure;
- the type of structure to be protected and their orientation in space; temperature and humidity conditions of operation;
- increasing the load on the structure due to the weight of the fire protection, aesthetic requirements for structures, etc.

References

1. Ramanenkov, I.G., Levites, F.A.: Fire Protection of Building Structures. Stroyizdat, Moscow (1991)
2. Absimetov, V.E., Kalmagambetova, A.S.: Anticorrosive and flame-retardant materials, technologies, production. In: Proceedings of the 1st Center, Asian. Geotechnical Symposium, 1, pp. 342–347. Astana (2000)
3. Absimetov, V.E., Kalmagambetova, A.S.: Anticorrosive materials for surface preparation and painting of metal structures in repair conditions. Akmolinsk polygraphy, Astana (1999)
4. Merkulov, S.I.: Development of the theory of constructive safety of objects in conditions of corrosive effects. Bulletin of BSTU named after V.G. Shukhov **3**, 44–46 (2014)
5. Absimetov, V.E., Presnyakov, N.I., Vostrov, V.K.: Development of the national and interstate regulatory technical base in metal construction taking into account the second generation of Eurocodes. Ind. Civil Eng. Mag. **12**, 6–12 (2013)
6. Solodov, N.V.: Strength and deformability in collapse in a bolted connection. Bulletin of BSTU named after V.G. Shukhov **1**, 82–87 (2017)

7. Gorokhov, E.V., Shapovalov, S.M., Udod, E.I.: Monograph Improving the Reliability and Durability of Power Grid Structures. Tekhnika, Kiev (1997)
8. Absimetov, V.E.: Proposals for the development of harmonized standards to substantiate the requirements of technical regulations for the safety of buildings and structures IOP Conference Series. Mater. Sci. Eng. **698**(2), 022025 (2019). https://doi.org/10.1088/1757-899X/698/2/022025
9. Solodov, N.V., Peshkova, E.V.: Investigation of the stability of rods. Bulletin of BSTU named after V.G. Shukhov **4**, 25–27 (2015)
10. Doronina, O.I., Shevchenko, N.Y., Bakhtiarov, K.N.: Assessment of the reliability of overhead power transmission lines taking into account climatic factors. Int. J. Appl. Fundam. Res. **9**(2), 226–323 (2015)

Methodology for the Selection of Optimal Parameters of the Finite Element Mesh in Composite Materials Calculation

Nickolay Lubimyi$^{(\boxtimes)}$, Gerasimov Mihail , Polshin Andrey ,
and Shurinov Arseniy

Department of Hoisting-and-Transport and Road Machines, Belgorod State Technological University Named After V.G. Shukhova, St. Kostyukov 46, 308012 Belgorod, Russia
`nslubim@bk.ru`

Abstract. The paper presents a methodology for evaluating the convergence of the results of composite part model calculations. The aim of the paper is to describe an algorithm for optimizing the strength calculations of the composite part structure by adjusting the parameters of the finite element mesh. The convergence is evaluated by sequentially varying the dimensions of the finite element mesh. The paper describes the difference of nonlinear calculation and its peculiarities relevant to the calculation of composite parts having surface contact of different materials. NX Nastran SolidEdge ST10 is used as the solver. Calculations of a composite specimen made of metal and metal-polymer were used to analyze the results. The parameters of the materials used in the calculations were used both from the built-in reference books and from the manufacturers' data sheets. Among the analyzed calculation data, the parameters of safety margin, deformations and stresses were used. The results of the calculations have been systematized and presented in the form of appropriate graphs. The influence of the finite element mesh size on the accuracy of the results obtained and the expediency of using a finite element mesh with minimum dimensions are evaluated. The conclusion describes recommendations for the use of the proposed methodology for use by design engineers in the development of composite and other component designs in a nonlinear analysis.

Keywords: Convergence · Finite element analysis · Metal polymer · Composite · Strength · Element mesh

1 Introduction

Finite element calculations are widely used by research engineers in the design of various products. Numerical modeling makes it possible to calculate in advance the strength of a product, its deformations, safety margins and other parameters before launching the designed product into production. There is a large variety of software products that allow performing finite element calculations [1–3]. SolidEdge, NX, SolidWorks, TFlex are some of them. Pre-calculations allow changing the design, optimizing the shape, making

other changes to the design, reducing the material intensity using generative design of the product shape [4–8]. Calculations require basic data. The basic data for calculations include: availability of a digital model of the product or assembly, knowledge of physical and mechanical material parameters of the product model under study, knowledge of load parameters and places of its application, knowledge of restrictions of model degrees of freedom. In addition to these parameters, other calculation settings, such as the size and type of the finite element mesh, etc., have a great influence on obtaining adequate calculation results. It is especially important to take into account additional settings of calculation parameters when solving the so-called "nonlinear analysis" problems, which include the problems of solving models in which geometrical and physical nonlinearity should be taken into account. This means that the properties of the model, such as plasticity, creep and other parameters change at each iteration of the calculation. Since in reality the part experiences time-varying loads, that is, the properties of the part without load and the part when loaded with half of the specified loads will be different. That is why the problems of solving nonlinear analysis require iterative problem solving. A legitimate question arises, but how much iteration is necessary and sufficient to obtain adequate results of calculations. 90% of calculations performed nowadays refer to linear analysis, because it does not take much time and computing resources. Nevertheless, for the calculation of composite parts, such as metal–metal-polymer parts [9–11], when there is surface interaction between the contact surfaces of different materials, geometric nonlinearity (deformations), exactly the solution of the nonlinear problem is required.

2 Materials and Methods

The aim of the paper is to describe an algorithm for optimizing the strength calculations of a composite part structure by adjusting the parameters of the finite element mesh. The process of solving the problem of optimization of calculation parameters of the model, described in the paper, is performed using the SolidEdge ST10 software product. In the used program NX Nastran is used as a solver, which since the mid 70 s of the last century has repeatedly proved its reliability, accuracy and speed.

The solution algorithm used in nonlinear analysis differs in that the loads are applied gradually, so the solver solves many problems iteratively, that is, the loads are applied gradually. The input data for each step in the nonlinear analysis is the previous state of the model at the previous step. It is necessary to take into account that energy parameters reflecting external and internal forces should be balanced with an admissible error (see Fig. 1), called convergence criterion. As a rule, the convergence criterion is set as a percentage of the applied loads.

The need for a multi-iteration solution is due to the fact that when loading an elastic–plastic structure at which the stress will be greater than the yield strength of the material, the solver does not independently determine at what load this stress in individual model nodes will be exceeded. Some software products allow using the "Nonlinear History" tool in the solver. This tool allows you to see a real-time graph of the solution, keep track of the number of repeated solutions produced and the level of achieved load. This graph allows you to analyze the convergence rate of the solution results. It should be noted that the NX Nastran solver used most often in SolidEdge ST10 uses the Mises
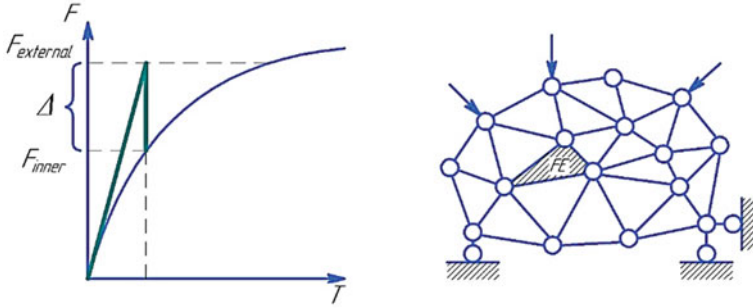
Fig. 1 The error Δ balancing the external and internal forces of the model

plasticity criterion, for a plastic material. The analysis setup window in SolidEdge ST10 looks as shown in Fig. 2. Unlike earlier versions of the software, in SolidEdge ST10 the non-linearity of the solution is specified by specifying the contacts of the two materials that make up the composite part. The iterability of the solution and its accuracy are adjusted by the corresponding tabs marked by positions 1, 2 and 3 in Fig. 2.
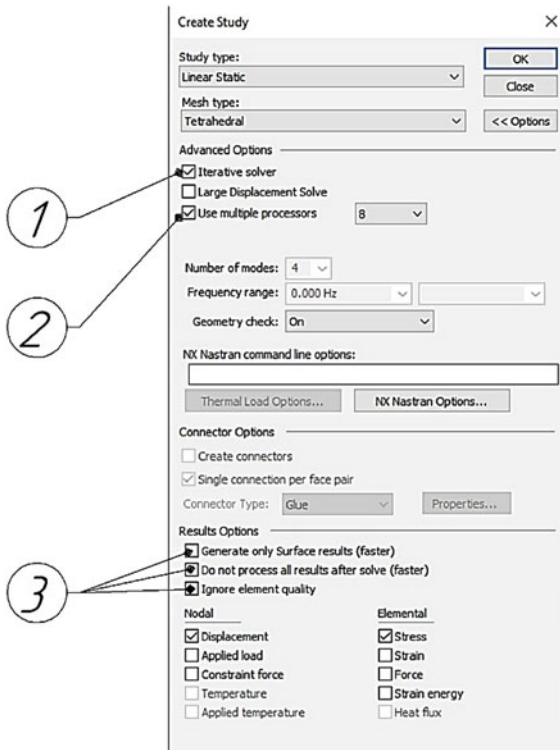
Fig. 2 Setup menu for finite element solutions in SolidEdge ST10

At first glance it seems that all parameters in SolidEdge ST10 are easy to configure and the convergence check of the solution results is also performed automatically. If the results do not converge, the solver simply displays a solution error and breaks the calculation. However, there is another condition that cannot be taken into account in automatic mode: the size of the finite element mesh. In the case of a simple model, the use of the computational resources of the model can be neglected. Optimizing the mesh size will not significantly affect the computational result and the time spent.

However, if the computational model has large dimensions, includes an assembly of different materials in contact with each other, different material properties, and complex geometry, then the creation of the finite element mesh itself, as well as the calculations, can take quite a long time and still not come together. This will lead to calculation errors and calculation interruptions. Therefore, it is very important to choose the size of the finite element mesh that will allow us to correctly calculate the model with the least amount of computational resources.

The use of an optimally sized finite element mesh will subsequently allow, by changing the material parameters of the model, to calculate quickly and accurately the composite part model in various material variations for the purpose of conducting engineering surveys.

3 Results

The method of comparing the results of calculations on different parameters of the finite element meshes is shown in Fig. 3. The lever arm model was chosen as the specimen model on which the calculations were performed.
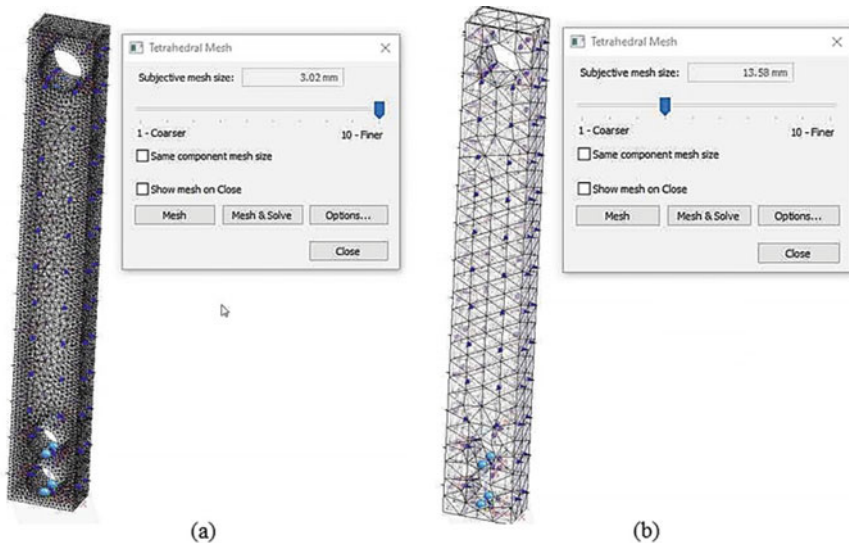
Fig. 3 Varying the finite element mesh of the lever model: level 10 (**a**), level 4 (**b**)

Calculated data for the convenience of analyzing the convergence results, the data were summarized in Table 1. Figure 4 shows the convergence plots for the stress, strain, and safety margin parameters. The graphs show the calculated parameters for each variation of the finite element mesh quality in the range from 1 to 10.

Table 1 Calculated parameters of the composite specimen

Mesh size	Deformations max, mm	Stress min, MegaPa	Stress max, MegaPa	Stress max, MegaPa	Margin of safety min	Margin of safety max
1	0.91	0.048	123	0.532	1360	0.048
2	0.917	0.0558	120	0.546	1170	0.0558
3	0.918	0.0544	116	0.567	1200	0.0544
4	0.923	0.0443	124	0.528	1410	0.0443
5	0.924	0.0464	124	0.528	1480	0.0464
6	0.928	0.0551	133	0.491	1190	0.0551
7	0.93	0.0561	129	0.507	1170	0.0561
8	0.931	0.0398	135	0.486	1640	0.0398
9	0.931	0.0429	141	0.465	1530	0.0429
10	0.931	0.0275	153	0.429	2380	0.0275

4 Discussion

Despite the fact that at any size of the finite element mesh the solution was performed without errors, the most optimal mesh size is number 7. Mesh size number 7 has the smallest safety margin, which is preferable. The deformations at number 7 reach a plateau. The maximum stresses in general differ insignificantly over the entire range of mesh size variations. According to the totality of parameters, mesh size number 7 is the most preferable. The projection relationship of the graphs on mesh size number 7 is shown by the dashed line.

5 Conclusions

The procedure described in the paper for evaluating the convergence of the results of the study based on varying the size of the finite element mesh in nonlinear analysis, allows the research engineer to evaluate the influence of the mesh size on the adequacy of the calculation results. This is most clearly shown by the convergence graph of the deformations (see Fig. 4). Increasing the quality of the finite element mesh, that is, decreasing the mesh size after level 7, does not lead to significant changes in calculation results. Consequently, decreasing the size of the finite element mesh leads to increasing
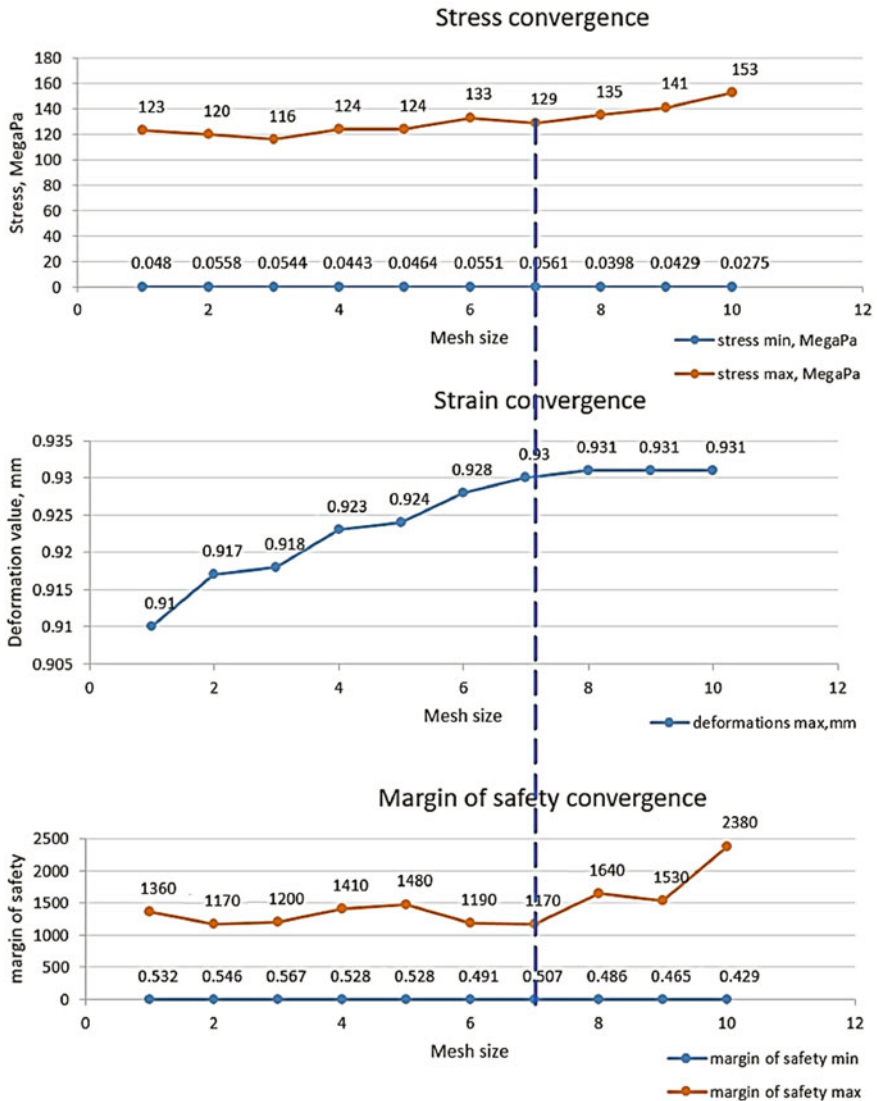
Fig. 4 Graphs of convergence of calculation results

the computational resources, increasing the computational time, but does not give any significant results of increasing the computational accuracy.

The application of the convergence analysis of calculation results while varying the quality of the finite element mesh construction, can have a significant impact on the speed of calculations, which is a key factor in designing a composite product model.

References

1. Jeng, Y.R., Liu, D.S., Yau, H.T.: Fast numerical algorithm for optimization mold shape of direct injection molding process. USA Mater. Manuf. Process. **6**, 689–694 (2013). https://doi.org/10.1080/10426914.2012.727119

2. Lubimyi, N.S., Chepchurov, M.S., Evtushenko, E.I., Voronenko, V.P.: Calculation of fixing element of metal-polymeric mold-forming surface of mold in metal cage. Actual Issues Mech. Eng. **133**, 433–438 (2017). https://doi.org/10.2991/aime-17.2017.70

3. Lubimyi, N.S., Polshin, A.A., Gerasimov, M.D., Tikhonov, A.A., Antsiferov, S.I., Chetverikov, B.S., Ryazantsev, V.G., Brazhnik, J., Ridvanov, I.: Justification of the use of composite metal-metal-polymer parts for functional structures. Polymers **14**, 340–352 (2022). https://doi.org/10.3390/polym14020352

4. Khan, S., Gunpinar, E., Moriguchi, M., Suzuki, H.: Evolving a psycho-physical distance metric for generative design exploration of diverse shapes. J. Mech. Des. Trans. ASME **141**, 111101 (2019). https://doi.org/10.1115/1.4043678

5. Nisar, M.M., Zia, S., Fenoon, M., Alquabeh, O.: Generative design of a mechanical pedal. Int. J. Eng. Manag. Sci. **6**, 48–58 (2021). https://doi.org/10.21791/ijems.2021.1.5

6. Shrestha, P.R., Timalsina, D., Bista, S., Shrestha, B.P., Shakya, T.M.: Generative design approach for product development. In: Proceedings of the AIP Conference Proceedings 2397 (2021)

7. Leary, M.: Generative design. Des. Add. Manuf. 203–222 (2020) https://doi.org/10.1016/B978-0-12-816721-2.00007-5

8. Filippo, A. Di, Lombardi, M., Marongiu, F., Lorusso, A., Santaniello, D.: Generative design for project optimization. In: 27th International DMS Conference on Visualization and Visual Languages, KSIR Virtual Conference Center, USA, June 29–30, (2021). https://doi.org/10.18293/DMSVIVA21-014

9. Jahan, S.A., Hazim, E.M.: Optimal conformal cooling channels in 3D printed dies for plastic injection molding. Procedia Manuf. **5**, 888–900 (2016). https://doi.org/10.1016/j.promfg.2016.08.076

10. Liang, J., Narahara, H., Koresawa, H., Suzuki, H.: Verification and evaluation of automatically designed cooling channels for block-laminated molds. Int. J. Adv. Manuf. Technol. **75**, 1751–1761 (2014). https://doi.org/10.1007/s00170-014-6260-2

11. Romanovich, A.A., Ebrahim, A., Romanovich, M.A.: Improving the efficiency of the material grinding process. IOP Conf. Series: Mater. Sci. Eng. **945**, 012060 (2020). https://doi.org/10.1088/1757-899X/945/1/012060

Review Study of Recycled Aggregate Concrete Column Under Eccentric Loading

Al-K. A. F. Qasim , A. I. Nikulin$^{(\boxtimes)}$, and M. Z. Zahidi

Department of Civil Conctruction, Belgorod State Technological University Named After V.G. Shukhov, Kostyukov St., 46, Belgorod 308012, Russia
nikulin137@yandex.ru

Abstract. The construction process is one of the main sources of consumption of a lot of raw materials which causes a huge amount of waste around the world. Finding reusable materials has become a challenge for many countries around the world. This paper presents a literature review that includes several experimental studies dealing with the behavior of reinforced columns using recycled aggregate concrete. Among the most important variables that have been focused on is the ratio of recycled aggregate concrete, centricity, and eccentricity of the applied loads, in addition to the behavior of columns using this type of concrete. Based on the results obtained from previous studies, it was shown that the comparison between normal reinforced concrete and recycled aggregate concrete showed a little difference in the performance and behavior, as concrete with recycled gravel has a structural performance that is slightly lower than normal reinforced concrete, which emphasizes the need to use concrete with recycled aggregate. Recycled in construction applications. In addition, the percentage of water content in concrete with recycled aggregates must be taken into account, as it is preferable that the water content must be enough in purpose of the saturation of aggregates well to provide a high resistance close to the resistance of natural concrete.

Keywords: Reinforced recycled aggregate concrete · Compressive behavior · Columns · Eccentricity

1 Introduction

At the beginning of the previous century, the productivity of factories doubled several times as a result of the increase in the world population, in addition to the migration from the countryside to the cities and the expansion of cities which calls for the need to use reusable materials again, to preserve the environment on the one hand, and to save the construction cost of buildings that require high costs. According to Franklin Associates [1] in the USA, the waste generated from construction operations amounted to 136 tons of building and demolition materials, which while this amount increased until 2003 to 170 million tons. A total of 39% of the waste material as a result of the residential building and 61% by the non-residential sources [2].

The amount of debris was calculated by Bossink and Brouwers [3], during which it was found that the amount of debris resulting from building houses in the Netherlands

is 9% of the materials purchased. This percentage is considered a high percentage, which economists consider to be a high percentage of losses and squandering, and these materials need to be reused in order to benefit from them. The study, which dealt with several models, concluded that between 1 and 10% of the materials used are finished with It leads to waste that cannot be used again, which causes environmental and economic damage. According to several previous studies, the most important study is presented by Sáez et al. [4], Europe produced quantities of industrial and construction waste estimated at 890 million tons. In Asia, Seo and Hwang [5] reported that the volume of C and D debris in Seoul, South Korea's capital, was over 8.63 million tons in 1999 and would continue to rise in the coming years. The following statistics demonstrate how serious the construction industry's environmental impact is: (1) Energy consumption of building industry accounts for 25–40% of global usage of energy. (2) Waste from the construction industry accounts for 20–40% of overall debris. (3) One-third of all noise comes from building projects. (4) Cement industry is responsible for 7% of total CO_2 emissions. Research on recycling construction materials, notably Waste construction materials such as concrete which began early in affluent and developed countries such as the United States, Japan, and several European countries. The recycling rate of waste concrete in these countries currently exceeds 90%. Despite the massive amount of building waste generated by war actions in Iraq, this ratio remains modest. Usage of recycled aggregates concrete (RAC) has become more common, especially in normal concrete and pre-stressed concrete, but the effect of recycled aggregate on the general behavior of concrete needs more and extensive studies, as its presence reduces workability, shrinkage and creep. According to the obtained outcomes from the previous studies, its found that comparing the results between recycled aggregate concrete and normal concrete, it was found that the structural behavior of recycled aggregate concrete is weaker than that of normal concrete because its mechanical properties are weaker. Recycled aggregate concrete lacks some characteristics such as the high deformability of normal concrete, in addition to its durability and ductility, which makes some designers retract the idea of using recycled aggregate concrete in construction projects, especially those that require high specifications and requirements. Recycling and re-use materials will provide great advantages and benefits for the composite building in addition to its role in protecting the environment in the disposal of debris. Waste concrete is mostly sourced from the following sources, according to research conducted in various countries:

(1) The largest source of concrete waste was discovered to be buildings that had reached the end of their useful lives and had been demolished. (2) Demolition waste concrete produced as a result of eminent domain or municipal planning changes. This form of waste concrete is becoming more prevalent as a result of fast economic growth and urbanization. (3) The debris generated on the construction site during the building of a new structure [6].

2   Materials and Methods

Due to the physical properties differences between coarse recycled aggregates (CRA) and natural coarse aggregates, the quality, performance, and behavior of concrete will be different as a result of the above difference. The most essential mechanical characteristic

of RAC is compressive strength, which acts as a foundation for evaluating other mechanical parameters. According to researchers Buck [7], Sri and Tam [8], and Gupta [9], it found that recycled concrete is weaker than normal concrete in term of the compressive strength but It is possible to increase the recycled concrete trength of to the same level as that of conventional concrete through a treatment of concrete that improves the strength of concrete to a higher level. According to Nixon [10], the compressive strength of RAC has been reduced by 20% when the concrete was replaced by recycled concrete. Subsequently, similar effects were reported in the lab tests by Bcs[11], and the compressive strength of RAC was found to decrease from the NAC by 14–32%. When Wesche and Schulz [12] evaluated the test findings from Buck [7] and Frondistou-Yannas [13] at an early stage, they determined that the compressive strength of RAC was around 10% lower than NAC. Sri and Tam [8] concluded that when RAC was compared to NAC, the compressive strength of RAC reduced by 8–24%. Gerardu and Hendriks [14] claimed that RAC's compressive strength is approximately 95% that of NAC. In according to Hansen [15], the compressive strength of RAC is usually 5–24% lower than that of NAC. While the conclusion of researchers Mandal and Gupta [16] was similar, they concluded that the compressive strength of RAC at any curing time is approximately 15% lower than the compressive strength of NAC.

But some researchers had an opinion and conclusion contrary to what the previous researchers mentioned, where they discovered that recycled concrete had an 8.5% better compressive strength than normal concrete as presented by Yoda et al. [17], while Ridzuan et al. [18] added a conclusion that it is higher by about 2–20% than the compressive strength of ordinary concrete Hansen and Narud [19] and Salem[20] have also confirmed this conclusion. When the water-cement ratio (w/c) is lower, Gupta test showed that RAC's compressive strength is lower than the NAC. As a result of the high absorption of water by the reused aggregate, this is due to the cement mortar sticking to the surfaces of the recycled aggregate, and this would cause the concrete mixture to lose water content, making it less resistant than enough to complete the reaction inside the concrete [9]. Increase of w/c leads to larger RAC's compressive strength, and RAC's compressive strength does not drop when the w/c ratio rises. When the w/c ratio is 0.6, RAC has the highest compressive strength, and when the w/c ratio is 0.55, it has the lowest compressive strength. The replacement Proportion of RCA, the proportion of recycled fine aggregates (RFAs), the source of RCA, the w/c ratio, and other parameters all influence the compressive strength of RAC, according to all of the current research.

Regarding the other mechanical properties, and according to Ahmad et al. [21], the splitting tensile strength of RAC is nearly comparable to that of NAC, however, Ikeda et al. [22] revealed that the tensile strength of RAC is 6% less than those of NAC. RAC has a 10% lower splitting tensile strength than NAC, according to Hansen [19], and Ravindrarajah et al. [23]. Salem [20] showed that the mathematical approaches of the ACI code that used to obtain the mechanical properties such as the tensile and compressive strength can be used to obtain the mechanical properties of the RAC. In addition to the effect of water content on the compressive strength of recycled concrete, the tensile strength of the concrete itself is also affected by the decrease in its water content. Lower water content causes lower the tensile strength of the reused concrete,

according to Gupta [9]. Moreover, it was revealed that the tensile strength increase produced by RAC curing is the same as that produced by NAC curing.

In a test conducted by Ahmad et al. [21] and Ikeda et al. [22], the flexural strength of RAC was shown to be substantially similar to that of NAC. Ravindrarajah et al. [23], Mandal and Gupta [16] claim that the flexural strength of RAC is 10% lower than that of NAC. RAC's flexural strength, was 12.5–20% of its compressive strength, according to Bcs [11], which is nearly the result of that NAC. Salem [20] showed that the relationship between the tensile strength and the compressive strength of NAC, when applied to RAC, is too conservative according to ACI standards. Gupta [9] had expressed his opinion regarding the mechanical properties of recycled concrete, where he investigated the effect of the water-cement ratio when he found that whenever water reduction occurs, the flexural strength also decreased when compared to ordinary concrete. Concerning the strength of concrete towards compressive strength and axial loads, the researchers Ajdukiewicz and Kliszczewicz [24], Choi and Yun [25], and Hao et al. [26] studied the effect of using recycled gravel concrete on the behavior of concrete columns.

In 2012, Choi and Yun [25] investigated the behavior of $40 \times 40 \times 200$ cm columns used the pre-saturation equivalent effective water approach. The ratio of recycled aggregate was (0%, 30%, 60%, and 100%) was utilized in the tested columns. Ajdukiewicz and Kliszczewicz [24] investigated three distinct classes of concrete compressive strength (25, 45, and 95 MPa) with a size of $15 \times 15 \times 90$ cm. To manufacture the test specimens, they considered three main types of RCAs, namely: rounded river sand mainly of quartz, crushed basalt, and crushed granite. In high-strength RAC mixes basalt ($w/c = 0.216$) and medium-strength granite ($w/c = 0.36$), Ajdukiewicz and Kliszczewicz [24] used the equivalent total water approach, while in the rest mixes they used the equivalent effective water approach.

Hao et al. [26] used the equivalent effective water methodology with compensating water and $w/c = 0.315$ to analyze a set of concentrically and eccentrically loading columns with diameters of 15, 20, and 140 cm, with recycled aggregate proportion (r) 50 and 70%. Figures 1 and 2 illustrate the compressive behavior of RRAC columns at both the material and structural levels from the experiments previously reported. In the figure's caption, the w/c employed in various experiments is indicated. For simplicity of comparison, it is advisable to adopt the same terminology as presented by Ajdukiewicz and Kliszczewicz [24]. The relationship between the compressive strength ratio of RAC mixes at the material level and r is depicted in Fig. 1. The compressive strength ratio compares the compressive strength of an analogous NAC to the compressive strength of a RAC with a particular r value.

It is important to note that when producing recycled aggregate, it will be noticed that there are quantities of cement mortar stuck to the aggregate, which makes its ability to absorb water higher than natural concrete. It was found that keeping the water percentage less than 0.36, increasing the proportion of recycled aggregate becomes more effective in increasing the concrete's resistance, but the excessive increase in water at a rate higher than 0.36 will reduce the concrete's resistance. RAC mixes developed with the equivalent total water method have compressive strength ratios greater than 1. Because of the significant water absorption of these RAC mixes, the effective w/c ratio decreases, resulting in an increase in compressive power [27]. The ultimate axial load capacity ratio
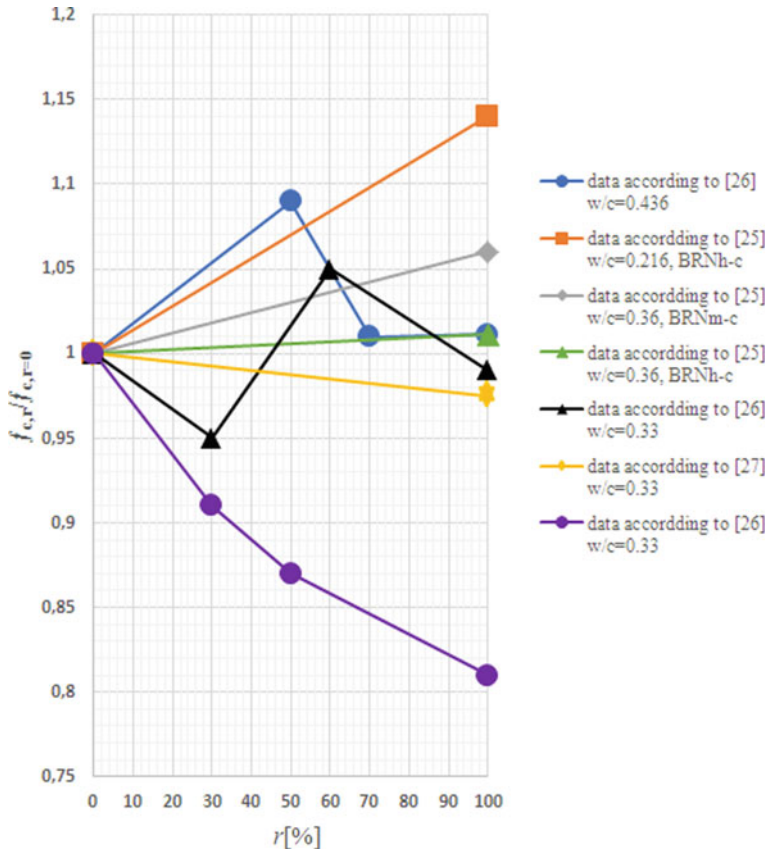
Fig. 1 RCA content influence on the compressive strength of recycled concrete

compares the ultimate axial load capacities of an RRAC column with a given r value to those of an identical RNAC column. Figure 2 shows that increasing r decreases the axial load capacity of RRAC columns. In some cases, the ultimate axial load power ratio of RRAC columns is significantly higher than unity. The compressive strength of columns $f_{c,r}/f_{c,r=0}$, ranges from 0.78 to 1.13 (Fig. 1), while their ultimate axial load capacity, $P_{u,r}/P_{u,r=0}$, ranges from 0.85 to 1.01. (Fig. 2).

The influence of stirrups beside the longitudinal reinforcement is significant on the behavior of the RRAC and RANC. According to Choi and Yun [25], the value of the Poisson ratio for the recycled aggregate concrete is 0.2 which is independent of the recycled aggregate proportion. Regarding the failure mode, Ajdukiewicz and Kliszczewicz [24], Choi and Yun [25]; Hao et al. [26] proved that tested column under axial concentric load revealed the same behavior regardless of the percentage of recycled aggregates.

Despite the importance of studies on the recycling and reusing of aggregates due to their economic and environmental benefits, there are a few studies that investigated the compressive strength of concrete columns with recycled aggregates. One of the
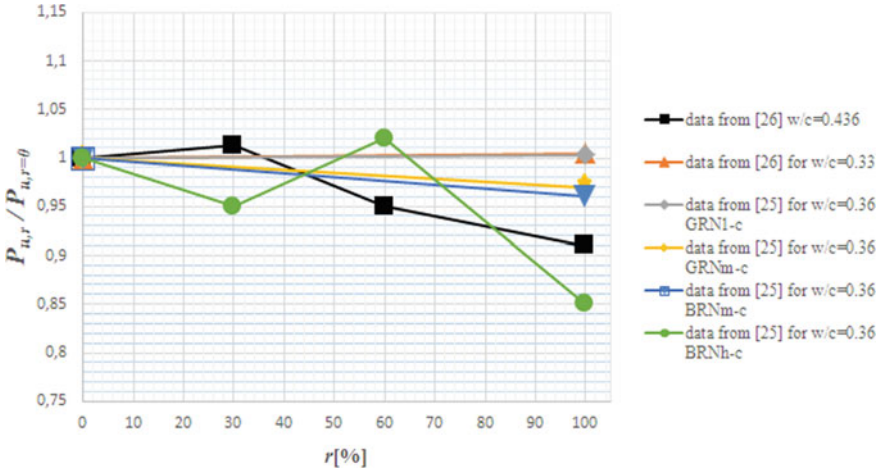
Fig. 2 RCA content influence on the axial load capacity of recycled concrete

important studies that dealt with the study of concrete columns with recycled aggregate exposed to eccentric loads with e equal to 0, 6, 9.4, and 1.4 cm with using of recycled aggregates ratios of (0, 50, and 70%). The effect of the used variables is illustrated in Fig. 3. In general, as e increases, the axial load capacity decreases [26].
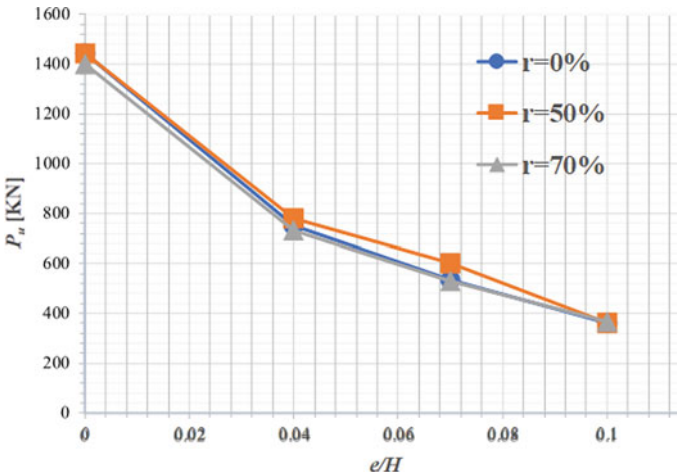
Fig. 3 The influence of the eccentricity's ratio on RRAC axially loaded columns [26]

3   Results and Discussions

Regardless of the eccentricity of the load, RRAC and RNAC columns have the same axial ultimate strength capacity. The presence of eccentricity in the loading of columns greatly

affects the failure pattern of concrete columns, as the greater the eccentricity distance (140 mm), the failure will occur with more brittleness, as crushing of concrete occurs with the reach of the rebar to the yield stress, while it was not observed that the steel reached the yield stress by reducing the eccentricity to 60–94 mm. Concerning the effect of the proportion of recycled aggregates, it directly affects the strength of the column against the axial loads, which increase the recycled aggregate caused a decrease in the strength capacity of the column as shown in Fig. 2. Khelil A et al. [28] presented a study to investigate the effect of the proportion of recycled aggregates on the behavior of concrete columns with the manufacture of a reference column in which natural aggregates were used, as shown in Table 1.

Table 1 Load–displacement details

Columns	Formulations	0R-0R	30R-30R	0R-100R	100R-100R
Experimental	Ultimate load (kN)	502.0	500.0	475.0	431.0
	Maximum displacement (mm)	2.620	4.480	2.960	4.850
Numerical eccentricity	Ultimate load (kN)	535.0	522.0	522.0	535.0
	Maximum displacement (mm)	3.10	3.20	3.20	3.0
Numerical adapted eccentricity	Ultimate load (kN)	535.0	524.0	524.0	417.0
	Maximum displacement (mm)	3.10	3.20	3.20	5.0

An eccentric compression loading mechanism was developed for the testing of the columns and for determining the effects of proportions of recycled fine and coarse aggregations on the compression behavior. The analysis showed good findings were achieved for low-recycled concretes; however, the behavior law appeared to be flawed for more extensively recycled concretes. Regardless of the recycled material ratios, the damage mechanism of the several studied columns was the same experimentally and numerically. According to the results of the last-mentioned study, under concentric and eccentric loads, RRAC columns respond similarly to RNAC columns in terms of crack development and failure pattern. As r rises, the maximum axial load capacity diminishes slightly. RRAC columns have a higher concrete strain than RNAC columns, indicating that RACs have a lower stiffness. In terms of eccentric loading, RRAC columns perform similarly to RNAC columns. The increase in *e* leads to a decrease in the maximum axial load capacity. Due to the lack of suggested methods that can be used to determine the ultimate load capacity of RRAC columns taking into account the variation of recycled aggregate concete structural properties, specially the modulus of elasticity, it can be suggest to use the methodology proposed by the authers in recently published article [29]. The proposed new approach to improving the methodology for calculating the ultimate load of eccentrically compressed reinforced concrete elements with different eccentricities

loading cases. The developed technique is based on a modified deformation model version for the resistance internal forces of reinforced concrete. Main feature of this model is the energy approach to transforming reference diagrams of concrete in compression and tension of into non-uniform deformation diagrams, identical to the stress–strain state of concrete compressed and stretched zones in the cross section of reinforced concrete structures subjected to eccentrical compression. Thus, by this method, no falling branch in the obtained concrete diagrams. For steel reinforcement deformation diagram with a physical yield point a calculation partial function was taken consisting of one linear and two non-linear equations. Based on the suggested methodology the authors developed design software named KOLON_1 for the personal computer registered by Russian Federal Service For Intellectual Property with a registeration number (2,020,616,266). The advantage of the developed software that the more easier strict use the ectual testing properties of the RCA concrete which may be different for each concrete mix used to manufacture RRAC columns. The program is designed to calculate the strength and crack resistance of eccentrically compressed hinged reinforced concrete elements of rectangular cross-section at small [30] and large [29] eccentricities of application of the longitudinal force, considering the bending of the center line. It can be seen from the results as shown in Table 2 that calculated bearing capacity using program KOLON_1 is more accurate with comparsion to the experimental and calculation results given by study [26], this accuracy is recommended with the use of RCA concrete due to the variation of recycled concrete aggregate properties.

Table 2 Bearing capacity comparsion of eccentrically compressed RRAC columns

Member	Experimental bearing capacity from study [26] [kN]	Calculated bearing capacity from study [26] [kN]	Calculated bearing capacity using program KOLON_1 [kN]
PZ-0-1	740	667.4	638.3
PZ-5-1	785	702.8	676.8
PZ-7-1	725	671.3	642.4
PZ-0-2	510	489.2	473.8
PZ-5-2	605	510.9	499.1
PZ-7-2	505	491.6	467.3
PZ-0-3	340	339.3	317.9
PZ-5-3	327	345.8	324.4
PZ-7-3	320	340.1	318.6

Similar comparsion results obtained from the analysis of other studies data using the developed software.

4   Conclusions

One of the most important conclusions obtained from previous studies is the value of compressive strength. It was found that when the same percentage of water is maintained, the compressive strength of both types of concrete (normal and recycled aggregates concrete) is approximately equal and without a noticeable difference. In addition, the percentage of water content in concrete with recycled aggregates must be taken into account, as it is preferable that the water content must be enough in purpose of the saturation of aggregates well to provide a high resistance close to the resistance of natural concrete. And the RAC compressive strength increase is nearly identical to that of the NAC over time. Factors such as the proportion of recycled aggregate, *w/c*, and RCA source have been shown to have a significant impact on RAC strength. RRAC columns' compressive behavior can be studied at the material level using standard specimens (such as prisms or cylinders) or at the structural level using full-scale columns. For reinforced RAC members, serviceability and limit state design criteria have yet to be defined. The creation of such guidelines is essential for their implementation. Further experimental investigation will be done by the authers to improve and proof the use the developed software for structural analysis.

References

1. Franklin Associates: characterization of building-related construction and demolition debris in the United States. EPA530-R-98–010. US Environmental Protection Agency, Washington DC, USA (1998)
2. US Environmental Protection Agency (USEPA): Estimating 2003 Building Related Construction and Demolition Materials Amounts. EPA530-R-09-222. Washington, DC, USA (2009)
3. Bossink, B., Brouwers, H.: Construction waste: quantification and source evaluation. J. Constr. Eng. Manage. **122**(1), 55–60 (1996)
4. Sáez, P.V., Merino, M.R., Amores, C.P.: Estimation of construction and demolition waste volume generation in new residential buildings in Spain. Waste Manage. Res. **30**(2), 137–146 (2012)
5. Seo, S., Hwang, Y.: An estimation of construction and demolition debris in Seoul, Korea: waste amount, type, and estimating model. J. Air Waste Manage. Assoc. **49**(8), 980–985 (1999)
6. Xiao, J.: Recycled Aggregate Concrete Structures. Springer Tracts in Civil Engineering. https://doi.org/10.1007/978-3-662-53987-3_1
7. Buck, A.D.: Recycled concrete as a source of aggregate. J. Proc. **74**(5), 212–219 (1977)
8. Sri, R., Tam, C.T.: Properties of concrete made with crushed concrete as coarse aggregate. Mag. Concr. Res. **37**(130), 29–38 (1985)
9. Gupta, S.M.: Strength characteristics of concrete made with demolition waste as coarse aggregate. In: Proceedings of the International Conference on Recent Development in Structural Engineering, pp. 364–373 (2001)
10. Nixon, P.J.: Recycled concrete as an aggregate for concrete–a review. Mater. Struct. **11**(5), 371–378 (1978)
11. Bcs, J.: Study on recycled aggregate and recycled aggregate concrete. Concr. J. **16**(7), 18–31 (1978)

12. Wesche, K., Schulz, R.R.: Beton aus aufbereitetem Altbeton-Technologie und Eigenschaften. Betontechnische, Berichte (1984)
13. Frondistou-Yannas, S.: Waste concrete as aggregate for new concrete. J. Proc. **74**(8), 373–376 (1977)
14. Gerardu, J.J., Hendriks, C.F.: Recycling of road pavement materials in the Netherlands. Dienst Weg-en Waterbouwkunde, Rijkswaterstaat (1985)
15. Hansen, T.C.: Recycled aggregates and recycled aggregate concrete second state-of-the-art report developments 1945–1985. Mater. Struct. **19**(3), 201–246 (1986)
16. Mandal, S., Gupta, A.: Strength and durability of recycled aggregate concrete. IABSE Symp. Rep. **86**(6), 33–46 (2002)
17. Yoda, K., Yoshikane, T., Nakashima, Y., Soshiroda, T.: Recycled cement and recycled concrete in Japan. In: Proceedings of the International Conference on Demolition and Reuse of Concrete and Masonry, pp. 527–536 (1988)
18. Ridzuan, A.R., Diah, A.B., Hamir, R., Kamarulzaman, K.B.: The influence of recycled aggregate on the early compressive strength and drying shrinkage of concrete. Struct. Eng. Mech. Comput. **2**, 1415–1422 (2001)
19. Hansen, T.C., Narud, H.: Strength of recycled concrete made from crushed concrete coarse aggregate. Concr. Int. **5**(01), 79–83 (1983)
20. Salem, R.M.: Strength and durability characteristics of recycled aggregate concrete (1996)
21. Ahmad, S.H., Fisher, D.G., Sackett, K.W.: Properties of concrete made with north carolina recycled coarse and fine aggregates. Center for Transportation Engineering Studies. North Carolina State University, Department of Civil Engineering (1996)
22. Ikeda, T., Yamane, S., Sakamoto, A.: Strengths of concrete containing recycled aggregate. In: Proceedings of the 2nd International RILEM Symposium on Demolition and Reuse of Concrete and Masonry, pp. 7–11. Japan, Tokyo (1988)
23. Ravindrarajah, R.S., Loo, Y.H., Tam, C.T.: Recycled concrete as fine and coarse aggregates in concrete. Mag. Concr. Res. **39**(141), 214–220 (1987)
24. Ajdukiewicz, A.B., Kliszczewicz, A.T.: Compressive behavior of reinforced concrete columns with recycled aggregate under uniaxial loading. J. Adv. Concr. Technol. **5**(2), 259–273 (2007)
25. Choi, W.C., Yun, H.D.: Compressive behavior of reinforced concrete columns with recycled aggregate under uniaxial loading. Eng. Struct. **41**, 285–293 (2012)
26. Hao, T., Zhao, L., Du, Z.: Experimental study on compressive performance of R.C. columns with recycled aggregate. Key Eng. Mater. **517,** 589–594 (2012)
27. Xu, J.J., Chen, Z.P., Ozbakkaloglu, T.: A critical assessment of the compressive behavior of reinforced recycled aggregate concrete columns. Eng. Struct. **161**, 161–175 (2018)
28. Khelil, A., Boissière, R., Al Mahmoud, F., Wurtzer, F., Blin-Lacroix, J.-L.: Experimental and numerical investigation on axial compression of reinforced concrete columns made from recycled coarse and fine aggregates. Struct. Concr. **22**(1), 1–14 (2020)
29. Nikulin, A.I., Qasim, A.-K.A.F.: Improving the methodology for calculating the bearing capacity of eccentrically compressed reinforced concrete elements based on the use of the refined curvilinear deformation diagrams of concrete and reinforcement. Mater. Sci. Forum **974**, 570–576 (2019)
30. Nikulin, A.I., Qasim, A.-K.A.F.: About the formation of the strength calculation method of the eccentrically loaded reinforced concrete elements with small excentricity. Bulletin of BSTU named after V.G.Shukhov **6**, 48–53 (2017). https://doi.org/10.12737/article_5926a05 95ccb32.33696422

Surface Modification of ZrH$_2$ with an Organosilicon Oligomer

N. I. Cherkashina$^{(\boxtimes)}$, O. V. Kuprieva , A. I. Gorodov , and D. S. Romanyuk

Belgorod State Technological University Named After V.G. Shukhov, Belgorod, Russia
cherkashina.ni@bstu.ru

Abstract. The paper presents data on the hydrophobization of the surface of powdered particles of zirconium hydride ZrH$_2$ with polyethylhydrosiloxane. The surface morphology of ZrH$_2$ particles was studied by scanning electron microscopy. The particle sizes range from 1 to 5 µm; there are nanoparticles up to 100 nm in size. The association of zirconium hydride particles into agglomerates is observed. Data on the granulometric composition of the ZrH$_2$ powder are presented. According to the granulometric analysis, the transverse particle size of zirconium hydride does not exceed 31 µm, while most of the powder (80%) has a size not exceeding 10 µm. The specific surface of the particles is 25592 cm^2/cm^3, the modal particle diameter is 7.69 µm. Schemes are presented for modifying the surface of ZrH$_2$ particles with ethylhydrosiloxane in a solution of a nonpolar solvent. The creation of a polyethylhydrosiloxane shell led to a significant increase in the wetting angle of the zirconium hydride surface from 71.5 ± 1.3° to 136.2 ± 1.6°. It was established that the modification of zirconium hydride led to a change in the hydrophilic surface to a hydrophobic.

Keywords: Zirconium hydride · Hydrophobization · Adsorption isotherm · Wetting angle · Neutron radiation · Composite material

1 Introduction

When creating composite materials, special attention is paid to the compatibility of the matrix and filler. When using highly dispersed fillers, a strong aggregation of particles occurs, which leads to a significant decrease in the physical properties of materials [1, 2]. To exclude the aggregation of highly dispersed and nanoparticles in the synthesis of composite materials, various technological methods are used [3, 4]. One of the promising methods for introducing a filler powder into a polymer matrix is ultrasonic cavitation [5, 6]. The use of ultrasonic cavitation makes it possible to carry out the physicochemical modification of the components of polymer composites, which improves the technical and operational properties of materials [7]. Despite the improved performance of composites obtained using ultrasonic cavitation, this method can not be applied to all polymers. Polymers such as fluoroplastic, polyimide, etc. are practically insoluble and therefore it is impossible to use the ultrasonic dispersion method for them. To create

composite products from sparingly soluble polymers, mixing of polymer and filler powders in dry form is most often used [8]. In [9], a new melt mixing method under a high-pressure fluid situation was presented for the synthesis of polymer composites.

For uniform distribution of filler particles in the polymer, it is also possible to use preliminary modification of the filler surface [10–12]. The purpose of the modification is to transform the hydrophilic surface of the filler particles into a hydrophobic one. An analysis of studies on the modification of the surface of highly dispersed powder components shows that the use of particles with a hydrophobic surface makes it possible to introduce up to 60 wt% filler into a nonpolar polymer matrix [13–15]. For surface hydrophobization, it is possible to use organosilicon oligomers, which form a siloxane shell on powder particles during polycondensation [16–18].

This paper presents data on surface modification of zirconium hydride. Zirconium hydride is a promising material for protection against neutron radiation [19, 20]. The development of polymer composite materials with zirconium hydride as a filler will make it possible to create effective protective materials. Such materials can be used both for biological protection at nuclear power plants and for protecting astronauts from secondary neutron radiation in the living compartments of the spacecraft.

2   Methods and Materials

Zirconium hydride ZrH_2 powder (Hebei Suoyi New Material Technology Co., Ltd, China) was used for the study. The chemical elemental composition of zirconium hydride is presented in Table 1.

Table 1 Chemical elemental composition of zirconium hydride

Chemical composition	Test results (%)
Fe	0.12
Si	0.023
Al	0.025
Ni	0.0071
Cu	0.014
Mg	0.012
Ca	0.014
Cr	0.0077

The powder was modified by creating a polyethylhydrosiloxane shell on the surface of zirconium hydride particles. The modification was carried out by dissolving the polyethylhydrosiloxane in a non-polar solvent. Then, powdered zirconium hydride was added to the resulting solution, and the suspension was shaken for 60 min. at a temperature of 25 °C and the precipitate was separated. The equilibrium concentration was

determined from the calibration curve. Optical density was measured using a SmartSpec Plus spectrophotometer (Bio-Rad Laboratories, Inc., USA).

To study the surface morphology of zirconium hydride particles, a MIRA3 TESCAN scanning electron microscope (Tescan, Czech Republic) was used.

Granulometric analysis of zirconium hydride powder was studied using an Analysete 22 Nano Tec Plus diffraction analyzer (Fritsch GmbH, Germany).

The contact angle was determined by the sessile drop method using a Krüss DSA30 instrument (KrüssGmbH, Germany).

3   Results and Discussion

Figure 1 shows the SEM-image of the initial particles of zirconium hydride.
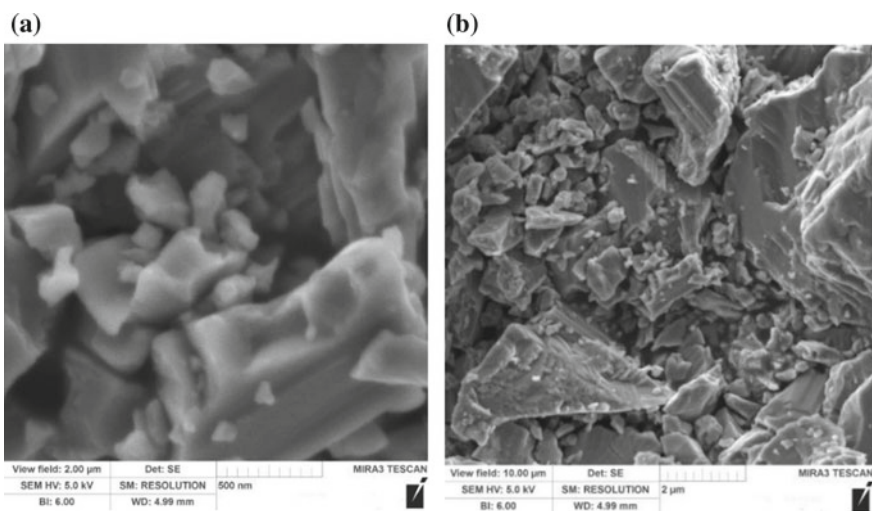
Fig. 1 SEM-image of zirconium hydride particles

According to the SEM data (Fig. 1), it can be seen that most of the particles have an irregular shape. Sometimes there are elongated particles. The dimensions of the largest side of the particles range from 1 to 5 μm. In addition, there are nanoparticles with a size of up to 100 nm. The association of zirconium hydride particles into agglomerates is observed. Figure 2 presents data on the granulometric composition of zirconium hydride powder. The measurements were carried out in distilled water using ultrasonic treatment and Dusazin 901 dispersant.

According to the granulometric composition, the transverse particle size of zirconium hydride does not exceed 31 μm, while most of the powder (80%) has a size not exceeding 10 μm. The specific surface of the particles is 25,592 cm²/cm³, the modal particle diameter is 7.69 μm.

To modify the surface of zirconium hydride, a polyethylsiloxane liquid dissolved in a nonpolar solvent was used. Hexane was used as a nonpolar solvent. It is known that when
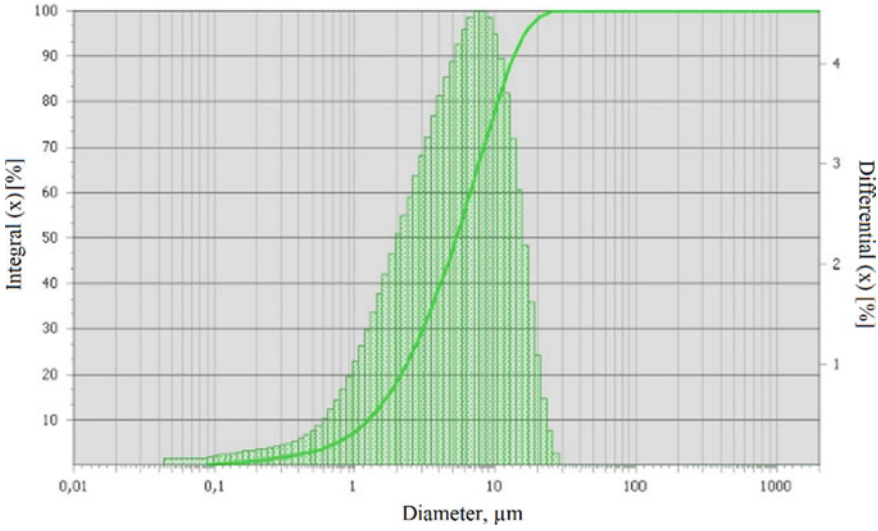
Fig. 2 Granulometric composition of zirconium hydride

hydroxides of materials are treated with ethylhydrosiloxane, the formation of a water-repellent hydrophobic surface film can occur as a result of the interaction of the Si–H bond of the hydrophobizator with the (–OH) group in the hydroxide [21]. Therefore, to create groups (–OH) on the surface of zirconium hydride, the powder was treated in a boiling water layer. Processing in a fluidized bed leads to forced hydroxylation of the surface according to Scheme (1):

$$\text{ZrH}_2 \quad \Bigg| \quad + \ \text{H}_2\text{O} \quad \longrightarrow \quad \text{ZrH}_2 \ - \ \Bigg|{\overset{\text{—OH}}{\underset{\text{—OH}}{}}} \tag{1}$$
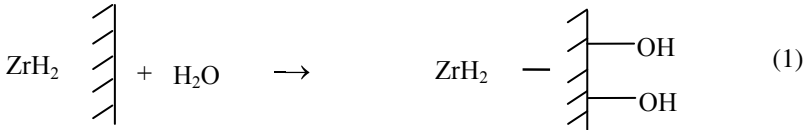
A significant role in the formation of a hydrophobic surface during the treatment of materials with ethylhydrosiloxane is played by the ability of the Si–H bond to hydrolyze and transform into the Si–OH bond in the presence of a catalyst. In the work, metal oxides were used as a catalyst. Then the hydrolysis of ethylhydrosiloxane occurs according to Scheme (2).

$$
\begin{array}{ccc}
\overset{|}{\text{OH}}\!-\!\text{Si}\!-\!\text{C}_2\text{H}_5 & & -\text{O}\!-\!\overset{|}{\text{Si}}\!-\!\text{C}_2\text{H}_5 \\
| & \text{Me}_x\text{O}_y & | \\
\text{O} & & \text{O} \\
| & + \text{H}_2\text{O} \longrightarrow & | \quad + \text{H}_2 \\
\overset{|}{\text{OH}}\!-\!\text{Si}\!-\!\text{C}_2\text{H}_5 & & -\text{O}\!-\!\text{Si}\!-\!\text{C}_2\text{H}_5 \\
| & & |
\end{array}
\tag{2}
$$
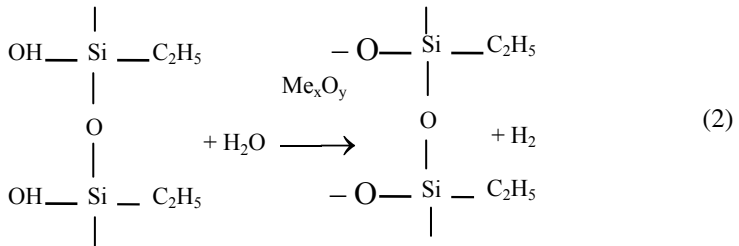
It can be assumed that the adsorption of oligoethylhydrosiloxane on the surface of zirconium hydride occurs due to the presence of (–OH) groups on its surface, obtained

by treating the powder in a fluidized bed and interacting with the Si–OH bonds of the oligomer. The proposed interaction scheme is shown in Scheme (3):

$$
\text{ZrH}_2 \!\!\begin{array}{c} \text{—OH} \\[1.5em] \text{—OH} \end{array} \;+\; \begin{array}{c} \text{OH}—\overset{|}{\underset{|}{\text{Si}}}—\text{C}_2\text{H}_5 \\[0.5em] \text{O} \\[0.5em] \text{OH}—\overset{|}{\text{Si}}—\text{C}_2\text{H}_5 \\ | \end{array} \;\xrightarrow[{-\,\text{H}_2\text{O}}]{\text{ZrH}_2}\; \text{ZrH}_2 \!\!\begin{array}{c} \text{—O}—\overset{|}{\underset{|}{\text{Si}}}—\text{C}_2\text{H}_5 \\[0.5em] \text{O} \\[0.5em] \text{—O}—\overset{|}{\text{Si}}—\text{C}_2\text{H}_5 \\ | \end{array}
\tag{3}
$$
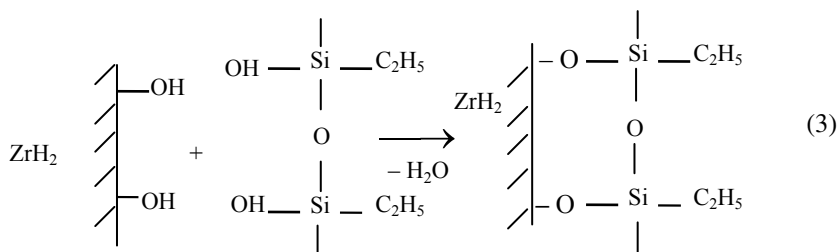
To confirm the hydrophobization of the surface of zirconium hydride, studies were carried out to measure the wetting angle before and after modification. Figure 3 shows photographs of a water drop on unmodified zirconium hydride particles (Fig. 3a) and on modified particles (Fig. 3b). It can be noted that the creation of a polyethylhydrosiloxane shell led to a significant increase in the wetting angle of the zirconium hydride surface from $71.5 \pm 1.3°$ to $136.2 \pm 1.6°$. Thus, the modification of zirconium hydride led to a change in the hydrophilic surface to a hydrophobic one.
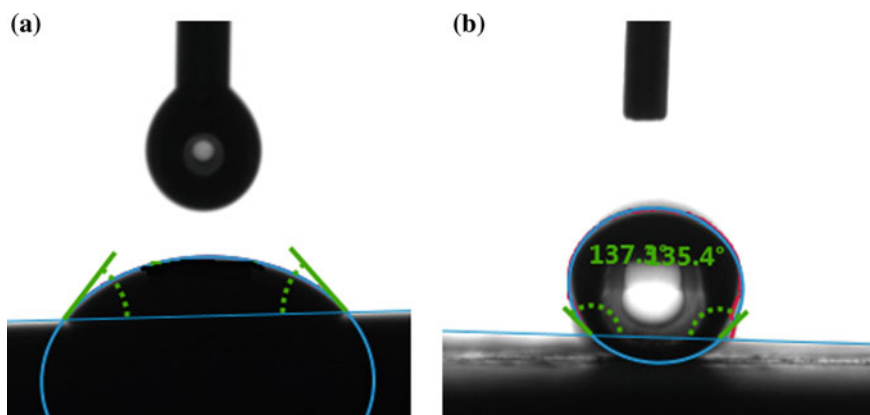
Fig. 3 Photographs of a water drop on unmodified (**a**) and modified particles (**b**) of zirconium hydride

To determine the optimal concentration of ethylhydrosiloxane in the solvent, studies were carried out to determine the adsorption of the modifier on the surface of zirconium hydride particles. It was found that at an equilibrium concentration of the oligomer up to 2.5 wt% adsorption values increase, and at concentrations of more than 2.5 wt% value is constant and amounts to 8.9 mg/g.

4   Conclusion

The possibility of modifying zirconium hydride powder with an organosilicon oligomer has been established. The modification leads to a significant increase in the wetting angle

of zirconium hydride (from $71.5 \pm 1.3°$ to $136.2 \pm 1.6°$) and transforms its surface from hydrophilic to hydrophobic.

The developed method of surface modification can be used for the synthesis of composite materials. The use of a hydrophobic zirconium hydride filler will allow it to be evenly distributed in a nonpolar polymer matrix. Polymer composites with modified zirconium hydride can be used for protection against neutron radiation both at nuclear power plants and for protection against neutrons in space.

Further research should be directed to the development of compositions and technology for the synthesis of composite materials with modified zirconium hydride.

References

1. Poovarodom, S., Hosseinpour, D., Berg, J.C.: Effect of particle aggregation on the mechanical properties of a reinforced organic−inorganic hybrid sol−gel composite. Ind. Eng. Chem. Res. **47**(8), 2623–2629 (2008). https://doi.org/10.1021/ie071563n
2. Zare, Y.: Study of nanoparticles aggregation/agglomeration in polymer particulate nanocomposites by mechanical properties. Compos. A Appl. Sci. Manuf. **84**, 158–164 (2016). https://doi.org/10.1016/j.compositesa.2016.01.020
3. Sun, Z., Yang, L., Chen, S., Wu, X.: Promoting the removal of fine particles by turbulent agglomeration with the coupling of different-scale vortexes. Powder Technol. **367**, 399–410 (2020). https://doi.org/10.1016/j.powtec.2020.03.062
4. Kochergin, Y.S., Popova, O.S., Grigorenko, T.I.: Properties of epoxy composite materials, calcium carbonate fabrics. In: Bulletin of BSTU named after V.G. Shukhov 2, pp 53–56 (2017)
5. Khmelev, V.N., Lopatin, R.A., Golykh, R.N., Minakov, V.D., Petrekov, P.V., Shalunov, A.V.: Experimental study of the influence of the ultrasonic cavitation on raw components of the polymer composite material. In: 20th International Conference of Young Specialists on Micro/Nanotechnologies and Electron Devices (EDM) 2019, pp. 175–179 (2019). https://doi.org/10.1109/EDM.2019.8823287
6. Yu, Y., Wang, J.: Preparation of graphene/PMMA composites with assistance of ultrasonic wave under supercritical CO_2 conditions. Ultrason. Sonochem. **73**, 105487 (2021). https://doi.org/10.1016/j.ultsonch.2021.105487
7. Kolosov, A.E., Sivetskii, V.I., Kolosova, E.P., Vanin, V.V., Gondlyakh, A.V., Sidorov, D.E., Ivitskiy, I.I.: Creation of structural polymer composite materials for functional application using physicochemical modification. Adv. Polym. Technol. **2019**, Article ID 3501456 (2019). https://doi.org/10.1155/2019/3501456
8. Delogu, F., Gorrasi, G., Sorrentino, A.: Fabrication of polymer nanocomposites via ball milling: present status and future perspectives. Prog. Mater Sci. **86**, 75–126 (2017). https://doi.org/10.1016/j.pmatsci.2017.01.003
9. Kihara, S., Tsukuda, Y., Asada, M., Takishima, S.: Development of polymer composites containing nano-carbon materials by highpressure fluid mixing method. AIP Conf. Proc. **2055**, 090001 (2019). https://doi.org/10.1063/1.5084879

10. Yastrebinsky, R.N., Pavlenko, V.I., Matukhin, P.V., Cherkashina, N.I., Kuprieva, O.V.: Modifying the surface of iron-oxide minerals with organic and inorganic modifiers. Middle East J. Scien. Res. **18**(10), 1455–1462 (2013)

11. Matyukhin, P.V., Pavlenko, V.I., Yastrebinsky, R.N., Cherkashina, N.I.: The high-energy radiation effect on the modified iron-containing composite material. Middle East J. Scien. Res. **17**(9), 1343–1349 (2013)

12. Fronza, B.M., Lewis, S., Shah, P.K., Barros, M.D., Giannini, M., Stansbury, J.W.: Modification of filler surface treatment of composite resins using alternative silanes and functional nanogels. Dent Mater. **35**(6), 928–936 (2019). https://doi.org/10.1016/j.dental.2019.03.007

13. Pavlenko, V.I., Zabolotny, V.T., Cherkashina, N.I., Edamenko, O.D.: Effect of vacuum ultraviolet on the surface properties of high-filled polymer composites. Inorg. Mater. Appl. Res. **5**(3), 2219–2231 (2014). https://doi.org/10.1134/S2075113314030137

14. Stöckelhuber, K.W., Svistkov, A.S., Pelevin, A.G., Heinrich, G.: Impact of filler surface modification on large scale mechanics of styrene butadiene/silica rubber composites. Macromolecules **44**(11), 4366–4381 (2011)

15. Pavlenko, V.I., Cherkashina, N.I.: Synthesis of hydrophobic filler for polymer composites. Int. J. Eng. Technol. **7**(2.23), 493–495 (2018)

16. Telysheva, G., Dizhbite, T., Paegle, E., Shapatin, A., Demidov, I.: Surface-active properties of hydrophobized derivatives of lignosulfonates: effect of structure of organosilicon modifier. J. Appl. Polym. Sci. **82**(4), 1013–1020 (2001). https://doi.org/10.1002/app.1935

17. Syrkov, A.G., Kabirov, V.R., Pomogaibin, A.P., Kkhan, N.K.: Electrophilic-nucleophilic properties as a factor in the formation of antifriction and hydrophobic properties of surface-modified metals with ammonium and organosilicon compounds. Kondensirovannye Sredy I Mezhfaznye Granitsy = Conden. Matt. Interphases **23**(2), 282–290 (2021). https://doi.org/10.17308/kcmf.2021.23/3478

18. Gökaltun, A., Kang, Y.B.(A.), Yarmush, M.L., Usta, O.B., Asatekin, A.: Simple surface modification of poly(dimethylsiloxane) via surface segregating smart polymers for biomicrofluidics. Sci. Rep. **9**, 7377 (2019). https://doi.org/10.1038/s41598-019-43625-5

19. Hayashi, T., Tobita, K., Nakamori, Y., Orimo, S.: Advanced neutron shielding material using zirconium borohydride and zirconium hydride. J. Nucl. Mater. **386–388**, 119–121 (2009). https://doi.org/10.1016/j.jnucmat.2008.12.073

20. Fantidis, J.G.: The comparison between simple and advanced shielding materials for the shield of portable neutron sources. Int. J. Radiat. Res. **13**(4), 287–295 (2015). https://doi.org/10.7508/ijrr.2015.04.001

21. Pashchenko, A.A., et al.: Hydrophobization. Institute of Colloidal Chemistry and Water Chemistry, Academy of Sciences of the Ukrainian SSR, 240 p. Naukova Dumka, K. (1973)

Formation of Copper Coating on the Surface of Titanium Hydride Using Quadruple Magnetron Sputtering

S. V. Zaitsev[(⊠)] , D. S. Prokhorenkov , N. V. Kashibadze ,
and M. V. Limarenko

Belgorod State Technological University Named After V.G. Shukhov, Belgorod, Russia
`sergey-za@mail.ru`

Abstract. Copper coating on the surface of titanium hydride shot was successfully obtained by quadrupole magnetron sputtering. The quadrupole magnetron system includes 4 rectangular magnetrons with an unbalanced closed magnetic system and a pulsed power supply. During the coating process, this system provides a significantly higher plasma homogeneity along the entire trajectory of the substrate products and the production of high-quality coatings with good adhesion. The microstructure of the copper coating was analyzed by scanning electron microscopy (SEM) and X-ray diffraction (XRD). It has been established that the thickness of the deposited coating is almost the same distributed over the entire surface of the shot and is ~986 nm. The interface between the deposited copper coating and titanium hydride shot can be traced over the entire survey area. The XRD results show that the copper coating deposited on the titanium hydride shot has a polycrystalline structure with a face-centered cubic lattice. The root mean square (RMS) surface roughness of the copper coating was ~3.67 nm.

Keywords: Surface microstructure · Titanium hydride · Copper coating · Magnetron sputtering

1 Introduction

Coating methods using plasma sources have attracted a lot of attention in many areas of industry. Magnetron sputtering is the main technology used for the deposition of various types of coatings, both high-quality metallic and multi-phase nanocomposite [1–4]. This method allows application at low temperatures, and also guarantees the reproducibility of coating properties, uniformity of their thickness and adhesion to various substrates [5–7].

Many types of magnetron systems have been developed in recent years. Each of these magnetrons has its own specific advantages and applications. The quadruple magnetron system is a well established coating process. The quadruple magnetron system includes 4 rectangular magnetron-cathodes with an unbalanced magnetic system (magnetic lines of force bypass the counter electrodes to a large extent) and with a pulsed power supply (meander). This ensures significantly higher plasma uniformity during the coating

process along the entire trajectory of the substrate products and virtually eliminates the presence of shadow zones with a low degree of ionization and a low flux density of metal atoms. In addition, due to a certain magnetic configuration and a special mode of synchronization of the magnetrons, the quadruple system generates pulsating magnetized plasma with a higher degree of ionization. An increased degree of ionization favors the implementation of phase nanosegregation in the synthesis of coatings. All this leads to the production of nanostructured coatings with unique properties and characteristics. [8, 9].

The paper presents the results of modifying the surface of titanium hydride shot by the method of quadrupole magnetron sputtering.

2 Methods and Materials

Titanium hydride shot with a diameter of 0.2–2.5 mm developed by OAO VHTRII (Moscow, Russia) was used as the material under study. In this work, titanium hydride shots were modified by depositing metallic copper (Cu) on the surface. The Cu coating was deposited in a QUADRA 500 TM vacuum unit (ElanPraktik, Dzerzhinsk, Russia) equipped with an unbalanced quadruple magnetron sputtering system. The installation diagram is shown in Fig. 1. A planetary mechanism is located in the center of the vacuum chamber, and four magnetron plasma sources are installed along its perimeter.
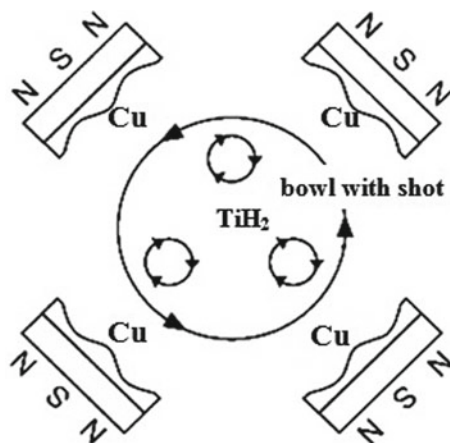
Fig. 1 Scheme of the formation of magnetron coatings on a titanium hydride shot

Before coating, the titanium hydride shot was carefully cleaned of contamination with acetone in ultrasound, then washed with deionized water and dried with dry nitrogen.

The formation of a uniform coating on titanium hydride shots used the technical solution published in the article [10]. A bowl with titanium hydride shot was installed in the vacuum chamber on the planetary mechanism at an angle of 45° from the normal position. The chamber with samples was evacuated to a pressure of 9×10^{-3} Pa. After that, using an automatic gas purge device, the working gas argon was supplied to the

chamber up to a pressure of 6×10^{-2} Pa. The bowl was turned on and ion purification was performed for 10 min at a voltage of 1800 V and a current of 110 mA. Microcontaminants were removed from the surface of the titanium hydride shot, which prevented the formation of strong bonds between surface atoms and deposited coating atoms. Vacuum pre-treatment significantly improves the adhesion of the coating to the surface of the titanium hydride shot. After the end of the ion purification process, the copper coating was deposited. The distance from the bowl with titanium hydride shot to the magnetron was 70 mm and the deposition time was 30 min. In Table 1 shows the conditions for the deposition of a copper coating.

Table 1 Copper deposition process conditions

Parameter	Description
Targets	Cu (purity 99.999%, 372 × 74 × 6 mm), 4 pcs. installed vertically
Working gas	Ar (о.ч. 99.999%)
The flow of argon in the chamber, SCCM	90
Working pressure, Pa	0.22
Discharge current of the magnetron, A	5
Voltage, V	510–514
Frequency, kHz	218
Rotation of the carousel with samples, rpm	18

The study of the morphology of the original and modified titanium hydride shots was carried out by high-resolution scanning electron microscopy (SEM) on a TESCAN MIRA 3 LMU. SEM images were taken at an accelerating voltage of 5 kV. The phase analysis was assessed using X-ray diffraction on an ARL X'TRA diffractometer (ThermoTechno) with Cu-Kα radiation ($\lambda = 0.1541744$ nm). $\theta - 2\theta$ scans were obtained in the range of 30–80° in increments of 0.05°. Phase identification and peak indexing were performed using the JCPDF database. The microrelief of the surface of the copper coating was studied using an NT MDT NanoEducator scanning probe microscope.

3   Results and Discussion

The surface of the titanium hydride shot was examined by scanning electron microscopy to determine the surface morphology. On Fig. 2 shows SEM micrographs of the initial titanium hydride shot at different magnifications. From these micrographs it can be seen that the shot has small irregularities, mainly small depressions and cracks. The presence of short cracks on the surface is explained by the presence of stresses caused by the difference in the specific volumes of titanium and hydrogen [11–13].

On Fig. 3 shows the microstructure of the surface of copper-coated shot at different magnifications. The copper coating completely covers the surface of the shot, which
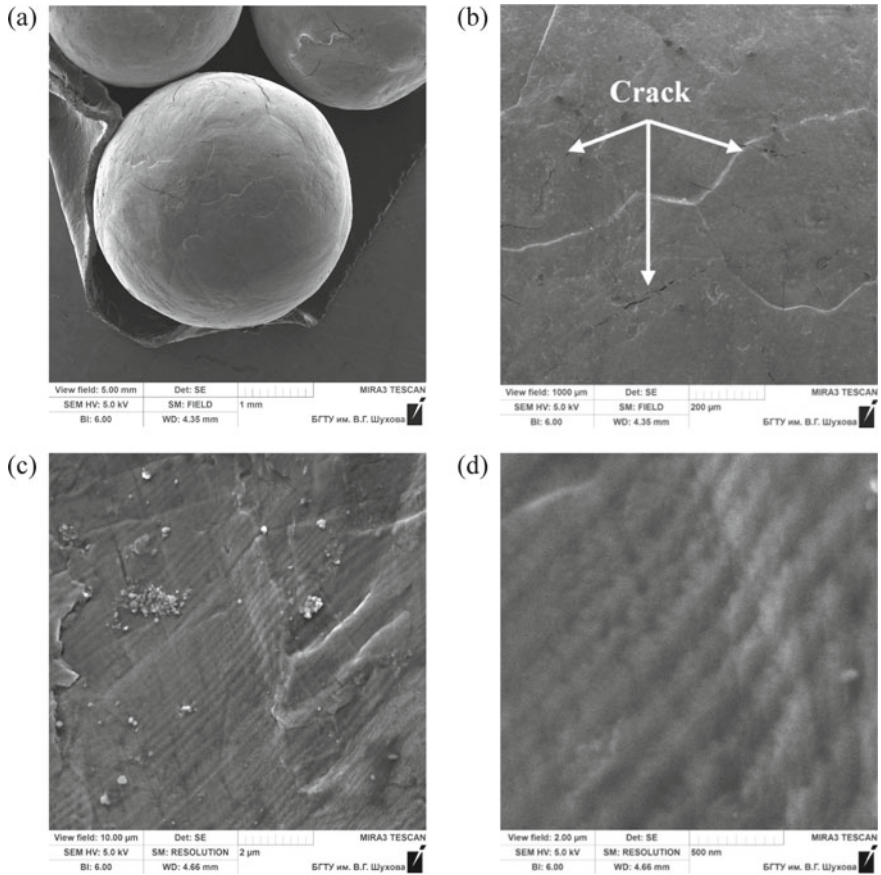
Fig. 2 Micrographs of the surface of titanium hydride shot

indicates a uniform distribution of the coating over the surface. The coating has a poly-crystalline structure with a grain size of 25 to 50 nm. In some areas of the coating (Fig. 3c), small longitudinal cracks are observed along the grain boundaries. Apparently, there was a partial "healing" of cracks due to the penetration of copper into them and further growth of the coating. In addition, the copper coating has an uneven surface and a large number of pores. The roughness of the coating surface is associated with the surface relief of the titanium hydride shot. The formation of pores in the copper coating is associated with a high deposition rate and a very low diffusion energy of adatoms on the surface, i.e. copper atoms tend to pin at the lowest surface energy. As a result of weak coalescence, pores are formed in the coating.

The radiograph and topology of the copper coating surface are shown in Fig. 4. The X-ray pattern shows (Fig. 4a) diffraction lines at 2θ angles of 43.36°, 50.42° and 74.14° corresponding to the (111), (200) and (220) crystal orientations, with (111) being the preferred orientation. For this structure, the (111) plane is the most stable, since it has the lowest surface energy [14]. The copper coating consists of a face-centered cubic lattice
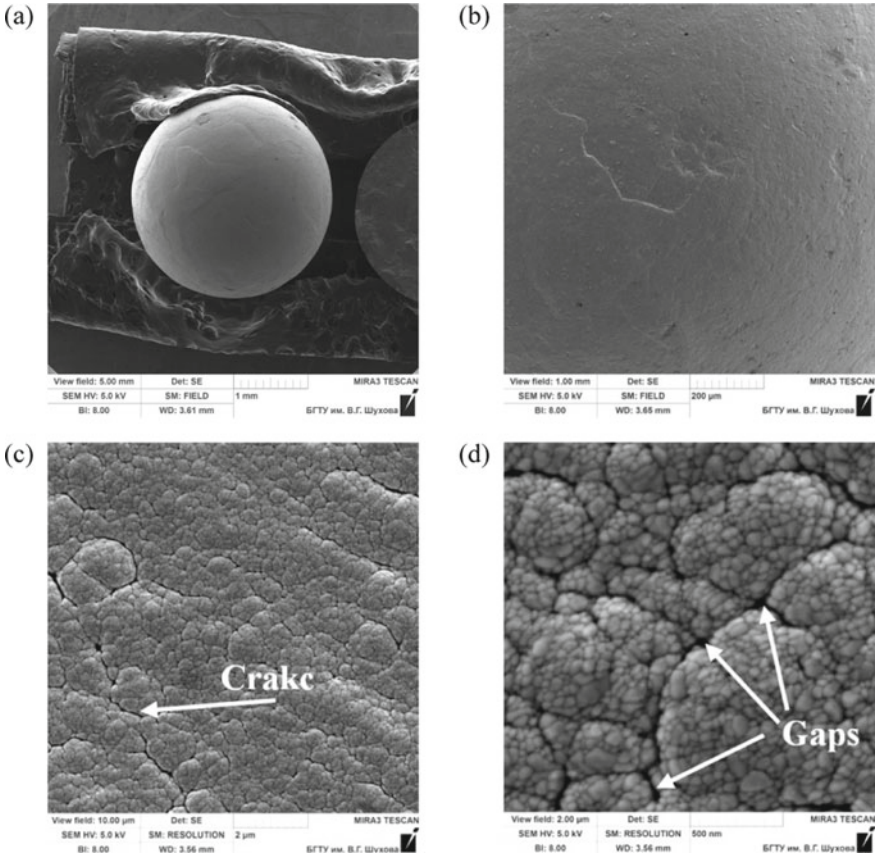
Fig. 3 Surface micrographs of copper-coated titanium hydride shot

(fcc) with space group Fm-3 m (Cu) [JCPDS 4–836]. The root mean square (RMS) surface roughness of the copper coating was ~3.67 nm (Fig. 4b).
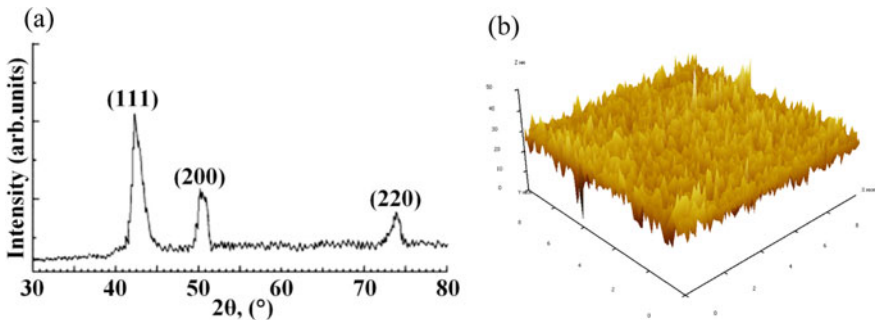
Fig. 4 X-ray pattern (**a**) and surface topology (**b**) of a copper coating on titanium hydride shots

Figure 5 shows the chipping of a titanium hydride fraction with a copper coating. The thickness of the copper coating is almost the same along the entire length of the shot surface and is ~986 nm. The interface between the copper coating and the titanium hydride fraction can be traced throughout the survey area. The coating has a homogeneous structure, fits snugly to the surface of the fraction.
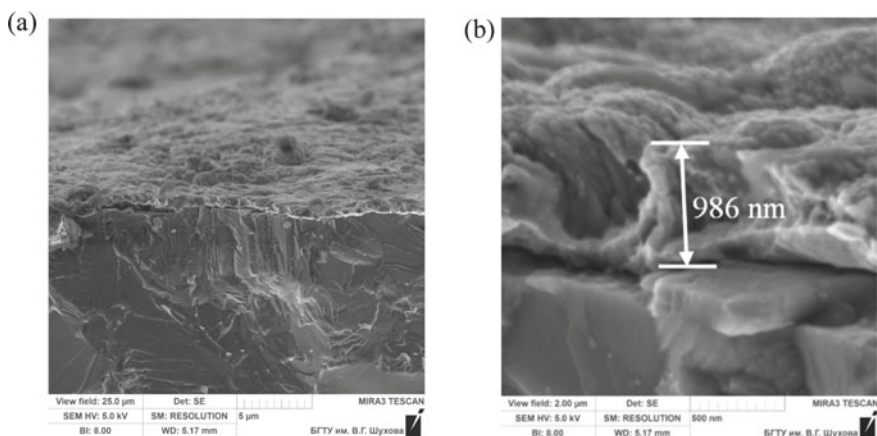
Fig. 5 Fracture morphology of titanium hydride shot with a copper coating

4 Conclusion

In this work, a new approach to the deposition of a copper coating on the surface of a titanium hydride shot by the method of quadruple magnetron sputtering was tested. It has been established that the applied copper coating is evenly distributed over the surface of the shot. The coating thickness is almost the same over the entire surface of the shot and is ~986 nm. The uniformity of the distribution of the coating is associated with the correct mixing and high uniformity of the plasma along the entire trajectory of the titanium hydride shot during sputtering. According to X-ray diffraction data, the coatings have a polycrystalline structure with a face-centered cubic lattice. The RMS surface roughness of the copper coating was ~3.67 nm.

References

1. Figuet, D., Billard, A., Savall, C., Creus, J., Cohendoz, S., Grosseau-Poussard, J.L.: A comparison between the microstructure and the functional properties of NiW coatings produced by magnetron sputtering and electrodeposition. Mater. Chem. Phys. **276**, 125332 (2022). https://doi.org/10.1016/j.matchemphys.2021.125332

2. Su, Y., Huang, W., Zhang, T., Shi, C., Hu, R., Wang, Z., Cai, L.: Tribological properties and microstructure of monolayer and multilayer Ta coatings prepared by magnetron sputtering. Vacuum **189**, 110250 (2021). https://doi.org/10.1016/j.vacuum.2021.110250

3. Deeleard, T., Buranawong, A., Choeysuppaket, A., Witit-Anun, N., Chaiyakun, S., Limsuwan, P.: Structure and composition of TiVN thin films deposited by reactive DC magnetron co-sputtering. Procedia Eng. **32**, 1000–1005 (2012). https://doi.org/10.1016/j.proeng.2012.02.045

4. Stanishevsky, A.V., Walock, M.J., Zou, Y., Imhoff, L., Zairi, A., Nouveau, C.: Growth of WC–Cr–N and WC–Al–N coatings in a RF-magnetron sputtering process. Vacuum **90**, 129–134 (2013). https://doi.org/10.1016/j.vacuum.2012.05.026

5. Priedeman, J.L., Thompson, G.B.: Conformal coating of powders by magnetron sputtering. Surf. Coat. Technol. **436**, 128242 (2022). https://doi.org/10.1016/j.surfcoat.2022.128242

6. Kelly, P.J., Arnell, R.D.: Magnetron sputtering: a review of recent developments and applications. Vacuum **56**(3), 159–172 (2000). https://doi.org/10.1016/S0042-207X(99)00189-X

7. Zaitsev, S.V., Cherkashina, N.I., Pavlenko, V.I., Prochorenkov, D.S.: Formation and stability of W coating on a flexible polyimide substrate. Thin Solid Films **715**, 138424 (2020). https://doi.org/10.1016/j.tsf.2020.138424

8. Nartsev, V.M., Zaitsev, S.V., Prokhorenkov, D.S., Evtushenko, E.I., Vashchilin, V.S.: Microstructure and morphology of AlN coatings on sapphire depending on nitrogen concentration and conditions at the initial stages of dual magnetron sputter deposition. J. Fund. Appl. Sci. **8**(2S), 82–101 (2016). https://doi.org/10.4314/jfas.v8i2s.561

9. Miletić, A., Panjan, P., Škorić, B., Čekada, M., Dražič, G., Kovač, J.: Microstructure and mechanical properties of nanostructured Ti–Al–Si–N coatings deposited by magnetron sputtering. Surf. Coat. Technol. **241**, 105–111 (2014). https://doi.org/10.1016/j.surfcoat.2013.10.050

10. Schmid, G.H.S., Eisenmenger-Sittner, C.: A method for uniformly coating powdery substrates by magnetron sputtering. Surf. Coat. Technol. **236**, 353–360 (2013). https://doi.org/10.1016/j.surfcoat.2013.10.012

11. Hruška, P., Čížek, J., Knapp, J., Lukáč, F., Melikhova, O., Mašková, S., Drahokoupil, J.: Characterization of defects in titanium created by hydrogen charging. Int. J. Hydrogen Energy **42**(35), 22557–22563 (2017). https://doi.org/10.1016/j.ijhydene.2017.05.104

12. Pavlenko, V.I., Gorodov, A.I., Yastrebinsky, R.N., Cherkashina, N.I., Karnauhov, A.A.: Increasing the adherence of metallic copper to the surface of titanium hydride. ChemEngineering **5**(4), 72 (2021). https://doi.org/10.3390/chemengineering5040072

13. Ma, M., Wang, L., Tang, B., Lyu, P., Xiang, W., Wang, Y., Tan, X.: Kinetics of hydrogen desorption from titanium hydride under isothermal conditions. Int. J. Hydrogen Energy **43**(3), 1577–1586 (2018). https://doi.org/10.1016/j.ijhydene.2017.11.103

14. Wu, B.H., Wu, J., Jiang, F., Ma, D.L., Chen, C.Z., Sun, H., Huang, N.: Plasma characteristics and properties of Cu films prepared by high power pulsed magnetron sputtering. Vacuum **135**, 93–100 (2017). https://doi.org/10.1016/j.vacuum.2016.10.032

Investigating of the Residual Stresses During the Extraction of a Polymer Product from an Extruder

Stepan Litvinov[1,2(✉)] , Dmitriy Vysokovsky[1] , Lyubov Lesnyak[1] ,
Batyr Yazyev[1,2] , and Linar Sabitov[2,3]

[1] Don State Technical University, 1 Gagarin Sq., Rostov-On-Don 344000, Russia
litvstep@gmail.com
[2] Kazan Federal University, 18 Kremlyovskaya Street, Kazan 420008, Russia
[3] Kazan State Power Engineering University, 51 Krasnoselskaya Street, Kazan 420066, Russia

Abstract. The accumulation of residual stresses during the manufacturing process of a product can affect its performance in the future. Under the action of an inhomogeneous temperature field, polymeric materials can acquire indirect inhomogeneity, which is a change in physical and mechanical parameters (elastic and rheological), which are a strong function of temperature. The article provides information about definition of the stress–strain state of a polymer cylinder removed from an extruder. The heat exchange with the environment is taken into account, the temperature field is determined, and the change in stresses in the polymer body is studied, taking into account the development of creep deformations. It is shown that as a result of the development of stresses only from the inhomogeneity of the material caused by an uneven temperature field, the values of residual stresses in the body are very small and can be neglected.

Keywords: Residual stresses · Indirect inhomogeneity · Polymer creep · Temperature inhomogeneity

1 Introduction

One of the main tasks in mechanics is the problem of determining the residual stresses that arise in the manufactured polymer product during its cooling. Similar problems have already been considered in the works [1–3], however, in them, the boundary conditions were set as a certain function, without taking into account the heat exchange with the environment. In the process of solving the problem, it becomes necessary to take into account many individual processes: determination of the temperature field; determination of indirect inhomogeneity caused by uneven distribution of the temperature field and, accordingly, different distribution of physical and mechanical parameters of the product at each moment of time in its thickness; determination of the stress–strain state at each moment of time; determination of rheological processes occurring in the product.

A special limitation is imposed by the fact that stresses and deformations can be reversible in time, which does not allow taking into account such common complexes as ANSYS, Abaqus, SolidWorks and others.

Works [4, 5] are devoted to the calculation of polymer cylindrical bodies, taking into account the pressure on the internal and external surfaces. The work [6] considers the study of a polymer cylinder during its rotation.

In [7], a multilayer polymer pipe is studied under the action of internal pressure.

In Russia, academician Andreev [8–11] studied the study of the heterogeneity of polymer cylinders, which occurs due to the gradient of the temperature field along the polymer body. The work [12] shows how the induced inhomogeneity can be used to control the stress–strain state of the body.

An attempt to determine the change in the stress–strain state is shown in [13]. The authors consider a rotating body subjected to an alternating temperature field and inertial forces. At the second stage, the rotation of the body stops and the body cools down. Thus, the development of reversible deformations is observed, which, without special techniques, cannot be studied in the widespread FEM complexes listed earlier. Most of the earlier works considered models of a polymer body either under conditions of a plane stress state or under conditions of a plane deformed state.

The study of the stress–strain state of a polymer cylinder removed from an extruder requires the creation of a higher-dimensional model: a two-dimensional axisymmetric problem.

2 Methods and Materials

The main purpose of this article is a comprehensive study of residual stresses in a polymer cylindrical body removed from an extruder over time. In this case, uneven cooling of the cylinder along its length and thickness leads to material inhomogeneity, expressed in the variation of its physical and mechanical parameters. In general, the general deformation of the material consists of several components: elastic, temperature and creep:

$$\varepsilon = \varepsilon_{el} + \varepsilon_T + \varepsilon_{cr}; \tag{1}$$

where ε is the total strain; ε_{el} is the elastic deformation; ε_T is the temperature component of deformation; ε_{cr} is the creep strain.

The process of extracting a polymer cylinder from a dryer is considered. The material of the product is EDT-10 thermal curing epoxy resin; the thermal and physical–mechanical parameters of the material are given below. The calculation model is shown in Fig. 1. Three stages are considered:

1. The initial moment of time (Fig. 1a). The sample is in the extruder and it is assumed that its entire temperature is equal to the temperature of the extruder itself.
2. Extracting of the cylinder (Figs. 1b and 2). The sample is partially withdrawn from the cylinder, on the lower face and the outer face, which is located in the extruder, the temperature is equal to the temperature of the extruder. On the inner face, the heat exchange in the air layer is considered, the temperature of which is also assumed to be equal to the temperature of the extruder. On the upper face and the outer face that came out of the extruder, heat exchange with the external environment is considered.
3. Cooling (Fig. 1c). The sample was removed from the extruder during t = 1.2 h; heat exchange with air is considered on all four faces.
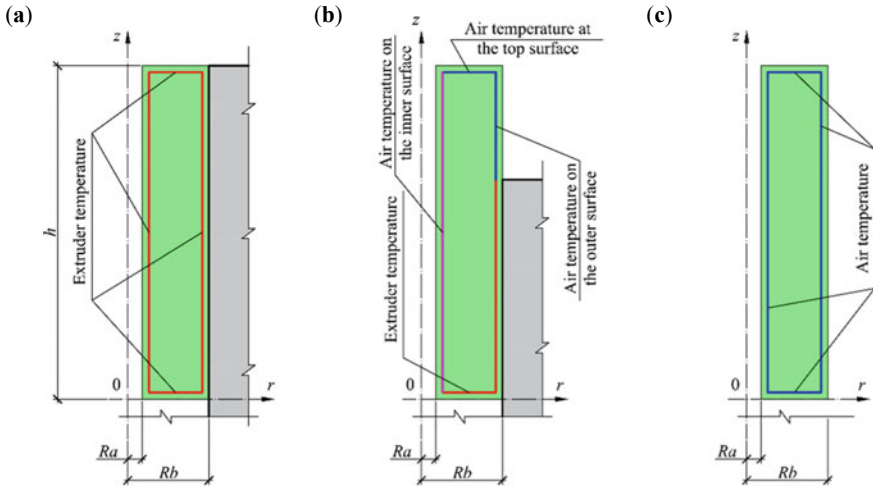
Fig. 1 Calculation model of polymer cylinder drawing (green color) from the extruder (gray color): **a** is the initial moment of time; **b** is the time point within the cylinder drawing time; **c** the hood is completed, full contact with the environment
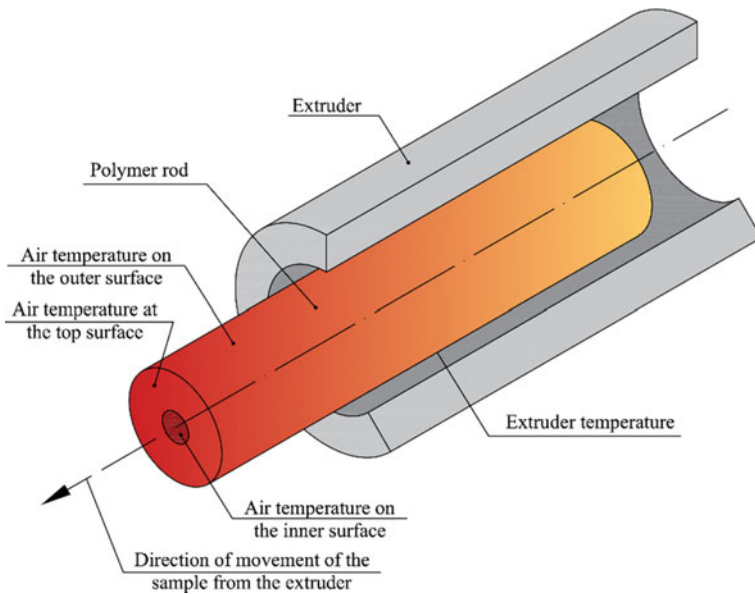
Fig. 2 The visual diagram of the calculation model, which shown in Fig. 1b

The temperature of the extruder and the temperature of the air inside the extruder is 100 °C. This is because the curing process of epoxy resin should be carried out at temperatures of 100–130 °C, however, since mechanical calculation is carried out, the

temperature should not exceed the glass transition temperature of EDT-10, equal to about 102 °C. The temperature of the external air is 20 °C.

The dimensions of the polymer cylinder are $Ra = 0.008$ m; $Rb = 0.028$ m; $h = 0.5$ m. There are no mechanical loads at all ends.

The full settlement period was 3.6 h. The total number of time intervals was $h_t = 100$ pcs; the number of rectangular finite elements approximating the polymer cylinder was the same in the vertical and radial directions and amounted to $h_r = h_z = 51$ pcs.

The calculations performed taking into account the dependence of all physical and mechanical parameters of the cylinder material on temperature in a non-linearized formulation.

The problem was solved using the finite element method. A rectangular area was considered, the diagonal corners of which had the coordinates $[Z_i, R_i]$ and $[Z_k, R_k]$.

The determination of the variable temperature field in time was carried out by minimizing the temperature field functional [14]:

$$\text{Im}(T) = \int_V \left[\lambda (\text{grad } T)^2 + \frac{\rho c}{h_t} T^2 \right] dV + \int_{\Gamma 3} \alpha T^2 d\Gamma - 2 \int_{\Gamma 3} \alpha T_0 T \, d\Gamma - 2 \int_V fT \, dV, \tag{2}$$

where T is the product temperature; λ is the thermal conductivity coefficient; c is the isobaric heat capacity; ρ is the density of the material; $\Gamma 3$ is the boundary of the region.

Minimization of expression (2) and further solution led to the system of equations of the finite element method

$$\left[K^{(T)} \right] \cdot \left\{ T^{(T)} \right\} = \left\{ f^{(T)} \right\}.$$

The coefficients of the resulting system of equations are not given in detail in this article.

To determine the stress–strain state, a system of equations of the finite element method was obtained, which has the form:

$$[K] \cdot \{U\} = \{F\},$$

where $[K]$ is the global stiffness matrix; $\{U\}$ is the global load vector.

$$[K] = \sum_{e=1}^{E} \int_{Z_i}^{Z_k} \int_{R_i}^{R_k} r[B]^T [D][B] \, dr \, dz;$$

$$[F] = \sum_{e=1}^{E} \int_{Z_i}^{Z_k} \int_{R_i}^{R_k} r[B]^T [D]\{\varepsilon_T\} \, dr \, dz + \sum_{e=1}^{E} \int_{Z_i}^{Z_k} \int_{R_i}^{R_k} r[B]^T [D]\{\varepsilon_{cr}\} \, dr \, dz.$$

The coefficients of the resulting system of equations are also not given in detail in this article.

Creep deformations are described using the nonlinear Maxwell-Gurevich constraint equation:

$$\frac{\partial \varepsilon_{cr,ij}}{\partial t} = \frac{f_{ij}^*}{\eta^*}, \tag{3}$$

where $\partial\varepsilon_{cr,ij}/\partial t$ is the creep strain rate along the directions of the ij axes; f_{ij}^* is the stress function; η^* is the coefficient of relaxation viscosity.

$$f_{ij}^* = \sigma_{ij} - E_\infty \varepsilon_{cr,ij}; \quad \frac{1}{\eta^*} = \frac{1}{\eta_0^*} \exp\left\{ \frac{|f_{rr}^*|_{max}}{m^*} \right\}, \tag{4}$$

where E_∞ is the modulus of high elasticity of the polymer; η_0^* is the coefficient of initial relaxation viscosity; m^* is the speed modulus.

The methods for determining the elastic and rheological parameters of polymers are detailed in [15–17].

Thus, the coefficient of relaxation viscosity η^* directly depends on the maximum value of the stress function f_{rr}^* for the principal directions.

Physical and mechanical (rheological and thermophysical) characteristics used are as follows: $\lambda = 0.17$ W/(m × deg); $\rho = 1250$ kg/m³; $c = 0.35$ J/(kg × deg); $\nu = 0.3$; $E = -17.5\,T + 3525$ MPa; $E_\infty = -30\,T + 3150$ MPa; $m^* = -0.011\,T + 4.75$ MPa; $\eta^* = \eta_0^* \exp(-0.0275\,T)$ MPa × h.

3 Results and Discussion

The calculation was implemented in the MATLAB environment. The calculation results are shown in Figs. 3, 4, 5 and 6.
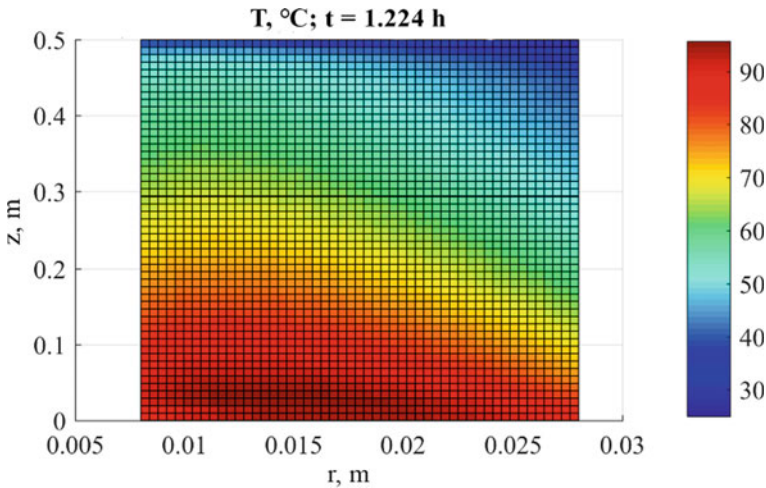
Fig. 3 The temperature field for the moment when the cylinder is completely removed from the extruder, t = 1.2 h

Figure 3 shows the temperature field for the moment when the cylinder is completely removed from the extruder, $t = 1.2$ h. As a result of the existing temperature field gradient, the material of the polymer cylinder acquires a pronounced induced indirect
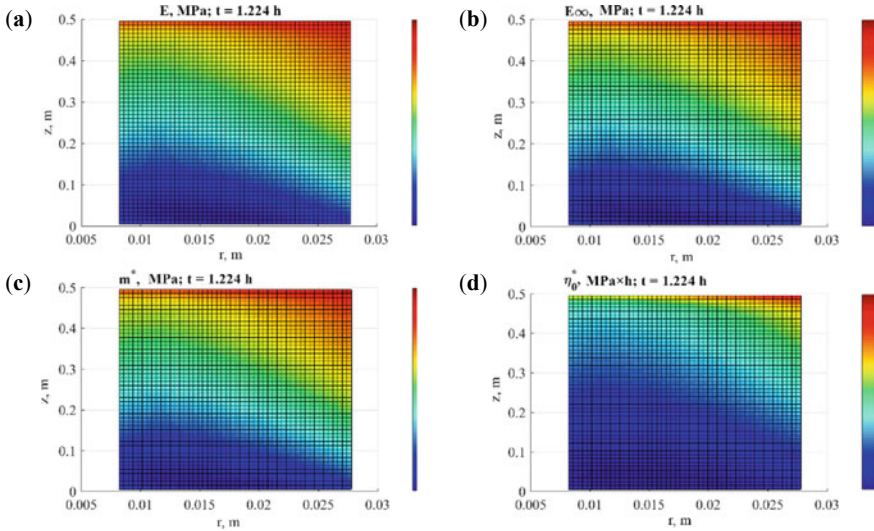
Fig. 4 Changing in the physical and mechanical parameters of the material depending on the temperature field at the moment of complete extraction of the polymer cylinder from the extruder, t = 1.2 h
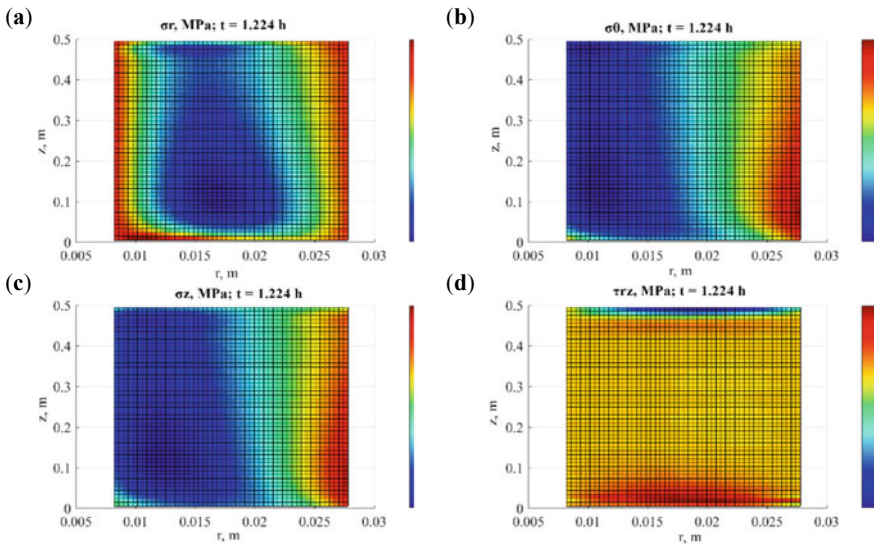
Fig. 5 Distributing of the axial and shear stresses in the polymer cylinder at the moment of its complete extraction from the extruder, t = 1.2 h

inhomogeneity in the form of a difference in physical and mechanical parameters (elastic and highly elastic) in the thickness of the body (Fig. 4).
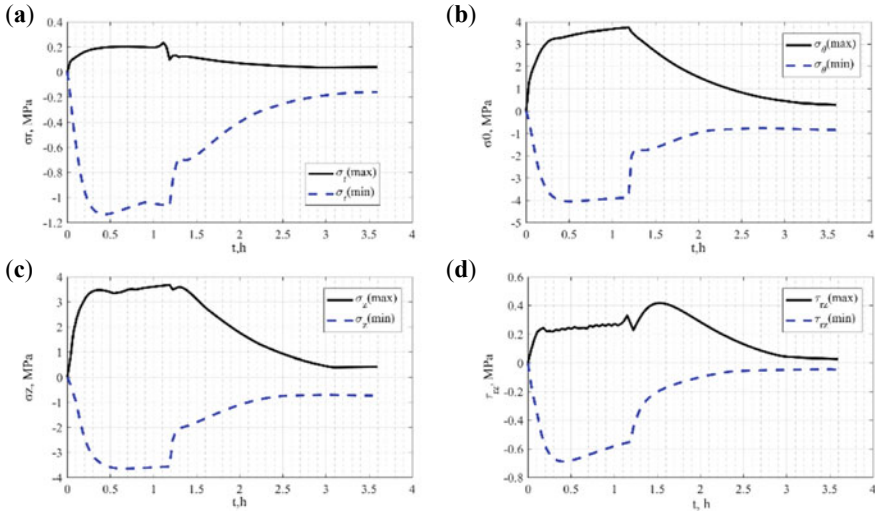
Fig. 6 Changing in the maximum and minimum stresses in the thickness of the polymer cylinder at the moment of removing the body from the extruder, t = 1.2 h

In the process of extracting material from the extruder, stresses arise in the body due to the occurrence of induced inhomogeneity of the material (Fig. 5). An analysis of the stress fields shows that they have a somewhat different nature of their distribution in the thickness of the body, but the same order of magnitude. For the convenience of analyzing the change in values over time, at each calculation step, the maximum and minimum values of stresses in the body were determined, after which graphs of their change were plotted, which are shown in Figs. 6. The maximum tensile and maximum compressive axial stresses over the entire calculation period have a level of about 4 MPa.

An analysis of the data obtained shows that a stress state of a sufficiently high level may occur in the body, which can adversely affect the subsequent processing of the product without the possibility of cooling and holding it under normal conditions. During cooling of the body and its settling under normal conditions, due to the development of highly elastic deformations in the polymer several hours after the cylinder is drawn from the extruder, the stresses take on a value that can be neglected in the subsequent operation of the sample.

4 Conclusion

The task of determining the residual stresses in the body remains very relevant, since there can be an infinite number of different combinations of loadings: temperature and force.

It is interesting to study a different class of materials that can be used in construction, taking into account changes in their properties [18–21].

In the future, it is possible to study the stress–strain state of such products, but at different times of their extraction from the extruder, as well as when considering linear and nonlinear creep laws.

References

1. Litvinov, S.: Nonlinear creep of inhomogeneous multilayer cylinders and spheres. Moscow State Building University, 200 p (2010)
2. Klyuev, S.V., Klyuev, A.V., Shorstova, E.S.: The micro silicon additive effects on the fine-grassed concrete properties for 3-D additive technologies. Mater. Sci. Forum **974**, 131–135 (2019)
3. Yazyev, B.: Features of relaxation properties of network and linear polymers and composites based on them. Kabardino-Balkarian State University named after H.M. Berbekov, 352 p (2009)
4. Sharma, S., Sahni, M., Kumar, R.: Elastic-plastic transition of transversely isotropic thick-walled rotating cylinder under internal pressure. Def. Sci. J. **59**(3), 260 (2009)
5. Sharma, S., Sahni, M., Kumar, R.: Thermo elastic—plastic transition of transversely isotropic thick—walled rotating cylinder under internal pressure. Adv. Theor. Appl. Mech. **2**(3), 113–122 (2009)
6. Sahni, M., Sharma, S.: Analysis of safety measure in creep transversely isotropic thick-walled rotating cylinder by finitesimal deformation under external pressure, pp. 1–5. IEEE (2014)
7. Yazyev, S., Litvinov, S., Dudnik, A., Doronkina, I.: Rheological aspects of multilayered thick-wall polymeric pipes under the influence of internal pressure. Key Eng. Mater. **869**, 209–217 (2020)
8. Polyakova, L.S., Andreev, V.I.: Solution of the problem of thermoelasticity for nonlinear elastic inhomogeneous thick-wall cylindrical shell. Int. J. Comput. Civ. Struct. Eng. **15**, 133–142 (2019)
9. Andreev, V.: Approximate method for calculating a thickwalled cylinder with rigidly clamped ends. E3S Web Conf., 02026 (2018)
10. Andreev, V.I., Polyakova, L.S.: Calculation of a thick-walled inhomogene-ous cylinder of nonlinear-elastic material. In: Advanced Materials and Structural Engineering. Proceedings of the International Conference on Advanced Materials and Engineering Structural Technology, pp. 715–718 (2015)
11. Andreev, V.I.: Axisymmetric thermo-elastic deformation of the cylinder with two-dimensional inhomo-geneity of material. MATEC Web Conf., 05008 (2016)
12. Chepurnenko, A., Litvinov, S., Meskhi, B., Beskopylny, A.: Optimization of thick-walled viscoelastic hollow polymer cylinders by artificial heterogeneity creation: theoretical aspects. Polymers **13**(15), 2408 (2021)
13. Lesnyak, L.I., Yazyev, S.B., Avakov, A.A., Andreev, V.I., Doronkina, I.G.: Analysis of residual stresses in a polymer cylinder when it is stopped and then cooled in a nonlinear and linearized problem settings. Key Eng. Mater. **899**, 486–492 (2021)
14. Litvinov, S.: Simulating of rheological processes in polymeric and composite materials under thermal force influence [Modelirovanie reologicheskih processov v polimernyh i kompozicionnyh materialah pri termosilovom vozdejstvii]. Kabardino-Balkarian State University named after H.M. Berbekov, 289 p (2022)
15. Chepurnenko, A.S., Beskopylny, A.N., Jazyev, B.M., Andreev, V.I.: Determination of rheological parameters of polyvinylchloride at different temperatures. MATEC Web Conf. SMAE **2016**, 06059 (2016)
16. Dudnik, A.E., Chepurnenko, A.S., Litvinov, S.V.: Determining the rheological parameters of polyvinyl chloride, with change in temperature taken into account. Int. Polym. Sci. Technol. **44**(1), 30–33 (2017)
17. Yazyev, S.B., Chepurnenko, A.S., Litvinov, S.V.: Determination of rheological parameters of polymeric materials using nonlinear optimization methods. Constr. Mater. Prod. **3**(5), 15–23 (2020). https://doi.org/10.34031/2618-7183-2020-3-5-15-23

18. Zhuikov, S.V.: The use of nanotechnology for the design of building structures. Constr. Mater. Prod. **4**(6), 26–47 (2021). https://doi.org/10.34031/2618-7183-2021-4-6-26-47
19. Klyuev, S.V., Abakarov, A.J., Lesovik, R.V., Muravyov, K.A., Tatlyev, R.D.: Optimal engineering of rod spatial construction. J. Comput. Theor. Nanosci. **16**(1), 200–203 (2019)
20. Klyuev, S.V., Garkin, I.N., Klyuev, A.V., Sabitov, L.S.: Results of endurance testing of prefabricated crane structures. Constr. Mater. Prod. **5**(4), 39–49 (2022)
21. Shorstov, R.A., Yaziev, S.B., Chepurnenko, A.S., Klyuev, A.V.: Flat bending shape stability of rectangular cross-section wooden beams when fastening the edge stretched from the bending moment. Constr. Mater. Prod. **5**(4), 5–18 (2022)

Compatibility of Polymer and Plasticizer—As a Key Factor in the Formation of Degradation-Resistant Bituminous Binder

M. A. Vysotskaya[1]([✉]) [iD], D. P. Litovchenko[1] [iD], E. V. Korolev[2] [iD], and A. O. Shiryaev[1] [iD]

[1] Department of Roads and Railways, Belgorod State Technological University Named After V.G. Shukhov, Kostyukov St., 46, Belgorod 308012, Russia
`roruri@rambler.ru`

[2] St. Petersburg State University of Architecture and Civil Engineering, 2nd Krasnoarmeyskaya St., 4, St. Petersburg 190005, Russia

Abstract. The work is focused on assessing the effect of compatibility of polymer and various plasticizers on the properties and stability over time of the final product—polymer modified bitumen (PMB). To obtain the regularities of the influence of plasticizers on the stability of PMB at the initial stage of the research, the basic set of characteristics of the initial materials (bitumen and plasticizer) was determined. Control of structure formation of investigated binders was carried out by varying the concentration of plasticizer, which was used as: fuel oil M 200, oil I-50, "Uniplast", the extract of selective oil purification (SPE), "Katgol". For plasticizing additives such characteristics as: sample mass loss (volatility) in the range of technological temperatures of PMB preparation, aniline point indicator were investigated, as well as the group composition of plasticizing components was evaluated. In the course of the experiment the dynamics of changes of indicators of standard properties of modified binders was revealed, as well as their thermal stability (tendency to delamination and loss of weight during thermotreatment) due to the composition of plasticizer and its compatibility with the polymer used. It is suggested to investigate compatibility of components: plasticizer and polymer, at the preparatory stage, before preparation of laboratory PMB compositions. Recommendations on the use of plasticizers for obtaining effective compositions of polymer-bitumen binders have been developed. The contribution of polymer-plasticizer system compatibility on PMB resistance to destructive stratification and aging processes was studied. The importance of the raised topics for the industry is caused by the lack of a unified regulatory framework governing the requirements for plasticizers to modify bituminous binders, including the preparation of PMB. The conducted studies show that the compatibility of polymer and plasticizer has a key impact on the quality indicators of modified bituminous binders, but this aspect for the systems under consideration at the present time is not properly studied.

Keywords: Polymer Modified Bitumen (Pmb) · Plasticizer · Polymer · Compatibility · Destruction · Bitumen

1 Introduction

Active development of the road industry, causes high requirements to the quality of raw components that ensure the durability of asphalt concrete in the road pavement. One of the main directions of scientific search in the road construction industry was the study of the effect of various polymeric and plasticizing additives on organic binders [1–5] in order to increase the operating properties of asphalt concrete by strengthening its structure.

The analysis of scientific and technical literature shows that bitumen modification can be carried out by one or several additives [3]. However, when they are introduced together, it is necessary to take into account their compatibility not only with bitumen, but also with each other. Otherwise, it may lead to their antagonistic influence and bitumen modification will not be effective [1]. Thus, the search for effective additives, the development of optimal formulations of additive complexes for bitumen modification, as well as the analysis of the effectiveness and feasibility of their combined use, started in the last century, remain relevant today. To impart the ability of polymer modified bitumen in real life operation of road pavement to withstand the tensile loads without destruction and to prepare PMB it is advisable to use oil bitumen with a needle penetration depth at 25 °C of the order of 130–200 or 200–300 mm^{-1}. But, due to the specifics of oil refining, for road construction is primarily used raw materials on the residual principle, from which the bitumen with low penetration is derived. From such bitumen, in accordance with the existing studies in the industry [1], it is impossible to obtain a good quality PMB without plasticizing the binder [4]. At present it is difficult to choose an effective plasticizer that helps to achieve the design properties of the binder and asphalt concrete on its basis. Considering in detail the effect of plasticizer on PMB, it can be noted that a reasonable choice of plasticizer allows:

- provide a temperature of preparation of modified binder not more than 160 °C,
- optimize the cost of preparing PMB by reducing energy costs for the heating of PMB with an increase in the efficiency of the introduction of the polymer,
- to expand significantly the plasticity interval of the modified binder by increasing the brittleness temperature of PMB to − 46 °C, using a minimum amount of polymer [5].

The benefits of using plasticizers are clear. There is evidence of their positive effect on the properties of PMB and asphalt concrete in road pavement. However, regulatory documents regulating the application, requirements for plasticizers and their properties have not been developed at present. In this regard, the paper formulated the requirements, which, in our opinion, should meet the plasticizer for bituminous binders:

- have a high boiling point and flash point;
- characterized by low losses during heating, must be volatile;
- must be free of a pungent smell;
- it must be able to be compatible with the system components and effectively plasticize;
- have danger class III or IV.

It is clear that the compatibility of polymer and plasticizer is an important criterion in selecting the component composition of PMB. The methods used in the chemical industries show the colloidal stability of the final product [6] when the conditions of component compatibility are met. However, in the road industry none of the methods of preliminary assessment of polymer and plasticizer compatibility has not found application in practice. There is used, and to a limited extent, the method of assessing the resistance to delamination, but already the final product—PMB. According to the testing methodology, only the sample thermostating process takes 72 h, not counting the time for selection, preparation and testing of the laboratory sample at the stage of PMB formulation development. Therefore, the main purpose of the work was to investigate the compatibility of the polymer and plasticizer and assess its impact on the quality indicators of PMB. In carrying out the study the following tasks were solved:

- analyzed the known methods of assessing the compatibility of the polymer and plasticizer in various branches of knowledge;
- studied indicators of the properties of plasticizers used in the industry;
- two-phase systems "polymer—plasticizer" were made to evaluate the compatibility;
- influence of two-phase "polymer—plasticizer" system on PMB 90 indicators was studied.

2   Materials and Methods

In this work was considered a line of plasticizers, presented in Table 1. There are also given indicators of their properties. The plasticizers accepted for the study were tested for compliance with the formulated requirements. As a polymer was used SBS L 30-01A.

Table 1 Plasticizers used in the work and their properties

Sample	Aniline point, °C	Change of plasticizer mass after 5 h of heating at 165 °C, %
Fuel oil M 200	57.7	3.4
Oil I-50	> 100.0	7.8
Uniplast	< 30.0	5.1
Selective Purification Extract (SPE)	40.6	2.3
Katgol	< 30.0	94.3

There is an opinion that the quality of bitumen is not the key parameter that determines the nature of the modifying effect of the polymer. The main thing is the chemical composition of the maltene part of bitumen and its structure. It is logical that the forced introduction of plasticizer into bitumen increases its maltene part. Therefore, to evaluate the effectiveness of plasticizer it is necessary to have data on its composition and potential response to high process temperatures.

At the first stage of the experiment the following characteristics of plasticizers were studied:

- mass change after heating at 165 °C for 5 h;
- aniline point, characterizing the content of the limiting hydrocarbons (paraffins);
- group chemical composition of plasticizers.

By the opinion of [1], when using plasticizers with aromatic compounds to modify bitumens with polymers, compatible compositions are obtained. It is known [7] that the ability of aniline to dissolve hydrocarbon groups is different: the higher the aniline point [7], the more paraffin-containing is the oil product, so the higher is the content of saturated hydrocarbons in it; the lower the value of the index, the more aromatic hydrocarbons in it; naphthenic and unsaturated hydrocarbons are of intermediate importance. In turn [8], paraffins have a negative effect on the low-temperature characteristics of PMB. It can be assumed that this rapid method, suitable for low-viscosity, light, oily substances, may be applicable to the evaluation of bitumen plasticizers at the initial stage of research. The aniline point determination temperature range is from 30 to 100 °C. The results obtained, Table 1, indicate that out of a series of plasticizers, two of them—ESO and fuel oil—contain aromatic hydrocarbons. The value of aniline point for oil I-50 indicates a significant content of paraffins, which negatively affects the PMB indicators. Determination of aniline point for plasticizers "Katgol" and "Uniplast" demonstrates the limit beyond the sensitivity range of the method, obviously, this is due to the absence of aromatic hydrocarbons and paraffins in their composition. As seen in Table 1, plasticizers respond differently to temperature control at 165 °C for 5 h: the change in mass "Katgol" was 94.3%, which characterizes it as highly volatile. The value of this property for other plasticizers is in a comparable range and may characterize them as low-volatile. For detailed understanding of the nature of plasticizers used at the next stage was determined by SARA-analysis of their group composition (Table 2).

Table 2 Group composition of plasticizers

Sample	Saturated hydrocarbons, %	Aromatic hydrocarbons, %	Resins, %	Asphaltenes, %
Fuel oil M 200	12.1	38.2	24.3	25.4
Oil I-50	72.74	19.31	7.95	0
Uniplast	0	0	100	0
Selective purification extract (SPE)	17.97	64.47	17.57	0
Katgol	0	0	100	0

Table 2 shows that the plasticizers under consideration significantly differ in group chemical composition. Fuel oil M 200 by group chemical composition is the closest to bitumen and contains a significant amount of asphaltenes. The highest content of aromatic hydrocarbons is observed in the composition of SPE. The maximum amount of saturated hydrocarbons is contained in the oil I-50. Uniplast and Katgol plasticizers

are of the greatest interest because they are represented by monocompounds—resins. Their composition contains no aromatic hydrocarbons, which allows us to argue that the method of determining the "aniline point" can be used as a primary express method of assessing the effectiveness and suitability of plasticizers for the preparation of PMB. In accordance with the technological process in the production of PMB there are two main steps: emulsification of the polymer in the melt bitumen, through a colloidal mill, followed by its swelling in the maltene medium. It can be assumed that in this case, it is fair to speak primarily about compatibility at the level of two-phase structures "polymer—maltene medium" [9]. In this case, it is natural, if the polymer is easily soluble in plasticizer, then also at complex modification of bitumen by polymer using plasticizer will be observed combination of polymer modifying and plasticizing additives [10]. To confirm the hypothesis put forward, two-phase systems were prepared—concentrates consisting of the plasticizers and polymer under study. Concentrates were prepared in a laboratory IKA high-speed stirrer at 165 °C. When the experiment was set, the temperature was constant, and the stirring time was varied depending on the dissolution of the polymer. The homogeneity of the mixture was determined visually using a glass rod. Simplified, if the polymer is easily dissolved in the plasticizer, or combined with the plasticizer at low thermodynamic influences, it is considered that the polymer has an affinity to the plasticizer. An important factor determining the compatibility of polymer and plasticizer is the interaction parameter X, which is determined from the formula [9]:

$$\frac{1}{T_m} = 0.002226 + 0.1351\frac{1 - |X|}{V_1}, \tag{1}$$

$$|X| = \frac{0.002226V_1 + 0.1351 - \frac{V_1}{T_m}}{0.1351}, \tag{2}$$

where

$|X|$ parameter of compatibility of polymer and plasticizer (the value of the indicator was taken in the work by module):
T_m interaction temperature, dissolution of the polymer;
V_1 molar volume of plasticizer;

Then, on the basis of the prepared concentrates by identical methodology PMB 90 was prepared. For all compositions, the ratio "plasticizer—polymer—bitumen" was constant.

The validity of the hypothesis on the influence of polymer and plasticizer compatibility on physical and mechanical properties of PMB was based on a comparative analysis of the compatibility coefficients of the two-phase system "polymer—plasticizer" and generalized efficiency coefficients of obtained compositions of PMB 90, calculated by multi-criteria optimization [11].

When calculating the effectiveness criteria and generalized coefficient of effectiveness, the formulas below were used.

$$K_{\text{eff}}^i = \frac{Z_{\text{ind.}}^i}{Z_{\text{Gost}}^i}, \tag{3}$$

where

K_{eff}^i specific performance criterion i of the indicator;
$Z_{\text{ind.}}^i$ actual value i of the indicator;
Z_{Gost}^i required value i of the indicator.

Formula (4) is valid in the case of analysis of indicators with inverse dependence: $Z_{\text{chan.mass}}$ и Z_{sta}, – in which the lowest value of the parameter indicates the quality of the product:

$$K_{sta}^i = \frac{Z_{Gost}^i}{Z_{\text{ind}}^i}, \tag{4}$$

where

K_{sta}^i specific performance criterion i of the indicator;
$Z_{\text{ind.}}^i$ actual value i of the indicator;
Z_{Gost}^i required value i of the indicator.

The calculation of the generalized performance criterion for each PMB composition was based on a base of individual performance criteria.

$$K_{\text{eff.}}^{\text{gen}} = \sqrt[n]{N_{n=1}^i \cdot K_{\text{eff}}^i}, \tag{5}$$

where

$K_{\text{eff.}}^{\text{gen}}$ generalized performance criterion i of the indicator.
$K_{\text{eff.}}^i$ individual criteria i of the indicator.

3 Results and Discussions

In the first part of the study, by changing the stirring time, the dissolution efficiency of the polymer in different plasticizers was evaluated (Table 3).

Obviously, the plasticizers used are characterized by different solubility. The analysis showed that the presence of resins and marginal hydrocarbons in the plasticizer composition significantly increases the time of preparation of the concentrate. The minimum time for dissolution of the polymer was required when using SPE and fuel oil, characterized by the presence of aromatic compounds, and the minimum content of saturated hydrocarbons. These data also correlate with a numerical evaluation of the compatibility of two-phase "polymer-plasticizer" systems based on the thermodynamic compatibility determination approach used in the polymer industry (form. 1.2).

To determine the necessary parameters a reverse experiment was conducted when the mixing time of the two-phase system was taken as a constant, the variable parameter was temperature, which was chosen experimentally. The molar volume of each plasticizer

Table 3 Assessment of the compatibility of the two-phase system "polymer—plasticizer"

Sample	Dissolution time, min.	Compatibility parameter X
Fuel oil M 200	85	4.0
Oil I-50	130	2.9
Uniplast	115	2.8
Selective purification extract (SPE)	70	3.7
Katgol	155	2.7

was also determined. The obtained values of the compatibility factor are presented in Table 3.

In accordance with [6], plasticizers for the polymer industry, depending on the parameter X, it was proposed to divide into two groups: plasticizers "promoting swelling" ($1.2 \leq X \leq +3.0$) and plasticizers "promoting dissolution" ($X \geq 3.0$).

Implementation and confirmation of the identified patterns was carried out at the second stage of the study in the preparation of compositions of the modified bitumen binder PMB 90 The concentration of the input systems "polymer—plasticizer" was 10.5%, in addition for fuel oil 15%. Prepared compositions were tested for compliance with the requirements of GOST 52056, Table 4. Analysis of Table 4 illustrates that all plasticizers contribute to a change in the physical and mechanical properties of the modified bitumen. By the introduction of plasticizer in bitumen can significantly increase the range of variation of performance factors PMB relative to the original bitumen [12]. However, not all plasticizers provide modification of the binder, with a set of desired (projected) properties. As can be seen, when using fuel oil, other things being equal, to achieve the property index PMB 90 was not possible, it was necessary to increase its content. Significant interest is represented by indicators evaluating the stability of PMB structure to destructive processes. In the work were the change in mass of samples after heating, Table 4, and the thermostability of PMB according to EN 13399 were studied.

In accordance with the data obtained, the greatest change in weight of samples of PMB after thermostatting is observed in samples made on plasticizers (in descending order): Katgol and Oil I-50. The same plasticizers were characterized by the maximum value of plasticizer mass change after heating. Obviously, the stability of disperse systems as colloids, which is a bitumen, depends on the degree of interaction between the maltene medium and the disperse phase of the modified binders. In the case of instability, the systems tend to separate phases, which is clearly seen in the study of delamination [12] of the system after heating in a tube, by the difference of softening temperatures between the upper and lower part of the sample of PMB, Fig. 1. The results on the stratification of systems performed with the use of two-phase concentrates based on fuel oil and SPE, builds a logical chain of resulting patterns on the influence of polymer and plasticizer compatibility on the physical and mechanical properties of the PMB.

Despite the importance of the problem under consideration, for the road construction industry as a whole, none of the methods of preliminary assessment of the compatibility of the polymer and plasticizer has not found application in practice.

Table 4 Effect of the two-phase system "polymer—plasticizer" on the performance of PMB 90

Indicator name	GOST requirements	Name of plasticizer						
		–	Fuel oil M 200		Oil I-50	Uniplast	SPE	Katgol
			10.5%	15.0%				
Needle penetration depth, mm^{-1} 25 °C, 0 °C	91–130	67	70	93	99	107	104	110
	At least 40	23	31	44	49	41	43	52
Stretchability, cm:25 °C, 0 °C	At least 30	≥ 150	63.7	65.7	60.3	68.8	73.4	61.8
	At least 15	–	23.4	45.1	17.8	43.7	44.3	40.1
Temperature, °C: soften fragility according to Fraas	At least 51	54	65.3	66.5	69.4	61.1	65.0	60.4
	Not higher − 25	− 18	− 21	− 25	− 27	− 21	− 26	− 25
Elasticity, %: 25 °C, 0 °C	At least 85	–	92	98	92	95	96	95
	At least 75	–	68	77	70	79	78	78
Mass change after warming up, %	No more 1	0.34	0.54	0.61	1.98	0.67	0.45	4.66
Flash point, °C	At least 220	268	288	290	274	276	279	258
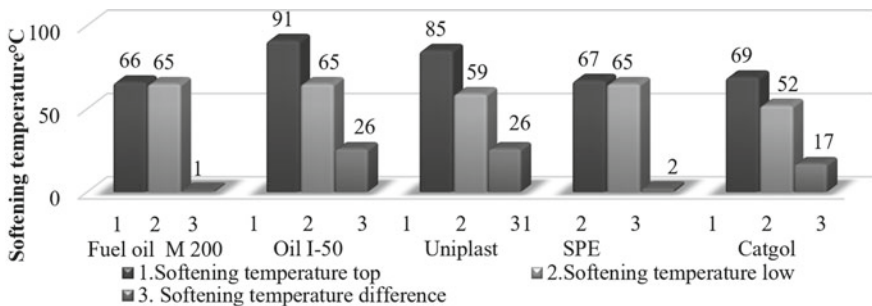
Fig. 1 Bituminous binder storage stability for 72 h at 185 °C

At the same time, if we analyze the results obtained in the course of the study (Table 5 and Fig. 2), we can note the dependence of the effectiveness of the obtained formulations of the PBV on the compatibility of the system "polymer—plasticizer".

Table 5 Partial performance criteria for PMB-90, depending on the type of plasticizer

Indicator name	Name of plasticizer				
	SPE	Katgol	Uniplast	Oil I-50	M 200
Needle penetration depth 25 °C	1.16	1.22	1.19	1.10	0.78
Needle penetration depth 0 °C	1.08	1.30	0.98	1.23	0.78
Stretchability 25 °C	2.45	2.06	2.29	2.01	2.12
Stretchability 0 °C	2.95	2.67	2.91	1.19	1.56
Temperature soften	1.27	1.18	1.20	1.36	1.28
Temperature fragility according to Fraas	1.04	1.00	0.84	1.08	0.84
Elasticity 25 °C	1.13	1.12	1.12	1.08	1.08
Elasticity 0 °C	1.04	1.04	1.05	0.93	0.91
Flash point	1.27	1.17	1.25	1.25	1.31
Mass change after warming up	2.22	0.21	1.49	0.50	1.81
Stability in tubes	2.5	0.29	0.19	0.19	5.00
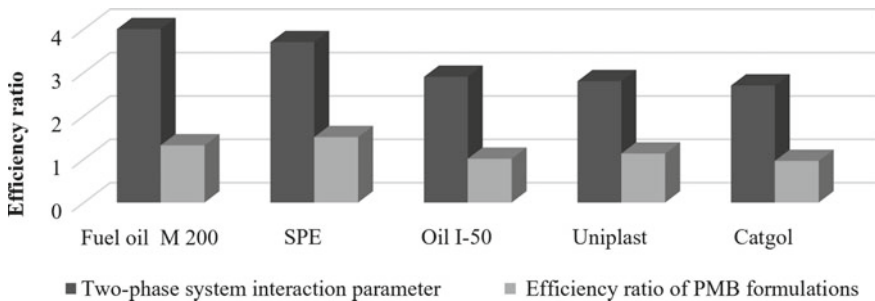
Fig. 2 Indicators of the generalized performance criteria for PMB 90 formulations and the compatibility parameter of the two-phase system "polymer—plasticizer"

Comparison of the results of calculating the generalized efficiency criteria for formulations of PMB 90 and compatibility coefficients of the two-phase system "polymer—plasticizer" are shown in Fig. 2.

Despite the fact that the application of polymer modified bitumen binders is preceded by a feasibility study, which is associated with an increase in its cost relative to the basic bitumen [4, 5], there are almost no industry works devoted to the raised problem. This necessitates the development of laboratory tests at the stage of selecting the composition of polymer-bitumen, allowing in a short time with high reliability to obtain information about possible destructive processes of modified binder at various stages of its life cycle to minimize production costs and the possibility of fulfilling the contractor's warranty obligations.

4 Conclusion

1. The problem of imperfect methodological approach to the choice of plasticizers for modifying bituminous binders and evaluation of their compatibility with bitumen and polymer has been revealed, which is an actual production problem that needs to be solved.
2. It has been established that at the stage of evaluating the initial characteristics of the raw components (polymer, plasticizers) and their compatibility by studying the two-phase systems, it is possible to predict the efficiency of polymer-modified bituminous binder.
3. It is shown that the compatibility of polymer and plasticizer is a key control factor in the formation of resistant to destructive processes polymer-bitumen matrix that determines the effectiveness of physical and mechanical properties of the PMB.

References

1. Kataware, A.V., Singh, D.E.: Evaluating effectiveness of WMA additives for SBS modified binder based on viscosity, Superpave PG, rutting and fatigue performance. Constr. Build. Mater. **146**, 436–444 (2017). https://doi.org/10.1016/j.conbuildmat.2017.04.043
2. Santagata, E., Baglieri, O., Tsantilis, L.: Experimental investigation on the combined effects of physical hardening and chemical aging on low temperature properties of bituminous binders. RILEM Bookseries **11**, 631–641 (2016). https://doi.org/10.1007/978-94-017-7342-3-51
3. Galeev, R., Nizamov, R., Abdrakhmanova, L., Khozin, V.: Resource-saving polymer compositions for construction purposes. In: IOP Conference Series: Materials Science and Engineering (2020). https://doi.org/10.1088/1757-899X/890/1/012111
4. Litovchenko, D.P., Shiryaev, A.O., Vysotskaya, M.A., Lashin, M.V.: Use of plasticizers in the production of PMB, as a tool for creating effective binders. CTESiberia (2019). https://doi.org/10.1051/e3sconf/202015706034
5. Kumar, K., Singh, A., Maity, S., Srivastava, M., Sahai, M., Singh, R., Garg, M.O.: Rheological studies of performance grade bitumens prepared by blending elastomeric SBS (styrene butadiene styrene co-polymer in base bitumens. J. Ind. Eng. Chem. **44**, 112–117 (2016). https://doi.org/10.1016/j.jiec.2016.08.017
6. Fernandes, S.R.M., Silva, H.M.R.D., Oliveira, J.R.M.: Developing enhanced modified bitumens with waste engine oil products combined with polymers. Constr. Build. Mater. **160**, 714–724 (2018). https://doi.org/10.1016/j.conbuildmat.2017.11.112
7. Munera, J.K., Ossa, E.A.: Polymer-modified bitumen: optimization and selection. Mater. Des. **62**, 91–97 (1980–2015). https://doi.org/10.1016/J.matdes.2014.05.009
8. Vysotskaya, M.A., Kuznetsov, D.A., Litovchenko, D.P., Barkovsky, D.V., Shiryaev, A.O.: The need for a plasticizer in the production of polymer-bitumen binders. Bull. Belgorod State Technol. Univ. named after VG Shukhov **5**, 16–22. https://doi.org/10.34031/article-5cd6df466bb9e0

9. Vysotskaya, M.A., Litovchenko, D.P., Korolev, E.V., Shiryaev, A.O.: The effect of polymer and plasticizer compatibility. Proc. Kazan State Univ. Arch. Civ. Eng. **2**(56), 22–36. https://doi.org/10.52409/20731523_2021_2_22

10. Inozemtsev, A.S., Korolev, E.V.: Multicriteria optimization. Int Res J **11**(4), 55–60 (2017). https://doi.org/10.18454/IRJ.2016.53.201

11. Sun, L., Wang, Y., Zhang, Y.: Aging mechanism and effective recycling coefficient of modified SBS asphalt. Constr. Build. Mater. **70**, 26–35 (2014). https://doi.org/10.1016/j.conbuildmat.2014.07.064

12. Zani, L., Giustozzi, F., Harvey, J.: Effect of storage stability on chemical and rheological properties of polymer-modified asphalt binders for road pavement construction. Constr. Build. Mater. **145**, 326–335 (2017). https://doi.org/10.1016/j.conbuildmat.2017.04.014

Improving the Method of Assessing the Bearing Capacity of Complex Technical Systems

N. V. Pirumyan[1]([✉]) [iD], M. G. Stakyan[1] [iD], and S. B. Yazyev[2] [iD]

[1] National University of Architecture and Construction of Armenia, Yerevan, Armenia
pirumyannarine@gmail.com
[2] Don State Technical University, Rostov-On-Don, Russian Federation

Abstract. The new method for assessing the bearing capacity of structural elements of complex technical systems, taking into account single and complex factors in a wide range of durations ($N = 10^3 \ldots 10^8$ cycles) with different amounts and combinations of their actions is proposed. Based on the system analysis, the classification of negative and positive impact factors was performed and it was shown that the main one of them, that reduces the bearing capacity, is a combination of corrosion and fatigue processes. As positive factors that increase the cyclic strength and durability of structural elements, the technologies for surface strengthening of welds and the application of new corrosion-resistant polymer coatings on stressed sections of elements are proposed. To assess the influence of the acting factors, 5 series of model tests were performed on the corrosion fatigue of steel samples with various combinations and numbers of factors (open air, corrosive environment, stress concentration, weld coatings, strengthening), which made it possible to form mathematical models of the action of these factors in the form of functions of corrosion coefficients for strength and durability. Unlike the current calculation method, which assess the bearing capacity only at the inflection point of the branches of the corrosion fatigue lines ($N \approx 7 \cdot 10^6$ cycles), the new method makes it possible to evaluate the strength and durability in the entire range of $N = 10^3 \ldots 10^8$ cycles and, by clarifying the calculation procedures, to ensure high productivity and reliable uptime of specified elements with minimal material consumption.

Keywords: Complex technical systems · Structural elements · Bearing capacity · Fatigue · Corrosion · Durability · Polymer coating · Strengthening · Influencing factors

1 Introduction

The increasing volumes of production and services in various industries, energy, transport infrastructures and the social sphere, as well as the tightening of natural and climatic conditions, have put forward the need to develop and implement a complex of design, technological, operational procedures, maintenance and restoration work of complex technical systems (CTS)—structures and technological equipment for various purposes, complexes of agricultural machinery, transport infrastructure, etc. [1]. In relation to the

methods of CTS design developments, significant innovations have been introduced over the past decades, from which probabilistic methods for calculating the main parameters of influencing factors and characteristics of the bearing capacity of structural elements can be isolated, which contributed by clarifying the strength indicators of elements of system to achieve an increase in operating speeds and productivity, reducing the material consumption of structural elements and clarifying their actual service life [2, 3]. The next stage of clarifying the calculation procedures is a comprehensive account of the impact of factors that, as a rule, are acting together, in different numbers and combinations, and if their combination is unfavorable, they can significantly reduce the bearing capacity characteristics of the CTS. This requires a systematic analysis and classification of factors, as a result of which it is possible to achieve the optimal option of their number and combinations, as well as to propose new design and technological nature measures that compensate for the effect of negative factors. Traditional calculation methods do not take into account the influence of complex factors, and calculations are mainly performed for strength using constant magnitudes of these values corresponding only to certain point magnitudes of durability, i.e. calculations for durability are performed indirectly and incompletely, without covering the entire interval of the service life of the elements of system. These omissions require additions and clarifications of the current calculated procedures in order to ensure the necessary level of reliability of the CTS operation.

2 Methods and Materials

The actual operating conditions of the elements of CTS differed from other technical systems due to the diverse impact of a number of factors of a material science, design, technological, operational and climatic nature (there are about 11-s.), the number and different combinations of which are variable for each CTS. Among the factors according to the degree of damage, corrosion and fatigue processes are distinguished, which in most cases are acting together and initiate the development of damage in stressed sections of structural elements [4, 5]. Therefore, for ensure a given level of CTS productivity for each specific case, by applying of principles of system analysis, it is necessary to determine the type, number and combination of influencing factors in order to compensate for the negative appearance of separate factors [1].

   The purpose of the study is to develop a new computational method for assessing the strength and durability of CTS elements, taking into account the single or complex impact of influencing factors with their various combinations, in a wide range of cyclic durations, covering the impact of corrosion and fatigue processes in areas of limited and long endurance [6–9]. To achieve this, it is planned to solve the following tasks: analysis and classification of active factors by type, number and combinations of their effects; study of the possibility of using surface strengthening and new anticorrosive coatings on stressed sections of CTS elements; model fatigue tests conducting and fatigue line equations in the studied interval of cyclic durations obtaining; functions of corrosion coefficients receiving by the joint solution of the equations of comparative fatigue lines; calculations performing on the cyclic strength and durability of CTS elements under the different influence of the studied factors [10].

3   Results and Discussion

Installation and assemblage of CTS elements in open area with using of elements made of low-carbon structural steels of general purpose, after welding leads to significant corrosion phenomena caused by temperature changes during welding ($T = 350...1150\,°C$), as well as environmental influences (air humidity, precipitation, industrial and transport gases, daily and seasonal temperature fluctuations, etc.) [5]. Under the total impact of these factors, corrosion damages occur and develop in welds, in which complex electrochemical processes occur that initiate oxidative reactions in the surface layers, as well as micropores appearance and a further increase of these defects. These processes are also intensified under the influence of variable loading caused by fluctuations in loading mode, ambient temperature changes, elements structure vibrations (geological, anthropogenic), which are acting in different sections, and are forming a variable complex-stressed state. If there is a stress concentration ($K_\sigma = 1.8...2.5$) in the weld area, this condition can cause fatigue damage and microcracks. To increase the corrosion resistance of structural elements, the latest anti-corrosion protective polymer coating of the Belzona 1111FN10132 brand can be used. Static tests of steel samples with this protective coating applied in a corrosive environment ($FeCl_3$ 10% aqueous solution) confirmed the high corrosion-resistant property of this coating. Another important way to increase the welds corrosion-fatigue strength is to strengthening the surface layers by using various physical and mechanical methods of influence, that regulate the microstructure and stress state of the surface layers of the weld and the adjacent zone. For low-carbon structural steels, which are sensitive to plastic deformation, the most acceptable of these methods is the method of surface plastic deformation (SPD) of weld and the adjacent zone, which is carried out by using a relatively simple tool with deforming rollers operating on the principle of a friction planetary mechanism and having the shape of a working surface similar to the profile of the weld. In the interval of cyclic durations $N = 10^3...10^8$, which coincides to the actual service life of the CTS elements, the limits of corrosion endurance are falling and with a different gradient in the intervals of $N \leq 7 \cdot 10^6$ and $N > 7 \cdot 10^6$ cycles due to the different fatigue processes (adsorption, electrochemical) in progress, which in the ($\lg\sigma$, $\lg N$) coordinate system, the mathematical model of corrosion fatigue is represented, unlike open air tests, in the form of two-link fatigue lines with different slopes. This assumes that in the design calculations, the limits of long-term corrosion endurance for a given value N_i from the specified durability intervals are used as limit stresses. In traditional calculations, only the σ_{RG} value for $N \approx 7 \cdot 10^6$ cycles is taken, which differs from the values of the endurance limits for $N_i > 7 \cdot 10^6$ cycles and requires clarification by using the equation of the right branch of the corrosion fatigue curve. The experiments provide the performance of fatigue comparative model tests according to the "open air-corrosive environment" scheme, the initial of which are tests of flat samples (St10 steel, GOST 1050-74 regulatory document) in open air, and comparative tests—for corrosion fatigue of samples: smooth; with a stress concentrator (galtel); with a protective anticorrosive coating (*Belzona 1111*); hardened in the galtel zone (see Figs. 1, 2 and 3), with various combinations and the number of these factors. Corrosion fatigue tests were performed on a special installation operating on the principle of a closed loop force flow and loading samples with joint circular bending and torsion. A mobile corrosion chamber is installed in the working area of the sample, where, with the assistance of a

controlled hydraulic system, a corrosive liquid is supplied to the surface of the rotating sample by a drip or continuous flow.
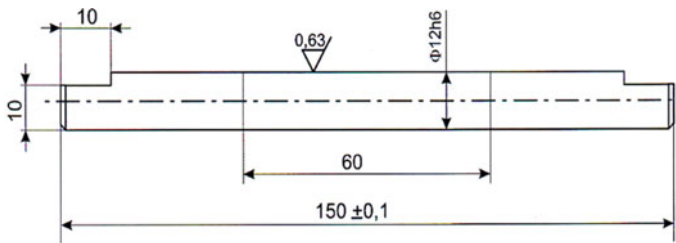

Fig. 1 Flat steel samples
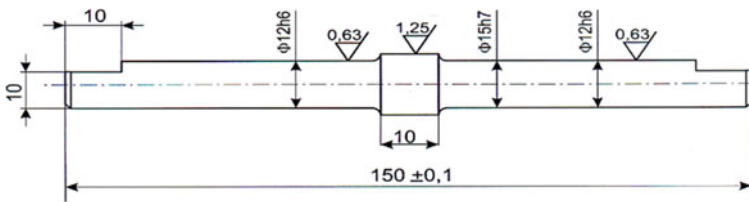
Fig. 2 Steel samples with a galtel

Fig. 3 Steel samples: with an anticorrosive coating (**a**), with a strengthened surface (**b**)

As a mathematical model of the fatigue process, the function is adopted, which in the ($\lg\sigma$, $\lg N$) coordinate system is represented

$$\text{as}\quad \lg N = C - m\lg\sigma \quad\text{or}\quad \lg\sigma = (C - \lg N)/m. \tag{1}$$

For the mathematical description of the experimental results in the entire interval $N = 10^3\ldots10^8$ loading cycles, according to (1) the following functions are adopted:

- for testing samples in open air:

$$\text{at } N \le N_G - \lg N = C - m\lg\sigma, \text{ and at } N > N_G - \lg\sigma_{RG} = const \tag{2}$$

- for testing samples in a corrosive environment:

$$\text{at } N \le N_G - \lg N = C - m\lg\sigma, \text{ and at } N > N_G - \lg N = C^I - m^I\lg\sigma, \tag{3}$$

where $\lg\sigma_{RG}$, $\lg N_G$ are the coordinates of the inflection point of the fatigue lines; and C, m and C^I, m^I are the parameters of the fatigue lines (2) and (3).

5 series of model tests were carried out (6 samples in each series) and the functions of parameters (2), (3) were obtained, which actually are integral characteristics of the fatigue process and are probabilistic in nature, obeying the logarithmically normal distribution law. According to GOST 25.C04-82 regulatory documents, the corrosion fatigue of the structure is estimated by the coefficient of corrosion impact

$$K_{\sigma k} = \sigma_{RK}/\sigma_{R0} < 1, \tag{4}$$

where σ_{RK}, σ_{R0} are the endurance limits of structural elements in a corrosive environment and in the open air.

Such an approach to assessing the bearing capacity of a structure corresponds only to the inflection point of the fatigue lines, which significantly limits the possibilities of the current calculation methodology. Taking into account the variability of endurance limits in the entire interval of loading cycles $N = 10^3...10^8$ as well as the two-link type and the different gradient of fatigue functions, the coefficient $K_{\sigma k}$ can be represented as a functional dependence $K_{\sigma k} = f(N)$ in the $N \leq N_G$ and $N > N_G$ intervals and (zones of limited and long endurance, Fig. 4), expanding the possibilities of $K_{\sigma k}$ application (4). Another way to expand the capabilities of the new calculation methodology is to quantify the cyclic durability of the structure by a similar coefficient

$$K_{Nk} = N_{Rk}/N_{RG} \gtrless 1 \tag{5}$$
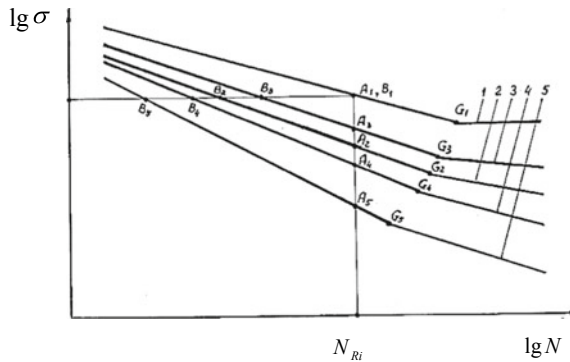
Fig. 4 Two-link fatigue lines: 1—for flat samples tested in open air; 2, 3, 4, 5—for samples tested in a corrosive environment: 2—for flat ones; 3—for strengthening ones; 4—for samples with a protective coating; 5—for samples with a galtel. $G_1(\lg \sigma_{RG1}, \lg N_{G1}), ..., G_2(\lg \sigma_{RG5}, \lg N_{G5})$-inflection points of fatigue lines $A_1(\lg \sigma_{R1}, \lg N_{R1}), ..., A_5(\lg \sigma_{R5}, \lg N_{R1})$ and $B_1(\lg \sigma_{R1}, \lg N_{R1}), ..., B_5(\lg \sigma_{R1}, \lg N_{R5})$—calculated points for $K_{\sigma k}$ and K_{Nk} at $N \leq N_G$.

where N_{Rk}, N_{RG} is the cyclic durability for endurance limits in a corrosive environment and in the open air, which is also not be taken into account in the current calculation methodology and can be represented as a $K_{Nk} = \phi(\sigma)$ function.

Functional dependencies $K_{\sigma k} = f(N)$ and $K_{Nk} = \phi(\sigma)$ (4), (5) have the following advantages:

- by specifying the strength characteristics of structural elements, it is possible to increase the production capacity of the CTS or to guarantee minimal material consumption of the system [4];
- by calculating the durability parameters, it is possible to specify the actual service life of the structure, within which the established level of reliability of the system is ensured;
- classifying the factors of materials science, design, technological and operational nature, by the method of system analysis of their distribution, it is possible to determine the bearing capacity of system structures under the complex impact of these factors.

This predetermined the compilation of a new calculation methodology using experimental data obtained during the fulfillment of complex fatigue tests and drawing up a graphical diagram of the location of two-link fatigue lines. For the organization and execution of 5 test series ($N_1, \dots, N_5$) the principle of single and complex impact of factors with their various numbers and combinations, which are grouped into 5 possible options (I, ..., V) found in real structural elements designs, is adopted. The method of system analysis logically approves the selection and compilation of 10 calculation schemes for determining coefficients (4), (5), which are taking into account a different combination and number of Influencing factors, and the formation of their functions $K_{\sigma k} = f(N)$ and $K_{Nk} = \phi(\sigma)$. Taking into account the two-link type of fatigue lines (Fig. 4), these calculation schemes are classified and separately presented in zones of limited ($N_{Ri} \leq N_{G1}$) and long-term ($N_{Ri} > N_{G1}$) endurance. During open air tests in the $N_{Ri} > N_{G1}$ zone, the fatigue line of flat samples takes a horizontal position, which changes the structure of the parameters of the calculation schemes. The rest design schemes are structurally identical to the case $N_{Ri} \leq N_{G1}$, but with the parameters of the corrosion fatigue lines for the right branch. As an example, the calculation scheme N5 is considered, which is covering the impact of four factors (*"corrosive environment, open air, stress concentration, strengthening"*), which are evaluated by coefficients:

$K_{\sigma k1} = \sigma_{R2}/\sigma_{R1}, K_{Nk1} = N_{R2}/N_{R1}$—"corrosive environment, open air"; $K_{\sigma k2} = \sigma_{R2}/\sigma_{R5}, K_{Nk2} = N_{R2}/N_{R5}$—"stress concentration"; $K_{\sigma k3} = \sigma_{R3}/\sigma_{R5}, K_{Nk3} = N_{R3}/N_{R5}$- "strengthening of the weld surface"; $K_{\sigma k5} = \sigma_{R3}/\sigma_{R5}, K_{Nk5} = N_{R3}/N_{R5}$—the total factor of accounting for all these factors, which, according to the method of independent impact of factors adopted in the applied mechanics, is defined as

$$K_{\sigma k5} = K_{\sigma k1} \cdot K_{\sigma k3}/K_{\sigma k2}, \quad K_{Nk5} = K_{Nk5} = K_{N1} \cdot K_{N3}/K_{N2} \qquad (6)$$

The $K_{\sigma k5} = f_5(N)$ and $K_{\sigma k5} = \phi_5(\sigma)$ functions in areas of limited and prolonged endurance, according to (1)–(6), take the form

(a) at $\sigma_{R5} \geq \sigma_{RG1}$—

$$\lg K_{\sigma k5} = \left(\frac{C_3}{m_3} - \frac{C_1}{m_1} \right) - \left(\frac{1}{m_3} - \frac{1}{m_1} \right) \lg N = S_5 - M_5 \lg N \qquad (7)$$

(b) at $\sigma_{R5} \geq \sigma_{RG1}$—

$$\lg K_{\sigma k5} = \left(\frac{C_3^1}{m_3^1} - \lg \sigma_{RG1} \right) - \frac{1}{m_3^1} \lg N = S_5^1 - M_5^1 \lg N \qquad (8)$$

(c)　at $N_{R5} \leq N_{G1}$—

$$\lg K_{Nk5} = (C_3 - C_1) - (m_3 - m_1) \lg \sigma = \Delta C_5 - \Delta m_5 \lg \sigma \qquad (9)$$

(d)　at $N_{R5} > N_{G1}$—

$$K_{Nk5} = \left(C_3^1 - \lg N_{G1}\right) - m_3^1 \lg \sigma = \Delta C_5^1 - m_5^1 \lg \sigma \qquad (10)$$

To deduce the parameters of functions (7)–(10), the principle of constancy $\lg N_{Rk} = const$ for the $K_{\sigma k}$ and $\lg \sigma_{Rk} = const$ coefficients—for K_{Nk} is adopted, according to the graphical representation of this procedure in Fig. 4 (relations of coordinates of A_1, ..., A_5 and B_2, ..., B_5 points).. For all variants of comparable test series it is similarly possible to make calculation schemes for the formation of $K_{\sigma ki} = f_i(N)$ and $K_{Nki} = \phi_i(\sigma)$ coefficient functions and, sequentially performing calculations according to expressions (6)-(10). This procedure makes it possible to create an algorithm of a new calculation method for obtaining functions (7)–(10), and using them—to determine the essential parameters of the bearing capacity of structural elements, taking into account the option of complex interaction of factors.

4　Conclusion

In order to increase the resistance to corrosion fatigue of butt welded joints, which are significant stress concentrators, the technology of surface plastic deformation of welds has been applied; in welds, due to the appearance of residual compression stresses, the influence of working loading has been significantly compensated and the fatigue resistance of structural elements has been increased. Corrosion and fatigue tests of 5 series of steel samples were carried out under the complex impact of these factors, according to the results of which a new calculation method for assessing the fatigue strength and durability of welded joints of structural elements in the entire range of corrosion endurance ($N = 10^3...10^8$ cycles) was developed. Unlike to the existing standard and reference calculation methods, the implementation of which is limited at the inflection point of the corrosion fatigue lines ($N \approx 7 \cdot 10^6$ cycles), and calculations are performed only on fatigue strength, the new method proposes functions of corrosion coefficients for strength and durability in the entire specified interval of the number of cycles. Calculation schemes have been compiled to assess corrosion-fatigue strength and durability under the complex impact of factors that are not fulfilled in the current calculation methods. The use of statistical characteristics of the equations of corrosion fatigue lines to form the functions of these coefficients allows calculations to be performed at a given level of probability of non-destruction of structural elements, as well as their equal levels of reliability for various types of arrangement (sequential and parallel) to be established.

References

1. Volgina, N., Shulgin, A., Khlamkova S., Sharipzyanova, G., Vorobyov, Y.: Analysis of the causes of destruction of gas pipelines. MATEC Web Conf. **329** (2020). https://doi.org/10.1051/matecconf/202032903010
2. Aliyev, M., Zaytsev S., Ismagilova Z., Bayburova M.: Evaluating the load-bearing capacity of a section of the Orenburg-Zainsk main gas pipeline using static and cyclic loading methods. E3S Web Conf. **225**, 01012 (2021). https://doi.org/10.1051/e3sconf/202122501012
3. Pirumyan, N.V., Stakyan, M.G.: Measures to increase the building steel structures' bearing capacity. IOP Conf. Ser.: Mater. Sci. Eng. **913**, 1–7, 022006 (2020). https://doi.org/10.1088/1757-899X/913/2/022006
4. Pirumyan, N.V., Stakyan, M.G., Khazaryan, H.A.: Mathematical modeling of the process of reduction of the material consumption of gas transmission system elements. Key Eng. Mater. **906**, 115–124 (2022). https://doi.org/10.4028/www.scientific.net/KEM.906.115
5. Krastev, D.: Improvement of corrosion resistance of steels by surface modification, pp.295–316. IntechOpen, London (2012). https://doi.org/10.5772/33247
6. Pirumyan, N.V., Stakyan, M.G.: Assessment of corrosion fatigue strength of gas-transport system constructions under atmospheric forcing. IOP Conf. Ser.: Materials Sci. Eng. **698**, 1–7, 022077 (2019). https://doi.org/10.1088/1757-899X/698/2/022077
7. Stenberg, T., Lindgren, E., Barsoum, Z., Barmicho, I.: Fatigue assessment of cut edges in high strength steel—influence of surface quality. Mat.-wiss. u. Werkstofftech. **48**, 1–14 (2017). https://doi.org/10.1002/mawe.201600707
8. Rowiński, S.: Effect of steel-cutting technology on fatigue strength of steel structures. Tests Anal. Mater. **14**, 6097 (2021). https://doi.org/10.3390/ma14206097
9. Parareda, S., Lara, A., Sieurin H., D'Armas, H., Casellas, D.: Increasing fatigue performance in AHSS thick sheet by surface treatments. MATEC Web Conf. **165**, (2018). https://doi.org/10.1051/matecconf/201816522015
10. Praca, M., Uehara, S., Ferreira, M., Mian, O.: New polymeric coating on sputtered bearings for heavy duty diesel engines. SAE Int. J. Engines **6**(1), 623–628 (2013). https://doi.org/10.4271/2013-01-1724

Optimization of Foam Fiber Concrete Mix Design by Mathematical Modeling

A. S. Pilipenko ⓘ, O. B. Lyapidevskaya ⓘ, and A. M. Minaeva⁽✉⁾ ⓘ

Department of Building Materials Science, Moscow State University of Civil Engineering,
Yaroslavskoye Shosse 26, Moscow 129337, Russia
`20anna00@list.ru`

Abstract. The purpose of the conducted research was to optimize the foam fiber concrete technology and develop a methodology for selecting its composition based on the methods of mathematical planning of the experiment and analytical processing of its results. Processing and optimization of experimental data made it possible to establish the influence of variable factors on the properties of foam fiber concrete samples. It has been established that the fiber consumption has a significant effect on the strength and density of concrete, and the length of the basalt fiber affects only the strength of the samples. The graphical interpretation of the data obtained makes it possible to determine the consumption of basalt fiber depending on the required strength of the products and the consumption of Portland cement. The specific strength of foam fiber concrete is adopted as an optimization parameter. The research results can be used in the development of methods for selecting the composition of foam concrete reinforced with basalt fiber.

Keywords: Foam fiber concrete · Specific strength · Basalt fiber · Modeling · Density · Compression strength

1 Introduction

The current level of technological development of the construction industry and, in particular, the production of building materials, involves the active introduction of advanced methods that allow raising the organizational level of production and obtaining highly efficient materials. Particular attention is paid to the implementation of BIM and digital technologies [1–3]. If the implementation of digitalization opportunities in the conditions of a construction site is problematic, then in the technologies of building materials, in the conditions of existing production facilities, the use of such technologies is justified and already gives positive results [4–6]. Modeling of technological processes in the conditions of improving existing production facilities and designing new ones makes it possible to solve both technological and organizational problems [7–9]. The group of technological tasks may include selection and optimization of the composition of the material; selection of technological, transport and heating equipment, as well as

coordination of internal logistics interactions; control and optimization of technological parameters and processes; visualization of technological parameters and processes; predicting the properties of products with varying technological parameters on the model.

The group of organizational tasks includes: control and regulation of environmental parameters in production and household premises; remote control of technological processes; accounting and control of warehousing; external logistics and systematization of the supply of raw materials for production and products to customers. The existing modeling methodology is based on the fact that the technological process is considered as a cybernetic system, for which only external factors are important: the inputs and outputs of the system. All physical, physicochemical, thermal, mass transfer and other processes are not considered [10, 11]. Such an approach makes it possible to formalize the technology and use either the "black box" model or a set of similar models, each of which can be adequate to the technological stage. The model considers: (1) input variable factors (X_i … X_k) and control parameters (X_{k+1} … X_n), (2) output parameters—response functions (Y_1 … Y_z)—as a rule, product properties or process efficiency indicators (economic, energy), including optimization parameters (Y_{opt}) (Fig. 1). Optimization parameters, depending on the optimization goal, can be taken either product quality indicators, or heat consumption for technological processes, or financial result [12, 13].
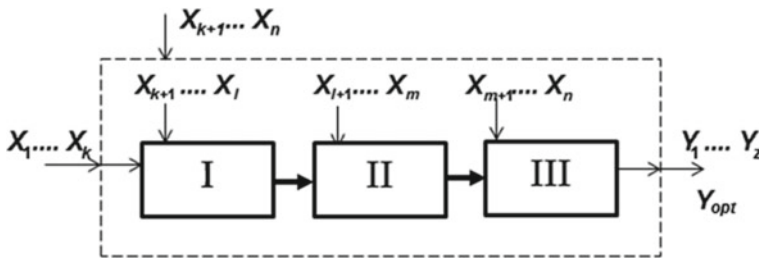
Fig. 1 General view of the cybernetic model of the technological process: I, II, III—technologic blocks; X_i … X_k—*variable input factors;* X_{k+1} … X_n—*control parameters;* Y_1 … Y_z—output parameters (response functions); Y_{opt}—optimization parameters

The purpose of this research is to optimize the foam fiber concrete technology and develop a methodology for selecting its composition based on the methods of mathematical planning of the experiment and analytical processing of its results.

2 Materials and Methods

The basis of the experiment conducting is the methodology for planning, processing the results of the experiment and their analytical optimization, developed at NRU MGSU. This methodology includes the planning and implementation of an experiment at two levels; analytical optimization and interpretation of results. The technique has been tested in the analysis of the technologies of cellular concrete, textile concrete, polymer-cement concrete, ceramic products, as well as various types of heat-insulating materials [14].

First level of the experiment covers the main technological factors of a statistical nature and concerning both the composition of the material and the parameters characteristic of each of the technological stages. The list of such factors is formed on the basis of a passive experiment (observation of the technological process) and from the analysis of a priori information [10–13]. Deterministic factors are not considered in the experiment, but are taken as external constants.

Fractional replicas of rotary-time plans of orders IV…VII are used as a basis for planning an experiment. An experiment is carried out according to the results of which linear dependences of the response functions ($Y_1 … Y_z$) on the variable factors ($X_1 … X_k$) are obtained. A coefficient for each of these factors makes it possible to estimate the magnitude and direction of this factor's influence on the result. According to the results of the first level of the experiment, 3–5 of the most significant factors are selected and move to the second level. Second level experiment is carried out on the basis of D-optimal rotatable plans that allow obtaining full quadratic regression equations. The resulting quadratic polynomials after checking the significance of the coefficients and their adequacy are considered as mathematical models of the processes under study.

The influence of each factor on the result (response functions) is assessed and the results are analyzed. The result of the analysis is conclusions about the causes (physical and chemical etc.) that determine the impact; about the presence of significant paired interactions (synergistic or antagonistic), as well as about possible directions for further research going into the field of building materials science.

Optimization of equations that have significant coefficients at the second degrees of variable factors (X_n^2) is carried out by the analytical method. This method is based on the following provisions: the obtained regression equations adequately describe the studied technological process; each equation is an algebraic function of several variables (according to the number of significant variable factors), and methods of mathematical analysis are applicable to study this function [13, 14]. Each equation is differentiated by factors of the second order and partial extreme of the response functions are determined. The obtained digital values or optimization functions are substituted into the regression equations and the optimized functions are obtained.

Results of optimization process were taken for usage in experimental part. This technology was aimed to produce light wall blocks, which are ones of the most common types of building wall materials in Russia.

3 Results and Discussion

The production of foam fiber concrete includes the following technological stages: preparation of the binder and pretreatment of fiber; preparation of resistant foam and dosing of all components; mixing the components in the mixer and obtaining a foam concrete mixture of the required flowability, workability and density; product molding and heat treatment.

In the experiment, the response functions are the following: foam fiber concrete density (Y_1), kg/m^3; compression strength of foam fiber concrete (Y_2), MPa. Specific strength (strength/density ratio, R_{sp}, MPa) is taken as an optimization parameter. The total number of factors (excluding deterministic and non-statistical evaluations), on which the

material manufacturing process depends, exceeds 50. Based on the results of the analysis of a priori information about technological processes similar to the one being designed, sampling of 19 factors that have the highest influence on the results of the experiment (strength and density) was made.

A material assessment of the degree of influence of sample factors was carried out during the first stage of the experiment and processing data. The estimated factor was the calculated coefficients b_i for single X_i. The experimental conditions of the first stage are presented in Table 1 in columns 1–4. In accordance with the conditions, series of experiments were carried out to determine the strength and density of the samples. Processing the results and calculating the coefficients for linear values of the factors made it possible to determine the coefficients of the regression equations for single values of the factors (Table 1, columns 5 and 6). The coefficients less (in modulus) than the confidence interval $\Delta b = 3.5$ MPa were taken insignificant and equated to zero ($b_i = 0$). Four factors—basalt fiber consumption (C_f), length of basalt fibers (L_f), Portland cement consumption (C_{Pc}) and foaming agent consumption (C_{fa}) had highest influence on the compressive strength These factors became the basis of the second stage of the experiment, which was carried out according to the plan based on the quadratic matrix of the four-factor experiment.

The experimental conditions of the second stage are presented in Table 2. The two-stage foam concrete technology has been studied well and concrete compositions have been extensively tested. The use of basalt fiber has a novelty; therefore, special attention was paid to this aspect of the technology in the experiment. Accordingly, one of the goals of the experiment was the development of the foundations of the methodology for selecting the composition of foam fiber concrete.

Processing the results of the experiment, and determining only significant factors made it possible to obtain the following polynomials:

- for density:

$$Y_1 = 560 - 20X_2 - 60X_4 + 12X_2^2 \tag{1}$$

- for compressive strength:

$$Y_2 = 2.81 + 0.25X_1 + 0.12X_2 + 0.32X_3 - 0.22X_4 - 0.11X_1X_2 + 0.13X_2X_3 \tag{2}$$

The confidence intervals for the density were taken as 10 kg/m^3, for the strength—as 0.10 MPa. The analysis of polynomials shows that the change in the density of foam fiber concrete is significantly influenced by the consumption of the foaming agent and the length of the basalt fibers (to a lesser extent). At the same time, a significant coefficient at X_2^2 allows us to draw the following conclusions. First, the influence of the fiber length is ambiguous, and at its values approaching the maximum of the factor definition range, the strength of the samples may decrease. Secondly, analytical optimization can be applied to the obtained polynomials.

Strength significantly depends on each of the variable factors, while the consumptions of basalt fiber and Portland cement have the highest impact on strength. Significant coefficients for paired interactions suggest the presence of a synergistic or antagonistic

Table 1 Experimental conditions for ranking and determining the significance of factors

Factor's name	Coding symbol, X_i	Average factor, $\overline{X_i}$	Variation interval, ΔX_i	The value of the coefficient at X_i	
				Y_1	Y_2
Basalt fiber consumption (C_f), [kg/m^3]	X_1	0.75	0.25	4	0.27
Basalt fiber length (L_f), [mm]	X_2	5	1	-20	0.14
Portland cement consumption (C_{Pc}), [kg/m^3]	X_3	265	25	3	0.34
Foaming agent consumption (C_{fa}), [kg/m^3]	X_4	10	2	-60	-0.23
Basalt fiber diameter (d_f), [μm]	X_5	5	1	-6	0.09
Sand consumption (C_s), [kg/m^3]	X_6	120	40	7	-0.08
Water consumption (C_w), [dm^3/m^3]	X_7	110	20	3	-0.07
Sand grinding time (τ_1), [min]	X_8	40	10	6	0.05
Mill load factor (α)	X_9	0.5	0,2	5	0.07
Duration of foam preparation (τ_2), [min]	X_{10}	12	4	10	-0.04
Rotational speed of the foam mixer shaft (n_1), [min^{-1}]	X_{11}	40	10	9	-0.05
Mixing duration (τ_3), [min]	X_{12}	10	4	8	0.09
Mixer shaft rotation frequency (n_2), [min^{-1}]	X_{13}	25	5	10	0.10
Exposure before heat treatment (τ_4), [h]	X_{14}	3	1	4	0.09
Exposure temperature (t_1), [°C]	X_{15}	30	10	5	0.08

(*continued*)

Table 1 (*continued*)

Factor's name	Coding symbol, X_i	Average factor, $\overline{X_i}$	Variation interval, ΔX_i	The value of the coefficient at X_i	
				Y_1	Y_2
Rise of temperature in the heat treatment chamber (τ_5), [h]	X_{16}	4	1	5	0.07
Exposure at constant temperature (τ_6), [h]	X_{17}	6	1	6	0.09
Heat treatment temperature (t_2), [°C]	X_{18}	80	15	7	0.11
Decrease in temperature to 30 °C, (τ_7), [h]	X_{19}	4	1	6	0.08
Confidence interval Δb				8	0.06

Table 2 Experimental conditions

Factor's name	Coding symbol, X_i	Average factor, $\overline{X_i}$	Variation interval, ΔX_i	Factor's value on variation levels	
				-1	$+1$
Basalt fiber consumption, [kg/m³]	X_1	0.75	0.25	0.5	1.0
Basalt fiber length, [mm]	X_2	5	1	4	6
Portland cement consumption, [kg/m³]	X_3	265	25	240	290
Foaming agent consumption, [kg/m³]	X_4	10	2	8	12

effect of these interactions. The nature of the influence should be determined by the results of the material structure study, which was not the task of these study.

Analytical optimization includes the determination of the optimal fiber length, the formation of optimization dependences for the density and strength, obtaining the dependence for specific strength and graphic interpretation of the results.

(1) The optimal fiber length is determined using the analytical optimization method:

$$\partial Y_1 / \partial X_2 = -20 + 24 X_2 = 0 \tag{3}$$

$$X_2 = \frac{20}{24} = 0.83 \tag{4}$$

In physical terms, the optimal length of basalt fiber will be:

$$\tilde{X}_2 = \overline{X_2} + \Delta X_2 \cdot 0.83 = 5 + 1 \cdot 0.83 = 5.83 \, \text{mm} \tag{5}$$

(2) Solving the Eq. (1) with $X_2 = 0.83$:

$$Y_1 = 560 - 20 \cdot 0.83 - 60X_4 + 12 \cdot 0.83^2 = 552 - 60X_4 \tag{6}$$

(3) Solving the Eq. (2) with $X_2 = 0.83$:

$$Y_2 = 2.9 + 0.16X_1 + 0.43X_3 - 0.22X_4 \tag{7}$$

(4) The foaming agent consumption (X_4) is determined by calculation. In the model, it is equated to the value $X_4 = 0$ and substituted into Eq. (7). Accordingly, Y_1 becomes equal to 552 kg/m^3, and the equation for the strength of foam fiber concrete takes its final form:

$$Y_2 = 2.9 + 0.16X_1 + 0.43X_3 \tag{8}$$

For ease of use, the Eq. (7) is converted into a graphical form (Fig. 2).
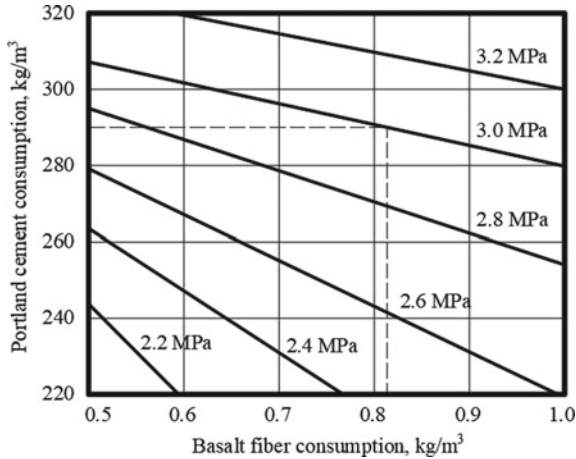

Fig. 2 Consumption of Portland cement and basalt fiber, depending on the required strength of products (with a design density of 552 ± 11 kg/m^3)

The consumption of the main components is set using the data of analytical optimization and Fig. 3. For foam fiber concrete with a density of 400 kg/m^3, optimal mix design includes 240 kg/m^3 of Portland cement, 73 kg/m^3 of siliceous component and

0.8 kg/m^3 of basalt fiber. The specific strength (R_s) is accepted as the optimization parameter of foam fiber concrete. Following optimization function was used to determine it numerically:

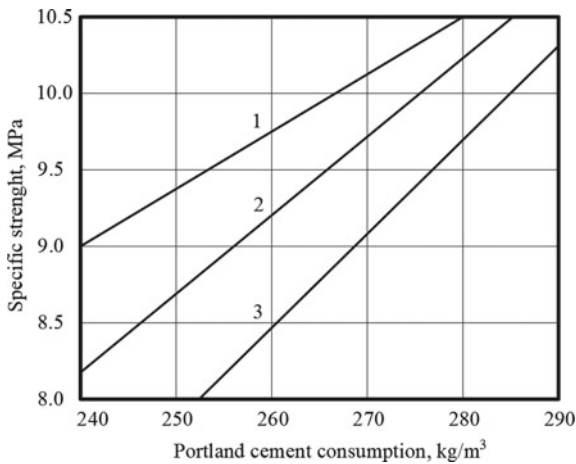$$R_s = \frac{Y_2}{Y_1} = \frac{1}{552}(2.9 + 0.16X_1 + 0.43X_3) \tag{9}$$

Fig. 3 Influence of Portland cement and basalt fiber consumption on specific strength of foam fiber concrete; basalt fiber: 1—1.0 kg/m^3; 2—0.75 kg/m^3; 3—0.5 kg/m^3

The graph of function (9) for the optimal values range is shown at Fig. 3.

As a result of the implementation of two stages of the experiment and the analytical optimization of the results and their graphic interpretation, the factors most influencing the strength and density of foam fiber concrete have been established; mathematical models of the influence of factors on the results have been obtained. A nomogram has been constructed that allows to determine the consumption of basalt fiber depending on the required strength of products and the consumption of Portland cement, as well as a nomogram for choosing the optimal parameters depending on the specific strength. The obtained dependencies can be used in the development of a method for selecting the composition of foam fiber concrete.

4   Conclusion

The article presents the main provisions of the methodology of a two-level experiment based on mathematical planning, system research and optimization of building materials technologies. On the example of the study of the main production processes, methods for assessing the significance of factors characterizing technological processes, constructing nonlinear regression polynomials, analytical optimization, selecting the composition and evaluating the characteristics of raw materials were tested.

It was found that the consumption of the foaming agent and the length of basalt fibers have the greatest effect on the density of the material, and the consumption of basalt fiber and Portland cement has a significant effect on the strength characteristics of the foam fiber concrete. The graphic interpretation of the optimized experimental results makes it possible to assess the influence of the consumption of basalt fiber and Portland cement, depending on the required strength characteristics of the products and to estimate the density values of the products depending on the strength and the established value of specific strength of foam fiber concrete.

References

1. Gudkov, P.: Use of thermal insulation systems for low-rise buildings as a component of information models. E3S Web Conf. **97**(4), 01039. https://doi.org/10.1051/e3sconf/201997 01039
2. Zhukov, A.: Mathematical methods for optimizing the technologies of building materials. In: VIII International Scientific Siberian Transport Forum, pp. 413–421. Springer Nature, Cham (2020). https://doi.org/10.1007/978-3-030-37919-3_40
3. Rumyantsev, B., Zhukov, A.: Experiment and modelling in the creation of new insulating and finishing materials, 1st edn. Moscow State University of Civil Engineering, Moscow (2013)
4. Zhukov, A.: Technological modeling, 1st edn. Moscow State University of Civil Engineering, Moscow (2013). ISBN 978-5-72640-780-7
5. Akhmadiev, F., Gilfanov, R.: Mathematical modeling and optimization methods, 1st edn. IPR MEDIA, Moscow (2017). https://doi.org/10.23682/116448
6. Klyuev, S., Klyuev, A., Vatin, N.: Fine-grained concrete with combined reinforcement by different types of fibers. MATEC Web Conf. **245**, 03006 (2018)
7. Amran, M., Fediuk, R., Vatin, N., Lee, Y., Murali, G., Ozbakkaloglu, T., Klyuev, S., Alabduljabber, H.: Fibre-reinforced foamed concretes: a review. Materials **13**(19), 1–36, 4323 (2020). https://doi.org/10.3390/ma13194323
8. Paulava, I.: Properties of basalt fiber sulfo-aluminate modified cement binders. E3S Web Conf. **212**, 02011. https://doi.org/10.1051/e3sconf/202021202011
9. Pettersson, M., Thorsson P.: FE-modelling of textile reinforced concrete facade elements. Mater. Struct. **54**(5), Gothenburg (2014)
10. Kodzoev, M., Isachenko, S., et al: Ceramic products and energy-efficient systems. IOP Conf. Ser.: Mater. Sci. Eng. **869**(3), 032006. https://doi.org/10.1088/1757-899X/869/3/032006
11. Zhukov, A., Shokodko, E., et al.: Internal acoustic materials and systems. In: International Scientific Conference Energy Management of Municipal Facilities and Sustainable Energy Technologies EMMFT 2018, pp. 740–747. Springer Nature, Cham (2019). https://doi.org/10.1007/978-3-030-19868-8_72
12. Zhukov, A., Bobrova, E., et al.: Modelling of Technology of mineral wool products. In: International Scientific Conference Energy Management of Municipal Facilities and Sustainable Energy Technologies EMMFT 2018, pp. 828–838. Springer Nature, Cham (2019). https://doi.org/10.1007/978-3-030-19868-8_81.
13. Meschke, G., Pichler, B., Rots, J.: Computational modelling of concrete structures, 1st edn. CRC Press, Austria (2018)
14. Suryavanshi, D., Akhtar, S.: Design optimization of reinforced concrete slabs using various optimization techniques. Int. J. Trend Scien. Res. Dev. **3**(5), 45–48 (2019). https://doi.org/10.31142/ijtsrd25231

Analysis of Intermediates Produced During the Synthesis of Alkyd Resins

V. A. Poluektova [ORCID], N. I. Cherkashina[(✉)] [ORCID], E. P. Kozhanova [ORCID], and D. S. Matveenko [ORCID]

Belgorod State Technological University Named After V.G. Shukhov, Belgorod, Russia
cherkashina.ni@bstu.ru

Abstract. The paper considers the possibility of using the FT-IR spectroscopy method in the production of alkyd varnishes and resins to control various stages of synthesis. A number of samples were analyzed at different stages of synthesis, selected under production conditions at the stages of transesterification and polycondensation. The formulation of pentaphthalic resin is presented, the chemistry and features of obtaining alkyd resins are analyzed. Having considered the issues of express control of the production of alkyd varnishes, the possibility of controlling the studied stages by infrared spectra in the laboratory was investigated and analyzed. It has been established that the IR spectra of samples taken sequentially during the synthesis can be used to control the course of the chemical reaction of polycondensation in the technological process. Control can be carried out according to three main absorption bands, taking into account the identified patterns observed in the synthesis process: stretching vibrations—OH; C–H stretching vibrations of olefins (oils) and arenes (phthalates); valence antisymmetric and symmetric C–H methyl and methylene groups; bending vibrations of four aromatic ring hydrogens.

Keywords: Catalyst · Sodium carbonate · FT-IR spectra · Polycondensation · Alkyd coatings

1 Introduction

The development of new materials, including polymers, is one of the promising areas of modern materials science. Particular attention is paid to the development of technologies and conditions for the industrial synthesis of macromolecular compounds, taking into account the economic and environmental aspects [1, 2].

In the process of production of polymer systems (varnishes, paints), the control of the parameters of the technological process of synthesis plays a very important role [3]. One of the main reasons for the high level of energy consumption and accident rate in the production of synthesis of alkyd varnishes and resins is the lack of operational control of the chemical state of the reaction mass and control of the synthesis reaction. In this regard, the task of developing instruments for monitoring and controlling the flow of chemical reactions of interesterification and polycondensation in the synthesis of alkyd

varnishes and resins becomes important. The means of control will improve the safety of the synthesis of alkyd varnishes and minimize the possibility of accidents at synthesis plants.

One of the methods for studying polymer systems is the spectrometric method [4, 5]. At present, there are a significant number of instruments and methods that make it possible to obtain infrared spectra and analyze the changes that occur during the synthesis of macromolecular compounds [6–8].

The most common method for express control of the course of chemical reactions in the production of alkyd resins is the Fourier-IR spectroscopy method. This method is used to analyze and identify unknown chemicals. It is suitable not only for the identification of macromolecular compounds, but also for polymer composite materials, including composite materials based on plant materials [9]. It can be used to determine the chemical structure, structure and composition of substances [10].

The object of this study was the improvement of methods for controlling the production process of alkyd resins as the basis for semi-finished alkyd varnishes. The purpose of the work is to study the possibility of express control by IR spectroscopy of the stages of transesterification and polycondensation of the synthesis of alkyd varnishes in order to improve production safety and minimize the possibility of accidents.

2 Methods and Materials

The compounds obtained at various stages of the industrial synthesis of alkyd resins were subjected to research. We selected 11 compounds obtained at various stages of the synthesis. The compounds were selected at the paint and varnish plant LLC "Yamshchik" (Russia, Belgorod). The sampling points on the production line are shown schematically in Fig. 1.
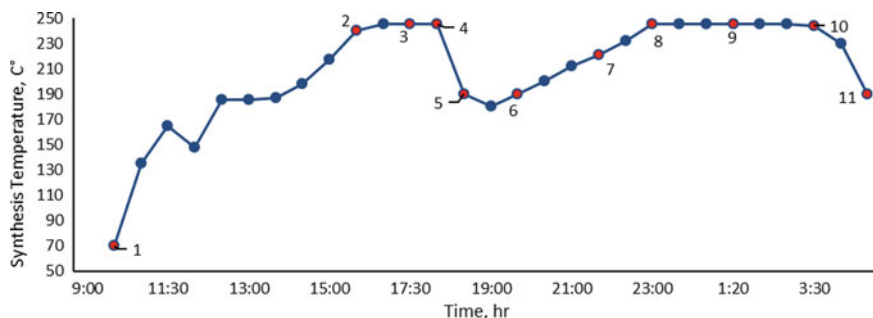

Fig. 1 Marking sheet for sampling IR analysis on a temperature–time program for the synthesis of alkyd resin PF-060: 1—sunflower oil, 2—sunflower oil + pentaerythritol + soda, 3—the middle of alcoholysis, 4—completion of alcoholysis, 5—before loading phthalic and maleic anhydride, 6—after loading phthalic and maleic anhydride, 7—set temperature, 8—exit for temperature conditions, the first sample, 9—the second sample, 10—the third (last) sample, 11—before unloading

Fourier IR spectra were obtained on a VERTEX 70 IR spectrometer (Bruker, Germany). The weight ratio of the components of the formulation of pentaphthalic resin is presented in Table 1.

Table 1 The composition of the semifinished pentaphthalic resin

Component	Weight ratio, %
Vegetable oil (sunflower)	60.0
Pentaerythritol	14.5
Phthalic anhydride	25.0

As a catalyst in the production of alkyd resins, compounds such as sodium and potassium carbonates can be used; calcium hydroxide, lithium hydroxide, sodium oxide, lead oxide, zirconium octoate, etc. [11–13]. Sodium carbonate was used as an interesterification catalyst in this work.

3 Results and Discussion

Semi-finished pentaphthalic alkyd varnishes are a solution of pentaphthalic resin. The process of obtaining alkyd resins for varnishes of different brands, depending on the raw materials used, is classically carried out in two stages. At the first stage, the interesterification of vegetable oil with a polyhydric alcohol, most often pentaerythritol or glycerin, occurs. At the second stage, the transesterification products obtained are condensed with a dibasic acid, phthalic anhydride is most often used (polycondensation reaction) to form a pentaphthalic or glyphthalic oligomer (base) with the required performance.

In the production under consideration, the first stage is the process of transesterification (alcoholysis) of vegetable oil with pentaerythritol. The scheme of this process is shown in Fig. 2.
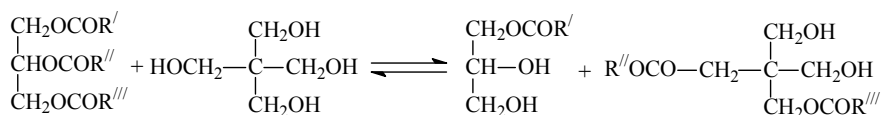
$$
\begin{array}{l}
CH_2OCOR^{/} \\
CHOCOR^{//} \\
CH_2OCOR^{///}
\end{array}
+ HOCH_2-\overset{CH_2OH}{\underset{CH_2OH}{C}}-CH_2OH
\;\rightleftharpoons\;
\begin{array}{l}
CH_2OCOR^{/} \\
CH-OH \\
CH_2OH
\end{array}
+ R^{//}OCO-CH_2-\overset{CH_2OH}{\underset{CH_2OCOR^{///}}{C}}-CH_2OH
$$

Fig. 2 Scheme of transesterification (alcoholysis) of vegetable oil with pentaerythritol

The spectrum of the feedstock (vegetable oil) and the spectrum of the mixture are shown in Fig. 3a. Comparison of the spectra showed the appearance of an absorption band in the region of 3200–3600 cm^{-1} and 1070–1080 cm^{-1}, due to the presence of OH-groups, which are characteristic of fragments of both triatomic and tetrahydric alcohols. The intensity of the stretching vibrations of the carbonyl group $> C=O$ in the ester groups 1720–1740 cm^{-1} increased significantly.
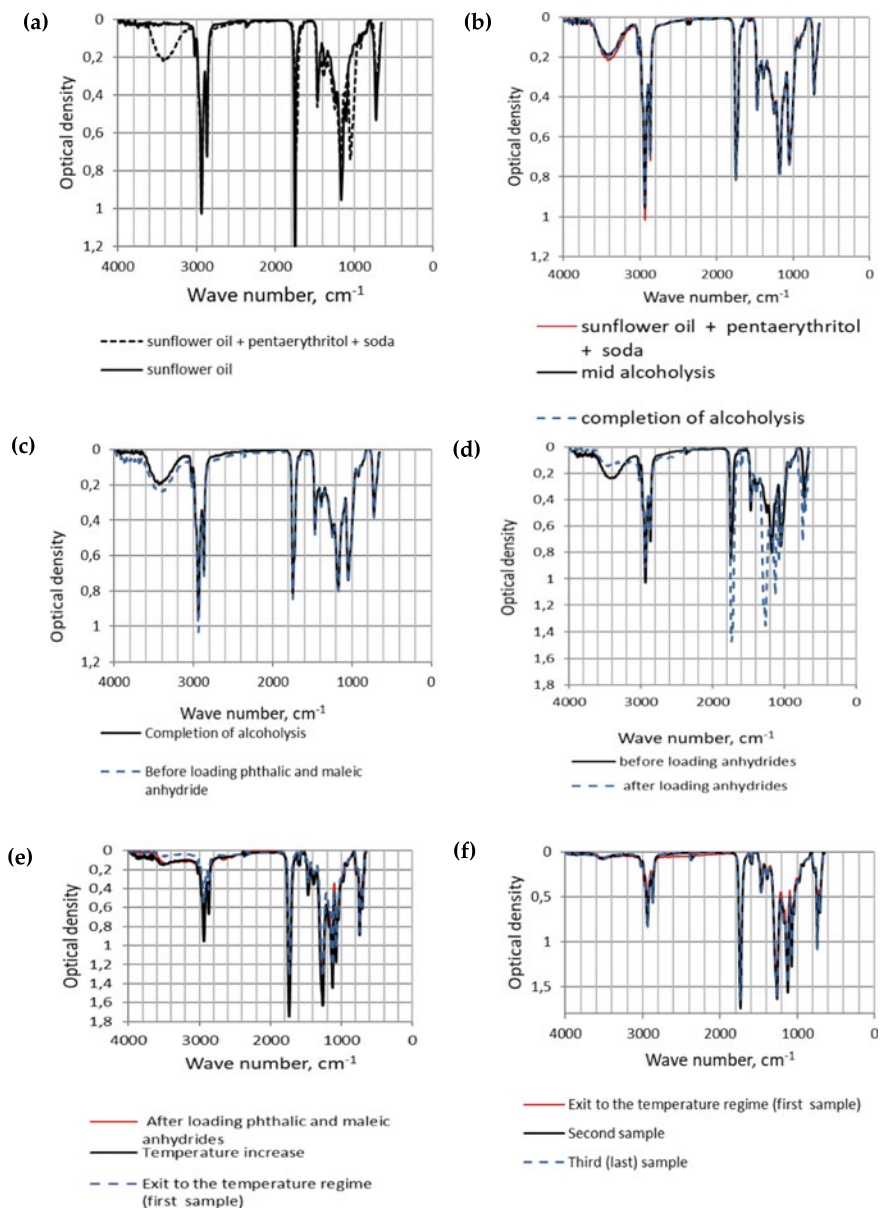
Fig. 3 IR spectra of samples: **a**—taken in the beginning of synthesis, **b**—selected in a process alcoholysis, **c**—taken after alcoholysis (cooling process), **d**—taken after addition of anhydrides, **e**—taken at the stage of temperature rise and exit to the temperature regime (before the stage of polycondensation), **f**—selected in a process polycondensation

Then, at this stage, two more samples were taken: in the middle (in terms of time) of alcoholysis and at the end of the interesterification reaction. Comparing the spectra, it can be noted that no obvious changes are observed (Fig. 3b).

An analysis of the alcoholysis stage showed that during this stage, the intensity of vibrations of symmetric and antisymmetric C–H (sp^3 hybridization) methyl (–CH_3) and methylene (–CH_2) groups decreases. The intensity and location of the stretching vibrations of the carbonyl group > C=O (1720–1700 cm^{-1}) in ester groups remain unchanged.

At the first stage (transesterification) there is a side reaction—the formation of polypentaerythritol. A sign is water released in small quantities. In addition, the reactions are reversible and during cooling before loading phthalic and maleic anhydrides part of the monoglycerides are converted back into diglycerides.

This process is undesirable, since a larger amount of diglycerides in the reaction mixture leads to some decrease in the gloss of the finished varnish. In order to reduce this effect, we recommend loading phthalic anhydride in the form of a melt at a temperature of the reaction mixture of 210–215 °C.

The direction of changes in the intensities of all characteristic absorption bands in the IR spectrum (Fig. 3c) during cooling changes in the opposite direction, which confirms the beginning of the reverse process before equilibrium in the system.

Thus, the completion of the transesterification step is difficult to control by qualitative analysis of IR spectroscopy.

Analyzing the IR spectra before and after loading anhydrides (Fig. 3d), we observed significant changes in the position and intensities of the main absorption bands, and the appearance of new ones. These changes are due to the combination of the IR spectra of various substances.

In the region of 3200–3600 cm^{-1}, the band of stretching vibrations of OH groups decreases significantly, and in the region of 2850–2900 cm^{-1}, the intensity of symmetric and antisymmetric vibrations of the methyl (CH_3) and methylene (C–H) groups in sp^3 hybridization decreases. The intensity of the stretching vibrations of the carbonyl group > C=O in ester groups 1720–1740 cm^{-1} increases significantly.

At the stage of temperature rise (Fig. 3e), the intensity of stretching vibrations of the carbonyl group > C=O in ester groups continues to increase, antisymmetric stretching and symmetric C–O–C ester groups $\overset{}{\underset{}{>}}C-O-\overset{}{\underset{|}{C}}=O$.

The transition to the temperature regime was accompanied by a continued decrease in the intensities of stretching vibrations of OH– groups, stretching vibrations of the carbonyl group > C=O in ester groups, antisymmetric stretching and symmetrical C–O–C of ester groups.

Thus, reaching the temperature regime (1 sample) is accompanied by a decrease in almost all intensities of the main absorption bands.

The second stage is polycondensation. At this stage, a low molecular weight product, water, is released. In order to shift the equilibrium towards the final products, it was removed continuously from the reaction mixture by the azeotropic method. Xylene was used as an azeotropic agent. Therefore, in the second stage, starting from a temperature of 190–192 °C, water and xylene were present in the reaction mixture until the very end of the process.

At this stage, mono- and diglycerides interact with phthalic anhydrides to form partial acid esters. The scheme of this process is shown in Fig. 4.
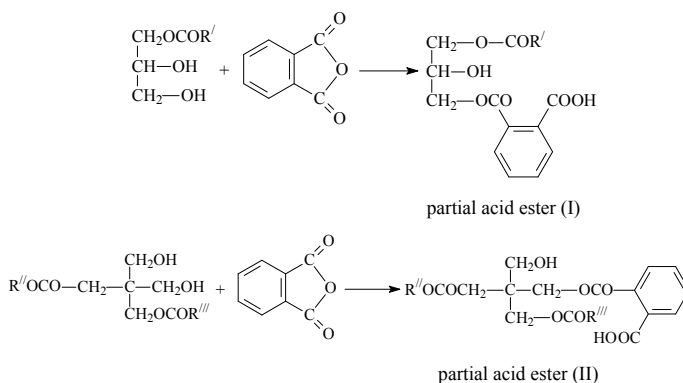

partial acid ester (I)

partial acid ester (II)

Fig. 4 Scheme of the formation of partial acid esters

The general view of the spectrum of the first polycondensation sample (Fig. 3f) qualitatively differs from samples 2 and 3: a sharp increase in the intensities of all absorption bands is observed.

The spectra of the second and third samples are almost indistinguishable, except for the bands 1720–1740 (stretching vibrations of the carbonyl group $>$ C=O), 1080 and 1130 cm^{-1} (stretching symmetric C–O–C), the intensity of which began to decrease in the 3rd sample.

Analysis of the samples after the condensation stage made it possible to conclude that there were no statistically significant changes in the IR spectra of the 3rd polycondensation sample and the sample after unloading from the reactor.

4 Conclusion

Having considered the issues of express control of the production of alkyd varnishes, the possibility of controlling the stages of transesterification and polycondensation by IR spectroscopy was investigated and analyzed in order to increase production safety and minimize the possibility of accidents. It has been found that the IR spectra of samples sequentially taken during the synthesis can be used to control the progress of the reactions of the polycondensation stage in the technological process. Control can be carried out according to three main absorption bands, taking into account the identified patterns observed in the synthesis process:

- gradual decrease in the bands characteristic of stretching vibrations –OH (3200–3600 cm^{-1});
- gradual decrease in the intensity of C–H stretching vibrations of olefins (oils) and arenes (phthalates) (3010–3100 cm^{-1}), stretching vibrations of both antisymmetric (2950, 2920 cm^{-1}) and symmetrical C–H methyl and methylene groups (2850 cm^{-1});

- gradual increase in the intensity of deformation vibrations of four aromatic ring hydrogens (740–710 cm^{-1}).

References

1. Grishin, D.F., Grishin, I.D.: Modern trends in controlled synthesis of functional polymers: fundamental aspects and practical applications. Russ. Chem. Rev. **90**, 231–264 (2021)
2. Gandini, A., Lacerda, T.M.: Monomers and macromolecular materials from renewable resources: state of the art and perspectives. Molecules **27**(1), 159 (2022). https://doi.org/10.3390/molecules27010159
3. Dubovik, N.S., Matyas, D.S., Dubovik, S.A., Lyubushkin, R.A.: Method for controlling reaction mass parameters during the synthesis of alkyd resins. J. Phys.: Conf. Ser. **1926**, 012009 (2021). https://doi.org/10.1088/1742-6596/1926/1/012009
4. Wang, F., Du, C., Chen, J., Shi, L., Li, H.: A new method for determination of pectin content using spectrophotometry. Polymers **13**(17), 2847 (2021). https://doi.org/10.3390/polym13172847
5. Li, X., Guo, L., Casiano-Maldonado, M., Zhang, D., Wesdemiotis, C.: Top-down multidimensional mass spectrometry methods for synthetic polymer analysis. Macromolecules **44**(12), 4555–4564 (2011)
6. Poluektova, V.A., Cherkashina, N.I., Starchenko, S.A., Romanyuk, D.S.: Features of the chemical interaction of 2-furaldehyde and 1,3,5-trihydroxybenzene in an alkaline medium to obtain a plasticizing additive. ChemEngineering **5**, 84 (2021). https://doi.org/10.3390/chemengineering5040084
7. Dwyer, J.L., Zhou, M.: Polymer characterization by combined chromatography-infrared spectroscopy. Int. J. Spectrosc. **2011**. Article ID 694645 (2011). https://doi.org/10.1155/2011/694645
8. Ramírez-Hernández, A., Aguilar-Flores, C., Aparicio-Saguilán, A.: Fingerprint analysis of FTIR spectra of polymers containing vinyl acetate. DYNA **86**(209), 198–205 (2019)
9. Loganina, V.I., Mazhitov, E.B., Averin, I.A., Karmanov, A.A.: Evaluation of the structure of a polysilicate binder with the addition of glycerin. Bull. BSTU named after V.G. Shukhov **2**, 14–20 (2019)
10. Fadlelmoula, A., Pinho, D., Carvalho, V.H., Catarino, S.O., Minas, G.: Fourier transform infrared (FTIR) spectroscopy to analyse human blood over the last 20 years: a review towards lab-on-a-chip devices. Micromachines **13**, 187 (2022). https://doi.org/10.3390/mi13020187
11. Uzoh, C., Nwabanne, J.: Investigating the effect of catalyst type and concentration on the functional group conversion in castor seed oil alkyd resin production. Adv. Chem. Eng. Sci. **6**, 190–200 (2016). https://doi.org/10.4236/aces.2016.62020
12. Elba, M.E., Rehim, E.M.A., Ashery. R.E.: Progress in organic coating: synthesis and characterization alkyd resin based on soya bean oil and glycerin using zirconium octoate as catalyst. Chem. Technol. Ind. J. **13**(1), 118 (2018)
13. Simpson, N., Maaijen, K., Roelofsen, Y., Hage, R.: The evolution of catalysis for alkyd coatings: responding to impending cobalt reclassification with very active iron and manganese catalysts using polydentate nitrogen donor ligands. Catalysts **9**(10), 825 (2019). https://doi.org/10.3390/catal9100825

Surface Structure of Modified Titanium Hydride Fraction

V. I. Pavlenko [ID], N. I. Bondarenko[(✉)] [ID], R. N. Yastrebinsky [ID], and Z. V. Pavlenko [ID]

Belgorod State Technological University Named After V.G. Shukhov, Belgorod, Russia
`bondarenko-71@mail.ru`

Abstract. This paper presents studies of the surface of titanium hydride fraction samples modified by applying to its surface an organic silicon oligomer and boric acid chemically from aqueous solutions, using methods of optical and scanning electron probe microscopy. To determine the surface topography of a solid, we used high-resolution scanning probe (atomic force) microscopy using the MFP-3D Stand Alone (MFP-3D-SA) AFM microscope. The presence of hydroxyl OH-groups on the surface of the initial titanium hydride was established by infrared spectroscopy methods. A significant increase in the intensity of absorption bands at 3480 and 3490 cm^{-1} (OH-groups) was recorded. Activation of the titanium hydride fraction surface with an organic silicon oligomer significantly increased the concentration of hydroxyl OH-groups on the surface of vacuum-dried titanium hydride fraction at 100 °C. We observed a difference in the surface structure of the initial and activated titanium hydride due to the formation of polysiloxane shell, as well as a difference in the surface structure of titanium hydride fraction containing polysiloxane and borosilicate shells due to the vitrification of boron oxide at 300 °C. The surface of a modified titanium hydride fraction containing a borosilicate shell showing a 4.2 µm atomic force scanning microscope probe stroke relative to the OX axis, small reductions of characteristic probe dips and elevations with height and depression differences to up 10 nm throughout the scanning area are visible.

Keywords: Borosilicate coating · Heat treatment · Titanium hydride · Sodium methylsilicate · Modification

1 Introduction

One of the directions of work on the technology of titanium hydride fraction production is the study of methods and modes of titanium hydride fraction surface modification in order to improve its thermal stability at high temperatures and to protect titanium from oxidation [1, 2].

It is known that the main glass-forming components of boroaluminosilicate coatings based on frites for metals are oxides SiO_2, Al_2O_3 and boric anhydride B_2O_3. To improve the technological properties (flowability, wetting ability), alkaline oxides are inserted into the coatings [3].

Modification of the titanium hydride fraction surface with a boron-containing component is due to the high neutron absorption cross-section in the thermal and suprathermal spectral areas by boron atoms, which leads to a decrease in the thermal neutron flux density and the level of trapped gamma rays [4, 5]. Experiments showed that it was not possible to achieve noticeable adsorption of boric acid (H_3BO_3) from aqueous solution on the surface of titanium hydride fraction [6–8].

The general requirement for coatings is to ensure protection of the titanium hydride fraction surface against destructive processes in the fraction at macro- and microlevels at elevated temperatures (over 250 °C). The composition of the coating is chosen so that during heat treatment of titanium hydride formed a continuous, stable at a given temperature film, reliably insulates the surface of titanium hydride from dissociation and subsequent oxidation of titanium [9, 10].

2   Methods and Materials

To prepare the experimental samples we used titanium hydride series GTK-D in the form of spherical granules (fraction) with a diameter of 1–4 mm; boric acid H_3BO_3 grade "hch", sodium methyl siliconate (GKZH-11M, $RSi(OH)_2ONa$, where $R = CH_3$. Infrared spectra were obtained using the following instruments: Specord-75IR infrared spectrometer (Germany) in the frequency range 400–4000 cm^{-1}; Nexus-470 FT-IR spectrometer (Thermo Nicolet, USA) with high resolution (0.5 cm^{-1}). Spectral range is 400–7000 cm^{-1}. High-resolution scanning probe (atomic force microscopy) was performed on the MFP-3D Stand Alone (MFP-3D-SA) AFM microscope (Asylum Research Inc., USA) to determine the surface topography of a solid. An optical microscope POLAM-P321 was used to determine optical microscopy.

3   Results and Discussion

The technology of titanium hydride modification consists of preliminary chemical activation of the fraction surface by silicon oligomer—sodium methyl siliconate with subsequent treatment with boric acid, release of solid phase of titanium hydride and subsequent drying at 100 °C.

Microscopic examination of the surface of the original titanium hydride fraction showed the presence of porosity, irregularities and defects with rough edges (Fig. 1).

The titanium hydride layer porosity is the result of brittle hydride cracking due to stresses in the layer as well as different specific volumes of titanium and hydride.

Activation of titanium hydride fraction surface by an organic silicon oligomer as an example of sodium methyl siliconate, due to chemical adsorption from aqueous solution, significantly increases the concentration of hydroxyl OH-groups on the vacuum dried titanium hydride fraction surface at 100 °C. A significant increase in the intensity of the absorption bands at 3480 and 3490 cm^{-1} (OH groups) was recorded. The absorption bands at 1080–1120 cm^{-1} correspond to siloxane bonds (Si–O–Si) in chemisorbed sodium methylsiliconate on the titanium hydride surface (Fig. 2).

Optical studies of the surface of titanium hydride fration activated by sodium methyl siliconate are shown in Fig. 3.
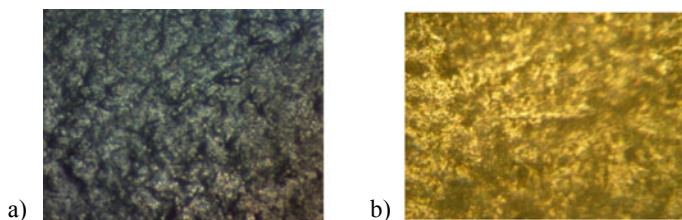
Fig. 1 The surface of the initial titanium hydride fraction: **a** magnification by 300 times; **b** magnification by 750 times
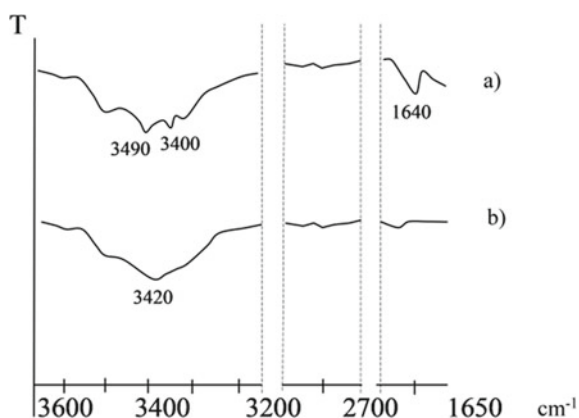

Fig. 2 IR spectra of the initial titanium hydride (**a**) and dried for 10 h at 100 °C (**b**)
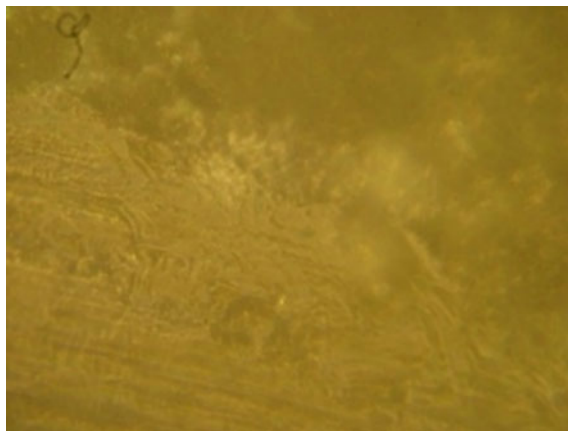

Fig. 3 Titanium hydride fraction surface activated by sodium methyl siliconate, magnified by 750 times

A difference in the surface structure of the initial and activated titanium hydride was observed due to the formation of a polysiloxane shell.

Studies of the surface structure of a titanium hydride fraction activated with sodium methyl silicate using an atomic force scanning probe microscope are presented in Figs. 4 and Fig. 5.

a)

b)
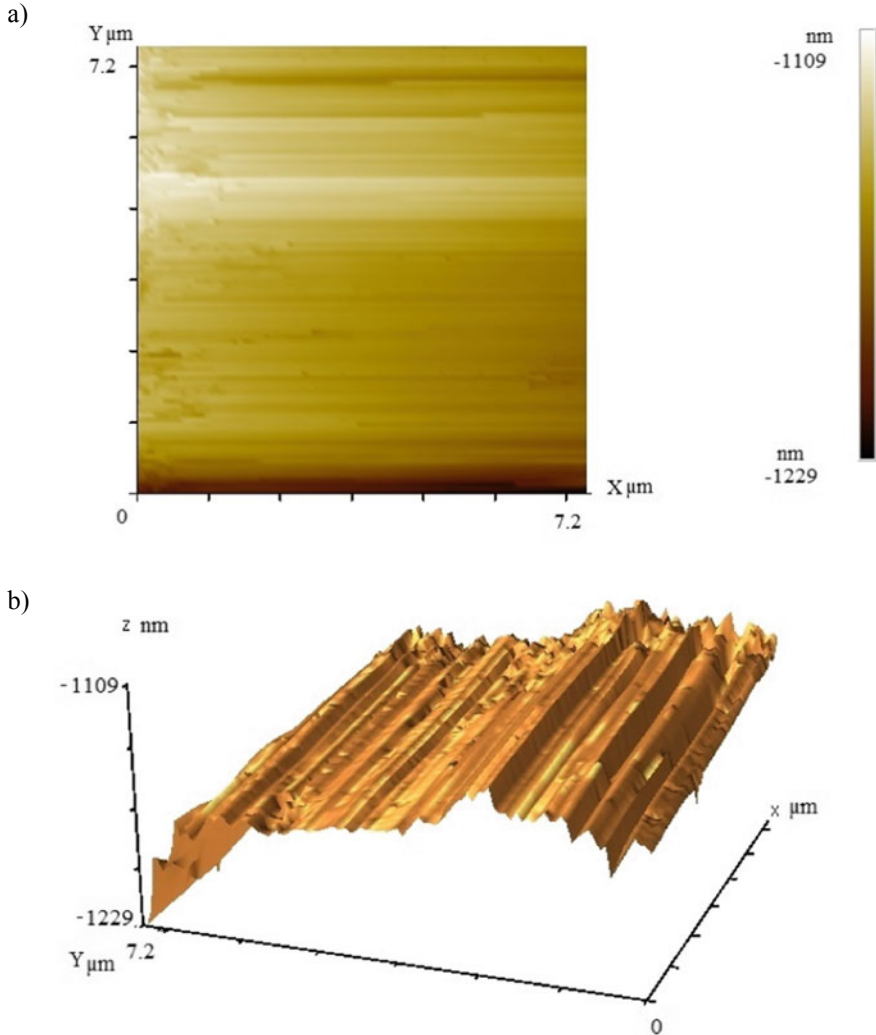
Fig. 4 The surface of titanium hydride fraction activated by sodium methylsilicate (ASSZM): **a** the study area 2D 7.2 × 7.2 microns; **b** 3D surface relief

Analyzing the microdiagram of titanium hydride fraction surface activated by sodium methylsiliconate showing the probe stroke of an atomic force scanning microscope with a 4 µm cross section relative to the OX axis, one can notice a significant decrease of characteristic dips and rises of the probe with height difference and depressions up to 14 nm throughout the scanning area (in the range from 0 to 7. 2 µm), the surface of
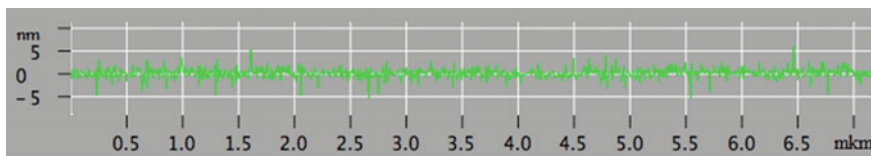
Fig. 5 Microdiagram of the surface of titanium hydride fraction activated with sodium methyl-siliconate (ASSZM)

the fraction has a smoother structure due to the adsorbed organic siloxane oligomer like methylsiliconate. Optical studies of the modified surface of titanium hydride fraction containing a borosilicate shell are shown in Fig. 6.

Fig. 6 The surface of a modified titanium hydride fraction containing a borosilicate shell magnified by 300 times

A difference in the surface structure of titanium hydride fraction containing polysiloxane and borosilicate shells is observed due to the vitrification of boron oxide at 300 °C.

Studies of the structure of a modified titanium hydride fraction surface containing a borosilicate shell using an atomic force scanning probe microscope are shown in Fig. 7.
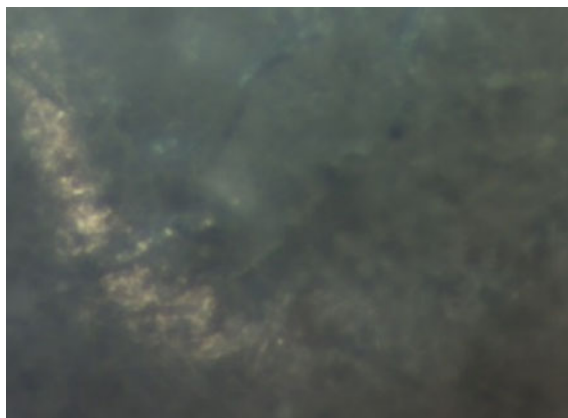
Analyzing the surface microdiagram of a modified titanium hydride fraction containing a borosilicate shell showing the probe stroke of an atomic force scanning microscope with a 4.2 μm section relative to the OX axis (Fig. 7a), small reductions of characteristic probe dips and rises with height and depression differences up to 10 nm throughout the scanning area (in areas from 0 to 7.2 μm) can be seen. The surface of modified titanium hydride fraction containing a borosilicate shell has a smoother structure due to the vitrification of boron oxide during heat treatment (Fig. 8).

a)

b)

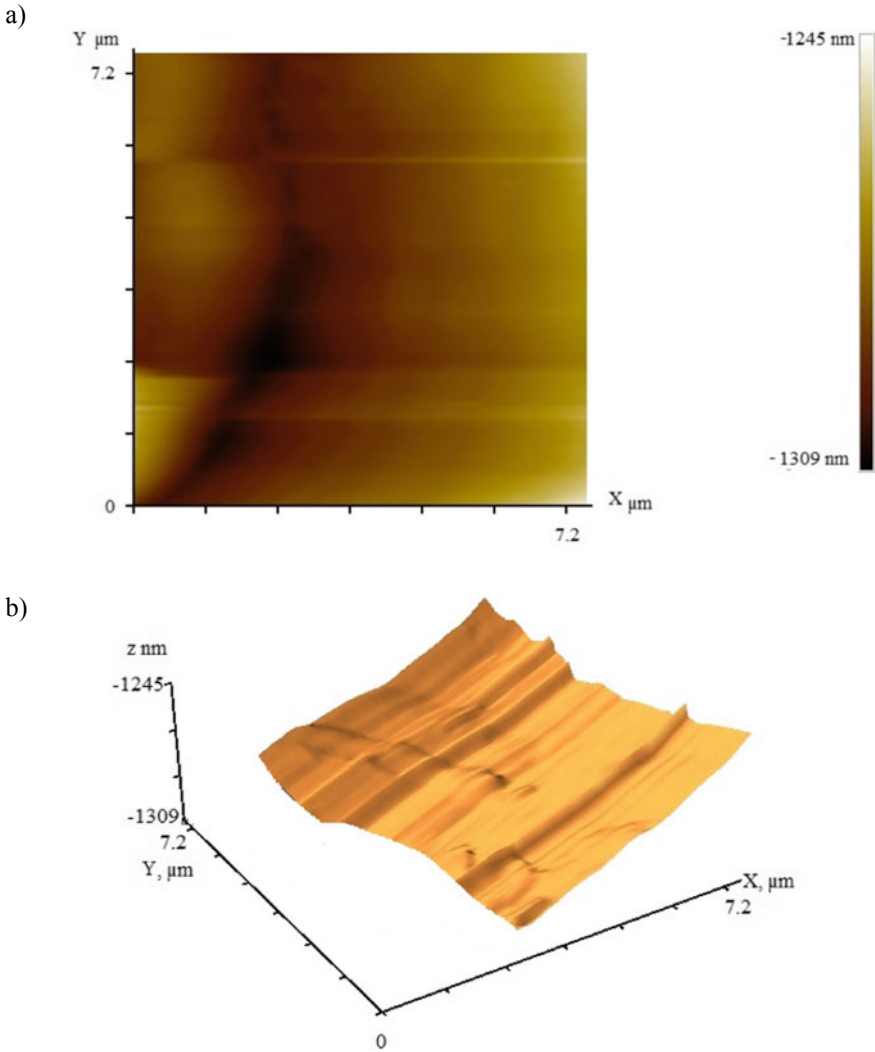**Fig. 7** Surface of the modified titanium hydride fraction containing borosilicate shell (ASSZM):
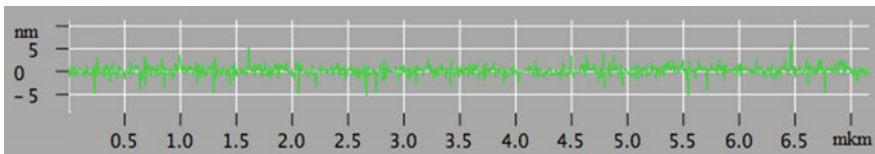**a** 7.2 × 7.2 μm 2D study area; **b** 3D surface relief

Fig. 8 Microdiagram of the surface of a modified titanium hydride fraction containing a borosilicate shell (ASSZM)

4   Conclusion

It was revealed that the surface of titanium hydride fraction is covered by a polymolecular layer of both physically adsorbed water and chemisorbed water in the form of crystalline hydrates. Physically sorbed water on the surface of titanium hydride fraction is easily removed during drying (100 °C), as evidenced by the marked decrease in the intensity of absorption bands for the valence vibrations of OH-groups (3400 and 1640 cm^{-1}). We observed a difference in the surface structure of the initial and activated titanium hydride due to the formation of a polysiloxane shell.

References

1. Gkomoza, P., Lampropoulos, G., Vardavoulias, M., Pantelis, D., Karakizis, P., Sarafoglou, C.: Microstructural investigation of porous titanium coatings, produced by thermal spraying techniques, using plasma atomization and hydride-dehydride powders, for orthopedic implants. Surf. Coatings Technol. **357**, 947–956 (2018). https://doi.org/10.1016/j.surfcoat.2018.10.072

2. Pavlenko, V.I., Yastrebinsky, R.N., Pavlenko, Z.V., Bondarenko, N.I.: Features of titanium hydride crystal oxidation at heat treatment. Lect. Notes Civ. Eng. **173**, 53–58 (2022). https://doi.org/10.1007/978-3-030-81289-8_8

3. Pavlenko, Z.V., Cherkashina, N.I., Demchenko, O.V.: Creating a protective coating on the surface of titanium hydride shot. Bull. BSTU named after V.G. Shukhov **10**, 166–171 (2016). https://doi.org/10.12737/22094

4. Cherkashina, N.I., Kuprieva, O.V., Kashibadze, N.V.: Investigation of the effect of mechanical activation of powder components on the properties of polyimide composites. Mater. Sci. Forum **992**, 353–358 (2020). https://doi.org/10.4028/www.scientific.net/MSF.992.353

5. Chernov, V.M.: Structural materials for fusion power reactors—the RF R&D activities. Nucl. Fusion **8**(47), 839–848 (2007). https://doi.org/10.1088/0029-5515/47/8/015

6. Gavrish, V., Chayka, T., Gavrish, O., Cherkashina, N.: Studies of highly dispersed titanium carbide powder obtained from scrap tungstenless cemented carbide alloys. In: Materials Research Proceedings. Modern Trends in Manufacturing Technologies and Equipment, pp. 214–219 (2022). https://doi.org/10.21741/9781644901755-38

7. Cherkashina, N.I., Pavlenko, A.V.: Modification of optical characteristics of a polymer composite material under irradiation. Tech Phys. **63**(4), 571–575 (2018). https://doi.org/10.1134/S1063784218040072

8. Cherkashina, N.I., Pavlenko, A.V.: Synthesis of polymer composite based on polyimide and Bi$_{12}$SiO$_{20}$ sillenite. Polymer Plast. Tech. Eng. **57**, 1923–1931 (2018). https://doi.org/10.1080/03602559.2018.1447129

9. Pavlenko, V.I., Yastrebinsky, R.N., Bondarenko, N.I., Kuprieva, O.V.: Features of thermal decomposition of titanium hydride fraction. J. Phys.: Conf. Ser. **1926**, 012049 (2021). https://doi.org/10.1088/1742-6596/1926/1/012049

10. Cherkashina, N.I., Popova, E.V., Pilavidou, E.O., Klopot, E.P.: Polymer composite material based on titanium hydride. IOP Conf. Series: Mater. Sci. Eng. **945**, 012079 (2020). https://doi.org/10.1088/1757-899X/945/1/012079

Optimization of Parameters for the Production of Gypsum Binders Based on Gypsum-Containing Waste

N. I. Alfimova[1,2(✉)] , S. Y. Pirieva[1,3] , K. M. Levickaya[1,3] ,
and N. I. Kozhukhova[1,3]

[1] Belgorod State Technological University Named After V.G. Shukhov, 46 Kostyukova Str.,
308012 Belgorod, Russia
`alfimovan@mail.ru`
[2] National Research Tomsk State University, 36 Lenin Ave., Tomsk 634050, Russia
[3] Laboratory of Advanced Materials and Technologies, Belgorod National Research University,
85 Pobedy Str., 308015 Belgorod, Russia

Abstract. Gypsum-containing wastes are a promising source of raw materials for the production of gypsum binders. However, they have specific features that require the development of alternative approaches and technological regimes in order to ensure the high quality of the final product. The purpose of the article was to study the influence of moisture content of gypsum-bearing waste and firing temperature on the specific surface of the gypsum binder, as well as the compressive strength and average density of gypsum paste based on it. The gypsum-bearing material was citrogypsum. It is a waste product of the biochemical synthesis of citric acid. The experiment was carried out using the method of mathematical planning. Burning of citrogypsum was carried out in a laboratory oven according to a given temperature regime. Using the statistical computer processing of experimental data, regression equations were obtained; graphic dependence as nomograms are constructed; the influence of variable factors on the controlled parameters was assessed. It has been established that the optimal, from the standpoint of energy consumption, is the binder burning at a temperature of 150 °C and the lowest possible raw material moisture content of 5%. Increasing the burning temperature above 150 °C is not economically workable and adversely affects the compressive strength of the gypsum stone, as well.

Keywords: Gypsum-bearing waste · Cytrogypsum · Mathematical experiment planning

1 Introduction

Gypsum-bearing waste (GBW) from various industrial enterprises such as phospho-gypsum, FGD gypsum, citrogypsum, etc., is a promising raw material for the production of gypsum binders and can be used as an excellent alternative to natural gypsum. The possibility of obtaining gypsum binders based on GBW has been proven by many studies conducted throughout the world [1–7]. However, it should be noted that it is practically impossible to obtain a high-quality binder based on gypsum-bearing waste using standard technological approaches. This is due to the specifics and significant differences between gypsum-bearing waste and natural gypsum. For example, gypsum-bearing waste is characterized by high humidity, high specific surface area, and a lot of impurities. All this makes it necessary to develop new technological methods and make adjustments to existing ones, taking into account the features of the GBW used [3, 8–10]. In this connection, the purpose of this article was to study the influence of the moisture content of gypsum-bearing waste (citrogypsum) and the burning temperature on the specific surface of the gypsum binder, as well as the compressive strength and average density of the gypsum paste based on it [11–15].

2 Materials and Methods

The object of the study was citrogypsum. This is a gypsum-bearing waste, which is a by-product in the biochemical synthesis of citric acid (Belgorod, Russia) [16].

The experiment was carried out using the method of mathematical planning. The burning temperature of citrogypsum (150–250 °C, with a variation interval of 50 °C) and the moisture content of citrogypsum (0–10 wt%, variation interval of 5%) were chosen as variable parameters (Table 1). Burning of citrogypsum was carried out in a laboratory oven. The curing time for GBW in the oven at the set temperature (150, 200, and 250 °C) was 30 min.

Table 1 Conditions for the mathematical planning of the experiment

Input parameter		Variability range			Unit variation
Origin form	Coded form	− 1	0	1	
Burning temperature, °C	X_1	150	200	250	50
Humidity, % by wt	X_2	0	5	10	5

Using the experimental design conditions (Table 1), an experiment design matrix was developed that includes 9 different mixes of citrogypsum-based binder (Table 2).

According to the planning matrix (Table 2), the 9 mixes of citrogypsum-based binder were molded. The output parameters for determining the effect of variable input parameters were the specific surface area (SSA), average density and compressive strength of the gypsum paste. The compressive strength of the gypsum paste was determined for sample cubes 3 × 3 × 3 cm in size, molded at an equal "water-hard" ratio (W/S = 0.4).

Table 2 Experiment design matrix

	Input parameter			
	X_1		X_2	
1	− 1	150	− 1	0
2	− 1	150	+ 1	10
3	− 1	150	0	5
4	+ 1	250	− 1	0
5	+ 1	250	+ 1	10
6	+ 1	250	0	5
7	0	200	− 1	0
8	0	200	+ 1	10
9	0	200	0	5

3   Results and Discussions

After statistical computer processing of experimental data, regression equations (Eqs. 1–3) were obtained. Based on the equations, graphical dependencies were plotted that allow assessing the effect of varying input parameters (Figs. 1, 2 and 3) on controlled output parameters.

$$SSA = 330.1 + 5.217 \cdot X_1 + 2.0667 \cdot X_2 + 39.42 \cdot X_1^2 + 5.367 \cdot X_2^2 - 1 \cdot X_1 \cdot X_2 \tag{1}$$

$$R_{comp} = 4.479 - 0.668 \cdot X_1 - 0.293 \cdot X_2 - 0.168 \cdot X_1^2 - 0.26 \cdot X_2^2 + 0.59 \cdot X_1 \cdot X_2 \tag{2}$$

$$P_{average} = 1028 - 4.933 \cdot X_1 + 1.1333 \cdot X_2 + 13.2 \cdot X_1^2 - 16.3 \cdot X_2^2 - 0.8 \cdot X_1 \cdot X_2 \tag{3}$$

The nature of the presented graphical dependence as monograms (Fig. 1) showed that an increase in humidity and burning temperature contributes to an increase in the specific surface of the citrogypsum-based binder. There is a decrease in the specific surface area in the entire humidity range for citrogypsum-based binders obtained at a temperature of 200 °C.

The maximum compressive strength is observed for citrogypsum-based binder mixes obtained at a burning temperature of 150 °C and humidity up to 5%. A further increase in temperature leads to a decrease in compressive strength. This is most likely due to the formation of a larger amount of anhydride, which has a higher porosity and lower compressive strength vs. calcium sulfate hemihydrate. It should be noted that the gypsum paste obtained on this mix of citrogypsum-based binder is characterized by the maximum values of the average density (Fig. 2).
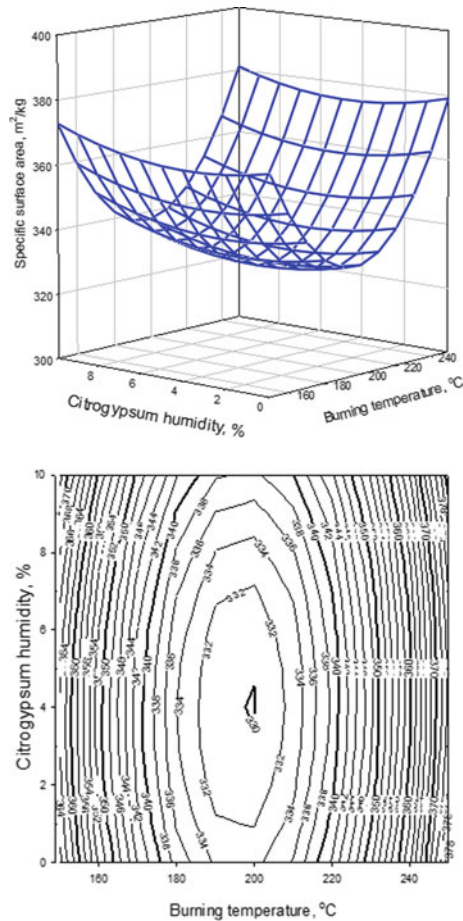
Fig. 1 Dependency of the specific surface area of the gypsum binder on the humidity of the citrogypsum and the burning temperature

With an increase in the initial humidity above 5%, I also observed a decrease in the compressive strength of the gypsum paste. This can be explained by an increase in the porosity of the binder particles due to evaporation and removal of water as steam at high temperature (Fig. 3).

The minimum values of the average density are typical for samples of citrogypsum-based binding paste, which has the minimum specific surface area, which is quite natural.

4 Conclusion

Based on the results obtained, the following conclusions are proposed:

- optimal, in terms of energy consumption, is the burning of the binder at a temperature of 150 °C and the lowest possible raw material moisture content of 5%;
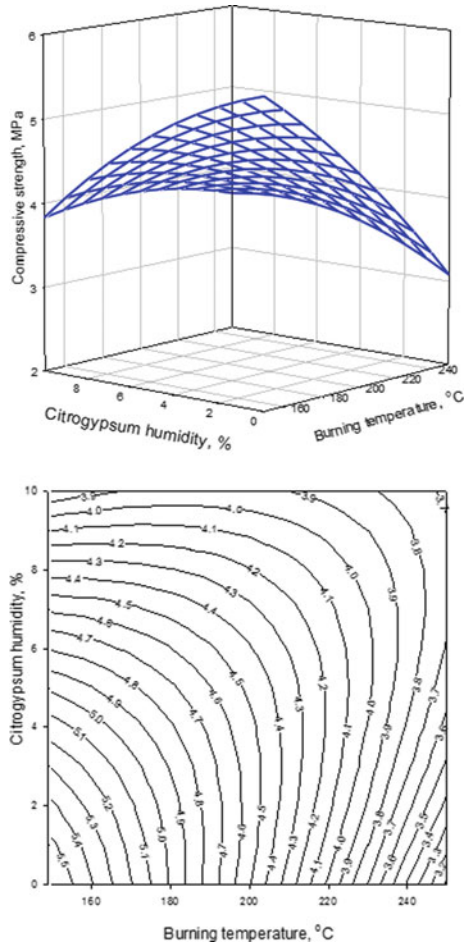
Fig. 2 Dependency of compressive strength of gypsum paste on citrogypsum humidity and burning temperature

- Increasing the burning temperature above 150 °C is not economically feasible, and adversely affects the compressive strength of the citrogypsum-based binding paste, as well.

Fig. 3 Dependency of average density of gypsum paste on citrogypsum hymidity and burning temperature

References

1. Rashad, A.M.: Phosphogypsum as a construction material. J. Clean. Prod. **166**, 732–743 (2017). https://doi.org/10.1016/j.jclepro.2017.08.049

2. Li, X., Zhang, Q., Ke, B., Wang, X., Li, L., Li, X., Mao, S.: Insight into the effect of maleic acid on the preparation of α-hemihydrate gypsum from phosphogypsum in Na_2SO_4 solution. J. Cryst. Growth **493**, 34–40 (2018). https://doi.org/10.1016/j.jcrysgro.2018.04.025
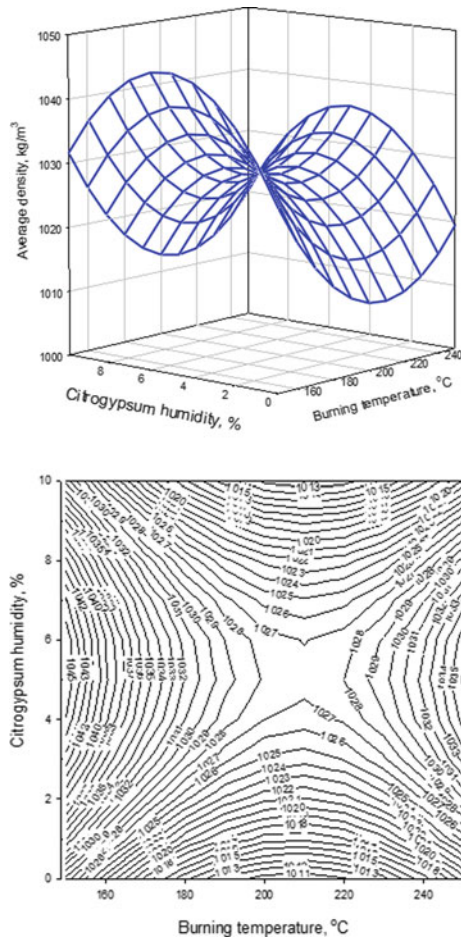
3. Li, X., Zhang, Q., Shen, Z., Li, L., Li, X., Ma, S.: L-aspartic acid: a crystal modifier for preparation of hemihydrate from phosphogypsum in $CaCl_2$ solution. J. Cryst. Growth **511**, 48–55 (2019). https://doi.org/10.1016/j.jcrysgro.2019.01.027

4. Guan, B., Yang, L., Wu, Z., Shen, Z., Ma, X., Ye, Q.: Preparation of α-calcium sulfate hemihy-drate from FGD gypsum in K, Mg-containing concentrated $CaCl_2$ solution under mild conditions. Fuel **88**, 1286–1293 (2009). https://doi.org/10.1016/j.fuel.2009.01.004

5. Alfimova, N.I., Pirieva, S.Y., Titenko, A.A.: Utilization of gypsum-bearing wastes in materials of the construction industry and other areas. Constr. Mater. Prod. **4**(1), 5–17 (2021). https://doi.org/10.34031/2618-7183-2021-4-1-5-17

6. Guan, B., Kong, B., Fu, H., Yu, J., Jiang, G., Yang, L.: Pilot scale preparation of a-calcium sul-fate hemihydrate from FGD gypsum in Ca–K–Mg aqueous solution under atmospheric pressure. Fuel **98**, 48–54 (2012). https://doi.org/10.1016/j.fuel.2012.03.032

7. Kozhukhova, N., Kozhukhova, M., Teslya, A., Nikulin, I.: The effect of different modifying methods on physical, mechanical and thermal performance of cellular geopolymers as thermal insulation materials for building structures. Buildings **12**(2), 241 (2022). https://doi.org/10.3390/buildings12020241

8. Moalla, R., Gargouri, M., Khmiri, F., Kamoun, L., Zairi, M.: Phosphogypsum purification for plaster production: a process optimization using full factorial design. Environ. Eng. Res. **23**(1), 36–45 (2018). https://doi.org/10.1016/j.tca.2018.01.011

9. Alfimova, N.I., Pirieva, S.Y., Elistratkin, M.Y., Kozhuhova, N.I., Titenko, A.A.: Production methods of binders containing gypsum-bearing wastes: a review. Bull. BSTU named after V.G. Shukhov. **11**, 8–23 (2020). https://doi.org/10.34031/2071-7318-2020-5-11-8-23

10. Lu, W., Ma, B., Su, Y., He, X., Jin, Z., Qi, H.: Preparation of a-hemihydrate gypsum from phosphogypsum in recycling $CaCl_2$ solution. Constr. Build. Mater. **214**, 399–412 (2019). https://doi.org/10.1016/j.conbuildmat.2019.04.148

11. Chernysh, L.I.: Improving the efficiency of building composites obtained using industrial waste. Ecol. Indus. **4**(41), 87–89 (2014)

12. Petropavlovskaya, V.B., Belov, V.V., Novichenkova, T.B., Buryanov, A.F., Poleonova, Y.Y., Petropavlovsky, K.S.: Resource-saving non-fired gypsum composites. Build. Mater. **6**, 79–81 (2015)

13. Alfimova, N.I., Pirieva, S.Y., Elistratkin, M.Y., Nikulin, I.S., Titenko, A.A.: Binders from gypsum-containing waste and products based on them. IOP Conf. Ser.: Mater. Sci. Eng. **945**(1), 012057 (2020). https://doi.org/10.1088/1757-899X/945/1/012057

14. Petropavlovskaya, V.B., Novichenkova, T.B., Buryanov, A.F.: Improving the technologi-cal properties of non-fired hyper-pressed gypsum products. Bull. BSTU named after V.G. Shukhov. **6**, 75–78. (2013)

15. Jin, Z., Ma, B., Su, Y., Lu, W., Qi, H., Hu, P.: Effect of calcium sulphoaluminate cement on mechanical strength and waterproof properties of beta-hemihydrate phosphogypsum. Constr. Build. Mater. **242**, 118198 (2020). https://doi.org/10.1016/j.conbuildmat.2020.118198

16. Pirieva, S., Alfimova, N., Levickaya, K.: Citrogypsum as a raw material for gypsum binder production. Constr. Unique Build. Struct. **100**, 10007 (2022). https://doi.org/10.4123/CUBS.100.7

Heat-Shielding Properties of Concrete Structures Reinforced with Composite Reinforcement

L. A. Suleymanova(✉) 📷, I. S. Ryabchevskiy 📷, D. S. Anoprienko 📷, and A. V. Rafaelyan 📷

Belgorod State Technological University Named After V.G. Shukhov, Belgorod, Russia
`ludmilasuleimanova@yandex.ru`

Abstract. Corrosion of steel reinforcement is the main cause of failure of concrete structures. The most effective way to prevent degradation of concrete structures is to replace the steel with a corrosion-resistant reinforcing material, such as a fiber-reinforced composite. The types of composites that are best suited for reinforcing concrete provide high strength, stiffness, and compatibility with concrete. They are rod-shaped elements, molded and processed in such a way that the surface texture and irregularities provide mechanical adhesion to concrete. The authors considered the types of rods made of fiber-reinforced composite, such as fiber-glass, carbon fiber, basalt-reinforced plastic and aramidoclast, in comparison with steel as a reinforcement material. The reduced resistance to heat transfer of an inhomogeneous part of the structure is determined taking into account linear and point thermal inhomogeneities using the example of a coating slab with a reinforced frame. Based on this calculation, it was found that the least energy efficient model is a plate reinforced with steel reinforcement, in which additional specific linear heat losses are 14.5 times lower than the rods made of fiber-reinforced composite, the reduced heat transfer resistance is 10%, the heat transfer resistance of a homogeneous part of the structure is 13%.

Keywords: Concrete · Reinforcement · Fiberglass · Reduced heat transfer resistance · Steel reinforcement

1 Introduction

The use of fiber-reinforced composite rods to replace steel reinforcement is one of the most effective methods for increasing the corrosion resistance of reinforced concrete structures [1–3]. When used correctly, these rods can improve strength-to-weight ratio, corrosion and chemical resistance, controlled thermal expansion characteristics, and electromagnetic neutrality, which can lead to increased safety and service life, as well as savings in production, equipment and maintenance costs.

Fiberglass is usually composed of synthetic or organic high-strength brominated materials in a polymer matrix. The most commonly used fiber reinforced materials for

civil engineering are carbon, aramid basalt and glass. They are used in practice as reinforcement for reinforced concrete and prestressed concrete elements, ground anchors, as well as for repairing or strengthening existing concrete structures [4–7]. Comparative characteristics of fiber-reinforced composites with respect to steel are presented in Table. 1 [8].

Table 1 Comparative characteristics of fiber-reinforced composites in relation to steel

Characteristic	Material				
	Carbon	Glass	Aramid	Basalt	Steel
Density, g/sm^3	1.50–2.10	1.25–2.50	1.25–1.45	1.90–2.10	7.85
Tensile strength, Mpa	600–3920	483–4580	1720–3620	600–1500	483–690
Modulus of elasticity, Gpa	37–784	35–86	41–175	50–65	200
Relative extension, %	0.5–1.8	1.2–5.0	1.4–4.4	1.2–2.6	6.0–12.0
Coefficient of linear expansion, 10^{-6}/°C	– 9.0–0.0	6.0–10.0	– 6.0–2.0	9.0–12.0	11.7

Carbon fiber is inherently an anisotropic material manufactured at 1300 °C. The main advantages of this fiber include low density, low electrical conductivity, high fatigue strength, high modulus of elasticity, good creep, chemical resistance, and no water absorption. However, low compressive strength and anisotropy (reduced radial strength) are the weaknesses of carbon fiber. In addition, the relatively high energy requirement for carbon fiber production leads to higher costs, which is considered another weak feature [9, 10].

Glass fiber is isotropic in nature and is a widely used fiber. E-glass, S-glass, C-glass and AR-glass are popular types of fiberglass. High strength, resistance to moisture and chemicals at low cost are the main characteristics of fiberglass. The relatively low cost compared to other types of fiberglass makes fiberglass the most widely used in the construction industry. However, the relatively low elastic modulus, low alkali resistance with low long-term strength due to stress fracture are the main disadvantages of fiberglass [10, 11].

Aramid fiber is anisotropic in nature and is usually yellow in color. This fiber has low density, high tensile strength, high modulus of elasticity and sufficient stiffness. The fiber can be used for static and shock-resistant structures. However, its use is limited due to low long-term (tensile) strength as well as low radial strength. Moreover, the difficulty of cutting and processing is another disadvantage of aramid fiber [10].

Basalt fiber is a type of igneous rock that was formed as a result of the rapid cooling of lava on the surface of the planet. The production of basalt fiber is similar to the production of fiberglass. Crushed basalt rocks are the only raw material needed for fiber production. Basalt fibers have recently appeared in composites and structural materials based on fiberglass. Such fibers have high tensile strength, excellent resistance to high

temperatures, and good wear resistance (Table 1). Other advantages are excellent electromagnetic performance and resistance to corrosion, acid, radiation, UV radiation and vibration [10].

Despite the knowledge of the physical and mechanical characteristics of fiber-reinforced composite rods, the question of the effect of the reinforcement material on the energy efficiency of concrete structures remains open.

2 Methods and Materials

To justify the choice of material used for reinforcing concrete, the authors calculated the reduced resistance to heat transfer of the structure, taking into account heat-conducting inclusions. For the calculation, fragments of roof slabs (Fig. 1), each with an area of 1 m^2, are considered, made of concrete of optimal composition, reinforced with glass-composite, basalt-plastic, carbon-fiber, steel reinforcement and aramid fiber rods, which is a reinforcing cage, consisting of upper and lower belts of rods with a diameter of 10 mm.
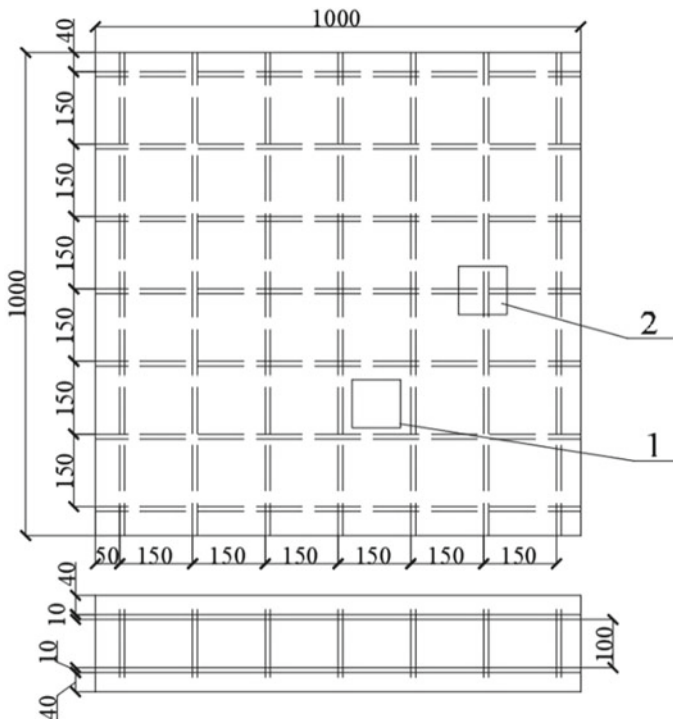
Fig. 1 Cross section and general view of fragments of floor slabs: 1—section of concrete in the structure; 2—section of reinforcement of the structure

The calculation of the reduced heat transfer resistance of energy-efficient masonry and aerated concrete masonry with transverse bonding through a row is carried out in accordance with [12, 13].

To determine additional specific linear heat losses through the joints, the authors adopted values based on the calculation of the two-dimensional temperature field of the joint of homogeneous parts of the structure (Fig. 2).
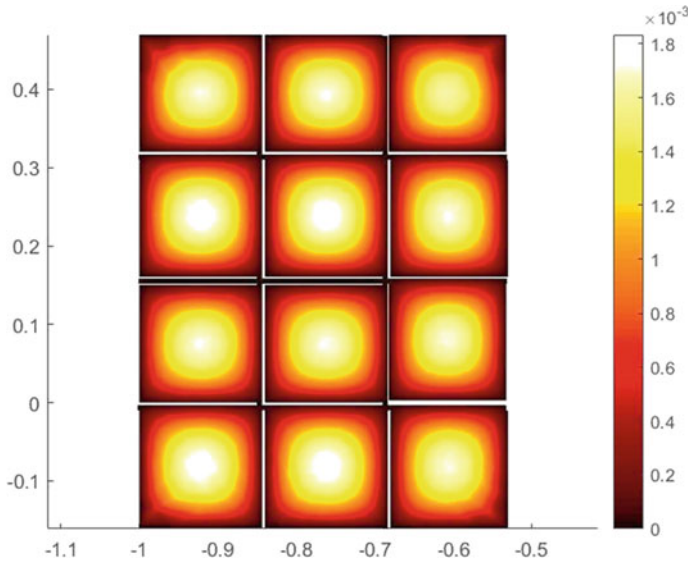
Fig. 2 Temperature field of a fragment of the floor slab under consideration, taking into account reinforcement

3   Results and Discussion

The nature of the distribution of the heat flux through the floor slab under consideration, based on the calculation of the two-dimensional temperature field of the joint of homogeneous parts of the structure, is shown in Fig. 3.

The heat flux distribution diagram through the floor slab under consideration is shown in Fig. 4.

The fragments under consideration are represented by two types of a homogeneous part of the structure:

- a section of concrete in the structure (Fig. 1, pos. 1);
- section of the reinforcement of the structure (Fig. 1, pos. 2);

The reduced resistance to heat transfer of the design of the calculated fragment is determined by formula (1) [12, 13]:

$$R_o^r = \sum A_i / \left(\sum A_i / R_{o,i} + \sum L_j \psi_j \right) \qquad (1)$$
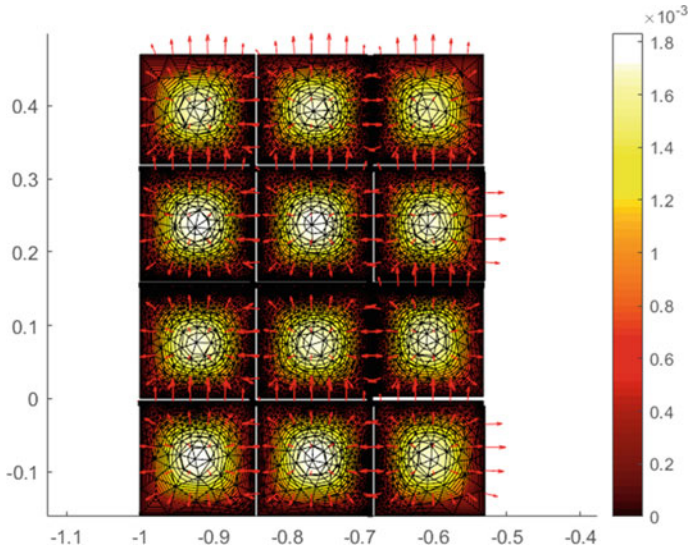
Fig. 3 The nature of the heat flux distribution through the floor slab under consideration
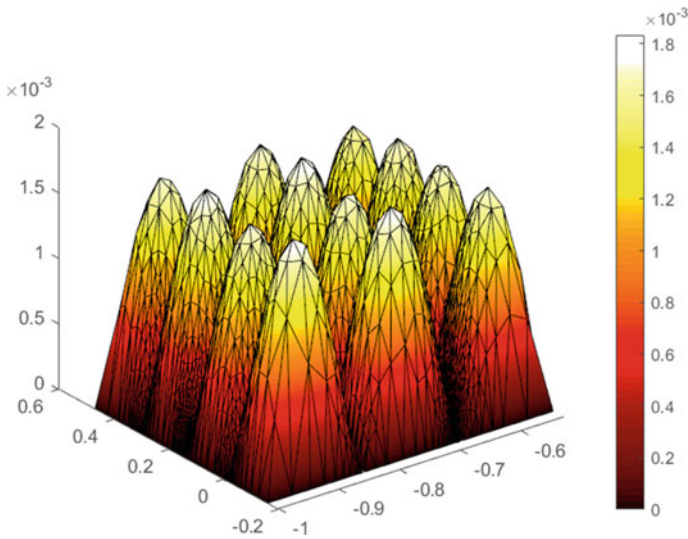
Fig. 4 Heat flow distribution diagram through the floor slab under consideration

where A_i—the area of the structure of the i-th type in the fragment under consideration, m^2; L_j—the length of all joints of the j-th type in the fragment under consideration, m; $R_{o,i}$—heat transfer resistance of the homogeneous part of the structure of the i-th type, (m^2·°C)/Вт; ψ_j—additional specific linear heat loss through the joint of the j-th type, W/(m·°C).
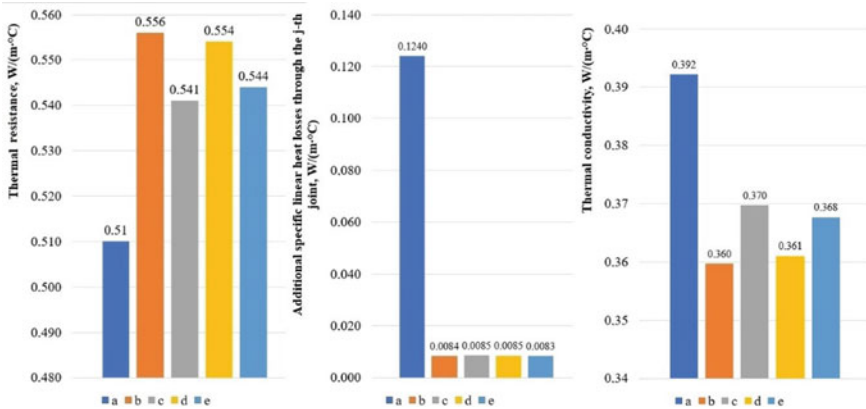
Fig. 5 Average values of the main thermal parameters of floor slab models reinforced with: **a**—steel reinforcement; **b**—fiberglass reinforcement; **c**—carbon fiber reinforcement; **d**—basalt-plastic reinforcement; **e**—aramidoplastic reinforcement

The reduced resistance to heat transfer of fragments of roof slabs made of concrete of optimal composition, reinforced with glass-composite, basalt-plastic, carbon fiber, steel reinforcement and aramid fiber rods is determined. The calculation data are presented in Fig. 5.

From the data presented in Fig. 5, we can conclude that the best thermal performance of floor slab models reinforced with fiberglass and basalt reinforcement. It should be noted that the values of the reduced resistance to heat transfer of models of floor slabs reinforced with carbon fiber and aramidoplastic reinforcement are 1–2% lower than those with fiberglass reinforcement with equal additional specific linear heat losses through the j-th type joint, which also confirms their energy efficiency. According to research data, the least energy efficient model is a plate reinforced with steel reinforcement, in which additional specific linear heat losses are 14.5 times lower than rods made of fiber-reinforced composite, the reduced heat transfer resistance is by 10%, and the heat transfer resistance of a homogeneous part of the structure is by 13%.

4 Conclusion

To determine the energy efficiency of a concrete structure with fiber-reinforced composite rods, the authors calculated the reduced heat transfer resistance of an inhomogeneous part of the structure, taking into account linear and point thermal inhomogeneities of a fragment of the coating slab, and established conclusions.

The use of fiberglass and basalt-reinforced reinforcement allows to increase the tensile strength, high modulus of elasticity, corrosion resistance and durability of the concrete structure, while ensuring high thermal uniformity.

References

1. Sardar, S., Mahmod, M., Shakir, I.: Nonlinear pushover analysis for steel beam-column connection. Eurasian J. Sci. Eng. **3**(1), 83–98 (2017). https://doi.org/10.23918/eajse.v3i1sip83

2. Lye, M.L., Mohammed, B.S., Liew, M.S., Wahab, M.M.A., Al-Fakih, A.: Bond behaviour of CFRP-strengthened ECC using response surface methodology (RSM). Case Stud. Constr. Mater. **12**, e00327 (2020). https://doi.org/10.1016/j.cscm.2019.e00327

3. Mussa, M.H., Abdulhadi, A.M., Abbood, I.S., Mutalib, A.A., Yaseen, Z.M.: Late age dynamic strength of high-volume fly ash concrete with nano-silica and polypropylene fibres. Crystals. **10**(4), 243 (2020). https://doi.org/10.3390/cryst10040243

4. Rahim, N.I.: Strengthening the structural behavior of web openings. RC deep beam using CFRP. Mater. **13**(12), 2804 (2020). https://doi.org/10.3390/ma13122804

5. Siddika, A., Mamun, M.A.A., Ferdous, W., Alyousef, R.: Performances, challenges and opportunities in strengthening reinforced concrete structures by using FRPs—a state-of-the-art review. Eng. Fail. Anal. **111**, 104480 (2020). https://doi.org/10.1016/j.engfailanal.2020.104480

6. Weli, S.S., Abbood, I.S., Hasan, K.F., Jasim, M.A.: Effect of steel fibers on the concrete strength grade: a review. IOP Conf. Ser.: Mater. Sci. Eng. **888**, 012043 (2020). https://doi.org/10.1088/1757-899X/888/1/012043

7. Benmokrane, B., Chaallal, O., Masmoudi, R.: Glass fibre reinforced plastic (GFRP) rebars for concrete structures. Constr. Build. Mater. **9**, 353–364 (1995). https://doi.org/10.1016/0950-0618(95)00048-8

8. Ahmed, A., Guo, S., Zhang, Z., Shi, C., Zhu, D.: A review on durability of fiber reinforced polymer (FRP) bars reinforced seawater sea sand concrete. Constr. Build. Mater. **256**, 119484 (2020). https://doi.org/10.1016/j.conbuildmat.2020.119484

9. Günaslan, S.E., Karasin, A., Öncü, M.E.: Properties of FRP materials for strengthening. Int. J. Innov. Sci. Eng. Technol. **1**(9), 656–660 (2014)

10. Abbood, I.S., Odaa, S., Hasan, K.F., Jasim, M.A.: Properties evaluation of fiber reinforced polymers and their constituent materials used in structures—a review. Mater. Today: Proc. **43**, 1003–1008 (2021). https://doi.org/10.1016/j.matpr.2020.07.636

11. Wang, R.-M., Zheng, S.-R., Zheng, Y.-P.: 3-matrix materials. In: Polymer Matrix Composites and Technology, pp 101–548. Woodhead Publishing, Cambridge (2011). https://doi.org/10.1533/9780857092229.1.101

12. Suleymanova, L.A., Pogorelova, I.A., Marushko, M.V., Ryabchevsky, I.S.: Energy-efficient double-row masonry of the exterior walls in the buildings made of cellular concrete blocks. IOP Conf. Series: Mater. Sci. Eng. **913**, 022044 (2020). https://doi.org/10.1088/1757-899X/913/2/022044

13. Suleymanova, L.A., Pogorelova, I.A., Suleymanov, K.A.: Energy efficiency improvement of aerated concrete block wall fences. IOP Conf. Series: Mater. Sci. Eng. **945**, 012006 (2020). https://doi.org/10.1088/1757-899X/945/1/012006

Erosive Wear of Alumina Coated Polyimide Composite

V. I. Bedina[(✉)] [iD], A. A. Skiba [iD], and M. V. Limarenko [iD]

Belgorod State Technological University Named After V.G. Shukhov, Belgorod, Russia
vera_bedina@mail.ru

Abstract. A layer of aluminum oxide on the surface of a highly filled polymer composite based on polyimide and tungsten oxide was obtained by the method of detonation spraying. The thickness of the resulting coating is from 80 to 120 μm. The X-ray diffraction pattern of the coating showed the presence of only one modification of aluminum oxide—α-Al_2O_3. The erosion resistance of coated and uncoated polymer composite specimens at 25 °C was studied in accordance with ASTM G76-02. The test time for all samples was 1 h, the abrasive material consumption was 2.2 g/min, and corundum powder (Al_2O_3) with an average fraction of 50 μm was used as the abrasive material. The air pressure was 0.35 bar. The impact of the abrasive material jet was carried out at angles of 30, 60, and 90°. It has been established that the erosion wear of specimens with a ceramic coating of α-Al_2O_3 is almost an order of magnitude lower than that of specimens without a coating.

Keywords: Erosive wear · Alumina coating · Polyimide composite · Detonation spraying

1 Introduction

Traditionally, metals and their alloys have been used to protect spacecraft from radiation. Currently, new composite materials are being actively developed that have better radiation-protective properties compared to aluminum [1, 2]. The effectiveness of a protecting material is measured by its ability to attenuate the intensity of radiation as it passes through the material. When cosmic radiation passes through heavy metal materials, secondary radiation occurs, which causes even more harm than primary radiation [3]. To reduce the contribution of secondary particles to the total dose equivalent, it is more efficient to use lightweight materials for radiation protection, such as polymers. However, the use of pure polymers in space is limited due to their low thermal stability, low resistance to atomic oxygen, and a number of other negative space factors [4, 5]. The introduction of inorganic fillers into polymers makes it possible to create composites with improved thermal, physical–mechanical, and radiation-protective properties [6].

This paper discusses the impact of a jet of abrasive material (the impact of micrometeorite particles) on highly filled polymer composites based on polyimide and tungsten

oxide, as well as the effect of an aluminum oxide coating as a way to increase wear resistance. A polymer composite based on polyimide with the addition of tungsten oxide, which showed high radiation-protective properties, was chosen as the material under study. The choice of thermoplastic polyimide as a polymer matrix is due to its properties necessary for use in space—high physical and mechanical properties at low and elevated temperatures [7]. The use of polyimide as a binder can provide high radiation resistance of composites, which affects the durability of materials. The use of WO_2 creates reliable protection against γ-radiation [8]. The ceramic coating has a higher resistance to erosive wear and is used to improve wear resistance under the influence of space dust.

2 Methods and Materials

Were prepared samples of polyimide composites containing 60 wt. %WO_2. Previously, it was found that the maximum content of WO_2 in a polyimide composite, at which high strength parameters are maintained, is 60 wt. % [9]. A detailed description of the method for manufacturing a polymer composite is presented in Ref. [9]. Mixing of polymer particles and filler was carried out in a jet-vortex mill. Then the homogeneous mixture was placed into steel molds and hot pressing was carried out at a pressure of 80 MPa and a temperature of 360–380 °C. As a result, composite plates were obtained with a size of 25 × 50 mm and a thickness of 5 mm. Next, the plates were cut into samples of 25 × 25 mm and 25 × 20 mm.

The ceramic layer was deposited on the polyimide composite by detonation spraying [10]. Al_2O_3 powder with an average size of 26 μm was used as the applied material (see Fig. 1). The particle size distribution was measured by the laser scattering method using a particle size analyzer (Analysette 22 NanoTec Plus, Fritsch GmbH). The powder was dried in an electric oven at 200 ± 5 °C for 60 min to reduce agglomeration and prevent sticking during the coating process.
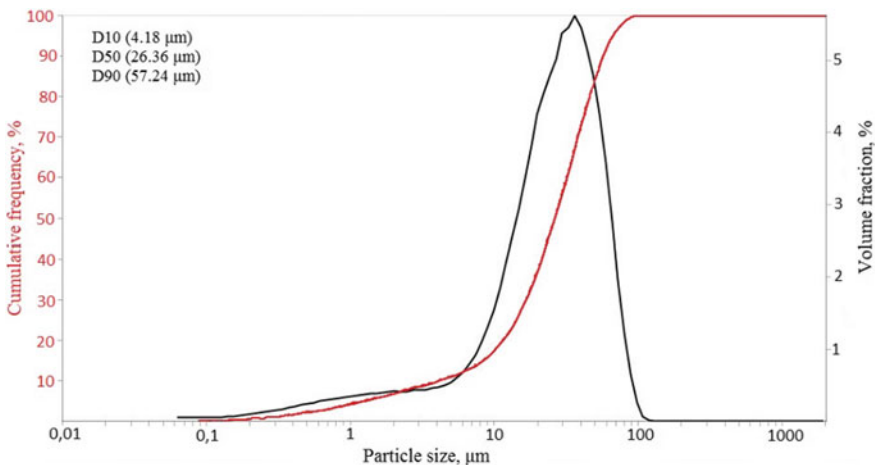
Fig. 1 A granulometric composition of the powder Al_2O_3

The ceramic layer was deposited using a multi-chamber detonation accelerator (MCDS) [11, 12]. The robotic complex detonation spray coatings process was manufactured by IntelMashin LLC (Russia) for Belgorod State Technological University named after V.G. Shukhov (Belgorod, Russia). The powder was applied to polyimide composite plates 25×25 mm and 25×20 mm in size. Before coating, the plates were cleaned of oil contamination with hexane. The operating mode of the detonation spraying plant during the application of ceramic coating is shown in Table 1.

Table 1 Parameters of detonation spray coating (DSC) process

Consumption of combustible mixture components [m^3/h]			Powder supply [g/h]	Spray distance [mm]	Travel speed [m/h]
Air	Oxygen	Propane			
1.41*/1.08**	2.87/3.26	0.54/0.65	500	65	100

*—cylindrical combustion chamber, **—annular combustion chamber

The structure and thickness of the coating were studied by scanning electron microscopy (SEM, Tescan MIRA 3 LMU, Czech Republic). X-ray diffraction (XRD) pattern of Al_2O_3-coating was recorded at room temperature using X-ray diffractometer (Thermo Fisher Scientific ARL 9900 WorkStation, Switzerland) with Co k-alpha radiation.

The erosion resistance of the samples was studied at a temperature of 25 °C in accordance with ASTM G76-02 "Standard Test Method for Conducting Erosion Tests by Solid Particle Impingement Using Gas Jets" using Air Jet Erosion Testing Machine TR-471-400 (Ducom Instruments, India). The test time for all samples was 1 h, the abrasive material consumption was 2.2 g/min, corundum powder (Al_2O_3) with an average fraction of 50 μm was used as the abrasive material. The air pressure was 0.35 bar. Abrasive wear was carried out at angles of 30, 60, and 90°. A composite material without coating and with a ceramic coating was chosen as the test samples.

3   Results and Discussion

As a result of the process of detonation spraying on the surface of plates from a polyimide composite, Al_2O_3 coatings with a thickness of 80 to 120 μm were obtained, the X-ray diffraction pattern of which showed the presence of only one modification of aluminum oxide—α-Al_2O_3 (corundum) (see Fig. 2).

The results of tests for erosive wear are presented in Table 2 Erosive wear spots of coated and uncoated samples Table 2 and in Fig. 3. From the graph (see Fig. 3a) it can be seen that the areas of erosion wear for samples with a ceramic coating are less than for samples without a coating. In 1.76, 1.57 and 1.76 times for angles of 30, 60 and 90°, respectively. The erosive values was calculated from the ratio of the volume loss of the sample material to the total mass of abrasive particles that acted on the sample,
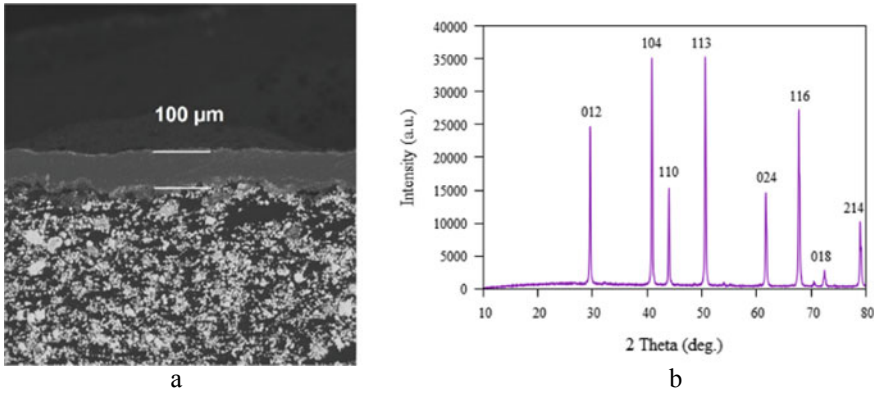
Fig. 2 A cross section micrograph of the coated composite (**a**) and an X-ray diffraction pattern of the coating (**b**)

according to the formula (1):

$$\frac{(m_0 - m_1)}{\rho} / \frac{S}{t},$$

(1)

where m_0—the mass of the sample before the start of the test, g; m_1—the mass of the sample after testing, g; ρ—sample density (coating or system coating + base), g/cm^3; S—the abrasive consumption rate, g/min; t—the duration of the test, min.
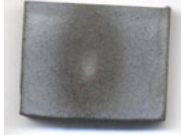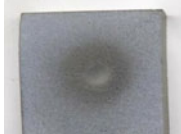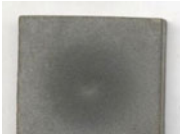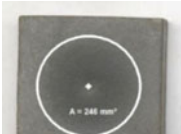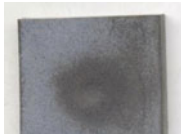
It follows from the graph (see Fig. 3b) that erosive wear increases with decreasing angle of incidence of the abrasive powder flow. This dependence is due to the fact that as the angle of incidence decreases, the abrasive jet is reflected from the surface in the direction of its movement and, without intersecting with the incident jet, carries away the eroding material. At an angle of 60 and 90°, the incident flow and the reflected flow intersect, complex cavitation processes occur, preventing erosion of the test material, especially at 90°, to the extent that in some zones the material can penetrate into a soft substrate, therefore, mass loss much less and, as a consequence, less erosive wear.

The calculated erosive wear for specimens with a ceramic coating of α-Al$_2$O$_3$ is almost an order of magnitude lower than for specimens without a coating. This is due to the high hardness of the ceramic coating, and it is consistent with qualitative observations of the erosive wear area for ceramic-coated and uncoated specimens.

4 Conclusion

Studies of the resistance of the developed polymer composite to the impact of micrometeorite particles were carried out. The tribological characteristics of a polyimide composite coated with a corundum coating based on α-Al$_2$O$_3$ have been evaluated. It has been established that a coating 100 μm thick increases the wear resistance of the filled polyimide composite by an order of magnitude.

Table 2 Erosive wear spots of coated and uncoated samples

Erosive wear angle	Uncoated		Coated with α-Al_2O_3	
	Image	Erosive wear spot area	Image	Erosive wear spot area
30°				
60°				
90°				
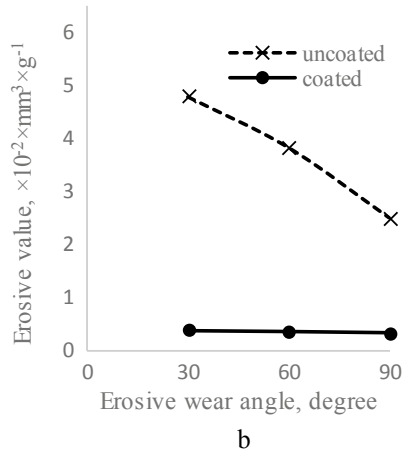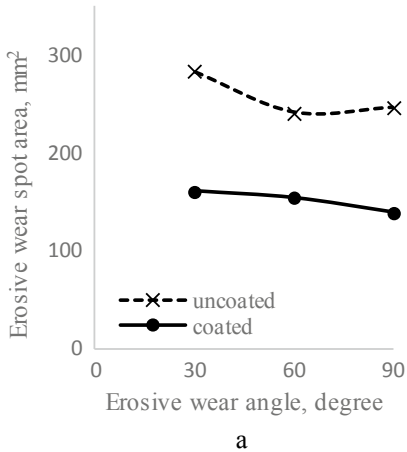
Fig. 3 Value of erosive wear (**a**) and erosive wear spot area (**b**) from the angle of processing

References

1. Vilkov, F.E., Lozovan, A.A., Bazhanov, A.V., Kasitsyn, A.N., Schekoturova, O.E., Solovev, M.K.: Investigation of the radiation-protective properties of a highly filled liquid glass material. J. Surf. Investig. **11**, 912–916 (2017). https://doi.org/10.1134/S1027451017050160
2. Cherkashina, N.I., Pavlenko, V.I., Ivanitskiy, D.A.: Investigation of the mechanisms of synthesis and modification of nanocrystalline fillers of polymeric matrices. Bull. BSTU named after V. G. Shukhov **1**, 185–190 (2016). https://doi.org/10.12737/22101
3. Keating, A., Goncalves, P., Pimenta, M., Brogueira, P., Zadeh, A., Daly, E.: Modeling the effects of low-LET cosmic rays on electronic components. Radiat. Environ. Biophys. **51**, 245–254 (2012). https://doi.org/10.1007/S00411-012-0412-2
4. Cherkashina, N.I., Pavlenko, V.I., Noskov, A.V.: Radiation shielding properties of polyimide composite materials. Radiat. Phys. Chem. **159**, 111–117 (2019). https://doi.org/10.1016/J.RADPHYSCHEM.2019.02.041
5. Ortner, H.M., Stadermann, F.J.: Degradation of space exposed surfaces by hypervelocity dust bombardment, and refractory materials for space. Int. J. Refract. Met. Hard Mater. **27**, 949–956 (2009). https://doi.org/10.1016/J.IJRMHM.2009.05.009
6. Pavlenko, V.I., Cherkashina, N.I., Noskov, A.V.: Calculation of proton passage through a highly filled polyimide composite. J. Surf. Investig. **15**, 147–151 (2021). https://doi.org/10.1134/S1027451020060129
7. Fang, X., Yang, Z., Zhang, S., Gao, L., Ding, M.: Synthesis and properties of polyimides derived from cis- and trans-1,2,3,4-cyclohexanetetracarboxylic dianhydrides. Polymer (Guildf) **45**, 2539–2549 (2004). https://doi.org/10.1016/J.POLYMER.2004.02.008
8. Cherkashina, N.I., Pavlenko, V.I., Noskov, A.V., Sirota, V.V., Zaitsev, S.V., Prokhorenkov, D.S., Sidelnikov, R.V.: Gamma radiation attenuation characteristics of polyimide composite with WO2. Prog. Nucl. Energy **137**, 103795 (2021). https://doi.org/10.1016/J.PNUCENE.2021.103795
9. Cherkashina, N.I., Pavlenko, V.I., Noskov, A.V.: Synthesis and property evaluations of highly filled polyimide composites under thermal cycling conditions from $-190\,°C$ to $+200\,°C$. Cryogenics (Guildf) **104**, 102995 (2019). https://doi.org/10.1016/J.CRYOGENICS.2019.102995
10. Sirota, V.V., Zaitsev, S.V., Prokhorenkov, D.S., Limarenko, M.V., Skiba, A.A., Kovaleva, M.G.: Detonation spraying of composite targets based on Ni, Cr and B4C for magnetron multi-functional coating (2022). https://doi.org/10.4028/p-74w31h
11. Kolisnichenko, O.V., Tyurin, Y.N., Tovbin, R.: Efficiency of process of coating spraying using multichamber detonation unit. Autom. Weld. **2017**, 28–34 (2017). https://doi.org/10.15407/AS2017.10.03
12. Kovaleva, M., Goncharov, I., Novikov, V., Yapryntsev, M., Vagina, O., Pavlenko, I., Sirota, V., Tyurin, Y., Kolisnichenko, O.: Effect of heat treatment on the microstructure and phase composition of ZrB2-MoSi2 coating. Coatings **9** (2019). https://doi.org/10.3390/COATINGS9120779

Biological and Climatic Resistance of Cement Composites Based on Biocidal Binders

V. T. Erofeev[1] , A. I. Rodin[1] , S. N. Karpushin[1] , Ya. A. Sanyagina[1] ,
S. V. Klyuev[2(✉)] , and L. S. Sabitov[3,4]

[1] Ogarev Mordovia State University, Saransk, Russia
[2] Belgorod State Technological University Named After V.G. Shukhov, Belgorod, Russia
Klyuyev@yandex.ru
[3] Kazan State Power Engineering University, Kazan, Russia
[4] Kazan Federal University, Kazan, Russia

Abstract. The aim of this work is to study the durability in biological media of cement composites based on biocidal cements. Formulation of biocidal cements was carried out using the following components: Portland cement clinker (JSC "Mordovcement", Russia); calcium sulfate dihydrate (Poretskoe deposit, Nizhny Novgorod region); fly ash of Krasnoyarsk CHP-3 (Russia), biocide preparations: sulfuric acid sodium, sodium fluoride. The finished specimens were incubated in a medium consisting of 10 species of mycelial fungi. Identification of dominant micromycetes infesting the surface of composites made on ordinary Portland cement and several types of biocidal cements obtained using different biocidal preparations was carried out. No more than 2 species of mycelial fungi were found around specimens based on biocidal cements as opposed to ordinary ones—against 7–8. At the same time, it is important that the absence of the most dangerous for human health micromycetes (Aspergillusniger) around the composites made with biocidal cements was revealed. Long-term tests (up to 180 days) revealed high fungal resistance and fungicidity of individual compositions with biocidal additives and insignificant variability of properties both in standard biological environment and in the products of their metabolism. The biocidal properties of the developed composites were tested in full-scale climate conditions of the Black Sea coast and the Leningrad Region. Developed biocidal cements with active mineral additives are recommended for use in buildings with biologically active media in the manufacture of concrete and other cement composites with increased biological resistance.

Keywords: Biocidal cements · Compositions · Study of properties · Change in mass content · Strength · Fungal resistance · Fungicidity · Climatic resistance · Properties of cements

1   Introduction

Concretes of various types are widely used in the construction industry. This contributes to the development of conducting numerous researches in the world practice. To date, rational compositions of concretes and other cement composites with improved indicators of physical and mechanical properties and increased durability have been developed [1–6]. Portland cement, which is produced by grinding Portland cement clinker with calcium sulfate dihydrate, is the most widely used as a binder in the production of concrete and products based on them. In the construction industry cements of grades 400, 500, 550, 600 are used. In addition to strength, cements have a number of other requirements, such as technological (normal density, setting time), for durability. Information is given on special binders, including mixed, composite, activated. Improving the properties of cement composites is achieved by introducing plasticizers and other additives.

The introduction of fine-grained active fillers into both cements and concrete mixes is particularly effective, leading to improvements in a number of properties of cement-based concretes.

It is shown that the use of industrial wastes in the process of obtaining various construction materials, including binders and concretes, allows increasing their physical and mechanical properties and simultaneously solving such problems as: environmental protection and the creation of waste-free technologies of production of construction materials. The most promising direction, according to a number of experts, is the use of ash as a component of mixed cements.

Recently, more and more researchers and practitioners pay attention to improving the biostability of materials and products and the elimination of the negative fact of biodeterioration of buildings and structures [7, 8].

The economic damage from bio-damage worldwide is estimated at tens of billions of dollars annually, and the list of human diseases caused by microscopic organisms is growing [9, 10].

Both in our country and abroad there is intensive research on improvement of known and development of new types of cements. Many authors have established that the most corrosive for cement and other construction composites are the following types of bacteria: Nitrosomonas, Ciostridium, Micrococcus, Tiobacillus, Desulfovibrio, Acetobakter, и мицелиальных грибов: Aspergillus, Penicillium, Trichoderma, Mycor, Cladosporium, Cepfalosporium, Torula, Saccharomyces, Pichia, Coniophora, Poria, Serpula.

In addition to destruction processes, microorganisms have a negative impact on human life. The population living in contaminated premises is prone to diseases of the respiratory, circulatory, digestive, nervous, musculoskeletal and connective tissue systems, endocrine and genitourinary systems, etc. The main causative agents of diseases associated with biodegradable microbes are micromycetes. The most common pathogens are fungi of the genus Aspergillius, which cause aspergillosis. In addition, certain species of mold fungi are potentially oncogenic.

The paper considers the issues of chemical and biological corrosion of cement concrete, durability of products based on them under the influence of aggressive media. Mechanisms of destruction of cement composites under the influence of mycelial fungi,

bacteria and products of their metabolism are analyzed. Various fouling and waste products of bacteria and fungi have a destructive effect on concrete and other materials. The destruction of concrete structures, building elements is further aggravated by the combined effects of microorganisms in the presence of mechanical damage, climatic factors.

One of the effective ways to increase the biostability of cement composites is the introduction of fungicidal and bactericidal additives in their composition.

The expediency of increasing the biostability of cement composites through the use of special cements with biocidal properties is substantiated below.

The aim of the study is to investigate the durability of cement composites based on biocidal cements with active mineral additives.

1. To study the durability of composites based on biocidal cements with an active mineral additive in the environment of mycelial fungi and products of metabolism of fungi and bacteria, in laboratory conditions, in sea water, climatic conditions of the sea coast in full-scale tests.
2. To select biocidal additives effective for use in cement composites based on the results of strength and biostability studies.
3. To establish quantitative indicators of resistance of composites based on biocidal cements with an active mineral additive in biological media, water and aqueous acid solutions.
4. To study the climatic resistance of cement composites composed on the basis of biocidal Portland cement with an active mineral additive.

2 Materials and Methods

The following components were used for the manufacture of biocidal cements: Portland cement clinker (JSC "Mordovcement") of mineralogical composition: $3CaOSiO_2$ (59–63%), $2CaOSiO_2$ (16–18%), $3CaOAl_2O_3$ (6–7.5%), $4CaOAl_2O_3Fe_2O_3$ (11–12%), calcium sulfate dihydrate (GOST 4013–82) (Poretskoe deposit), biocidal preparations: sodium sulphate (GOST 4166–76), sodium fluoride (GOST 4463–76), fly ash of the Krasnoyarsk CHP-3.

Biocidal cements were produced by grinding cement clinker, calcium sulfate dihydrate and biocidal additive (Na_2SO_4, NaF, PHMG-C) to achieve a specific surface area of 2900–3000 cm^2/g.

When evaluating the biostability of cement composites for comparison with the developed materials as binders were used ordinary and white Portland cement of domestic and foreign production: Shchurovsky, Volsky, Mordovsky, Danish, Egyptian and many others, the chemical and mineralogical composition of which was also determined in the work [11].

Standard Volsky sand $M_k = 2.45$ (GOST 6139–91) and natural quartz sand for the manufacture of concrete and mortars $M_k = 1.4$ (GOST 8736–93) (Smolninskoye deposit of Republic of Mordovia) were used as aggregates.

The technology for making specimens is described in Ref. [11].

Physical and mechanical properties of cements and composites based on them were determined according to GOST 310.3–76, GOST 30,744–2001, GOST 310.6–85. Physical and mechanical methods of research (RFA, TG, DTG, DSC, calorimetry, etc.), as well as biological methods (method of imprints, method of sampling, method of determining fungal resistance and fungicidity according to GOST 9049–91) were used in the work.

Biological, climatic and chemical resistance of cement composites with an active mineral additive was studied in comparison with cement composites made on ordinary Portland cement. Specimens of composites were tested for fungal resistance and the presence of fungicidal properties in accordance with GOST 9049–91. The following species of micromycetes were used as test organisms: Aspergillusoryzae, Aspergillusniger, Aspergillusterreus, Chaetomiumglobosum, Paecilomycesvariotii, Penicilliumfuniculosum, Penicilliumchrysogenum, Penicilliumcyclopium, Trichodermaviride.

3 Results and Their Analysis

Studies of resistance of biocidal cement composites with an active mineral additive in a standard biological medium and products of metabolism of mycelial fungi and bacteria have been conducted. The results of their tests for fungal resistance according to GOST 9.049–91 are given in Table 1.

Identification of dominant species of micromycetes on the surface of composites based on cements from 10 national and foreign manufacturers with differences in chemical and mineralogical composition after 1 month of testing in a standard medium of mycelial fungi was carried out.

Species dominance has been established on almost all decorative cement composites: Aspergillusniger, Penicilliumcyclopium и Penicilliumchrysogenum. On the surface of composites on ordinary cements two dominant species of micromycetes of the genus Penicillium (Penicilliumchrysogenum and Penicilliumcyclopium) are distinguished. In addition to micromycetes of the genus Penicillium, two species of the genus Aspergillus were identified - Aspergillusniger, on all composites made on national cements, which is associated with increased content of Mg, K, Na in them, and Aspergillusterreus, identified on the surface of composites on Krasnoyarsk and Mordovian standard composition cements. It should also be noted the presence of Trichodermaviride on the surface of composites on cement of JSC "Volskcement" and JSC "Mordovcement", which is associated with an increased content of P and Mn in their composition, and on the surface of composites on cement of French production Paecilomycesvariotii, which has a lower content of Mg, K, Na, P and Mn.

After 6 months of keeping in standard medium of mycelial fungi strength of cement stone samples of normal density on white cements decreased by 15–20%, and on ordinary cements by 20–30% depending on pore space of composites, chemical and mineralogical composition of cements and on dominating micromycetes in vicinity and on surface of composites (see Table 1).

Table 1 Fouling and coefficient of biostability of composites based on cements of national and foreign production

№ of composition	Name of cement. Producer	Assessment of fungi growth, points		Characteristics according to GOST 9.049-91	Biological resistance coefficient		
		Method 1	Method 3		1 month	3 months	6 months
1	M 600 D0 (France)	0	4	Fungal resistant	1.04	0.93	0.88
2	M 500 D0 (Russia, Krasnoyarsk)	0	4	Fungal resistant	1.05	0.9	0.8
3	M 500 D0N(Russia, Chamzinka village)	0	4	Fungal resistant	1.05	0.9	0.85
4	M 500 D0 (Russia, Volsk)	1	3	Fungal resistant	1.07	0.87	0.78
5	M 500 D0N (Russia, Volsk)	0	4	Fungal resistant	1.06	0.92	0.83
6	M 400 D0 (Russia, Stary Oskol)	0	4	Fungal resistant	1.09	0.85	0.73
7	M 500 D0 (Russia, Ulyanovsk)	0	4	Fungal resistant	1.07	0.85	0.76
8	M 500 D0 (Russia, Chamzinka village)	0	4	Fungal resistant	1.03	0.93	0.82
9	White M 500 D0 (Russia, Kolomna)	0	4	Fungal resistant	1.04	0.96	0.85
10	White M 600 D0 (Egypt)	0	4	Fungal resistant	1.05	0.90	0.8
11	White M 600 D0 (Denmark)	1	4	Fungal resistant	1.04	0.95	0.83

(*continued*)

Table 1 (*continued*)

№ of composition	Name of cement. Producer	Assessment of fungi growth, points		Characteristics according to GOST 9.049-91	Biological resistance coefficient		
		Method 1	Method 3		1 month	3 months	6 months
12	White M 600 D0 (Italy)	1	4	Fungal resistant	1.05	0.93	0.82

The biostability of cement composites modified with sodium sulfate, sodium fluoride and polyhexamethylene guanidine stearate has been established. The following cement compositions modified with biocidal preparations were tested: 1—100 wt. h. clinker, 6 wt. h. CaSO4 2H2O, 4.5 wt. h. Na2SO4; 2—100 wt. h. clinker, 0–8 wt. h. CaSO4 2H2O, 3–4.5 wt. h. NaF; 3—100 wt. h. clinker, 0–6 wt. h. CaSO4 2H2O, 1–2 wt. h. PHMG–C. At this content of components cement composites have fungicidal properties. After 6 months of incubation in a standard medium of mycelial fungi the strength of composites based on cements with fungicidal properties decreased only by 3–8% in comparison with non-added compositions, the strength of which decreased by 25–40% (see Tables 2, 3 and 4).

The dominant species of micromycetes near specimens made with biocidal cements were identified after long-term tests in standard mycelial fungi medium. Around the specimens based on cements modified with sulfuric acid sodium there is a dominance of species—Aspergillusterreus and Penicilliumcyclopium; modified with sodium fluoride—Aspergillusterreus, Penicilliumcyclopium and Aspergillusoryzae; modified with polyhexamethyleneguanidine stearate—Aspergillusoryzae. At the same time, the presence of the most dangerous for human health micromycetes (Aspergillusniger) around the composites made with biocidal cements was not detected.

On the basis of the conducted complex research the following compositions of cements for the manufacture of materials, products and structures, resistant in biologically active media are recommended: 1—100 wt. h. clinker, 4.5 wt. h. Na_2SO_4, 6 wt. h. $CaSO_4 * 2H_2O$; 2—100 wt. h. clinker, 3 wt. h. NaF, 0–8 wt. h. $CaSO_4 * 2H_2O$; 3—100 wt. h. clinker, 4.5 wt. h. NaF, 0–6 wt. h. $CaSO_4 * 2H_2O$; 4—100 wt. h. cklinker, 1–2 wt. h. PHMG–C, 0–6 wt. h. $CaSO_4 * 2H_2O$.

In a study of the fouling properties of cement composites made of Portland cement, biocidal Portland cement, Portland cement with an active mineral additive in laboratory conditions in a standard biological environment found that the composites based on Portland cement without biocidal additive have fungal resistance 0 and 1 point in the test by method 1, but fouled in the test by method 3 (3 and 4 points), that is, they are non-fungicidal.

Based on the studies of the biostability of cement composites, the following biocidal compositions of binders were identified, which showed a fungistatic effect

Table 2 Effect of CaSO$_4$ * 2H$_2$O and Na$_2$SO$_4$ content on fouling and bioresistance coefficient of cement stone

№ of composition	Content of CaSO$_4$ * 2H$_2$O, wt.h	Content of Na$_2$SO$_4$, wt.h	Assessment of fungi growth, points		Characteristics according to GOST 9.049-91	Biological resistance coefficient		
			Method 1	Method 3		1 month	3 months	6 months
1	0	0	0	4	Fungal resistant	0.99	0.8	0.60
2	2	0	0	4	Fungal resistant	1.06	0.87	0.76
3	4	0	0	4	Fungal resistant	1.02	0.88	0.75
4	6	0	0	4	Fungal resistant	1.07	0.86	0.75
5	8	0	0	4	Fungal resistant	1.07	0.79	0.63
6	0	1.5	2	4	Fungal resistant	1.07	0.94	0.79
7	2	1.5	2	4	Fungal resistant	1.06	1.00	0.86
8	4	1.5	0	4	Fungal resistant	1.06	1.02	0.85
9	6	1.5	2	4	Fungal resistant	1.09	0.98	0.82
10	8	1.5	2	4	Fungal resistant	1.06	0.92	0.77
11	0	3	0	2	Fungal resistant	1.02	0.86	0.70
12	2	3	2	3	Fungal resistant	1.05	0.99	0.92
13	4	3	2	4	Fungal resistant	1.05	1.05	0.91
14	6	3	2	4	Fungal resistant	1.01	0.97	0.93
15	8	3	2	4	Fungal resistant	1.08	0.94	0.82
16	0	4.5	0	3	Fungal resistant	1.05	0.99	0.90
17	2	4.5	0	3	Fungal resistant	1.00	0.98	0.95
18	4	4.5	0	3	Fungal resistant	1.02	1.05	0.98
19	6	4.5	0	0 (0)	Fungicidal	1.07	1.02	0.98
20	8	4.5	0	3	Fungal resistant	1.05	1.00	0.96
21	0	6	1	3	Fungal resistant	1.05	1.03	0.97
22	2	6	1	4	Fungal resistant	0.99	0.95	0.89
23	4	6	1	3	Fungal resistant	0.95	0.92	0.88
24	6	6	0	4	Fungal resistant	0.97	0.94	0.88
25	8	6	2	4	Fungal resistant	0.97	0.94	0.91

(wt. h.): (1) Portland cement clinker—100, CaSO4·2H2O—6.0–11.2, Na$_2$SO$_4$—7.0, fly ash—10.0—20.0 wt. h.; (2) Portland cement clinker—100, CaSO4·2H2O—6.0–8.6, Na2SO4—3.5, fly ash 13—10.0–20.0 wt. h.; (3) Portland cement clinker—100, CaSO4·2H2O—6.0–11.2, NaF—2.0–4.0, fly ash—10.0–20.0 wt. h. It follows from the research results that cement composites without a biocidal additive become overgrown with microorganisms, therefore, even high-density materials will be exposed to the aggressive effects of metabolic products.

The results of tests to establish the species composition of microorganisms contaminating the surface of specimens of cement composites aged in the open area and under a canopy on the Black Sea coast and in the climate of the Leningrad region, as well as after aging in sea and ground water are presented. The Black Sea coast is characterized by a

Table 3 Effect of CaSO$_4$ * 2H$_2$O and NaF content on fouling and bio-resistance coefficient of cement stone

№ of composition	Content of CaSO$_4$ * 2H$_2$O, wt.h	Content of NaF, wt.h	Assessment of fungi growth, points		Characteristics according to GOST 9.049-91	Biological resistance coefficient		
			Method 1	Method 3		1 month	3 months	6 months
1	0	0	0	4	Fungal resistant	0.99	0.8	0.61
2	2	0	0	4	Fungal resistant	1.06	0.87	0.76
3	4	0	0	4	Fungal resistant	1.02	0.88	0.75
4	6	0	0	4	Fungal resistant	1.07	0.86	0.75
5	8	0	0	4	Fungal resistant	1.07	0.79	0.63
6	0	1.5	0	3	Fungal resistant	1.05	0.88	0.81
7	2	1.5	0	3	Fungal resistant	1.07	0.90	0.81
8	4	1.5	0	3	Fungal resistant	1.08	0.92	0.85
9	6	1.5	0	3	Fungal resistant	1.08	0.95	0.86
10	8	1.5	0	3	Fungal resistant	1.05	0.93	0.85
11	0	3	0	0 (40 mm)	Fungicidal	0.99	0.97	0.92
12	2	3	0	0 (40 mm)	Fungicidal	1.00	0.98	0.93
13	4	3	0	0 (40 mm)	Fungicidal	0.98	0.96	0.94
14	6	3	0	0 (40 mm)	Fungicidal	0.99	0.97	0.95
15	8	3	0	0 (40 мм)	Fungicidal	0.98	0.96	0.94
16	0	4.5	0	0 (40 mm)	Fungicidal	0.97	0.94	0.88
17	2	4.5	0	0 (40 mm)	Fungicidal	0.95	0.92	0.86
18	4	4.5	0	0 (40 mm)	Fungicidal	0.94	0.93	0.89
19	6	4.5	0	0 (40 mm)	Fungicidal	0.83	0	0
20	8	4.5	0	0 (40 mm)	Fungicidal	0.72	0	0

warm climate, in which case the samples are exposed to variable humidity, salt spray, wind, and, in the open area, also to ultraviolet irradiation. Leningrad Region belongs to the zone with moderate climate, which is characterized by high humidity. It is known that such conditions intensify the processes of biodegradation.

The species composition of microorganisms isolated from the surface of specimens aged in warm and temperate climatic zones are shown in Tables 5 and 6.

Climatic zone Exposure conditions of specimens Species composition of microorganisms on specimens 100 wt.h. clinker, 8.6 wt.h. CaSO4·2H2O, 10.

The test results showed that the species and quantitative composition of mycobiota, contaminating cement composites is ambiguous, and depends on the formulation of materials and the effect on them of environmental factors.

Table 4 Effect of CaSO$_4$ * 2H$_2$O and PHMG–C content on fouling and the coefficient of wear resistance of cement stone

№ of composition	Content of CaSO$_4$ * 2H$_2$O, wt.h	Content of PHMG–C, wt.h	Assessment of fungi growth, points		Characteristics according to GOST 9.049-91	Biological resistance coefficient		
			Method 1	Method 3		1 month	3 months	6 months
1	0	0	0	4	Fungal resistant	0.99	0.80	0.61
2	2	0	0	4	Fungal resistant	1.06	0.87	0.76
3	4	0	0	4	Fungal resistant	1.02	0.88	0.75
4	6	0	0	4	Fungal resistant	1.07	0.86	0.75
5	0	0.5	0	3	Fungal resistant	1.03	0.89	0.78
6	2	0.5	0	2	Fungal resistant	1.04	0.91	0.82
7	4	0.5	0	2	Fungal resistant	1.04	0.95	0.87
8	6	0.5	0	2	Fungal resistant	1.05	0.94	0.88
9	0	1	0	1	Fungicidal	1.02	0.97	0.92
10	2	1	0	0 (0)	Fungicidal	1.02	1.00	0.95
11	4	1	0	0 (0)	Fungicidal	1.01	1.00	0.95
12	6	1	0	1	Fungicidal	1.01	1.01	0.95
13	0	2	0	0 (3 mm)	Fungicidal	1.01	1.00	0.97
14	2	2	0	0 (5 mm)	Fungicidal	1.01	1.01	0.98
15	4	2	0	0 (5 mm)	Fungicidal	1.02	1.02	0.98
16	6	2	0	0 (4 mm)	Fungicidal	1.02	1.01	0.97

4   Conclusions

1. The resistance of cement composites under the influence of water and chemical aggressive media: acid solutions, machine oil, gasoline were experimentally investigated. Using Excel table processor the functions describing the change in mass content and resistance coefficient of biocidal cements with active mineral additive were obtained. After 110 days of exposure the highest resistance has the following compositions, (wt.h.): (1) clinker—100, CaSO4·2H2O—8.6, Na2SO4—3.5, fly ash—20; (2) clinker—100, CaSO4·2H2O—8.6, NaF—4.0, fly ash—10.

2. The degree of fouling by mycelial fungi was revealed and the resistance of the investigated cement composites to microbiological aggressive media was established. Composites compositions modified with biocidal additives showed fungistatic effect. The kinetic dependences of changes in mass content and strength of cement composites specimens on the duration of soaking in the media were analyzed. Quantitative dependences of changes in strength and mass content of cement compositions in a standard biological medium depending on the formulation factors were revealed. Compositions of biocidal cements were revealed (wt. h.): (1) clinker—100, CaSO4·2H2O—6.0, Na2SO4—3.5; (2) clinker—100, CaSO4·2H2O—6.0,

Table 5 Test results of specimens exposed in the warm zone

Climatic zone	Specimen exposure conditions	Species composition of microorganisms on the specimens	
		100 wt.h. clinker, 8.6 wt.h. $CaSO_4 \cdot 2H_2O$, 10 wt.h. fly ash, 7.0 wt.h. sodium sulfate	100 wt.h. clinker, 11.2 wt.h. $CaSO_4 \cdot 2H_2O$, 20 wt.h. fly ash, 4.0 wt.h. sodium sulfate
Warm (Novorossiysk)	In an airy environment under a canopy	*Alternaria brassicae, Alternaria tenuissima*	*Aspergillus oryzae, Cladosporium herbarum*
Warm (Novorossiysk)	In an open air environment	*Botryotrichum piluliferum, Fusarium miniliforme*	***Not found***
	On the open area after aging in seawater	***Not found***	*Cladosporium elatum, Penicillium claviforme, Penicillium cyclopium*

Na2SO4—7.0; (3) clinker—100, CaSO4·2H2O 8.6–11,2, NaF—2,0; (4) clinker—100, CaSO4·2H2O—8.6–11.2, NaF–2.0.

3. The efficiency of using biocidal cement composites with an active mineral additive in full-scale conditions of exposure to media characteristic of bacteria and mycelial fungi was confirmed. It was established that composites on the developed compositions within the wide limits of the formulation were more resistant in comparison with materials on ordinary cement in the climatic conditions of the Black Sea coast and Leningrad region.

Table 6 Test results of specimens exposed in the temperate zone

Climatic zone	Specimen exposure conditions	Species composition of microorganisms on the specimens	
		100 wt.h. clinker, 8.6 wt.h. $CaSO_4 \cdot 2H_2O$, 10 wt.h. fly ash, 7.0 wt.h. sodium sulfate	100 wt.h. clinker, 11.2 wt.h. $CaSO_4 \cdot 2H_2O$, 20 wt.h. fly ash, 4.0 wt.h. sodium sulfate
Temperate (St. Petersburg)	In an airy environment under a canopy	–	*Alternaria brassicae, aspergillus ustus, Fusarium moniliforme*
Temperate (St. Petersburg)	In an open air environment	–	***Not found***
	On the open area after aging in groundwater	–	*Aspergillus fumigatus,Aspergillus niger, Botryotrichum piluliferum, Cladosporium elatum, Cladosporium macrocarpum, Fusarium moniliforme, Penicillium claviforme, Penicillium lanosum, Penicillium nigricans, Trichoderma viride*

References

1. Dyer, T.: Influence of cement type on resistance to organic acids. Mag. Concr. Res. **69**(4), 175–200 (2017)
2. Janfeshan, Araghi, H., Nikbin, I.M., Rahimi Reskati, S., Rahmani, E., Allahyari, H.: An experimental investigation on the erosion resistance of concrete containing various PET particles percentages against sulfuric acid attack. Constr. Build. Mater. **77**, 461–471 (2015)
3. Klyuev, S.V., Bratanovskiy, S.N., Trukhanov, S.V., Manukyan, H.A.: Strengthening of concrete structures with composite based on carbon fiber. J. Comput. Theor. Nanosci. **16**(7), 2810–2814 (2019)
4. Klyuev, S.V., Khezhev, T.A., Pukharenko, Y.V., Klyuev, A.V.: Fibers and their properties for concrete reinforcement. Mater. Sci. Forum MSF **945**, 125–130 (2018)
5. Lesovik, R.V., Klyuyev, S.V., Klyuyev, A.V., Netrebenko, A.V., Yerofeyev, V.T., Durachenko, A.V.: Fine-grain concrete reinforced by polypropylene fiber. Res. J. Appl. Sci. **10**(10), 624–628 (2015)
6. Erofeev, V., Dergunova, A., Piksaikina, A., Bogatov, A., Kablov, E., Startsev, O., Matvievskiy, A.: The effectiveness of materials different with regard to increasing the durability. MATEC Web Conf. 04021 (2016)

7. Erofeev, V., Bobryshev, A., Shafigullin, L., Khalilov, I., Sibgatullin, K., Igtisamov, R., Lakhno, A.: Theoretical evaluation of rheological state of sand cement composite systems with poly-oxyethylene additive using topological dynamics concept. Solid State Phenom. **871**, 96–103 (2016)
8. De Belie, N.: Microorganisms versus stony materials: a love-hate relationship. Mater. Struct. Materiaux et Constr. **43**(9), 1191–1202 (2010)
9. Strigác, J., Martauz, P.: Fungistatic properties of granulated blastfurnace slag and related slag-containing cements. Ceramics Silikaty **60**(1), 19–26 (2016)
10. Wei, S., Jiang, Z., Liu, H., Zhou, D., Sanchez-Silva, M.: Microbiologically induced deterioration of concrete—a review. Braz. J. Microbiol. **44**(4), 1001–1007 (2013)
11. Travush, V.I., Karpenko, N.I., Erofeev, V.T., Rodin, A.I., Rodina, N.G., Smirnov, V.F.: Development of biocidal cements for buildings and structures with biologically active environment. Power Technol. Eng. **51**(4), 377–384 (2017)

Calculation of the Parameters of the Grinding Load in a Ball-Tube Mill for the Production of Construction Materials

V. S. Bogdanov ⬤, D. V. Bogdanov ⬤, E. A. Sychev ⬤, and A. V. Karachevtseva^(✉) ⬤

Belgorod State Technological University Named After V.G. Shukhov, Belgorod, Russia
karachevtseva.anastasiia@gmail.com

Abstract. The paper deals with the main construction materials used in the construction, repair and reconstruction of buildings and structures, which include gypsum, lime, and clinker. Obtaining building materials is associated with technological processes, grinding is the most energy-intensive of them. Grinding of construction materials is carried out in ball-tube mills, the design of which is constantly being improved. The new design of the ball-tube mill is equipped with an inclined partition. The grinding bodies in the new scheme of the ball-tube mill, unlike conventional designs, move not only in the cross section of the crushing cylinder, but also in the longitudinal direction, which significantly affects the kinetics of motion. The fundamental differences in the kinematics of motion, velocity and energy modes of grinding bodies during the cycle compared to conventional ball-tube mills are considered. The calculation diagrams and graphical results of calculations are given: the coordinates, velocities and inertia of the ball at the moment of its collision with the mill crushing cylinder and the energy value of the ball under the conditions of its cross-longitudinal motion. The characteristic sections of the phases of motion of grinding bodies during the full cycle of rotation of the crushing cylinder and the behavior of grinding bodies in each of the sections is considered. The most effective zones of the work of grinding bodies are indicated. A comprehensive analysis of the loading operation is given. The main difference between the kinetics of motion of grinding bodies in a mill with an inclined chamber partition from conventional ball-tube mills, consisting in different values of the angle of incidence, velocity and energy of the ball at the same angle of separation, is considered. The generalizing conclusions of the energy and speed parameters of the ball-tube mill in the grinding of construction materials are made.

Keywords: Ball-tube mill · Inclined partition · Ball · Loading · Speed · Kinetic energy · Grinding

1 Introduction

In construction, most materials go through various technological processes during their production. The main of these processes is the grinding of construction materials. Construction materials are defined as materials that are used in the construction, repair and

reconstruction of buildings and structures. Grinding construction materials is a very energy-intensive process. Various types of equipment are used to grind construction materials. For more than a century tube mills have been widely used for grinding construction materials. But tube mills have a significant disadvantage, high energy consumption. The main materials grinded in tube mills are clinker, lime, gypsum, etc. Also in tube mills, polymeric materials are milled, which are becoming more widespread in the national economy.

When grinding clinker to produce cement, the degree of grinding has a great influence on the properties of the final product, which affects the activity of the clinker.

Due to the high energy intensity of the grinding process, work is currently underway to reduce energy consumption for grinding by installing internal energy exchange devices, such as inclined inter-chamber partitions. The movement of grinding bodies in our developed design of a ball-tube mill equipped with an inclined inter-chamber partition differs significantly from the known designs of mills [1–3]. In conventional ball-tube mills, the grinding bodies move exclusively in the cross-section of the crushing cylinder. In our proposed design of the mill, grinding bodies, along with the cross motion, make additional longitudinal one, which significantly changes the kinematics of motion, speed and energy mode of their work [4, 5].

2 Materials and Methods

To calculate the parameters of grinding load operation in mills with cross-longitudinal motion of grinding bodies it is not possible to use the classical theory of Davis assuming that the ball in the crushing cylinder first moves in its cross section along a circular path together with the crushing cylinder, and then at the breakaway point it changes to a free parabolic trajectory of falling [6, 7]. In the methodology we are considering, new approaches are proposed based on the introduction of an additional movable coordinate system located in the plane of an inclined inter-chamber partition.

This will allow us to calculate not only the trajectory of the balls during the full cycle, but also their speeds, accelerations, potential and kinetic energy, impact forces at the point of the balls falling.

3 Results and Discussion

3.1 Parameters of the Ball Movement Along the Inclined Partition

To calculate the trajectory of the ball on the inclined partition, based on the calculation scheme shown in (Fig. 1), we must determine the angle α at which the ball will detach from the crushing cylinder, the angle γ characterizing the position of the ball on the inclined partition and determine the corresponding moment angle ξ of rotation of the inclined partition.

The angle ξ of rotation of the inclined partition, at which the ball will detach from the crushing cylinder of the mill, is calculated by the formula:

$$\xi = -\theta + (-1)^k arcsin\psi^2 r^{-1}\left(1 - cos^2\beta cos\varepsilon\right) + \pi R, \tag{1}$$
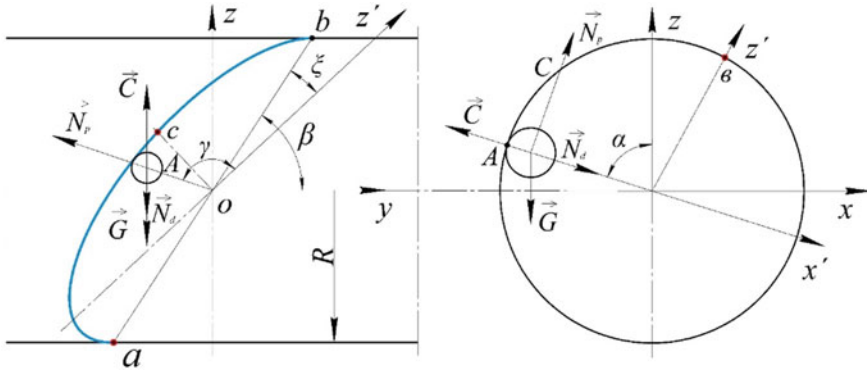
Fig. 1 The calculated coordinate system and the forces acting on the ball: fixed *OXYZ* and movable *X'OZ'* coordinate systems at $\varepsilon = 0°$; α—the angle of separation of the ball from the crushing cylinder; γ—the angle of the ball position on the inclined partition; β—the angle of inclination of the partition; ε—the angle of rotation of the crushing cylinder; $\vec{G}$, $\vec{C}$, $\overrightarrow{N_p}$, $\overrightarrow{N_d}$—the forces, respectively, of the weight of the ball, centrifugal one, the reaction of the partition, the crushing.

$$there\ r = \left[1 - cos^2 - \left(1 - sin^4\beta\right)\right]^{0.5};$$

$$\theta = arccossin - /r;$$

$$\varepsilon = arctg(tg\gamma/sin\beta).$$

The parameter k is selected in such a way that the value of the angle ξ is in the interval $0 < \xi < 2\pi$.

The angle α at which the ball breaks away from the crushing cylinder and begins its further movement along the inclined partition is equal to:

$$\alpha = arctg(tg\gamma/sin\beta) + arccossine/r - (-1)^k$$
$$\times arcsin\psi^2 r^{-1}\left(1 - cos^2\beta cos\varepsilon\right) - \pi R \tag{2}$$

3.2 Separation of the Ball from the Inclined Partition

The further movement of the ball along the inclined partition is determined by its weight $\vec{G}$ and force $\vec{N}$ of reaction of the inclined partition acting on the ball. Due to the fact that the ball rolls along the inclined partition, and does not slide, the friction force of the ball relative to the partition is neglected.

The relative coordinates of the ball on the inclined partition at any time (in the moving coordinate system $(OX'Z')$ are equal:

$$x' = -\sin[arctg(-x_i/z_i) + \xi_0 + \omega t_i]\left(x^2 + z^2\right)^2,$$

$$z' = cos[arctg(-x_i/z_i) + \xi_0 + \omega t_i)/sin\beta]\left(x^2 + z^2\right)^2. \tag{3}$$

The angle α_p of the ball's detachment from the inclined partition and the angle ξ_p of the crushing cylinder rotation at this time t_i are equal:

$$\alpha_p = arctg(-x_i/t_i); \quad \xi_p = \xi_0 + \omega t_i. \tag{4}$$

The analysis of the calculated graphical dependencies presented in Fig. 2 allows us to draw the following conclusions.
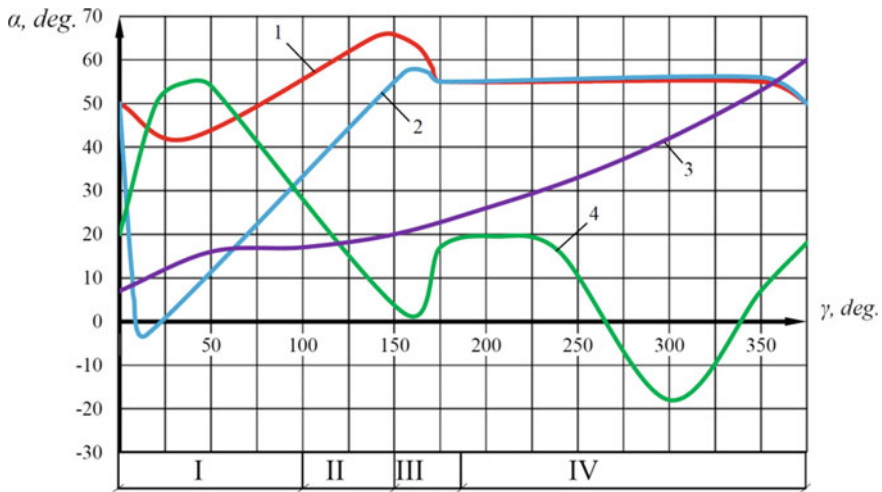
Fig. 2 Computational dependencies α_d; α_p; α; ε (γ):1—function α_d (γ); 2—function α_p (γ); 3—function α (γ); 1—function ε (γ); I, II, III, IV—characteristic areas of the phases of the ball movement ($\psi = 0.76$; $\beta = 50°$); α—angle of incidence of the ball on the "heel"

In the first section, limited by the angle of rotation of the crushing cylinder $0 < \xi < 100$ the grinding bodies from the crushing cylinder (curve 1, Fig. 2) and from the inclined partition (curve 2, Fig. 2) come off at smaller angles, i.e. rise to a greater height than in conventional mills and acquire more total energy (kinetic and potential), do more work of impact grinding [8, 9]. In this phase of motion, the inclined partition picks up the balls that have detached from the inner surface of the crushing cylinder, lifts them to the maximum height and throws them down to the grinding heel. Here we should pay special attention to the fact that in conventional mills, the ball, once detached from the inner surface of the crushing cylinder of the mill, goes to the path of free fall and moves exclusively in the cross section of the crushing cylinder. In this case, the ball receives additional longitudinal velocity when detached from the inclined partition and moves along a free-fall trajectory along the axis of the crushing cylinder [9]. Those balls that are on the inclined partition in the area bounded between $10 < \gamma < 27$ rise to the maximum height. In this case the angle of separation is $\alpha \leq 0°$. While in conventional mills, at the same speed of the crushing cylinder, equal to $\psi = 0.76$, the separation angle is 55°.

And at $\alpha = 0$ the balls start to centrifuge without committing grinding work. In our case balls are not centrifuged, and less energy is spent for their work.

In the second section, corresponding to a rotation angle of $0° < \xi < 150°$, the ball comes off with larger angles than in conventional mills (Fig. 2, curve 2), but it does not follow the free-fall trajectory, because the inclined partition "pulls" it against itself from the crushing cylinder inner surface. The ball is lifted by the inclined partition and goes into free fall only after detachment from the partition in this case the separation angle of the ball from the partition is within $34° < \alpha_p < 55°$, and the crushing cylinder in the rotation phase is $0° < \xi < 150°$ (Fig. 2, curve 2).

In the considered section of the crushing cylinder rotation, equal to 40% of the full crushing cylinder revolution, unlike conventional mills, the ball rises to a greater height and acquires significantly more energy.

At the third characteristic section, corresponding to the angle of rotation of the crushing cylinder $150° < \xi < 180°$ balls are caught with inclined partition at angles of separation from the crushing cylinder $\alpha_d = 72° - 55°$, lifted it to an angle of respectively $17° - 0°$ and then move on to the trajectory of free fall.

The fourth section corresponds to the phase of crushing cylinder rotation $180° < \xi_0 < 360°$, here the functions $\alpha_d(\gamma)$ and $\alpha_p(\gamma)$ intersect in the area $\gamma = 180°$ and have a linear characteristic in all subsequent phase of the crushing cylinder rotation (Fig. 2, cur.1;2). The ball from the crushing cylinder and the inclined partition is detached as in a conventional mill at the angle $\alpha_d, \alpha_p = 55°$.

In mills equipped with an inclined partition plate, the separation angle of the ball during one cycle (crushing cylinder revolution) varies within a wide range from 0° to 62°, while in conventional mills it is constant and during the cycle it is 55°. At 40% of a full cycle the ball rises to a higher height than in conventional mills, 10% to a lower height, and 50% it has the same separation angle as in conventional mills. It follows that the presence of an inclined partition in a drum mill at the same crushing cylinder speed provides more energy to the balls than in conventional mills.

3.3 Speed and Inertia of the Ball at the Moment of Its Collision with the Mill Crushing Cylinder

The coordinates of the ball and its velocity at the moment of impact on the inner surface of the crushing cylinder are equal:

$$x_d = x_1 + \vartheta_{x_1} t_d; \quad y_d = y_1 + \vartheta_{y_1} t_d; \quad z_d = z_1 + \vartheta_{z_1} t_d - g t_d^2/2. \tag{5}$$

$$\vartheta_x = \vartheta_{x_1}; \quad -\vartheta_y = \vartheta_{y_1}; \quad -\vartheta_z = \vartheta_{z_1} - gt. \tag{6}$$

The relative velocity of the ball at the moment of impact with the crushing cylinder is calculated by the formula:

$$\vartheta_{N_d} = \left[\left(\vartheta_{x_d} - \omega_{z_d} \right)^2 + \vartheta_{y_d} + \left(\vartheta_{z_d} + \omega_{x_d} \right)^2 \right]^{0.5}. \tag{7}$$

After colliding with the crusing cylinder, the ball loses kinetic energy and the cycle repeats again.

In the process of the ball movement after detachment from the crushing cylinder, it may repeatedly collide with the inclined partition and only then with the crushing cylinder.

The coordinates of the ball and its velocity at the moment of the first collision with the inclined partition after time t are equal:

$$x_p = x_1 + \vartheta_{x_1} t_p; \quad y_p = y_1 + \vartheta_{y_1} t_p; \quad z_p = z_1 + \vartheta_{z_1} t_p - g t_p^2/2, \tag{8}$$

$$\vartheta_x = \vartheta_{x_1}; \quad \vartheta_y = \vartheta_{y_1}; \quad \vartheta_z = \vartheta_{z_1} - g t_p. \tag{9}$$

Since we know the coordinates and velocity of the ball after its first collision with the inclined partition, its further motion is calculated by the formulas:

$$x_{p_i} = x_2 + u_{x_2} t_p; \quad y_p = y_2 + u_{y_2} t_p; \quad z_{p_i} = z_2 + u_{z_2} t_p - g t_p^2/2. \tag{10}$$

$$u_{x_2} = \vartheta_{x_2} + A\cos\beta\sin\xi_2; \quad u_{y_2} = \vartheta_{y_2} + A\sin\beta; \quad u_{z_2} = \vartheta_{z_2} + A\cos\beta\cos\xi_2. \tag{11}$$

There
$A = 2\left[\omega\cos\beta(z_2\sin\xi_2 - x_2\cos\xi_2) + \vartheta_{x_2}\cos\beta\sin\xi_2 - \vartheta_{y_2}\sin\beta + \vartheta_{z_2}\cos\beta\cos\vartheta_{x_2}\right]$,
$X_2; Y_2; Z_2; V_{x_2}; V_{y_2}; V_{z_2}$ are, respectively, the coordinates and velocity of the ball at the moment of impact with the inclined partition.

According to Davis' theory, in conventional ball mills with a known ball angle we can always unambiguously calculate the angle of incidence, velocity and energy of the ball, which ultimately characterizes its ability to grind the material.

In mills equipped with inclined partitions this is not possible. The balls have different angles of incidence, velocities and energies for the same separation angle (Figs. 3 and 4). This is the essential difference between the motion kinetics of grinding bodies in an inclined partition mill and conventional ball-tube mills.
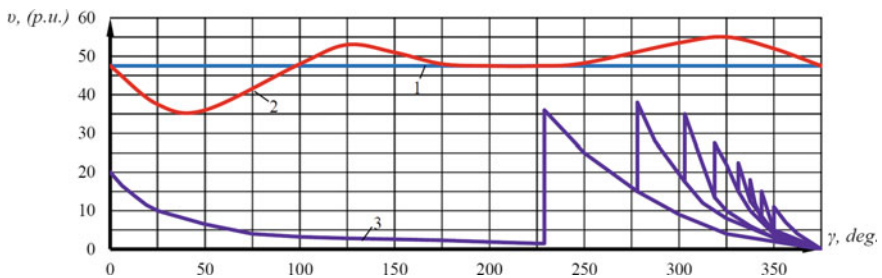
Fig. 3 Relative and longitudinal velocity of the ball at the moment of falling on the crushing cylinder ($\psi = 0.76; \beta = 50°$): 1—$\vartheta_r'(\gamma)$; 2—$\vartheta_r(\gamma)$; 3—$\vartheta_l(\gamma)$

The pattern of change in the relative velocity ϑ_0 of the ball at the moment of its collision with the crushing cylinder is of the greatest interest, because this very velocity determines the value of kinetic energy, and consequently the nature of the loads and the efficiency of the grinding process as a whole.
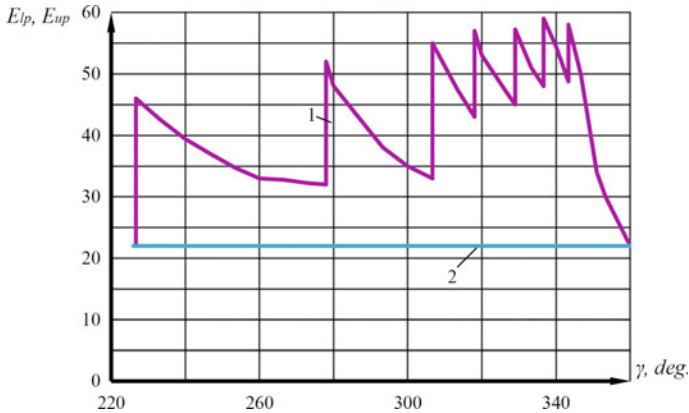
Fig. 4 Kinetic energy of balls at points of incidence: 1—$E_{lp}(\gamma)$; 2—$E_{up}(\gamma)$

In conventional ball mills at the optimum crushing cylinder velocity $\psi = 0.76$ the value of relative velocity does not change during the cycle and is equal to $\vartheta_r = 47$ r.u. (relative units)—Fig. 3; curve 1, then in mills with inclined partition it changes from 33 to 55 r.u.

In the crushing cylinder rotation phase $0° < \xi < 105°$ the relative velocity in the inclined partition mill is lower than in the conventional ones (Fig. 3) curve 3 is lower than curve 1. This is due to the fact that the incidence angles in this section of the inclined partition mill are larger than those of conventional mills (Fig. 2). However, in mills with inclined partition, the ball has a longitudinal velocity, which is absent in conventional mills and which is commensurate in magnitude with the relative velocities. Moreover, the absolute velocity of the ball in this phase of its motion corresponds to its speed in conventional mills [10].

In the $100° < \xi < 230°$ rotation phase of the crushing cylinder the balls move as in conventional mills the relative ball speed increases to 50 r.u. and the longitudinal speed becomes zero. In the area of crushing cylinder rotation $230° < \xi < 360°$ ° a sharp increase of the longitudinal velocity is observed (Fig. 3; curves 3; 2), the relative velocity of the ball also increases. The kinetic energy of the ball increases from 20 to 42 r.u., i.e., more than two times (Fig. 4; curve 1). Obviously, in this phase, the efficiency of the material grinding process increases significantly [9].

At $\xi > 275°$, the longitudinal velocity and kinetic energy change discontinuously (Fig. 3; curve 3; Fig. 4; curve 1). This corresponds to the moment of multiple collisions of the balls with the inclined partition. The kinetic energy and longitudinal velocity of the ball change in a wide range of values, which creates conditions for a selective process of grinding the material and rational use of ball loading energy.

In the subsequent phase of crushing cylinder rotation, the relative ball velocity and kinetic energy are greater than in conventional mills, and the presence of a longitudinal speed of up to 80% of the relative velocity ensures longitudinal movement of the balls

and intensive grinding of material by abrasion. In addition, the large value of longitudinal velocity indicates that the impact when the ball falls does not fall on the surface of the crushing cylinder (liner), but on the load, because the longitudinal velocity is directed along the axis of the crushing cylinder.

4   Conclusion

The peculiarity of grinding bodies motion in mills equipped with an inclined partition provides a reduction of liner wear in the zone of inclined partition work; actively destroys stagnant zones in the cross section of the load; creates conditions for in-mill classification of the crushed construction material; increases the probability of useful use of energy of grinding bodies. Changing the angles of separation and incidence of balls not only changes the value of velocities and energy of the ball at the point of falling, but also significantly increases the width of the zone in which the most intensive crushing of construction material occurs.

References

1. Fadin, Y.M., Khakhalev, P.A., Degtyarev, P.A.: Simulation of the ball mill loading movement and study of its operation modes depending on geometrical parameters of the lining. J. Phys. Conf. Ser. **1353**, 1–5 (2019). https://doi.org/10.1088/1742-6596/1353/1/012026
2. Latyshev, S.S., Voronov, V.V., Bogdanov, V.S., Fadin, Y.M., Bazhanova, O.I., Maslovskaya A.N.: Mathematical modeling of load's movement in lifter of intramill recirculation device inside tubular mill. In: IOP conference series: materials science and engineering, pp. 1–9. Iopscience, Tomsk, Russian Federation (2018). https://doi.org/10.1088/1757-899X/327/2/022046
3. Bondarenko, J.A., Khanin, S.I., Bestuzheva, O.V.: Investigation of stress-strain state of ball mill trunnion. In: Proceedings of the 5th international conference on industrial engineering, pp. 883–893. Springer, Cham (2019). https://doi.org/10.1007/978-3-030-22041-9_94
4. de Alessandro, L.R.: Oliveira, Luís Marcelo Tavares: Modeling and simulation of continuous open circuit dry grinding in a pilot-scale ball mill using Austin's and Nomura's models. Powder Technol. **340**, 77–87 (2018). https://doi.org/10.1016/j.powtec.2018.09.016
5. Bogdanov, V.S., Fadin, Y.M., Dontsova, Y.A., Bogdanov, N.E., Fyot, Sh.K.: Mechanics of crushing medium in ball mills with longitudinal-transverse motion of grinding bodies. Bull. BSTU named after V.G. Shukhov **3**(8), 117–125 (2018). https://doi.org/10.12737/article_5b6d586e6ed9b2.54424779
6. Bürger, R., Bustamante, O., Fulla, M.R., Rivera, I.E.: A population balance model of ball wear in grinding mills: an experimental case study. Miner. Eng. **128**, 288–293 (2018). https://doi.org/10.1016/j.mineng.2018.09.004
7. Bogdanov, V.S., Sharapov, R.R., Fadin, Y.M.: Fundamentals of calculation of machinery and equipment of enterprises of construction materials and products. Thin science-intensive technologies, Russian Federation (2013)
8. Bogdanov, V.S., Bogdanov, D.V., Semikopenko, I.A.: Processes in the production of construction materials. Thin science-intensive technologies, Russian Federation (2018)

9. Reichardt, R., Wiechert, W.: Event driven algorithms applied to a high energy ball mill simulation. Granular Matter **9**, 251–266 (2007). https://doi.org/10.1007/s10035-006-0034-y
10. Gupta, V.K., Sharma, S.: Analysis of ball mill grinding operation using mill power specific kinetic parameters. Adv. Powder Technol. **25**, 625–634 (2014). https://doi.org/10.1016/j.apt.2013.10.003

Dynamic Behavior of an "Earth Dam-Foundation" Plane System Within Wave Theory

K. D. Salyamova[1](✉) and A. T. Buriev[2]

[1] Institute of Mechanics and Seismic Stability of Structures of the Academy of Sciences of the Republic of Uzbekistan, Tashkent, Uzbekistan
klara_51@mail.ru

[2] Tashkent University of Architecture and Civil Engineering, Tashkent, Uzbekistan
abdulaziz.bt77@gmail.com

Abstract. The design, construction, and operation of high earth dams located in seismically active zones of the Republic Uzbekistan require constant improvement of the computational methods for their calculation to predict the loss of strength (formation of cracks, loss of slope stability, etc.). In the current normative method to calculate hydro-technical structures for seismic effects, a cantilever rod is considered; this method does not allow taking into account the non-one-dimensional nature of the oscillation and the real physical and mechanical characteristics of soil of the structure and foundation. The assessment of the dynamic stress–strain state of high earth dams under seismic action within the wave theory is the most difficult problem in mechanics. This article presents a mathematical formulation for the numerical solution of a non-stationary problem for an earth dam with a foundation in a plane elastic statement. The problem of studying the stress state of the high Charvak earth dam under shear dynamic impact on the foundation (in the form of a seismogram) was solved by the numerical method of finite differences. So-called radiation conditions were set at the boundaries of the studied finite domain of the foundation. The solution is represented as a distribution of lines of equal displacements, stresses over the dam body depending on time. At that, the most vulnerable zones of the considered earth dam were identified.

Keywords: Earth dam · Finite difference method · Explicit scheme · Rock foundation · Stress · Displacement · Seismogram

1 Introduction

Ensuring the seismic resistance of hydro-technical structures is the most important task that must be taken into account in the design, construction, and operation since their potential destruction during an earthquake can lead to catastrophic consequences and the death of people. The seismic safety of rockfill or earthfill dams is subject to the constant movements caused by earthquakes.

The design scheme of the current normative method for calculating hydro-technical structures for seismic impacts presents an elastic cantilever rod, which does not take into account the non-one-dimensional nature of the oscillation.

A detailed review of known publications, as well as studies of dynamic behavior and stress–strain state (SSS) of earth dams, considering the linear and nonlinear elastic and viscoelastic properties of soil and finite strains in a plane formulation, is given in [1–3]. Oscillations of structures in the pre-resonant, resonant, and post-resonant modes are considered.

In the studies of foreign researchers [4–8], a special place is given to solving specific problems related to the assessment of the SSS and dynamic behavior of earth dams, taking into account various factors [4–8].

This article considers a plane design model representing the cross-section of an earth dam on an aleurolite base. The finite difference method was chosen as a calculation method. The non-stationary problem for the "earth dam-foundation" plane elastic scheme is solved on the example of the high earth dam of the Charvak HPP (height 169 m).

2 Methods and Materials

The equations of motion of the "earth dam-foundation" system are written by the basic equations of continuum mechanics; they have the following form in a plane formulation

$$\rho_i \frac{\partial^2 u^i}{\partial t^2} = \frac{\partial \sigma_{xx}^i}{\partial x} + \frac{\partial \tau_{xy}^i}{\partial y},$$

$$\rho_i \frac{\partial^2 v^i}{\partial t^2} = \frac{\partial \tau_{yx}^i}{\partial x} + \frac{\partial \sigma_{yy}^i}{\partial y}, \ (i = 1, 2) \tag{1}$$

where index i = 1 refers to the foundation, and i = 2 refers to the dam, ρ_i– is the density; u^i, v^i,—are the displacement vector projections on the x, y coordinate axes; $\sigma_{xx}^i, \sigma_{yy}^i, \tau_{xy}^i$- are the normal and shear stresses.

The relationship between strains and displacements is determined by the Cauchy relations

$$\varepsilon_{xx}^i = \frac{\partial u^i}{\partial x}, \ \varepsilon_{yy}^i = \frac{\partial v^i}{\partial y},$$

$$\varepsilon_{xy}^i = \frac{\partial u^i}{\partial y} + \frac{\partial v^i}{\partial x}, \ (i = 1, 2). \tag{2}$$

Hooke's law expresses the constitutive equations relating the stress tensor and the strain tensor:

$$\sigma_{xx}^i = \frac{E_i}{1 - v_i^2}(\varepsilon_x^i + v\varepsilon_y^i)$$

$$\sigma_{yy}^i = \frac{E_i}{1 - v^2}(v_i\varepsilon_x^i + \varepsilon_y^i)$$

$$\tau_{xy}^i = \frac{E_i}{2(1 + v_i)}\varepsilon_{xy}^i, \ (i = 1, 2) \tag{3}$$

where E_i—is the linear strain modulus, v_i is Poisson's ratio.

Boundary conditions on the surface of the upstream face of the dam are

$$p_x = \sigma_{xx}^2 l_1 + \tau_{xy}^2 m_1,$$
$$p_y = \tau_{xy}^2 l_1 + \sigma_{yy}^2 m_1. \tag{4}$$

where p_x, p_y—are the stress components from the hydrostatic pressure on the upstream face surface, l_1, m_1,—are the direction cosines of the upstream face surface. In the absence of hydrostatic pressure, stress components p_x, p_y are zero.

Boundary conditions at the crest of the dam are

$$\tau_{xy}^2 = 0,$$
$$\sigma_{yy}^2 = 0. \tag{5}$$

Boundary conditions on the surface of the downstream face are

$$\sigma_{xx}^2 l_2 + \tau_{xy}^2 m_2 = 0,$$
$$\tau_{xy}^2 l_2 + \sigma_{yy}^2 m_2 = 0. \tag{6}$$

where l_2, m_2,—are the direction cosines of the downstream face surface.

At initial time ($t = 0$), the displacements and velocities in the entire area of the earth dam are zero

$$u^2 = 0, \quad \frac{\partial u^2}{\partial t} = 0,$$
$$v^2 = 0, \quad \frac{\partial v^2}{\partial t} = 0. \tag{7}$$

On the free surface of the dam foundation, the boundary conditions have the following form

$$\sigma_{yy}^1 = 0,$$
$$\tau_{yx}^1 = 0. \tag{8}$$

At the dam-foundation contact boundary, the following no-slip conditions are satisfied

$$u^1 = u^2, \quad v^1 = v^2,$$
$$\sigma_{xx}^1 = \sigma_{xx}^2, \quad \tau_{xy}^1 = \tau_{xy}^2, \tag{9}$$

$$u^1 = u^2, \quad v^1 = v^2,$$
$$\sigma_{yy}^1 = \sigma_{yy}^2, \quad \tau_{yx}^1 = \tau_{yx}^2. \tag{10}$$

The time point when the wave front approaches the lower part of the dam foundation is taken as the initial condition $t = 0$, i.e.

$$u^1 = u^0,$$

$$v^1 = v^0, \tag{11}$$

here the superscript ^{0} corresponds to displacements in the incident wave.

In the numerical calculation of the problem, an explicit scheme of the method of finite differences of the second-order accuracy is used in this study to solve a system of differential equations.

When solving the problem numerically, we select the calculated finite domain (fictitious boundary) and set the boundary conditions on the contour of this domain.

Since we are solving a linear problem, displacements of the dam foundation soil u^1, v^1 we represent as sums of incident ($u^{1,0}$, $v^{1,0}$) and reflected ($u^{1,1}$, $v^{1,1}$) waves, i.e. $u^1 = u^{1,1} + u^{1,0}$, $v^1 = v^{1,1} + v^{1,0}$. In boundary conditions, the displacements and stress for the dam foundation soil are represented as the sum of incident and reflected waves, and radiation conditions are set on fictitious boundaries.

The following conditions are set on the lower fictitious boundary of the foundation from the side of the upstream face slope

$$\sigma_{xx}^{1,1} = \rho_1 a_1 \frac{\partial u^{1,1}}{\partial t}, \quad \tau_{xy}^{1,1} = \rho_1 b_1 \frac{\partial v^{1,1}}{\partial t}. \tag{12}$$

The following conditions are set on the lower fictitious boundary of the foundation from the side of the downstream face slope

$$\sigma_{xx}^{1,1} = -\rho_1 a_1 \frac{\partial u^{1,1}}{\partial t}, \quad \tau_{xy}^{1,1} = -\rho_1 b_1 \frac{\partial v^{1,1}}{\partial t}. \tag{13}$$

The following conditions are set on the lower fictitious boundary of the foundation

$$\sigma_{yy}^{1,1} = \rho_1 a_1 \frac{\partial v^{1,1}}{\partial t}, \quad \tau_{xy}^{1,1} = \rho_1 b_1 \frac{\partial u^{1,1}}{\partial t}. \tag{14}$$

The problem is solved by the finite difference method using an explicit scheme. The calculated domains of the earth dam and deformable foundation are conditionally partitioned into three areas with steps: hx = hx1 in the horizontal line (the x-axis) (upstream retaining prism); hx = hx2 (a dam crest), hx = hx3 (downstream retaining prism); hy in the vertical line (Fig. 1).

We denote the value of the grid function at the point with coordinates $x_i = ih$, $y_j = jh$ at $t = k\tau$, (τ is the time step; hx, hy are the domain steps) by $F_{i,j}^k$, then the components of the strain tensor for the internal nodes of the computational domain (i + 1/2,j) at $k\tau$ in difference form are written as

$$\varepsilon_{xx,i+1/2,j}^k = \frac{u_{i+1,j}^k - u_{i,j}^k}{hx},$$

$$\varepsilon_{yy,i+1/2,j}^k = \frac{v_{i+1,j+1}^k + v_{i,j+1}^k - v_{i+1,j-1}^k - v_{i,j-1}^k}{4hy},$$

$$\varepsilon_{xy,i+1/2,j}^k = \frac{u_{i+1,j+1}^k + u_{i,j+1}^k - u_{i+1,j-1}^k - u_{i,j-1}^k}{4hy} + \frac{v_{i+1,j}^k - v_{i,j}^k}{hx}, \tag{15}$$
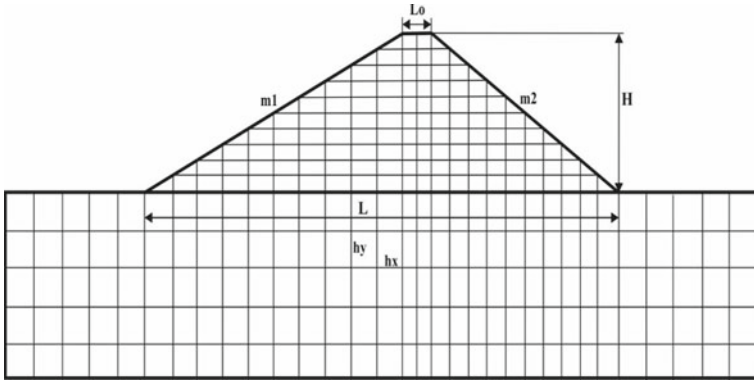
Fig. 1 Partitioning of the calculation domain of the dam

for node $(i, j + 1/2)$ at $k\tau$,

$$
\varepsilon_{xx,i,j+1/2}^{k} = \frac{u_{i+1,j+1}^{k} + u_{i+1,j}^{k} - u_{i-1,j+1}^{k} - u_{i-1,j}^{k}}{4hx},
$$

$$
\varepsilon_{yy,i,j+1/2}^{k} = \frac{\upsilon_{i,j+1}^{k} - \upsilon_{i,j}^{k}}{hy},
$$

$$
\varepsilon_{xy,i,j+1/2}^{k} = \frac{u_{i,j+1}^{k} - u_{i,j}^{k}}{hy} + \frac{\upsilon_{i+1,j+1}^{k} + \upsilon_{i+1,j}^{k} - \upsilon_{i-1,j+1}^{k} - \upsilon_{i-1,j}^{k}}{4hx}. \qquad (16)
$$

where hx takes the following values: on the upstream retaining prism hx = hx1, on the crest of the dam hx = hx2, on the downstream retaining prism hx = hx3.

Below we give expressions for calculating fictitious displacements of boundary nodes on the upstream face. Since the problem does not take into account the water pressure on the upstream face, i.e., $p_x = p_y = 0$, from condition (4) we obtain

$$
\sigma_{yy} = \sigma_{xx} d_1^2,
$$

$$
\tau_{xy} = -\sigma_{xx} d_1 \qquad (17)
$$

where $d_1 = l_1/m_1$.

Substituting Hooke's law (3) and Cauchy relations (2) into Eq. (17), we determine the first derivatives of displacements u, υ along the y coordinate

$$
\frac{\partial \upsilon}{\partial y} = D_{11} \frac{\partial u}{\partial x},
$$

$$
\frac{\partial u}{\partial y} = D_{21} \frac{\partial u}{\partial x} - \frac{\partial \upsilon}{\partial x} \qquad (18)
$$

where $D_{11} = \frac{d_1^2(\lambda+2G)-\lambda}{\lambda+2G-\lambda d_1^2}$, $D_{21} = -\frac{d_1(\lambda+2G+\lambda D_{11})}{G}$, $\lambda = \frac{2\nu G}{1-2\nu}$.

We use the central differences of the approximation of the first derivatives of the second order of error and from (18) we obtain an expression for determining the boundary displacements

$$v_{i,j+1}^k = 2hy\left(D_{11}\frac{u_{i+1,j}^k - u_{i-1,j}^k}{2hx1}\right) + v_{i,j-1}^k,$$

$$u_{i,j+1}^k = 2hy\left(D_{21}\frac{u_{i+1,j}^k - u_{i-1,j}^k}{2hx1} - \frac{v_{i+1,j}^k - v_{i-1,j}^k}{2hx1}\right) + u_{i,j-1}^k \qquad (19)$$

$i = j, j = 1,..., J1 - 1, k = 1,..., K.$

From boundary condition (6), similarly to (19), for the downstream face, we obtain

$$v_{i,j+1}^k = 2hy\left(D_{12}\frac{u_{i+1,j}^k - u_{i-1,j}^k}{2hx3}\right) + v_{i,j-1}^k,$$

$$u_{i,j+1}^k = 2hy\left(D_{22}\frac{u_{i+1,j}^k - u_{i-1,j}^k}{2hx3} - \frac{v_{i+1,j}^k - v_{i-1,j}^k}{2hx3}\right) + u_{i,j-1}^k \qquad (20)$$

$i = I2 + j, j = 1,..., J1 - 1, k = 1,..., K$

where $d_2 = l_2/m_2$, $D_{12} = \frac{d_2^2(\lambda+2G)-\lambda}{\lambda+2G-\lambda d_2^2}$, $D_{22} = -\frac{d_2(\lambda+2G+\lambda D_{12})}{G}$.

From the boundary condition on the crest of the dam (5) and Hooke's law (3), we obtain a formula for calculating normal stress σ_{xx}

$$\sigma_{xx} = \frac{4G(\lambda + G)}{\lambda + 2G}\frac{\partial u}{\partial x}$$

there is no need to calculate the boundary fictitious displacements on the crest of the dam. On the contour of the crest of the dam at the nodes with half-integer grid numbers, shear stresses τ_{xy}, and normal stresses σ_{yy} are known and they are zero, σ_{xx} is determined from (21) and in finite differences, it has the following form

$$\sigma_{xx,i+1/2,j}^k = \frac{4G(\lambda + G)}{\lambda + 2G}\frac{u_{i+1,j}^k - u_{i,j}^k}{hx2}, \qquad (21)$$

$i = I1,..., I2 - 1, j = J1, k = 1,..., K.$

Then, the finite-difference equation of motion of the dam and its foundation is solved for each domain

$$\rho\frac{(u_{i,j}^{k+1} - 2u_{i,j}^k + u_{i,j}^{k-1})}{\tau^2} = \frac{\sigma_{xx,i+1/2,j}^k - \sigma_{xx,i-1/2,j}^k}{hx} + \frac{\sigma_{xy,i,j+1/2}^k - \sigma_{xy,i,j-1/2}^k}{hy}$$

$$\rho\frac{(v_{i,j}^{k+1} - 2v_{i,j}^k + v_{i,j}^{k-1})}{\tau^2} = \frac{\tau_{yx,i+1/2,j}^k - \tau_{yx,i-1/2,j}^k}{hx} + \frac{\sigma_{xy,i,j+1/2}^k - \sigma_{xy,i,j-1/2}^k}{hy} \qquad (22)$$

(where, in each area of the dam, the horizontal step hx in formulas (21)–(22) takes the value hx1, hx2, and hx3, respectively) with boundary conditions (9)–(11), and initial

conditions (17); then the displacements are determined at the dam nodes for each time point. It can be seen from the difference Eq. (22) that three time layers are involved in it, and in order to derive the equation at each node (i, j) for two displacement components, it is necessary to calculate the stresses at four nodes with half-integer indices.

Difference Eq. (22) approximates the equation of motion (1), of order $O(\tau^2, hx^2, hy^2)$. The condition for the scheme stability is ($\tau \leq h/c_1$), where h = min(hx, hy).

3 Results and Discussion

A solution algorithm was developed based on the formulation of the dynamic problem. The reliability of the developed methods and algorithm for solving the problem was proved by comparison with the solution of the test problem (the Lamb problem) [9, 10].

A time process (the model proposed by I.L. Korchinsky [11]) is taken as a seismic effect

$$\frac{\partial^2 u_0}{\partial t^2} = Ae^{-st} \sin \omega t \tag{23}$$

where A is the maximum acceleration, s is the coefficient of exponential damping in time, ω is the prevailing frequency of the impact.

In calculations, the law of change of displacements in the horizontal direction (a seismogram) is taken as an external impact on the dam foundation in the following form

$$u_0 = \frac{A}{(\omega^2 + s^2)^2} \left(e^{-st} \left(s^2 \sin(\omega t) - \omega^2 \sin(\omega t) + 2\omega s \cos(\omega t) \right) - 2\omega s \right) \tag{24}$$

It corresponds to model (23), i.e. differentiating expression (24) twice, we obtain (23).

In calculations, the acceleration amplitude according to the Korchinsky formula [11] was taken as A = 0.2 g and coefficient $s = 0.3$, which corresponds to an 8-point magnitude earthquake.

Figure 2 shows the dependence of horizontal displacements (m) on time for three points of the dam at f = 1 Hz for the calculation time t = 10 s (solid line—foundation point with coordinates x = 375.6 m, y = 0; dashed line—downstream face point with coordinates x = 504.8 m, y = 112 m (at height $\frac{2}{3}H$); dotted line—point of the middle of the dam crest with coordinates x = 375.6 m y = 168 m). Under a possible 8-point magnitude earthquake, the maximum amplitude of oscillations of the dam foundation is 0.05 m; of the downstream face, it is 0.35 m, and the maximum amplitude of displacements on the crest is 0.5 m (10 times greater compared to the foundation).

Figure 2 shows the dependence of horizontal displacements (m) on time for three points of the dam at f = 1 Hz for the calculation time t = 10 s (solid line—foundation point with coordinates x = 375.6 m, y = 0; dashed line—upstream face point with coordinates x = 246 m, y = 112 m (at height $\frac{2}{3}H$); dotted line—point of the middle of the dam crest with coordinates x = 375.6 m, y = 168 m). Under a possible 8-point magnitude earthquake, the maximum amplitude of oscillations of the dam foundation is 0.05 m; of the upstream face, it is 0.12 m, and the maximum amplitude of displacements on the crest is 0.225 m (4,5 times greater compared to the foundation).
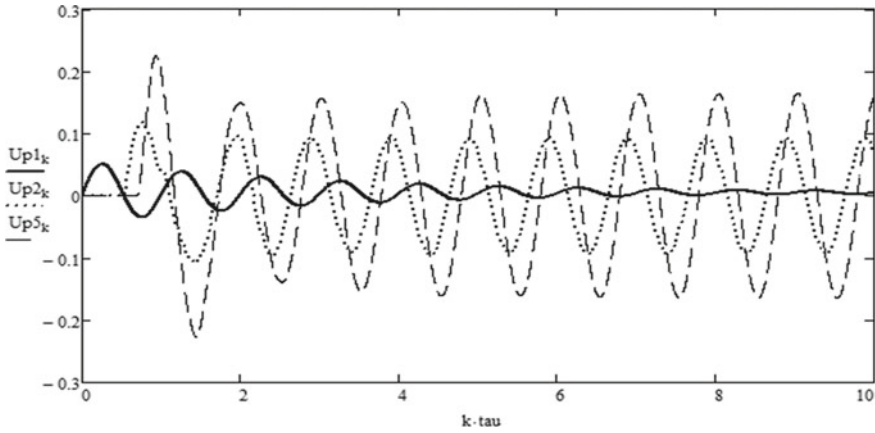
Fig. 2 Dependence of horizontal displacements (m) on time (solid line—dam foundation; dotted line—upstream face ($y = \frac{2}{3}H$); dashed line—dam crest) at impact frequency $f = 1$ Hz

Fig. 3 Dependence of shear stresses τ_{xy}(MPa) on time (solid line—dam foundation; dotted line—downstream face ($y = \frac{2}{3}H$)) at impact frequency $f = 1$ Hz

Figure 3 shows the dependence of shear stresses τ_{xy} (MPa) on time (solid line—dam foundation; dotted line—downstream face ($y = \frac{2}{3}H$), calculation time—10 s.

Although at the dam foundation, shear stresses are greater than on the downstream face, they are less dangerous compared to the stress values on the downstream face.

Figure 4 shows the time dependence of normal stresses σ_{yy} at the same points.

4 Conclusion

The calculations were conducted in accordance with the current normative documents, clause 2.2b of Building Code of the Republic "in design of retaining hydro-technical structures of classes I-II in areas with seismicity of more than 7 points, it is recommended
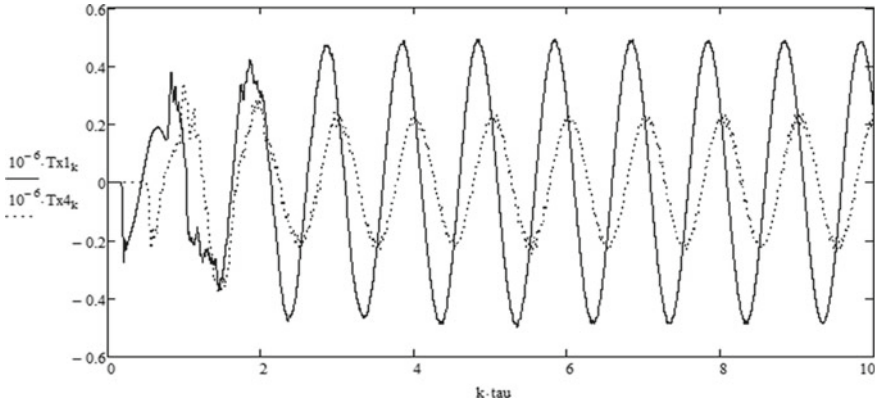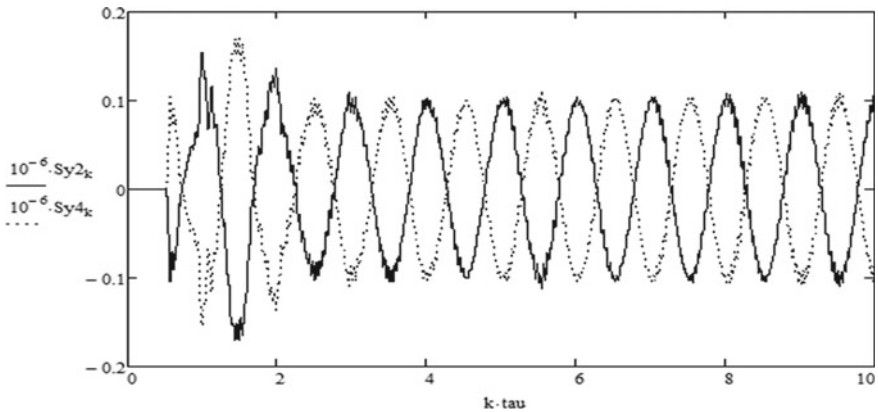
Fig. 4 Dependence of normal stresses σ_{yy} on time (solid line—dam foundation; dotted line—downstream face ($y = \frac{2}{3}H$)) at impact frequency f = 1 Hz

to conduct calculations based on the wave theory for the impacts specified by the earthquake records (accelelograms, etc.). Unlike other studies [1–8], these calculations use records of earthquakes, determined in accordance with the specified paragraph 5.3 of the Building Codes for design, considering the mechanical properties of soils. Therefore:

- the formulation and solution of a non-stationary problem by the numerical method of finite differences for the study of the stress–strain state of a particular earth dam with the foundation were developed and solved, taking into account the geometric and physical–mechanical parameters of soil of the structure and foundation under shear seismic impacts;
- the results of solving the problem were the distribution of horizontal velocities, normal, shear, and maximum shear stresses in the body of the dam at the frequencies of seismic impact f = 1 Hz and f = 5 Hz, present in the frequency range of strong earthquakes; they are key frequency parameters of building regulations;
- it was shown that for the considered particular case of the dam calculation, low-frequency seismic effects are more unfavorable than high-frequency ones. At that, the crest and slopes of the dam are the most dangerous parts from the point of view of the possibility of soil sliding [12].

References

1. Mirsaidov, M.M., Sultanov, T.Z.: Evaluation of the stress-strain state of earth dams, taking into account the nonlinear deformation of the material and finite deformations. Eng. Constr. J. **5**, 73–82 (2014)
2. Mirsaidov, M.M., Sultanov, T.Z.: Development of theoretical foundations for assessing the dynamics of earth dams, taking into account their interaction with water and wave entrainment of energy from structure to foundation. Irrig. Melioration **2**, 32–38 (2016)

3. Sultanov, K.S., Salyamova, K.D., Khusanov, B.E.: Dynamic calculation of earth dams taking into account the structural change of soil. Probl. Dev. Transp. Eng. Commun. **1**, 137–140 (2011)
4. Xiong, B.-L., Wang, X.-L., Lu, C.-J.: Dynamic reaction analysis of tailing dams under earthquake. Adv. Environ. Geotech. **6**, 697–701 (2010)
5. Siyahi, B., Arslan, H.: Nonlinear dynamic finite element simulation of Alibey. Earth Dam Environ. Geol. **54**(1), 77–85 (2008)
6. Bauer, E., Fu, Z.Z., Liu, S.: Constitutive modeling of materials for rockfill dams. In: 6th International conference on dam engineering, vol. 15, issue 17, pp. 1–14. Lisbon, Portugal (2011)
7. Bauer, E., Fu, Z.Z., Liu, S.: Influence of pressure and density on the rheological properties of rockfills. Front. Struct. Civ. Eng. **15**(2), 25–34 (2012)
8. Matvienko, A.A.: Improving the methodology for calculating the seismic resistance of dams from soil materials based on wave theory. Dissertation Ph.D. in Technical Sciences. Kharkov (2015).
9. Buriev, A.T.: Non-stationary oscillation of an earth dam with a rigid foundation. Probl. Mech. **30**(2), 17–26 (2021)
10. Buriev, A.T., Salyamova, K.D., Turdikulov, KhKh., Takhirov, Sh.M.: Numerical analysis of a stress-strained earth dam under seismic impact, taking into account wave dynamics. Constr. Mater. Prod. **2**(3), 5–18 (2020). https://doi.org/10.34031/2618-7183-2020-3-3-5-20
11. Korchinsky, I.L.: Seismic-resistant construction of buildings. Higher school, Moscow (1971)
12. Akhmedov, M.A., Salyamova, K.D.: Analysis and assessment of damage to hydro-technical structures. Tashkent (2016)

Effect of Plasma Blast Furnace Slag Treatment on Properties of Blast Furnace Slag-Cement Mortar

S. I. Bazhenova$^{(\boxtimes)}$ [ID] and Dien Vu Kim [ID]

National Research Moscow State University of Civil, Engineering, d. 26, Yaroslavskoe Shosse, Moscow 129337, Russian Federation
sofia.bazhenova@gmail.com

Abstract. The paper presents the results of blast furnace slag treatment by low-temperature non-equilibrium plasma method. The blast furnace slag treatment process is carried out at the Moscow State University of Civil Engineering laboratory. An alternating current generator with voltages up to 8000 V and frequencies up to 40 kHz between the electrodes creates a low-temperature unbalanced plasma region. Research results show that, after blast furnace slag is treated by low-temperature non-equilibrium plasma method, cracks appear on the blast furnace slag surface. This leads to a decrease in grain size and an increase in the blast furnace slag Blaine fineness. In addition, the research results also show that the compressive and flexural strengths of the mortar sample using plasma-treated blast furnace slag are 71.08 MPa and 10.42 MPa, respectivel. That is higher than the mortar sample using the blast furnace slag untreated plasma, respectively 0.05 MPa and 8.70 MPa.

Keywords: Low-temperature non-equilibrium plasma · Blast furnace slag · Compressive strength · Flexural strength · Surface activity

1 Introduction

Blast furnace slag (BFS) is a non-metallic residue usually obtained from steel mills or ore reduction in a blast furnace. Blast furnace slag has a high cementitious capacity and a high content of calcium silicate hydrates (CSH), a strength-enhancing compound that improves concrete's strength, durability and appearance [1, 2]. Many methods have been developed for the treatment of blast-furnace slag. For example, BFS sent to a landfill. However, this is very expensive and causes environmental problems, such as organic soil contamination, heavy metal leaching, and secondary dusting. Therefore, the processing of BFS is a critical process before its storage. In addition, another method that is widely used to treat blast-furnace slags is mechanical grinding. This method can obtain finely ground BFS for admixture or fine aggregate in concrete [3]. However, the mechanical grinding method still has limitations, such as not being able to increase the surface activity of BFS. Therefore, the method of low-temperature non-equilibrium plasma can be used to improve the surface activity of blast-furnace slag [4–10].

Non-equilibrium plasmas are low pressure plasmas characterized by high electron temperatures and low ion and neutral temperatures. Low-temperature plasmas are frequently not in thermodynamic equilibrium [11–13]. The use of plasma technologies in building materials science is reflected in the works of Fedosov S.V., Akulova M.V., Bruyako M.G., Volokitin G.G., Ushkova V.A. and others [4, 5, 8, 14–17]. But studies aimed at studying the activation of the surface of blast-furnace slag in a low-temperature non-equilibrium plasma have not been identified, in comparison with studies aimed at processing binder, mixing water, and natural sand by this method. Therefore, this paper presents the effect of the non-equilibrium low-temperature plasma method on the absorption characteristics of blast-furnace slag.

2 Methods and Materials

2.1 Materials Used

– Portland cement CEM I 42.5 N manufactured by the But Son (VietNam) plant with a content of C_3S—56.15%, C_3A—5.14%, average particle size 29.58 MKM, blaine fineness $= 3670 \, cm^2/g$, $\rho = 3.11 \, g/m^3$, water demand 28.2% and compressive strength at age 28 days $= 48.24 \, MPa$. Chemical composition: $SiO_2 = 22.43\%$, $CaO = 62.52\%$, $MgO = 2.04\%$, $Fe_2O_3 = 3.44\%$, $Al_2O_3 = 5.32\%$, $SO_3 = 0.15\%$, $MgO = 2.04\%$, $K_2O = 0.29\%$, loss on ignition $= 1.97\%$.
– Blast furnace slag (BFS) from the Hoa Phat factory (Vietnam) with $\rho = 2.63 \, g/cm^3$. Chemical composition: $SiO_2 = 36.01\%$, $CaO = 40.46\%$, $MgO = 7.71\%$, $Al_2O_3 = 13.41\%$, $K_2O = 0.64\%$ loss on ignition $= 3.46\%$.
– Mixing water to obtain a concrete mixture meets the requirements of GOST 23,732–2011, pH $= 7.5$.

2.2 Methods

The process of processing blast-furnace slag by the method of low-temperature non-equilibrium plasma was carried out in a laboratory installation, where an alternating current source with a voltage of up to 8000 V and a frequency of up to 40 kHz creates a region of low-temperature non-equilibrium plasma between the electrodes. Processing time in 90 s.

Raman spectroscopy experiments were carried out on a Horiba Jobin Yvon T64000 Raman spectrometer.

Changes in the surface of blast-furnace slag before and after low-temperature non-equilibrium plasma treatment were determined using a LEVENHUK 320 microscope and a DCM500 digital ocular camera.

The setting time of the cement-slag mixture is determined according to GOST 310.3-76.

3 Results and Discussion

3.1 Analysis of Raman Spectroscopy

The study of the results of the Raman method revealed the presence of distinct changes in the position and intensity of the Raman spectra of modified samples obtained as a result of plasma treatment of minerals, which indicates the presence of phase transitions of the first and second order. Although it is difficult to accurately identify the Raman-active phases of slag samples during the measurement process, the obtained data show that the control variables (aperture, wavelength, and polarization of the excitation source) do not lead to a qualitative change in the response compared to the control. A comparison of the curves for the control and modified samples under plasma exposure shows that one of the effects of plasma-chemical treatment is an increase in the luminescence intensity (the continuous component of the response is not due to single-photon processes). As a result, functional group surface concentration increases as the metastable state exit time increases. The results allow us to conclude that the increase in the sorption capacity of the mineral carrier is not proportional to the time of exposure to low-temperature non-equilibrium plasma (Fig. 1).
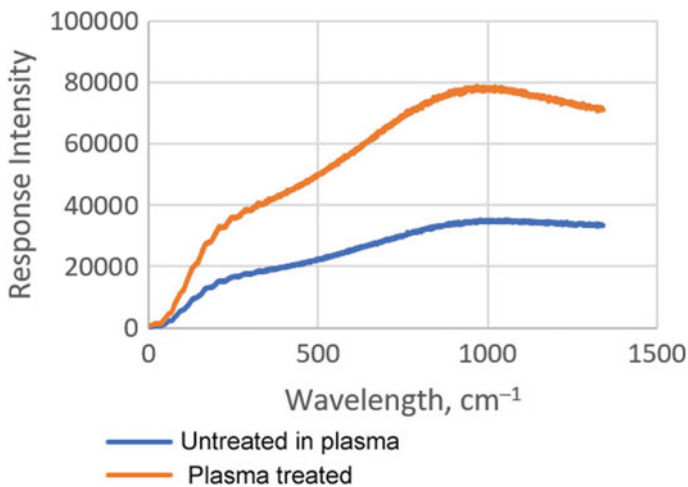
Fig. 1 Response-intensity dependence of the blast-furnace slag surface on the wavelength after treatment in low-temperature non-equilibrium plasma for 90 s

3.2 Investigation of the Blast-Furnace Slag Surface Before and After Treatment with Low-Temperature Non-Equilibrium Plasma

Changes in the macro-and microstructure of control blast-furnace slags and blast-furnace slags processed in a barrier discharge were studied by the method of optical registration. Using a LEVENHUK 320 microscope and a DCM500 digital eyepiece camera, a series of images were taken, some of which are shown below.

Figure 2 shows that the control sample of blast-furnace slag (before treatment with low-temperature non-equilibrium plasma) did not have cracks. Meanwhile, cracks form as the time of exposure to low-temperature non-equilibrium plasma increases, and the trajectory of the BFS is increased, going along the lines A, B, C, D, E, F, G, H (Fig. 2). The degree of imperfection increases when exposed to low-temperature non-equilibrium plasma, leading to irreversible damage. As a result, the dispersion increases, and the particle size decreases. In our opinion, forming new cells, including microparticles and macrophages, contributes to the absorption of more sorbate than previously thought.

BFS before plasma treatment   BFS after plasma treatment
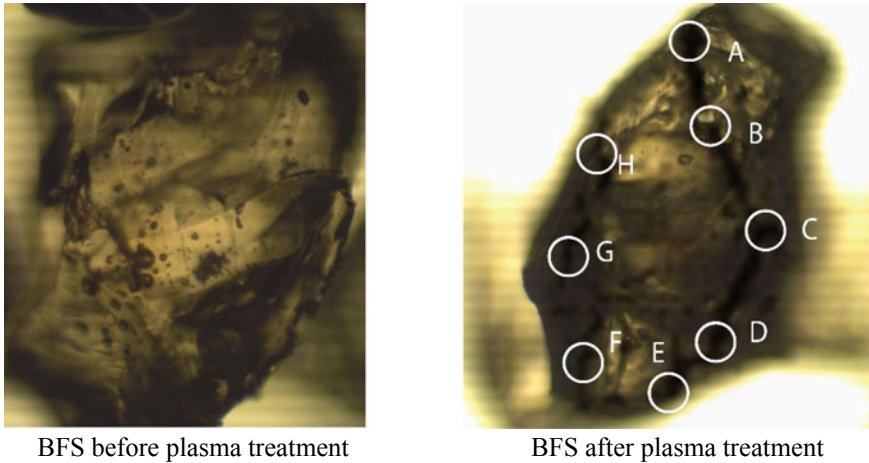
Fig. 2 Surface image of plasma blast-furnace slag and initial blast-furnace slag

3.3   Effect of Plasma Modified BFS on Properties of BFS -Cement Mortar

3.3.1   Setting Time of BFS -Cement Mortar

In the present study, the proportions and composition of the mixture are presented in Table 1.

Table 1 Mixing ratios of BFS -cement mortar

Mixture number	Mixing ratio	Cement (g)	BFS (g)	Water (g)
No-1	(50% Cement - 50% BFS without plasma treatment)	500	500	324
No-2	(50% Cement - 50% BFS with plasma treatment)	500	500	324

The setting period corresponds to a certain stage in the cement stone's structure formation. The setting period is distinguished by the most intensive development of

hydration processes and the most intense heat release associated with this process [2, 4]. Table 2 presents the results of the study.

Table 2 Determination of setting time

Mixture number	Setting time, hours-minutes	
	Setting start time	Setting end time
No-1	3 h 05 min	5 h 35 min
No-2	2 h 20 min	4 h 55 min

From Table 2, it can be seen that mixture No-2 has a faster setting start time and setting end time than the No-1 mixture. This is explained because the blast furnace slag after plasma treatment will increase the Blaine fineness. Therefore water demand is higher than the No-1 mixture.

3.3.2 Compressive and Flexural Strength

Analyzing the results, we found that the strength of the samples on the modified binder increased significantly during the first seven days. This indicates that the plasma-denatured mineral component actively acts in the cement binder, forming a microframework and imparting a microstructure to the material, acting as a binding center (Table 3).

Table 3 Compressive and flexural strength of experimental samples

Mixture number	Compressive strength (MPa), days				Flexural strength (MPa), days			
	3	7	14	28	3	7	14	28
No-1	27.5	46.5	56.3	60.05	4.01	6.78	8.28	8.70
No-2	30.06	50.2	65.02	71.08	4.42	7.38	9.56	10.42

Figure 3 shows that the strength of the plasma-treated blast-furnace slag sample is always higher than that of the control blast-furnace slag sample. It is explained that low-temperature plasma treatment contributes to forming a more significant amount of hydration products and a denser structure. The compressive strength at 28 days for samples on the treated slag increases by 18.4%, and the flexural strength at 19.8%.

It has been proven and experimentally confirmed that the use of modified blast-furnace slags on the resulting concrete's strength is due to the cement matrix's adhesive properties and plasma-modified slags.
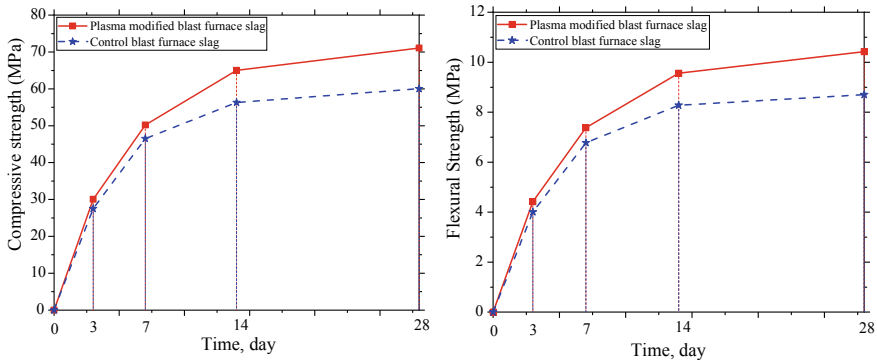
Fig. 3 Compressive strength and flexural strength versus time

4 Conclusion

Based on experimental results, we can conclude below.

The use of plasma-modified blast-furnace slag as an active mineral additive makes it possible to reduce the initial and final setting times of blast-furnace slag cement by up to 20% and increase the strength characteristics of mortars made from the modified substance. Binder (cement-blast furnace slag) at an early stage of hardening: an increase in strength at 7 days of age up to 70%.

The results allow us to conclude that the low-temperature plasma method effectively converts blast-furnace slag into a functional additive in the production of building materials and products. As a result, it is possible to obtain effective building materials, expanding the scope of their application and reducing energy costs for modification compared to other known methods.

References

1. Dien, K.V., Bazhenova, S.I., Nguyen, T.C., Tang, V.L., Do, M.C., Le, V.L., Hoang, M.T.: Insulation properties and performance of foam concrete using blast furnace slag. Struct. Integrity Life **22**(1), 48–56 (2022). https://doi.org/10.1016/j.jhazmat.2011.08.081
2. Kurti, I., Rani, D.A., Boccaccini, A.R., Cheeseman, C.R.: Geopolymers from DC plasma-treated air pollution control residues, metakaolin, and granulated blast furnace slag. J. Mater. Civ. Eng. **23**, 735–740 (2011). https://doi.org/10.1061/(ASCE)MT.1943-5533.0000170
3. Kim, D.V., Bazhenova, S.I., Trong, C.N., Van, L.T., Minh, C.D., Van, L.L., Van, D.N., Cong, L.N., Minh, T.H.: Blast furnace slag properties at different grinding times and its effect on foam concrete compressive and flexural strength. Civil Eng. J. **3**, 32–44 (2022). https://doi.org/10.14311/CEJ.2022.01.0003
4. Bruyako, M.G., Grigor'eva, L.S., Grigor'eva, A.I.: Plasmomodificated sorbing agents on the basis of zeolite containing earth materials of the Khotynets deposit occurrence. Constr. Sci. Educ. **7**(4) (25), 38–50 (2017). https://doi.org/10.22227/2305-5502.2017.4.3
5. Volokitin, O.G., Volokitin, G.G., Shekhovtsov, V.V: Physicochemical processes at plasma treatment of Quartz-Feldspar raw materials. Adv. Mater. Res. **1085**, 474–477 (2015). https://doi.org/10.4028/www.scientific.net/AMR.1085.474

6. Trung, H.T., Hoang, T., Huynh, D., Hung, Q.D., Giang, V.N.: Plasma treatment and teos modification on wood flour applied to composite of polyvinyl chloride/wood flour. Adv. Polym. Technol. **2019**(3974347), 8p (2019). https://doi.org/10.1155/2019/3974347

7. Valentin, V.S., Oleg, G.V., Nikolai, A.T., Gennady, G.V., Nelly, K.S., Ruslan, E.G.: Efficiency of Thermal plasma treatment of aluminosilicate particles. Key Eng. Mater. **769**, 23–28 (2018). https://doi.org/10.4028/www.scientific.net/KEM.769.23

8. Volokitin, G., Yu, A., Skripnikova, N., Volokitin, O., Shekhovtsov, V.: X-Ray diffraction analysis of bottom ash waste after plasma treatment. IOP Conf. Ser. Mater .Sci. Eng. **189**, 012021 (2017). https://doi.org/10.1088/1757-899X/189/1/012021

9. Jun, L., Kou, L., Shengjun, Y., Yaojian, L., Dan, H.: Application of thermal plasma technology for the treatment of solid wastes in China: an overview. Waste Manage. **58**, 260–269 (2016). https://doi.org/10.1016/j.wasman.2016.06.011

10. Mária, Č, Marián, L., Michal, P., Marta, L., Juraj, V., Ľubomíra, Š: Measurement and evaluation of properties of MSW fly ash treated by plasma. Measurement **62**, 155–161 (2015). https://doi.org/10.1016/j.measurement.2014.11.014

11. Shustin, E.G., Plasma technologies for material processing in nanoelectronics: problems and solutions, Vol. 62, No. 5, pp 454–465 (2017). https://doi.org/10.1134/S106422691704012X

12. Shekhovtsov, V.V., Volokitin, O.G, Kondratyuk, A.A., Vitske, R.E.: Fly ash particles spheroidization using low temperature plasma energy. IOP Conf. Ser. Mater. Sci. Eng. **156**, 012043 (2016). https://doi.org/10.1088/1757-899X/156/1/012043

13. Zhang, L., Chang, X., Jia, Y., Lei, Z., Shu, H., Luo, M., Wang, Y., Wen. X.: The denitration mechanism of fly ash catalysts prepared by low-temperature plasma technology. Vacuum **181**, 109695 (2020). https://doi.org/10.1016/j.vacuum.2020.109695

14. Ushkov, V., Nalbandyan, G., Soloviev, V.: Modification of components of fine-grained concretes by low-temperature nonequilibrium plasma. Mater. Today Proc. **19**, 1841–1844 (2019). https://doi.org/10.1016/j.matpr.2019.07.024

15. Bruyako, M.G., Glukhoedov, V.A., Kravtsova, D.V., Smirnov, V., Ushkov, V.A.: Plasma processing in industry of building materials. Adv. Mater. Res. **1040**, 730–734 (2014). https://doi.org/10.4028/www.scientific.net/AMR.1040.730

16. Fedosov S.V., Akulov, M.V., Tanicheva, M.V., Shutov, D.A.: Investigation of the effect of low-temperature glow discharge plasma on the hydrophilic properties of repair interlining. Bull. MGSU 63–67 (2012). https://doi.org/10.12737/article_5bab4a20598ad9.13288459

17. Ushkov, V.A., Kalyadin, A.Y., Nalbandyan, G.V., Soloviev, V.G., Bogdanova, A.A.: Plasma modification of construction mortar components, an efficient method of increasing their performance. Bull. MGSU 548–558 (2019). https://doi.org/10.22227/1997-0935.2019.5.548-558

Mechanical, Tribological, and Anticorrosion Properties of the Coating Produced by Magnetron Sputtering of a Ni–Cr–B$_4$C Composite Target

V. V. Sirota , S. V. Zaitsev$^{(\boxtimes)}$, D. S. Prokhorenkov , and M. V. Limarenko

Belgorod State Technological University Named After V.G. Shukhov, Belgorod, Russia
`sergey-za@mail.ru`

Abstract. In surface engineering technology, coatings have attracted widespread attention due to their ability to impart excellent tribological and anti-corrosion properties to the surface of materials. However, to improve the protective and functional properties of coatings, a more complex combination of elemental composition is largely assumed. In the present work, the mechanical, tribological, and anticorrosive properties of a Ni–B–Cr–C composite coating deposited by DC magnetron sputtering on a Ni–Cr–B$_4$C composite target are investigated. The composite film showed good mechanical properties with a hardness of 10 GPa and an elastic modulus of 271 GPa. Wear tests carried out with a ball-on-disk tribometer showed that the Ni–B–Cr–C coating had good wear resistance. The mechanical wear of the composite coating is dominated by abrasive, oxidative and adhesive wear in the atmospheric environment. The coefficient of friction of the composite coating is in the range from 0.84 to 1.01. It has been established that the Ni–B–Cr–C composite coating increases the corrosion resistance of the steel substrate.

Keywords: Composite coating · Magnetron sputtering · Tribology · Anti-corrosion

1 Introduction

The modern development of the aerospace, automotive and other industries is increasing the requirements for the properties of functional and protective coatings. Conventional one-component coatings cannot keep up with the increasing demands. It is necessary to research and develop new coatings that provide high heat resistance, wear resistance and corrosion resistance. World experience in recent years has shown that multicomponent coatings have a great development potential due to their unique functional and protective properties [1–6]. First, multi-component coatings demonstrate the advantages of constituent materials. Secondly, a combination of the elemental composition of the coating is possible in accordance with the structure and requirements for them. Thirdly, multi-component coatings can have properties that one material cannot have when performing

several functions. In connection with the above, the purpose of this work is to study the mechanical, tribological and anticorrosion properties of the Ni–B–Cr–C composite coating deposited by magnetron sputtering of a Ni–Cr–B$_4$C cermet composite target.

2 Methods and Materials

The Ni–B–Cr–C composite coating was deposited on a polished AISI 304 steel substrate in a UniCoad 200 vacuum unit by DC magnetron sputtering. The target was a copper plate with a Ni–Cr–B$_4$C ceramic–metal coating, the production of which is described in Ref. [7]. Steel substrates (AISI 304 steels) were subjected to ultrasonic cleaning in heptane and then washed with ethanol, after which they were dried in a stream of dry nitrogen and installed in a vacuum chamber. The distance from the magnetron and ion source to the substrate was 70 mm. After the base pressure in the vacuum chamber reached 2×10^{-3} Pa, ion purification was carried out with argon for 10 min at a pressure of 0.08 Pa and an ion source voltage of 2.2 kV. The coating was applied at an operating pressure of 0.17 ± 0.001 Pa in an argon gas medium. The target was pre-sprayed for 1 min to remove any surface contaminants. During the application of the composite coating, the substrate was not additionally heated. In Table 1 shows the conditions for applying a Ni–B–Cr–C composite coating.

Table 1 Ni–B–Cr–C composite coating conditions

Parameter	Description
Working gas	Ar (with a purity of 99,999%)
Discharge current of the magnetron, A	2
Voltage, V	495–502
Frequency, kHz	18
Rotation of the carousel with samples, rpm	18

The mechanical properties of the composite coating were tested on a Dynamic Ultra Micro Hardness Tester DUH-201S (Japan) using a Berkovich indenter at a maximum load of 0.2 mN to minimize the effects of the steel substrate. The tribological characteristics of the coatings were tested on an automated friction machine Tribometer (CSM Instruments) according to the "pin on the disk" scheme at a normal load of 2 N. Balls Ø6 mm made of corundum (hardness 19 GPa) and steel grade 100Cr6 (hardness 8 GPa) were used as a counterbody for tribological experiments. The surface and distribution of elements in the ball-coating contact zone were studied using a scanning electron microscope (TESCAN MIRA 3 LMU) and energy dispersive spectroscopy (EDS). SEM images were acquired at 5 kV acceleration voltage.

The anticorrosion characteristics of the composite coating were evaluated using an Elins P-20X8 multichannel potentiostat–galvanostat and ES8 software. To measure the potential of the open circuit Erc, a beaker-type cell with a vertically lowered sample

was used. 3.5% NaCl was used as a working solution. An ESr-10101 (Ag/AgCl/KCl) electrode was used as a reference electrode; the KCl concentration in the potential-forming half-cell was 4.2 mol/dm^3. Corrosion potential current densities were obtained from polarization curves using the Tafel slope crossing method.

3   Results and Discussion

The hardness (H) and modulus of elasticity (E), as well as the calculated values of H/E and H^3/E^2 of the composite coating are shown in Table 2. The measured hardness value and elastic modulus of the Ni–B–Cr–C composite coating were 10 GPa and 271 GPa, respectively. It is known that the ratio H/E is used to predict the elastic deformation of the coating, and the ratio H^3/E^2 is the resistance of the coating to plastic deformation [8, 9].

Table 2 Mechanical properties of the composite coating

Coating	H, GPa	E, GPa	H/E	H^3/E^2
Ni–B–Cr–C	10	271	0.04	0.01

On Fig. 1 shows the coefficient of friction, the SEM image of the wear mark of the composite coating, and the optical image of the wear mark of balls made of corundum and steel grade 100Cr6. As can be seen from Fig. 1a and d, the friction behavior of the composite coating on the steel substrate was the same, but the material of the ball affected the friction result. At the beginning, the coefficient of friction of the coating increases rapidly due to the running-in process. At this stage, the irregularities are leveled and the contact area of the ball with the coating is increased. After the running-in period, the friction process stabilizes until the end of the test, and the friction coefficient remains unchanged for the steel ball and the corundum ball, 1.01 and 0.84, respectively. The wear trace showed that when using a steel ball, as can be seen from Fig. 1b, the inner track is smooth with no cracks and no peeling of the coating from the substrate. There is a small groove in the center of the wear track due to ball abrasion, i.e. chafing occurs on the surface of the composite coating due to ball wear (Fig. 1c). The use of a corundum ball, as seen in Fig. 1e, the wear track is smooth with small grooves and small pits. There is a slight accumulation of abrasive particles on the surface of the worn track. As shown in Fig. 1f, the interior of the corundum ball also has a slight accumulation of abrasive particles.

On Fig. 2 shows the EDS map of the wear traces of the composite coating by steel and corundum balls. It can be seen that when steel and corundum balls are used, oxygen is present on the surface of the wear scar, indicating oxidation of the friction surface. The presence of iron in the wear track of the coating is due to the abrasion of the steel ball against the coating, which is indicative of adhesive wear. From Fig. 2b, it can be seen that a small amount of iron is present on the surface of the wear track due to the wear of the coating. As the ball rubs against the surface of the coating, there is a local
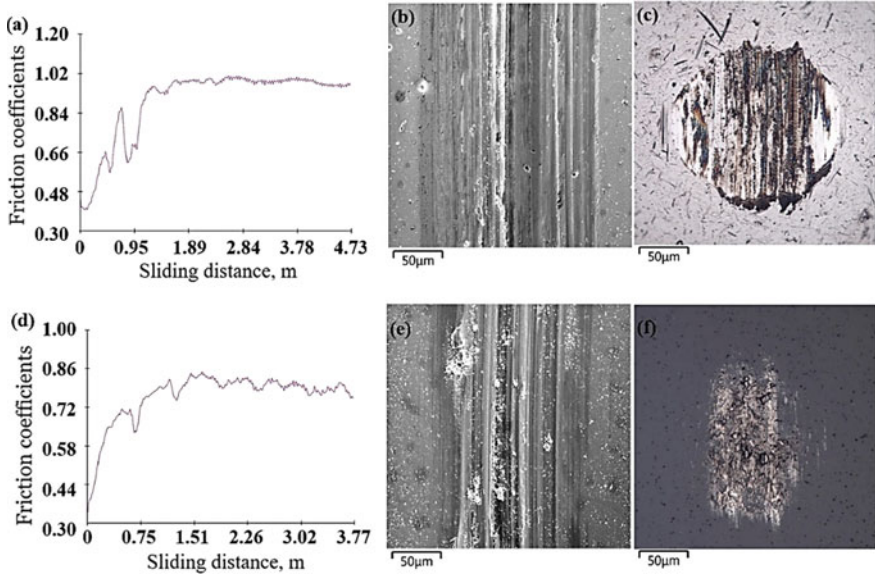
Fig. 1 Friction coefficient (μ), SEM image of the wear mark of the composite coating and optical image of the wear mark of the ball: (**a**, **b**, **c**) 100Cr6 steel ball; (**d**, **e**, **f**) ball of corundum

increase in temperature, and the unevenness of the coating or ball can break, creating loose debris particles that oxidize and adhere to surfaces. This may cause scratches on the surface, which will help remove the coating. As a result, when using a steel ball, the wear mechanism is adhesive and oxidative. When using a corundum ball, oxidative and abrasive wear occurs.
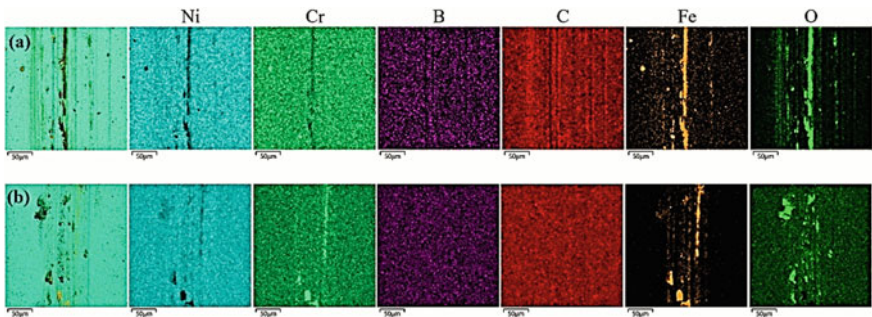
Fig. 2 EDS images of wear traces of the composite coating of the ball: **a** ball made of 100Cr6 steel, **b** corundum ball

On Fig. 3 shows the potentiodynamic polarization curves of the composite coating and AISI 304 steel substrate in 3.5% NaCl solutions. Using the Tafel extrapolation method, the results of the corrosion potential (E_{corr}) and current (I_{corr}) for the steel substrate and composite coating were obtained, shown in Table 3. The shift of the

polarization curve towards lower current and higher potential indicates an improvement in the corrosion resistance of the composite coated steel substrate. The value of the corrosion current and corrosion potential of the steel substrate was 248.80 mA and −153 mV. After applying the composite coating to the steel substrate, the values of E_{corr} and I_{corr} were 26.76 mA and −101 mV. This means that the composite coating improves the corrosion resistance of the steel substrate.
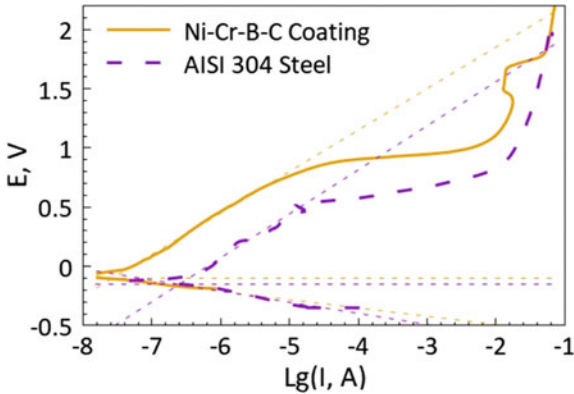
Fig. 3 Polarization curves of the steel substrate and composite coating

Table 3 Corrosion potential (E_{corr}) and corrosion current density (I_{corr}) of various materials

Material	E_{corr}, мВ	I_{corr}, мА
Steel AISI 304	−153	248.80
Coating Ni–B–Cr–C	−101	26.76

4   Conclusion

In this work, a Ni–B–Cr–C composite coating was deposited by DC magnetron sputtering of a Ni–Cr–B$_4$C cermet composite target in an Ar gaseous medium. It was found that the hardness and modulus of elasticity of the B–C–Ni–Cr composite coating were 10 GPa and 271 GPa, respectively. Tribological tests have shown that the material of the ball influences the result of friction. The composite coating showed the lowest coefficient of friction (with a corundum ball) and good wear resistance (with a steel and corundum ball) due to the balance of hardness and toughness. The wear mechanism of the composite coating with a steel ball is mainly adhesive and oxidative, and when using a corundum ball, it is mainly oxidative and abrasive.

It is found that the Ni–B–Cr–C composite coating exhibits good corrosion resistance with higher corrosion potential (−101 mV) and lower corrosion current (26.76 mA) than AISI 304 steel substrate.

References

1. Li, H., Zhang, L., Zeng, Q., Guan, K., Li, K., Ren, H., Cheng, L.: Structural, elastic and electronic properties of transition metal carbides TMC (TM= Ti, Zr, Hf and Ta) from first-principles calculations. Solid State Commun. **151**(8), 602–606 (2011). https://doi.org/10.1016/j.ssc.2011.02.005

2. Wu, F.B., Su, Y.M., Tsai, Y.Z., Duh, J.G.: Fabrication and characterization of the Ni–P–Al–W multicomponent coatings. Surf. Coat. Technol. **202**(4–7), 762–767 (2007). https://doi.org/10.1016/j.surfcoat.2007.06.070

3. Sha, C., Munroe, P., Zhou, Z., Xie, Z.: Effect of Ni content on the microstructure and mechanical behaviour of CrAlNiN coatings deposited by closed field unbalanced magnetron sputtering. Surf. Coat. Technol. **357**, 445–455 (2019). https://doi.org/10.1016/j.surfcoat.2018.10.052

4. Shakoor, R.A., Kahraman, R., Waware, U.S., Wang, Y., Gao, W.: Synthesis and properties of electrodeposited Ni–B–CeO$_2$ composite coatings. Mater. Des. **59**, 421–429 (2014). https://doi.org/10.1016/j.matdes.2014.03.024

5. Li, D., Li, B., Du, S., Zhang, W.: Synthesis of a novel Ni–B/YSZ metal-ceramic composite coating via single-step electrodeposition at different current density. Ceram. Int. **45**(18), 24884–24893 (2019). https://doi.org/10.1016/j.ceramint.2019.09.121

6. Mehr, M.S., Akbari, A., Damerchi, E.: Electrodeposited Ni-B/SiC micro-and nano-composite coatings: a comparative study. J. Alloy. Compd. **782**, 477–487 (2019). https://doi.org/10.1016/j.jallcom.2018.12.184

7. Sirota, V.V., Zaitsev, S.V., Prokhorenkov, D.S., Limarenko, M.V., Skiba, A.A., Kovaleva, M. G.: Detonation spraying of composite targets based on Ni, Cr and B$_4$C for magnetron multi-functional coating. Key Eng. Mater. **909**, 115–120 (2022) (Trans Tech Publications Ltd). https://doi.org/10.4028/p-74w31h

8. Levashov, E.A., Petrzhik, M.I., Shtansky, D.V., Kiryukhantsev-Korneev, P.V., Sheveyko, A.N., Valiev, R.Z., Smolin, A.Y.: Nanostructured titanium alloys and multicomponent bioactive films: mechanical behavior at indentation. Mater. Sci. Eng. A **570**, 51–62 (2013). https://doi.org/10.1016/j.msea.2013.01.034

9. He, D., Shang, L., Lu, Z., Zhang, G., Wang, L., Xue, Q.: Tailoring the mechanical and tribological properties of B$_4$C/aC coatings by controlling the boron carbide content. Surf. Coat. Technol. **329**, 11–18 (2017). https://doi.org/10.1016/j.surfcoat.2017.09.017

Correlation of Bitumen Emulsion Stability Factor with Aqueous Phase Parameters Evaluated at the Stage of Composition Design

M. A. Vysotskaya[1][✉] , A. V. Korotkov[2] , O. N. Voitenko[2] , and A. S. Kukin[2]

[1] Belgorod State Technological University Named After V.G. Shukhov, Belgorod, Russia
roruri@rambler.ru
[2] Gazpromneft—BM LLC, Saint Petersburg, Russia

Abstract. A fundamental factor in the proportioning of stable bitumen emulsions from a blending point of view is the choice of emulsifier and its effective concentration in the aqueous phase composition. The purpose of the work was to establish a correlation between the properties of the aqueous phase with different emulsifier content and the stability of the resulting bitumen emulsion. The indicators of surface tension of the systems and the wetting angle were taken as the criteria for evaluating the effectiveness and optimality of the emulsifier concentration in the aqueous phase. Research shows, that wetting efficiency of the aqueous phase, depending on the emulsifier concentration, correlates with the surface tension of the respective solutions. The greatest stability factor of the systems is characterized in samples of bitumen emulsions prepared in aqueous phases, previously noted as effective. The aggregative stability of bitumen emulsions is primarily associated with the flocculation and coalescence processes in the system, it is obvious that effective water-emulsifier solutions prevent these processes from initiation, maintaining the structure of the emulsions stable.

Keywords: Asphaltic emulsion · Bitumen emulsion · Emulsifier concentration · Aqueous phase · Stability

1 Introduction

A bitumen road emulsion is a complex colloidal system consisting of an immiscible dispersed phase distributed in a dispersion medium, the phase equilibrium of which is achieved through the use of emulsifiers or surfactants.

Often, bitumen emulsions are lyophobic thermodynamic (aggregatively) unstable [1] systems, which are characterized by a limited lifetime with a higher degree of interfacial tension parameters. Instability of the bitumen colloidal system manifests itself in the form of coalescence followed by sedimentation of the dispersed phase—bitumen.

It is known that surfactant acts as the regulator of the aggregative stability of emulsions [1]. In accordance with the Bancroft rule [2], in the construction of roads, the production and use of oil-in-water emulsions prevails, in which water acts as a dispersion medium, since it is a better solvent for surfactants than bitumen. Thus, purposefully

varying the nature and concentration of the emulsifier in an aqueous medium, it is possible to reduce the interfacial tension in the required range due to the adsorption of surfactant molecules at the phase boundary of the water-bitumen system and, as a result, the formation of stable bitumen emulsions.

2 Methods and Materials

In accordance with the recommendations of GOST R 58,952.1—2020, the content of bitumen in a bitumen emulsion, depending on its brand and application area, is strictly regulated and has a small variation interval. Thus, a fundamental factor in the proportioning of stable bitumen emulsions from a blending point of view is the choice of emulsifier and its effective concentration in the aqueous phase composition. It can be assumed that by revealing the correlation relationship between the characteristics of the water aqueous and the properties of emulsions prepared on its basis, it is possible to reduce the time of laboratory selections, including the operation of equipment and human resources, as well as to obtain a tool for predicting the stability of commercial bitumen emulsions.

In this regard, the purpose of the work was to establish a correlation between the properties of the aqueous phase with different emulsifier content and the stability of the resulting bitumen emulsion.

The indicators of surface tension of the systems and the wetting angle were taken as the criteria for evaluating the effectiveness and optimality of the emulsifier concentration in the aqueous phase.

Tests to study the effect of emulsifier concentration on surface tension were performed on the device "Lauda TVT 2". The principle of the method is to measure the volume of droplets when they fall from the dosing capillary. Droplet measurement accurate up to microliter provides high accuracy and reproducibility of surface or interfacial tension measurements.

Examination of the wetting angle was carried out by the "spreading droplet" method. Based on the data on the height and width of the droplet obtained experimentally, the wetting angles of the aqueous phases were calculated. Droplet images were recorded using a digital camera.

Based on the previously studied aqueous phases, bitumen emulsions were prepared and evaluated for the stability of the formed structure to determine the correlation between the characteristics of the aqueous phases and the finished emulsions.

The procedure proposed in Ref. [3] to determine the stability factor of bitumen emulsions was used as an evaluation test for emulsion stability. The meaning of the test is to determine the ratio of the amount of bitumen in the moving layer of the colloidal system before and after centrifugation. This indicator is determined using the formula:

$$\Phi = \frac{M_1}{M_2},\tag{1}$$

where M_1 is the bitumen content of the bitumen emulsion layer after centrifugation, wt%;

M_2 is the bitumen content in the initial emulsion before centrifugation, wt%;

Cationic emulsifiers manufactured by Nouryon: Redicote E-11 and Redicote EM-44 were considered as study subjects. Redicote EM-44 is a liquid emulsifier for cationic bitumen emulsions with rapid and medium break-up rate, also serves as an adhesion agent. The manufacturer recommended concentration for fast breaking systems (0.12–0.25)%, for medium breaking systems (0.25–0.6)%. Redicote E-11 is a liquid emulsifier for cationic emulsions with a slow break-up rate. Recommended concentration (0.6–1.5)%. Redicote additives are based on polyamines [4].

Also, to confirm the established dependencies, the domestic emulsifier Embit-BS produced by Selena was used. It is a liquid emulsifier for cationic bitumen emulsions.

In accordance with the statements of the manufacturer [5], on the basis of Embit-BS, varying the concentration (0.15–1.5)%, it is possible to obtain time-stable emulsions of various classes. In the work, an accent was put on obtaining an emulsion of the EBDK M class with recommendations for the emulsifier concentration (0.9–1.5)%. Derivatives of alkylpolyaminoamides and imidazolines obtained on the basis of vegetable raw materials are used as raw components in emulsifier.

BND 100/130 bitumen was used for the preparation of bitumen emulsions, with the indicators presented in Table 1.

Table 1 Bitumen property indicators

The name of the indicator	Requirements of GOST 33,133	Actual value
Needle penetration depth, 0.1 mm:		
at 25 °C	101–130	110
at 0 °C	min 30	30
Ring-and-ball softening point, °C	not lower than 45	45
Ductility, cm:		
at 25 °C	min 70	96
at 0 °C	min 4.0	5.0
Brittle temperature, °C	not higher than -20	-26
Flash point, °C	not lower than 230	246
Change in softening temperature after warming up, °C	max 7	5
Penetration index	-1.0 to $+1.0$	0.8

3 Results and Discussion

At the initial stage, aqueous phases were prepared and studied using the specified emul-sifiers in the range of concentrations recommended by manufacturers. The results are presented in Table 2.

The obtained aqueous phases were further investigated to determine the regularities of the influence of emulsifiers concentrations in their composition on the parameters of

Table 2 Aqueous phase formulations for bitumen emulsions

Type of emulsifier

REDICOTE E-11				REDICOTE EM-44				Embit–BS			
Formulation No.	Content, %		PH of the aqueous phase	Formulation No.	Content, %		PH of the aqueous phase	Formulation No.	Content, %		PH of the aqueous phase
	Emulsifier	Acid			Emulsifier	Acid			Emulsifier	Acid	
1	0.15	0.07	4.21	9	0.10	0.13	2.08	17	0.75	0.08	2.20
2	0.20	0.07	4.19	10	0.15	0.16	2.08	18	0.90	0.09	2.21
3	0.25	0.08	4.14	11	0.25	0.20	2.05	19	1.00	0.09	2.16
4	0.60	0.10	4.04	12	0.30	0.21	2.07	20	1.15	0.10	2.14
5	0.80	0.08	4.16	13	0.40	0.48	2.05	21	1.30	0.07	2.16
6	1.00	0.08	4.15	14	0.50	0.60	2.00	22	1.40	0.08	2.18
7	1.30	0.08	4.10	15	0.60	0.69	1.90	23	1.51	0.09	2.15
8	1.51	0.09	4.19	16	0.80	0.91	1.93	24	1.60	0.09	2.17

Note Formulations 1–12 and 17–24 were prepared using hydrochloric acid (HCl) Formulations 13–16—using orthophosphoric acid (H_3PO_4)

surface tension of the systems and the wetting angle, Table 3. Also, samples of bitumen emulsions were prepared using them.

Table 3 Characteristics of aqueous phases

Type of emulsifier								
REDICOTE E-11			REDICOTE EM-44			Embit–BS		
Formulation No.	Surface tension, mN/m	Wetting angle	Formulation No.	Surface tension, mN/m	Wetting angle	Formulation No.	Surface tension, mN/m	Wetting angle
Blank run	73.1	69	Blank run	73.1	69	Blank run	73.1	69
1	52.4	50	9	65.0	57	17	47.6	54
2	47.6	49	10	57.4	51	18	46.3	48
3	49.1	50	11	54.1	54	19	44.9	44
4	45.7	45	12	40.9	55	20	43.2	37
5	46.6	48	13	35.4	50	21	44.0	38
6	41.5	30	14	38.8	52	22	46.1	42
7	42.1	31	15	36.9	50	23	46.6	42
8	43.0	35	16	38.3	54	24	46.1	39

The wetting angle is a characteristic of hydrophilicity or hydrophobicity of the surface, and also serves as an adsorption characteristic that occurs when the aqueous phase and the mineral substrate contact. Such contact can be accompanied by chemical interaction of liquids and minerals, ion exchange, as well as dissolution and electrokinetic phenomena [6]. Given the importance in assessing the wetting angle of the characteristics and nature of the substrate on which the aqueous phase droplet is deposited, it was decided to use a glass plate.

The resulting data, Table 3, are consistent with the results obtained in the studies [7, 8]. As we can see, the wetting efficiency of the aqueous phase, depending on the emulsifier concentration, correlates with the surface tension of the respective solutions. Moreover, surface tension isotherms of the aqueous phase at a temperature of 20 °C demonstrate that there are ranges of surfactant concentrations for which the surface tension index reaches a small plateau, corresponding to the minimum wetting angle of the aqueous phase. In other words, by the totality of characteristics, such solutions can be called effective. According to Rebinder [9], the most universal stability factor of dispersed systems is reduced to emulsifiers, which must have both surface activity and the ability to form stable structured colloidal adsorption layers. In sum, it can be assumed that by using aqueous phases with minimal surface tension and wetting angle, stable bitumen emulsions can be obtained.

According to N.P. Peskov [10, 11], aggregative stability means the ability of a colloidal system to maintain a dispersed composition over time. To support thy proposed assumption, bitumen emulsions were selectively prepared and tested to assess the stability factor. The results are presented in Figs. 1, 2 and 3.

From the studies [3] it follows that the greater the stability factor, the more stable the emulsion is considered. As can be seen, the greatest stability factor of the systems is
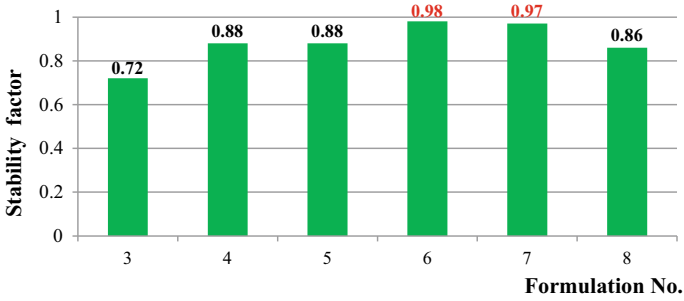
Fig. 1 Stability factor of the obtained emulsion samples (REDICOTE E-11)
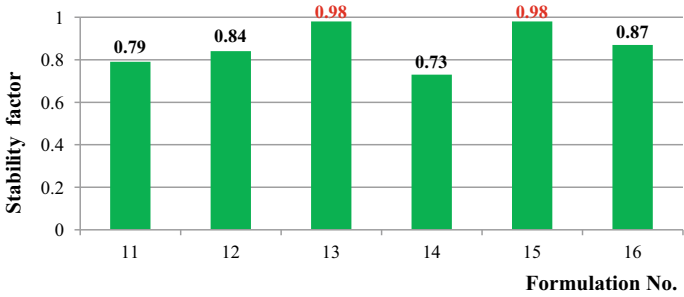

Fig. 2 Stability factor of the obtained emulsion samples (REDICOTE EM-44)
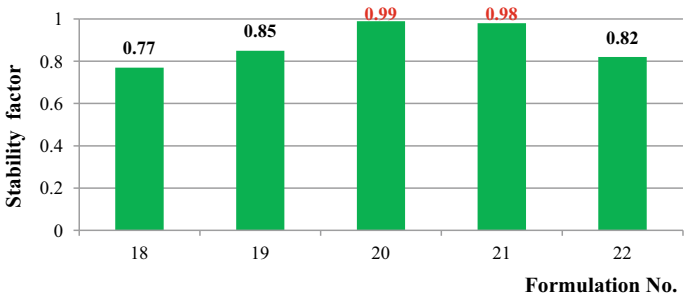

Fig. 3 Stability factor of the obtained emulsion samples (Embit–BS)

characterized in samples of bitumen emulsions prepared in aqueous phases, previously noted as effective. The aggregative stability of bitumen emulsions is primarily associated with the flocculation and coalescence processes in the system, it is obvious that effective water-emulsifier solutions prevent these processes from initiation, maintaining the structure of the emulsions stable.

4 Conclusion

Thus, the studies performed demonstrate the correlation of the stability factor of bitumen emulsions with the characteristics of the aqueous phase such as surface tension and wetting angle, as well as the possibility of predicting the stability of the compositions at the stage of their design according to express tests of the aqueous phases.

References

1. Chen, T., Ma, T., Huang, X., Ma, S., Tang, F., Wu, S.: Microstructure of synthetic composite interfaces and verification of mixing order in cold-recycled asphalt emulsion mixture. J. Clean. Prod. **263**, 121467 (2020). https://doi.org/10.1016/j.jclepro.2020.121467
2. Besnard, L., Protat, M., Malloggi, F., Daillant, J., Cousin, F., Pantoustier, N., & Perrin, P.: Breaking of the Bancroft rule for multiple emulsions stabilized by a single stimulable polymer. Soft Matter **10**(36), 7073–7087 (2014). https://doi.org/10.1039/C4SM00596A
3. Miljković, M., Radenberg, M.: Fracture behaviour of bitumen emulsion mortar mixtures. Constr. Build. Mater. **62**, 126–134 (2014). https://doi.org/10.1016/j.conbuildmat.2014.03.034
4. Keymanesh, M.R., Ziari, H., Zalnezhad, H., Zalnezhad, M.: Effects of lead time and manufacturing methods applied for polymer-modified bitumen emulsion (PMBE) on microsurfacing performance. Road Mater. Pavement Des., 1–22 (2021). https://doi.org/10.1080/14680629.2021.1963818
5. Emulsifiers for bituminous emulsions "Embit" [Electronic resource] // LLC "Selena". https://www.npfselena.ru
6. Vishal, B.: Foaming and rheological properties of aqueous solutions: an interfacial study. Rev. Chem. Eng. (2021). https://doi.org/10.1515/revce-2020-0060
7. Pal, N., Vajpayee, M., Mandal, A.: Cationic/nonionic mixed surfactants as enhanced oil recovery fluids: influence of mixed micellization and polymer association on interfacial, rheological, and rock-wetting characteristics. Energy Fuels **33**(7), 6048–6059 (2019). https://doi.org/10.1021/acs.energyfuels.9b00671
8. Vysotskaya, M.A., Korotkov, A.V.: Optimization of provide compositions bitumen emulsions, for example the cationic emulsifier. Appl. Mech. Mater. **725–726**, 517–522 (2015). https://doi.org/10.4028/www.scientific.net/AMM.725-726.517
9. Onoprienko, N.N., Salnikova, O.N.: Interconnection of intrinsic deformations and adhesive phenomena in modified disperse systems. Mater. Sci. Forum **974**, 440–445 (2019). https://doi.org/10.4028/www.scientific.net/MSF.974.440
10. Mcclements, D.J.: Critical review of techniques and methodologies for characterization of emulsion stability. Crit. Rev. Food Sci. Nutr. **47**(7), 611–649 (2007). https://doi.org/10.1080/10408390701289292
11. Fischer, P., Erni, P.: Emulsion drops in external flow fields—the role of liquid interfaces. Curr. Opin. Colloid Interface Sci. **12**(4–5), 196–205 (2007). https://doi.org/10.1016/j.cocis.2007.07.014

Electrochemical Co-deposition of Copper and Nanodispersed Tungsten Carbide on Titanium Hydride

A. I. Gorodov(✉) ⓘD, N. I. Cherkashina ⓘD, and R. V. Sidelnikov ⓘD

Belgorod State Technological University Named After V.G. Shukhov, Belgorod, Russia
gorodov-andreyy@mail.ru

Abstract. In radiation materials science, the issue of surface modification in order to improve the operational properties of materials is relevant. This manuscript describes an electrochemical method for obtaining co-deposited (alloyed) coatings from copper reinforced with nanodisperse particles of tungsten carbide, which contains carbon of the frame structure. Spherical granules of titanium hydride were used as a substrate. The advantages of this method are presented. The results of scanning electron microscopy of the obtained alloyed coatings are presented. Electrochemical co-deposition of copper and nanodispersed particles of tungsten carbide provided a simple and effective coating on the surface of spherical granules of titanium hydride, with a thickness of about $50\,\mu\mathrm{m}$. Obtaining an alloyed coating on pre-chemically modified titanium hydride granules contributes to obtaining a strong adhesive contact at the boundary between the surface of the titanium hydride sphere—an aggregate-like microrelief of hydroxytanyl—and a tungsten carbide-hardened copper shell, by increasing the contact area. This simple and effective electrochemical modification of the surface can be additionally used for various products or their individual parts. In addition to copper, nickel, cadmium, chromium or some alloys can be used as metal elements deposited by electrolytic means.

Keywords: Modifier · Neutron shielding · Titanium hydride · Surface · Scanning electron microscopy · Tungsten carbide · Co-deposition · Electroplating

1 Introduction

Currently, the nuclear industry is actively developing in the world, in particular, the development of new generation nuclear power technologies based on fast neutron reactors. In accordance with this, the issue of creating new materials that ensure the operational needs of new equipment and the protection of personnel from neutron irradiation remains relevant [1].

In works [2] show the prospects of using titanium hydride as filler in radiation-protective products. Since the operating temperature of fast neutron reactors is up to 600 °C, it is necessary to ensure the thermal stability (to reduce the thermal diffusion of hydrogen and titanium oxidation) of titanium hydride under these conditions. Therefore,

much attention is paid to the research of methods and modes of obtaining and modifying titanium hydride to obtain products resistant at high temperatures [3]. One of the main ways to increase the radiation-thermal stability of neutron-protective materials is based on strengthening their surface with dispersed particles that prevent the movement of dislocations. The function of dispersed phases can be performed by carbides, nitrides, borides and intermetallides. The method and kinetics of formation, composition and properties of hardening phases have a significant impact on the complex of physico-chemical properties of the materials being strengthened [4].

In studies [5], chemical modification of the surface of titanium hydride by an organosilicon oligomer and boric acid from aqueous solutions was reported. To fix boron-containing compounds, it is necessary to create additional adsorption centers on the surface of titanium hydride by preliminary chemical modification with an organosilicon oligomer. However, when chemically modifying the surface, it is quite difficult to accurately control the number of adsorption centers. Other modification methods are also found in the literature: catalytic alloying with amorphous or crystalline alloys based on TiCu, high-energy mechanochemical synthesis method [6], alloying by electric discharge treatment [7], by surface deposition of titanium metal by ion-plasma vacuum magnetron sputtering [8], ball milling using ultrasonic wave to improve the adhesion of epoxy resin [9]. However, these methods have some disadvantages, such as the requirement of a complex process, high cost, difficulties in controlling the degree of coverage and selective modification.

The electrochemical modification method may be a good option due to the relatively simple control of the degree of modification, the absence of the need for toxic chemicals and the possibility of selective coating on the substrate surface [10, 11].

Earlier we reported on electrochemical modification of the surface of spherical granules of titanium hydride with metallic copper [12]. Titanium hydride granules electrochemically coated with metallic copper with the Ti–O–Cu– coating demonstrated an increase in the thermal stability of the hydride phase by 236.8 °C.

In this publication, the possibility of obtaining a copper coating on spherical titanium hydride granules with inclusions of nanodispersed tungsten carbide containing carbon particles of a frame structure by electrochemical co-deposition is considered.

The prospects of the electrochemical co-deposition method for obtaining a coating lies in the high reliability and reproducibility of the results due to the possibility of regulating the electrolytic parameters, the number and size of the co-deposited particles. As a substrate, you can use finished products or their individual parts made in any form. In addition to copper, nickel, cadmium, chromium or some alloys can be used as metal elements deposited by electrolytic means. Dispersed particles will be embedded in this metal matrix.

2   Methods and Materials

The studies were carried out on unmodified and chemically modified (with the formation of hydroxotitanyl in the surface layer) spherical granules of titanium hydride with a diameter of 0.2–2.5 mm (RF Technical Conditions 162—2010). More details about the modification of spherical granules of titanium hydride with hydroxytanil are written in Refs. [12, 13].

To obtain a co-deposited (doped) coating, copper ions were electrochemically deposited on a substrate of titanium hydride granules in the presence of dispersed tungsten carbide particles. The tungsten carbide (WC) used is a black nanopowder synthesized by the method of obtaining nanoscale particles of refractory metals and their carbides from scrap of carbide products (manufacturer of the Sevastopol State University, Sevastopol, Russia). Particle sizes from 5 to 100 nm.

Electrodeposition was carried out on the IPC-Pro 3A "Potentiostat" installation in an electrolytic glass bath. The electrolytic solution consists of a 30% aqueous solution of copper sulfate ($CuSO_4 \cdot 5H_2O$), to which dispersed particles of tungsten carbide are added in an amount of 10% by weight of the solution. The solution was subjected to ultrasonic dispersion for 5–7 min. in order to break up agglomerates of tungsten carbide nanoparticles, to reduce them to the size of individual particles. In addition, it was assumed that ultrasonic dispersion for 5–7 min. it will lead to the formation of a more uniform particle distribution, which will significantly increase the hardness and wear resistance of the resulting coating. Copper plates pre-peeled from the oxide film, current density of 1.5–2 A/dm^2, electrolysis time of 10 min. were used as the anode.

In this work, periodic mechanical mixing of the solution was carried out together with ultrasonic cavitation. It is also worth noting that when obtaining a co-deposited coating, titanium hydride granules were located under the anode, so that dispersed tungsten carbide particles in the electrolytic solution settled on the surface of the fraction under the influence of gravity. This arrangement, in combination with preliminary ultrasonic dispersion of the electrolytic solution and periodic relative displacement, contributes to a more uniform introduction of dispersed tungsten carbide particles into the deposited copper metal matrix.

Titanium hydride granules with an alloyed coating were fixed in a polymer composition by the pouring method, a cut and a slot were made. The resulting sections were examined by scanning electron microscopy (SEM) with the removal of energy-dispersive X-ray spectra at different points (micro-regions). The study was carried out in BSE mode using a high-resolution scanning electron microscope TESCAN MIRA 3LMU with an integrated energy dispersive spectrometer X-MAX 50 Oxford Instruments (TESCAN ORSAY HOLDING, Czech Republic).

For thermal stability studies, the samples were subjected to heat treatment for 1.5 h at each test temperature (300, 500, 700 and 900 °C) in an air atmosphere. Since the thermal degradation of titanium hydride leads to significant changes in the chemical and phase compositions of the surface layers, after cooling the samples, their microstructure was analyzed by electron probe microscopy and the oxygen content in the surface and deep layers was determined.

3 Results and Discussion

As a result of electrochemical co-deposition on the surface of unmodified titanium hydride granules, an alloyed coating was obtained, the data obtained using the TESCAN MIRA 3LMU electron microscope are shown in Fig. 1.

The analysis of the microstructure of the slot of an unmodified titanium hydride granule with an alloyed coating (Fig. 1) showed that the titanium hydride granule is coated
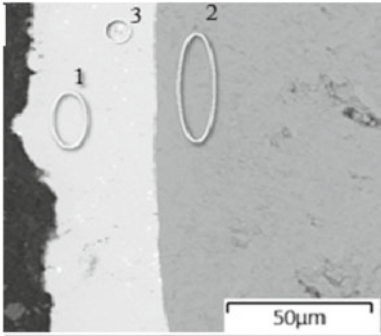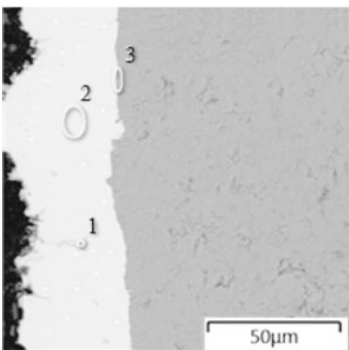
The elemental composition of the studied points

Elements	The content of elements at different points, mass %		
	Point 1	Point 2	Point 3
Cu	99.5	0.0	61.5
O	0.4	8.5	21.0
Ti	0.1	91.5	17.5
W	0.0	0.0	0.0

a)   b)

Fig. 1 Micrograph of a strip of unmodified titanium hydride granules with an alloyed coating (**a**) and the elemental composition of the studied points (**b**)

with a copper shell <50 μm thick, in which tungsten carbide particles are embedded (presence of light dots). It is worth noting that tungsten carbide particles are practically not collected into agglomerates, but are distributed evenly. Dispersed particles of tungsten carbide are located throughout the entire volume of the copper coating, including directly near the surface of titanium hydride.

The results of microstructural analysis of the surface of the doped layer of titanium hydride granules previously chemically modified to form hydroxotitanyl in the surface layer indicate the formation of a copper coating with a thickness of about 50 μm during electrodeposition, in which tungsten carbide particles are evenly distributed (Fig. 2). A feature characteristic of pre–chemically modified titanium hydride granules is the presence of an aggregate–like microrelief of hydroxytanyl at the boundary between the surface of the titanium hydride sphere and the alloyed shell.

The elemental composition of the studied points

Elements	The content of elements at different points, mass %		
	Point 1	Point 2	Point 3
Cu	10.1	99.0	21.1
O	1.7	0.8	9.2
Ti	1.2	0.2	69.3
W	87.1	0.0	0.4

a)   b)

Fig. 2 Micrograph of a strip of a pre-chemically modified titanium hydride granule with an alloyed coating (**a**) and the elemental composition of the studied points (**b**)

The thermal stability of titanium hydride granules with electrochemically applied coating containing embedded particles of nanodispersed tungsten carbide has been investigated, the results are shown in Figs. 3, 4, 5 and 6.
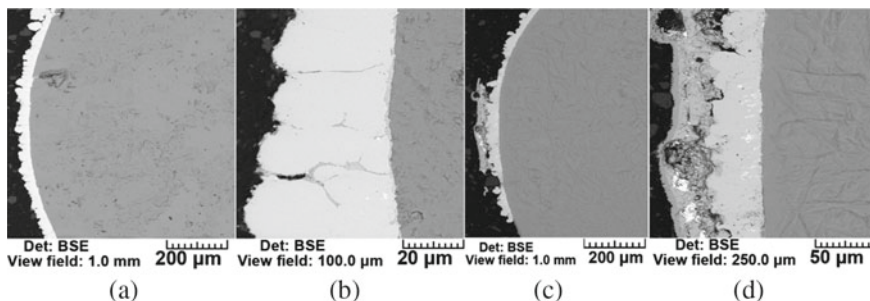

Det: BSE
View field: 1.0 mm 200 µm   Det: BSE
View field: 100.0 µm 20 µm   Det: BSE
View field: 1.0 mm 200 µm   Det: BSE
View field: 250.0 µm 50 µm

(a)   (b)   (c)   (d)

Fig. 3 Micrographs of samples of titanium hydride granules with an alloyed coating after heat treatment for 1.5 h at temperatures of 300 (**a–b**) and 900 °C (**c–d**)
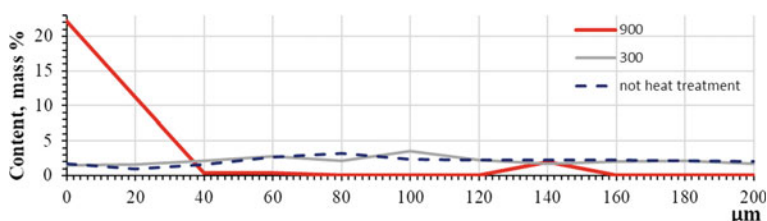
Fig. 4 Distribution profiles of oxygen atoms in samples of titanium hydride granules with an alloyed coating without heat treatment and heat treated at temperatures of 300 and 900 °C
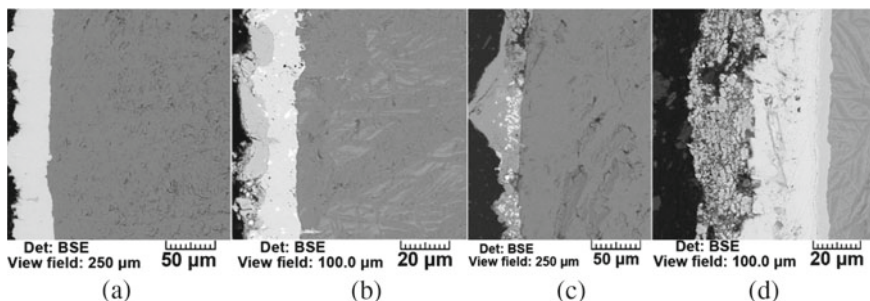

Det: BSE
View field: 250 µm 50 µm   Det: BSE
View field: 100.0 µm 20 µm   Det: BSE
View field: 250 µm 50 µm   Det: BSE
View field: 100.0 µm 20 µm

(a)   (b)   (c)   (d)

Fig. 5 Micrographs of samples of pre-chemically modified titanium hydride granules with an alloyed coating after heat treatment at temperatures of 300 (**a**), 500 (**b**), 700 (**c**) and 900 °C (**d**)

On microphotographs of titanium hydride grinds with an electrochemical coating applied already at 300 °C, the formation of darkened areas is observed, this is especially pronounced in the copper matrix of the alloyed coating (Fig. 3a, b). The presence of inhomogeneity's is probably due to the oxygen content at the grain boundaries. As a
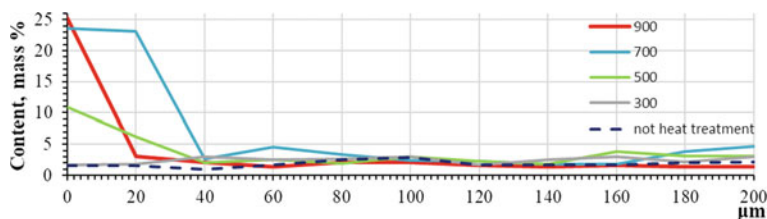
Fig. 6 Distribution profiles of oxygen atoms in samples of pre-chemically modified titanium hydride granules with an alloyed coating without heat treatment (**a**) and heat-treated at temperatures of 300, 500, 700 and 900 °C

result of heat treatment at 900 °C, an alloyed layer consisting of copper and dispersed particles of tungsten carbide is destroyed on the surface of titanium hydride granules, becomes loose, and torn areas are formed (Fig. 3 c, d).

The average oxygen concentration from the surface to a depth of 200 microns, both in non-thermally treated titanium hydride fraction (Fig. 4) and in heat-treated at 300 °C, is almost constant. An increase in the annealing temperature to 900 °C leads to a significant increase in the average oxygen concentration to 22 wt.% in the near-surface layer and a shift of the profile to the left. With increasing distance from the surface to a depth of 40 microns, the oxygen content decreases, after which it practically does not change to 200 microns. It can be assumed that an increase in the average oxygen concentration in the near-surface layer occurs due to the formation of CuO and Cu_2O oxides.

Figures 5 and 6 shows the results of thermal stability studies of samples of pre-chemically modified titanium hydride granules with an electrochemical coating applied. The microstructure of a pre-chemically modified titanium hydride fraction heat-treated at 300 °C (Fig. 5) has a similar character to the unmodified fraction described above under similar conditions. An increase in the temperature of heat treatment to 500 °C leads to an increase in the oxygen concentration in the near-surface layer to 11 mass % (Fig. 6), which is also visible on the micrograph (Fig. 5b) to increase the area of areas of heterogeneous areas.

With a further increase in the temperature of heat treatment, there is a gradual increase in the average oxygen concentration in the near-surface layer to 23 mass % at T = 700 °C and 25 mass % at T = 900 °C. It is worth noting that as the oxidation of the copper surface increases, the layer becomes loose, its thickness increases, which contributes to its destruction (Fig. 5b–d). In addition, at a temperature of T = 700 °C, as a result of hydrogen diffusion to the surface, voids begin to form between the surface of titanium hydride granules and the alloyed coating. After processing at a temperature of 900 °C, the structure of the alloyed coating can be divided into two zones: the upper one, with a thickness of 10…20 μm with a loose texture and the bottom, up to 30 μm thick with a layered texture. There is no great internal destruction.

4 Conclusion

To create a protective layer on spherical granules of titanium hydride to improve its operational properties, we have developed and demonstrated a simple and effective method of electrochemical co-deposition of metallic copper and tungsten carbide. Tungsten carbide particles are embedded in a layer of metallic copper by capturing them during electrochemical deposition. Micrographs of the grinds of modified titanium hydride granules indicate the formation of a copper coating with a thickness of about 50 μm, in which tungsten carbide particles are evenly distributed. We believe that this simple and effective electrochemical method of modifying the surface of titanium hydride granules can benefit radiation materials science and can be used in various fields of application.

References

1. Matyukhin, P.V.: The choice of iron-containing filling for composite radioprotective material. Paper presented at the IOP conference series: materials science and engineering, vol. 327, no. 3, p. 032036 (2018). https://doi.org/10.1088/1757-899X/327/3/032036
2. Cherkashina, N.I., Gavrish, V., Chayka, T.: Experiment—calculated investigation of composite materials for protection against radiation. Mater. Today Proc. (2019)
3. Chirico, C., Tsipas, S.A., Wilczynski, P., Gordo, E.: Beta titanium alloys produced from titanium hydride: effect of alloying elements on titanium hydride decomposition. Metals **10**(5) (2020). https://doi.org/10.3390/met10050682
4. Yastrebinskii, R.N.: Attenuation of neutron and gamma radiation by a composite material based on modified titanium hydride with a varied boron content. Russ. Phys. J. **60**, 2164–2168 (2018)
5. Pavlenko, V.I., Bondarenko, G.G., Kuprieva, O.V., Yastrebinskii, R.N., Cherkashina, N.I.: Modification of titanium hydride surface with sodium borosilicate. Inorg. Mater. Appl. Res. **5**(5), 494–497 (2014)
6. Zhou, C., Bowman, R.C., Fang, Z.Z., Lu, J., Xu, L., Sun, P., Liu, H., Wu, H., Liu, Y.: Amorphous TiCu-based additives for improving hydrogen storage properties of magnesium hydride. ACS Appl. Mater. Interfaces. **11**(42), 38868–38879 (2019)
7. Devgan, S., Sidhu, S.S.: Surface modification of β-type titanium with multi-walled CNTs/μ-HAp powder mixed electro discharge treatment process. Mater. Chem. Phys. **239** (2020). https://doi.org/10.1016/j.matchemphys.2019.122005
8. Pavlenko, V.I., Cherkashina, N.I., Yastrebinsky, R.N., Demchenko, O.V.: On enhancing the thermal stability of metal hydrides by ion–plasma vacuum magnetron sputtering. J. Surf. Invest. **11**(1), 254–258 (2017)
9. Chen, D., Zhang, Q., Ning, R., Bian, Z., Dai, H., Zhang, C.: Surface modification of titanium hydride with epoxy resin by ultrasonic wave-assisted ball milling. High Perform. Polym. **28**(3), 281–287 (2016). https://doi.org/10.1177/0954008315578465
10. Braem, A., Mattheys, T., Neirinck, B., Schrooten, J., Van Der Biest, O., Vleugels, J.: Porous titanium coatings through electrophoretic deposition of TiH$_2$ suspensions. Adv. Eng. Mater. **13**(6), 509–515 (2011)

11. Kulak, A.I., Kokorin, A.I., Sviridov, D.V.: Electrolyte electroreflectance study of TiO$_2$ films modified with metal nanoparticles. J. Mater. Res. **16**(8), 2357–2361 (2001)
12. Pavlenko, V.I., Gorodov, A.I., Yastrebinsky, R.N., Cherkashina, N.I., Karnauhov, A.A.: Increasing the adherence of metallic copper to the surface of titanium hydride. ChemEngineering **5**, 72 (2021). https://doi.org/10.3390/chemengineering5040072
13. Gorodov, A.I., Yastrebinsky, R.N., Karnauhov, A.A., Yastrebinskaya, A.V.: Regulation of the surface microrelief of titanium hydride by solutions of sulfuric acid salts. Environmental and Construction Engineering: Reality and the Future, Lecture Notes in Civil Engineering, vol. 160 (2021). https://doi.org/10.1007/978-3-030-75182-1_8

Light-Colored Ceramic Products from Red-Burning Clay Raw Materials

A. A. Naumov[(⊠)] and I. V. Maltseva

Don State Technical University, Rostov-on-Don, Russia
alexej_naumov@list.ru

Abstract. This article reveals the results of the conducted research on the production of ceramic products of light shades based on red-burning clay raw materials of the Doroganovskoye deposit. Based on the analysis of literary sources, it was found that the most common way to lighten a ceramic shard is the introduction of dispersed chalk into the mass. During the research, chalk was introduced into the composition of the mass in an amount of 10–30%. However, this led to a decrease in strength and an increase in water absorption in burnt products. In order to obtain light-colored ceramic products with high physical and mechanical properties, a modifying additive was additionally introduced into the composition of the masses, in addition to chalk. It was determined that this additive makes it possible to intensify the firing processes and makes it possible to obtain light-colored samples with a lower content of carbonate-containing material in the charge. X-ray phase studies have established that the mineralizing effect of this additive occurs due to its sufficiently low melting point. Due to this, the dark-colored mineral hematite is involved in the formation of new minerals characterized by low-intensity coloring, which ensures the production of light yellow samples. In addition, an increased content of anorthite and helenite is formed in the shard, which leads to an increase in the strength of the samples. Thus, laboratory studies have shown that it is possible to obtain light-colored ceramic products from the red-burning clay raw materials of the Doroganovskoye deposit by semi-dry pressing. The optimal composition of the ceramic mass and the production parameters for this are as follows: the amount of chalk in the mass should be 20%, the content of the mineralizing additive should be 1%, the preparation of the press powder should be carried out with preliminary plastic processing of the mass, the specific pressure of pressing samples is 20 MPa, the firing temperature is 1000 °C. This will make it possible to obtain burnt samples of light yellow color with a compressive strength of 36.1 MPa and a water absorption of 14.6%.

Keywords: Facing brick · Volumetric coloring · Modifying fdditive · Semi-dry pressing

1 Introduction

Trends in the modern market economy stimulate the constant upgrade of the range of manufactured products. In production of facial brick technology this task is often solved by changing the surface coloring of the bricks [1–3].

The coloring of bricks usually varies in red-brown tones, and the reserves of light-burning clay raw materials that used for the production of sanitary, household ceramics, and facing tiles are very limited. In this regard, obtaining light-colored ceramic bricks from common red-burning raw materials is an urgent task, and one of the ways to achieve this is volumetric lightening of ceramic tiles [4, 5].

Carbonate-containing materials—obtained from natural sources or various production wastes are usually introduced to lighten ceramics [6–8]. Additives of calcium and magnesium carbonates in the form of chalk, dolomite, marble and limestone are specially introduced into the composition of the masses to regulate technological and post-firing properties of the ceramic tiles.

The purpose of this study is to determine the lightening effect of finely dispersed chalk, together with a modifying additive on the color of a ceramic tiles made from red-burning clay raw materials.

2 Methods and Materials

When conducting research, low-melting clay raw materials from the Doroganovskoye deposit (Rostov region) were used as the main raw material. Clay from this deposit by its properties, is a fairly typical raw material for the southern Russia—it belongs to non-baking, moderately plastic, with high sensitivity to drying and giving a red-colored tiles during firing.

In order to lighten the ceramic tiles, finely dispersed chalk from the Belgorod deposit was used.

The samples were made by plastic molding and semi-dry pressing. By the method of plastic molding, samples-bricks were made in size 60 * 30 * 15 mm, while the raw materials was crushed until it completely passed through a 1 mm sieve and thoroughly mixed. The samples were fired in a laboratory electric kiln at a maximum temperature of 1000 °C.

Cylindrical samples with a diameter and height of 50 mm were made by semi-dry pressing with preliminary plastic processing of the mass. The initial raw materials were ground to sizes less than 1 mm, thoroughly mixed and moistened with water or a prepared solution of a modifying additive until plastic state, then the mass was passed through a laboratory granulator, dried to a moisture content of 9–10%, and to obtain a press-powder, the resulting granules were ground to sizes less than 3 mm. Cylindrical samples were pressed at a specific pressure of 20 MPa and burnt at a maximum temperature of 1000 °C.

The crystalline compounds in the ceramic shard were studied by X-ray phase analysis using a diffractometer.

3 Results and Discussion

To determine the possibility of lightening of the ceramic tiles, finely dispersed chalk was introduced into the composition of the clay masses based on clay raw materials from the Doroganovskoye deposit in the amount of 10, 20 and 30%. From them, as well as from pure clay raw materials, samples-bricks were made by the plastic molding method.

The results of the study on the effect of chalk content in the mixture on the characteristics of dried and fired samples are presented in Table 1.

Table 1 The composition of the mixtures and the characteristics of the fired samples of plastic molding

Code of samples	Charge composition by weight, %		Air shrinkage, %	Total shrinkage, %	Water absorption, %	Average density, kg/m3	Color of tiles
	Clay material	Chalk					
B 1–1	100	–	4.36	6.67	13.5	1832	Red
B 2–2	90	10	4.21	8.17	14.4	1839	Light-red
B 3–3	80	20	3.43	7.44	15.0	1799	Light-pink
B 4–4	70	30	3.16	5.67	23.6	1555	Light-yellow

It can be noted that the addition of chalk reduces air shrinkage of samples, while water absorption of fired samples increases from 13.5 to 23.6% and the average density of samples decreases from 1832 to 1555 kg/m3.

Figure 1 shows the dependence of the color of fired samples on the amount of chalk addition.

At a firing temperature of 1000 °C, the lightening effect of chalk is already manifested at its 10% presence in the mixture, which indicates the beginning of the formation of minerals that "lighten" the tiles. Significant lightening of fired tiles occurs in the presence of 20% of chalk. The color of the samples is light-pink. When the mixture contains 30% chalk, the color of the samples is light-yellow—almost white.

As the results of experiments showed, obtaining light-yellow color tiles is possible only by adding chalk in the amount of 30%, but in this case the water absorption of the samples increases sharply, which will not allow obtaining products corresponding to the front ones.

In further experiments, the effect of additives on the characteristics of cylindrical samples made by the semi-dry pressing method was determined.

Chalk and NaCl—a modifying additive in an amount of 1% were introduced into the clay mass [9].

This paper describes the technology of brick production using low-melting clays, which are fired at temperatures up to 1000 °C. As a result, a polymineral structure of ceramic stone in the form of crystalline (β-quartz, hematite) and X-ray amorphous (metakaolinite, glass-phase) phases is formed. Lightening of the brick color occurs only under conditions of oxidative firing when the mixture contains at least 15–20% $CaCO_3$ and a mineralizing additive. To lighten the bricks, the authors add chalk in an amount of 10 to 20% into the composition of the mixture, and NaCl is introduced as a modifying additive in an amount of 0.5 to 2%.
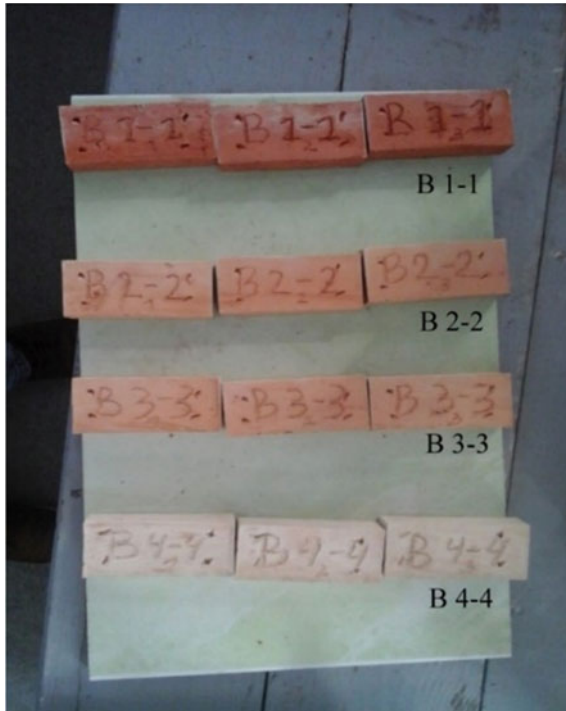
Fig. 1 The dependence of the color of fired samples on the amount of chalk additive

In order to determine the optimal content of chalk in the mixture for obtain products with the stated technical characteristics, it is necessary to determine the effect of chalk on water absorption, average density and change in the tone of the fired bricks.

To determine the possibility of lightening the ceramic tiles, finely dispersed chalk was introduced into the composition of clay masses in the amount of 10, 20 and 30%. Cylindrical samples were made by the method of semi-dry pressing with preliminary plastic processing of the mass.

Table 2 presented the physical and mechanical characteristics of semi-dry pressed cylindrical samples burnt at a temperature of 1000 °C.

Figure 2 shows the dependence of the color of the burnt samples on the amount of chalk additive with a modifier. Code of samples correspond to Table 2.

The results obtained show that the amount of addition of chalk affects the color of the fired brick tiles. With increasing the content of chalk, the lightening effect of chalk manifests itself already at its 10% presence in the mixture, indicating the beginning of the formation of minerals that "lighten" the brick tiles. Significant lightening of fired tiles occurs in the presence of 20% chalk and significantly changes its shade to light-yellow color. With a chalk content of 30% the samples acquired a lighter (almost white) tone.

From data in the Table 2, it is possible to identify that the optimal quantity of chalk is 20% with additional introduction of modifying additive. It can be seen that the fired

Table 2 Physical and mechanical characteristics of semi-dry pressing cylindrical samples

Code of samples	The composition of the mixture by weight, %			Air shrinkage, %	Total shrinkage, %	Water absorption, %	Strength, MPa	Color
	Clay raw materials	Chalk	NaCl					
C 0–0	100	–	–	2.15	3.95	13.7	42.5	Red
C 20–0	80	20	–	2.04	2.64	15.1	34.6	Light-pink
C 10–1	89	10	1	2.10	3.30	14.1	40.9	Light-pink
C 20–1	79	20	1	2.04	2.94	14.6	36.1	Light-yellow
C 30–1	69	30	1	1.92	2.52	24.9	28.8	Light-yellow
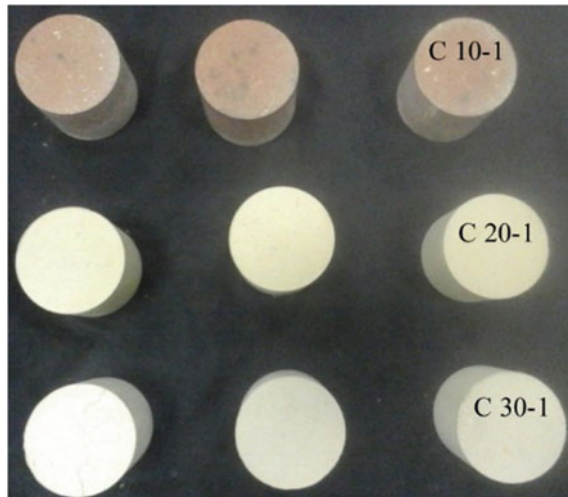
Fig. 2 The dependence of the color of burnt samples on the amount of chalk additive with modifier

samples have a stable light-yellow color, their strength in compression is 36.1 MPa, and water absorption is 14.6%.

Figure 3 shows photos of burnt semi-dry pressed samples with chalk content of 20% and NaCl modifier in an amount of 1%.

It should also be noted that fired cylindrical specimens containing 20% chalk and 1% NaCl as modifying additive were tested for capillary suction to determine the presence of water-soluble salts in the tiles. After testing, no salt deposits were observed on the faces of the samples.

Figures 4 and 5 show X-ray patterns of samples fired at a temperature of 1000 °C, molded by semi-dry pressing based on clay from the Doroganovskoye deposit with the addition of chalk in an amount of 20% and the same, but with the addition of 1% NaCl (Fig. 5).

As it can be seen from the X-ray pattern of the brick specimens, which contains only clay raw materials and chalk, several minerals such as quartz, hematite, anorthite, and
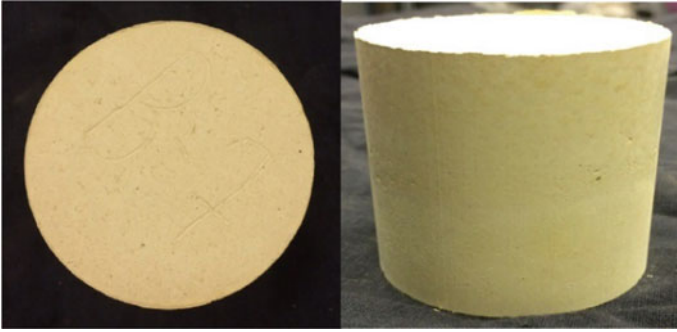
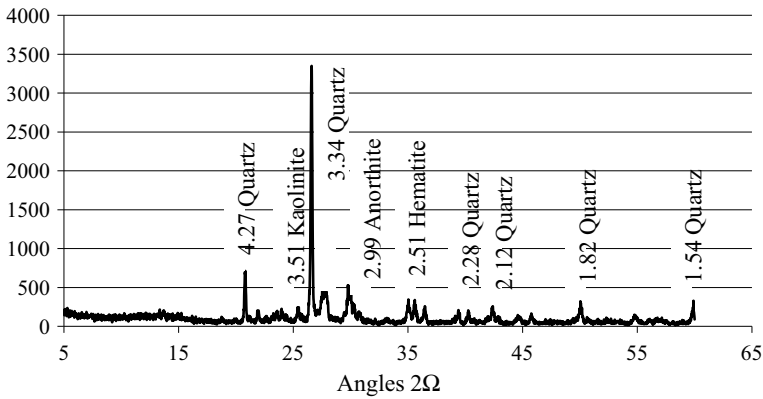**Fig. 3** Cylindrical samples of semi-dry pressing

Fig. 4 X-ray patterns of burnt samples with the addition of chalk

gehlenite are identified in its composition. The figure characterizing the brick specimen with chalk and modifier additive shows the mineralogical composition almost equivalent to the first sample. The introduction of NaCl into the mixture contributes only to a slight increase in the content of anorthite and gehlenite.

The conducted X-ray phase studies have established that the mineralizing effect of the NaCl additive occurs due to its sufficiently low melting point. Due to this, the dark-colored mineral hematite (Fe_2O_3) is involved in the formation of new minerals characterized by a low-intensity coloring, and an increased content of anorthite ($CaO \cdot Al_2O_3 \cdot 2SiO_2$) is also formed in the tiles, which ensures the production of light-yellow samples.

In the study [9], the authors indicate that a decrease in the color intensity of a ceramic tiles occurs as a result of the formation of anorthite, which depends on the content of Fe_2O_3 embedded into its structure. The intensity of anorthite crystallization is due to the presence of a significant amount of the melt, the formation of which occurs as a result of the action of the mineralizing additive NaCl, which ensures the formation of CaO at lower temperatures. An increase in the amount of the liquid phase and the presence of metakaolinite and CaO in the mass contributes to the crystallization of anorthite, in
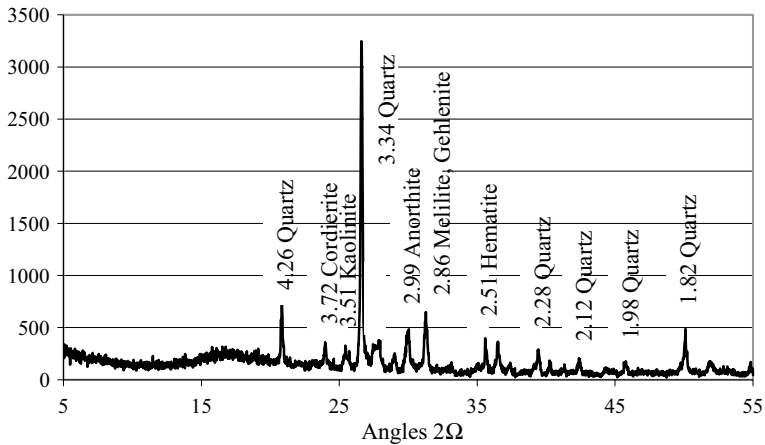
Fig. 5 X-ray patterns of burnt samples with the addition of chalk and NaCl

which iron oxides and other iron-containing compounds are dissolved, and the ceramic tile is clarified.

The effectiveness of NaCl additives can be explained in terms of the melting temperature [9, 10]. Thus, the melting point of NaCl is 800 °C. Crystallization processes occur in a completely different way when NaCl is added. The presence of metakaolinite, CaO, Fe_2O_3 and mineralizing additive NaCl in the mass ensures the formation of new phases at a lower temperature of 800–850 °C: $2NaCl + Al_2O_3 \cdot 2SiO_2 + Fe_2O_3 + 2CaO = CaO \cdot Al_2O_3 \cdot 2SiO_2 + CaCl_2 + 2NaFeO_2$. The quantity of low-melting compounds $CaCl_2$ and $NaFeO_2$ formed at the time of anorthite formation, melts and contributes to an increase in the anorthite content. This process causes the dissolution of iron oxide and the formation of other iron-containing compounds, and the lightening of the ceramic tiles.

4 Conclusions

Thus, the research revealed the following:

– the possibility of obtaining light-colored ceramic products based on clays of the Doroganovskoye deposit and finely dispersed chalk with a modifying additive has been proved. With a chalk content of 20% and NaCl modifier—1%, a light-yellow shard is obtained;
– regularities of the influence of the amount of addition of finely dispersed chalk on the properties of fired ceramic tiles based on clay raw materials from the Doroganovskoye deposit were established. The dependence of the main technical characteristics on the amount of the introduced additive is shown;
– the modifying effect of the NaCl additive on the ceramic tiles was revealed.

During the laboratory researches, we found that for the manufacturing of products with the necessary technical characteristics, the amount of chalk additive should be

20%, and the content of NaCl mineral additive should be 1%. The following optimal parameters for the semi-dry pressing method were also determined: the required press-powder fraction is less than 3 mm, the press powder moisture content is 9–10%, the pressing pressure is 20 MPa, and the maximum firing temperature is 1000 °C. This made it possible to obtain fired samples by the semi-dry pressing method of light-yellow color with a compressive strength of 36.1 MPa and water absorption of 14.6%. Based on the strength of laboratory samples, when manufacturing products of a standard size using a similar technology, it will be possible to obtain a facial brick of light-yellow color of grades M125, M150.

The conducted studies have shown the possibility of involving clay raw materials from the Doroganovskoye deposit for the production of light-yellow ceramic products that meet the requirements of current standards.

References

1. Valanciene, V., Siauciunas, R., Baltusnikaite, J.: The influence of mineralogical composition on the colour of clay body. J. Eur. Ceram. Soc. **30**, 1609–1617 (2010). https://doi.org/10.1016/j.jeurceramsoc.2010.01.017
2. Akst, D.V., Stolboushkin, A.Y., Fomina, O.A.: Calculation of the composition of granular charges for decorative wall ceramics. Constr. Mater. **12**, 25–33 (2020)
3. Pishch, I.V., Maslennikova, G.N., Gvozdeva, N.A., Klimosh, Yu.A., Baranovskaya, E.I.: Methods for ceramic bricks staining. Glass Ceram. **8**, 15–18 (2007)
4. Maslennikova, G.N., Pishch, I.V.: Ceramic pigments. Moscow: Stroymaterialy **224** (2009)
5. Bogdanov, A.N., Abdrakhmanova, L.A., Gordeev, A.S.: Evaluation of the effectiveness of a carbonate-containing additive in clay raw materials for the facial ceramics creating. Bull. KazGASU **2**(24), 215–220 (2013)
6. Maltseva, I., Kurilova, S., Naumov, A.: Utilization of waste from thermal power plants in high performance materials' production. Mater. Sci. Forum **1011**, 109–115 (2020)
7. Storozhenko, G., Stolboushkin, A.: Ceramic bricks from indusrial waste. Ceramic & Sakhteman. Seasonal Mag. Ceram. Build. **5**, 2–6 (2010)
8. Naumov, A., Mal'tseva, I., Kurilova, S.: Increase in frost resistance of a ceramic brick from clay raw materials of the Atyukhtinsky field. IOP Conference Series: Materials Science and Engineering: 21, Construction—The Formation of Living Environment. Institute of Physics Publishing, Moscow, 032003 (2018)
9. Yatsenko, N.D., Zubekhin, A.P.: Scientific basis of innovative technologies of ceramic bricks and its properties management, depending on the chemical and mineralogical composition of raw materials. Constr. Mater. **4**, 28–31 (2014)
10. Golovanova, S.P., Zubekhin, A.P., Likhota, O.V.: Whitening and intensification of ceramic sintering using iron-containing clays. Glass Ceram. **12**, 9–11 (2004)

On the Effect of Operating Conditions on the Coupling of Non-metallic External Reinforcement with Reinforced Concrete Structure

S. I. Merkulov[1(✉)] , S. M. Esipov[2] , N. V. Solodov[2] , and D. V. Esipova[2]

[1] Kursk State University, Kursk, Russia
sk31.sm@gmail.com
[2] Belgorod State Technological University V. G. Shukhov, Belgorod, Russia

Abstract. The reliability of reinforced concrete structure by external reinforcement with composite materials is ensured by the joint work of the reinforcement element and the main reinforced structure. The current standards do not contain provisions for the experimental evaluation of the adhesion of external composite reinforcement with concrete. The provisions on the design of reinforcement of reinforced concrete structures with external composite reinforcement do not take into account shear deformations in the contact seam, adhesion of composite material with concrete it is indirectly estimated by the introduction of the coefficient of the working conditions of the composite material when assigning its design resistance. A method of experimental evaluation of the adhesion of external composite non-metallic reinforcement with concrete is proposed, the patterns of deformation of composite reinforcement elements are revealed, the nature of the destruction of the adhesive joint of the adhesive joint of the composite material with concrete is established.

Keywords: External reinforcement · Carbon fiber · Composite material · Load

1 Introduction

When performing reinforcement by external reinforcement with composite materials, it is necessary to ensure the joint operation of the reinforcement element and the main reinforced structure. Reinforced reinforced concrete structure is a complex system in which an elastic reinforcement element is combined with a reinforced concrete structure by an adhesive composition with inelastic properties [1, 2]. Modern calculation methods do not take into account shear deformations in the contact seam, the adhesion of the composite material to concrete is indirectly estimated by introducing a coefficient of the working conditions of the composite material when assigning its design resistance [3]. Currently, there are no experimentally substantiated theoretical methods for assessing the adhesion of external composite reinforcement to concrete.

Current the standards do not contain provisions for the experimental evaluation of the adhesion of external composite reinforcement with concrete. When determining the

strength and deformative characteristics of composite materials (rod fittings, tapes, canvases) according to normative methods, the condition of fixing samples in the test facility has a significant impact on the results [4–6], which requires the use of special devices at the ends of the tested samples. Studies of the adhesion of composite reinforcement with concrete are carried out on concrete samples to which composite tapes are glued. The sample is rigidly fixed in the test rig, and a tensile force is applied in stages to the free end of the tape through a gripping device [7]. With this test method, the disadvantages associated with the use of gripping devices remain. Namely, a torque appears in the cross sections of the element, causing normal stresses in the adhesive seam, which is almost not found in real conditions. Also, an unrealistic picture of reinforcement, without end rods and framing, and sometimes even without rod reinforcement, negatively affects the receipt of adequate data on the distribution of tangential stresses. The task that the authors faced in this study was to develop a correct model of the test sample to determine the deformability and strength of the adhesive joint of non-metallic reinforcement with concrete, as well as to obtain data on the effective anchorage length, the excess of which does not cause an increase in the bearing capacity of the entire joint.

2   Methods and Materials

In order to obtain data on the strength and rigidity of the composite-concrete contact zone, 4 prototypes were tested, the design and layout of the measuring equipment of which is shown in Fig. 1.

The samples were tested in 2 series: OK-1 and OK-2. The OK-1 series includes samples OK-1–1 and OK-1–2: OK-1–1 has a rough surface in accordance with the operating conditions in which the design worked; OK-1–2 has a cleaned and leveled surface with more regular planes. The OK-2 series includes samples OK-2–1 and OK-2–2: OK-2–1 has a rough surface in accordance with the operating conditions in which the design worked; OK-2–2 has a cleaned and leveled surface with more regular planes.

All samples were loaded stepwise to destruction by two equal concentrated forces, being in the test bench according to the principle of three-point loading. The magnitude of the loading stage was 1.23 kN. The exposure time at each stage was 10 min. The prototypes were equipped with a system of strain gauges, group No. 1 of which (T1, T2, T3, T4) were glued to the concrete of the stretched zone under the adhesive seam, and group No. 2 (T5, T6, T7, T8)—to the composite material. The sensors were glued in such a way that the sensors of group No. 1 measured deformations only of concrete and their readings were not affected by deformations of glue and composite. This was achieved by supplying the sensors of group No. 1 with a protective film. Load cells of group No. 1 had a measurement base of 80 mm, groups No. 2–20 mm. The load cell readings were recorded using a device and two multi-channel adapters. Sensors located on concrete were connected to adapter No. 1, sensors located on composite material were connected to adapter No. 2. The prototypes of the OK-1 series were equipped with two mechanical strain gauges (I1, I2) so that I1 measured the absolute deformations of the blocks relative to each other, and I2 measured the deformations of the composite material on an identical measurement base. Taking into account the difference in absolute deformations in the form of readings I1 and I2 allowed us to correct the values of the
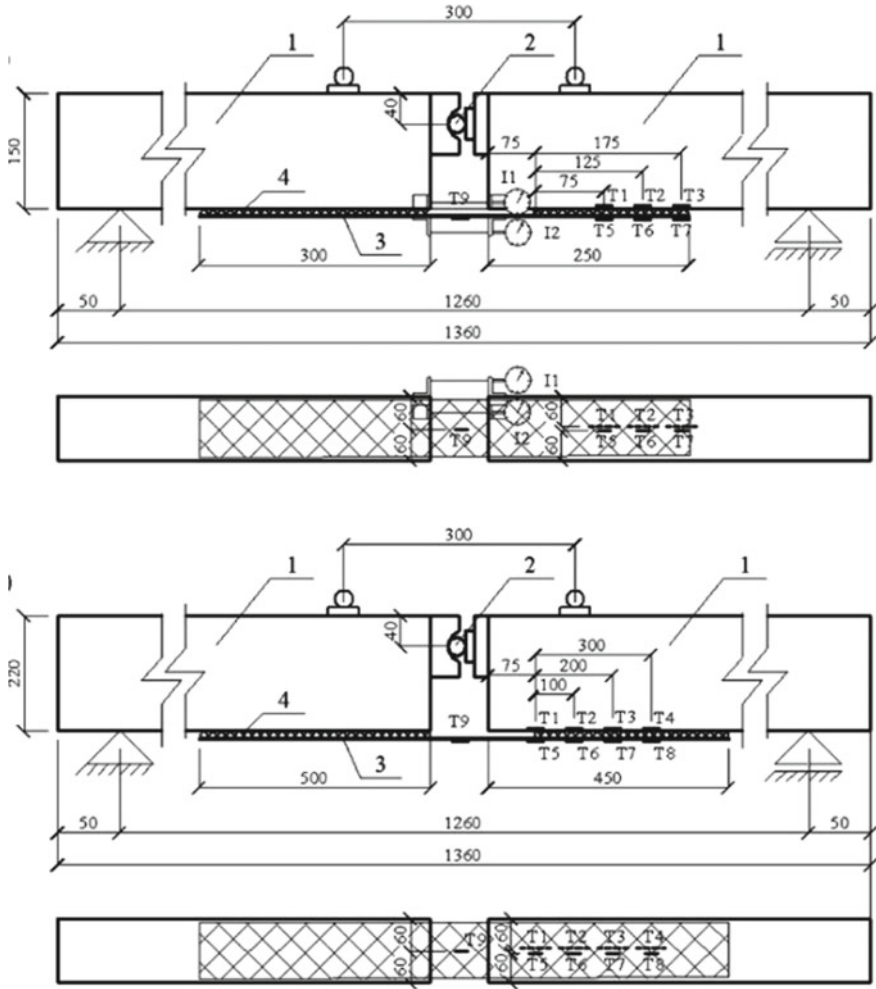
Fig. 1 Sample for separation tests of the OK-1 (above) and OK-2 (below) series: *1—beam; 2—hinge; 3—composite material; 4—glue*

difference in deformations and register the beginning of detachment of the composite from concrete (in cases of its occurrence).

The beams of all series were loaded with a short-term load until destruction. The three-point accepted calculation scheme allows you to create a clean bending zone between the concentrated forces for a more correct analysis of the VAT of the sample.

Loading using hydraulic jacks was chosen as the loading method, because it provides the possibility of applying loads of high values (up to 300 kN), allows you to determine the magnitude of the applied load with high accuracy, and also, unlike the gravitational type of loading method, to take readings of measuring instruments and monitor the work of samples under load without being distracted for loading the stand with piece loads. With this in mind, a test bench was designed and manufactured. The stand is

designed taking into account the placement of measuring instruments and samples, the possibility of conducting both long-term and short-term tests. According to preliminary calculations, the design of the stand and the cross-sections of its elements ensure its sufficient strength, rigidity and stability for the experiment. Deformations of the elements of the stand in the conditions of this experiment are negligible. The main parts of the stand are made of C285 steel.

Loading of the samples occurred by increasing the oil pressure in the pistons of the jacks, which caused the extension of their rods. The distributing traverses uniformly transmitted the load to the sample in the form of two concentrated forces located at a distance of 300 mm from each other symmetrically relative to the ends of the beam.

The concentrated loads of the beam were transmitted through metal plates. Loading was carried out stepwise. At the stages preceding the destruction and the moment of cracking, the magnitude of the stage decreased, which allowed us to consider in more detail the stress–strain state of the elements.

3   Results and Discussion

Tests of auxiliary samples were carried out in accordance with the stated test procedure within the established time frame. According to the established methodology, samples were tested to bring them to destruction. The values of the maximum loads on the samples are given in Table 1. The type of samples after destruction is shown in Fig. 2.

Table 1 Values of limit loads when testing samples for strength when detached from the concrete surface

Marking of the sample	Maximum external load on the sample P_{cr}, кN	The ultimate tensile force in a composite element T_{cr}, кN	The nature of the destruction
OK-1–1	10.50	21.00	Separation of concrete near the glued surface to the lower reinforcement in the absence of destruction of the composite element and its detachment
OK-1–2	10.66	21.32	
OK-2–1	21.58	31.11	
OK-2–2	22.26	32.05	

Because the destruction of the samples did not occur due to the loss of strength of the adhesive seam, it was not possible to determine the bearing capacity of the adhesive seam during shear operation. However, taking into account the data of experimental studies conducted by the author with the involvement of laboratories, it can be said that the condition of destruction of a different nature is unattainable within the framework of the presented test program. This is because the minimum adhesive strength of the adhesive is 4 MPa, which exceeds the calculated shear resistance of concrete of class up

Fig. 2 Type of sample OK-1–1 after destruction

to and including B60. The tests were carried out on primed metal plates, which made it possible to approach the calculated bearing capacity of the adhesive, equal to 20 ± 1 MPa under the condition of complete curing [8]. At the same time, during the tests of samples of the OK-1 and OK-2 series, it was possible to obtain the values of the maximum tangential stresses in the adhesive joint, at which the destruction of concrete begins. These values are shown in Table 2.

Table 2 Values of the limiting stresses in the elements of the adhesive joint when testing samples for strength when detached from the concrete surface

Marking of the sample	The limiting stress in the composite element corresponding to the destruction of the sample $\sigma_{f,cr}$, MPa	The ratio of the effective stresses in the composite element to its tensile bearing capacity, %	Limit stress in the adhesive seam $\sigma_{w,cr}$, MPa
OK-1–1	2038.83	42.50	6.94
OK-1–2	2069.90	43.20	7.07
OK-2–1	2449.60	51.14	6.75
OK-2–2	2523.62	52.70	6.98

According to the test data, diagrams of the dependence of the relative deformations of the composite element and the adhesive were constructed. These diagrams are shown in Figs. 3 and 4. The numbers in parentheses indicate the percentage ratio of the current tensile force in the composite element to the limit—the corresponding destruction of the sample. In Figs. 3 and 4, dotted lines show the dependences of the relative deformations of the protective layer of concrete bordering the adhesive joint (if there is a difference between them and the relative deformations of the composite element).

Analyzing the diagrams shown in Figs. 3 and 4, we can conclude about the attenuating nature of the distribution of relative deformations along the length, indicating the
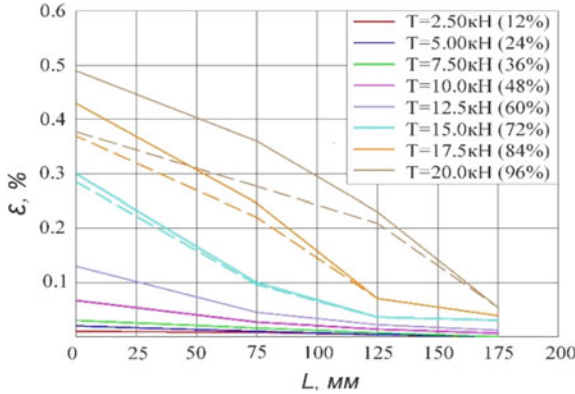
Fig. 3 Diagram of relative deformations of OK-1 series samples during separation tests
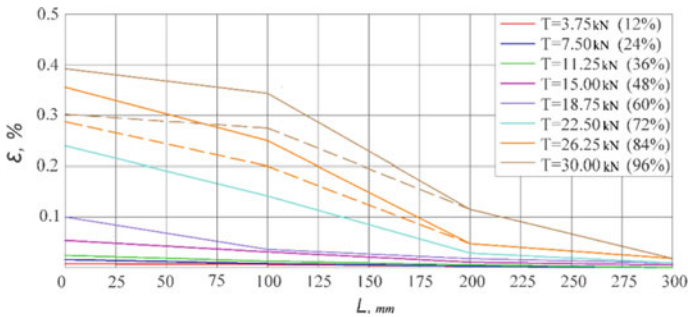
Fig. 4 Diagram of relative deformations of OK-2 series samples during separation tests

existence of a limit value of anchoring of the composite element. Within the framework of the conducted studies, this value was 300 mm, which, in general, corresponds to the conclusions obtained during the preliminary experimental studies of the author [5], as well as other authors [9–11]. A further increase in the anchoring of the composite element does not lead to an increase in the bearing capacity of the entire sample. The destructive forces within the same series differ slightly given in Table 2.

It was found that when the relative deformations exceed a value of 0.25…0.28%, there is a difference in sensor readings under the adhesive joint and on the composite material. Visually, it can be established that, at appropriate load levels, horizontal cracks are formed in the protective layer of concrete at the level of the longitudinal working reinforcement with a spreading front deep into the anchoring of the composite. This corresponds to the scenario of destruction of prototypes given in Ref. [4, 5].

4   Conclusion

The destruction of the prototypes occurred with the separation of the external composite element from the concrete without crushing the concrete of the compressed zone, with

the formation of normal cracks in the beams. Separation of the composite strip occurred with the destruction of concrete near the adhesive seam to a depth of 8–12 mm. It should be noted that the operation of the contact seam between the concrete surface depends on the degree of preparation of the surface to which the composite is glued. However, it does not have a serious impact on quantitative parameters. At the moment of destruction, the force in the composite element was 0.5–0.7 of the destructive value obtained during the tensile test.

The proposed scheme for testing the adhesion of external composite non-metallic reinforcement with concrete made it possible to determine quantitative and qualitative parameters, on the basis of which it is possible to propose a number of provisions for the design of reinforcement of reinforced concrete structures by external reinforcement with composite materials and formulate the tasks of studying structures of this class.

References

1. Dai, J., Ueda, T., Sato, Y.: Development of the nonlinear bond stress–slip model of fiber reinforced plastics sheet–concrete interfaces with a simple method. J. Compos. Constr. **9**, 52–62 (2005). https://doi.org/10.1061/(ASCE)1090-0268(2005)9:1(52)
2. Smerdov, D.N., Selivanova, E.A.: The study of the creep properties in the elements of the system of external reinforcement during prolonged exposure to load. Polytransport system materials IX International scientific-technical conference. Siberian state University of railway engineering, pp. 53–56 (2017)
3. Yushin, A.V., Morozov, V.I.: Experimental studies of two-span reinforced concrete beams reinforced with composite materials on an inclined section. Bull. Civil Eng. **5**(46), 50–57 (2014)
4. Rimshin, V.I., Merkulov, S.I., Esipov, S.M.: Concrete structures reinforced with composite material. Bull. Eng. Sch. Far Eastern Fed. Univ. **2**(35), 93–100 (2018). https://doi.org/10.5281/zenodo.1286034
5. Merkulov, S.I., Esipov, S.M.: Increase in the bearing capacity of reinforced concrete structures by strengthening the external reinforcement composite material // BST. Bull. Constr. Equip. **2**(1002), 56–57 (2018)
6. Bokarev, S.A., Smerdov, D.N.: Experimental studies of bent reinforced concrete elements reinforced with composite materials. Proc. High. Educ. Inst. Constr. **2**(614), 112–124 (2010)
7. Nevolin, D.G., Smerdov, D.N., Smerdov, M.N.: Experimental studies of the bearing capacity of reinforced concrete structures of mining buildings and structures. Proc. High. Educ. Inst. Min. J. **8**, 138–142 (2015)
8. Lu, X.Z., Teng, J.G., Ye, L.P., Jiang, J.J.: Bond–slip models for FRP sheets/plates bonded to concrete. Eng. Struct. **27**, 920–937 (2005). https://doi.org/10.1016/j.engstruct.2005.01.014
9. Smolyago, G.A., Obernikhina, Y.L.: Strength and deformation of bended reinforced concrete elements reinforced with carbon fiber. Bull. BSTU named after V.G. Shukhov **4**, 25–39 (2022). https://doi.org/10.34031/2071-7318-2021-7-4-25-38

10. Frolov, N.V.: Experimental studies of the kinetics of the developmental corrosive damages of concrete in bent reinforced concrete elements under force and environmental effects. Bull. BSTU named after V.G. Shukhov **2**, 34–44 (2020). https://doi.org/10.34031/2071-7318-2020-5-2-34-43

11. Suleymanova, L.A., Amelin, P.A., Adham, A.: Hameed: study of the strength of flexural elements made of cellular concrete. Lect. Notes Civil Eng. **173**, 107–155 (2021). https://doi.org/10.1007/978-3-030-81289-8_15

Research Study of Mixing Processes in the Pneumatic Mixer for Dry Construction Mixes

Yu. M. Fadin , O. M. Shemetova(✉) , V. P. Voronov , and V. S. Bogdanov

Belgorod State Technological University named after V.G. Shukhov, Belgorod, Russia
olga95kizilova@gmail.com

Abstract. This article discusses perspective directions of development of pneumatic mixers for mixing dry building mixes. Pneumatic mixers are modern equipment used for mixing dry building materials and fine materials that meet the requirements for environmental and industrial standards that surpass mechanical mixing units in their technical characteristics and do not harm the health of operators. Mixing materials with high-intensity movement of particles through the mixing chamber and with other material particles allows for obtaining a finished mixture with a high percentage of uniformity, which allows increasing the quality characteristics of the finished product, which is of no small importance in the manufacture of building materials. In this article, we present a new patented design of a pneumatic mixer, the distinctive quality of which it improves the properties of the final product and high uniformity of the finished mixture due to intensification of the mixing process. The method for calculating the process of mixing the components of bulk material in a pneumatic mixer is provided. According to the results which we obtained, the ratio that determines the change in the concentration of a selected component of bulk materials in the cylindrical volume of the mixing chamber. The results of this article can be used in the design of pneumatic mixers for mixing dry building mixtures.

Keywords: Pneumatic Mixer · Building Mixtures · Vortex Mixing · Mixer · Improvement · Dry Building Mixes

1 Introduction

The demand and increase in the production of modern building materials makes it necessary to improve the existing equipment for their production and develop new ones. In almost all technological lines for the production of building mixtures, there is a section with mixing equipment, in which various components are mixed to obtain finished products. The quality of the manufactured products will depend on the competent choice of this equipment, in our case, these are dry building mixes. Recently, the mixing equipment market has presented an extensive selection of equipment for mixing solid materials. The range of mixing equipment ranges from small to large volume mixers. Some faucets have long dominated certain market segments, and improved designs are the result of close collaboration with the end users.

Recently, pneumatic mixers have become the most popular. They meet the requirements according to environmental and production standards, they do not harm the health of operators and in terms of their technical characteristics they are in no way inferior to mechanical mixers [1–4].

In connection with this less-studied area, there are several areas of study, such as: obtaining new mixing opportunities through the development of an efficient mixing chamber; obtaining high-tech processing of dry multicomponent mixtures; reduction of metal consumption of the mixer. In accordance with the development of an air mixer and the calculations of obtaining a homogeneous mixture and mixing time, it is possible to obtain universal development of an air mixer with a degree of uniformity of more than 95%, with the possibility of high-quality mixing of components of different density, particle size and a large specific surface area [5–7].

2   Materials and Methods

In relation to opening new possibilities of using pneumatic mixers for the production of dry building mixes, several directions of their development can be distinguished [8–10].

The promising areas of development of pneumatic mixers include the following [11]:

- Development of high efficient mixing chambers, for achieving new types of mixed materials.
- Obtaining new modern methods of mixing dry components.
- Increasing the quality characteristics of the mixture, by increasing the percentage of homogeneity.
- Percentage reduction in metal consumption of mixing equipment.

Based on the above development possibilities, we propose a new design of a pneumatic mixer, the purpose of which is to improve the quality of the final product and increase the homogeneity of the product by intensifying the mixing process especially of materials with different densities.

The basic concept of a pneumatic mixer with a spiral energy-carrying tube (Fig. 1) for fine materials is based on the mixing of dry building mixtures in a turbulent flow of air [12, 13].

Components for mixing are fed into the housing 1 through the loading nozzles 5. In the housing 1 the material is picked up by the energy carrier supplied simultaneously with the material and flowing out of the holes in the spiral energy-carrying tube 4 extended upwards in the form of a truncated cone. The holes in the spiral energy-carrying tube 4 are arranged evenly in a checkerboard pattern, and the axes of the holes are directed upwards at an angle of 30°-35° relative to the vertical plane of the spiral energy-carrying tube 4. By pulling the spiral energy-carrying tube 4 with a cone upwards, the area of interaction of the energy carrier with the mixing components in housing 1 of the mixture, which improves the quality of the finished product due to the intensification of the mixing process. A vacuum is created in the conical bottom 2, and after the mixing cycle.

This solution helps to increase the degree of homogeneity of the finished product due to the intensification of the mixing process, which makes it possible to improve
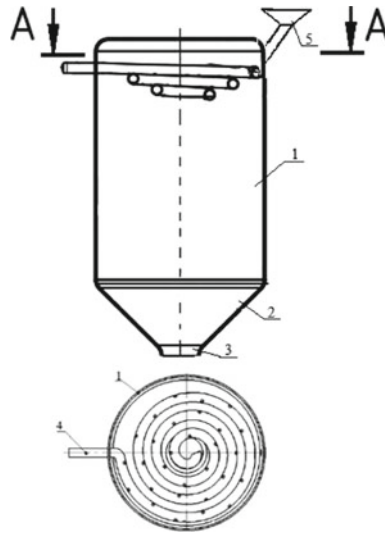
Fig. 1 Pneumatic mixer with a spiral energy-carrying tube

the quality and obtain dry building mixes with a high degree of distribution of the key component [14, 15].

3 Results and Discussions

Let us dwell on the method for calculating the mixing process in a pneumatic mixer of components in the bulk material for the production of building materials (Fig. 2).
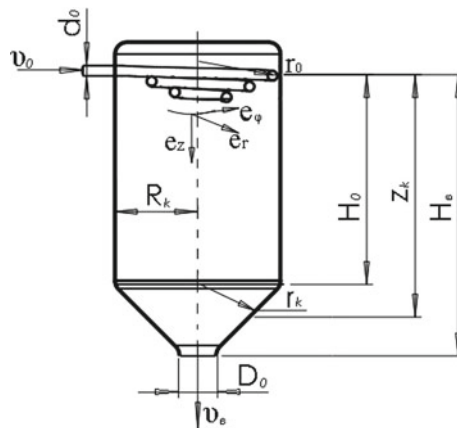

Fig. 2 Calculation scheme

The description of the process of mixing the components of bulk material in the volume of the mixer design under consideration can be carried out within the framework

of a two-parameter diffusion model:

$$\frac{\partial c}{\partial t} = D_z \frac{\partial^2 c}{\partial z^2} - \overline{\vartheta_z} \frac{\partial c}{\partial z} + \frac{D_r}{r} \frac{\partial}{\partial r}\left(r \frac{\partial c}{\partial r}\right). \tag{1}$$

where D_z and D_r the coefficients of longitudinal and radial mixing;—the speed of the longitudinal movement of the material $D_z D_r \overline{\vartheta_z}$.

In this model, it is assumed that the values,—are constant along the length and cross section $D_z D_r \overline{\vartheta_z}$.

The mixer model under consideration is characterized by the presence of a steady (time-independent) mixing mode. Therefore, it can be assumed that changes in the concentration "c" in this case will depend on only two variables c (z, r). Based on this fact, Eq. (1) can be expressed as:

$$D_z \frac{\partial^2 c}{\partial z^2} - \overline{\vartheta_z} \frac{\partial c}{\partial z} + \frac{D_r}{r} \frac{\partial}{\partial r}\left(r \frac{\partial c}{\partial r}\right) = 0. \tag{2}$$

The assumption that these coefficients of longitudinal and radial mixing are directly proportional to the average values of the speed of movement in the longitudinal and radial directions, as well as to the geometric dimensions. Based on this, we can express it as:

$$D_z = \overline{\vartheta_z} H_0, \tag{3}$$

$$D_r = \overline{\vartheta_r} R_k. \tag{4}$$

Further, we will assume that the average values of the velocities of the particles in the material differ from the average values of the velocities of the air flow by an infinity value. Therefore, on the basis of what has been said, the following relations can be written:

$$\overline{\vartheta_r} = \frac{1}{V} \int_0^{2\pi} d\varphi \int_{r_0}^{R_k} \int_0^{H_0} \vartheta_r \cdot dr \cdot dz, \tag{5}$$

$$\overline{\vartheta_z} = \frac{1}{V} \int_0^{2\pi} d\varphi \int_{r_0}^{R_k} \int_0^{H_0} \vartheta_z \cdot dr \cdot dz. \tag{6}$$

Here the volume of the cylindrical body of the mixer is equal to: V

$$V = \pi R_k^2 H_0. \tag{7}$$

Substituting (6) into (4) leads to the following result:

$$\overline{\vartheta_r} = \frac{A_0}{R_k^2 H_0} \int_{r_0}^{R_k} K_1(\lambda r) r dr \int_0^{H_0} \cos(\lambda z) dz, \tag{8}$$

where the following notation is introduced:

$$A_0 = \frac{\vartheta_0 \left(\frac{d_0}{D_0}\right)^2 I_0(\lambda r_0)}{\sin(\lambda H_B) K_0(\lambda r_0)}.$$ (9)

The calculation of the integrals in formula (8) for the value allows us to obtain the following result: $\lambda = \frac{\pi}{2H_0}$

$$\overline{\vartheta_r} = \frac{16 \cdot A_0 \cdot Y_1 \left(\frac{R_k}{H_0}, \frac{r_0}{H_0}\right) H_0^2}{\pi^2 R_k^2},$$ (10)

where the following notation is introduced:

$$Y_1 \left(\frac{R_k}{H_0}, \frac{r_0}{H_0}\right) = \int\limits_{\frac{\pi r_0}{2H_0}}^{\frac{\pi R_k}{2H_0}} K_1(x) \cdot x \cdot dx.$$ (11)

Substituting into relation (5) allows us to write the following expressions:

$$\overline{\vartheta_z} = \frac{2A_0\pi}{V} \int\limits_{r_0}^{R_k} K_0(\lambda r) r dr \int\limits_0^{H_0} \sin(\lambda z) dz.$$ (12)

Given that

$$\int\limits_0^{H_0} \sin(\lambda z) dz = \frac{1}{\lambda} \int\limits_0^{H_0} \sin(\lambda z) d(\lambda z) = \frac{2H_0}{\pi},$$ (13)

and according to reference data [Dwight]:

$$\int\limits_{r_0}^{R_k} K_0(\lambda r) r dr = \frac{1}{\lambda} [r_0 K_1(\lambda r_0) - R_k K_1(\lambda R_k)].$$ (14)

Relation (12), taking into account (7), (14), can be reduced to the following form:

$$\overline{\vartheta_z} = \frac{8 \cdot H_0 \cdot A_0}{\pi^2 R_k^2} \left[r_0 K_1 \left(\frac{\pi r_0}{2 \cdot H_0}\right) - R_k K_1 \left(\frac{\pi R_k}{2 \cdot H_0}\right) \right].$$ (15)

Equation (2) taking into account (3) and (4) will take the form:

$$\overline{\vartheta_z} H_0 \frac{\partial^2 c}{\partial z^2} - \overline{\vartheta_z} \frac{\partial c}{\partial z} + \frac{\overline{\vartheta_r} R_k}{r} \frac{\partial}{\partial r} \left(r \frac{\partial c}{\partial r} \right) = 0.$$ (16)

In Eq. (16) we have dimensionless variables according to the relations: $\xi_1 \xi_2 \xi_1 \xi_2$

$$z = \xi_1 H_0,$$ (17)

$$r = \xi_2 R_k. \tag{18}$$

In dimensionless variables, Eq. (16) can be expressed in the following form:

$$\gamma^2 \left[\frac{\partial^2 c}{\partial \xi_1} - \frac{\partial c}{\partial \xi_1} \right] + \frac{1}{\xi_2} \frac{\partial}{\partial \xi_2} \left(\xi_2 \frac{\partial c}{\partial \xi_2} \right) = 0. \tag{19}$$

where the following notation is introduced:

$$\gamma^2 = \frac{\overline{\vartheta_z} R_k}{\overline{\vartheta_r} H_0}. \tag{20}$$

Taking into account (10) and (15), formula (20) takes the following form:

$$\gamma^2 = \frac{r_0 K_1 \left(\frac{\pi r_0}{2 \cdot H_0} \right) - R_k K_1 \left(\frac{\pi R_k}{2 \cdot H_0} \right)}{2 \cdot \pi \cdot H_0 \cdot Y_1 \left(\frac{R_k}{H_0}, \frac{r_0}{H_0} \right)}. \tag{21}$$

The solution of Eq. (19) is sought in the form:

$$c = c_1(\xi_1) \cdot c_2(\xi_2). \tag{22}$$

Substituting (22) into (19) gives:

$$\gamma^2 c_2(\xi_2) \left[\frac{d^2 c_1}{d\xi_1^2} - \frac{dc_1}{d\xi_1} \right] + \frac{c_1(\xi_1)}{\xi_2} \frac{d}{d\xi_2} \left(\xi_2 \frac{dc_2}{d\xi_2} \right) = 0. \tag{23}$$

Based on (22), the following relation can be obtained:

$$\frac{\gamma^2}{c_1(\xi)} \left[\frac{d^2 c_1}{d\xi_1^2} - \frac{dc_1}{d\xi_1} \right] = -\frac{1}{c_2(\xi_2)\xi_2} \frac{d}{d\xi_2} \left(\xi_2 \frac{dc_2}{d\xi_2} \right). \tag{24}$$

The left side of relation (24) depends only on the variables ξ_1, and the right side on ξ_2 therefore the fulfilment of the equality in (24), is possible only if each of the parts is a constant value equal to $\beta^2 > 0 . \beta^2 > 0$.

According to the above relation (24), will be equivalent to the following two differential equations:

$$\gamma^2 \left[\frac{d^2 c_1}{d\xi_1} - \frac{dc_1}{d\xi_1} \right] = \beta^2 c_1, \tag{25}$$

$$\frac{d^2 c_2}{d\xi_2} + \frac{1}{\xi_2} \frac{dc_2}{d\xi_2} + \beta^2 c_2 = 0. \tag{26}$$

The solution of Eq. (26), limited at $\xi_2 \to 0$ according to the reference data [Special Functions Handbook] has the form:

$$c_2(\xi) = const \, \mathcal{J}_0(\beta \xi_2), \tag{27}$$

where $\mathcal{J}_0(\beta\xi_2)$– is a zero-order Bessel function of the first kind.

Functional dependence (27) in the transition according to (18) to dimensional quantities will take the form:

$$c_2(r) = const\,\mathcal{J}_0\left(\beta\frac{r}{R_k}\right). \tag{28}$$

Solution (28) must satisfy the boundary condition:

$$r = R_k, \quad c_2(R_k) = 0. \tag{29}$$

Applying (29) to (28) makes it possible to obtain:

$$const\,\mathcal{J}_0(\beta) = 0. \tag{30}$$

Functional dependence graph $\mathcal{J}_0(\beta)$ (Fig. 3) Based on this dependence, (30) is converted to the first zero at the value $\beta = \beta_1 = 2.4\ldots$.
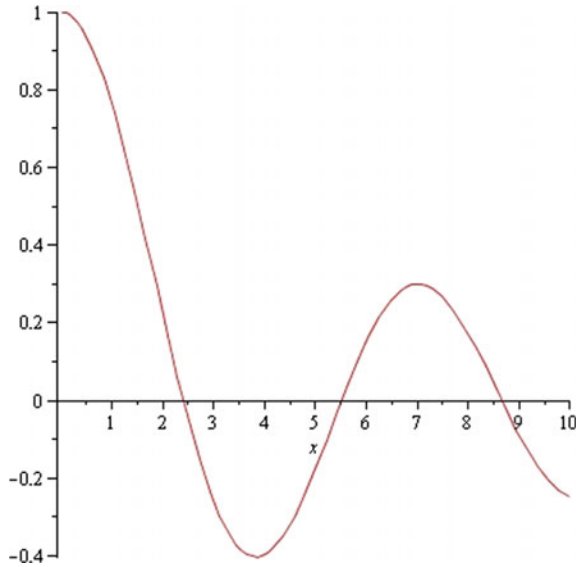
Fig. 3 Graph of integral functions $\mathcal{J}_0(x)$.

Based on the data obtained, solution (28) satisfying (29) can be written in the following form:

$$c_2(r) = const\,\mathcal{J}_0\left(\beta_1\frac{r}{R_k}\right). \tag{31}$$

Equation (25) can be represented as:

$$\frac{d^2c_1}{d\xi_1^2} - \frac{dc_1}{d\xi_1} - \frac{\beta_1^2}{\gamma^2}c_1 = 0. \tag{32}$$

To find a solution to the differential Eq. (32), it is necessary to write down the characteristic equation:

$$1.\ k^2 - k - \left(\frac{\beta_1}{\gamma}\right) = 0. \tag{33}$$

The quadratic Eq. (33) has two roots:

$$k_1 = \frac{1}{2} - \sqrt{\frac{1}{4} + \left(\frac{\beta_1}{\gamma}\right)^2}, \tag{34}$$

$$k_2 = \frac{1}{2} + \sqrt{\frac{1}{4} + \left(\frac{\beta_1}{\gamma}\right)^2}. \tag{35}$$

Since we are interested in the decreasing solution of the function $c_1\ (\xi_1)$, which corresponds to the negative value of the root of the characteristic equation. Based on the above $k_1 < 0$, the solution of Eq. (32) can be represented as:

$$c_1(\xi_1) = const \cdot e^{k_1 \xi_1}. \tag{36}$$

Passing to dimensional variables according to (17), we have:

$$c_1(z) = const\, e^{\frac{k_1 z}{H_0}}. \tag{37}$$

Substituting (31) and (37) results in:

$$c(r, z) = const \cdot e^{\frac{k_1 z}{H_0}} \mathcal{J}_0\left(\beta_1 \frac{r}{R_k}\right). \tag{38}$$

To determine the value *const* in (38) it is necessary to use the following boundary condition:

$$c(r = 0, z = 0) = c_0, \tag{39}$$

where c_0—is the initial value of the concentration of the isolated component of the dry mixture in the bulk material.

Applying (39) to (38) gives:

$$c_0 = const. \tag{40}$$

Based on (40) we find:

$$const = c_0. \tag{41}$$

Taking into account (41), formula (38) takes the form (Fig. 4):

$$c(r, z) = c_0 \mathcal{J}_0\left(\beta_1 \frac{r}{R_k}\right) e^{\frac{k_1 z}{H_0}}. \tag{42}$$
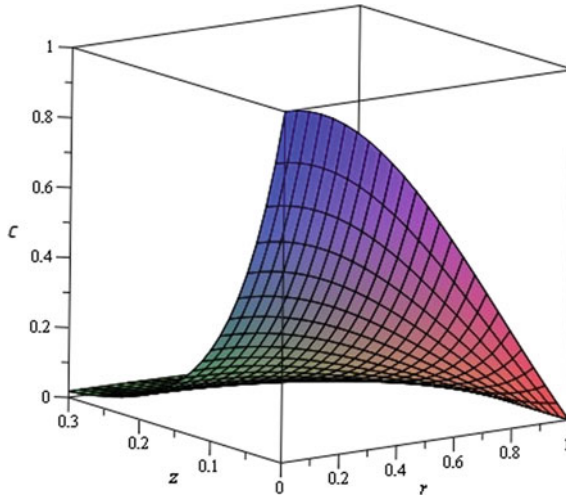
Fig. 4 Graph of concentration change from

The change in concentration is highly non-linear and strongly depends on the parameters of the mixing chamber.

Thus the obtained relation (42) determines the change in the concentration of the selected component of the mixture of bulk material in the cylindrical volume of the mixing chamber. The uniformity of the finished product and its physical and chemical characteristics directly depend on what concentration will be created in the mixing chamber. Those the lower the concentration, the worse the quality of the mixture and the greater the heterogeneity of the mixture, which directly leads to unsatisfactory performance of the finished product.

4 Conclusions

Mixing building materials with high-intensity movement of material particles through the mixing chamber and with other material particles allows obtaining a finished mixture with a high percentage of uniformity, increasing the quality characteristics of the dry building mixes. The movement of the particle in the mixing chamber at high speeds contributes to the mechanical activation of the mixture and in this way increases the strength characteristics of the finished mixture. The process of mixing the bulk material components in the volume of the mixer design under consideration describes the change in the concentration of the selected component of the bulk material mixture in the cylindrical volume of the mixing chamber, which makes it possible to clearly see how the material particles behave in the mixing chamber building mix. Considering what concentration will be created in the mixing chamber directly depends on what will be the homogeneity of the finished product and the physico-chemical characteristics of the finished building mixture.

References

1. Korneev, V.I.: Dry mixes. Stroimaterialy. St. Petersburg (2010).
2. Dury, C.M., Ristow, G.H.: Competition of mixing and segregation in rotating. Physics of fluids **11**, 1387–1394 (1999)
3. Orehova, T.N., Kachaev, A.E., Okushko, V.V., Shestakov, Y.G.: Suspended bed mechanics with polydisperse particles in continuous pneumatic mixers. Bulletin of BSTU named after V.G. Shukhov **3**, 121–127 (2020)
4. Fadin, Yu.M., Shemetova, O.M.: Dry building mixtures and mixing equipment for production. Bulletin of BSTU named after VG Shukhov **12**, 145–150 (2020)
5. Shemetova, O.M. Shemetov, E.G.: Mixture quality assessment criteria. Education. The science production. XIII International Youth Forum 1001–1003 (2021).
6. Bogdanov, V.S.: Mechanical equipment for enterprises of the building materials industry. BelGTASM, Belgorod (1996).
7. Orehova, T.N.: Determination of the performance of a pneumatic mixer of dry building mixtures, taking into account the analysis of the devices of mixing units. Bulletin of BSTU named after V.G. Shukhov **3**, 65–68 (2011)
8. Fadin, Y.M., Shemetova, O.M.: Development and calculation of mathematical model of pneumatic mixer for mixing dispersed materials, Samara (2021).
9. LNCS Homepage https://studfile.net/preview/7493544/page:15/. Last accessed 20 Oct 2020.
10. Weinekotter, R., Gericke, H.: Mixing of solids. Kluwer academic publishers. (2000).
11. Bolshakov, E.L. et al.: Current state and development prospects of production of dry building mixtures in Russia. sat. articles of the International Scientific and Technical Conference "Modern technologies of dry mixes in construction". Stroimaterialy, St. Petersburg, pp. 3–5 (2000).
12. Fadin, Y.M., Shemetova, O.M., Voronov, V.P., Shemetov, E.G.: Pneumatic mixer with a spiral energy-carrying tube. Lecture Notes in Civil Engineering **160**, 333–339 (2021)
13. Shemetova, O.M., Fadin, Y.M., Shemetov, E.G.: Study of the mixing process in a pneumatic mixer. News of the Tula State University. Technical Sci. **10**, 170–174 (2021)
14. Berthiaux, H., Mizonov, V.: Applications of Markov chains in particulate process. The Canadian Journal of Chemical Engineering **6**, 1143–1168 (2004)
15. Shemetova, O.M., Fadin, Yu.M., Bogdanov, V.S.: Obtaining homogeneous fine mixtures in a pneumatic mixer. STIN **3**, 22–24 (2022)

Improving the Calculation of Variable Cross Section Compressed Wooden Bars Stability

Roman Shorstov[1] , Anton Chepurnenko[2,3] , Linar Sabitov[3,4] ,
Batyr Yazyev[2,3(✉)] , and Stepan Litvinov[2,3]

[1] Belgorod State Technological University named after V.G. Shukhov, 46 Kostyukova Street, Belgorod, Russia 308012
[2] Don State Technical University, 1 Gagarin Sq., Rostov-on-Don, Russia 344000
`ps62@yandex.ru`
[3] Kazan Federal University, 18 Kremlyovskaya Street, Kazan, Russia 420008
[4] Kazan State Power Engineering University, 51 Krasnoselskaya Street, Kazan, Russia 420066

Abstract. The article presents a method for determining critical loads for centrally compressed wooden bars with a cross-sectional stiffness variable along the length. Rectangular cross-section bars are considered, the section height of which varies according to a linear law, and the width is constant. The solution is carried out in the elastic formulation. To obtain a solution that is valid for an arbitrary bar geometry, dimensionless parameters are introduced. When solving the stability problem, the basis is the static Euler criterion. The solution of the main resolving equation is performed numerically by the finite difference method. As a result, the task is reduced to the problem of matrix eigenvalues. The implementation of the calculation is performed in the MATLAB environment. Comparisons are made with the current Russian standards for the design of wooden structures. In Russian design standards, a controversial provision is that the variable stiffness of the bars is estimated by the same calculation formula, regardless of the type of fastening. It has been established that the error of Russian design codes for a bar hinged at the ends can in some cases exceed 5%. Corrected calculation formulas suitable for engineering calculations are proposed. In addition, to confirm the reliability of the results, a finite element analysis is performed in the LIRA-SAPR software package.

Keywords: Wood · Bar · Stability · Buckling · Variable Stiffness · Finite Difference Method · Finite Element Method

1 Introduction

Wood has been one of the main structural materials in construction for many centuries, due to its high physical, mechanical and technical qualities. At the present stage of the construction industry development, there has been significant progress in the field of design and construction of buildings and structures using wood due to the use of glued wooden structures [1–3].

To improve design solutions and reduce the material consumption of construction, it is necessary to develop scientifically based methods for calculating and optimizing building structures. In many designs, elements with a constant cross-sectional geometry along the length are used, however, for reasons of reducing material consumption, in some cases it is advisable to use elements of variable stiffness [4–9].

A lot of works are devoted to the solution of problems for compressed elements stability with a section variable along the length, including [10–14]. In the current Russian standards for the design of wooden structures (SP 64.13330.2017), for compressed elements with a cross-sectional height that varies along the length, the variable stiffness is taken into account by the coefficient k_{zhN}, which for various fastening options is proposed to be determined using the same calculation formula, with which one cannot agree.

The purpose of this work is to improve the normative methods for calculating the stability of compressed structural elements made of wood with a section variable in length.

2 Methods

We consider a centrally compressed rack hinged at the ends with a rectangular cross section (Fig. 1), the height of which varies according to a linear law. The law of height change can be written as:

$$h(x) = h_0\left(\beta + \frac{(1-\beta)x}{l}\right). \tag{1}$$

We assume that the rack material is elastic. To determine the critical load, we use the differential equation for the buckling of the bar:

$$EI(x)\frac{d^2w}{dx^2} + Fw = 0 \tag{2}$$

with the boundary conditions $w(0) = w(l) = 0$.

To make the solution valid for an arbitrary bar geometry, we introduce a dimensionless coordinate $\xi = x/l$, $\xi \in [0;1]$. Then expression (1) will take the form:

$$h(x) = h_0(\beta + (1-\beta)\xi) = h_0\varphi(\xi). \tag{3}$$

In case of stability loss in the xz plane, in Eq. (2) as the axial moment of inertia, the moment of inertia I_y should be substituted, which is determined by the formula:

$$I_y(\xi) = \frac{bh^3}{12} = \frac{bh_0^3}{12}\varphi^3(\xi) = I_y^0\varphi^3(\xi). \tag{4}$$

The transition from the derivative with respect to x to the derivative with respect to ξ in Eq. (2) is performed as follows:

$$\frac{dw}{dx} = \frac{dw}{d\xi}\frac{d\xi}{dx} = \frac{1}{l}\frac{dw}{d\xi};$$
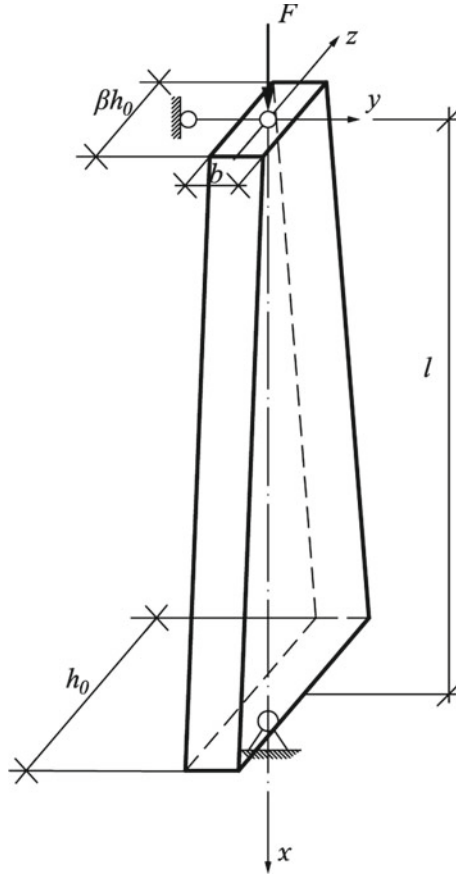$$\frac{d^2w}{dx^2} = \frac{1}{l^2}\frac{d^2w}{d\xi^2}. \tag{5}$$

Fig. 1 Design scheme

Substituting (5) and (4) into (2), we get:

$$EI_y^0 \varphi^3(\xi) \frac{1}{l^2} \frac{d^2 w}{d\xi^2} + Fw = 0 \qquad (6)$$

Or

$$\varphi^3(\xi) \frac{d^2 w}{d\xi^2} + \lambda w = 0, \qquad (7)$$

where $\lambda = \frac{Fl^2}{EI_y^0}$.

The critical force is expressed in terms of the dimensionless parameter λ as:

$$F_{cr} = \frac{\lambda EI_y^0}{l^2}. \qquad (8)$$

This formula coincides in structure with the Euler formula. For $EI(x) = \text{const}$, i.e. $\beta = 1$: $\lambda = \pi^2$.

In the current Russian standards for the design of wooden structures, the variable stiffness of the bar is taken into account by the coefficient k_{zhN}, which depends on the parameter β. This coefficient for a bar hinged at the ends is expressed in terms of the parameter λ as follows:

$$k_{zhN}(\beta) = \frac{\lambda(\beta)}{\pi^2}. \tag{9}$$

To solve Eq. (7), we use the finite difference method. On the interval [0; 1], a uniform grid with step $\Delta\xi$ is introduced. The finite difference approximation of Eq. (7) for the i-th node is written as:

$$\varphi^3(\xi_i)\frac{w_{i+1} - 2w_i + w_{i-1}}{\Delta\xi^2} + \lambda w_i = 0. \tag{10}$$

Compiling this equation for all grid nodes, except for the extreme ones, in which $w_0 = w_n = 0$, we obtain a system of linear algebraic equations:

$$([A] + \lambda[E])\{X\} = 0, \tag{11}$$

where $\{X\} = \{w_1 w_2 \ldots w_{n-1}\}^T$, $[E]$ is the identity matrix,

$$[A]\Delta\xi^2 = \begin{bmatrix} -2\varphi^3(\xi_1) & \varphi^3(\xi_1) & 0 & 0 & \ldots & 0 & 0 & 0 \\ \varphi^3(\xi_2) & -2\varphi^3(\xi_2) & \varphi^3(\xi_2) & 0 & \ldots & 0 & 0 & 0 \\ 0 & \varphi^3(\xi_3) & -2\varphi^3(\xi_3) & \varphi^3(\xi_3) & \ldots & 0 & 0 & 0 \\ \ldots & \ldots & \ldots & \ldots & \ldots \ldots & \ldots & & \ldots \\ 0 & 0 & 0 & 0 & \ldots & 0 & \varphi^3(\xi_{n-1}) & -2\varphi^3(\xi_{n-1}) \end{bmatrix}.$$

The system of Eqs. (11) is homogeneous and has a nonzero solution only if its determinant is equal to zero:

$$\|[A] + \lambda[E]\| = 0. \tag{12}$$

The parameter λ corresponding to the critical load is the minimum eigenvalue of the matrix $[A]$, taken with a minus sign:

$$\lambda = \min(-eig(A)), \tag{13}$$

where $eig(A)$ is a function returning the eigenvalues of the matrix $[A]$.

3   Results and Discussion

The calculation was implemented in the MATLAB environment. The first step to estimate the required number of intervals in ξ was to solve the problem for a bar of constant cross section. Table 1 shows the values of the parameter λ for a different number of intervals n in ξ, as well as the deviation from the exact result equal to π^2.

In further calculations, the number of intervals n was assumed to be 100.

Table 1 Dependence of the parameter λ for a bar of constant cross section on the number of intervals n in ξ

n	2	3	4	5	6	7	8	9	10
λ	8	9	9.37	9.55	9.65	9.71	9.74	9.77	9.79
$\delta, \%$	18.9	8.8	5.1	3.2	2.2	1.6	1.3	1.0	0.8
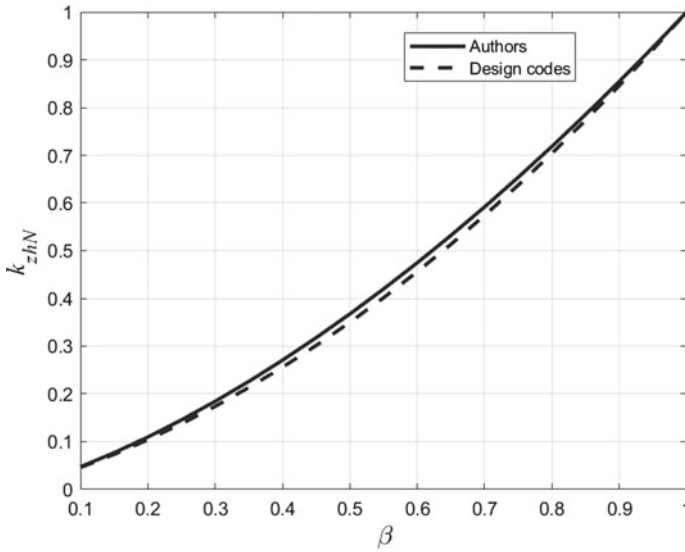
Fig. 2 The dependence of the coefficient k_{zhN} on the parameter β at loss of stability in the xz plane

Figure 2 shows the dependence of the coefficient k_{zhN} on the parameter β obtained as a result of the calculation. The dashed line corresponds to the formula presented in Russian standards:

$$k_{zhN} = (0.4 + 0.6\beta)\beta. \tag{14}$$

The greatest discrepancy between the results is 5.7% at β = 0.3. For the dependence $k_{zhN}(\beta)$ shown in Fig. 2 we have selected a refined approximating formula:

$$k_{zhN}(\beta) = 0.5116\beta^2 + 0.5004\beta - 0.0103. \tag{15}$$

We consider next the case of stability loss in the xy plane. In this case, the moment of inertia I_z should be substituted into Eq. (2) as $I(x)$, determined by the formula:

$$I_z(x) = \frac{b^3 h(x)}{12} = \frac{b^3 h_0}{12}\varphi(\xi) = I_z^0 \varphi(\xi). \tag{16}$$

The differential equation for buckling takes the form:

$$\varphi(\xi)\frac{d^2w}{d\xi^2} + \lambda w = 0, \tag{17}$$

where $\lambda = \frac{Fl^2}{EI_z^0}$.

This equation is solved similarly to Eq. (7). In Russian design standards for wooden structures with buckling in the xy plane, the coefficient k_{zhN} is determined by the formula:

$$k_{zhN} = 0.4 + 0.6\beta. \tag{18}$$

Figure 3 shows the graph of the coefficient k_{zhN} dependence on β obtained as a result of the calculation. The dashed line corresponds to a straight line constructed according to formula (18).
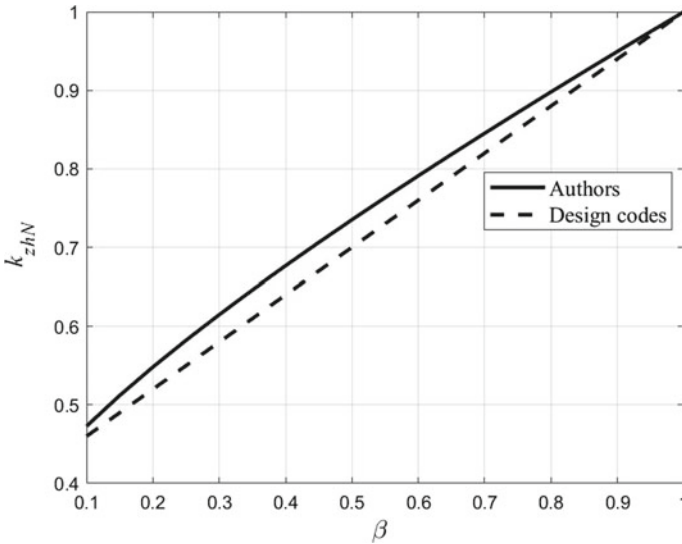
Fig. 3 The dependence of the coefficient k_{zhN} on the parameter β at loss of stability in the xy plane

The maximum deviation of the author's solution from the normative values is also observed at $\beta = 0.3$ and is, as before, 5.7%. We propose the following refined formula for the coefficient k_{zhN}:

$$k_{zhN} = -0.1305\beta^2 + 0.7193\beta + 0.4079. \tag{19}$$

To confirm the reliability of the results, a calculation was made for the stability of the bar with variable cross section in the LIRA-SAPR software package at $\beta = 0.5$, $h_0 = 15$ cm, $b = 10$ cm, $l = 3$ m. The critical force was 100.79 kN. The Euler force for a bar of constant section $b \times h_0$ is 137 kN. The actual coefficient $k_{zhN} = 0.735$. The normative value of the coefficient calculated by formula (18) was 0.7. According to the refined formula (19) proposed by us it is equal to 0.735. The model in LIRA-SAPR and the form of buckling are shown in Fig. 4.
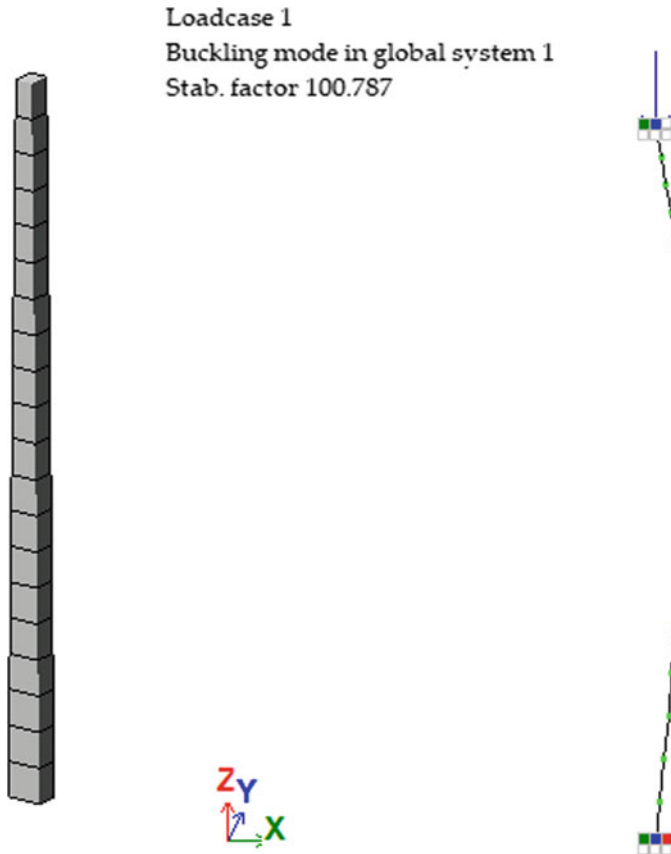
Fig. 4 Model of a bar with variable cross section and the form of buckling in LIRA-SAPR

4 Conclusion

A technique has been developed for determining the critical load for compressed wooden bars with a linearly varying cross-sectional height based on the finite difference method. A comparison was made with the calculation dependencies presented in Russian design codes SP 64.13330.2017. It is established that the error of normative formulas exceeds 5%. Using the least squares method, refined formulas are proposed. The reliability of the results obtained by the authors is confirmed by finite element modeling in the LIRA-SAPR software package.

References

1. Karamisheva, A.A., Yazyev, S.B., Avakov, A.A.: Calculation of plane bending stability of beams with variable stiffness. Procedia Engineering **150**, 1872–1877 (2016)
2. Lapina, A.P.: Wooden beam flat bending shape stability taking the creep into account. Construction and Architecture **9**(2), 6–10 (2021)

3. Chepurnenko, A., Ulianskaya, V., Yazyev, S., Zotov, I.: Calculation of wooden beams on the stability of a flat bending shape enhancement. MATEC Web Conf. **196**, 01003 (2018)
4. Klyuev, S.V., Khezhev, T.A., Pukharenko, Y.V., Klyuev, A.V.: Fibers and their properties for concrete reinforcement. MSF **945**, 125–130 (2018)
5. Zhuikov, S.V.: The use of nanotechnology for the design of building structures. Construction Materials and Products **4**(6), 26–47 (2021). https://doi.org/10.34031/2618-7183-2021-4-6-26-47
6. Klyuev, S.V., Abakarov, A.J., Lesovik, R.V., Muravyov, K.A., Tatlyev, R.D.: Optimal engineering of rod spatial construction. J. Comput. Theor. Nanosci. **16**(1), 200–203 (2019)
7. Klyuev, S.V., Garkin, I.N., Klyuev, A.V., Sabitov, L.S.: Results of endurance testing of prefabricated crane structures. Construction Materials and Products **5**(4), 39–49 (2022)
8. Shorstov, R.A., Yaziev, S.B., Chepurnenko, A.S., Klyuev, A.V.: Flat bending shape stability of rectangular cross-section wooden beams when fastening the edge stretched from the bending moment. Construction Materials and Products **5**(4), 5–18 (2022)
9. Yazyev, S.B., et al.: Flexural buckling of a revolving bar in a rigid pipe with a gap exposed to axial force and dead weight. IOP Conf. Ser.: Mater. Sci. Eng. **913**, 022021 (2020)
10. Litvinov, S.V., et al.: Buckling of glass reinforced plastic rods of variable rigidity. Mater. Sci. Forum **931**, 133–138 (2018)
11. Andreev, V.I., Tsybin, N.Y.: On the stability of rod with variable cross-section. Procedia Engineering **111**, 42–48 (2015)
12. Tsybin, N.Y., Turusov, R.A., Andreev, V.I.: Comparison of creep in free polymer rod and creep in polymer layer of the layered composite. Procedia Engineering **153**, 51–58 (2016)
13. Andreev, V.I., Barmenkova, E.V.: Iterative method of optimization of stress state of column under eccentric compression. Procedia Engineering **92**, 20–25 (2014)
14. Andreev, V., Barmenkova, E.: Optimization of the thin-walled rod with an open profile. MATEC Web Conf. **86**, 01033 (2016)

Characterization of a Polymer Composite with a Hybrid Filler

S. V. Zaitsev$^{(\boxtimes)}$, V. V. Sirota , D. S. Prokhorenkov , and A. A. Skiba

Belgorod State Technological University Named After V.G. Shukhov, Belgorod, Russia
`sergey-za@mail.ru`

Abstract. Polymer composites with radiation protection fillers play an important role in the space and nuclear industry. Along with radiation resistance, the multifunctionality of the polymer composite is also required to meet the needs of industry. The introduction of hybrid fillers into a polymer matrix can have a beneficial effect on protective properties, but also on the multifunctionality of polymer composites. This article examines the influence of the distribution of a hybrid filler in a polytetraforoethylene (PTFE) matrix on the microstructure and hardness of the composite. Tungsten carbide, boron carbide, bismuth oxide and titanium hydride—four types of filler with different average particles from submicron to the micron. The homogenization of the mixture was carried out in a jet-type mill. The molding of the polymer composite was carried out by hot pressing. It was established that the hybrid filler is evenly distributed by the PTFE matrix. The interfacial border between the matrix and the particles of the filler is very dense. It is shown that the maintenance of a hybrid filler into the PTFE matrix significantly increases the hardness of the polymer composite.

Keywords: Polymer Composite · Tungsten Carbide · Bismuth Oxide · Boron Carbide · Titanium Hydride Polytetraforoethylene

1 Introduction

In recent years, one of the leading areas of research in material science is the development of composite materials based on polymer matrices. The introduction of the filler into the polymer matrix has a very beneficial effect on the functional and protective properties of polymeric materials [1–5].

Polymer composites, filled with materials ensuring effective weakening of radiation intensity to the minimum level, can be used in the atomic and space industries [6–8]. Studies have shown that the introduction of Bi_2O_3 up to 44 wt% in polymethyl methacrylate matrix not only improves gamma-protective ability, but also increases the micro-hardness of the composite [9]. In another study, the carbide boron powder (B_4C) was mixed with a polyethylene matrix, and the results demonstrated good protective properties from neutrons and protons [10]. Soylu and others added from 50 to 70% boron carbide (WC) to the polypropylene matrix and showed that the composite has good properties of gamma radiation with high energy [11]. In addition, polymer composites with a filler are easier and flexible compared to lead in the same conditions.

In most of the above studies, it is devoted to composites with one type of aggregate. However, mixing three or four types of fillers of different sizes can show better properties than one type of filler in polymer composite. In this regard, the purpose of this study is to study the influence of the distribution of hybrid filler in a polytetraforoethylene (PTFE) matrix on the microstructure and firmness of the composite.

2   Methods and Materials

As a matrix for composites, polytetraforoethylene was chosen (PTFE, production "Fluroplast products", Belgorod, Russia), white powder with a particle size of 6–20 microns. The temperature range of operation is from -269 °C to $+260$ °C, a tensile strength at a stretch of 250 kgf/cm^2, the strength of the strength during compression is 120 kgf/cm^2, the elasticity module when compressed 7000 kgf/cm^2.

Hybrid filler is a powder of tungsten carbide (WC, production "Sevastopol State University", Sevastopol, Russia), powder of carbide boron F2500 (B$_4$C, production "plasmotherm", Moscow, Russia), powder oxide bismuth (Bi$_2$O$_3$, production "Plant of Rare Metals", Novosibirsk, Russia) and Titan Hydrid powder (TiH$_2$ developed by "VHTRII" Moscow, Russia).

Mixing polymer particles and fillers was carried out in a jet-type mill. The composition of the polymer composite is shown in Table 1. Such a composition is due to the fact that the filled polytetraforoethylene retains valuable properties of the polymer matrix. Then the homogeneous mixture was placed in a steel shape and hot pressing was carried out at a pressure of 80 MPa and a temperature of 360–380 °C. At the end of the pressing, a shaped sample of 25 × 50 × 5 mm was cooled in the air.

Table 1 Compositions of a polymer composite

Component content, wt%				
PTFE	Bi$_2$O$_3$	WC	TiH$_2$	B$_4$C
42.5	38.7	3.2	14.1	1.5

The distribution of particles in size was measured by Laser Scattering using (Analysette 22 NanoTec Plus, Fritsch GmbH).

The morphology and microstructure of the polymer composite were investigated using a scanning electron microscope (Tescan Mira 3 LMU, Czech Republic) in combination with energy dispersion X-ray spectroscopy (SEM–EDS). SEM images were acquired at 5 kV acceleration voltage.

The hardness of the Vickers of the compositional polymer was measured using a micro-hardness meter for Vickers (Nexus 4505-IMP, "Innovatest Europe BV", the Netherlands). The measurement was carried out at 5 points in the direction from the edge to the center with a constant step. Then the obtained values were averaged and the resulting number was taken as the final hardness of the polymer composite.

3 Results and Discussion

The distribution of particles of the initial powders in size measured the Laser Scattering method and are presented in Fig. 1. The result of granulometric analysis for Bi_2O_3 showed that the average particle size is 8 μm (Fig. 1a). In Fig. 1b shows the size of small WC particles in the submicron range, and larger B_4C particles showed a range from 10 to 100 microns (Fig. 1d). The dimensions of the TiH_2 particles are in the range from 0.1 to 107 μm (Fig. 1c), and most particles are in the range from 10 to 70 microns.
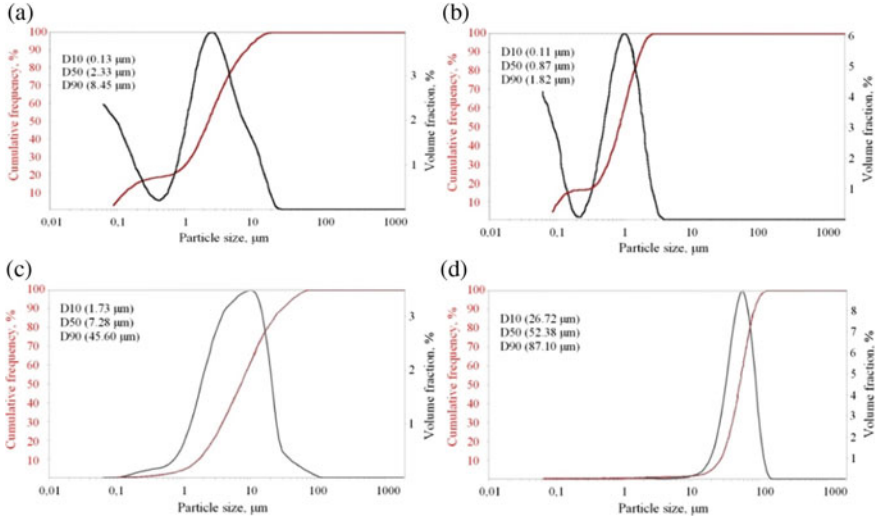
Fig. 1 The size of the particles of the source powders: **a** Bi_2O_3; **b** WC; **c** TiH_2; **d** B_4C

In Fig. 2 shows the microstructure of the PTFE cross section with a hybrid filler. On microphotography (Fig. 2a) it is clear that the particles of the hybrid filler are evenly distributed in the PTFE matrix. The polymer composite demonstrates good homogeneity.

With a greater increase in the microphotography of the transverse section, the composite shows a dense and compact structure (Fig. 2b). Defects, micropores and cracks are not observed. The interfacial border between the PTFE matrix and the particles of the filler TiH_2, B_4C and Bi_2O_3 is very dense. The conglomeration of the hybrid filler in the PTFE does not occur. In this regard, the lack of visible defects in the structure and uniform distribution of the filler in the polymer matrix can increase the physical and mechanical properties and the radiation protection characteristics of the composite [12, 13].

In Fig. 3 shows the image of EDX PTFE with a hybrid filler. It can be seen that in the polymer composite there are all the elements of the hybrid filler and PTFE (F, B, C, Bi, W and O). Element F indicates that the PTFE powder is distributed homogeneous in the composite. Elements of Bi and Ti are evenly distributed throughout the volume of the PTFE matrix. Compared to Bi_2O_3 and TiH_2 powders, the WC and B_4C powder content is very small. As a result, small sections of the W and B elements are evenly distributed in the volume of the composite.
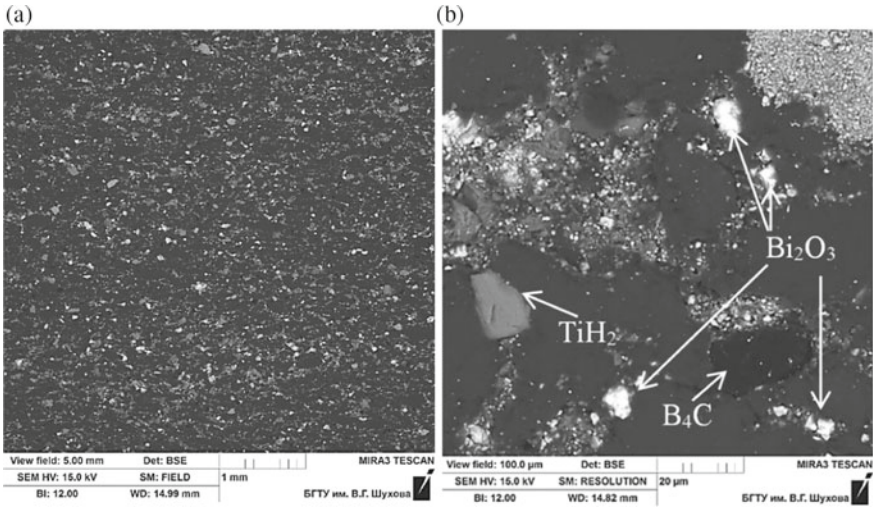
Fig. 2 Microstructure of the polymer composite

The composition of individual plots of the cross section of the polymer composite in accordance with Fig. 3 is shown in Table 2.

The test for hardness is a very important characteristic of a composite with a hybrid filler. Firmness indicates the ability of a hybrid composite to resist pressing. In the current research work, the values of microstality were evaluated, and the results for the composite with a hybrid filler are given in Table 3. Analysis of data Table 3 showed that the introduction of a hybrid filler into the PTFE matrix significantly increases the hardness of the polymer composite. An increase in the hardness of Vickers of the polymer composite with a hybrid filler is explained by the fact that the hybrid filler has a higher hardness. The hardness of individual fillers according to Vickers is [14–16]. The Vicker hardness of pure PTFE is only 19 MPa. It is known that the introduction of inorganic particles significantly increases the mechanical characteristics of composites, including hardness [17].

4   Conclusion

In this work, a nanostructured polymer composite based on PTFE with a hybrid filler was fabricated by solid-phase mixing and hot pressing. Tungsten carbide, boron carbide, bismuth oxide and titanium hydride were used as a hybrid filler with different average particle sizes from submicron to micron. It has been established that the hybrid filler, regardless of the particle size, is evenly distributed over the PTFE matrix. Defects, cracks and pores were not found in the polymer composite. It is shown that the hardness of PTFE with hybrid filler increased to 27 MPa.
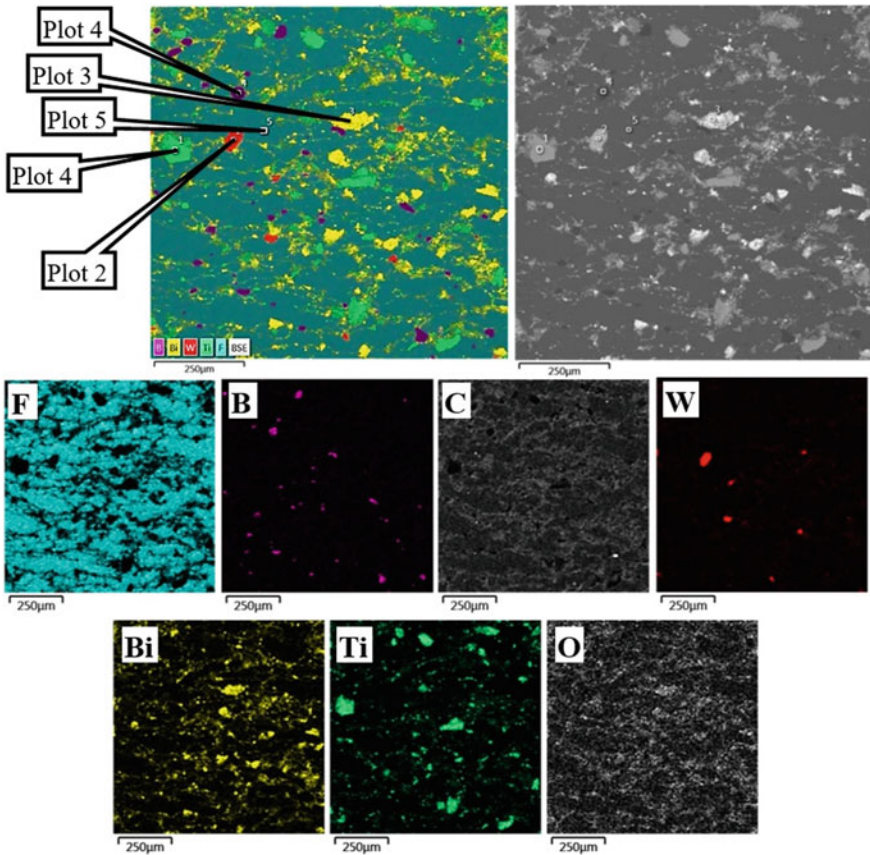
Fig. 3 EDX spectroscopy of the transverse section of the polymer composite

Table 2 The composition of the cross section of the polymer composite in individual plots

Location	EDX-spectroscopy, wt%						
	F	B	C	Bi	W	Ti	O
Plot 1	0.82	–	1.90	–	–	91.37	5.91
Plot 2	5.18	–	38.56	–	50.71	–	4.71
Plot 3	2.45	–	24.98	63.49	–	–	9.08
Plot 4	0.13	68.85	29.82	–	–	0.08	1.08
Plot 5	70.48	–	29.52	–	–	–	–

Table 3 Hardness of the developed composites

Material	Hardness, MPa
PTFE	19 ± 0.67
PTFE with filler	27 ± 0.56

References

1. Lv, M., Zheng, F., Wang, Q., Wang, T., Liang, Y.: Friction and wear behaviors of carbon and aramid fibers reinforced polyimide composites in simulated space environment. Tribol. Int. **92**, 246–254 (2015)
2. Hu, Y., Zhang, Y., Liu, H., Zhou, D.: Microwave dielectric properties of $PTFE/CaTiO_3$ polymer ceramic composites. Ceram. Int. **37**(5), 1609–1613 (2011)
3. Liu, S., Dong, C., Yuan, C., Bai, X., Tian, Y., Zhang, G.: A new polyimide matrix composite to improve friction-induced chatter performance through reducing fluctuation in friction force. Compos. B Eng. **217**, 108887 (2021)
4. Lyashkov, A.Y., Makarov, V.O., Plakhtii, Y.G.: Structure and electrical properties of polymer composites based on tungsten oxide varistor ceramics. Ceram. Int. **48**(6), 8306–8313 (2022)
5. Pavlenko, V.I., Cherkashina, N.I., Yastrebinsky, R.N.: Synthesis and radiation shielding properties of polyimide/Bi_2O_3 composites. Heliyon **5**(5), e01703 (2019)
6. Kaçal, M.R., Akman, F., Sayyed, M.I.: Evaluation of gamma-ray and neutron attenuation properties of some polymers. Nucl. Eng. Technol. **51**(3), 818–824 (2019)
7. Nambiar, S., Yeow, J.T.: Polymer-composite materials for radiation protection. ACS Appl. Mater. Interfaces. **4**(11), 5717–5726 (2012)
8. Aldhuhaibat, M.J., Amana, M.S., Jubier, N.J., Salim, A.A.: Improved gamma radiation shielding traits of epoxy composites: evaluation of mass attenuation coefficient, effective atomic and electron number. Radiat. Phys. Chem. **179**, 109183 (2021)
9. Cao, D., Yang, G., Bourham, M., Moneghan, D.: Gamma radiation shielding properties of poly (methyl methacrylate)/Bi_2O_3 composites. Nucl. Eng. Technol. **52**(11), 2613–2619 (2020)
10. Uddin, Z., Yasin, T., Shafiq, M., Raza, A., Zahur, A.: On the physical, chemical, and neutron shielding properties of polyethylene/boron carbide composites. Radiat. Phys. Chem. **166**, 108450 (2020)
11. Soylu, H.M., Yurt Lambrecht, F., Ersöz, O.A.: Gamma radiation shielding efficiency of a new lead-free composite material. J. Radioanal. Nucl. Chem. **305**(2), 529–534 (2015)
12. Noor Azman, N.Z., Siddiqui, S.A., Haroosh, H.J., Albetran, H.M., Johannessen, B., Dong, Y., Low, I.M.: Characteristics of X-ray attenuation in electrospun bismuth oxide/polylactic acid nanofibre mats. J. Synchrotron Radiat. **20**(5), 741–748 (2013)
13. Kaloshkin, S.D., Tcherdyntsev, V.V., Gorshenkov, M.V., Gulbin, V.N., Kuznetsov, S.A.: Radiation-protective polymer-matrix nanostructured composites. J. Alloy. Compd. **536**, S522–S526 (2012)

14. Thevenot, F.: Boron carbide a comprehensive review. J. Eur. Ceram. Soc. **6**(4), 205–225 (1990)
15. Csanádi, T., Bl'anda, M., Chinh, N.Q., Hvizdoš, P., Dusza, J.: Orientation-dependent hardness and nanoindentation-induced deformation mechanisms of WC crystals. Acta Materialia **83**, 397–407 (2015)
16. Mwamba, I.A., Chown, L.H.: The use of titanium hydride in blending and mechanical alloying of Ti-Al alloys. J. South Afr. Inst. Min. Metall. **111**(3), 159–165 (2011)
17. Xu, J., Yan, H., Gu, D.: Friction and wear behavior of polytetrafluoroethene composites filled with Ti_3SiC_2. Mater. Des. **61**, 270–274 (2014)

Finite Element Modeling of the Work of Bent Reinforced Concrete Elements of Rectangular Section in the Abaqus Software Environment

P. A. Amelin[1]([✉]) , V. I. Rimshin[2] , A. A. Kryuchkov[1] , and D. V. Obernikhin[1]

[1] Belgorod State Technological University Named After V.G. Shukhov, Belgorod, Russia
`p.amelin@inbox.ru`
[2] National Research Moscow State University of Civil Engineering, Moscow, Russia

Abstract. In this work, by numerical simulation using the Abaqus software package, the stress–strain state of a bent reinforced concrete element of a rectangular cross section is investigated. Numerical modeling of the element is performed by volumetric finite elements, taking into account the non-linear (actual) state diagram of concrete, described by the model of plastic fracture of concrete with damage (CDP). Reinforcement is specified by rod finite elements, with a combination of elastic properties and metal plasticity model. The loading of the beam element in the model is performed statically with the application of concentrated forces at the centers of the thirds of the design span. As a result of the finite element calculation, the distribution of stresses in concrete and reinforcement according to Mises, deformations of finite elements along the main axes, as well as a model of concrete damage with increasing load were obtained. The results obtained showed a high convergence with the experimental data of testing beams for bending along a normal section, which allows using this algorithm for automated finite element analysis in the design of bending reinforced concrete structures.

Keywords: Finite Element Method (FEM) · Plastic Damage Model (CDP) · Abaqus · Strength · Deformability · Breaking Moment

1 Introduction

For the calculation of building structures, automated software systems based on the finite element method (FEM) are increasingly used, which is a numerical method for solving partial differential equations, as well as integral equations that arise in solving problems of applied physics [1].

An urgent problem in the calculation of reinforced concrete structures using automated finite element analysis systems is to take into account the nonlinear relationship between stress and deformation of concrete, the formation of cracks and their propagation caused by tensile deformation, the joint work of concrete and reinforcement.

Many researchers have been developing methods for calculating the strength of normal sections of bending elements using a nonlinear (actual) state diagram concrete [2–6]. It has been established that due to the complexity and number of mathematical

iterative processes, these calculations can only be performed using computer technology using special programs.

Simulia Abaqus is one of the advanced finite element modeling software packages for structural performance, which has the ability to calculate the stress–strain state under static and dynamic loading, taking into account the physically and geometrically non-linear behavior of materials (including concrete creep), as well as the contact interaction between structural elements [7].

In the Abaqus software package, the nonlinear behavior of concrete is specified using the plastic fracture model for damaged concrete (CDP) [8]. The plastic fracture model of damaged concrete has its own characteristics:

- provides a general possibility of modeling concrete and other quasi-brittle materials in all types of structures;
- uses the principle of isotropic elastic damage in combination with isotropic plasticity to model non-linear concrete;
- designed for conditions in which concrete is subjected to various types of loading—smoothly increasing, cyclic or dynamic;
- consists of a combination of unbound multilevel plasticity and scalar (isotropic) elastic damage to describe the irreversible damage that occurs during the cracking process;

The development of the concrete failure mechanism is controlled by two variables $\tilde{\varepsilon}_t^{pl}$ and $\tilde{\varepsilon}_c^{pl}$, , which are respectively tensile and compressive equivalent plastic deformations. Theoretical regularities describe the effects of irreversible damage accumulation in concrete and other quasi-brittle materials at sufficiently low stresses. According to the model, the uniaxial behavior of concrete in compression and tension is characterized by plastic fracture (Fig. 1).
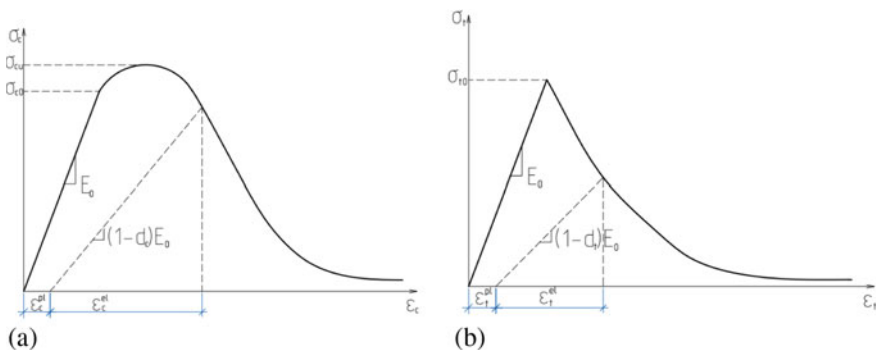

Fig. 1 Behavior of concrete in uniaxial: **a** compression; **b** tension

When a concrete sample is unloaded from any point in the stress–strain curve, the unloading response is weakened, the elastic stiffness of the material is damaged. Elastic stiffness degradation is characterized by two damage coefficients d_t and d_c, ranging from 0 (for undamaged materials) to 1 (completely destroyed material), which are functions of plastic deformations, temperature and other variables.

If E_0 is the initial (intact) elastic stiffness of the material, then the ratios of stresses and strains under uniaxial tension and compression load are equal to:

$$\sigma_t = (1 - d_t)E_0\left(\varepsilon_t - \tilde{\varepsilon}_t^{pl}\right) \tag{1}$$

$$\sigma_c = (1 - d_c)E_0\left(\varepsilon_c - \tilde{\varepsilon}_c^{pl}\right) \tag{2}$$

Nonlinear deformations of concrete during compression and tension are determined by the formulas:

$$\varepsilon_b^{in} = \varepsilon_b - \frac{\sigma_b}{E_b} \tag{3}$$

$$\varepsilon_{bt}^{in} = \varepsilon_{bt} - \frac{\sigma_{bt}}{E_{bt}} \tag{4}$$

Plastic deformations of concrete during compression and tension are determined by the formulas:

$$\varepsilon_b^{pl} = b_c \cdot \varepsilon_b^{in} \tag{5}$$

$$\varepsilon_{bt}^{pl} = b_t \cdot \varepsilon_{bt}^{in} \tag{6}$$

where b_c и b_t—parameters of cyclic loading under compression and tension according to [9].

The coefficients of damage to heavy concrete in compression and tension are determined by the formulas:

$$d_b = 1 - \frac{\sigma_b}{E_b \cdot \left(\varepsilon_b - \varepsilon_b^{pl}\right)} \tag{7}$$

$$d_{bt} = 1 - \frac{\sigma_{bt}}{E_b \cdot \left(\varepsilon_{bt} - \varepsilon_{bt}^{pl}\right)} \tag{8}$$

2   Methods and Materials

In this work, the author simulated the operation of a reinforced concrete beam of rectangular cross section during a bending test, the results of which are compared with experimental data [9] for a reinforced concrete beam of rectangular cross section made of concrete, which has compressive strength class B225 and density 2300 kg/m³. Reinforcement of the beam is carried out by a single frame, hot rolled steel rebar was used as the working and structural reinforcement of the frames with diameter Ø 12 mm tensile strength class A500 and with diameter Ø 8 mm tensile strength class A240. The role of transverse reinforcement is performed by cold-drawn wire Ø 5 mm from low carbon steel tensile strength class B500. The geometric dimensions and the reinforcement scheme of the reinforced concrete beam are shown in Fig. 2.
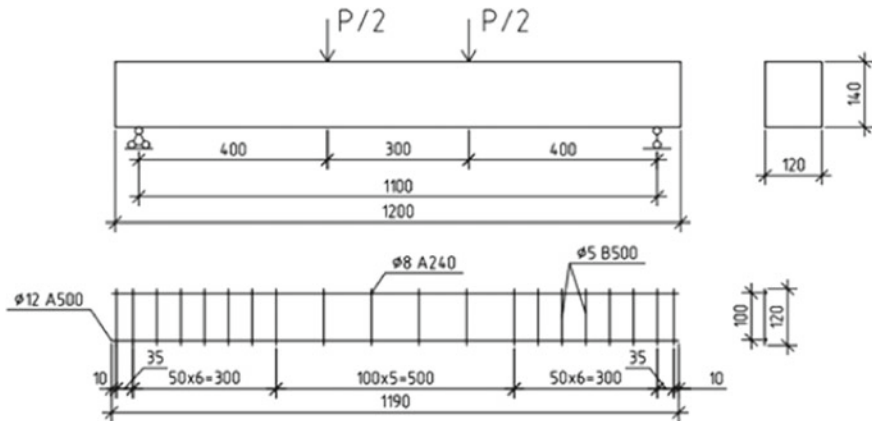
Fig. 2 Scheme of reinforcement and loading of a reinforced concrete beam

The geometric characteristics of the reinforced concrete beam were set by volumetric and bar elements for the concrete body and reinforcement bars, respectively.

The physical and mechanical characteristics of concrete were set by elastic and plastic properties (Table 1), which were determined by formulas (3–8).

The initial dependences of compressive and tensile stresses σ_c and σ_t, as well as concrete deformations in compression and tension ε_c и ε_t were obtained from the experimental diagram of the state of concrete given in [10]. For reinforcement, a combination of elastic properties and metal plasticity models, presented in Table 2, was also used.

The beam was loaded in increments of 5% of the breaking load Pcp, which was 40,218 кН. The task of the static load was carried out using two steel plates 120 × 50 × 20 mm, which were located along the edges of the central third of the calculated span. Calculation scheme—hinged beam on two supports.

The first support was limited in moving along the planes U1, U2, U3, the second— along the planes U1 и U2. Further, the places of contact interaction of the studied beam, supports and load application elements were determined. Ultimately, the model of the concrete body and supports was divided into three-dimensional finite elements; the reinforcement was divided into segments.

3 Results and Discussion

As a result of the finite element calculation, the Mises stress distributions in concrete and reinforcement were obtained (Fig. 3), deformations of finite elements along the main axes (Fig. 4), as well as a concrete damage model with increasing load.

To verify the results of this study with experimental data, the criteria were chosen: the load of cracking and the value of the maximum deflection of the beam f at loads of 16, 24 and 32 кН. The cracking load in this case is the load value at which the relative deformations in the tensile concrete zone reach the limit values ε_{bt}, equal to 0.00012 (Fig. 5).

Based on the results of numerical simulation and experimental data presented in Table 3, the following conclusions can be drawn:

Table 1 Physical and mechanical characteristics of concrete

Initial modulus of elasticity Eb, MPa		Poisson's ratio	
31,500		0.2	
Stresses and strains in compression		Compressive damage to concrete	
Yield stress σ_b, MPa	Inelastic strain ε_b^{in}	Damage parameter d_b	Inelastic strain ε_b^{in}
12.5	0	0	0
14.779363	0.000015	0	0.000015
16.897181	0.00004	0	0.00004
18.815096	0.000079	0	0.000079
20.499689	0.000132	0	0.000132
21.925443	0.000202	0	0.000202
22.354643	0.001964	0.105814	0.001964
20.860155	0.002386	0.165594	0.002386
19.314226	0.002811	0.227431	0.002811
18.549152	0.003023	0.258034	0.003023
17.069142	0.003445	0.317234	0.003445
15.682397	0.00386	0.372704	0.00386
14.404665	0.004268	0.423813	0.004268
13.23977	0.004669	0.470409	0.004669
12.184584	0.005062	0.512617	0.005062
11.69608	0.005257	0.532157	0.005257
9.977867	0.006019	0.600885	0.006019
8.905476	0.006576	0.643781	0.006576
7.5	0.007448	0.7	0.007448
Tensile stresses and strains		Tensile damage to concrete	
Yield stress σ_{bt}, MPa	Cracking strain ε_{bt}^{in}	Damage parameter d_{bt}	Cracking strain ε_{bt}^{in}
3	0	0	0
1.664354	0.000281	0.445215	0.000281
1.179148	0.000507	0.606951	0.000507
0.76383	0.000923	0.74539	0.000923
0.573836	0.001324	0.808721	0.001324
0.512265	0.001522	0.829245	0.001522
0.463463	0.00172	0.845512	0.00172
0.423761	0.001917	0.858746	0.001917

(*continued*)

Table 1 (*continued*)

Initial modulus of elasticity Eb, MPa		Poisson's ratio	
31,500		0.2	
Stresses and strains in compression		Compressive damage to concrete	
Yield stress σ_b, MPa	Inelastic strain ε_b^{in}	Damage parameter d_b	Inelastic strain ε_b^{in}
Parameters of the plastic fracture model for damaged concrete (CDP)			
Dilation angle	Eccentricity	f_{b0}/f_{c0}	Viscosity Parameter
35	0.1	1.16	0.667

Table 2 Metal plasticity model parameters

Initial modulus of elasticity E_s, MPa		Poisson's ratio
210,000		0.3
	Tensile stresses and strains	
Yield stress σ_s, MPa		Plastic strain ε_s^{in}, %
	Rebar A240	
160		0
240		0.19
	Rebar A500	
372		0
500		0.23
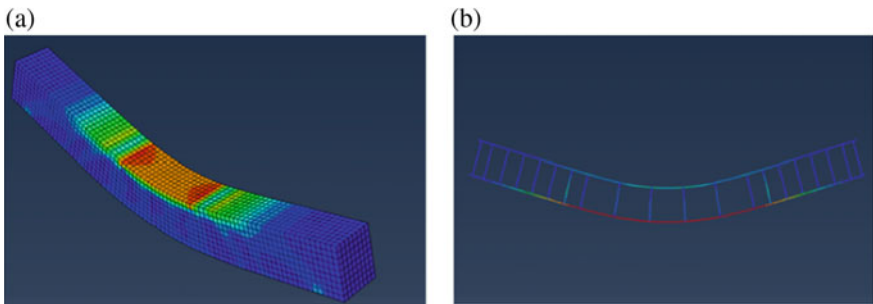
Fig. 3 Mises stress distribution, MPa: **a** concrete; **b** reinforcement

- calculated deflection of the beam at a load of 16 kN is 2% less, at a load of 24 kN it is 3.6% more, and at a load of 36 kN it is 1.8% less than the average experimental values of deflections, respectively;
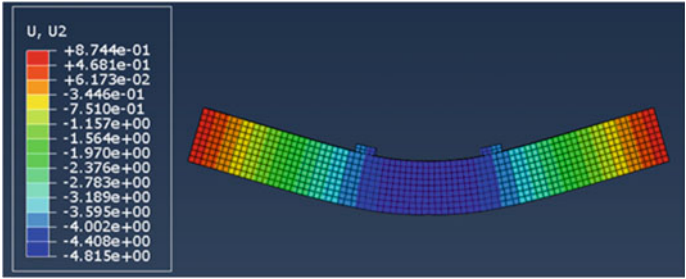
Fig. 4 Deformations along the vertical axis U2 (beam deflections f) at a load of 32 kN
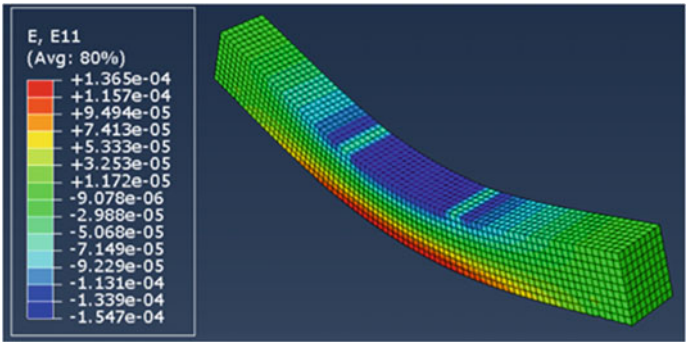
Fig. 5 Relative deformations in concrete at a load of 6.85 kN

Table 3 Metal plasticity model parameters

Load кН	Maximum stresses of concrete (according to Mises), MPa	Maximum reinforcement stresses (according to Mises), MPa	Deflection, mm	Fracturing load, кН
16	10.97	152.5	1.726	6.85
24	17.05	279.1	3.343	
32	21.3	372.6	4.815	

- concrete in the tensile zone reaches the limiting tensile value at a load of 6.85 kN, which is the moment of cracking. The calculated load turned out to be 4.9% more than the experimental one.

4 Conclusion

The above results confirm the high convergence with the experimental values, which indicates the accuracy of the applied ductile failure model for damaged concrete (CDP) in Simulia Abaqus.

References

1. Karpunin, V., Golubeva, E.: Computer modeling of building structures of buildings and structures. Architecton: Proceedings of Higher Education **4**(68), 17 (2019)
2. Raghu, P., Rajagopal, A., Reddy, J.N.: Nonlocal nonlinear finite element analysis of composite plates using TSDT. Compos. Struct. **185**, 38–50 (2018). https://doi.org/10.1016/J.COMPST RUCT.2017.10.075
3. Bondarenko, V., Rimshin, V.: Quasi-linear equations of force resistance and the diagram σ - ε of concrete. Structural Mechanics of Engineering Constructions and Buildings **6**, 40–44 (2014)
4. Varlamov, A.: Models of concrete behavior. Behavior models of concrete. General theory of degradation. Moscow: Limited Liability Company "Scientific Publishing Center INFRA-M", 436 (2019). https://doi.org/10.12737/monography_5c8a716e3c4460.52838016
5. Kryuchkov, A.A., Frolov, N.V., Smolyago, G.A.: Stress-strain state of normal sections of precast-monolithic reinforced concrete beams. Lecture Notes in Civil Engineering **95**, 38–44 (2021). https://doi.org/10.1007/978-3-030-54652-6_6
6. Travush, V.: Issues of improving building standards. In: Travush, VI, Sharipov, R.S., Volkov, Y.S. (eds.) Concrete and reinforced concrete. No. 4(606), pp. 3–7 (2021)
7. Abaqus/CAE User,s Guide 2016. http://manualzilla.com/doc/5731215/abaqus-cae-user-s-manual. Last accessed 24 June 2022
8. Nikaido, Y., Mihara, Y., Sawada, S., Takahashi, Y.: Improvement and enhancement of concrete damage plasticity model. Simulia Community Conference Proceedings (2015)
9. Obernikhin, D., Nikulin, A.: Experimental studies of the strength, crack resistance and deformability of reinforced concrete beams of trapezoidal and rectangular cross sections. Innovative Science. **8–2**, 73–77 (2016)
10. Popov, V.M., Plyusnin, M.G.: Influence of deformation characteristics of concrete on the bearing capacity of flexible reinforced concrete elements. Industrial and Civil Construction **8**, 5–10 (2015)

Clay-Slag Autoclaved Composite Materials with the Usage of Activated Aluminosilicate Raw Materials

Yu. L. Makridina , I. V. Starostina(✉) , A. S. Lushnikov , and R. G. Shevtsova

Belgorod State Technological University Named After V.G. Shukhov, Belgorod, Russia
starostinairinav@yandex.ru

Abstract. In order to expand the raw materials base of building materials industry, not only industrial waste, but the off-grade natural aluminosilicate raw materials— clay minerals of incomplete mineral-forming stages,—have been more and more involved into the industrial usage. As initial materials the steelmaking slag with basicity factor 1.15 and characterized as neutral and the clay-containing component—sandy loam—were used in this study. The paper presents the results of dry milling and MW (microwave) treatment of sandy loam influence on strength properties of clay-slag autoclaved silicate concretes. It has been demonstrated that dry milling of sandy loam provides the highest gain of specific surface—26.15%, while using the MW-field (power 800 W, 2 min.) increases the specific surface by only 8.83% in comparison with the original sample. Then the reactive properties of mechanically activated sandy loam are considered. The reactive properties of sandy loam, modified with microwave radiation, are composed of the increased sorption capacity to $Ca(OH)_2$ of the dispersed clay minerals and reactive polymorphic modifications of quartz. At the optimal ratio, wt%, clay component: slag = 40:60 the highest strength properties were obtained at using the sandy loam, activated in the microwave field at the following radiation parameters—power 800 W, treatment time 2 min. The gain of strength properties made up 60% as compared to the non-activated sandy loam.

Keywords: Off-Grade Aluminosilicate Raw Materials · Sandy Loam · Mw (Microwave Radiation) Treatment · Mechanical Activation · Dry Milling · Specific Surface · Reactivity · Ultimate Compressive Strength

1 Introduction

In recent years, for the purpose of building materials industry raw material base expansion, not only the industrial waste, but the off-grade natural aluminosilicate raw materials as well, have been more and more involved into the industrial application.

Research works by scientists from BSTU named after V.G. Shukhov in the field of obtaining autoclaved silicate materials of compact or cellular structure [1, 2] have confirmed the efficiency of using the off-grade, including by-product, raw materials, containing a significant amount of clay minerals of incomplete mineral-forming stages. The usage of high-calcium fly ash, formed at solid-fuel combustion, is also known.

In the work [3] the application of nanostructured aluminosilicate modifier on the basis of magmatic acidic rock—granite—in the raw charge for autoclaved gas silicate production is substantiated. Research has shown that adding the nanostructured modifier instead of cement provides the structure-forming action of the component in the process of materials curing before autoclaving, which stabilizes the strength of raw materials. At the same time the modifier interacts with calcium hydroxide, forming different-sized formations of various compositions, which increases the strength of not only the raw material body, but also improves the strength and performance properties of finished products and structures in atmospheric conditions. Adding nanostructured granite-based modifier in the range of 20–40% increases strength properties by 5–15% in comparison with the control samples.

In the work [4] it has been determined that thermal and electron-beam treatment of silica-containing aggregates and active mineral admixtures—quartz sand, metakaolin and microsilica—influences their chemical activity to alkaline-silicate reactions in sand-cement mortars and concretes. After electron-beam treatment the building quartz sand takes on the properties of a reactive aggregate, which is due to polymorphic transformations of quartz into high-temperature modifications of SiO_2—tridymite, cristobalite, α-quartz.

To improve the quality of ceramic bricks, a two-stage activation of argillous raw materials was used. The combination of mechanical-thermal treatment of clay rock (grinding in a ball mill) with the shock-wave activation of slip clay, obtained on the basis of clay raw material's dust fraction, was tested. It was demonstrated that the combination of drying (heat carrier temperature 200–400 °C) and milling to particle size 0.06 mm provided partial dehydration of clay minerals, increasing their amorphicity and structure imperfection. The activation of slip clay increases the content of particles less than 5 μm, which increases the viscosity and stability of slip clay. The usage of activation methods allows producing facing brick with low content of clay fractions and high strength properties.

It is known that the mechanical-chemical activation of clinkerless binders on the basis of natural and by-product Trans-Baikal raw materials allows reducing the autoclaving time of silicate materials with these components, or even switching to out-of-autoclave treatment while retaining their physical–mechanical characteristics.

In a number of works [5–7] the usage of super-high-frequency (microwave) electromagnetic radiation treatment of sand-cement mortars to intensify cement hydration processes is shown. Microwave radiation intensifies and accelerates the processes of dissolving and hydration of cement, which results in fine-crystalline structures formation, reduces porosity, increases the density, strength, frost-resistance and durability of materials in general.

The purpose of this work is to study the influence of various methods of argillous raw materials activation—microwave electromagnetic radiation treatment and mechanical activation,—on physical–mechanical characteristics of clay-slag autoclaved composite materials.

2 Methods and Materials

As original raw component for carrying out the research the steelmaking slag of JSC «United Metallurgical Company Stal» (JSC «UMC-Stal»), Vyksa, Russia, was used, the chemical composition of which is presented in Table 1. A distinctive feature of this slag is low content of MgO and high content of Al_2O_3 and iron oxides.

Table 1 Chemical composition of slag, wt%

CaO	SiO$_2$	MnO	MgO	SO$_3$	Cr$_2$O$_3$	Fe$_2$O$_3$	Al$_2$O$_3$	R$_2$O	TiO$_2$	Basicity factor, M$_o$
33.11	19.85	3.73	4.95	0.22	1.17	27.47	7.70	0.50	0.48	1.15

According to the data in Table 1, the slag has basicity factor 1.15, and, consequently, is neutral, characterized with structure stability, and can be classified as non-slaking.

According to the X-ray phase analysis data (Fig. 1), the basic minerals of the slag include β-dicalcium silicate (larnite), melilite, iron oxides—wustite and magnetite, and some amount of free calcium hydroxide.
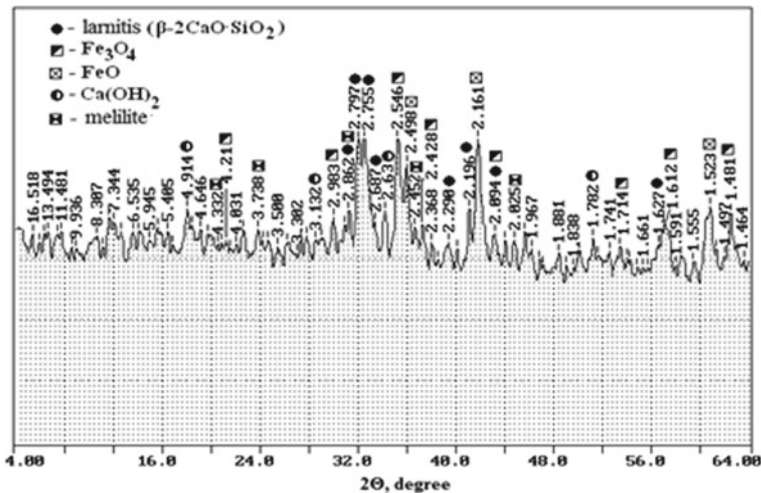
Fig. 1 X-ray phase analysis of steelmaking slag from JSC «UMC-Stal», Vyksa, Russia

As an argillous raw material for obtaining clay-slag autoclaved composite materials the sandy loam from deposit in Volokonovka settlement, Belgorod region, Russia, was used.

This sample is presented with light-brown medium-density loose rock, the chemical composition of which is presented in Table 2. The mineral composition of sandy loam was evaluated on the basis of integrated research—the X-ray phase analysis and differential thermal analysis findings (Fig. 2, Table 3).

Table 2 Chemical composition of sandy loam, wt%

SiO_2	Al_2O_3	CaO	Fe_2O_3	MgO	K_2O	TiO_2	Na_2O	P_2O_5	SO_3	MnO
67.97	13.88	6.15	4.43	2.92	1.96	0.69	0.75	0.10	0.90	0.06
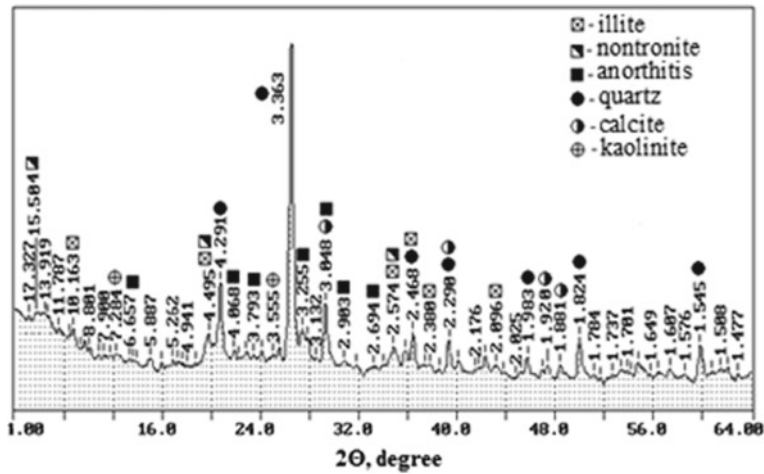
Fig. 2 X-ray phase analysis of sandy loam

Table 3 Differential thermal analysis results

Mineral	Ionic formula	Effects: endothermic (–), exothermic (+)	
		By Ramachrandran temperature, ℃	Analyzed sample temperature, ℃
Illite	$K_{<1}Al_{<2}[(Si,Al)_4O_{10}][OH]_2\,nH_2O$	(–) 110–125	(–) 114.5
		(–) 500–650	(–) 512.8
Kaolinite	$Al_2O_3·2SiO_2·2H_2O$	(–) 105–115	(–) 114.5
Calcite	$CaCO_3$, containing magnesite	(–) 700	(–) 752.7

According to the research findings, the sandy loam is characterized with polymineral composition, and contains three groups of clay minerals—kaolinite, minerals of montmorillonite group (nontronite) with prevailing hydromicaceous components (illite, anorthite). The presence of some impurity minerals—calcite, hematite and free silica—should be also noted.

The microwave treatment of sandy loam was carried out in a microwave oven Samsung at radiation power 300, 600 and 800 W for 2, 4 and 6 min. Mechanical activation of sandy loam was performed by dry milling in a porcelain mill for 5 h.

The weighed raw components were mixed and moistened with water to moisture content 28%. The cylindrical samples of clay-slag composite materials 3 cm high and 3 cm in diameter were shaped by semidry molding at specific pressure 20 MPa, and autoclaved under factory conditions at steam pressure 1 MPa.

The samples of raw sandy loam and sandy loam after various activation methods were researched for their grain-size composition and sorption activity to $Ca(OH)_2$ from a saturated water solution. The sorption capacity of sandy loam, mg/g, was determined by the formula 1:

$$A = \frac{(C_i - C_f) \cdot V}{m_a} \tag{1}$$

where C_i and C_f—initial and final concentrations of $Ca(OH)_2$, mg/dm^3; V—volume of $Ca(OH)_2$ solution, dm^3; ma—mass of sandy loam, g.

3 Results and Discussions

Based on the research findings it has been determined that the increase of microwave treatment power of sandy loam results in the increase of its specific surface and its activity to alkaline components—$Ca(OH)_2$.

The dry milling of loam provides the highest gain of specific surface—26.15%, while using the MW-field (800 W, 2 min.) increases the specific surface by only 8.83% in comparison with the original sample (Fig. 3). The reactive properties of mechanically activated sandy loam are considered below (Table 4).

It is safe to assume that the increase of sandy loam's specific surface under the action of microwave radiation is explained, first of all, by dispergation of clay minerals. The treatment of siliceous component, according to [8], results in its considerable activation without dispergation, and, according to findings in work [4], the polymorphic transition of quartz into cristobalite and/or tridymite is possible.

The reactive properties of sandy loam, modified by magnetic radiation of microwave frequencies, are made of the increased sorption capacity to $Ca(OH)_2$ of the dispersed clay minerals and reactive polymorphic modifications of quartz.

In case of sandy loam dry milling, the increase of its specific surface is explained, most of all, by pulverization of its quartz component, which also determines its increased adsorption properties to $Ca(OH)_2$ in comparison with the initial material.

So, after microwave treatment the sandy loam takes on the properties of a reactive component for silicate concrete.

The results, presented in Fig. 4, have demonstrated that at the optimal ratio, wt%, clay component: slag = 40:60 the highest strength properties were obtained at using the sandy loam, activated in the microwave field at the following radiation parameters—power 800 W, treatment time 2 min. The gain of strength properties made up 60% in comparison with using the initial sandy loam.

So, the microwave treatment of sandy loam promotes its considerable activation, manifested in the alteration of physical–chemical processes of clay-slag silicate concrete hardening products in conditions of autoclave curing. The gain of strength properties made up 60% as compared to the initial sandy loam.
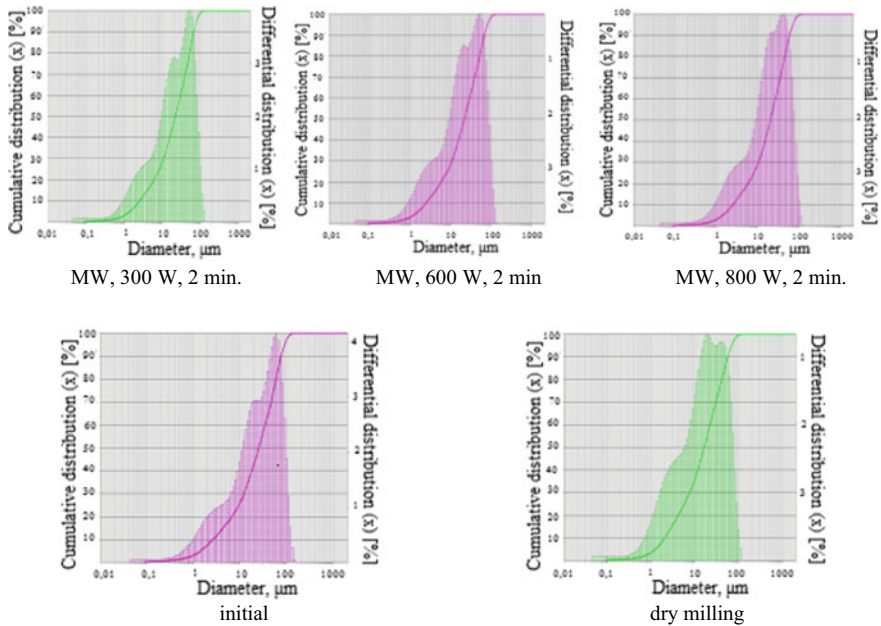
MW, 300 W, 2 min.   MW, 600 W, 2 min   MW, 800 W, 2 min.

initial   dry milling

Fig. 3 The influence of sandy loam activation conditions on its grain-size composition

Table 4 The influence of sandy loam activation conditions on some its characteristics

Material	Activation conditions	Specific surface, cm^2/g	Sorption capacity, mg/g
Initial sandy loam	–	3828	28.3
Activated sandy loam	MW field, power 300 W, 2 min	4074	36.3
	MW field, power 600 W, 2 min	4095	50.7
	MW field, power 800 W, 2 min	4166	98.6
	Dry milling	4829	73.1

4 Conclusion

Based on the results of the research, the following conclusions can be drawn:

- the reactive properties of sandy loam, modified by magnetic radiation of microwave frequencies, are made of the increased sorption capacity to $Ca(OH)_2$ of the dispersed clay minerals and reactive polymorphic modifications of quartz;
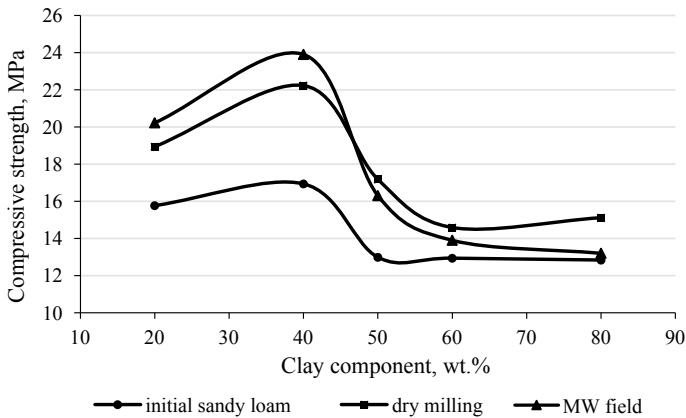
Fig. 4 Strength properties of clay-slag autoclaved silicate materials with the use of activated argillous raw materials

- optimal conditions for microwave processing of sandy loam—power 800 W, processing time 2 min;
- the use of sandy loam activated in a microwave field leads to a change in the physico-chemical processes of synthesis of autoclave hardening products of clay-slag silicate materials, which provides an increase in their strength properties by 60% compared with the use of untreated (initial) sandy loam.

References

1. Volodchenko, A.N., Lesovik, V.S., Zagorodnjuk, L.H., Glagolev, E.S.: On the issue of reducing the energy intensity of the silicate composites production with the unconventional aluminosilicate raw materials use. MSF **974**, 20–25 (2020)
2. Volodchenko, A.N., Nelybova, V.V.: Reactivity of the clay component of rocks at the incomplete stage of mineral formation to lime during autoclave processing. Lecture Notes in Civil Engineering **95**, 86–91 (2021)
3. Kapustin, F., Vishnevsky, A.: The use of fly ash in the production of concrete and products based on it. Solid State Phenom. **309**, 8–13 (2020)
4. Brykov, A.S., Panfilov, A.S., Mokeev, M.V.: Effect of metakaolin structure on its binding properties in alkaline hydration. Russ. J. Appl. Chem. **85**(5), 722–725 (2012). https://doi.org/10.1134/S1070427212050060
5. Avrenyuk, A.N., Rusyaev, E.L., Vilinchuk, V.L., Abutalipova, E.M.: Research of physical-mechanical properties of sand-cement mortars under the action of super-high-frequency electromagnetic radiation. Nanotechnologies in Construction **20**(6), 63–76 (2018)

6. Abutalipova, E.M., Bugai, D.E., Avrenyuk, A.N., Streltsov, O.B., Sungatullin, I.R.: Investigation of the effect of microwave-radiation energy flux on the structure and properties of polymeric insulating materials. Chem. Pet. Eng. **52**(3–4), 212–216 (2016). https://doi.org/10.1007/s10556-016-0177-6

7. Avrenyuk, A.N., et al.: Research of sand-cement mortars structure under the action of super-high-frequency electromagnetic radiation. Nanotechnologies in Construction **9**(5), 53–66 (2017). https://doi.org/10.15828/2075-8545-2017-9-5-53-66

8. Lapteva, S.N., Pavlenko, V.I., Gladkikh, Y.P.: MW-treatment of surface-modified quartz sand and its influence on hardening and strength of gypsum-sand composites. Bulletin of BSTU named after V.G. Shukhov **12**, 152–154 (2016). https://doi.org/10.12737/22649

Cellular Concrete Mixes with Bentonite Suspension

K. A. Suleymanov(✉) 🆔, V. S. Lesovik 🆔, and I. A. Pogorelova 🆔

Belgorod State Technological University Named After V.G. Shukhov, Belgorod, Russia
kloud09@mail.ru

Abstract. Bentonite is a clay obtained from volcanic rock. It is a type of smectite clay containing the mineral montmorillonite and a certain amount of quartz, feldspar, cristobalite, pyrite, illite, and mica. Montmorillonite is classified as a 2:1 clay mineral because it consists of two silicon tetrahedral sheets that share oxygen atoms with an octahedral aluminum sheet sandwiched between them. The authors studied the issue of using bentonite as an additive in gypsum plaster and putty mortars. The ability of bentonite to swell can be used to optimize the microstructure of threshold gypsum, increase the proportion of small pores, improve its thermal insulation and vapor permeability. A chemical and phase analysis of the composition of semi-aqueous gypsum and bentonite was carried out. At a ratio of bentonite/water of 1:5, unlike other ratios, there is no residual water on the surface of the mixture, bentonite is completely saturated with moisture. It is expedient to use such a ratio in further research to obtain a finely porous structure of threshold gypsum.

Keywords: Bentonite · Gypsum · Swelling Kinetics · Surface Sediment Volume · Pore Suspension

1 Introduction

The microclimate in a dwelling is an important aspect of a comfortable life of a person, since suitable relative humidity and indoor temperature have a beneficial effect on his health and well-being. To control temperature and humidity, heat-insulating (polystyrene foam, extruded polystyrene, porous material based on cement, airgel, etc.) and moisture-regulating materials (diatomite, sepiolite, zeolite, polymer resin, etc.) have been developed, respectively, inside buildings [1–3]. Gypsum plaster is also widely studied and used for energy saving in buildings due to fire resistance, low cost, safety and aesthetic appearance, heat insulation and moisture control abilities. However, the most important reason for the popularity of gypsum plasters is that calcium sulfate hemihydrates have been widely known as "green cements" due to their healthful contribution to environmental quality and reduced pollution by reducing CO_2 emissions [4]. Unfortunately, conventional gypsum plasters are less thermally insulating and moisture controlling than other porous materials, and several studies have focused on improving the thermal insulating and moisture controlling properties of gypsum plasters by adding modifiers,

lightweight aggregates, or air-absorbing materials [5, 6]. However, the high thermal conductivity and poor moisture control of lightweight gypsum plaster have hindered its development for interior applications.

An increase in the number of small pores in a porous material can reduce the thermal conductivity of air, as well as the transmission of gaseous components. This reduction leads to an improvement in thermal insulation properties. In addition, the increased and complex heat transfer path resulting from a higher proportion of fine pores for any given porosity can also contribute to a reduction in the thermal conductivity of porous materials [7]. Hardened gypsum plasters are composed of calcium sulfate dihydrate ($CaSO_4$ $2H_2O$), water and micron-sized voids, the void volume being increased by increasing the water content of the fresh plaster. However, the voids formed in this way are coarse (relatively large) and always result in low strength and high thermal conductivity for the same porosity due to the short heat transfer path and the relatively high thermal conductivity of the air, moreover it also leads to fresh paste bleeding [8]. In order to achieve a higher proportion of fine pores in gypsum without sacrificing setting properties, researchers are exploring other ways to introduce pores.

Bentonite is widely used, consisting mainly of montmorillonite. With inorganic binders together to meet application requirements [9], for example, bentonite is used as an additional binder to make up the shortage of raw materials and prepare cement-based raw materials, bentonite/cement mortar is used for waterproofing, stabilization and hardening of heavy metals. However, bentonite can swell when completely absorbed by water and lead to structural damage to engineering structures; gypsum, lime, cement, or combinations thereof are often used as stabilizers to prevent swelling. There are materials based on nanoporous cement by adding pre-swollen bentonite for thermal insulation of buildings, the formation of pores of which is due to the fact that pre-saturated bentonite consists mainly of several layers of montmorillonite and a large amount of water; water in pre-saturated bentonite cannot be completely absorbed by the hydration reaction, eventually forming tiny voids in the matrix [10]. If pre-swollen bentonite is added to the gypsum test, the volume of capillary voids in the gypsum may also increase. In addition, bentonite can be used to prevent gypsum from running out due to excess water, as montmorillonite layers strongly attract free water.

2 Methods and Materials

Bentonite (Tarbagatai region, Republic of Kazakhstan) consists mainly of montmorillonite with quartz. as shown in X-ray phase analysis (Fig. 1a).

Granulometric analysis was carried out in order to obtain information on the distribution of particles by size using a laser particle size analyzer and is presented in Fig. 2.

Gypsum hemihydrate was purchased from the Samara gypsum plant (Samara, Russia) and mainly consists of calcium sulfate hemihydrate, as shown in Fig. 1b.

A sample of powdered clay weighing 20 g was taken from the batch, placed in a pre-dried to constant weight and weighed bowl, and dried in an oven at a temperature of 106 °C for 30 min to constant weight. We weigh the bowl with a hinge. It was then dried for an additional 15 min and weighed again. The operation was repeated until the
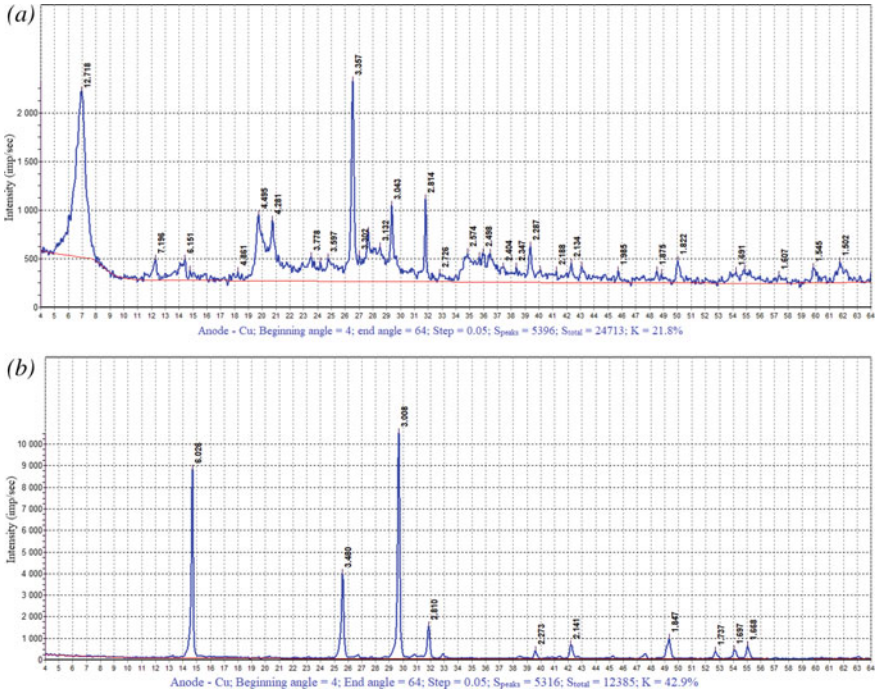
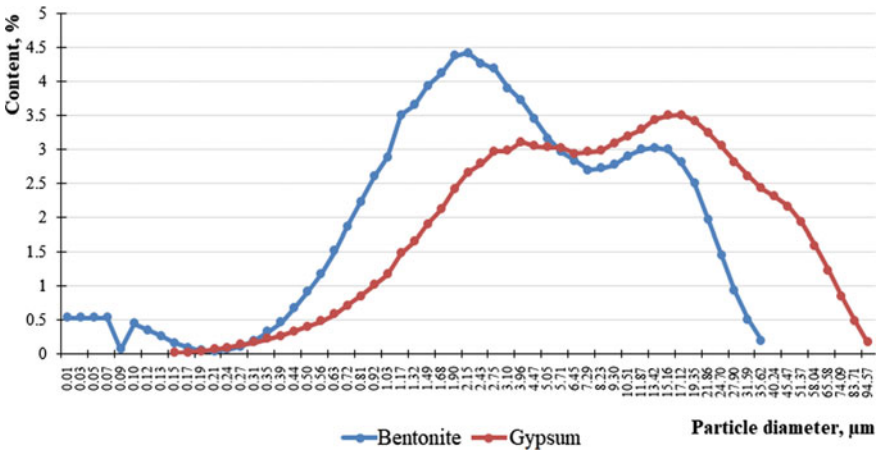**Fig. 1** X-ray phase analysis: **a** bentonite, **b** gypsum

Fig. 2 Granulometric composition of bentonite and gypsum

difference between the results of the last two weighing was no more than 0.02 g. The bowl with powdered clay dried to constant weight was cooled and weighed.

In the course of the data obtained, it was determined that the true moisture content of bentonite is 5.74%. In parallel, the moisture content of semi-aqueous gypsum was determined. The moisture content of gypsum was 4.55%.

In the course of the data obtained, it was determined that the true density of bentonite is 2.022 g/cm^3. In parallel, the true density of semi-aqueous gypsum was determined. The true density of gypsum was 2.453 g/cm^3.

Due to the inner surface and high dispersion, montmorillonite minerals in bentonite are characterized by a high specific surface area and cation exchange capacity, which determine their high physical and chemical activity, which decreases with an increase in the proportion of non-swellable interlayers [11, 12].

The specific surface area of bentonite and semi-aqueous gypsum was determined using a PSKh-10a instrument. The specific surface of bentonite was S = 3186 cm^2/g; semi-aqueous gypsum—S = 4874 cm^2/g.

The chemical compositions of the bentonite and gypsum were then determined by X-ray fluorescence spectroscopy on an ARL 9900 WorkStation X-ray fluorescence spectrometer.

The chemical composition of bentonite and gypsum is presented in Table 1 and in Figs. 3 and 4.

Table 1 Chemical composition of materials

Material	Chemical composition, %								
	SiO$_2$	Al$_2$O$_3$	CaO	MgO	SO$_3$	Fe$_2$O$_3$	Na$_2$O	TiO$_2$	Rest
Bentonite	58.07	23.51	4.75	3.97	–	3.61	3.8	0.66	1.63
Gypsum	1.32	0.47	47.69	1.36	48.77	0.18	–	0.01	0.20
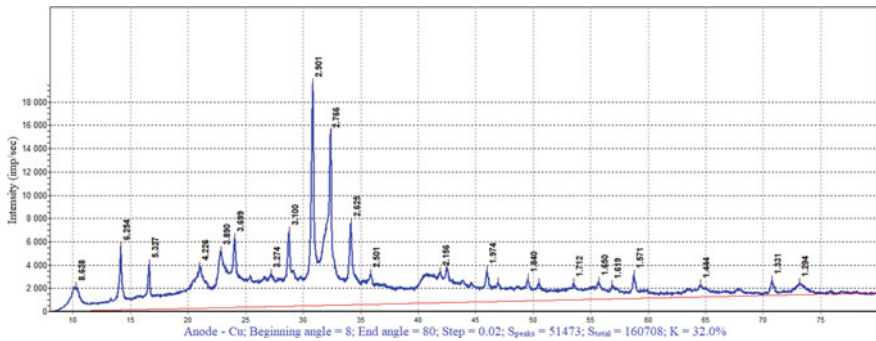
Fig. 3 The spectrum of chemical analysis of bentonite

3 Results and Discussion

The study of the microstructure of samples of bentonite and semi-aqueous gypsum was carried out using a scanning electron microscope (Figs. 5 and 6).
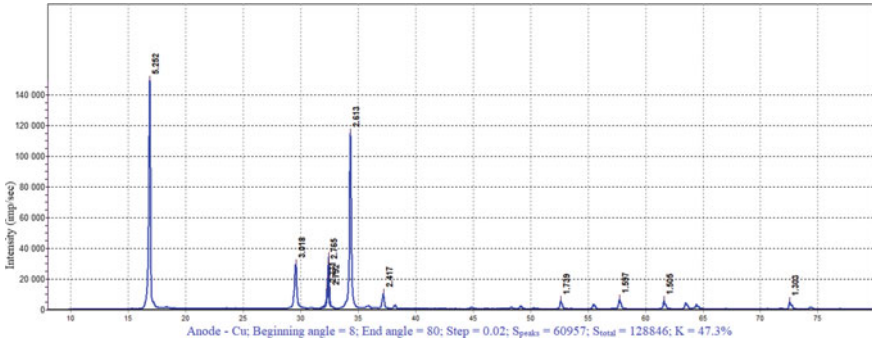
Fig. 4 Spectrum of chemical analysis of semi-aqueous gypsum
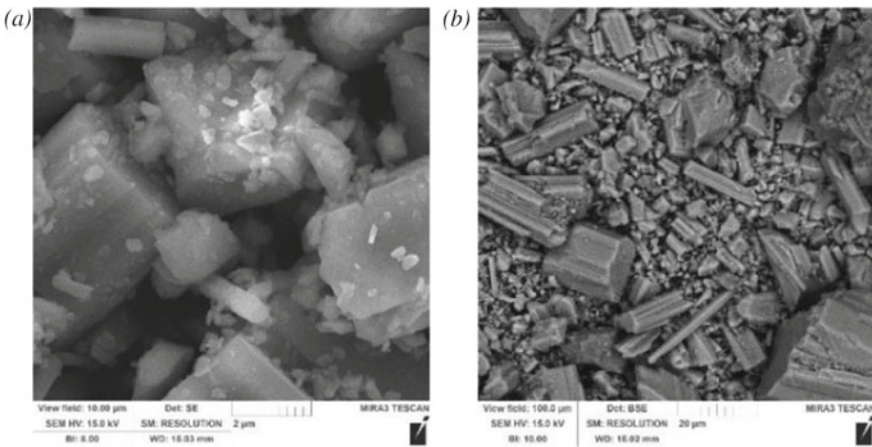
Fig. 5 Scanning electron microscopy of bentonite: **a** view area 10 μm; **b** view area 100 μm

The structure of bentonite consists of ultramicroaggregates of lamellar, leaf-shaped form with sizes up to 2 μm, consisting of aluminosilicate particles, micro- and macroaggregates up to 100 μm in size with a chaotic arrangement, and grains of quartz and hydromica.

The crystal structure of bentonite is based on two basic structural elements: silicon-oxygen tetrahedra $(SiO_4)^{4-}$ and octahedrons consisting of atomic cores of oxygen, OH groups and aluminum, magnesium, iron in octahedral position.

Visualization of the microstructure of gypsum hemihydrate showed that the samples consisted of small crystals of low density without a characteristic crystalline pattern.

When determining the optimal amount of bentonite in the threshold-gypsum mixture, it is necessary to strictly take into account the quality and quantity of liquid and solid phases capable of exchanging ions, as well as the kinetics of swelling of bentonites and structure formation of pore suspensions. As a result, an experiment was planned and carried out to determine the volume of surface sediment (water) at different bentonite/water ratios equal to 1:5, 1:10, 1:15, 1:20, 1:40, 1:50. Bentonite slurry was prepared by mixing
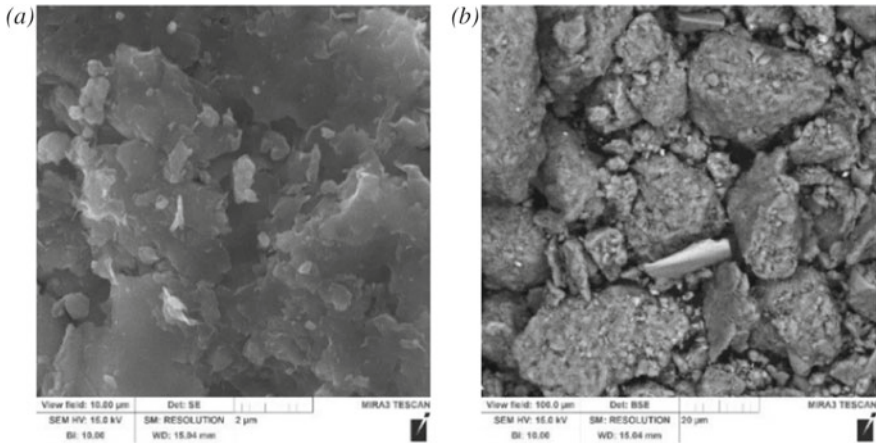
Fig. 6 Scanning electron microscopy of semi-aqueous gypsum: **a** view area 100 μm, **b** view area 1000 μm

tap water and bentonite for 1 h, and then leaving the mixture alone for 24 h to ensure complete hydration of the bentonite (Fig. 7).
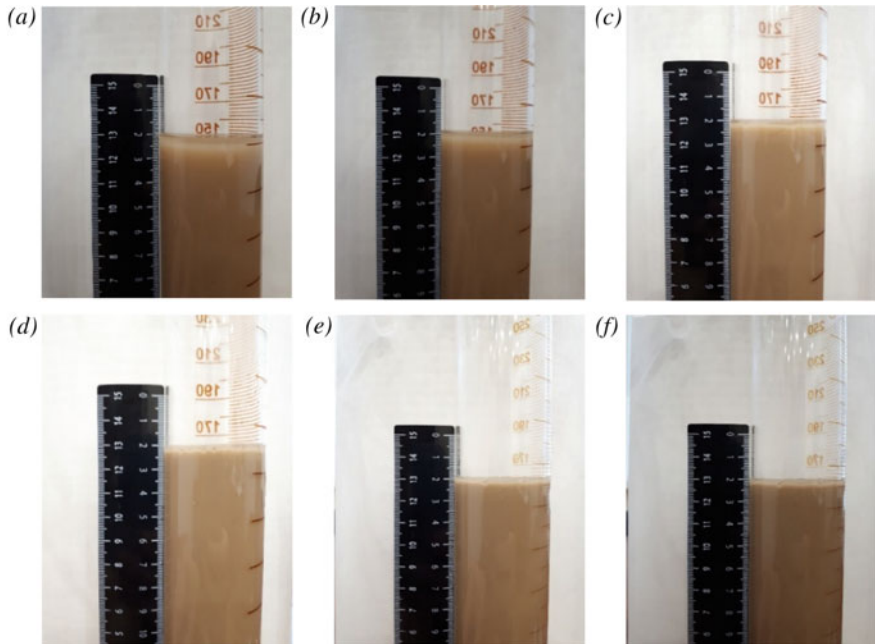
Fig. 7 Determination of surface sediment (water) of bentonite suspension at different ratios of bentonite: water: **a** 1:50 (6 mm), **b** 1:40 (4 mm), **c** 1:20 (3 mm); **d** 1:15 (2,5 mm); **e** 1:10 (1,5 mm); **f** 1:5 (0 mm)

The volume of surface sediment (which was mostly water) decreased significantly at bentonite/water ratios from 1:50 to 1:5, and was negligible at ratios less than 1:10. A visual study of the volume of the released surface sediment in the form of water at different ratios is shown in Fig. 7.

4   Conclusions

In this study, the issue of using bentonite as an additive in gypsum plaster and putty mortars was studied. The ability of bentonite to swell can be used to optimize the microstructure of threshold gypsum, increase the proportion of small pores, improve its thermal insulation and vapor permeability. A chemical and phase analysis of the composition of semi-aqueous gypsum and bentonite was carried out.

Bentonite consists of ultramicroaggregates of lamellar, leaf-shaped form with sizes up to 2 μm, consisting of aluminosilicate particles, micro- and macroaggregates up to 100 μm in size with a chaotic arrangement, and grains of quartz and hydromica.

Semi-aqueous gypsum consists of small crystals of low density without a characteristic crystalline pattern.

At a ratio of bentonite/water of 1:5, unlike other ratios, there is no residual water on the surface of the mixture, bentonite is completely saturated with moisture. It is expedient to use such a ratio in further research to obtain a finely porous structure of threshold gypsum.

References

1. Gao, T., Ihara, T., Grynning, S., Jelle, B.P., Lien, A.G.: Perspective of aerogel glazings in energy efficient buildings. Build. Environ. **95**, 405–413 (2016)
2. Hu, Z., Zheng, S., Tan, Y., Jia, M.: Preparation and characterization of diatomite/silica composite humidity control material by partial alkali dissolution. Mater. Lett. **196**, 234–237 (2017)
3. Cao, L., Yang, H., Zhou, Y., Zhao, F., Xu, P., Yao, Q., Yu, N., Hu, Z., Peng, Z.: A new process for preparation of porous polyacrylamide resins and their humidity control properties. Energy Build. **62**, 590–596 (2013)
4. Jiang, J., Yang, Y., Hou, L., Lu, Z., Li, J., Niu, Y.: Facile preparation and hardened properties of porous geopolymer-supported zeolite based on swelled bentonite. Constr. Build. Mater. **228**, 117040 (2019). https://doi.org/10.1016/j.conbuildmat.2019.117040
5. Cheng, Y., Jiang, Q., Zhang, Y., Li, D.: Study of preparation and performance of gypsum–based light thermal insulation material. Mater. Rev. **4**, 135–147 (2014)
6. Bicer, A., Filiz, K.: Thermal and mechanical properties of gypsum plaster mixed with expanded polystyrene and tragacanth. Therm. Sci. Eng. Prog. **1**, 59–65 (2017)
7. Cao, W., Cheng, X., Gong, L., Li, Y., Zhang, R., Zhang, H.: Thermal conductivity of highly porous ceramic foams with different agar concentrations. Mater. Lett. **139**, 66–69 (2015)

8. Zhu, C., Zhang, J., Yi, W., Cao, W., Peng, J., Liu, J.: Research on degradation mechanisms of recycled building gypsum. Constr. Build. Mater. **173**, 540–549 (2018)

9. Papatzani, S., Badogiannis, E.G., Paine, K.: The pozzolanic properties of inorganic and organomodified nano–montmorillonite dispersions. Constr. Build. Mater. **167**, 299–316 (2018)

10. Jiang, J., Lu, Z., Li, J., Xie, Y., Luo, K., Niu, Y.: Preparation and properties of nanopore–rich lightweight cement paste based on swelled bentonite. Constr. Build. Mater. **199**, 72–81 (2019)

11. Suleymanova, L.A., Pogorelova, I.A., Kara, K.A.: Non-autoclaved aerated concrete porosity and factors affecting it. Mater. Sci. Forum **992**, 218–227 (2020)

12. Suleymanova, L.A., Pogorelova, I.A., Marushko, M.V., Ognev, N.V.: Vibration-vacuum gypsum-containing composites. Bulletin of the BSTU V.G. Shukhov **12**, 62–66 (2017). https://doi.org/10.12737/article_5a27cb86c33964.15907428

Foundation Type Influence on the Construction Site Seismicity

M. A. Zubritskiy[1,2(✉)] , L. S. Sabitov[1,2] , O. Yu. Ushakov[3] , L. R. Mailyan[4] , and S. V. Klyuev[5]

[1] Kazan State Power Engineering University, Kazan, Russia
`zubtickiy_maksim@mail.ru`
[2] Kazan Federal University, Kazan, Russia
[3] Ural Federal University Named After the First President of Russia B.N. Yeltsin, Ekaterinburg, Russia
[4] Don State Technical University, Rostov-on-Don, Russia
[5] Belgorod State Technological University Named After V.G. Shukhov, Belgorod, Russia

Abstract. The construction site geotechnical conditions are an important factor in the structures seismic resistance estimation. Based on the earthquakes consequences analysis to buildings with the same structural schemes and overall dimensions, the construction site estimated seismicity dependence on the base soil seismic stiffness and the transverse waves speed is fixed in the seismic building design code. In the research, a math modeling experiments for completely identical structures, but with different foundations types on identical soil conditions, were performed. The performed calculations analysis showed a significant discrepancy in the structures response under seismic impact for different foundations types.

Keywords: Seismic Impact · Time History Analysis · Soil Conditions · Microseismic Zoning

1 Introduction

Strong earthquakes consequences analysis showed many examples of various damage to same design schemes buildings and structures, but located in different geotechnical conditions [1–4]. Seismic building design code links the seismic impact intensity with the soil density and its water saturation. This dependence was obtained on the long-term observations' basis of the strong earthquakes' consequences.

For example, some buildings and structures after the earthquake in 1964 in the Niigata city (Japan) withstood the seismic impact, but were significantly damaged as a result of the earth foundation destruction. Due to the sands compaction, about a third of the city's territory suffered sharp subsidence, in some places reaching two meters.

After the earthquake in Alaska in the same 1964, the city of Anchorage, located 130 km from the earthquake epicenter, was badly damaged, and the Valdez and Seward cities were less damaged, although their distance from the epicenter is identical. The reason for the destruction is unstable thixotropic clays significant thickness that form

the base in the Anchorage area. These soils are subjected to structural changes under dynamic influences.

Perform the calculation together with the soil base in an explicit form (3D soil model) both in terms of computer capacity and creating such models. As part of the technical documentation audit, it was noted the following approach prevalence in the calculation schemes formation: the structures seismic impact calculation is performed separately from the base, or with soil reaction coefficient usage. These approaches do not allow assessing the soil mass real stress–strain state, that may lead to consequences similar to the earthquakes in Anchorage and Niigata.

Under performing microseismic zoning, the construction site design seismicity is specified depending on the base soil seismic stiffness and the speed transverse waves. According to Table 4.1 SP 14.13330.2014 «Seismic Building Design Code», the design seismicity can be reduced by 1 point for category I soils and vice versa it can be increased for category IV.

This design code desire to provide soft soils design "margin" is quite reasonable, but does this assumption reflect the actual system response during earthquakes? Are the soft soils dissipative properties taken into account during seismic impact? Is it correct to reduce the construction site design seismicity for the category I soils? And does the foundation type choice affect the overall system response under earthquake?

2 Methods and Materials

Seismic impact math modeling by time history method was performed using the Plaxis 2D software package.

The research object is a four-tiered flat equipment structure 10 m wide and 12 m high (floor height—3 m). Foundation thickness—600 mm, slabs and column thickness—300 mm. Structures material—concrete B25. The calculation is performed in the elastic formulation. Damping in the structures is taken into account using the Rayleigh equation [5, 6].

The structure foundation is composed of three engineering-geological elements (see Fig. 1):

Fig. 1 Structure base

- Upper layer—silty gray loams, indistinctly layered, with plant remains, fluid-plastic;

- Middle layer—silty gray sandy loam with gravel, pebbles, with interlayers of loam, plastic;
- Bottom layer—granite.

For the upper and middle layers, a Hardening Soil with Small Strain Stiffness (HSS) material model was adopted. In fact, to describe the change in stiffness with the amount of deformation, only two additional parameters are needed:

- Initial shear modulus or shear modulus for ultra-small strains G_0;
- Shear deformation level $\gamma_{0,7}$, at which the secant shear modulus G_S decreases to about 70% of the value G_0.

Depending on the type of foundation, three calculation models are modeled:

- Direct foundation (see Fig. 2);
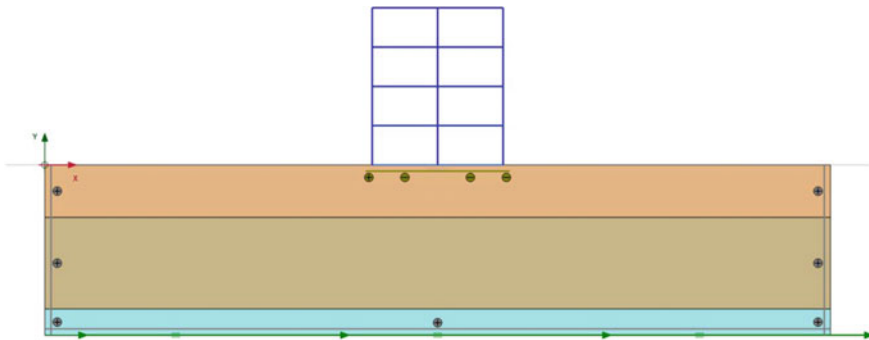
Fig. 2 Calculation model with direct foundation

- Pile foundation: compression piles with a cross-section of 400×400 mm (see Fig. 3);
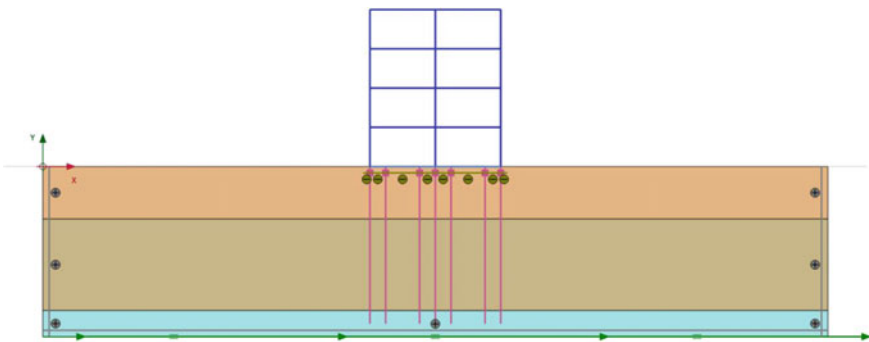
Fig. 3 Calculation model with compression piles

- Pile foundation: friction piles with a cross-section of 400×400 mm (see Fig. 4).
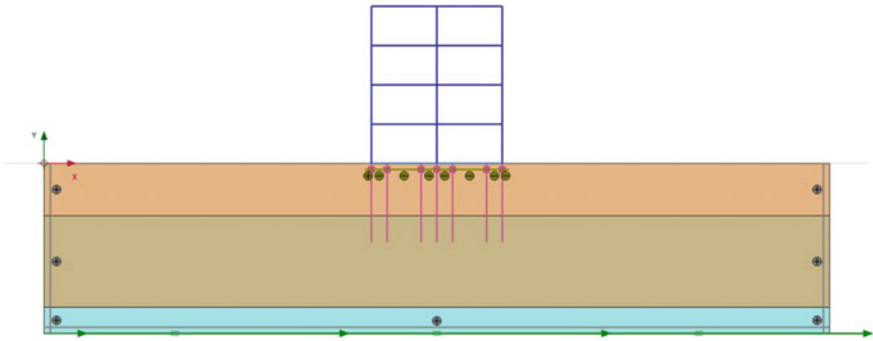
Fig. 4 Calculation model with friction piles

The boundary conditions choice depends on the vibration source location:

- The source is located inside the model. The generated and reflected waves go beyond the model boundaries;
- The source is outside the model. The generated waves remain inside the model, while the reflected waves must go beyond it.

The boundaries were assigned according to the second variant: the earthquake source is located outside the model at significant depth.

At the lower boundary, Compliant base (special boundary condition) was used. The left and right boundaries are set using the Free field boundary conditions.

Seismic impact is modeled by applying a seismogram (Line Displacement) at the lower boundary. Earthquake intensity—8 points [4, 7–10] (Fig. 5).
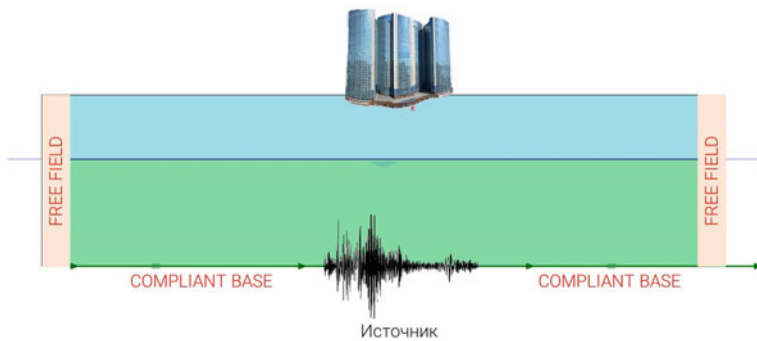
Fig. 5 Calculation model boundary conditions

3 Results and Discussion

According to the calculation results, dynamic models' responses were obtained.

Structure natural vibrations periods with foundations on a natural foundation, with pile foundations (compression and friction piles) are respectively equal to 0.9, 0.75, 0.725 s (see Fig. 6). The difference between the maximum and minimum periods is 19.4% (Figs. 7, 8, 9, 10).
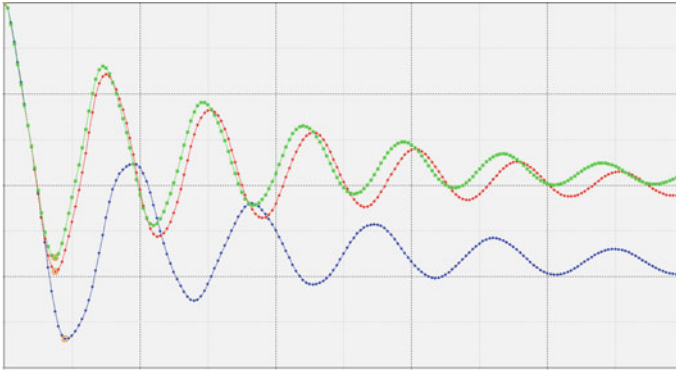
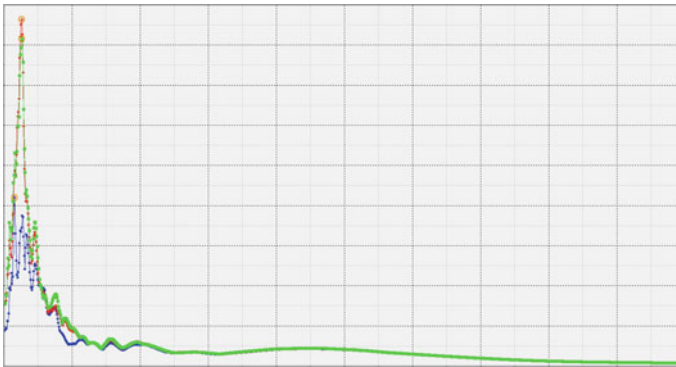**Fig. 6** Top point displacement graph

Fig. 7 The response spectrum at foundation level

Under analyzing the structures response, significant discrepancies were obtained in the results for pile foundations and direct foundation (Table 1):

- The natural period difference is 19.5%;
- Peak accelerations differ by more than 2 times.
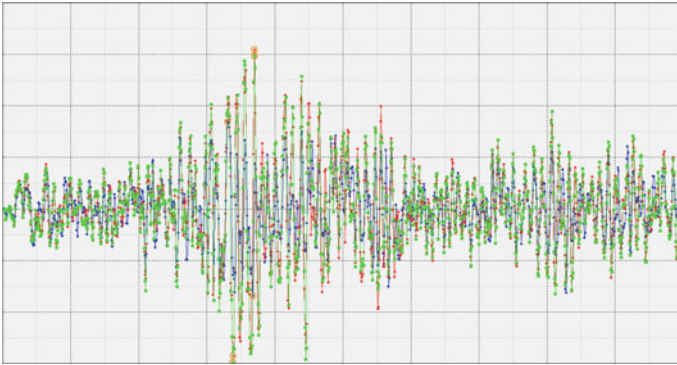
Fig. 8 Accelerogram at foundation level
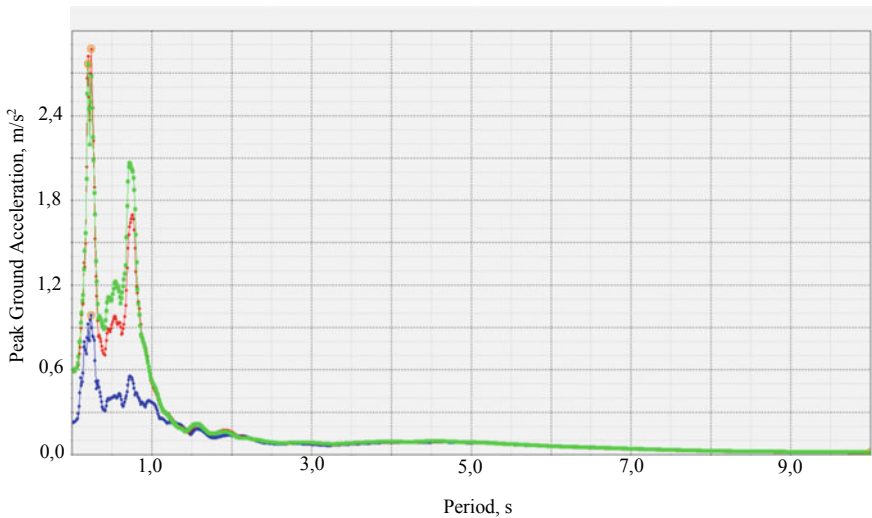
Fig. 9 Response spectrum at top point level: -•-Natural Base, -•-Friction Piles, -•-Piles Racks

4 Conclusion

In the process of research, number of calculations were performed by time history analysis using acceleration records, top point displacement graphs, response spectrum at the foundation and top point level were plotted. The resulting discrepancies are explained by the soil dissipative properties that lead to the seismic impact reduce.

The structures seismic resistance estimation should be carried with the "structure-foundation-base" system usage. This approach makes it possible to make cost-effective decisions, taking into account the soils damping properties. Accelerations graphs of the top point and in the foundations level show significant differences depending on the foundations type. Thus, the foundations design features affect the overall response
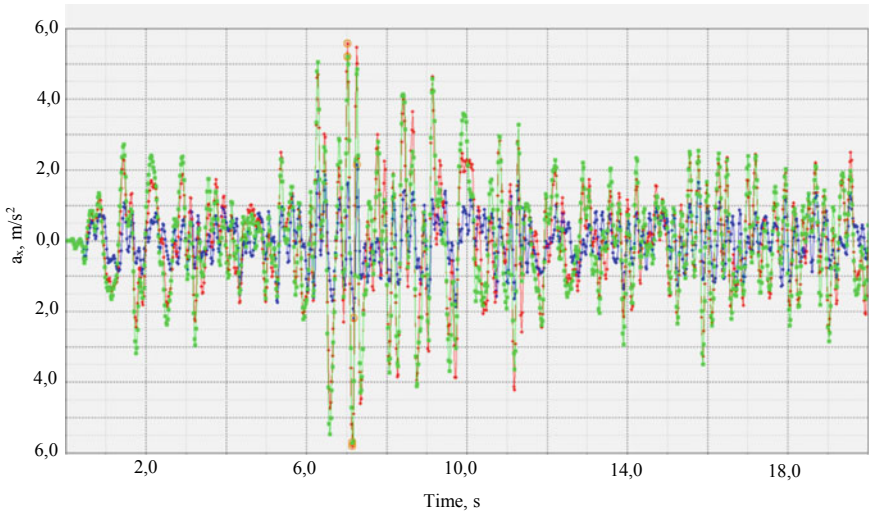
Fig. 10 Accelerogram at top point level: -•-Natural Base, -•-Friction Piles, -•-Piles Racks

Table 1 Results comparison table

Comparison parameter	Foundation type		
	Direct foundation	Compression piles	Friction piles
Natural period, s	0.9	0.725	0.75
Top point displacement, mm	36.5	27.3	29.6
Peak acceleration at foundation level, m/s^2	1.63	3.02	2.98
Peak acceleration at top point level, m/s^2	2.26	5.64	5.51

during earthquakes. To clarify the seismic impact intensity, it is necessary to develop a system for taking into account the foundation type influence during engineering surveys.

References

1. Klyuev, S.V., Khezhev, T.A., Pukharenko, Y.V., Klyuev, A.V.: Fibers and their properties for concrete reinforcement. MSF **945**, 125–130 (2018)
2. Klyuev, S.V., Bratanovskiy, S.N., Trukhanov, S.V., Manukyan, H.A.: Strengthening of concrete structures with composite based on carbon fiber. J. Comput. Theor. Nanosci. **16**(7), 2810–2814 (2019)
3. Klyuev, S.V., Khezhev, T.A., Pukharenko, Y.V., Klyuev, A.V.: To the question of fiber reinforcement of concrete. MSF **945**, 25–29 (2018)
4. Klyuev, S.V., Khezhev, T.A., Pukharenko, Y.V., Klyuev, A.V.: Experimental study of fiber-reinforced concrete structures. MSF **945**, 115–119 (2018)

5. Zubritskiy, M.A., Ushakov, O.Y., Sabitov, L.S.: Account for the contribution of higher modes under system seismic resistance estimation by nonlinear static method. IOP Conference Series: Materials Science and Engineering **570**(1), 012109 (2019)
6. Zubritskiy, M.A., Ushakov, O.Y., Sabitov, L.S.: Performance-based seismic evaluation methods for the estimation of inelastic deformation demands. IOP Conference Series: Materials Science and Engineering **570**(1), 012108 (2019)
7. Zubritskiy, M.A., Ushakov, O.Y., Sabitov, L.S., Kolesnikov, A.V.: Account for the contribution of higher vibration modes under seismic resistance estimation of system with elastomeric supports by nonlinear static method. J. Phys: Conf. Ser. **1425**(1), 012032 (2020)
8. Mailyan, L.R., Zubritsky, M.A., Ushakov, O.Y., Sabitov, L.S.: Calculation of high-rise structures under the seismic effect of "controlling earthquake" level by a nonlinear static method on the example of Adyghe wind power plant. Construction Materials and Products **3**(1), 14–20 (2020). https://doi.org/10.34031/2618-7183-2020-3-1-14-20
9. Kurbatskiy, E.N., Mondrus, V.L., Pestriakova, E.A.: On the question of the correct assignment of the seismic input information. Academia. Architecture and Construction **1**, 134–143 (2021)
10. Kurbatskiy, E.N., Titiov, E.U., Golosova, O.A., Kosaurov, A.P.: Vibration and seismic action abatement method for structures. Building and Reconstruction **1**(75), 55–66 (2018)

Model of the Catastrophic Stage of Wood Damage Accumulation Under Uniaxial Compression

T. A. Gavrilov[(✉)] [ID]

Petrozavodsk State University, Lenin Avenue, 33, Petrozavodsk, Russia 185910
`gtimmo@mail.ru`

Abstract. It is known that the failure of quasi-brittle materials such as wood is accompanied by an accumulation of damage and a decrease in the effective cross-sectional area of the specimen. At a certain stage of loading the process of damage accumulation significantly accelerates and is characterized as a catastrophic process. Purpose of work: developing a model of catastrophic stage of damage accumulation under uniaxial compression of wood. Damage accumulation is characterized by a damage function. The choice of the damage function is not the only one. Two such sigmoid functions are discussed. Only one of the two functions provided the ability to quantify the rate and acceleration of catastrophic damage accumulation. It is shown that the rate of damage accumulation increases with increasing axial strain and reaches an extremum in the middle of the theoretical process duration. The theoretical dependence is not fully realized, since the failure occurs in the vicinity of the point of rate extremum, but does not reach it. Analytical and graphical estimates of the rate and acceleration of damage accumulation were obtained. The simulation results are in agreement with the data known from the literature.

Keywords: Quasi-Brittle Materials · Wooden Structures · Architectural Monuments · Damage Function · Catastrophic Damage Stage · Destruction

1 Introduction

At present, the problems of strength of brittle materials remain relevant. Depending on the temperature and humidity, wood breaks down as a brittle material under sufficiently high load [1]. Wood is an ecological, renewable resource and is often used to make wooden building structures. However, unprotected from external influences of temperature and humidity wood as a material degrades under the influence of wood-destroying fungi [2]. Biodegradation of wood in building structures significantly reduces their service life and causes great material losses. For example, about 20% of the business wood harvested in Russia is consumed only to compensate for its losses from biodegradation [3]. The problem of partial or complete loss of cultural heritage objects due to the biodegradation of wooden structures of monuments of architecture is no less important.

Micro- and mesoscale pores and cracks are a feature of the structure of quasi-brittle materials, the development of which with increasing load leads to a gradual destruction of the conglomerate of material particles [4], which is manifested in the non-linearity of the load-deformation diagram [5]. It is known that the process of destruction of solids is ordered, and the hierarchy of scales of destruction begins with the size of the crystal lattice and continues up to the size of tectonic plates in geospheres [6]. Taking into account these circumstances, the array (or specimen) of quasi-brittle material can be considered as a certain structure, the mechanical state and properties of which depend on the impact on it [7, 8]. Such a structure can be considered as a macroobject consisting of mesoscale elements, the mechanical state of which and their interaction with each other determine the strength and stiffness of the quasi-brittle material.

As the load on the structure increases, the "weakest" mesoscale elements or their conglomerates are destroyed, so that the load is redistributed to other elements that remain undestroyed. The mechanical stresses in these elements increase, which leads to the failure of the next "weak" link, etc. Consequently, the average stress values in such a process continuously increase until the quasi-brittle material fracture stage is completed. For the mathematical description of this process, a phenomenological model is developed within the presented research, in which two parameters corresponding to the point of extremum on the diagram "load—displacement" are used as input data, namely, the value of force external to the specimen and the displacement caused by this force, equal to the change in the length of the specimen. These parameters are determined in standard tests as a result of measurements and are the primary data in strength calculations. The above-mentioned average stresses in uniaxial compression or tension tests of the specimen at each point in time should theoretically be determined by dividing the load value by the cross-sectional area of the specimen, which, due to mesoscale damage, is continually decreasing. The area determined taking into account the damage is called the effective area, and the corresponding stresses are called effective stresses [9, 10]. The effective properties of quasi-brittle materials are determined using the damage parameter [10]. The values of this parameter vary in the range [0, 1], i.e. the parameter is a function depending on the properties of the material and the history of external influence. The growth of deformations and destruction of the material can take place without increasing the creep load [10]. These issues are discussed in more detail in articles [11, 12].

In standard methods, for example ASTM-C39, the result of dividing the external force for the specimen by the initial cross-sectional area of the sample is identified with the internal stress in the sample material. This approach does not take into account the reduction of the cross-sectional area of the sample noted above, so the stress found in this way is referred to in the literature [11] as apparent stress. In other words, the known approaches assume that the law of change of force external to the sample has no fundamental differences from the law of change of internal stresses during deformation of the specimen.

However, it is known that at a certain stage of deformation the processes of damage accumulation are significantly accelerated [13], which is accompanied by a decrease in the effective cross-sectional area of the specimen [14]. The problems of modeling such a stage of material deformation are among the most relevant and highly complex, and

modern numerical and experimental methods are used to solve them [15]. In the present work, only certain issues related to the mentioned problem are considered, namely, an attempt is made to analyze the rate and acceleration of the damage accumulation process under uniaxial compression. Accordingly, the aim of the work is to develop a model of damage accumulation in quasi-brittle materials under uniaxial compression.

2 Methods and Materials

The starting point for describing the physical model was the well-known interpretation of a quasi-brittle material as a macrostructure with supporting mesoscale elements [7]. The proposed model is built using the following assumptions [9]: material of each element (before cracks appear in it) obeys Hooke's law; elastic modulus, strength and other physical and mechanical properties of material of each element without cracks do not depend on its size and force impact history; with increase of external load on macrostructure some mesoscale elements or their conglomerates reach the limit state and collapse, as a result of which effective area decreases and load is redistributed to elements remaining undestroyed. As a consequence, the average statistical value of the effective stresses in the material of the remaining undestroyed mesoscale elements increases; the destruction of mesoscale elements and their conglomerates leads to a decrease in the effective area and the reduction of the macrostructure resistance to external force action, which corresponds to the downward branch of the "load–displacement" diagram. The well-known phenomenon of fracture of the above macrostructure on the descending branch of the diagram suggests that the effective stresses (i.e., stresses in the material of the mesoscale elements) are increasing. The growth of effective stresses is limited by the strength of the mesoscale elements.

3 Results and Discussion

3.1 Damage Functions

The damage function can be obtained in different ways. In this paper, two methods are briefly considered. One of these functions, which we will consider in more detail, is based on the results of tests on marble, sandstone and granite known from the literature. The corresponding review is given in the article [11]. The above decrease in the effective area is quantified using the damage function $D(\varepsilon)$ where ε is the relative deformation ($\varepsilon = \Delta L/L_0$ for a specimen of length L_0). The function $D(\varepsilon)$ changes from zero (no damage) to one (the material is completely damaged). It has been observed that an adequate model of the function $D = D(\varepsilon)$, can be a curve belonging to the class of sigmoid; such functions often appear in various applications. The existence of a set of functions of this class predetermines, respectively, the non-uniqueness of the damage function.

In [11] the sigmoid function $D(\varepsilon)$ is obtained using the following logic. Let for some value of ε the number of defects (damage) be determined by the value of D. As the deformation ε increases, the number of defects increases, i.e. $dD/d\varepsilon = rD$, where r is the coefficient of proportionality. However, the amount of undamaged material (as well as the effective area) decreases as ε increases. In an almost completely damaged specimen,

defect growth will stop. Such a process in [11] is modeled using the equation $dD / d\varepsilon = rD(1 - D)$. Solution of this equation: $D = 1/(1 + \exp(a - r\varepsilon))$ where a and r are model fitting parameters. Values of parameters and graphs of function D for granite, marble and sandstone are given in article [11]. Regarding this function, the question arises: are the parameters a and r redundant (even if not for all materials and conditions)? The validity of such a question can be explained by the following. Most likely, these parameters depend on the experimentally found deformations $\varepsilon_{extr}^{test}$ and stresses σ_{extr}^{test} corresponding to the extremum of the function (if such an extremum exists). Deformations ε and effective stresses $\tilde{\sigma}$, in turn, are related to the potential energy of deformation per unit volume of the linearly deformable material $w = \tilde{\sigma}\varepsilon/2 = \tilde{\sigma}^2/(2\tilde{E}) = \varepsilon^2\tilde{E}/2$. Therefore, within the framework of a heuristic approach, it can be assumed that the test results contain information sufficient to construct a damage function. This possibility was tested in [16], in which the function of changing the effective area $\tilde{A}$ in the form of:

$$\tilde{A} = A_0 \, e^{-\frac{1}{3}\left(\frac{\varepsilon}{\varepsilon_{extr}^{test}}\right)^3}. \tag{1}$$

There A_0—initial cross-sectional area.

It follows from (1) that the function $\Theta = \tilde{A}/A_0$ is a function of the residual resource:

$$\Theta = e^{-\frac{1}{3}\left(\frac{\varepsilon}{\varepsilon_{extr}^{test}}\right)^3}. \tag{2}$$

Using function (2), we define the damage function as $D = 1 - \Theta$:

$$D = 1 - e^{-\frac{1}{3}\left(\frac{\varepsilon}{\varepsilon_{extr}^{test}}\right)^3}. \tag{3}$$

The adequacy of the approach used in the justification of function (1) was confirmed in [16] by comparing the simulation results with the experimental data known in the literature. However, the functions (1), (2), (3) were not applied to the simulation of blow-up regime.

3.2 Simulation of Blow-Up Regime

In the considered problem, a necessary element of the mathematical description of the physical model is a function that determines the change in the effective area depending on the deformation. The choice of variable ε as an argument of functions (1)–(3) is explained by the fact that in modern testing machines the rate of deformation in uniaxial compression can be set constant or variable; the graphs of change of load F on displacement of its application point are automatically plotted in the axes ΔL (or ε) and F (or σ). Therefore, if necessary, it is possible to convert the argument into units of time.

Let us consider the application of relations (1)–(3) by an example. We will use the results of solving model problems from [8] as input data. In this paper, the characteristics for four specimens are given. Let us consider three specimens, marked on the graph in the cited work by numbers 1, 2, and 4. For these specimens we determine $\varepsilon_{extr}^{test}$, respectively:
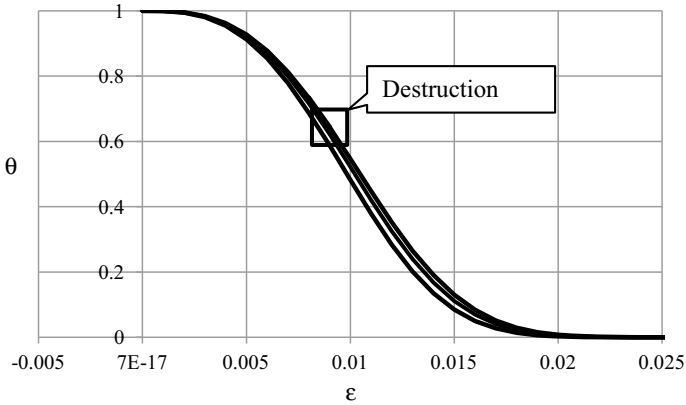
Fig. 1 Residual life function $\Theta = \tilde{A}/A_0$

0.0080; 0.0077; 0.0082. For these data the graphs of the residual life function (2) are shown in Fig. 1.

The simulation results show that specimen failure occurs if ε is between 0.0079 and 0.0093 (Fig. 1).

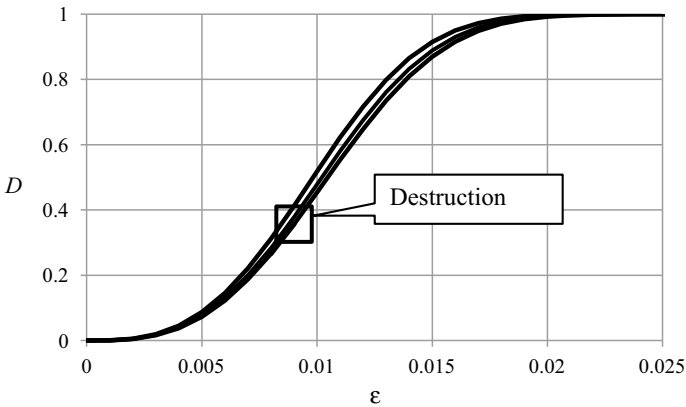The graph of the damage function (3) for the samples in question is shown in Fig. 2.

Fig. 2 Damage function D (3)

Figure 2 shows that destruction occurs if the damage is less than ~40%.

The fracture velocity characteristic v can be determined numerically [using the values of function (3)] or analytically [9]:

$$v = \frac{\mathrm{d}D}{\mathrm{d}\varepsilon} = \varepsilon^2 \frac{\exp\left(-\frac{1}{3}b^3\right)}{b^3} \tag{4}$$

Here $b = \varepsilon/\varepsilon_{extr}^{test}$.

From relation (4) it follows that the rate of the fracture process increases in proportion to the cube of the decrease in the above value $\varepsilon_{extr}^{test}$. The graphs of function (4) for the above three samples are shown in Fig. 3.
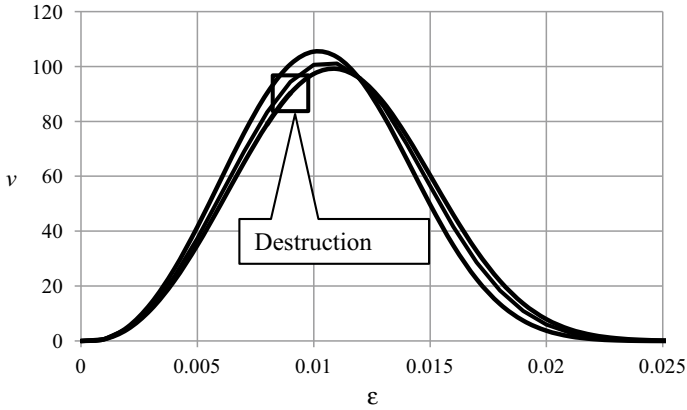
Fig. 3 Changes of the damage rate v (4)

Figure 3 shows that the rate of damage growth is irregular, increases rapidly with increasing strain, and reaches an extremum approximately in the middle of the theoretical duration of the entire deformation process. The theoretical dependence (4) is not realized completely, because the destruction of the specimens occurs in the vicinity of the point of extremum of the function $v(\varepsilon)$. In this case, the velocity value approaches the extremum, but does not reach it. At the extremum point of the function (4), the volumes of damaged and undamaged material are the same. After passing the point of extremum, the growth of damage slows down due to the fact that the amount of undamaged material, in which only new damage can appear, decreases.

Focusing on the aggravation of the damage process, we note the following. At the start of the process, when $\varepsilon = 0.001$, the rate characteristic is $v \approx 0.65$. At the point of extremum $v \approx 105$. Thus, the blow-up regime is characterized by a catastrophic increase in the rate of material damage growth (approximately by 160 times).

The characteristic of the acceleration of the damage process can be determined numerically [using the values of function (4)] or analytically:

$$a = \frac{dv}{d\varepsilon} = -\varepsilon \frac{\exp\left(-\frac{1}{3}b^3\right)\left(-2\left(\varepsilon_{extr}^{test}\right)^3 + \varepsilon^3\right)}{\left(\varepsilon_{extr}^{test}\right)^6}. \tag{5}$$

It follows from relation (5) that the acceleration of the damage process increases in proportion to the cube of the decrease in the above value of $\varepsilon_{extr}^{test}$. The graphs of function (5) are shown in Fig. 4.

Figure 4 shows that the acceleration of the damage process, increases rapidly with increasing strain and reaches a maximum before the specimen fails. At the start of the process, when $\varepsilon = 0.001$, the acceleration characteristic $a \approx 650$, $a_{\max} \approx 15{,}900$ (Fig. 4).
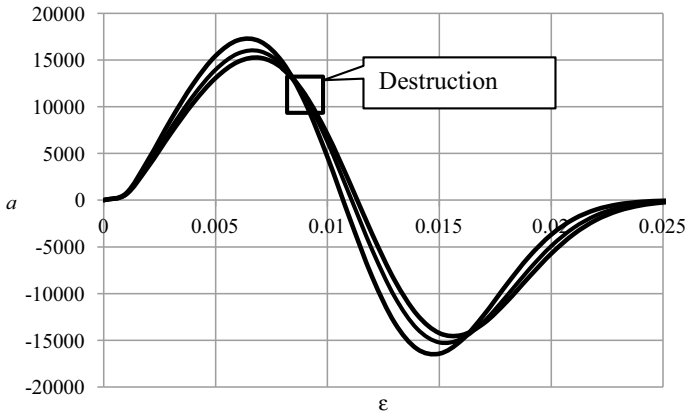
Fig. 4 Change of the damage process acceleration a (5)

Thus, in the considered case the blow-up regime is characterized by an increase in the acceleration of damage growth of the material approximately by 24 times.

4 Conclusion

The model has been developed to determine the characteristics of the speed and acceleration of the catastrophic stage of damage accumulation and destruction of such quasi-brittle materials as wood under uniaxial compression. Calculation formulas are obtained and an example of the analysis of these characteristics is given. The presented patterns of damage accumulation and destruction of quasi-brittle materials do not contradict known works [7, 8, 11–14, 16]. However, taking into account the variability of the properties of wood, an additional analysis of the correspondence of the simulation results and experimental data known from the literature is necessary.

References

1. Soares, B.C.D., Lima, J.T., de Assis, C.O.: Influence of density and lignin content on cleavage strength of *Eucalyptus grandis*. Trees **36**, 1185–1192 (2022). https://doi.org/10.1007/s00468-022-02279-z
2. Maeda, K., Ohta, M., Momohara, I.: Relationship between the mass profile and the strength property profile of decayed wood. Wood Sci. Technol. **49**, 331–344 (2015). https://doi.org/10.1007/s00226-014-0696-2
3. Kononov, G.N., Verevkin, A.N., Serdyukova, Y.V., Zaitsev, V.D.: Mycolysis of wood, its products and their use. II. Biological and morphological processes of mycological destruction of wood. Lesnoy vestnik/Forestry Bulletin **24**(2), 81–87 (2020). https://doi.org/10.18698/2542-1468-2020-5-89-96

4. Mohammadnejad, M., Liu, H., Chan, A., Dehkhoda, S., Fukuda, D.: An overview on advances in computational fracture mechanics of rock. Geosystem Engineering **24**(4), 206–229 (2021). https://doi.org/10.1080/12269328.2018.1448006

5. Deng, Z., Liu, B., Ye, B., Xiang, P.: Mechanical behavior and constitutive relationship of the three types of recycled coarse aggregate concrete based on standard classification. J. Mater. Cycles Waste Manage. **22**(1), 30–45 (2020). https://doi.org/10.1007/s10163-019-00922-5

6. Makarov, P.V., Eremin, M.O.: Fracture model of brittle and quasibrittle materials and geomedia. Phys. Mesomech. **16**, 207–226 (2013). https://doi.org/10.1134/S10299599130 30041

7. Kolesnikov, G., Gavrilov, T.: Modeling the drying of capillary-porous materials in a thin layer: application to the estimation of moisture content in thin-walled building blocks. Appl. Sci. **10**, 6953 (2020). https://doi.org/10.3390/app10196953

8. Smolin, I.Y., Eremin, M.O., Makarov, P.V., Evtushenko, E.P., Kul'kov, S.N., Buyakova, S.P.: Brittle porous material mesovolume structure models and simulation of their mechanical properties. AIP Conf. Proc. **1623**, 595 (2014). https://doi.org/10.1063/1.4899015

9. Kolesnikov, G.: Damage function of a quasi-brittle material, damage rate, acceleration and jerk during uniaxial compression: model and application to analysis of trabecular bone tissue destruction. Symmetry **13**, 1759 (2021). https://doi.org/10.3390/sym13101759

10. Stepanova, L.V., Igonin, S.A.: Rabotnov damage parameter and description of delayed fracture: results, current status, application to fracture mechanics, and prospects. Journal of Applied Mechanics and Technical Physics **56**(2), 282–292 (2015). https://doi.org/10.15372/PMTF20150214

11. Liu, D., He, M., Cai, M.: A damage model for modeling the complete stress–strain relations of brittle rocks under uniaxial compression. Int. J. Damage Mech **27**(7), 1000–1019 (2018). https://doi.org/10.1177/1056789517720804

12. Volegov, P.S., Gribov, D.S., Trusov, P.V.: Damage and fracture: classical continuum theories. Phys. Mesomech. **20**(2), 157–173 (2017). https://doi.org/10.1134/S1029959917020060

13. Smolin, I.Y., Makarov, P.V., Kulikov, A.S., Eremin, M.O., Bakeev, R.A.: Blow-up modes in fracture of rock samples and earth's crust elements. Phys. Mesomech. **21**, 297–304 (2018). https://doi.org/10.1134/S1029959918040033

14. Makarov, P.V., Smolin, I.Y., Peryshkin, A.Y., Kulkov, A.S., Bakeev R.A.: Experimental and numerical investigation of the catastrophic stage of failure on different scales from rock sample to coal mine. Physical Mesomechanics **23**(5), 43–55 (2020). https://doi.org/10.24411/1683-805X-2020-15004

15. Sun, B., Zheng, Y., Li, Z.: Random beam lattice modeling method for catastrophic crack growth simulation of brittle-like materials. Constr. Build. Mater. **244**, 118396 (2020). https://doi.org/10.1016/j.conbuildmat.2020.118396

16. Kolesnikov, G.N., Meltser, R.A.: Damage model to trabecular bone and similar materials: residual resource, effective elasticity modulus, and effective stress under uniaxial compression. Symmetry **13**, 1051 (2021). https://doi.org/10.3390/sym13061051

Improving the Operational Reliability of Complex Technical Systems Operating in Corrosive Conditions

N. V. Pirumyan[1]([✉]) [iD], M. G. Stakyan[1] [iD], and B. M. Yazyev[2,3] [iD]

[1] National University of Architecture and Construction of Armenia, Yerevan, Armenia
`pirumyannarine@gmail.com`
[2] Don State Technical University, Rostov-On-Don, Russia
[3] Kazan Federal University, Kazan, Russia

Abstract. The responsible heavily loaded structural elements (butt welds and sections of their location) of the complex technical systems, which are mainly operated outdoors, are impacted by atmospheric influences and cyclic stresses, which are caused by load fluctuations, nature vibration processes, ambient temperature and changing weather conditions. These factors cause the appearance and development of corrosion-fatigue damage and can lead to cracking and fatigue destruction of structural elements. The factors affecting on the bearing capacity of structural elements, which are occurred in a complex form, in different amounts and combinations, are classified. The surface strengthening of the junction outside surfaces and usage of anticorrosive protective plating on them are selected from a number factors. So that, to magnify fatigue strength and durability is suggested to use a strengthening technology-surface plastic deformation of welds. The physical and mechanical phenomena of the appearance and development of corrosion-fatigue processes are considered and ways to enlarge the strength and durability of elements using new corrosion-protective polymer platings (Belzona 1111) in the location of butt welded junctions are outlined. A series of techniques, e.g., static tests of steel samples with and without platings in a corrosive solution was performed and its effectiveness for application in the critical nodes was confirmed. The effectiveness of the implementation of these, process operations which enlarge the bearing capacity of the complex technical system, has been proven.

Keywords: Complex Technical Systems · Structural Elements · Corrosion · Fatigue · Cyclic Durability · Polymer plating · Strengthening · Affecting Factors

1 Introduction

The development of industry, agriculture, transport infrastructures is related to the reliability of the operation of the various purposes Complex technical systems (CTS). The extension of the CTS network is the solution of this problem, that is implemented by surmounting the difficult terrain, various natural and climatic zones and water spaces.

As the main CTS are mainly operated in an area free of settlements, therefore the laying of the network, maintenance, technical examination, as well as scheduled maintenance of the system are relatively complex. This problem is also complemented by the peculiar properties of the CTS operation under conditions of corrosion and atmospheric influences, as well as fatigue processes associated with the cyclical loading of the network, ambient temperature fluctuations and various vibration phenomena. This factors inevitably leads to the cyclical stress–strain state in the structural elements, to the occurrence of corrosion and fatigue damage, and if there are surface and internal defects of welded junction of elements—to the development of cracks and destruction of separate structural elements [1–4].

These phenomena prescribe the requirement for the formation of the stages of development, creation and operation of the CTS, consisting of the procedures listed below: research of the location of the CTS; application of design, technological, testing, maintenance and routine repair that guarantee a given level of operability and reliable operation of the CTS [5–7].

The stages of design and technological development of the CTS are considered. The operation of CTS assumed the classification of factors causing damage and the accounting of their complex impact on the bearing capacity of the responsible structural elements of CTS [4]. It is possible to perform this by using in calculations the advanced features of the affecting factors (type and parameters of the loading mode and physical and mechanical characteristics of structural materials, terrain and atmospheric influences, as well as indicators of heat, corrosion, wear resistance and fatigue resistance of structures), as well as taking into account the influence of their complex interaction.

2 Methods and Materials

The real working conditions of the CTS are characterized by the appearance and development of various types of damages, which are continuous and complex in nature and may reduce the strength, durability and reliability of the structure. In some cases, they can result in the breakdown of the most loaded elements of the CTS, consequently—in significant downtime and reduced productivity, and to the appearance of fatigue cracks and fractures [1].

The number of factors affecting on the bearing capacity of structural elements is significant and, according to the principle of appearance and the nature of the impact, they can be united in the following groups:

I.   Geometry and physic-mechanical condition of the CTS construction material;
II. System location surroundings and loading modes;
III. Corrosion-fatigue phenomena in CTS structural elements;
IV. Technological aspects of the construction and maintenance of CTS:

The factors include:

(1) Geometry and configuration of contours of CTS structural elements;
(2) Physical and mechanical condition of structural materials of elements;

(3) Nonstationary and cyclicity of the CTS loading mode;
(4) Environmental corrosion,
(5) Daily and seasonal ambient temperature fluctuations;
(6) Vibration phenomena (geodetic and anthropogenic) in the system;
(7) Flaws and damages of CTS structural elements;
(8) Fatigue processes in CTS structural elements;
(9) Technological methods to increase the bearing capacity of the system;
(10) Using of anticorrosive polymer plating in loaded sections of the structural elements;
(11) Rational schedule of maintenance, examination and repair work of the system.

According to the calculation scheme, adopted in the methodology of system analysis, for these 11 factors, all possible options of sets of factors are composed, depending on their number and combinations. Analysis and classification of possible options of these factors have shown that in the elements of the CTS, the most responsible are cases of combinations with 4 factors that significantly affect the efficiency of the CTS. These are: points (4) and (8)—factors of corrosion (C) and fatigue (F) processes, as well as points (9) and (10) are the factors of strengthening (S) and corrosion resistance (CR), which are opposite in nature and in total determine the bearing capacity of the CTS. Another peculiarity of significant factors—points (4), (8), (9), (10) is their presence in the vast majority of options of combinations and the level of strength and corrosion resistance of structural elements depends on their number in these combinations. Grouping of factors in combinations is carried out according to the number of inclusion of these significant factors in them:

- just one factor: F, C, S, CR—86 pcs.;
- two factors: (FC), (FS), (F CR), (CS), (C CR), (S CR)—48 PCs.;
- three factors: (FCS), (FC CR), (CS CR), (FH CR)—28 PCs.;
- four factors: (FCS CR)—1 PC.

At the second stage of the procedures, the principle of independent action of factors within the selected group was adopted, which is more often used in applied tasks for assessing the total influence effect of factors and to determine the generalized parameter of the entire group by multiplying the values of their separate parameters (the scheme of sequential influence of factors).

The aim of the study is selection of optimal technologies for increasing the bearing capacity of structural elements on the base of research and classification of complex affecting factors of CTS structural elements. To achieve that objective, it is necessary to solve the following tasks: the study of the physical and mechanical nature of corrosion and fatigue processes in low-carbon structural steels used in structural elements; the selection of the type of strengthening technique for welds; the selection of the optimal type of anti-corrosion protective plating and the technique of its usage to the welds. The mathematical model of fatigue destruction can be represented by a system of three linear equations $\lg N = F(\lg \sigma)$ corresponding to the specified sections N and σ with indices: 1, … ,3—for the initial fatigue and *1k, … ,3k; 1k, … ,3k*—for comparative

corrosion-fatigue processes. The classification of the main parameters and equations of these fatigue lines is presented in Table 1.

Table 1 Equations and parameters of fatigue on the 1, … ,3, 1_k, … ,3_k and $1'_k$, …, $3'_k$ sections

No.	Conditions of fatigue processes	Calculation scheme	Section of the fatigue line	N and σ * intervals		Equations of fatigue lines
				N	σ	
1	Fatigue in a protective environment (in the open air)	–	1	$N_0...N_{G1}$	$\sigma_{R1} \ldots \sigma_{\beta 1}$	$\lg N = C_1 - m_1 \lg \sigma$
2			2	$N_{G1}...N_{G2}$	$\sigma_{R2}...\sigma_{R1}$	$\lg N = C_2 - m_2 \lg \sigma$
3			3	$N_{G2}...10^8$	$\sigma_{R2} = const$	$\lg \sigma = \lg \sigma_{R2} = const$
4	Corrosion fatigue (comparable to points 1, 2, 3)	N1	1_k	$N_0...N_{G\kappa 1}$	$\sigma_{R\kappa 1} \ldots \sigma_{\beta \kappa 1}$	$\lg N = C_{\kappa 1} - m_{\kappa 1} \lg \sigma$
5			2_k	$N_{G\kappa 1}...N_{G\kappa 2}$	$\sigma_{R\kappa 2} \ldots \sigma_{R\kappa 1}$	$\lg N = C_{\kappa 2} - m_{\kappa 2} \lg \sigma$
6			3_k	$N_{G\kappa 2} \ldots 10^8$	$\sigma_{R\kappa 1} \ldots \sigma_{R\kappa 2}$	$\lg N = C_{\kappa 3} - m_{\kappa 3} \lg \sigma$
7	Corrosion fatigue (comparable to points 4, 5, 6)	N2	$1'_k$	$N_0 \ldots N'_{G\kappa 1}$	$\sigma'_{R\kappa 1} \ldots \sigma'_{\beta \kappa 1}$	$\lg N = C'_{\kappa 1} - m'_{\kappa 1} \lg \sigma$
8			$2'_k$	$N'_{G\kappa 1} \ldots N'_{G\kappa 2}$	$\sigma'_{R\kappa 2} \ldots \sigma'_{R\kappa 1}$	$\lg N = C'_{\kappa 2} - m'_{\kappa 2} \lg \sigma$
9			$3'_k$	$N'_{G\kappa 2} \ldots 10^8$	$\sigma'_{R\kappa 1} \ldots \sigma'_{R\kappa 2}$	$\lg N = C'_{\kappa 3} - m'_{\kappa 3} \lg \sigma$

* Coordinates of the starting points of the three-link fatigue lines: $(\sigma_{\beta 1}, N_0)$, $(\sigma_{\beta \kappa 1}, N_0)$, $(\sigma'_{\beta \kappa 1}, N_0)$; $N_0 = 10$ cycles—initial durability; $\sigma_{\beta 1}, \sigma_{\beta \kappa 1}, \sigma'_{\beta \kappa 1}$—strength limits; coordinates of inflection points between $(\sigma_{R\kappa 1}, N_{G\kappa 1})(\sigma_{R1}, N_{G1})$, $(\sigma'_{R\kappa 1}, N'_{G\kappa 1})$ sections of—low- and multi-cycle fatigue; (σ_{R2}, N_{G2}), $(\sigma_{R\kappa 2}, N_{G\kappa 2})$, $(\sigma'_{R\kappa 2}, N'_{G\kappa 2})$—of multi-cycle and long-term fatigue

2.1   Analysis of Corrosion Processes in CTS Structural Elements

Maintenance and operating conditions of CTS are characterized by a great amount and combinations of periodically affecting factors that damage the structure or increase the efficiency of the system, with different nature and gradient of actions, as well as the duration and sequence of their manifestations.

Corrosion processes in CTS structural elements have a significant impact on the occurrence and development of corrosion and fatigue damage [8, 9]. The mounting of system and the creation of a network in an open area is accomplished by welding, therefore the welds are exposed to temperature fluctuations and the environment, which cause corrosion phenomena and accelerate the processes of occurrence and development of fatigue cracks. As a result, this results in the reduction of the endurance limit of welded junctions by 1.5 … 2.5 times, and durability—by 3 … 5 times. Simultaneously, the weakest sections are the locations of butt welds, where the stress concentration reaches up to $\kappa_\sigma = 1.8 \ldots 2.5$. As a result of the execution of the technical examination and processing of statistical data, fixed that 70 … 75% of structural elements damages and failures are of a corrosion-fatigue nature, and 20 … 25%—only from corrosion effects. So, the replacement of damaged sections of structural elements is 25 … 30% of the total mass, and 5 … 7% is irretrievably lost in the form of chemical compounds. The nature and speed of corrosion processes depend on many factors that characterize the physical and mechanical state of the surface layers of structural materials: technological features of the manufacture and processing of structural elements; the nature, duration and operating conditions of the system; temperature fluctuations and cyclical loading; contact with the environment, etc. This complex of factors requires a detailed classification and a systematic approach to assess their joint and diverse impact on the bearing capacity of the CTS structure, of which corrosion and fatigue processes are the most significant [10]. A reducing production costs, increasing the requirements of efficiency and environmental safety, as well as increasing the durability of the system are the main requirements for the conditions of trouble-free operation of structural elements [2].

The method of system analysis logically approves the selection and compilation of 10 calculation schemes for determining coefficients $K_{\sigma k}$, K_{Nk}, which are taking into account a different combination and number of Influencing factors, and the formation of their functions $K_{\sigma k} = f(N)$ and $K_{Nk} = \phi(\sigma)$. Taking into account the two-link type of fatigue lines, these calculation schemes are classified and separately presented in zones of limited ($N_{Ri} \leq N_{G1}$) and long-term ($N_{Ri} > N_{G1}$) endurance (Tables 2, 3). The changes presented in Table 3 are as follows: during open air tests in the $N_{Ri} > N_{G1}$ zone, the fatigue line of flat samples takes a horizontal position, which changes the structure of the parameters of the calculation schemes (Table 2, points 1, 5–7).

2.2   Application of Strengthening Technology in CTS Elements Welded Joints

The development of the CTS network in an open area is accompanied by an increase in the scope of welding work. The ensuring of necessary operability, durability and reliability of the entire system are depending on quality of welding work. Considering that the main types of defects and damages are located on the section of butt welds and cause stress concentration, reducing the physical and mechanical characteristics of the

Table 2 The structure of the coefficients of corrosion $K_{\sigma k}$ and K_{Nk} (for $N_{Ri} \leq N_{G1}$)

For $N_{Ri} \leq N_{G1}$ $N_{Ri} \leq N_{G1}$

No.	Test series comparison	Groups options	Open air corrosion coefficient $K_{\sigma k}$		Ratio σ_{Ri}	Open air corrosion coefficient K_{Nk}		Ratio N_{Ri}	Factors impact — Types and groups of factors	Legends*
			$K_{\sigma ki}$	Ratio		K_{Nki}	Ratio			
1	N2-N1	I	$K_{\sigma k1}$	σ_{R2}/σ_{R1}	< 1	K_{Nk1}	N_{R2}/N_{R1}	< 1	Corrosive environment—open air	CE-A
2	N2-N5	II	$K_{\sigma k2}$	σ_{R2}/σ_{R5}	> 1	K_{Nk2}	N_{R2}/N_{R5}	> 1	Stress concentration (in corrosive environment)	SC (CE)
3	N3-N5		$K_{\sigma k3}$	σ_{R3}/σ_{R5}	> 1	K_{Nk3}	N_{R3}/N_{R5}	> 1	Strengthening	S (CE)
4	N4-N5		$K_{\sigma k4}$	σ_{R4}/σ_{R5}	> 1	K_{Nk4}	N_{R4}/N_{R5}	> 1	Coating	C (CE)
5	N3-N1	III	$K_{\sigma k5}$	σ_{R3}/σ_{R1}	< 1	K_{Nk5}	N_{R3}/N_{R1}	< 1	Corrosive environment—open air-stress concentration- strengthening	CE-A-SC-S
6	N4-N1		$K_{\sigma k6}$	σ_{R4}/σ_{R1}	< 1	K_{Nk6}	N_{R4}/N_{R1}	< 1	Corrosive environment—open air—stress concentration—coating	CE-A-SC-C
7	N5-N1		$K_{\sigma k7}$	σ_{R5}/σ_{R1}	< 1	K_{Nk7}	N_{R5}/N_{R1}	< 1	corrosive environment—open air—stress concentration	CE-A-SC
8	N3-N2	IV	$K_{\sigma k8}$	σ_{R3}/σ_{R2}	< 1	K_{Nk8}	N_{R3}/N_{R2}	< 1	Stress concentration-strengthening (In corrosive environment)	SC- S (CE)
9	N4-N2		$K_{\sigma k9}$	σ_{R4}/σ_{R2}	< 1	K_{Nk9}	N_{R4}/N_{R2}	> 1	Stress concentration- coating	SC-C(CE)
10	N3-N4	V	$K_{\sigma k10}$	σ_{R3}/σ_{R4}	> 1	K_{Nk10}	N_{R3}/N_{R4}	> 1	Strengthening—coating	S -C (CE)

Table 3 The structure of the coefficients of corrosion $K_{\sigma k}$ and K_{Nk} (for $N_{Ri}. > N_{G1}$)

For $N_{Ri}. > N_{G1}$ $N_{Ri}. > N_{G1}$

No.	Test series comparison	Groups options	Open air corrosion coefficient $K_{\sigma k}$			Open air corrosion coefficient K_{Nk}			Factors impact	
			$K_{\sigma ki}$	Ratio	Ratio σ_{Ri}	K_{Nki}	Ratio	Ratio N_{Ri}	Types and groups of factors	Legends*
1	N2-N1	I	$K_{\sigma k1}$	σ_{R2}/σ_{RG1}	< 1	K_{Nk1}	N_{R2}/N_{G1}	> 1	Corrosive environment—open air	CE-A
5	N3-N1	III	$K_{\sigma k5}$	σ_{R3}/σ_{RG1}	< 1	K_{Nk5}	N_{R3}/N_{G1}	> 1	Corrosive environment—open air—stress concentration—strengthening	CE-A-SC-S
6	N4-N1		$K_{\sigma k6}$	σ_{R4}/σ_{RG1}	< 1	K_{Nk6}	N_{R4}/N_{G1}	> 1	Corrosive environment—open air-stress concentration—coating	CE-A-SC-C
7	N5-N1		$K_{\sigma k7}$	σ_{R5}/σ_{RG1}	< 1	K_{Nk7}	N_{R5}/N_{G1}	> 1	Corrosive environment—open air-stress concentration	CE-A-SC

*Note. * Symbols: **A**—in the open air, **CE**—in the corrosive environment, **SC**—with stress concentration, **S**—strengthening, **C**—with protective coating*

material (strength and endurance limits, hardness, recrystallization of microstructure, tempering and aging from variable temperatures T = 250 … 1100 °C, etc.), the need to reduce the effects of these damages, by using various physical and technological procedures (hydrodynamic, temperature, supersonic, high-frequency electricity, laser exposure, plastic deformation, etc.), must become priority [10]. Of these technological procedures for CTS structural elements, the most acceptable is the technique of surface plastic deformation (SPD) of the weld section, which is a relatively simple and affordable method by using a special tool with rolling balls or rollers operating according to the kinematic scheme of the planetary friction mechanism. The break-in rollers (balls) under the action of normal force smooth out the surface micro-roughness of the weld and form a deformed layer with residual compression stresses compensating for the influence of external load, which ultimately leads to a decrease in the stress state in the seam [11].

Previously performed researches indicate that the widespread usage in structural elements the low-carbon and low-alloy structural steels, which are easily amenable to plastic deformation and have a relatively low cost, after performing strengthening techniques leads to an increase in endurance limits by 50 … 70%, and cyclic durability by 3 … 4 times, also ensuring the cost-effectiveness of the installation of a system [12].

The efficiency of SPD prescribes the necessity of a wide application of this method in order to regulate the stress state in the weld and in the transition section to the main metal, which remains the main cause of the appearance and development of fatigue damage. The effectiveness of the impact of strengthening processes can also be increased by preliminary grinding of the seam surface in order to remove defects and irregularities of welding work, which creates favorable conditions for influencing the stress concentration, hence increasing the bearing capacity of the seam [13].

3   Results and Discussion

The process of corrosion of responsible elements of the CTS abruptly reduces the reliability and operability of the system, which requires the use of new effective instruments and methods to increase the corrosion resistance of these elements. One of the concrete solutions to increase anticorrosive properties is the application of new highly effective protective coatings on loaded sections of system, which, interacting with surface micro-irregularities, fills their micro-depressions and micro-defects of welds and by simple technological operations increases the corrosion resistance of system. To apply these coatings, the outer surface of the seam is subjected to a preliminary examination to eliminate welding defects and to create surface micro- irregularities, then thoroughly cleaned and degreased to increase the degree of adhesion of the coating to the seam surface. After the coating is applied, it is exposed to pressure for its final formation. These operations are usually performed at $T \geq 5$ °C ambient temperature and at the absence of precipitation, and to increase the degree of adhesion after 2–4 h of its application, approximately 2 h the coating is treated with an air heater at T = 60 … 100 °C. It is recommended to start the work of the structural elements after 4.0 … 0.5 days (if the welding work is performed, respectively, at ambient temperatures T = 5 … 30 °C), and in the presence of volatile chemical compounds, gases and dust in the environment—after 5.0 … 1.0 days.

To assess the influence of corrosion and the possibility of application of effective anti-corrosive coatings, comparative static corrosion resistance tests were performed on flat metal samples made of structural steel *St10*, which were accurately weighed, thoroughly cleaned and degreased before testing. The newest polymer material of the Belzona 1111 FN10132 (SuperMetal) brand was used as an anticorrosive coating, which, according to the results of production tests, shows:

- high level of corrosion resistance—under influence of alcohols, gases, hydrocarbons, technical and vegetable oils, various types salt solutions, pure- and seawater;
- satisfactory level—with organic and inorganic acids of medium concentration (up to 50%);
- unsatisfactory level—with the same acids, but in a high concentration ($\approx 95\%$).

Of the 6 tested samples (N1, … N6), three were the initial options (*NN* 1, 2, 6), and on the rest ones (*NN* 3, 4, 5), according to the coating technology from the Belzona 1111 material, strong anticorrosive protective layers were created (Fig. 1b). Corrosion resistance tests were carried out in a 10% aqueous solution of $FeCl_3$ for 24 h and at the temperature of $T = 20\ °C$.

(a)   (b)   (c)
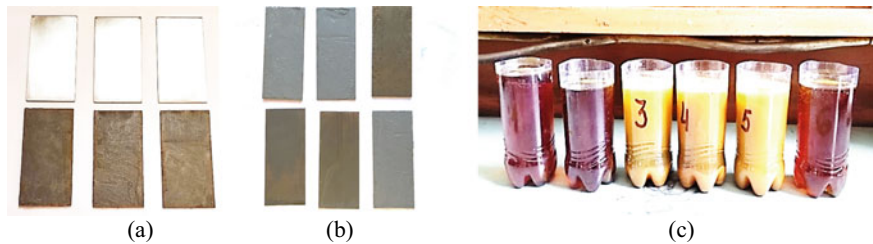
Fig. 1 Tests of flat steel samples in a corrosive solution with 10% $FeCl_3$ **a** before testing: *NN 1, 2, 6*—initial samples, *NN 3, 4, 5*—with an anticorrosive coating; **b** samples after testing; **c** the state of the corrosive solution after testing

For samples *NN 1, 2,* 6 changes in the microstructure of the surface layers and a decrease in the initial mass in the range of 4.5 … 10.0% are observed. The study of the surface condition of these samples on a *ZEISS AXIO VERT* A1 electron microscope (magnification $\times$ 1000 times) indicates the presence of corrosion damage with a depth of 20 … 22 mm, which in the sequel may become center for the development of corrosion-fatigue cracks (Fig. 2). For samples NN 3, 4, 5, these defects are not observed, which proves the high efficiency of applying this durable anticorrosive coating.

4   Conclusions

Reducing the design time of new CTS involves the clarification of the parameters of the affecting factor, based on the analysis, classification of their operating conditions and loading modes, by using productive design and technological measures that allow

(a)	(b)	(c)
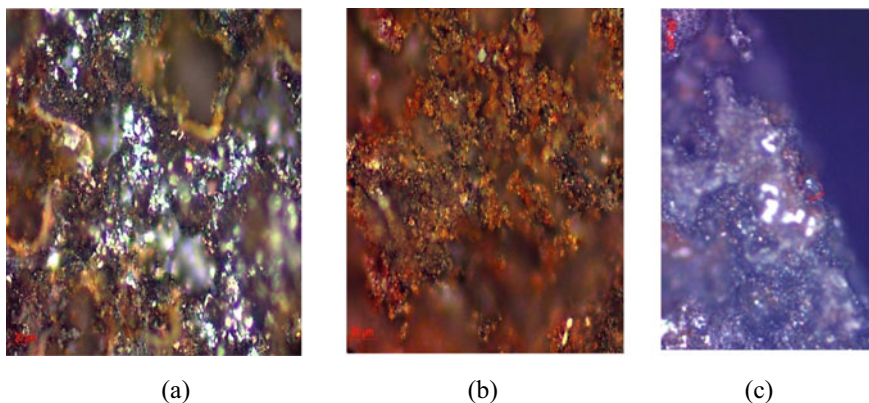
Fig. 2 Surface microstructure after static tests on samples *NN 1, 2, 6* **a** and *NN 3, 4, 5* **b**; **c** surface cracks in samples *NN 1, 2, 6*

determining and using their limit values. Simultaneously, the presence of a significant number of diverse factors (11 pieces) acting together and with various combinations predestine the task of their study and classification by the applying the principle of system analysis. These factors are presented in 4 groups. The features of the expression of the most significant factors—stress concentration, the corrosive effect of the environment and fatigue phenomena, as well as strengthening and corrosion protection techniques, which in most cases come into a single composition, are considered as a total.

The mechanism of appearance and development of corrosion-fatigue damages, which, unlike other factors, working in the entire range of durations of limited and long term endurance, has been studied. To increase the bearing capacity of structural elements the application of a new corrosion-resistant polymer plating of the Belzona 1111 brand is recommended. The numbers of static corrosion-proof tests in a $FeCl_3$ corrosion solution were performed, which confirmed the effectiveness of using of this plating.

So that, to increase the resistance to corrosion fatigue of structural elements butt welded junctions, which are significant stress concentrators, the technique of surface plastic deformation of welds has been applied, where, due to the appearance of residual compression stresses, the effect of working loading of CTS has been largely compensated and the fatigue resistance of structural elements has been increased [14].

References

1. Chibukhchyan, G., Stakyan, M., Chibukhchyan, O.: Improving the carrying capacity of structural elements of vehicles by the corrosive strength criterion. J. Mach. Manuf. Reliab. **48**, 551–556 (2019). https://doi.org/10.3103/S1052618819060037
2. Ibatullin, I.D.: Kinetics of fatigue damage and destruction of surface layers. Samara (2008)
3. Pirumyan, N.V., Stakyan, M.G.: Measures to increase the building steel structures' bearing capacity. IOP Conf. Se.: Materials Sci. Eng. **913**(1–6), 022006 (2020). https://doi.org/10.1088/1757-899X/913/2/022006
4. Korolov, V., Vysotskiy, Y., Filatov, Y.: Design criteria of reliability and safety in the design of corrosion protection of structural steel. EUROCORR-2014. The European Corrosion Cogress: "Improving materials durability: from cultural heritage to industrial applications", Pisa (2014)
5. Kogaev, V.P.: Calculations for strength under stresses variable in time. Mashinostroenie, Moscow (2003)
6. Krastev, D.: Improvement of corrosion resistance of steels by surface modification, pp. 295–316. IntechOpen, London (2012). https://doi.org/10.5772/33247
7. Orlov, B.N.: Innovative technologies for ensuring the reliability of working elements of machines and equipment. Moscow (2013)
8. Pirumyan, N.V., Stakyan, M.G.: Asessment of corrosion fatigue strength of gas-transport system constructions under atmospheric forcing. IOP Conf. Se.: Materials Sci. Eng, **698**(1–6), 022077 (2019). https://doi.org/10.1088/1757-899X/698/2/022077
9. Bazhenov, Y.V., Bazhenov, M.Y.: Fundamentals of reliability and operability of technical systems. Publishing House of the VlSU, Vladimir(2017)
10. Kirpichev, V.A., Saushkin, M.N., Smyslov, V.A.: On mathematical modeling of fields of plastic deformations arising from various types of strengthening treatment. Mat. Mod. Phys., Economy. Tech. Social. Systems and Processes: Proceedings of XVII International Conference. Ulyanovsk, pp. 116–117 (2009)
11. Pirumyan, N.V., et al.: Mathematical modeling of the process of reduction of the material consumption of gas transmission system elements. Key Engineering Materials **906**, 115–123 (2022). https://doi.org/10.4028/www.scientific.net/kem.906.115
12. Dashchenko, A.F., Kravchuk,V.S., Iorgachev, V.D.: Bearing capacity of strengthening of machine parts. "Astroprint", Odessa (2004)
13. Gubanov, V.F.: Parameters of roughness of smoothed surfaces. Strengthening Technologies and Coatings **11**, 6–9 (2010)
14. Zharskiy, I.M., et al.: Technological methods for ensuring the reliability of machines. Higher School, Minsk (2010)

Power Calculation of Ball-Tube Mill Drives in the Construction Materials Industry

V. S. Bogdanov , S. I. Antsiferov$^{(\boxtimes)}$, D. V. Bogdanov , and E. A. Sychev

Belgorod State Technological University Named After V.G. Shukhov, Belgorod, Russia
`anciferov.sergey@gmail.com`

Abstract. The article deals with the production of construction materials and products based on them, the main ones of which are cement, concrete, brick, stone, lime. The source for obtaining construction materials is natural resources that are subjected to various technological processes: grinding, classification, dosing, mixing, molding, heat treatment. The most energy-intensive process is grinding. The main equipment for grinding construction materials are ball-tube mills, which are actively used in industry and are constantly being improved. The main issue of improvement is to reduce the power consumption of a ball-tube mill with cross-longitudinal movement of the load. A comparative analysis and the possibility of using the known methods for calculating the power consumption of the drive of a ball-tube mill with cross-longitudinal movement of grinding bodies is given. The calculation scheme of the ball-tube mill, equipped with an inclined partition, is considered, and a detailed analysis of the mode of motion of the grinding bodies is described and given. Conclusions were obtained about the change in the value of power consumption of the ball-tube mill drive from minimum to maximum, due to the change in the level of the grinding bodies in both chambers of the mill during the cycle from maximum to minimum. Generalizing conclusions were made and it was proposed to reduce the mass of grinding bodies in proportion to the value of additional power consumption, in order to reduce the amplitude of the torque fluctuation on the shaft of the crushing cylinder.

Keywords: Ball-Tube Mill · Inclined Partition · Grinding Bodies · Loading · Power Consumption · Angle of Inclination · Grinding

1 Introduction

A wide range of building materials is used in the construction of buildings and structures. The main construction materials in industrial and civil construction are cement, concrete, bricks, stone, wood, lime, sand, ferrous metals, glass, roofing materials, plastic and others. The source for obtaining construction materials are natural resources that are subjected to various technological processes. These processes include: grinding, classification, dosing, mixing, molding, heat treatment.

The most energy-consuming technological process is grinding, which in most enterprises is carried out with such type of equipment as a ball-tube mill.

One of the directions of use of ball-tube mills is grinding raw materials, which are further required for obtaining materials such as air binders—gypsum binders, air lime, magnesia binders, Portland cement, mortars, dry construction mixtures, etc. The most common material in construction is Portland cement, a hydraulic binder with a predominance of calcium silicates. Portland cement is made by finely grinding clinker and dihydrate gypsum.

Today Portland cement is used as one of the main components for the production of reinforced concrete, commercial concrete, mortars, unburnt wall products, asbestos cement. In the production of Portland cement the grinding process plays an important role, due to the fact that the grinding fineness of the raw materials depends on the quality indicators of the cement stone, such as setting rate, hardening and strength. To achieve the required fineness, large energy costs are required, and during the operation of a ball-tube mill most of the drive power is wasted on ensuring the movement of grinding bodies in the mill body and overcoming the friction forces in the mechanical gears.

In conventional ball-tube mills (BTM), the grinding bodies move in the cross-section of the crushing cylinder in a plane perpendicular to the longitudinal axis of the crushing cylinder [1–4].

The theoretical calculation of the kinematics of grinding bodies and the energy modes of the ball-tube mill is based on the two-phase ball motion model proposed by Davis, according to which the ball first moves along a circular path together with the crushing cylinder, and then at the selection point it changes to a parabolic free-fall path, hitting the crushing cylinder or balls at the drop point. Then the cycle is repeated [1–6]. The longitudinal movement of grinding bodies inside the BTM was not considered and was not allowed due to the possible occurrence of longitudinal loads on the bearing supports, which would lead to emergency situations—the possibility of destruction of the bearing support.

The basis for calculating the power consumption of the BTM drive is the dependence:

$$N = A\gamma V S D^{0.5}, \tag{1}$$

there

A   S.E. Andreev's constant;
γ bulk weight of grinding bodies (GB);
V   crushing cylinder volume;
S   speed coefficient, $S(\psi, \varphi)$;
D   inner diameter of the mill body;
ψ relative rotation frequency of the crushing cylinder;
φ load factor.

All known theoretical studies are based on the refinement of the type of function $S(\psi, \varphi)$.

Due to the fact that in conventional BTM the load factor is constant, then the power consumption of the drive remains unchanged [7–10]. A significant disadvantage of the known structures of the BTM is that only 50% of the GB have an active effect on the

grinding process, while the remaining 50% form a stagnant zone, move in a dense compact layer in the central part of the grinding load, preventing the longitudinal movement of the crushed material.

2 Materials and Methods

2.1 The Power of the BTM Drive with Cross-Longitudinal Movement (CLM) of Grinding Bodies

The nature of the movement of GBs in our proposed design of the BTM with CLM loading (Fig. 1) differs significantly from their movement in conventional BTMs. This is ensured by the fact that the inter-chamber partition 3 in the crushing cylinder is set at an angle β to its longitudinal axis (y).
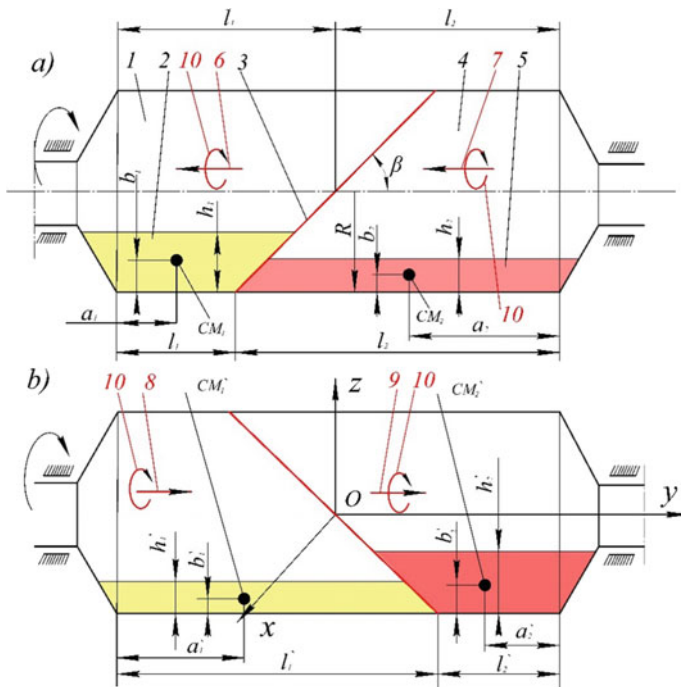
Fig. 1 Calculation scheme of a ball-tube mill: 1,4—mill chambers; 3—inclined partition; 2,5—grinding bodies; 6, 7, 8, 9, 10—directions of movement of grinding bodies

In position a (Fig. 1a) the length l_1 of the lower part of the chamber 1 is minimal, the grinding bodies 2 in it are located at the maximum level h_1. Center of masses (CM$_1$) of grinding bodies (GB) in chamber 1 is located at the minimum distance a_1 from the filling bottom and at the distance b_1 from the crushing cylinder body. The length l_2 of the lower part of the chamber 4 is maximum; the grinding bodies 5 are located at minimum level h_2. CM$_2$ is located at maximum distance a_2 from the discharge bottom and minimum b_2

from the crushing cylinder body. The subsequent rotation of the crushing cylinder after half a turn will take the characteristic position b (Fig. 1b).

The lower part of chamber 1 will become maximum l'_1. GBs will move in the longitudinal direction 8 under the inclined partition 3 simultaneously making a rotary movement in the direction 10 in the cross section of the crushing cylinder. The stagnant zones in the load are destroyed. At this point, the length l'_2 of the lower part of chamber 4 becomes minimal. The level h'_2 of GB becomes maximum. CM_2 of the load will move to the position characterized by the distance a'_2 from the unloading bottom and b'_2—the distance from the inner surface of the crushing cylinder. The GB will move along the longitudinal axis of the crushing cylinder in the direction 9 toward the discharge cover, making a cross-sectional movement in the direction 10.

After that, the crushing cylinder will take the position a. On this basis, the grinding bodies perform both cross and reciprocating longitudinal motion.

As the level of grinding bodies in both chambers of the mill during the cycle varies from maximum to minimum and, of course, CM loading also varies from minimum to maximum, it is obvious that the amount of power consumed by the drive of the BTM also changes.

The intensity of CLM of grinding bodies depends primarily on the angle of inclination β of the partition 3, the angle ε of the natural slope of the grinding bodies, the frequency ψ of rotation of the crushing cylinder, and the factor φ of loading. A significant influence on the intensity of CLM of grinding bodies has the length of the chambers. We have found that the greatest influence on the mode of movement of the grinding balls by an inclined partition has only in a certain zone, located under the partition. It is in this zone there is an intensive redistribution of energy consumed by the mill for the cross/longitudinal movement of the grinding bodies.

First of all, we are interested in the additional power consumption at the GB CLM in the zone of active influence of the inclined partition. Behind this zone, calculation of power consumption is carried out according to the known methods used for calculation of waterfall and cascade modes of GB movement [6–8].

The additional power consumption at the GB CLM in chamber 1 is equal to:

$$N = N_u + N_f, \tag{2}$$

there N_u—power spent on the vertical movement of the GB; N_f—power spent on overcoming the frictional forces in the longitudinal motion of the GB.

Based on the calculation scheme (Fig. 1), the coordinates of CM loading in the final form are calculated by the equations:

$$X_c = R^4 L_x / V, \tag{3}$$

$$Y_c = R^4 L_y / V, \tag{4}$$

$$Z_c = R^4 L_z / V, \tag{5}$$

there:

$$L_x = 0.25\pi\phi \sin\xi/\text{tg}\beta + \sin\xi/\text{ctg}\beta(\cos\xi/\lambda\text{tg}\beta - bx)(1 - x^2)^{1.5}, \tag{6}$$

$$L_y = (1 - 4\beta^2)\pi\vartheta/8\text{tg}^2\beta$$
$$+ [\cos\xi(\cos\xi - bx - 4b\cos\xi(b - x\cos\xi)](1 - x^2)^{1.5}/12b\text{tg}^2\beta$$
$$L_z = 0.25\pi\vartheta\cos\xi/\text{tg}\beta$$
$$+ [\cos\xi(\cos\xi - bx) - 4b(b - x\cos\xi)](1 - x^2)^{1.5}/6b\text{tg}\beta$$

there: ξ—crushing cylinder rotation angle; x, λ—dimensionless parameters, equal, respectively, to, $x = (R - h)/R$, $\lambda = l_1/R$.

3 Results and Discussion

Figure 2 shows an example of calculation of CM loading displacement in the first chamber of the mill 4×13.5 m, from which it follows that for each cycle CM loading makes a complex movement—along the axis of O$\mathcal{Y}$ this trajectory is an elongated ellipse (Fig. 2a), the major axis of which coincides with the longitudinal axis of O$\mathcal{Y}$ crushing cylinder, and relative to the plane ZO$\mathcal{Y}$ (Fig. 2b)—slanted line whose slope angle is equal to the angle ε of natural inclination of GB. In CLM mills, the CM loading of the grinding bodies moves more intensively during the cycle (Fig. 2) with respect to all coordinate axes than in conventional mills, hence the GBs perform more grinding work and, naturally, additional energy is required for this.

Figure 3 shows the dependence of the amplitude of oscillations of the loading CM on the size of the zone of active influence of the inclined partition relative to all coordinate axes. The analysis of the graphical dependencies gives a reason to conclude that with practically unchanged amplitude of oscillations of the loading CM relative to the axis O$\mathcal{Y}$, the amplitude of oscillations along the axes OX and OZ increases by three times. Moreover, large amplitudes of CM loading oscillations are achieved at smaller CM natural slope angles and the larger the amplitude of CM loading oscillations, the more intensive the grinding process in mills with GB CLM. This is practically an important conclusion—mills with CLM loading should have the lowest possible ε angle of natural slope of the GB, which intensifies the process of grinding the material as a whole.

To determine the amount of power required to move vertically M, let us calculate the corresponding work, which is equal:

$$A_u = g\gamma\Delta z_c V. \tag{7}$$

there: V—the volume of GB moved by the inclined partition in one chamber of the mill; Δz_c—change of coordinate of the loading CM along the axis OZ.

The corresponding power to lift the GB is:

$$N_u = g\gamma V z_c = g\gamma R^4 L_z. \tag{8}$$

Simultaneously with the movement of GBs relative to the vertical axis, they move along the O$\mathcal{Y}$ axis. The work spent on overcoming the frictional forces of GBs at their horizontal movement is equal:

$$A_f = f_c g\gamma s V, \tag{9}$$

there:
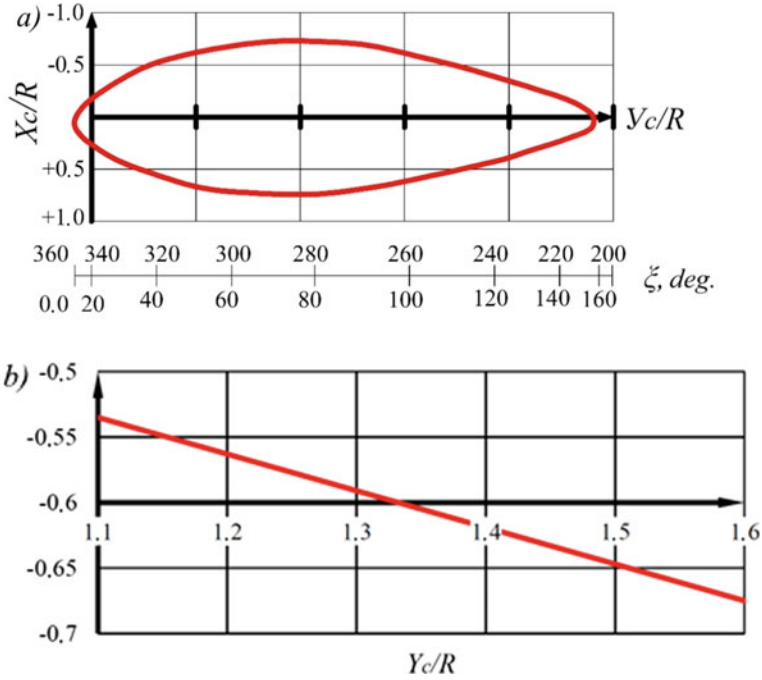
Fig. 2 Relocation of the load center of mass in the first mill chamber 4×13.5 m: **a** in relation to the axis OY, **b** in relation to the plane ZOY: $\varphi = 0{,}3$; $\psi = 0.76$; $\beta = 50°$; $\lambda_1 = \lambda_p = 2.63$
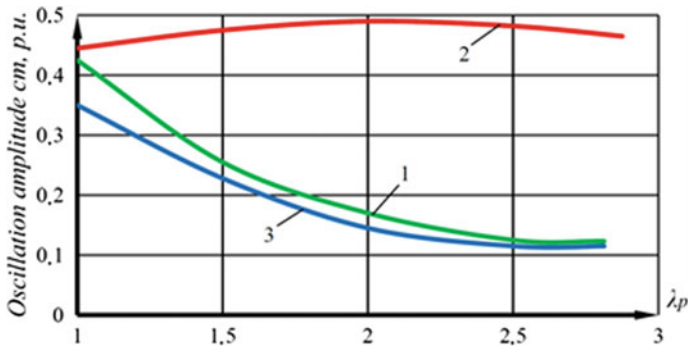
Fig. 3 Dependence of the oscillation amplitude of the center of mass of the load on the size of the active influence zone of the inclined partition. Relocation of CML: 1—along the axis OX; 2—along the axis OY; 3—along the axis OZ

f_c sliding friction coefficient;
s the distance by which the center of the grinding bodies moves along the axis OY.

Taking into account (9), the power consumed by the horizontal movement of the GB relative to the axis OY is equal:

$$N_f = f_c g \gamma s V. \tag{10}$$

Taking into account (4), (5), we present formula (10) in the form

$$N_f = f_c g \gamma R^4 \left[L_x^2 + L_y^2 \right]^{0.5}. \tag{11}$$

Then the total additional power expended by the inclined partition to move the GB will be equal:

$$N_{A1} = g \gamma R^4 \left(v_{1z} + f_1 \left(v_{1x}^2 + v_{1y}^2 \right)^{0.5} \right). \tag{12}$$

In the second chamber 4 GB of mills in the zone of active influence of the inclined partition move as well as in the chamber 1, only the process of their movement is shifted by 180°.

Therefore, for the second chamber of the mill, the additional power consumption is written in the form:

$$N_{A2} = g \gamma_1 R_1^4 \left(v_{1z} + f_1 \left(v_{1x}^2 + v_{1y}^2 \right)^{0.5} \right), \tag{13}$$

there: γ_1, R_1, f_1—parameters characterizing the size and loading of the second chamber.

The total additional power required to move the GB by the inclined partition in the BTM is equal:

$$N_A = N_{A1} + N_{A2}. \tag{14}$$

Figure 4 shows the results of the calculation of additional power consumption for the movement of GB in one chamber of the mill 4×13.5 m. The graphical dependences have a sinusoidal character and equal phase—π. The longitudinal displacement of GBs N_f requires more energy than their vertical displacement, as evidenced by the larger amplitude of the function $N_f(\xi)$, than the function $N_u(\xi)$. In the area of the rotation angles of the crushing cylinder $0° < \xi < 180°$ the function $N_u(\xi)$ has a negative value. This is explained by the fact that the GBs store energy when the chamber length decreases, some of which is subsequently spent on the longitudinal movement of the load when the chamber length increases.

It is known from the theory of the BTM [2–4] that the maximum level of power consumption corresponds to the maximum efficiency of the grinding process. In our case, when the rotation of the crushing cylinder in the area of the angle $180° < \xi < 360°$ the GBs possess the maximum energy. The mode of GB motion is avalanche-like, the angle of GB selection is maximal, the height of GB fall is maximal and, naturally, the impact energy at the point of fall is also maximal. From the graphs shown in (Fig. 4) it follows that the share of impact grinding consumes about 40% of the additional energy, and 60% of the share of grinding by abrasion.

As additional energy consumption is required for the CLM of grinding bodies, the modernization of the existing BTM requires, respectively, an increase in the installed electric motor power, or, in proportion to the value of the additional power, a reduction in the mass of the GB.
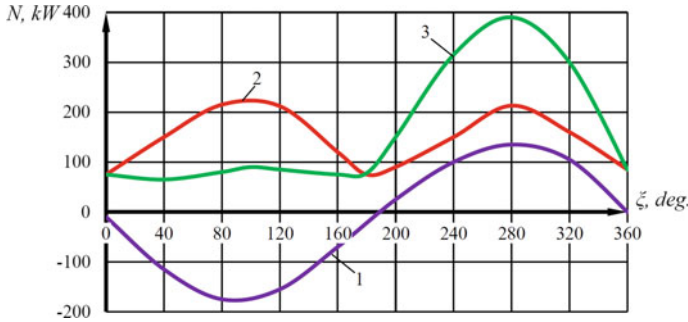
Fig. 4 Calculated dependence $N(\xi)$: 1—$N_u(\xi)$; 2—$N_f(\xi)$; 3—$N_A(\xi)$

4 Conclusion

Thus, the equations allowing to calculate the total additional power consumed by the BTM drive during the CLM of grinding bodies, as well as its components consumed for the lifting and longitudinal movement of the GB, were obtained. A comparative analysis of the values of the additional power consumption components showed that the mode of GB movement is characterized by their avalanche-like fall, which significantly increases the efficiency of the grinding process by impact, which consumes up to 40% of the additional consumed energy. The remaining 60% of the energy is spent on intensive grinding by abrasion at CLM of GB. In order to reduce the amplitude of torque fluctuations on the shaft of the crushing cylinder, it was proposed to reduce the mass of GB in proportion to the value of additional power consumption.

References

1. Fadin, Y.M., Khakhalev, P.A., Degtyarev, P.A.: Simulation of the ball mill loading movement and study of its operation modes depending on geometrical parameters of the lining. J. Phys: Conf. Ser. **1353**, 1–5 (2019). https://doi.org/10.1088/1742-6596/1353/1/012026
2. Latyshev, S.S., Voronov, V.V., Bogdanov, V.S., Fadin Y.M., Bazhanova, O.I., Maslovskaya, A.N.: Mathematical modeling of load's movement in lifter of intramill recirculation device inside tubular mill. In: IOP conference series: materials science and engineering, pp. 1–9. Iopscience, Tomsk, Russian Federation (2018). https://doi.org/10.1088/1757-899X/327/2/022046
3. Bondarenko, J.A., Khanin, S.I., Bestuzheva, O.V.: Investigation of stress-strain state of ball mill trunnion. In: Proceedings of the 5th international conference on industrial engineering, pp. 883–893. Springer, Cham (2019). https://doi.org/10.1007/978-3-030-22041-9_94
4. de Alessandro, L.R.: Oliveira, Luís Marcelo Tavares: modeling and simulation of continuous open circuit dry grinding in a pilot-scale ball mill using Austin's and Nomura's models. Powder Technol. **340**, 77–87 (2018). https://doi.org/10.1016/j.powtec.2018.09.016

5. Bogdanov, V.S., Sharapov, R.R., Fadin, Y.M.: Fundamentals of calculation of machinery and equipment of enterprises of building materials and products. Thin science-intensive technologies, Russian Federation (2013)
6. Bogdanov, V.S., Bogdanov, D.V., Semikopenko, I.A.: Processes in the production of construction materials. Thin science-intensive technologies, Russian Federation (2018)
7. Reichardt, R., Wiechert, W.: Event driven algorithms applied to a high energy ball mill simulation. Granular Matter **9**, 251–266 (2007). https://doi.org/10.1007/s10035-006-0034-y
8. Gupta, V.K., Sharma, S.: Analysis of ball mill grinding operation using mill power specific kinetic parameters. Adv. Powder Technol. **25**, 625–634 (2014). https://doi.org/10.1016/j.apt.2013.10.003
9. Bogdanov, V.S., Fadin, Y.M., Dontsova, Y.A., Bogdanov, N.E., Fyot, S.K.: Mechanics of crushing medium in ball mills with longitudinal-transverse motion of grinding bodies. Bulletin of BSTU named after V.G. Shukhov **3**(8), 117–125 (2018). https://doi.org/10.12737/article_5b6d586e6ed9b2.54424779
10. Bürger, R., Bustamante, O., Fulla, M.R., Rivera, I.E.: A population balance model of ball wear in grinding mills: an experimental case study. Miner. Eng. **128**, 288–293 (2018). https://doi.org/10.1016/j.mineng.2018.09.004

Calculation of Reliability of Beam with Corrugated Wall with Limited Information About the Controlled Parameters at the Stage of Operation

N. L. Galaeva[(✉)] [iD]

Moscow State University of Civil Engineering, Moscow, Russia
`Natalia-fdf@rambler.ru`

Abstract. Today a significant number of buildings and structures, which have already exhausted their resource, require inspection and diagnostics that aims to assess the technical condition, as well as making decisions on the possibility of their further operation, the need for overhaul, reconstruction, etc. When examining the construction of buildings and structures and assessing their technical condition it is not always possible to obtain complete statistical information about the monitored parameters, and there may be a situation in which complete statistical information may be obtained for part of the monitored parameters that allows to identify the distribution law and parameters of this distribution, and for another part of the parameters—incomplete. In such cases, when carrying out reliability calculations of a structure, the use of probabilistic-statistical methods can lead to inaccurate results and become incorrect. The combination of random and fuzzy variables in such situations when carrying out reliability calculations of building structures allows a more complete use of all statistical information obtained as a result of the survey of structures. The paper proposes a particular methodology for calculating the reliability of a beam with a corrugated wall by the criterion of compressed chord bending in the plane of the wall.

Keywords: Reliability of building structures · Corrugated wall beam · Random variable · Fuzzy variable · Reliability interval

1 Introduction

Ensuring the safe operation of buildings and structures is one of the key issues of the construction industry. Throughout the entire life cycle of buildings and structures are exposed to various factors that can have a negative impact on their technical condition, as well as lead to accidents, the consequence of which can be the collapse of building structures or the building as a whole, which, in turn, not to mention the material damage, can lead to more significant and serious consequences, namely the injury and possible loss of life. It is worth noting that accidents of building structures and buildings in general rarely occur without any preceding signs indicating the possible beginning of the exit

of the structure from the serviceable (normal) state, i.e. in most cases before the onset of emergency condition there is always a period of time during which visible defects and damages appear in the form of developing unacceptable deformations, subsidence, cracks, etc. With timely monitoring and inspection of building structures, there is an opportunity to identify early signs that precede the onset of emergency conditions, to take appropriate measures to restore, strengthen, prevent further destruction of structures, as well as to address the issue of further operation of the building or structure.

Recently, both in Russia and abroad there have been a number of emergency collapses of buildings and structures: the collapse of the Bassman Market structures in Moscow (Russia, 2006); the collapse of a residential building in Henan Province (China, 2015.); the collapse of a bridge at the entrance to the village of Egorovo (Russia, Perm Region, 2015); the collapse of part of a residential building in Perm (Russia, 2015); the collapse of part of a barracks building in Omsk (Russia, 2015); the collapse of a road bridge in Genoa (Italy, 2018), etc. The causes of these accidents were mainly: the unsatisfactory condition (deterioration) of individual structural elements, their insufficient carrying capacity, carrying out the restructuring (reconstruction) of buildings without assessing the residual carrying capacity and reliability of building structures, the lack of timely conducted inspections and monitoring of the technical condition of building structures. The presented examples of emergency destructions confirm the relevance of the problem of assessing the reliability of building structures of buildings and structures, especially at the stage of operation, in order to prevent and exclude such destructive consequences.

To date, quite a large number of scientific works of Russian and foreign scientists is devoted to the issues of development of calculations and reliability assessment of building structures. A considerable part of these works is based on the use of probabilistic-statistical methods for reliability calculation [1–6]. It is suggested to use these methods to assess reliability in the current normative and technical documentation, provided that there is a sufficient amount of complete and reliable information about the monitored parameters, allowing for its statistical analysis. Infrequently at the stage of operation of building structures there are situations when it is not always possible to get full and reliable information about controlled parameters, in this case the probabilistic-statistical methods cannot be applied at an estimation of reliability as they can lead to inaccurate results. There is no information about how to calculate and evaluate the reliability of building structures in this situation in the existing normative documents. In scientific works of V. S. Utkin and his followers [7–9], B. D. Kaufman, S. G. Shulman [10, 11] and others [11–13] the questions of calculations and reliability evaluation under the limited statistical information about the controlled parameters are considered. In the absence of complete statistical information, the provisions of fuzzy sets theory and possibility theory, random sets theory, the theory of interval averages or generalized probabilities can be used in calculations of reliability to describe uncertainties and simulate the lack of sufficient background information. In order to receive the most exact and informative result at calculation of reliability of a building structure it is necessary to aspire to the fullest use of all available statistical information. So, for example, in practice there can be a situation, when as a result of building structure inspection it is possible to receive the full statistical information on a part of controlled parameters, and on other controlled parameters the received statistical information is incomplete, i.e. in this case a part of

parameters can be represented in the form of random variables, and another part—in the form of fuzzy variables. Using the possibility method for reliability calculation in such a situation, based on the theory of possibilities, representing all the parameters in the form of fuzzy variables, will lead to the loss of useful statistical information about a random variable, which will reduce the informational content of the obtained result of reliability index calculation, because it will lead to its wider interval. Combining random variables and fuzzy variables in calculations of the reliability of building structures allows the most complete use of all available information.

This paper is a continuation of the work on the development of private methods of calculating the reliability of building structures on the basis of the modernized method.

2 Methods and Materials

The reliability calculation based on the upgraded method consists in the fact that the probability of an event $(X \leq Y)$ is established from the initial information. In this paper, we will consider the case in which: X is a generalized load with limited information (fuzzy variable), and Y is a generalized strength that has complete information (random variable). X will be characterized by a distribution function of the form:

$$\pi_X(x) = e^{-[(x-a_x)/b_x]^2}, \tag{1}$$

there $a_x = (X_{\max} + X_{\min})/2$, $b_x = (X_{\max} - X_{\min})/(2\sqrt{-\ln \alpha})$, $\alpha \in [0; 1]\,[0; 1]$, α—the level of risk (for tasks of construction mechanics we take $\alpha = 0.2$).

The fuzzy variable X can also be graphically characterized by probability distribution functions $\underline{P}_X(x)$ and $\overline{P}_X(x)$. Figure 1 shows these functions and their relation to $\pi_X(x)$ according to Eq. (1).
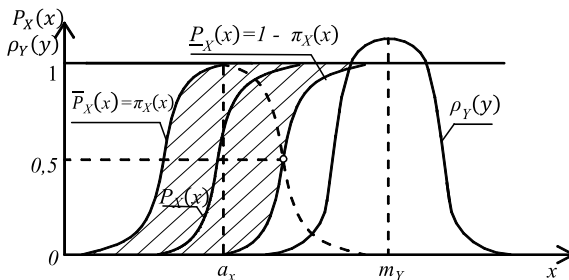
Fig. 1 Distribution function $(\underline{P}_X(x) \leq P_X(x) \leq \overline{P}_X)$ and probability density function $\rho_Y(y)/$

The random variable Y will be characterized, for example, by a normal distribution with a probability distribution density:

$$\rho_Y(y) = \frac{1}{\sqrt{2\pi}\,S_Y} e^{-\frac{(y-m_Y)^2}{2S_Y^2}}, \tag{2}$$

there m_Y—mathematical expectation; S_Y—standard deviation.

Figure 1 conventionally shows the function according to Eq. (2) (conventionally because they have different units of ordinates and the same notation of the argument x and $y = x$ are adopted hereafter).

Using the theory of reliability calculation by the modernized method to determine the reliability interval, we present formulas for the lower and upper values of failure-free operation:

$$\underline{P} = \int\limits_{S}^{\infty} \rho_Y(y)\underline{P}_X(x)\mathrm{d}x \text{ and } \overline{P} = \int\limits_{S}^{\infty} \rho_Y(y)\overline{P}_X(x)\mathrm{d}x, \tag{3}$$

there S—failure-free operation area.

Let us take it according to Fig. 1: $\underline{P}_X(x) = 1 - \pi_X(x) = 1 - e^{-[(x-a_x)/b_x]^2}$ at $x > a_x$, $\overline{P}_X(x) = \pi_X(x) = e^{-[(x-a_x)/b_x]^2}$ at $x \le a_x$. Taking into account the Eqs. (1), (2), (3) and Fig. 1 the calculation formulas will look like:

$$\left.\begin{aligned}
\underline{P} &= \int\limits_{0}^{a_x} \frac{1}{\sqrt{2\pi}S_Y} e^{-\frac{(x-m_Y)^2}{2S_Y^2}} \cdot 0\,\mathrm{d}x + \int\limits_{a_x}^{\infty} \frac{1}{\sqrt{2\pi}S_Y} e^{-\frac{(x-m_Y)^2}{2S_Y^2}} \cdot \left(1 - e^{-[(x-a_x)/b_x]^2}\right)\mathrm{d}x \\
\overline{P} &= \int\limits_{0}^{a_x} \frac{1}{\sqrt{2\pi}S_Y} e^{-\frac{(x-m_Y)^2}{2S_Y^2}} \cdot e^{-[(x-a_x)/b_x]^2}\,\mathrm{d}x + \int\limits_{a_x}^{\infty} \frac{1}{\sqrt{2\pi}S_Y} e^{-\frac{(x-m_Y)^2}{2S_Y^2}} \cdot 1(x)\,\mathrm{d}x
\end{aligned}\right\} \tag{4}$$

The reliability of a structural element according to the criterion $X \le Y$ will be characterized by the interval of failure-free operation values $[\underline{P}; \overline{P}]$, the true value of reliability will be within this interval.

3 Results and Discussion

Let us consider the calculation of reliability of a beam with corrugated wall, operating in the elastoplastic stage, according to the criterion of stability of the compressed chord bending in the plane of the wall. The mathematical model of the limit state in deterministic formulation will have the form:

$$\frac{N_f}{\varphi_f A_f R_y \gamma_c} \le 1 \text{ or } \frac{N_f}{\varphi_f A_f \sigma_T} \le 1 \text{ or } \sigma \le \sigma_T, \tag{5}$$

there N_f—belt compression force ($N_f = M_1/h_1$, there M_1—maximum bending moment occurring in the middle third of the beam length between the bracing points); φ_f—coefficient, which is determined as for a centrally-compressed rod; A_f—the area of the compressed belt (gross); R_y—the strength of steel to the yield strength (for the limit state, instead of R_y, we take the yield strength σ_T); γ_c—coefficient of working conditions.

When determining the reliability of elements of building structures at the stage of operation it is not always possible to obtain complete statistical information about the parameters of the mathematical model of the limiting state. Let us write Eq. (5) taking into account the variability of some parameters denoted by the symbol "~":

$$\tilde{\sigma} = \frac{\tilde{M}_1}{\varphi_f A_f h_1} \le \tilde{\sigma}_T, \tag{6}$$

there φ_f, A_f, h_1—we take as deterministic values. The moment from the operating load M_1 is defined as the sum of the bending moments (M_{perm}) from the permanent and (M_{tem}) temporary load. The bending moment M_{perm} from the permanent load on the beam can be assumed to be a deterministic value and determined by the methods of strength of materials. The bending moment M_{tem} from the temporary load can be determined from the results of measurements of deformations in the chords of the beam, and since the information obtained about the temporary load acting on the beam can be limited and non-uniform, $\tilde{M}_1 = M_{perm} + \tilde{M}_{tem}$ and respectively $\tilde{\sigma}$ will be assumed a fuzzy variable. The yield strength $\tilde{\sigma}_T$ of the beam material can be determined, for example through the hardness of the steel using the experimental and theoretical scratch method. The use of this method in some cases allows complete statistical information about the yield strength, as a result $\tilde{\sigma}_T$ can be considered as a random variable. Thus, to calculate the reliability of a beam with a cross-corrugated wall, we consider the case in which:

$\tilde{\sigma}$—a fuzzy variable with a distribution function of the form:

$$\pi_\sigma(\sigma) = e^{-[(\sigma - a_\sigma)/b_\sigma]^2}, \tag{7}$$

there $a_\sigma = (\sigma_{\max} + \sigma_{\min})/2$, $b_{M_1} = (\sigma_{\max} - \sigma_{\min})/(2\sqrt{-\ln\alpha})$, $\alpha \in [0; 1]$.

$\tilde{\sigma}_T$—a random variable that varies according to the normal distribution law with a probability density distribution:

$$\rho_{\sigma_T}(\sigma_T) = \frac{1}{\sqrt{2\pi}S_{\sigma_T}} e^{-\frac{(\sigma_T - m_{\sigma_T})^2}{2S_{\sigma_T}^2}}, \tag{8}$$

there m_{σ_T}—mathematical expectation; S_{σ_T}—standard deviation.

We use Eqs. (4), (7), (8) to determine the reliability of the beam:

$$\left.\begin{array}{l} \underline{P} = \int\limits_{a_\sigma}^{\infty} \frac{1}{\sqrt{2\pi}S_{\sigma_T}} e^{-\frac{(x - m_{\sigma_T})^2}{2S_{\sigma_T}^2}} \cdot \left(1 - e^{-[(x - a_\sigma)/b_\sigma]^2}\right) dx \\[3mm] \overline{P} = \int\limits_{0}^{a_\sigma} \frac{1}{\sqrt{2\pi}S_{\sigma_T}} e^{-\frac{(x - m_{\sigma_T})^2}{2S_{\sigma_T}^2}} \cdot e^{-[(x - a_\sigma)/b_\sigma]^2} dx + \int\limits_{a_\sigma}^{\infty} \frac{1}{\sqrt{2\pi}S_{\sigma_T}} e^{-\frac{(x - m_{\sigma_T})^2}{2S_{\sigma_T}^2}} dx \end{array}\right\}. \tag{9}$$

The reliability of a beam with corrugated wall according to the criterion of stability of the compressed chord bending in the wall plane will be characterized by the interval of failure-free operation values $[\underline{P}; \overline{P}]$, the true value of reliability will be within this interval.

We suppose the following data were obtained as a result of the beam survey: $m_{\sigma_T} = 283$ MPa, $S_{\sigma_T} = 24$ MPa, $a_\sigma = 215$ MPa, $b_\sigma = 20$ MPa. Let us determine the reliability of the beam with corrugated wall by the criterion of stability of the compressed chord bending in the plane of the wall (Eq. 6). By substituting all the necessary data into Eq. (9) we obtain the interval of failure-free operation values [0.974; 0.999]. We consider this example by presenting the parameters: $\tilde{\sigma}$ and $\tilde{\sigma}_T$—in the form of fuzzy variables. In this case to calculate the reliability we will use the possibility method. We will use the possibility distribution function of the form (1) to describe fuzzy variables: $\tilde{\sigma}$ and $\tilde{\sigma}_T$.
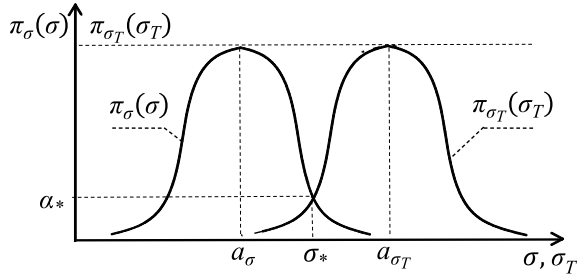
Fig. 2 Opportunity distribution functions $\pi_\sigma(\sigma)$ and $\pi_{\sigma_T}(\sigma_T)$

Let us present the possibility distribution functions $\pi_\sigma(\sigma)$ and $\pi_{\sigma_T}(\sigma_T)$ on the graph (Fig. 2).

As $a_\sigma = 215$ MPa $< a_{\sigma_T} = 283$ MPa, the failure probability of the beam by the condition of Eq. (6) is considered equal to one ($R = 1$). To determine the possibility of failure Q at $a_\sigma < a_{\sigma_T}$ we find the value of σ_* abscissa of the intersection of the opportunity distribution functions $\pi_\sigma(\sigma)$ and $\pi_{\sigma_T}(\sigma_T)$: $|(\sigma_* - 215)/20| = |(\sigma_* - 283)/24|$. We find the root of the equation, which is in the interval $[a_\sigma; a_{\sigma_T}]$, $\sigma_* = 245.9$ MPa. Possibility of failure is $Q = \alpha_* = \pi_\sigma(\sigma_*) = e^{-[(245.9-215)/20]^2} = 0.092$, the need for failure-free operation is $N = 1 - Q = 1{-}0.092 = 0.908$. The reliability of the beam under consideration according to criterion (6) will be characterized by the interval [0.908; 1].

Let us carry out additionally several variants of beam reliability calculations according to the considered model of limiting state (Eq. 6) with different initial data, modernized and possibility methods. The obtained results of calculations are presented in Tables 1 and 2.

Table 1 Results of beam reliability calculations according to criterion (6) by the modernized method

Initial data				Reliability interval
a_σ	b_σ	m_{σ_T}	S_{σ_T}	$[\underline{P}; \overline{P}]$
210	19.8	282	23.9	[0.983; 0.999]
217	20	270	23.5	[0.918; 0.998]
220	21	281	24	[0.948; 0.999]
225	21.1	267	23.4	[0.821; 0.993]
231	21.8	280	23.9	[0.873; 0.997]
235	22	284	24	[0.871; 0.996]
238	22	273	23.7	[0.728; 0.985]
241	23.3	278	23.8	[0.736; 0.989]
245	23.5	275	23.7	[0.640; 0.978]
250	24	274	23.7	[0.545; 0.963]

Table 2 Calculation results of beams reliability according to criterion (6) by the method of possibility

Initial data				Reliability interval
a_σ	b_σ	a_{σ_T}	b_{σ_T}	$[N; R]$
210	19.8	282	23.9	[0.934; 1]
217	20	270	23.5	[0.773; 1]
220	21	281	24	[0.841; 1]
225	21.1	267	23.4	[0.590; 1]
231	21.8	280	23.9	[0.683; 1]
235	22	284	24	[0.678; 1]
238	22	273	23.7	[0.444; 1]
241	23.3	278	23.8	[0.460; 1]
245	23.5	275	23.7	[0.332; 1]
250	24	274	23.7	[0.223; 1]

Having compared the obtained results of reliability intervals calculation, we can notice that when calculating reliability of beams by the probabilistic method (by presenting $\tilde{\sigma}_T$ by fuzzy variable) useful statistical information about $\tilde{\sigma}_T$ is lost, which leads to a wider reliability interval and reduces its informational content.

4   Conclusion

In this paper, a private method for calculating the reliability of a beam with corrugated wall by the criterion of compressed chord bending in the plane of the wall has been proposed. As a result of comparison of the obtained calculation results, it has been shown that the modernized method is more informative in comparison with the possible method of reliability calculation. Combining random and fuzzy variables in calculating the reliability of building structures allows using more fully all the statistical information obtained as a result of the survey.

References

1. Kala, Z., Seitl, S., Krejsa M., Omishore, A.: Reliability assessment of steel bridges based on experimental research. In: Simos, T., Tsitouras, C. (eds.) International Conference on Numerical Analysis and Applied Mathematics, ICNAAM-2018, AIP Conference Proceedings, vol. 2116, pp. 120005-1–120005-4. AIP Publishing (2019). https://doi.org/10.1063/1.5114107
2. Krejsa, M., Janas, P., Krejsa, V.: Structural reliability analysis using DOProC method. Proc. Eng. **142**, 34–41 (2016). https://doi.org/10.1016/j.proeng.2016.02.010
3. Krejsa, M., Kralik, J.: Probabilistic computational methods in structural failure analysis. J. Multiscale Modell. **6**(3), 1550006 (5 pages) (2015). https://doi.org/10.1142/S1756973715500067

4. Mkrtychev, O., Savenkov A.: Reliability of building structures in case of an air blast wave. IOP Conference Series: Materials Science and Engineering 2020, vol. 869, pp. 052–054. IOP Publishing Ltd. (2020). https://doi.org/10.1088/1757-899X/869/5/052054

5. Mkrtychev, O.V., Dzhinchvelashvili, G.A., Busalova M.S.: Assessing the reliability of a multi-storey monolithic concrete building with a base. In: XXIV R-S-P Seminar, Theoretical Foundation of Civil Engineering (24RSP) 2015. Procedia Engineering, vol. 111, pp. 550–555 (2015). https://doi.org/10.1016/j.proeng.2015.07.041

6. El Ghoulbzouri, A., Kissi, B., Khamlichi, A.: Reliability analysis of reinforced concrete buildings: comparison between FORM and ISM. Proc. Eng. **114**, 650–657 (2015). https://doi.org/10.1016/j.proeng.2015.08.006

7. Utkin, V.S.: Calculation of the reliability of the ground foundations of buildings and structures by the criterion of deformation with limited information about loads and soils. Eng. Constr. J. **1**(61), 4–13 (2016). https://doi.org/10.5862/MCE.61.1

8. Utkin, V.S.: Calculation of the reliability of the ground foundation base by bearing capacity (shear) at the stage of operation. Eng. Constr. J. **1**(45), 90–100 (2014). https://doi.org/10.5862/MCE.45.10

9. Utkin, V.S., Shepelina, E.A.: Calculation of the reliability of the foundations by the strength criterion with limited information about the load. Eng. Constr. J. **1**(36), 48–56 (2013). https://doi.org/10.5862/MCE.36.6

10. Kaufman, B.D.: Evaluation of design reliability of apron-slab stabilization based on incomplete parameter information on design models. Power Technol. Eng. **47**, 244–248 (2013). https://doi.org/10.1007/s10749-013-0431-4

11. Ivanova, T.V., Albert, I.U., Kaufman, B.D., Shulman, S.G.: The load-bearing capacity of hanging piles by the strength criterion of a pile or soil material. Mag. Civil Eng. **7**(67), 3–12 (2016). https://doi.org/10.5862/MCE.67.1

12. Ginzburg, S.M., Yudelevich, A.M.: Reliability assessment of hydraulic structures. Power Technol. Eng. **6**(54), 793–801 (2021). https://doi.org/10.1007/s10749-021-01289-0

13. Yudelevich, A.M.: Uncertainty of initial information in reliability assessment of concrete dams (within the framework of structural theory). Power Technol. Eng. **5**(51), 545–551 (2018). https://doi.org/10.1007/s10749-018-0871-y

White Cement Clinker Roasting Intensification

D. A. Mishin[✉] [iD], S. V. Kovalev [iD], S. I. Antsiferov [iD], A. V. Karachevtseva [iD], and N. S. Lubimyi [iD]

Belgorod State Technological University Named After V.G. Shukhov, Belgorod, Russia

Abstract. This article is devoted to the study of the intensifying ability of mineralizers in the production of white cement. Dried raw sludge was used as the initial raw mixture Limited Liability Company «Holcim (Rus) Construction Materials». The reagents CaF_2 and NaF of "pure" qualification were used as mineralizers. The intensifying ability of mineralizers of calcium fluoride and sodium fluoride was studied under conditions of circulation and accumulation of alkali metal salts, depending on the input method. To simulate the circulation and accumulation of alkali metal salts, the reagent Na_2CO_3 of "pure" qualification was introduced into the raw sludge in the amount of 3.5 wt% Na_2O on clinker. Calcium fluoride was introduced in the amount of 1.5 wt% CaF_2, and sodium fluoride in the amount of 1.615 wt% NaF on clinker. Traditional (in the initial mixture) and separate input of mineralizers were used. It has been found that the circulation and accumulation of alkali metal salts lead to a decrease in the whiteness of the clinker. With the traditional input, the efficiency of the mineralizer at 1400 °C is low. The traditional input of mineralizers has practically no effect on the whiteness of the clinker at 1400 °C. Separate input makes it possible to increase the efficiency of the action of mineralizers and achieve a comparable degree of assimilation of free calcium oxide in similar samples even at 1300–1350 °C. Separate input has a positive effect on the whiteness of the clinker. The greatest efficiency was shown by separate injection of calcium fluoride under conditions of circulation and accumulation of alkali metal salts.

Keywords: White cement · Intensifier roasting · Mineralizer · Separate input · CaF_2 · NaF · Na_2CO_3

1 Introduction

The production of white cement is characterized by an increased cost compared to the production of conventional cement. One of the factors that increase the cost is the special composition of the raw mix. To obtain cement of high whiteness, the content of iron oxide in clinker should not exceed 0.5% [1, 2]. As a result of the decrease in the content of iron oxide, which is flux, the sinter ability of the raw mixture deteriorates. This makes it necessary to increase the firing temperature to 1500 °C and above. This is one of the reasons leading to an increase in the specific fuel consumption for clinker burning.

The way out of this situation can be the use of roasting mineralizers [3–7]. At present, the operation of rotary kilns in the cement industry is characterized by the presence of

circulation and accumulation of alkali metal salts [8, 9]. According to studies [10, 11], in the production of gray cement, the effectiveness of mineralizers depends on the presence of circulation and accumulation of alkali metal salts in the system and on the method of introducing mineralizers. Similar studies in the preparation of white cement have not been carried out. Therefore, the purpose of this work is to study the effectiveness of the action of mineralizers in the conditions of circulation and accumulation of alkali metal salts, depending on the method of introducing the mineralizer.

2 Materials and Methods

Dried raw sludge was used as the raw mix Limited Liability Company «Holcim (Rus) Construction Materials» (Table 1). Sludge has the following modular characteristics: КН = 0.89; n = 3.56; p = 21.16.

Table 1 Chemical composition of dried sludge Limited Liability Company «Holcim (Rus) Construction Materials» and clinker based on it (composition in mass %)

Page	LOI	CaO	SiO$_2$	Fe$_2$O$_3$	Al$_2$O$_3$	MgO	SO$_3$	Other
Sludge	36.03	43.85	15.00	0.19	4.02	0.40	0.1	0.41
Clinker	–	68.55	23.45	0.3	6.28	0.63	0.16	0.64

To simulate the circulation and accumulation of alkali metal salts, the Na$_2$CO$_3$ reagent of "pure" qualification was introduced into the raw mixture in the amount of 3.5% Na$_2$O in terms of clinker.

The reagents CaF$_2$ and NaF of "pure" qualification was used as mineralizers. Calcium fluoride was introduced in the amount of 1.5%, and NaF in the amount of 1.615%, which corresponds to the input of 0.73% F$^-$. All concentrations of mineralizers are taken as mass percent of the mass of clinker.

Mineralizers were introduced by traditional and separate methods [11].

The traditional input of the mineralizer is made into the initial raw mixture.

Simulation of the separate input of the mineralizer was carried out as follows. The dried raw sludge or the dried raw sludge with Na$_2$CO$_3$ introduced into it was fired at a temperature of 1100 °C. The isothermal holding time is 30 min. The roasting product was crushed and crushed mineralizer was introduced into it. The resulting mixture was returned to the furnace, heated to 1100 °C. Further firing was carried out at the required temperature and isothermal holding time.

For firing, raw mixtures were molded into tablets weighing 2 g on a hydraulic press by manual effort.

The clinker was fired in a laboratory furnace with silicon carbide heaters. Furnace heating rate 10 °C/min. Isothermal exposure time 10 min.

As a result, the following mixture compositions were obtained:

N 1—control composition without additives;

N 2—3.5% Na_2O;
N 3—1.5% CaF_2 (traditional mineralizer input);
N 4—1.615% NaF (traditional mineralizer input);
N 5—3.5% Na_2O + 1.5% CaF_2 (traditional mineralizer input);
N 6—3.5% Na_2O + 1.615% NaF (traditional mineralizer input);
N 7—1.5% CaF_2 (separate input of the mineralizer);
N 8—1.615% NaF (separate input of the mineralizer);
N 9—3.5% Na_2O + 1.5% CaF_2 (separate input of the mineralizer);
N 10—3.5% Na_2O + 1.615% NaF (separate input of the mineralizer).

The effectiveness of mineralizers was evaluated by the content of free calcium oxide in clinker samples after firing. The content of free calcium oxide in clinker was determined using the ethyl glycerate method [12].

The whiteness of the clinker was evaluated by the brightness coefficient (BC) determined using an PhG-2 photoelectric gloss meter. Standard—white polished $BaSO_4$ plate.

3 Results and Discussion

When comparing the samples obtained with the traditional input of the mineralizer (Fig. 1a), one can see that the mineralizing ability of the mineralizers manifests itself at temperatures of 1300–1350 °C.
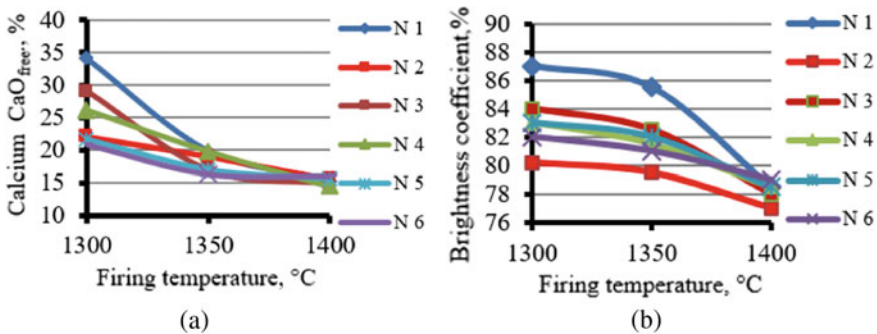
Fig. 1 The influence of the traditional input of mineralizers on a) the content of free calcium oxide; b) clinker brightness coefficient; N 1—control composition without additives; N 2—3.5% Na_2O; N 3—1.5% CaF_2; N 4—1.615% NaF; N 5—3.5% Na_2O + 1.5% CaF_2; N 6—3.5% Na_2O + 1.615% NaF

At a firing temperature of 1300 °C, the highest content of free calcium oxide is observed in composition N 1 and is 34.1%. The lowest content of free calcium oxide is observed in composition N 6 and is 20.8%. There is a significant difference in the efficiency of the introduced mineralizers. In this case, the highest brightness coefficient (Fig. 1b) is observed in composition N 1 (BC = 87%), and the smallest is observed in composition N 2 (BC = 80.5%).

At a firing temperature of 1350 °C, the highest content of free calcium oxide is observed in composition N 1 and is 19.8%. The lowest content of free calcium oxide is observed in composition N 6 and is 16.2%. The difference in the efficiency of mineralizers is not as pronounced as at 1300 °C. In this case, the highest brightness coefficient (Fig. 1b) is observed in composition N 1 (BC = 85.5%), and the smallest is observed in composition N 2 (BC = 79.5%). Free calcium oxide is a white crystalline substance, so a high content of it in clinker will increase the brightness coefficient. Therefore it is necessary to compare samples with comparable free calcium oxide content.

At a firing temperature of 1400 °C, for compositions N 2–N 6, the content of free calcium oxide is almost at the same level as the control composition N 1 (CaO_{free} = 15.4%). For example, N 5—15.7%; N 6—15.9%. Therefore, at a given temperature, the difference in the efficiency of various types of mineralizers is minimal.

At the same time, the brightness coefficient of the clinker (Fig. 1b) when mineralizers are introduced (compositions N 3–N 6) is almost identical to the brightness coefficient of the control sample N 1 (BC = 78.5%). Entering Na_2CO_3 (composition N 2) reduces the brightness coefficient of the clinker (BC = 77%).

With the introduction of mineralizers in a separate way, an increase in the effectiveness of the action of mineralizers occurs (Fig. 2a).
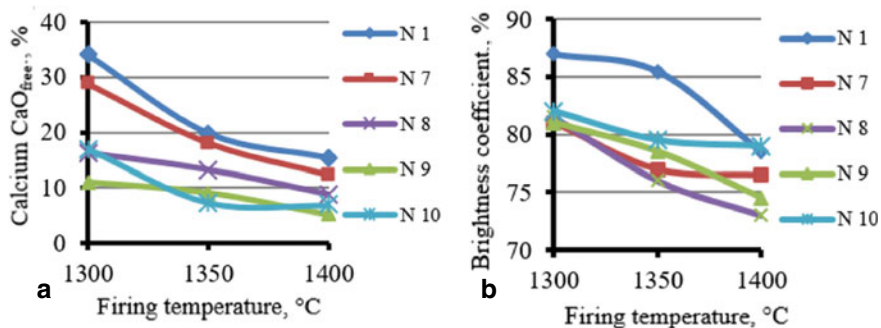
Fig. 2 The effect of separate input of mineralizers on **a** the content of free calcium oxide; **b** clinker brightness coefficient; N 1—control composition without additives; N 7—1.5% CaF_2; N 8—1.615% NaF; N 9—3.5% Na_2O + 1.5% CaF_2; N 10—3.5% Na_2O + 1.615% NaF

At a temperature of 1300 °C, the lowest content of free calcium oxide is observed in composition N 9 and is 11.1%. Differences in the efficiency of mineralizers are pronounced.

At a temperature of 1350 °C, the lowest content of free calcium oxide is observed in composition N 10 and is 7.4%. Differences in the efficiency of mineralizers are pronounced.

Therefore, at a firing temperature of 1300–1350 °C, the separate input of the mineralizer (compositions N 7–N 10) causes a more complete assimilation of free calcium oxide than at 1400 °C in similar samples with the traditional input of the mineralizer (N 3–N 6). For example, in composition N 5, the content of free calcium oxide at 1400 °C is 15.7%, and in composition N 9 at 1300 °C, it is 11.1%.

The lowest content of free calcium oxide at 1400 °C is observed in the composition of N 9 ($CaO_{free} = 5.2\%$), while in the control sample it is 15.4%.

At a firing temperature of 1400 °C, the maximum brightness coefficient (Fig. 2b) of the clinker ($BC = 79\%$) is observed for composition N 10 at $CaO_{free} = 6.9\%$ compared to the control sample N 1 ($BC = 79\%$) at $CaO_{free} = 15.4\%$. From this we can conclude that with an equal degree of assimilation of free calcium oxide, clinker with the use of a separate input of the mineralizer will have a higher clinker brightness coefficient.

4 Conclusion

The presence of circulation and accumulation of alkali metal salts during the firing of white clinker leads to a decrease in its whiteness.

With the traditional input of mineralizers in the production of white cement, they are characterized by low efficiency.

Entering mineralizers in a separate way increases the intensifying ability of mineralizers.

Clinker with the use of a separate mineralizer input has a higher clinker brightness coefficient.

The greatest efficiency was shown by separate injection of calcium fluoride under conditions of circulation and accumulation of alkali metal salts.

References

1. Zubekhin, A.P., Golovanova, S.P., Kirsanov, P.V.: White Portland cement. Rostov State University, Rostov-on-Don (2004)
2. Zubekhin, A.P., Golovanova, S.P., Kirsanov, P.V.: Super white Portland cement. Phase composition, technology. News of higher educational institutions. North Caucasus Region. Engineering, vol. 1, pp. 41–44 (2004)
3. Klyuev, S.V., Khezhev, T.A., Pukharenko, Y.V., Klyuev, A.V.: Fibers and their properties for concrete reinforcement. Mater. Sci. Forum 945 MSF, 125–130 (2018)
4. Timoshenko, T.I., Zalogina, A.V., Khudasov, V.I.: The effect of ZnO and $BaSO_4$ additives on the construction and technical properties of low base white cements. Constr. Mater. Prod. **1**(3), 17–24 (2018)
5. Moresová, K., Skvára, F.: White cement—properties, manufacture, prospects. Ceram. Silikáty **45**(4), 158–163 (2001)
6. Kulabukhov, V.A., Dmitriev, A.M., Chistyakov, G.I., Kozhevnikov, V.N., Alyoshina, O.K., Shutova, A.V.: Domestic technology of white and colored cements. To the 70th Anniversary of Industrial Production of White Cement. Part 1. Cement and Its Application, vol. 5, pp. 22–24 (2007)
7. Kulabukhov, V.A., Dmitriev, A.M., Chistyakov, G.I., Kozhevnikov, V.N., Alyoshina, O.K., Shutova A.V.: Domestic technology of white and colored cements. To the 70th Anniversary of Industrial Production of White Cement. Part 2. Cement and Its Application, vol. 6, pp. 101–104 (2007)

8. Klassen, V.K., Ermolenko, E.P., Michin, D.A., Novosyolov, A.G.: Problem of impurity of salts of alkali metals in cement raw materials. Middle-East J. Sci. Res. **17**(8), 1130–1137 (2013). https://doi.org/10.5829/idosi.mejsr.2013.17.08.7087
9. Luginina, I.G.: Selected articles. Publishing House of BSTU named after V.G. Shukhov, Belgorod (2002)
10. Mishin, D.A., Kovalev, S.V., Chekulaev, V.G.: The reason for the decrease in the effectiveness of mineralizers for firing Portland cement clinker. In: Bulletin of BSTU named after V.G. Shukhov, vol. 5, pp. 161–166 (2016)
11. Mishin, D.A., Kovalev, S.V., Chekulaev, V.G.: The effect of the input method of the mineralizer on the strength characteristics, morphology and color of Portland cement. Cem. Appl. **4**, 112–117 (2016)
12. Klyuev, S.V., Bratanovskiy, S.N., Trukhanov, S.V., Manukyan, H.A.: Strengthening of concrete structures with composite based on carbon fiber. J. Comput. Theor. Nanosci. **16**(7), 2810–2814 (2019)

The Influence of Electric Current on the Water Separation of Cements

D. A. Mishin[✉] 🄳, A. O. Erygina 🄳, Z. V. Tarallo 🄳, S. I. Antsiferov 🄳, and E. V. Lazko 🄳

Belgorod State Technological University Named After V.G. Shukhov, Belgorod, Russia

Abstract. With the constant development of the cement industry, the requirements for quality indicators of the produced Portland cement are being tightened, which creates some difficulties in cement production. But at the same time, these requirements have a positive impact on the construction industry. One of such indicators of quality is the water separation of cements. It is believed that the process of water separation is influenced by many factors, such as: the presence of active mineral additives, surface-active substances, the specific surface of cement, the chemical activity of tricalcium aluminate, clinker and the type of gypsum. In the construction industry, there is a practice of using electricity to heat concrete during the winter period of concrete work. In this case, both reduced (down to 100 V) and increased (up to 400 V) voltages are used. Also, the main effect leading to an increase in the strength of concrete is hardening at elevated temperatures. The process of water separation is strongly influenced by the sedimentation stability of the cement slurry. And the sedimentation stability is affected by the ζ-potential of the particles. By itself, the ζ-potential has an electrical nature, so it must be influenced by an electric current. This fact should lead to a change in water separation. However, the effect of low voltage electric current on the processes of hydration and water separation has not been studied. Therefore, the purpose of the scientific work is to study the effect of an electric current with a voltage of 1.5 V on the process of water separation of cements. In this work, the effect of an electric current of 1.5 V on the water separation of cements from various manufacturers was studied using 5 different arrangements of positive and negative electrodes in a cylinder with cement mortar. A salt battery (manganese-zinc) was selected as a power source. It has been established that a low-voltage direct electric current equal to 1.5 V affects the process of water separation. The greatest impact was made on factory cements CJSC «Maltsovsky Portland cement» CEM I 42.5N and CJSC «Oskolcement» CEM I 42.5N. For cement CJSC «Maltsovsky Portland cement» CEM I 42.5N, a direct electric current with a voltage of 1.5 V reduces water separation by 86%, and for CJSC «Oskolcement» CEM I 42.5N water separation increases by 327%.

Keywords: Portland cement · Water separating · Electric current · Tricalcium aluminate · Gypsum dehydrate · ζ-potential · Sediment stability · Slag

1 Introduction

Water separation is one of the important indicators of cement quality. This phenomenon is a form of segregation in which some of the water in the mixture tends to rise to the surface of the freshly placed concrete. The high value of water separation prevents the production of a homogeneous product and the adhesion of cement hardening in concrete with aggregate, which leads to a decrease in the strength of the concrete product, frost resistance and a decrease in the corrosion resistance of concrete. It is believed that the process of water separation is influenced by many factors, such as: the presence of active mineral additives, surfactants, the specific surface area of cement, the chemical activity of tricalcium aluminate, clinker, and the type of gypsum [1–11]. These factors change the ζ-potential of cement particles. A change in the ζ-potential changes the sedimentation stability of the cement suspension in water. It should be noted that the rate of the ettringite formation reaction has the main effect on water separation [5, 12]. And the rate of formation of ettringite is probably affected by a change in the specific surface area, the use of surface-active substances and active hydraulic additives.

During hydration processes, the formation of ettringite proceeds through the dissolution of gypsum in water and the diffusion of ions to particles of tricalcium aluminate [13]. It is possible to influence the rate of diffusion in aqueous solutions and, consequently, to control the rate of formation of ettringite by using an electric current.

In the construction industry, there is a practice of using electricity to warm up concrete in winter concreting. In this case, reduced (down to 100 V) and increased (up to 400 V) voltages are used [14–17]. When an electric current passes through the laid concrete, it heats up. Therefore, many authors believe that the main effect that increases the strength of concrete is hardening at elevated temperatures. Other effects have been little studied. Due to the fact that the use of high voltages is expensive, it was decided to study the effect of low voltage currents ($\approx$ 1.5 V) on the water separation process.

Therefore, the purpose of the scientific work is to study the effect of an electric current with a voltage of 1.5 V on the process of water separation of cements.

2 Materials and Methods

To determine the effect of electric current on the water separation process, cements from various manufacturers were used (Table 1). Diagrams for connecting electric current to cement mortar when determining water separation are shown in Fig. 1. In the installation, positive graphite electrodes from salt batteries were used. The electrodes are connected by a PuGV 1 × 0.75 wire to a regulated DC power supply MCH K3010DW with an output voltage of 0–30 V (adjustable) and an output current of 0–10 A (adjustable).

The method for determining the water separation of cements is carried out in accordance with GOST 310.6-2020.

Table 1 List of cements used in the study of the effect of electric current on the process of water separation

№	Cement	Manufacturer
1	PC 500 D0	JSC «Belarusian Cement Plant»
2	PC 500 D0	JSC «Krichevcementnoslate
3	CEM I 42.5N	JSC «Krichevcementnoslate»
4	CEM I 42.5N	CJSC «Maltsovsky Portland cement»
5	CEM ЦЕМ I 42.5N	CJSC «Oskolcement»
6	PC 500 D0	JSC «HeidelbergCement Volga»
7	CEM II/A–III 32.5B	CJSC «Belgorod cement»
8	CEM III/A–III 32.5B	CJSC «Belgorod cement»
9	CEM I 42.5N	JSC «Novoroscement»

a) **Scheme 1**

b) **Scheme 2**

$h_{cylinder} = 380$ mm

$h_{cylinder} = 380$ mm
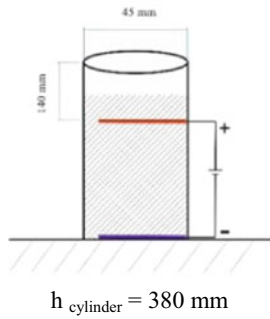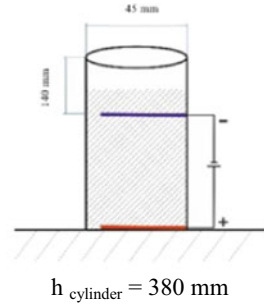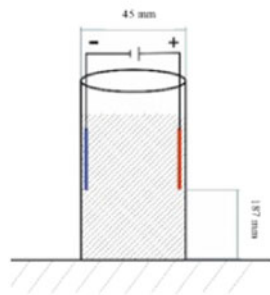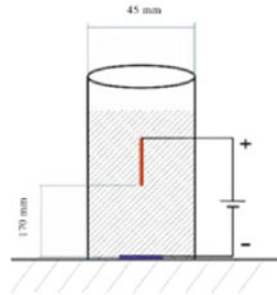
c) **Scheme 3**

d) **Scheme 4**

e) **Scheme 5**
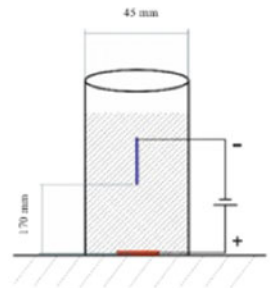
Fig. 1 Schemes for connecting electric current to cement mortar when determining the water separation of cements: scheme 1 (**a**), scheme 2 (**b**), scheme 3 (**c**), scheme 4 (**d**), scheme 5 (**e**)

3   Results and Discussion

To study the effect of electric current on the water separation of cements, a number of experiments were carried out. For each of 9 cements from different manufacturers (Table 1), water separation was determined without the action of an electric current and under the influence of an electric current with a voltage of 1.5 V using 5 different arrangements of positive and negative electrodes in a cylinder with cement mortar (Fig. 1). The results are presented in Table 2.

Table 2 Influence of 1.5 V electric current on water separation of cements from different manufacturers

№	Cements	Water separation under the action of electric current voltage 1.5 V (%)					Water separation without electric current (%)
		Scheme 1	Scheme 2	Scheme 3	Scheme 4	Scheme 5	
1	JSC «Belarusian cement plant» PC 500 D0	–	10.9	13.9	9.2	9.3	11.6
2	JSC «Krichevcementnoslate» PC 500 D0	15.8	17.9	18.2	16.1	17.1	19.0
3	JSC «Krichevcementnoslate» CEM I 42.5N	19.6	19.1	17.9	18.8	18.3	20.3
4	CJSC «Maltsovsky Portland cement» CEM I 42.5N	3.4	3.4	3.0	3.2	3.0	22.0
5	CJSC « Oskolcement» CEM I 42.5N	21.1	20.9	22.8	23.7	22.8	4.9
6	JSC «Heidelberg Cement Volga» PC 500 D0	20.7	21.3	21.5	21.1	21.2	19.2
7	CJSC «Belgorod cement» CEM II/A–SH 32.5B	23.7	24.5	24.7	24.8	19.2	24.5
8	CJSC «Belgorod cement» CEM III/A–SH 32.5B	19.6	20.9	21.8	20.0	20.1	21.0
9	JSC «Novoroscement» CEM I 42.5N	27.1	26.6	27.7	26.7	25.9	27.1

According to the data obtained (Table 2), it was noted that an electric current with a voltage of 1.5 V in most cases helps to reduce the water separation of various cements, but, for example, in CJSC Oskolcement CEM I 42.5N and JSC HeidelbergCement Volga PC 500 D0 water separation, on the contrary, it increased. Of the 9 different manufacturers,

it is worth noting the cements of CJSC "Maltsovsky Portlandcement" CEM I 42.5N and CJSC "Oskolcement" CEM I 42.5N. If at CJSC "Maltsovsky Portlandcement" CEM I 42.5N an electric current with a voltage of 1.5 V significantly reduces water separation by 86%, then at CJSC "Oskolcement" CEM I 42.5N, on the contrary, it contributes to its increase by 327%.

These indicators confirm the ability of electric current to regulate the water separation of cement.

Also during the experiment, it was found that in the cements of CJSC «Belgorod cement» CEM II/A–SH 32.5B and CJSC «Belgorod cement» CEM III/A–SH 32.5B, water separation decreases with increasing wt.% of slag in cement, and the electric current actually does not affect this process (Fig. 2).
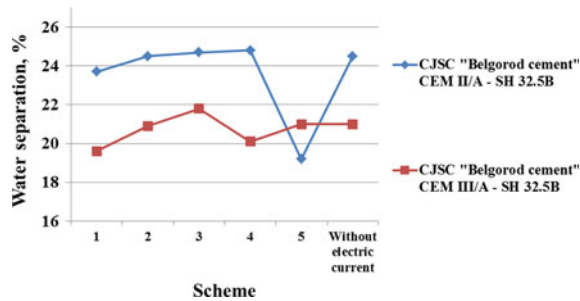
Fig. 2 Graph comparing the results of water separation of cements with slag

This fact is due to the fact that slag is more difficult to grind than clinker. Because of this, the cement component will be greatly over-grinded. The sedimentation stability of the entire system is determined by the particle size. Due to the over-grinded cement part, there is an increase in the stability of the system. On such a system, the effect of electric current will be negligible.

4 Conclusion

As a result of the data obtained, it can be argued that the low-voltage direct current equal to 1.5 V can regulate the process of water separation.

The greatest impact was made on factory cements CJSC «Maltsovsky Portland cement» CEM I 42.5N and CJSC «Oskolcement» CEM I 42.5N. For cement CJSC «Maltsovsky Portland cement» CEM I 42.5N, a constant electric current with a voltage of 1.5 V reduces water separation by 86%, and for CJSC «Oskolcement» CEM I 42.5N it increases by 327%.

References

1. Klyuev, S.V., Bratanovskiy, S.N., Trukhanov, S.V., Manukyan, H.A.: Strengthening of concrete structures with composite based on carbon fiber. J. Comput. Theor. Nanosci. **16**(7), 2810–2814 (2019)
2. Klyuev, S.V., Khezhev, T.A., Pukharenko, Y.V., Klyuev, A.V.: Fibers and their properties for concrete reinforcement. Mater. Sci. Forum 945 MSF, 125–130 (2018)
3. Frolov, Y.G.: Colloidal chemistry course. LLC TPH "Alliance", Moscow (2004)
4. Fediuk, R., Mugahed Amran, Y.H., Mosaberpanah, M.A., Danish, A., El-Zeadani, M., Klyuev, S.V., Vatin, N.: A critical review on the properties and applications of sulfur-based concrete. Materials **13**(21), 1–23, 4712 (2020)
5. Normantovich, A.S.: Regulation of the process of water separation of cement-water dispersed systems: specialty 05.17.11 "Technology of silicate and refractory non-metallic materials". Abstract of the dissertation of the Candidate of Technical Sciences. Belgorod State Technological University named after V. G. Shukhov, Belgorod, pp. 16 (2005)
6. Uspanova, A.S., Khadzhiev, M.R., Ismailova, Z.H., Basnukaev, I.: Analysis of the effect of methods of introduction of organomineral additive into mortars on fine sands. Constr. Mater. Prod. **4**(4), 32–40 (2021)
7. Stark, J., Wicht, B.: Zement und Kalk: Der Baustoff als Werkstoff. Basel, Birkhäuser (2000)
8. Luginina, I.G.: Chemistry and Chemical Technology of Inorganic Binders, vol. 2, no. 1. BSTU, Belgorod (2004)
9. Luginina, I.G.: Chemistry and Chemical Technology of Inorganic Binders, vol. 2, no. 2. BSTU, Belgorod (2004)
10. Kozhukhova, N.I., Shurakov, I.M., Titenko, A.A., Alfimova, N.I., Zhernovskaya, I.V., Bukovtsova, A.I.: Effect of the curing conditions on the characteristics of citrogypsum-containing alkali-activated binders. Constr. Mater. Prod. **4**(5), 24–34 (2021)
11. Erygina, A.O., Mishin, D.A., Klassen, V.K.: The sequence of Na_2O interactions with clinker mineral in their various combinations. Bull. BSTU Named V.G. Shukhov **12**(12), 98–104 (2018). https://doi.org/10.1007/978-3-030-54652-6_27
12. Normantovich, A.S., Konovalov, V.M.: Electrokinetic properties of cement pastes at an early stage of hydration. The current state and prospects for the development of building materials science. Eighth Academic Readings of the Department of Building Sciences Russian Academy of Architecture and Construction Sciences. Publishing House of Samara State University of Architecture and Civil Engineering, Samara, pp. 380–382 (2004)
13. Erygina, A.O., Mishin, D.A.: Effect of cubic and orthorhombic crystal systems of tricalcium aluminate to form ettringite in the presence of dihydrate calcium sulfate. Lect. Notes Civil Eng. **147**, 316–321 (2021)
14. Bakhtin, A.S., Lyubomirsky, N.V., Fedorkin, S.I., Bakhtina, T.A., Belenko, G.R.: The influence of forced carbonization on the properties of gypsum-lime systems based on secondary raw materials. Constr. Mater. Prod. **4**(6), 69–81 (2021)
15. Lesnichenko, E.N., Chernysheva, N.V., Drebezgova, M.Y., Kovalenko, E.V., Bocharnikov, A.L.: Development of a multicomponent gypsum cement binder using the method of mathematical planning of the experiment. Constr. Mater. Prod. **5**(2), 5–12 (2022)

16. Klimenko, V.M.: Electrophysical treatment of concrete mixtures with chemical additives. Abstract of the Dissertation of the Candidate of Technical Sciences. Saratov, pp. 17 (2002)
17. Nakhaev, M.R., Salamanova, M.S., Ismailova, Z.K.: Regularities of the processes of formation of the structure and strength of a clinker-free binder of alkaline activation. Constr. Mater. Prod. **3**(1), 21–29 (2020)

Analysis of the Effect of Cyclic Loading Mode on the Change in the Properties of Polymer Materials

T. A. Nizina(✉) , N. S. Kanaeva , and D. R. Nizin

National Research Mordovia State University, Saransk, Russia

Abstract. We studied the change in elastic-strength parameters of polymers based on epoxy resin Etal-247 and hardeners Etal-45M, Etal-1472, Etal-45TZ2 depending on the intensity of the cyclic tensile load (soft loading mode). The cycling levels were 40, 60 and 80% of the sample tensile strength without pre-cycling. We found that the tensile strength and relative elongation after cycling and subsequent stage of destruction for all levels of cyclic exposure vary in fairly narrow ranges. We revealed that for samples after pre-cycling, the strength characteristics are slightly higher compared to similar indicators without cyclic exposure, which is typical for cyclically hardening materials. We offer an algorithm for estimating the effect of cyclic loads on the kinetics of failure accumulation in polymeric materials. We studied the effect of cyclic loading level on the kinetics and the specific index of failure accumulation in samples of epoxy polymers. It is shown that a decrease in the level of tensile cyclic stresses from 80 to 40% with a simultaneous increase in the number of loading cycles (to achieve one level of loading) leads to an in-creased total failure rate, by 1.4–1.9 times on average. Stability of the specific index recorded at the stage of breaking and significantly lower values of the total number of accumulated failures of the Etal-247/Etal-1472 composition indicate the greatest prospects for the use of this polymer subjected to cyclic loads.

Keywords: Epoxy polymers · Failure accumulation · Low cycle fatigue · Hysteresis losses · Cyclically hardening materials

1 Introduction

Various polymer materials are currently widely used in the construction industry. Modern technologies make it possible to make materials with increased performance characteristics in combination with a lower cost, material consumption and labor intensity of the production process. The introduction of new building materials requires developing research on the laws of the destruction process and increasing the reliability of forecasting the polymer material durability.

One of the most important operational properties of materials is dynamic fatigue—gradual accumulation of micro-failures in the material subjected to repeatedly variable stresses (or deformations), leading to a change in its structure and properties, formation and development of cracks, and subsequent destruction [1]. According to the results of

studies [2–4], the strength indicators of polymer composite materials when tested for dynamic fatigue differ significantly from similar indicators determined when exposed to static loads. Under the variable loads, both hardening and softening processes can occur, associated with compaction or loosening of the polymer structure as a result of repacking macromolecules, formation and redistribution of residual microstresses, changes in the structure due to various mechanochemical processes [5].

The nature of fatigue failure depends on the level of stresses [6]. Thus, at maximum cycle stresses less than the elastic limit, the material is deformed elastically, however, due to the complex multicomponent structure of materials, alternating microplastic deformation occurs in individual weak grains, which multiple repetition leads to the origin of microscopic cracks, their development, fusion into a main crack and final destruction of the part (multi-cycle fatigue). In cases where the maximum stresses of the cycle exceed the elastic limit, plastic deformations occur in much greater volumes of the material (compared to the size of the structural elements), accumulating, they reach the limit value, which, as a consequence, leads to the sample destruction (low-cycle fatigue).

This paper determines the dependence of elastic-strength characteristics of epoxy polymers, determining the change in the total failure rate, the achievement of which leads to the destruction of samples, depending on the level and number of cycles of tensile stresses, as well as the type of polymer under study.

2 Methods and Materials

The object of the study were samples of polymer material based on epoxy resin Etal-247 (TU 2257-200-18826195-02 ed.1) and hardeners Etal-45M (TU 2257-045-18826195-01), Etal-1472 (TU 2257-1472-18826195-04), Etal-45TZ2 (TU 2257-045-18826195-01). Dumbbell samples were tested in accordance with GOST R 57143-2016 "Polymer composites. Method of fatigue testing under cyclic tension" subjected to mild cyclic amplitude loading. The target cycling levels are 40, 60 and 80% of the sample tensile strength without pre-cycling. Stress levels were rounded to a multiple of 5 MPa in order to compare the results obtained for different compositions of polymer materials tested in parallel. The number of cycles for the cyclic impact levels of 40 and 60% is calculated based on the value of the total loading work equivalent to 5 cycles of tensile load for the 80% level (Table 1).

Table 1 Cyclic load levels in MPa adopted to achieve the same level of operation at different loading amplitudes

Cyclic load level (%)	Loading level (number of cycles) depending on the epoxy polymer hardener, MPa (pcs.)		
	Etal-45M	Etal-1472	Etal-45TZ2
40	10 (25)	20 (27)	15 (20)
60	15 (10)	30 (11)	20 (10)
80	20 (5)	40 (5)	25 (5)

Movement speed of the clamps of AGS-X series tensile testing machine with the TRAPEZIUM X software was 2 mm/min, reading frequency was 0.01 s. Test temperature was 23 ± 2 °C and relative air humidity was 50 ± 5%. At least 5 samples were tested at each cyclic load level.

The study used an approach based on the of fractal analysis methods of time series recorded with a high frequency of taking readings (0.01 s.) to assess the failure accumulation kinetics under the action of tensile loads, the expediency of which was proved earlier [7–10]. For calculations, we used a software package in Python (Certificate of registration of the computer software No. 2022612647 "Calculation of local and integral fractal indices of deformation curves of polymer materials samples").

3 Results and Discussion

When processing the data of studying the dependences of elastic-strength characteristics on the level and number of cycles of tensile stresses, as well as the type of polymer under study, it was found that the tensile strength and elongation after cycling and the subsequent stage of destruction for all levels of cyclic action on samples of polymer materials vary in fairly narrow intervals (Fig. 1). Therefore, for a polymer based on epoxy resin Etal-247 and hardener Etal-45M, the tensile strength after cyclic exposure to various levels is in the range from 30 to 33 MPa, for Etal-1472—54.5–55.8 MPa, for Etal-45TZ2—31.6–32.7 MPa. The range of variation of relative elongation at tension does not exceed 0.6% (Fig. 1b). This stability of elastic-strength characteristics of the polymer materials under study at different scales of cyclic loading is obviously due to the fact that the calculated total loading work for all deformation cycles was taken as a constant in the study.
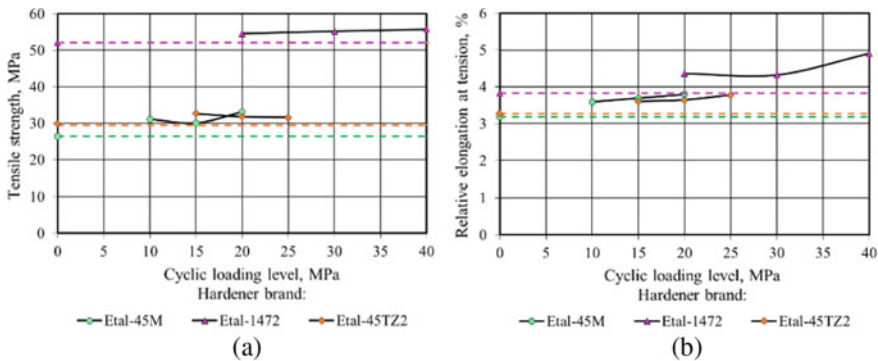
Fig. 1 Dependence of the tensile strength (**a**) and relative elongation (**b**) at tension on the cyclic loading level with the corresponding number of cycles (horizontal dashed lines show the levels of properties registered for samples tested without the cyclic exposure)

For samples without pre-cycling, the strength characteristics (see horizontal dashed lines in Fig. 1a are slightly lower compared to similar indicators after cyclic exposure. The tensile strength for polymer Etal-247/Etal-45M is lower by 14–25%, Etal-247/Etal-1472—5–7%, Etal-247/Etal-45TZ2—6–15%; elongation at tension for the above compositions—respectively, by 12–19, 13–28 and 10–15%.

Materials experiencing variable loads during operation, depending on the structural condition, loading conditions and operating temperature, can either harden (the width of the hysteresis loop decreases with soft loading, with hard loading—the stress increases with increasing number of cycles), or soften (with soft loading, the width of the hysteresis loop increases with increasing number of loading cycles, and under severe loading, an increase in the number of loading cycles is accompanied by a drop in tension in cycles), or remain stable, demonstrating the constancy of deformation parameters (the width of the hysteresis loop or tension in cycles) throughout the entire service life [6, 11].

Figure 2 shows graphical dependences of hysteresis losses under cyclic loading for 40 (a), 60 (b) and 80% (c) of the applied load on the tensile strength without pre-cycling. It is established that at all levels of cyclic deformation, samples of polymer materials show a decrease in hysteresis losses from cycle to cycle, which indicates the material hardening (within the selected number of cycles). The cyclic hardening process has a damped asymptotic character and practically stops after the first 10–20 (depending on the material) loading cycles.

Figure 3 shows graphical dependences of changes in the accumulated failure rate and specific indicators of polymers based on epoxy resin Etal-247 cured by Etal-1472, calculated only for the failure stage, as well as jointly for all loading stages. For compositions Etal-247/Etal-45M and Etal-247/Etal-45TZ2, these dependencies are of a similar nature; quantitative indicators for all compositions are given in Table 2.

We found that the failure stage (taking into account the previous cyclic loads at the 80% level of mechanical exposure) corresponds to the accumulation of defective elements in the polymer structure, amounting to 16.1–18.4% of their total number. A decrease in the level of tensile cyclic stresses from 80 to 40% with a simultaneous increase in the number of loading cycles (to achieve one level of loading operation) leads to an increase in the total failure rate (ω), on average, by 1.6 times when using the Etal-1472 hardener, by 1.9 times for Etal-45M, and by 1.4 times for Etal-45TZ2. At the same time, the accumulated failure rate only for the destruction stage ($\omega_{dest.}$) varies in a fairly narrow range—4.5–5.4% for Etal-1472, 5.0–5.8% for Etal-45 M, and 4.3–5.3% for Etal-45TZ2. This additionally confirms the sufficiently high stability of the studied polymers under low-cycle loading.

To assess the effect of the tensile load intensity, we compared total failure rate accumulated over the first 5 cycles (Table 2). We found a monotonous increase in this indicator for all the studied polymers with an increase in the applied tension level from 40 to 80%, which, regardless of the composition, is about 240%. When comparing the total number of failures accumulated during the first 5 cycles of mechanical action of the same level (20 MPa), we found an increase in this indicator in a number of polymers cured by Etal-1472, Etal-45TZ2 and Etal-45M, from 5.3 to 10.6%. Significantly lower values of the total number of accumulated failures, as well as the specific index stability recorded at the stage of destruction of the polymer based on Etal-247/Etal-1472
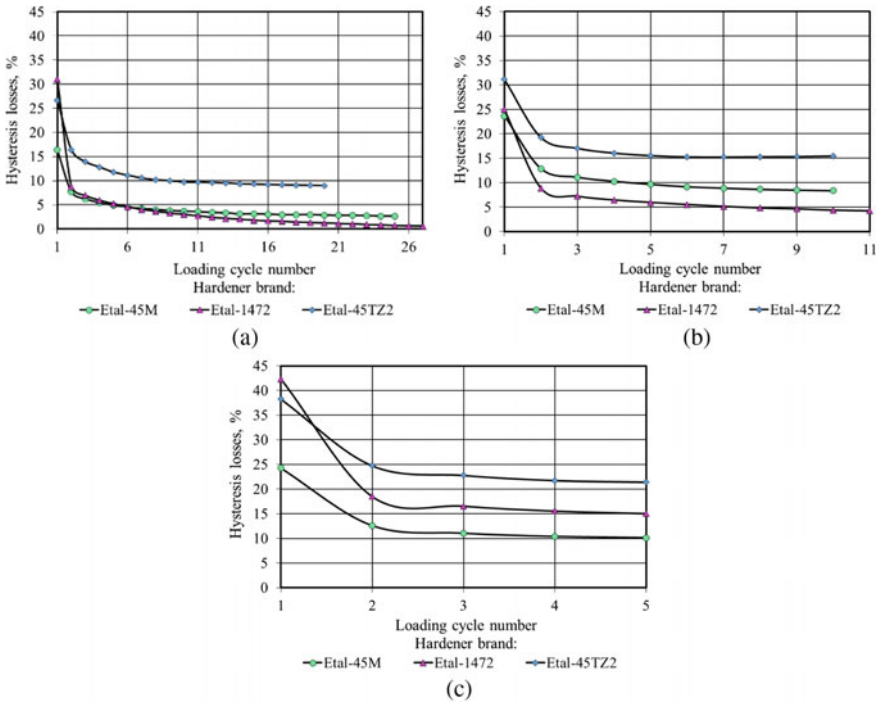
Fig. 2 The change in the values of hysteresis losses depending on the sequence number of cyclic loading at the level of 40 (**a**), 60 (**b**) and 80% (**c**) of the tensile strength without prior cycling of samples of polymer materials based on epoxy resin Etal-247 and hardeners Etal-45M, Etal-1472, Etal-45TZ2
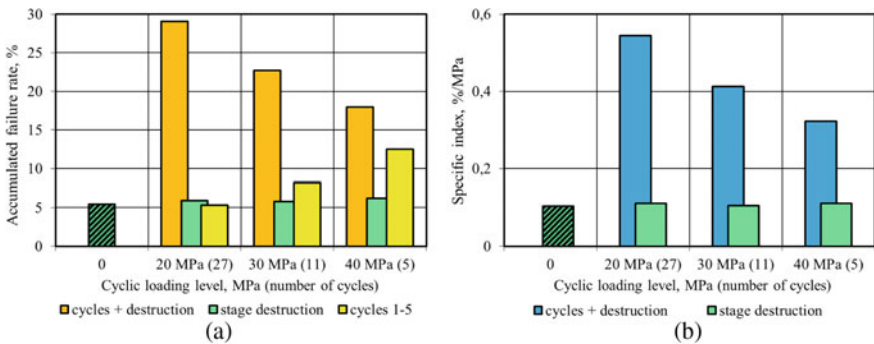
Fig. 3 The change in the accumulated failure rate (**a**) and specific index (**b**) of the polymer based on epoxy resin Etal-247 cured by Etal-1472, VS the cyclic loading level

$(\theta_{dest.} = 0.08 - 0.10\%/\mathrm{MPa})$, indicate the greatest prospects for the use of this polymer under cyclic loads.

Table 2 The change in the average accumulated failure rate and the average specific index of polymers based on epoxy resin Etal-247 cured by Etal-45M, Etal-1472, Etal-45TZ2 VS the cyclic loading level

Grade of hardener	Cyclic loading level, MPa (number of cycles)	Accumulated failures[a], %				Specific index[b], %/MPa	
		$\sum_1^m \omega_i$	$\sum_1^5 \omega_i$	$\omega_{dest.}$	ω	$\theta_{dest.}$	θ
45 M	0	–	–	5.8	–	0.22	–
	10 (25)	25.5	4.5	5.0	30.5	0.16	0.98
	15 (10)	14.3	7.3	5.0	19.3	0.17	0.64
	20 (5)	10.6	10.6	5.4	16.1	0.16	0.49
1472	0	–	–	5.4	–	0.10	–
	20 (27)	24.6	5.3	4.5	29.1	0.08	0.54
	30 (11)	18.0	8.2	4.7	22.7	0.09	0.41
	40 (5)	12.5	12.5	5.4	17.9	0.10	0.32
45TZ2	0	–	–	5.3	–	0.18	–
	15 (20)	21.7	5.5	4.3	25.9	0.12	0.75
	20 (10)	19.2	9.8	4.6	23.8	0.15	0.79
	25 (5)	13.5	13.5	4.9	18.4	0.16	0.58

[a]the average total number of failures in a series of samples: $\sum_1^m \omega_i$—when exposed only to cyclic loads; $\sum_1^5 \omega_i$—when exposed to 5 loading cycles; $\omega_{dest.}$—when exposed to a destructive load; ω—accumulated throughout the sample testing
[b]specific index, defined as the ratio of the total share of accumulated failure to the ultimate strength of a polymer material sample: $\theta_{dest.}$—only when analyzing the stage of failure; θ—when analyzing of the whole loading history (cyclic impacts and failure stage)

4 Conclusion

The proposed approach for assessing the kinetics of failure accumulation in polymer materials samples under cyclic loads and subsequent destruction stage allows us to separate the loading stages by calculating the accumulated number of failures for each loading cycle and for the destruction stage. The proposed criteria for evaluating the behavior of polymers under mechanical loads (accumulated failure rate and specific index) make it possible to describe the behavior of polymer material samples regardless of loading conditions. It is also advisable to use this approach to assess the durability of materials in various conditions of aggressive exposure.

The studies on the analysis of the effect of cyclic loading mode on the change in the physical and mechanical parameters of polymers based on epoxy resin Etal-247 cured by Etal-45M, Etal-1472 and Etal-45TZ2, demonstrates the greatest prospects for the use of Etal-247/Etal-1472 polymer.

References

1. Arutyunyan, A.R.: Formulation of the fatigue fracture criterion of composite materials. Vestnik of Saint Petersburg University. Math. Mech. Astron. **7**(65), 3, 511–517 (2020). https://doi.org/10.21638/spbu01.2020.313

2. Bondar, V.S., Danshin, V.V., Makarov, D.A.: Mathematical modelling of deformation and damage accumulation under cyclic loading. PNRPU Mech. Bull. **2**, 125–152 (2014). https://doi.org/10.15593/perm.mech/2014.2.06

3. Gots, A.N., Glinkin, S.A.: Review of models of fatigue fracture under cyclic loading. Fundam. Res. **9**(3), 478–482 (2016)

4. Gorokhov, V.A.: Numerical modeling of the processes of elastic-viscoplastic deformation and destruction of structural elements under quasi-static thermosilic, cyclic and thermoradiative effects. Ph.D. Thesis, UNN (2018)

5. Baraz, V.R., Filippov, M.A.: Physical Foundations of Hardening and Destruction of Materials: Textbook. Ural University Publishing House, Ekaterinburg (2017)

6. Erasov, V.S., Nuzhny, G.A.: Rigid loading cycle during fatigue tests. Aviat. Mater. Technol. **4**(21), 35–40 (2011)

7. Nizina, T.A., Nizin, D.R., Kanaeva, N.S., Kuznetsov, N.M., Artamonov, D.A.: Applying the fractal analysis methods for the study of the mechanisms of deformation and destruction of polymeric material samples affected by tensile stresses. Key Eng. Mater. **799**, 217–223 (2019)

8. Nizina, T.A., Nizin, D.R., Kanaeva, N.S., Artamonov, D.A.: Method for analyzing the kinetics of damage accumulation in the structure of polymer materials under tensile stresses. AIP Conf. Proc. **2371**(1), 020010 (2021)

9. Nizina, T.A., Kanaeva, N.S., Nizin, D.R.: The effect of moisture state on kinetics of damage accumulation in the structure of epoxy polymer samples under tensile stresses. Lect. Notes Civil Eng. **151**, 208–214 (2021)

10. Yazyeva, S.V., Yazyev, B.M.: Manifestation of fractal dimensions in the architecture of buildings and structures. Constr. Mater. Prod. **2**(4), 89–95 (2019). https://doi.org/10.34031/2618-7183-2019-2-4-89-95

11. Romanov, A.N.: Problems of materials science in the mechanics of deformation and fracture at the stage of crack formation (part 1). Bull. Sci. Tech. Develop. **11**(75), 38–49 (2013)

Modification of Properties and Study of Electrical Conductivity of Citrogypsum

I. S. Nikulin[1,2](✉) , E. A. Pilyuk[1] , V. S. Zakhvalinskii[1] , V. B. Nikulichev[3] ,
and V. S. Voropaev[3,4]

[1] Belgorod National Research University, Pobeda 85, Belgorod 308015, Russia
ivanikulin@yandex.ru
[2] Engineering Center NRU "BelSU", Belgorod, 2a/712, Koroleva St., Belgorod, Russia
[3] Belgorod State Technological University Named After V.G. Shukhov, 46 Kostyukova St.,
Belgorod 308012, Russia
[4] Fund of Innovative Scientific Technologies, 1, Room 3.3 Perspektivnaya Str. (Novosadovy
Mkr.), Belgorod Region, Belgorod District, Novosadovy Settlement 308518, Russia

Abstract. Due to a complex chemical composition and microstructure of many functional materials the problem of optimizing their parameters for applied purposes is associated with determining of charge carrier transport mechanisms. To modify the properties of $CaSO_4 \cdot 0.5H_2O$ we prepared composite samples: $(CaSO_4 \cdot 0.5H_2O)_{0.95}-(FeSO_4 \cdot 7H_2O)_{0.05}$ and $(CaSO_4 \cdot 0.5H_2O)_{0.90}-(FeSO_4 \cdot 7H_2O)_{0.10}$. In a dry atmosphere all studied samples also had a specific conductivity of about 10^{-9} S cm^{-1}. It has been established that with an increase in relative humidity (RH) of the environment the specific conductivity increases according to a power law up to 10^{-7} S cm^{-1}. The measurements were carrying out at a constant temperature of 28 °C and RH range of 35–90%. To study a proton conductivity of studied compounds a method of impedance spectroscopy was using. Conductivity was measuring in the frequency range 20 Hz–5 MHz. In $(CaSO_4 \cdot 0.5H_2O)_{0.95}-(FeSO_4 \cdot 7H_2O)_{0.05}$ samples and $(CaSO_4 \cdot 0.5H_2O)_{0.90}-(FeSO_4 \cdot 7H_2O)_{0.10}$ at above 40% RH granular conductivity was observed, an additional linear section was observed in $(CaSO_4 \cdot 0.5H_2O)_{0.90}-(FeSO_4 \cdot 7H_2O)_{0.10}$ samples which is responsible for the conductivity along grain boundaries.

Keywords: Electrical conductivity · Citrogypsum · RH granular conductivity · Grain boundaries · Ferroelectric

1 Introduction

Recently, a role of functional materials has increased in technology and especially in electronics [1, 2]. The physical and chemical properties of functional materials are sensitive to external influences such as temperature, electric field, magnetic field, pressure, humidity, pH value, optical radiation wavelength, adsorbed gas molecules [3, 4]. Functional materials cover a wide range of organic and inorganic materials such as ferroelectric $BaTiO_3$, magnetic field sensor $La_{1-x}Ca_xMnO_3$, surface acoustic wave sensor $LiNbO_3$,

semiconductor light detectors CdS, CdTe, high temperature piezoelectric Ta_2O_5, fast ion conductor $Y_2(Sn_xTi_{1-x})_2O_7$, high temperature superconductors, etc. The need of the industry stimulates fundamental and applied research aimed at creating new solid-state functional materials, studying their structure and physical properties. Due to a complex chemical composition and microstructure of many functional materials the problem of optimizing their parameters for applied purposes is also associated with the determination of the mechanisms of charge carrier transfer and the study of ion transport processes in solids. This, in turn, led to the discovery of new objects with ionic conductivity. These materials, called ionic conductors, have begun to be actively used in a variety of devices used in electronics and energy. For example, all solid oxide fuel cells, lithium-ion batteries, gas discharge membrane sensors, etc., contain solid crystalline or polymer ion conductors and are never used in single crystal form. It is necessary to understand the features of ion transport in these systems. Even greater relevance to this problem is given by the use of common natural materials as functional materials and materials accumulated in the form of industrial waste, which are a by-product of technological processes. Calcium sulfate dihydrate ($CaSO_4 \cdot 2H_2O$) is a waste product of the production of food citric acid, called citrogypsum [5]. This by-product cannot be used directly due to its physical properties [6, 7]. This research aims to modify the properties of citrogypsum and find new applications.

2 Materials and Methods

The object of the study was the waste of biochemical production of citric acid—citrogypsum (Belgorod, Russia). Its physicochemical properties are described in detail in [8]. Calcium sulfate dihydrate ($CaSO_4 \cdot 2H_2O$) as a result of anhydration at 200 °C for 1 h, first transferred to anhydrous gypsum ($CaSO_4$). Then, as a result of exposure of anhydrous gypsum in the open air in order to gain moisture from atmospheric air for 24 h, semi-aqueous gypsum was obtained ($CaSO_4 \cdot 0.5H_2O$).

In order to modify the properties of $CaSO_4 \cdot 0.5H_2O$ we prepared composite samples of citrogypsum: $(CaSO_4 \cdot 0.5H_2O)_{0.95}–(FeSO_4 \cdot 7H_2O)_{0.05}$ and $(CaSO_4 \cdot 0.5H_2O)_{0.90}–$ $(FeSO_4 \cdot 7H_2O)_{0.10}$. Iron sulfate was used as an alloying element ($FeSO_4 \cdot 7H_2O$). From $CaSO_4 \cdot 0.5H_2O$ and $FeSO_4 \cdot 7H_2O$ stoichiometric samples were prepared using analytical balance LV 210-A with an accuracy of 0.0001 g. Ferrous sulfate was dissolved in water and citrogypsum was added to the resulting solution. The resulting mixture was pressed under a pressure of 22 MPa. After drying in air at room temperature for 2 h, samples were cut out in a parallelepiped form $9.2 \times 7.2 \times 2.2$ mm^3 in size. Silver was deposited on large faces by magnetron sputtering using a BH-2000 setup. Contacts for research were fixed by silver-containing glue.

To study a proton conductivity of the studied compounds the method of impedance spectroscopy was using. The conductivity was measuring using RLC meter AM-3026 AKTAKOM in the frequency range of 20 Hz–5 MHz at an alternating signal amplitude of 1 V without DC polarization. The measurements were carrying out at a constant temperature of 28 °C and a RH range of 35 to 90%. RH and temperature were measured using AOSONG DHT11 sensor.

3 Results and Discussions

Figure 1 shows the electrical conductivity values of three compositions: semi-aqueous citrogypsum ($CaSO_4 \cdot 0.5H_2O$) and composite samples with the addition of iron sulfate ($CaSO_4 \cdot 0.5H_2O)_{0.95}$–$(FeSO_4 \cdot 7H_2O)_{0.05}$ and $(CaSO_4 \cdot 0.5H_2O)_{0.90}$–$(FeSO_4 \cdot 7H_2O)_{0.10}$ depending from RH in the range of 35–90% at a temperature of 28 °C.
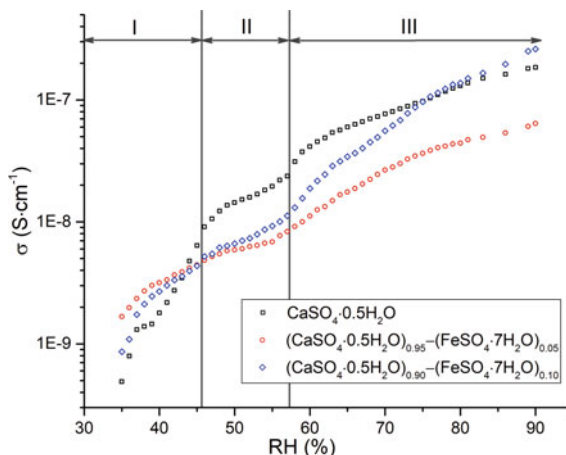
Fig. 1 Dependences of electrical conductivity of $CaSO_4 \cdot 0.5H_2O$, $(CaSO_4 \cdot 0.5H_2O)_{0.95}$–$(FeSO_4 \cdot 7H_2O)_{0.05}$ and $(CaSO_4 \cdot 0.5H_2O)_{0.90}$–$(FeSO_4 \cdot 7H_2O)_{0.10}$ on RH at 28 °C

At 35% RH all studied samples have a conductivity of about 10^{-9} S cm^{-1}. With an increase in the RH of the environment the specific conductivity increases according to a power law up to 10^{-7} S cm^{-1}. The dependence of electrical conductivity for all three samples has three linear segments that satisfy the equation:

$$\log_{10} s = a \times RH + b. \tag{1}$$

The coefficients a and b were determined from the linear plots of the $\log_{10}\sigma$ (RH) dependence and are shown in Table 1.

The proton conductivity of the studied samples was determined from the analysis of the impedance hodographs at 35, 40, 50, 60, 70, 80% RH. We further mean the Faraday impedance and its dependence on the frequency of the alternating current [9]. For all samples at 35% RH the impedance hodograph is a system of straight lines. A typical citrogypsum impedance hodograph is shown in Fig. 2.

The citrogypsum impedance hodograph with increasing humidity remains unchanged. However, for doped samples: $(CaSO_4 \cdot 0.5H_2O)_{0.95}$–$(FeSO_4 \cdot 7H_2O)_{0.05}$ at RH 40, 50, 60, 70, 80% and for $(CaSO_4 \cdot 0.5H_2O)_{0.90}$–$(FeSO_4 \cdot 7H_2O)_{0.10}$ at 40, 50, 60, 70% RH impedance hodograph is a semicircle. A typical hodograph for doped samples is shown in Fig. 3.

Table 1 The values of the coefficients a and b from the Eq. (1)

Sample	a	b	RH (%)
($CaSO_4 \cdot 0.5H_2O$)	0.1013 ± 0.0055	-12.77 ± 0.22	35–46
	0.0338 ± 0.0018	-9.55 ± 0.09	47–57
	0.0228 ± 0.0006	-8.73 ± 0.05	58–90
($CaSO_4 \cdot 0.5H_2O)_{0.95}$–($FeSO_4 \cdot 7H_2O)_{0.05}$	0.0386 ± 0.0025	-10.07 ± 0.10	35–46
	0.0175 ± 0.0013	-9.11 ± 0.06	47–57
	0.0266 ± 0.0011	-9.48 ± 0.08	58–90
($CaSO_4 \cdot 0.5H_2O)_{0.90}$–($FeSO_4 \cdot 7H_2O)_{0.10}$	0.0633 ± 0.0058	-11.16 ± 0.23	35–46
	0.0317 ± 0.0020	-9.76 ± 0.11	47–57
	0.0403 ± 0.0011	-10.10 ± 0.08	58–90
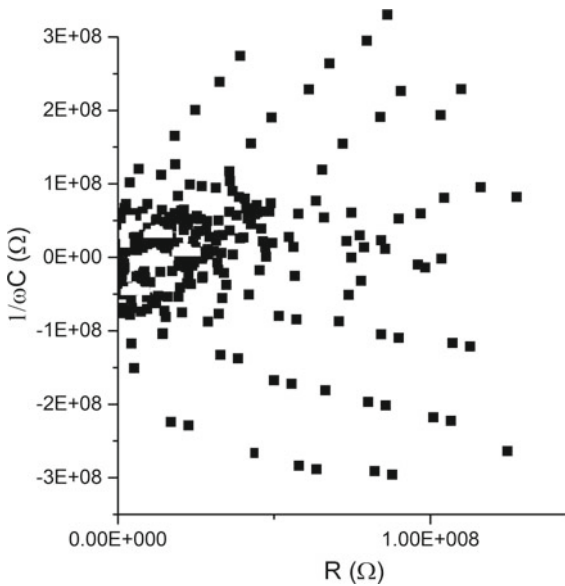
Fig. 2 Typical impedance hodograph $CaSO_4 \cdot 0.5H_2O$ at RH $= 35\%$ and $T = 28\ °C$

An electrochemical circuit can be described by constructing an electrical equivalent circuit from the simplest elements: resistors and capacitor [8]. According to this model representation the impedance hodograph ($CaSO_4 \cdot 0.5H_2O)_{0.95}$–($FeSO_4 \cdot 7H_2O)_{0.05}$ (Fig. 3) will correspond to a parallel connection of resistors and capacitor (Fig. 4) [8].

When the elements of the electrical circuit are connected in parallel, their conductivities add up. Therefore, with a known resistance of a resistor and capacitance of a capacitor for the circuit shown in Fig. 4, the reciprocals of the active and reactive resistances are added.
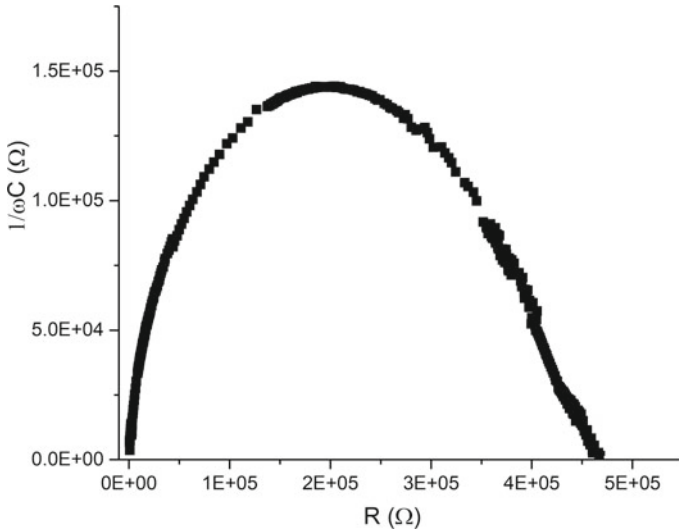
Fig. 3 Impedance hodograph $(CaSO_4 \cdot 0.5H_2O)_{0.95}–(FeSO_4 \cdot 7H_2O)_{0.05}$ at RH $= 60\%$ and $T = 28\,°C$
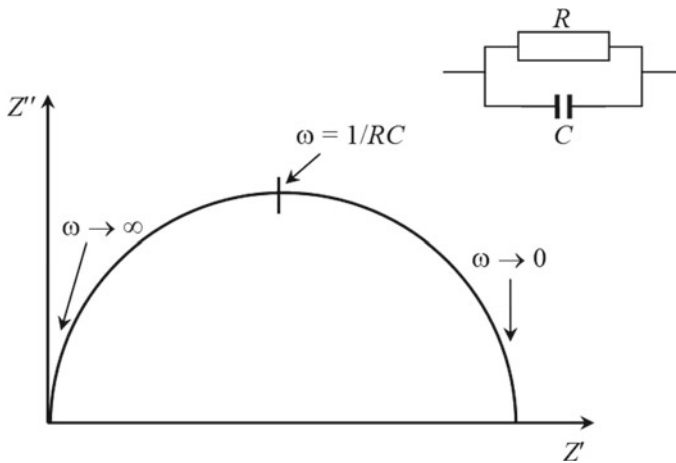
Fig. 4 Impedance for parallel connection of resistors and capacitor [2], axes: Z' and Z''—active and reactive resistance, respectively

The semicircle in Figs. 3 and 4 indicates ionic conductivity and corresponds to the grain boundary impedance [9] which makes it possible to calculate the capacitance of samples indicated in Table 2.

The right boundary of the semicircle of the impedance hodograph, a typical graph of which is shown in Fig. 3, shifts to the right with increasing RH. This suggests that with increasing RH in the samples the active resistance increases because based on Table 2

Table 2 Capacity of samples of citrogypsum doped with iron sulfate

RH (%)	C (nF)	
	$(CaSO_4 \cdot 0.5H_2O)_{0.95}-(FeSO_4 \cdot 7H_2O)_{0.05}$	$(CaSO_4 \cdot 0.5H_2O)_{0.90}-(FeSO_4 \cdot 7H_2O)_{0.10}$
40	0.114	0.117
50	0.112	0.103
60	0.108	0.102
70	0.106	0.093
80	0.110	0.109

the capacitance value remains almost constant and does not depend on humidity for both formulations.

For the sample $(CaSO_4 \cdot 0.5H_2O)_{0.90}-(FeSO_4 \cdot 7H_2O)_{0.10}$ at 80% RH the impedance hodograph is shown in Fig. 5.
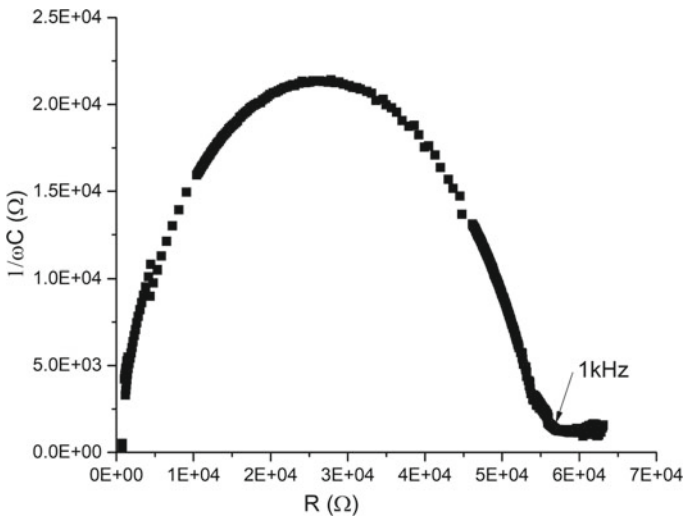
Fig. 5 Impedance hodograph of $(CaSO_4 \cdot 0.5H_2O)_{0.90}-(FeSO_4 \cdot 7H_2O)_{0.10}$ at RH $= 80\%$ and $T = 28\,°C$

The impedance hodograph is a semicircle corresponding to the grain conductivity and a linear segment responsible for the conductivity along grain boundaries [10].

4   Conclusions

Citrogypsum is a material obtained as waste in industrial processes for a production of citric acid and waste disposal is an important environmental issue. In order to expand the field of application of semi-aqueous gypsum $(CaSO_4 \cdot 0.5H_2O)$ an attempt was made

to optimize its parameters for applied purposes and study the mechanisms of charge carrier transfer. In order to modify its properties iron sulfate was used as an alloying element. Composite samples were obtained: $(CaSO_4 \cdot 0.5H_2O)_{0.95}$–$(FeSO_4 \cdot 7H_2O)_{0.05}$ and $(CaSO_4 \cdot 0.5H_2O)_{0.90}$–$(FeSO_4 \cdot 7H_2O)_{0.10}$. It was found that at 35% RH all the studied samples had a conductivity of the order of 10^{-9} S·cm^{-1}. With an increase in RH of the environment above 40% the conductivity increased according to a power law up to 10^{-7} S·cm^{-1}. In samples $(CaSO_4 \cdot 0.5H_2O)_{0.95}$–$(FeSO_4 \cdot 7H_2O)_{0.05}$ and $(CaSO_4 \cdot 0.5H_2O)_{0.90}$–$(FeSO_4 \cdot 7H_2O)_{0.10}$ granular conductivity was observed at RH above 40%, in the sample $(CaSO_4 \cdot 0.5H_2O)_{0.90}$–$(FeSO_4 \cdot 7H_2O)_{0.10}$ at above 80% RH is an additional linear region responsible for the conductivity along grain boundaries.

References

1. Goesmann, H., Feldmann, C.: Nanoparticulate functional materials. Angew. Chem. Int. Ed. **49**, 1362–1395 (2010). https://doi.org/10.1002/anie.200903053
2. Yi, J., Li, S.: Functional Materials and Electronics. Apple Academic Press Inc., Oakvill (2021)
3. Skinner, S.: Functional materials. Mater. Today **14**, 53 (2011). https://doi.org/10.1016/S1369-7021(11)70038-4
4. Ushkov, A.A., Shcherbakov, A.A.: Concurrency of anisotropy and spatial dispersion in low refractive index dielectric composites. Opt. Express **25**, 243–249 (2017). https://doi.org/10.1364/OE.25.000243
5. Sirimahasal, T., Kalhong, Y., Simasatitkul, L., Pranee, S., Seeyangnok, S.: The effect of solvent polarity on phase transformation of citrogypsum via hydrothermal process. Key Eng. Mater. **803**, 351–355 (2019). https://doi.org/10.4028/www.scientific.net/KEM.803.351
6. Nikulicheva, T.B., Nikulin, I.S., Pilyuk, E.A., Alfimova, N.I., Nikulichev, V.B., Saenko, M.Y.: Recycling and disposal of gypsum-containing waste generated in the production of citric acid. IOP Conf. Ser.: Earth Environ. Sci. **845**, 012152 (2021). https://doi.org/10.1088/1755-1315/845/1/012152
7. Alfimova, N.I., Pirieva, S.Y., Titenko, A.A.: Utilization of gypsum-bearing wastes in materials of the construction industry and other areas. Constr. Mater. Prod. **4**(1), 5–17 (2021). https://doi.org/10.34031/2618-7183-2021-4-1-5-17
8. Alfimova, N.I., Pirieva, S.Y., Elistratkin, M.Y., Nikulin, I.S., Titenko, A.A.: Binders from gypsum-containing waste and products based on them. IOP Conf. Ser.: Mater. Sci. Eng. **945**, 012057 (2020). https://doi.org/10.1088/1757-899X/945/1/012057
9. Chang, B.-Y., Park, S.-M.: Electrochemical impedance spectroscopy. Annu. Rev. Anal. Chem. **3**, 207 (2010). https://doi.org/10.1146/annurev.anchem.012809.102211
10. Irvine, J.T.S., Sinclair, D.S., West, A.R.: Electroceramics: characterization by impedance spectroscopy. Adv. Mater. **2**, 132 (1990). https://doi.org/10.1002/ADMA.19900020304

Improving the Quality of Building Materials Due to the Effect of Shear Deformation on the Parameters of the Grinding Process

A. A. Romanovich[(✉)] , S. A. Schastlivenko , M. A. Romanovich ,
and E. I. Vyskrebentsev

Belgorod State Technological University named after V.G. Shukhov, Belgorod, Russia
Alexejrom@yandex.ru

Abstract. The article presents the results of experimental studies of shear deformation on the process of grinding materials. The following values are taken as the investigated values: molding pressure, the angle of force exertion, the value of the weighted average size of the crushed particles and the pressing layer. As a result of mathematical planning of the experiment, regression equations were obtained and graphical dependences of the influence of the studied factors on the degree of material grinding and their final density were constructed. Organogenic limestone and clinker with an isotropic texture are the studied materials. The conducted studies allowed us to find out the range of rational values of the pressure value when grinding materials with different textures and physico-mechanical properties. The range within the limits for organogenic limestone is $P = 75$–150 MPa, and for clinker $P = 150$–225 MPa. The magnitude of shear deformations affects the degree of grinding. It is established that with an increase in the angle of application of force and shear deformations up to $45°$, the degree of grinding of the studied materials increases.

Keywords: Building material · Shear deformation · Grinding process · Mechanism of destruction

1 Introduction

Rocks used as raw materials in the production of various building materials are natural compounds formed in various geological, cosmochemical, sedimentary and other processes. These rocks include energy reserves that will enable to significantly reduce energy consumption. In our opinion, materials with anisotropic texture have huge reserves for energy saving.

In order to obtain the cement, millions of tons of clinker should be grinded. Its isotropic texture is formed in the decarburization zone of the furnace due to high temperatures followed by abrupt cooling [1, 2]. Scientists [3–5] from various countries are researching various technologies and equipment for grinding materials in order to improve the efficiency of raw material processing. Many scientists both in our country and abroad were engaged in energy saving issues when grinding materials, these are:

Gridchin A., Sopin M., Alferov V., Pustovoy K., Romanovich A., Amini E., Redkin G. M., Kolesnikov A. V., D. Elmo and others [6–11], who created modern ideas about the theory of destruction of brittle materials.

The provision of directional movement of materials to the working bodies of crushing equipment was applicable only for materials with anisotropic shale texture [12, 13]. However, this technique does not work with materials with anisotropic texture, such as rocks which received defects during their primary processing and semi-finished products because of these defects in a chaotic order.

In our opinion, the volume-shear deformation during grinding materials with an isotropic defective texture by pressure between the working bodies of roller will provide destruction in the direction of the cracks formed and thereby reduce the specific energy consumption. This can be ensured, since the force action in the units is carried out from the moment of capture by the working bodies until complete destruction. However, the process of volumetric shear destruction is influenced by a number of factors: the magnitude of the grinding force, the direction of shear deformation, the initial volume and size of pieces.

As a result, we conducted research to study the cumulative effect of these factors on the efficiency of the destruction process of materials with different textures and physical and mechanical characteristics [14–16].

2 Methods and Materials

The crushing process of materials and density after the particles deformation are significantly influenced by: the value of the extrusion pressure P, the angle of force action α, the weighted average size of the source material $d_{avg.}$ and the thickness of its layer during the grinding of H_{base} [2, 17]. The degree of shredding and the compaction coefficient were taken as output parameters.

The studies were carried out on a STU-50 hydraulic press with a measurement accuracy of $\pm$ 1 MPa, the maximum pressing force was $50 \cdot 104 \cdot N$. The studies were carried out in a cylindrical mold with a punch diameter $D_N = 40 \times 10^{-3}$ m, with a different cut angle on both sides of its working surface, which made it possible to change the direction of force application.

The degree of grinding of materials was determined by the following expression:

$$E = \left(1 - \frac{d_{\text{avg.}}}{D_{\text{avg.}}}\right) \cdot 100\% , \qquad (1)$$

where $D_{\text{avg.}}, d_{\text{avg.}}$ are the weighted average size before and after the force exertion.

To study their cumulative effect on the output parameters of the process, the method of mathematical planning of the experiment according to the central composite orthogonal plan of the CCOP-24 was applied.

The conducted studies enable to establish the levels and steps of variation of the studied factors (Table 1).

After processing the results of experimental studies on a computer, equations were obtained to determine the degree of grinding E and the compaction coefficient (2–5), depending on the magnitude of the extrusion pressure P, the angle of application of

Table 1 Levels of factor variation

	Variation step	The value of the variable parameters				
		-1414	-1	0	$+1$	$+1414$
P, MPa	80	37	70	150	230	263
α, degr.	15	8.8	15	30	45	49.2
$d_{avg.}$, 10^{-3} m	3.2	1.8	3.1	6.3	9.5	10.8
H_{base}, 10^{-3} m	10	20.9	25	35	45	49.1

force α, the weighted average size of the feedstock $d_{avg.}$ and the initial height of the compressible layer of H_{base}, which took the form for clinker E_i, K_k and organogenic limestone E_2, K_2:

$$E_i = 17.06 - 3.54\,P + 048\alpha + 1.736 \cdot d_{avg.} - 0.1736 \cdot H_{base}$$
$$- 0.001P^2 + 0.001\,P\alpha + 0.006P \cdot d_{avg.} +$$
$$+ 0.007\alpha \cdot d_{avg.} - 0.002\alpha \cdot H_{base} - 0.012 \cdot d_{avg.} \cdot H_{base}$$
$$+ 0.002 \cdot H_{base}^2 - 0.005\alpha^2 - 0.13d_{avg.}^2 \tag{2}$$

$$E_k = 26.14 + 0.216P + 0.574\alpha + 5.5d_{avg.} + 0.9 \cdot H_{base} - 0.001P^2 +$$
$$+ 0.003P \cdot d_{avg.} + 0.008\alpha d_{avg.} - 0.01 \cdot d_{avg.} \cdot H_{base}$$
$$- 0.008\alpha^2 - 0.239d_{avg.}^2 - 0.007 \cdot H_{base} \tag{3}$$

The study of the magnitude of the coefficients and their interaction in the regression equations allows us to draw conclusions:

- The molding pressure has the greatest influence on the amount of crushing of clinker and organogenic limestone, since the coefficient at P is the largest. The positive sign at α, $d_{avg.}$ indicates that the degree of grinding increases with increasing shear deformations and the weighted average particle size of the source material.
- A small value of the coefficients with a minus sign, at the H_{base}, indicates a slight decrease in the degree of grinding with an increase in the initial layer of the crushed product, which confirms the implementation of the self-grinding process in the material layer. All interaction effects, with the exception of H_{base}, increase the degree of grinding of the studied materials [12, 13].

$$K_k = 1.38 + 0.007\,P - 0.011 \cdot d_{avg.} + 0.004\alpha - 0.003H_{base} - 1.5 \times 10^{-5}P^2 +$$
$$+ 4.3 \times 10^{-5}P \cdot d_{avg.} - 7.6 \times 10^{-5}\alpha^2 + 6.3 \times 10^{-5}\alpha \cdot d_{avg.} - 2.1 \times 10^{-5}H_{base} \tag{4}$$

$$K_i = 2.63 + 0.004\,P - 0.046 \cdot d_{avg.} - 0.029 \cdot H_{base} + 5 \times 10^{-5}\,P \cdot d_{avg.}$$
$$+ 8 \times 10^{-5}\alpha^2 + 2.1 \times 10^{-5}\alpha \cdot d_{avg.} + 1.3 \times 10^{-5}\alpha H_{base} - 5.6 \times 10^{-4}H_{base}^2$$
$$- 1.4 \times 10^{-6}\,P^2 - 8.5 \times 10^{-6}\,P \cdot H_{base} + 2.5 \tag{5}$$

3 Results and Discussion

The analysis of Eqs. (3–4) shows that an increase in any of the parameters P, α, $d_{avg.}$ causes and increase in the compaction coefficients, while an increase in the thickness of the initial layer of particles of the H_{base} negatively affects its growth. But the effect of its interaction with α and P with a plus sign indicates that the compaction coefficient is influenced by the values of shear deformation and molding pressure rather than the size of the initial layer of the material. With an increase in shear deformation, the mobility of the grains of the crushed material increases, this leads to their better packaging.

According to the obtained Eqs. (2)–(5), graphical dependencies were constructed (Figs. 1, 2 and 3).
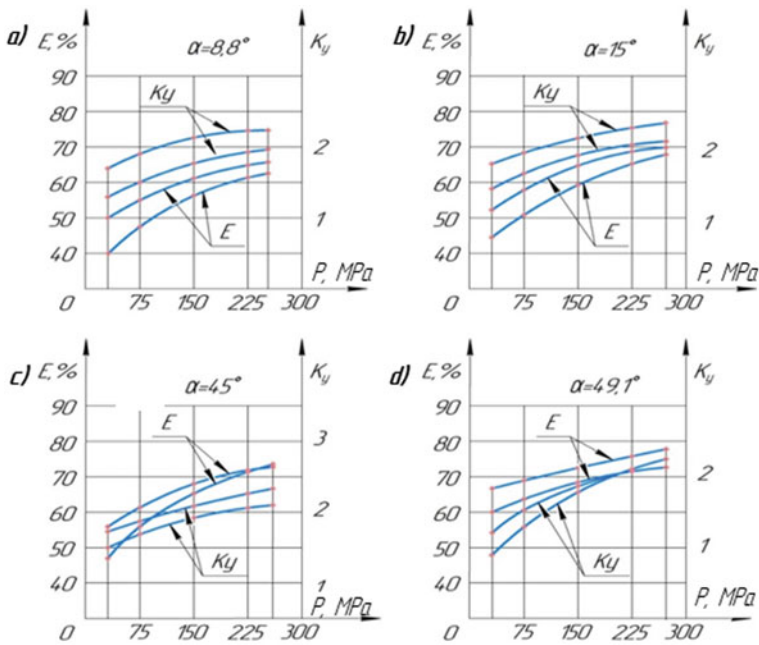
Fig. 1 Influence of the magnitude of shear deformation on the degree of fineness and compaction coefficient: at $(d_{avg.} = 6.3 \times 10^{-3}$ m, $N_{ix.} = 25 \times 10^{-3}$ m); 1—organogenic limestone, 2—clinker

The analysis of the graphical dependence E, $K_i = f (\alpha; P)$ for studied materials shows that an increase in the molding pressure to 150 MPa for organogenic limestone and up to 225 MPa for clinker leads to an intensive increase in the degree of grinding and compaction coefficient. A further rise in the pressing pressure up to 300 MPa leads to a slight increase in output indicators. For example, an increase in the molding pressure (Fig. 1a) from 37 to 150 MPa for organogenic limestone and up to 225 MPa for clinker leads to an increase in the degree of grinding and, from $E_i = 49.4\%$ to $E_i = 64.2\%$ and from $E_{avg.} = 40.8\%$ to 64.1%, i.e. by 14.7% and 13.2%, and their compaction coefficient increases by 24% and 49%, respectively.
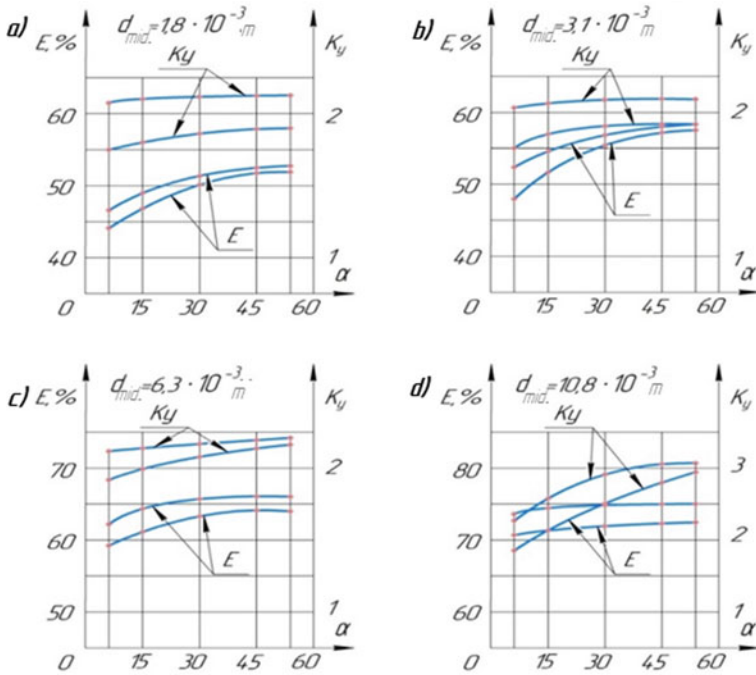
Fig. 2 Effect of shear value and weighted average particle size on fineness and compaction factor: ($P = 150$ MPa, $N_{ix.} = 35 \times 10^{-3}$ m); 1—organogenic limestone, 2—clinker

A further increase in the extrusion pressure to $P = 263$ MPa entails a slight increase in output parameters, so the density for organogenic limestone increased by 4%, and for clinker by 5%. This concludes that the saturation threshold for organogenic limestone occurs earlier than for clinker due to its lower strength. The rational values of the grinding pressure during the grinding of these materials are equal: for limestone $R_i = 150$ MPa and clinker $P_k = 225$ MPa, which indicates the effectiveness of their destruction.

With an increase in the angle of the punch cut from both sides from 0 to 45° (Fig. 1a–c), and, consequently, shear deformation, at $P = 150$ MPa, the degree of grinding for organogenic limestone and clinker increases from 64.2 to 70.6% and 58.7 to 68.6% by 10.0% and 16.8%, and the compaction coefficient increases from 2.1 to 2.2 and from 1.8 to 2.0, i.e. by 5% and 10%. This indicates the efficiency of using shear deformation when grinding materials.

A further increase in the value of the punch cut angle from $\alpha = 45°$ to $\alpha = 49.1°$ (Fig. 1d) does not raise output indicators for clinker and organogenic limestone. An increase in the angle of the double-sided section of the punch, and the shear deformation of the particles, in the range from 0 to 45 raises the efficiency of the grinding process, which effectively develops defects obtained in production or mining of rocks and their primary crushing.

The study of the dependence ($E, K_y = f(\alpha; d_{avg.})$) (Fig. 2a) made it possible to find out that an increase in the value of the angle of the two-sided cut of the punch α from
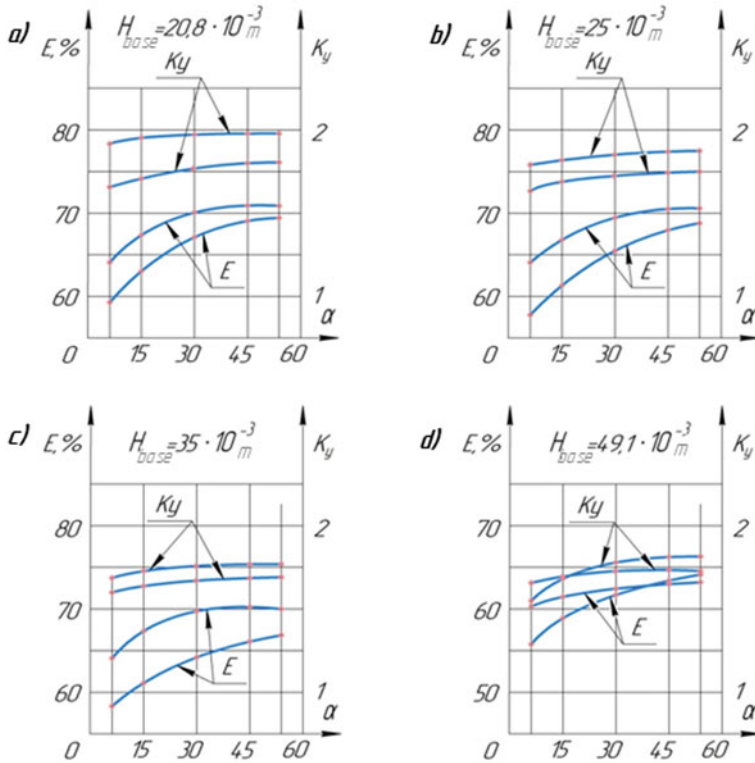
Fig. 3 Influence of the magnitude of shear forces and the initial thickness of the material on the degree of fineness and compaction coefficient: ($P = 150$ MPa, $d_{avg.} = 1.8 \times 10^{-3}$ m); 1—organogenic limestone, 2—clinker

8.8° to 45°, and, consequently, shear deformation, raises the degree of grinding and the density of the materials. Thus, for the fraction ($d_{avg.} = 1.8 \times 10^{-3}$ m), the degree of grinding increases for clinker from 44 to 52%, and for limestone from 47 to 53%.

With an increase in $d_{avg.}$ от 1.8×10^{-3} to 10.8×10^{-3} m, the degree of grinding for limestone increased from $E = 50.8\%$ to $E = 80.6\%$, i.e. by 29.8%, and for clinker from $E = 52.4\%$ to $E = 79.6\%$, i.e. by 27.4%, and the compaction coefficient by 15.8% and 14.3%, respectively (Fig. 2a–d).

A further increase in the angle of the double-sided cut of the punch to 49.20 does not lead to an increase in output indicators. It is concluded that shear deformation has a significant impact on the efficiency of the grinding process, and its rational parameter is limited by a two-sided cut of the punch at an angle of 45°.

The analysis of the graphical dependence ($E, K_y = f(\alpha; H_{base})$) (Fig. 3) showed that with an increase in the height of the crushed layer of the studied materials, the efficiency of the destruction process decreases but remains quite high, as evidenced by a slight change in the output values.

Thus, with an increase in the thickness of the layer from $H_{base} = 20.8 \times 10^{-3}$ m to $H_{base} = 49.1 \times 10^{-3}$ m ($\alpha = 45°$), the grinding degree of organogenic limestone and

clinker decreases from $E = 70.4\%$ to $E = 66.8\%$ and from $E = 67.1\%$ to $E = 64.1\%$, i.e. by 3.6% and 3%.

This study established rational parameters: the magnitude of shear deformation for organogenic limestone $P = 150$ MPa, for clinker $P = 225$ MPa, the inclination angle of the working surfaces $= 45°$. The influence of the initial weighted average size of the crushed material and the thickness of the layer on the output parameters of the process is studied. It was found that with an increase in the thickness of the layer from 20 to 50 mm, the fineness factor for the studied materials decreases by 3–4%. This indicates the effectiveness of shear deformation on the self-grinding of particles in the layer.

4   Conclusions

We can draw the following conclusions:

1. Many scientists who described the mechanism of destruction of solids with different textures have been engaged in energy saving issues when grinding materials of natural and man-made origin.
2. A technique has been developed to study the effect of the volume-shear deformation for different particle sizes of crushed materials with different textures and its initial layer thickness on the efficiency of the process.
3. Regression equations were obtained to determine the cumulative effect on the degree of grinding and compaction coefficient of organogenic limestone and clinker during their grinding of the following technological factors: the magnitude of the pressing pressure and the angle of application of force, the weighted average size of the initial product and the height of its layer.
4. As a result of the analysis of graphical dependencies obtained from regression equations, it was found that:

- The pressure value and the effective parameter and its rational value are within the limits of 150 MPa for organogenic limestone, and 225 MPa for clinker.
- Increasing the angle of the double-sided cut of the punch to 45°, as well as shear deformations raises the degree of grinding of the materials under study and increases the efficiency of the process.
- With an increase in the height of the initial layer from 20.8 to 49.1 mm, the degree of grinding for the studied materials is slightly reduced by 3–4%. This indicates the effectiveness of shear deformation on the self-grinding of their particles in the layer.

References

1. Alferov, V., Pustovoy, K.: Determination of energy costs in the crushing and grinding of materials. Constr. Road Mach. (5), 26–27 (1990)
2. Gridchin, A.M., Sevostyanov, V.S., Lesovik, V.S., Romanovich, A.A., Redkin, G.M., Kolesnikov, A.V.: Investigation of the grinding process of anisotropic materials in press-roll aggregates News of Universities. Construction **9**, 71–78 (2007)
3. Gridchin, A., Sopin, M., Strokova, V: Theoretical foundations of obtaining cube-shaped crushed stone from anisotropic rocks. In: Seventh Academic Readings of the RAACS Modern Problems of Construction Materials Science, pp. 94–97 (2001)
4. Kirpechev, V.: On the similarity of elastic phenomena. J. Russ. Phys. Chem. Soc. 152–155 (1974)
5. Mersman, M.: Technology for the modernization of cement plants of the company KHD Humboldt Wedag GmbH. Cem. Appl. (3), 40–43 (2005)
6. Reinhardt, J.: Effective Finishing Grinding World Cement, pp. 93–95 (2008)
7. Rodin, R.A.: The mechanization of crack development during the destruction of an elastic body News of Universities. Min. Mag. **10**, 5–12 (1991)
8. Romanovich, A.A., Alekhin P.V.,. Meshcheryakov, S.A.: Determination of the grinding force of anisotropic materials in a press-roll shredder Bulletin of the V.G. Shukhov BSTU 79-82 (2010)
9. Schwar, S.: Optimization of grinding using high-pressure roller grinding and downstream ball mills. World Cem. (9), 385–388 (1990)
10. Stroiber, V.: Grinding technology and energy consumption Part 1 V. Stroiber. Cem. Int. **2**, 44–52 (2003)
11. Sukkar, M., Kheshp, K., Shahid: Installations for the production of cement with roller press units of the company SPSS. Cem. Lime Gypsum (2), 60–64 (2006)
12. Romanovich, A.A., Amini, E., Romanovich, M.: IOP Conf. Ser.: Mater. Sci. Eng. **945**, 012060 (2020)
13. Romanovich, M., Romanovich, A.A., Chekhovskoy, E.: Bulletin of BSTU named after V. G. Shukhov (8), 131–137 (2018)
14. The road economy of Russia. Figures and facts Ministry of Transport of Russia. Fed. dor. Agency 18–26 (2010)
15. Elmo, D., Stead, D.: Rock Eng. (43), 3–19 (2010)
16. Singh, M., Rao, K.S., Ramamurthy, T.: Rock Mech. Rock Eng. **35**(1), 45–64 (2002)
17. Karakul, H., Ulusay, R., Isik, N.S.: Int. J. Rock Mech. Min. Sci. **47**(4), 657–665 (2010)

Water-Resistant Clay and Slag Composite Materials of Autoclaved Hardening

Yu. L. Makridina , I. V. Starostina(✉) , A. S. Lushnikov , and R. G. Shevtsova

Belgorod State Technological University named after V.G. Shukhov, Belgorod, Russia
starostinairinav@yandex.ru

Abstract. The water resistance of autoclaved silicate materials can change in a wide range. The strength of calcium-silicate brick in the water can decrease up to 30%, which is explained by its high open porosity and possible content of some free hydrated lime, which on contact with water after some time passes into its soluble state, forming pores and cavities. The most water-resistant are dense silicate concretes, the cementing bond of which consists of hydrosilicates CSH (B), tobermorite, xonotlite. The paper considers clay-slag autoclaved composite materials, obtained with the use of steelmaking slaking slags and polymineral clay, of the following composition, wt%: slag—60; clay—40; lime—5, over 100%. As a water-repelling admixture the usage of oil-extracting industry waste kieselguhr sludge, generated at winterization stage of oil refining during oil clarification from waxes and wax-like impurities, was considered. Kieselguhr sludge contains 65% of organic matter, including 3.8% of vegetable waxes and wax-like substances, which provides it with hydrophobic properties. The findings have demonstrated that the optimal sludge content makes up 0.8% of solid components weight, which provides consistent strength and reduces water sorption and capillary suction of clay-slag autoclaved composite concrete samples almost by half in comparison with control samples of concrete without the additive. The operating principle of the sludge consists in leaching of amorphous silica, contained in diatomite, and its participation in low-basic hydrated calcium silicates synthesis in autoclaving conditions with the subsequent impregnation of the silicate matrix with the released hydrophobic components of sludge, which contain, among other substances, vegetable waxes and wax-like components.

Keywords: Water-resistance · Clay and slag autoclaved composite material · Volumetric hydrophobization · Kieselguhr sludge · Compression strength · Water sorption · Capillary suction

1 Introduction

Among a wide variety of wall materials autoclaved silicate composites have found the most widespread application, which is due to their high physical–mechanical and performance properties.

The fundamental concept of obtaining silicate materials is solidification of lime-silica compositions as a result of synthesis of hydrated calcium silicates with various basicity grades at the increased temperature and vapor pressure.

From 20 to 50% of materials cost is made up by expenditures for raw components. So, the problem of increasing silicate materials production efficiency can be solved by cutting costs for key raw materials, technological processes intensification and improving the product quality by using technogenic raw materials or naturally-occurring materials, which are traditionally not used in autoclaving technology. The water resistance of autoclaved silicate materials can change in a wide range. The strength of calcium-silicate brick in the water can decrease up to 30%, which is explained by its high open porosity and possible content of some free hydrated lime, which on contact with water after some time passes into its soluble state, forming pores and cavities. The softening coefficient of silicate concretes in the water usually varies within the range 0.65–0.8.

The most water-resistant are dense silicate concretes, the cementing bond of which consists of hydrosilicates CSH (B), tobermorite, xonotlite. This is achieved by the proper selection of CaO and SiO$_2$ ratio, the proper fineness of grinding, adding blast-furnace slag as an admixture etc. Many researchers have experimentally proved that the water resistance of silicate concretes can be no lower than that of Portland cement concrete.

Water resistance of materials correlates well with their resistance to adverse environmental factors, and, consequently, their durability. Durability of building materials in structures is determined, on the one hand, with environmental effects of physical, chemical or mechanical nature, as well as their combinations. And, on the other hand, it is determined with endogenous processes, which to a great extent are conditioned by physical and chemical properties of building materials' components: chemical and mineralogical composition of clinker, pore space structure and permeability of material. So, the problem of increasing building materials durability can be solved in a variety of ways [1].

First of all, in order to improve technological and performance characteristics of concrete products it is necessary to effectively protect them from the adverse impact of water, in other words—to increase water resistance of concrete products.

Moisture, penetrating into the capillary system of materials, starts filling the pores and causes the increased water sorption, low water-resistance and frost-resistance, high shrinkage and water permeability, i.e., low materials durability in general. At soluble salts diffusion on the surface of materials the efflorescence is formed. The increase of building materials' water sorption over standard allowable values causes deterioration of their technological and performance characteristics—increase of porosity, decrease of strength, frost-resistance and corrosion resistance, which can result in decay of buildings and structures.

To increase water resistance of building materials and products various methods are used, which can be conveniently divided into two large groups (Fig. 1):

- technological methods, modifying the materials' structure;
- hydrophobization.

Technological methods compact the structure of materials by using air-entraining, plasticizing or thickening admixtures, or molding of harsh mixes by pressing or vibration pressing.
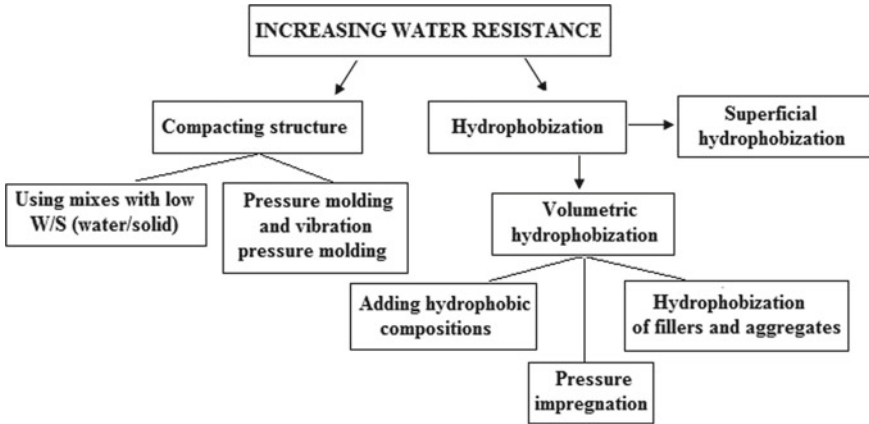
Fig. 1 Methods of increasing water resistance of silicate materials

Thus, in the work [2] the possibility of increasing strength and water resistance of press-formed articles based on gypsum binders and magnesium cement by changing their structure is shown. Such effect is achieved by adding carbonate-containing sludge of heat-and-power stations chemical water treatment and mono-ammonium phosphate to gypsum binders, and microsilica and fine-ground burnt mined rock—to magnesium cement. It is demonstrated that on the surface of microcrystalline structure elements of pressed gypsum materials the shielding protective films of poorly soluble calcium phosphates are formed. And the increase of strength and water resistance of press-formed articles made of modified magnesium cements is explained by the formation of poorly soluble magnesium hydrosilicates, hydroaluminates and hydroalumosilicates in the solidified material, and by the formation of a complex combined structure, which contains coagulation, condensation and crystallization phases. Concretes are usually considered to be hydrophilic materials, i.e. wettable with water. One of the efficient materials water-resistance increasing methods is hydrophobization—superficial and volumetric.

The most widely known modifiers of silicate concretes' hydrophilic mineral surface, providing it with hydrophobic (water-repelling) properties, are the compounds, which belong to different classes: long-chain alcohols, fatty acids, alkyl-substituted silanes, containing Si-Hal or Si-OR fragments, derivatives of phosphonic acids with long hydrocarbon radicals. With the increase of grafted hydrocarbon chains length, the hydrophobic behavior of the coating increases as well [3]. The most widely used class of water-repelling agents is organosilicon compounds [4, 5].

There is a practice of providing surfaces with superhydrophobic properties. These properties are achieved by the formation of microroughness and nanoroughness, created by a film, based on a dispersion or emulsion with the added aggregates from 0.1 to 200 μm. As the dispersed material titanium, aluminum or silicon oxides can be used, with the specific surface up to 200 m^2/g. [6]. Similar to a lotus leaf's rough surface, this structure facilitates the formation of water drops on the surface and the removal of mechanical impurities by their entraining with these drops [7].

The work [8] presents the research data concerning the waterproofing efficiency of dense concretes for paving and airfield slabs with an «Aquastat» impregnating compound. It has been determined that as a result of impregnating, a concrete sample is not wetted with water and acquires hydrophobic properties; with that, the water sorption of samples, treated during 24 h under atmospheric pressure is reduced by 3 times, and of samples, treated for 0.5 h under vacuum is reduced by 5.5 times. It has been revealed that the water-repelling properties of materials, impregnated with «Aquastat», allow the fine-grained concretes approximating the properties of dense concretes and increase the durability of pavement and airfield slabs, treated with the «Aquastat» compound.

The most promising is the volumetric hydrophobization method, based on adding a special component to the mix, which provides a finished item with water-repellent properties. Adding the admixture at mix preparation stage allows modifying the structure of material, and not only its surface.

There are various methods of adding water-repelling admixtures to a concrete mix: deposition of the admixture on a mineral excipient, mixed grinding, saponification of water-insoluble products, sulfonation, emulsification, agglomeration into granules, pellets, tablets, granulated powders. The usage of organic biogenic additives, recovered from peat raw material and added at cement milling in amount 0.5–10% of solid components weight of dry building mixes is also known.

In the works [9, 10] water-soluble organosilicon compounds FES-50, Tiprom S and GKZH 11 were used as water-repelling admixtures. The findings have demonstrated that the admixtures under study increase frost-resistance and reduce water sorption of fine-grained concrete, and inhibit the initial and final setting of cement paste, especially at high dosages. The application of Tiprom S admixture in amount 0.2% of the cement weight increases frost-resistance by 250 cycles in comparison with the control sample. The lowest water sorption of concrete was achieved at the combined adding of Tiprom S and FES-50 admixtures in amount 0.1% of the cement weight.

For volumetric hydrophobization of sand-cement concretes the application of paraffin emulsions, obtained from a mix of paraffin components (solid paraffin, paraffin slop wax) and non-ionic emulsifiers, is known. The usage of emulsions increases the workability, strength, water resistance and salt resistance of concretes.

The volumetric hydrophobization of pressed slag-lime cements (SLC), obtained from the Lipetsk metallurgical works slag and an alkaline activator NaOH, which various water-repelling materials, added in amount 2% of SLC weight, was studied. The findings have demonstrated that the most efficient are organometallic water-repelling agents—zinc stearate and calcium stearate, which have a long-term water resistance coefficient—0.99 and 0.98. With that, they do not affect the strength properties of materials, facilitating the active binder setting in aqueous media and the compression strength gain during 100-days aging in the water.

The most promising way for cost-cutting of both superficial and volumetric hydrophobization is using industrial production waste as water-repelling components. Thus, the usage of organosilicon fluids rectification vat residues, a hydrophobic organomineral modifier, based on technical-grade lignosulfonates, is known. In the work [11] it is suggested using heavy oil residues recycling products as water-repelling admixtures—a composite material in the form of fine powder. These recycling products contain

water-repelling wax compounds and silica-containing sorbents, which increase strength and water resistance of set cement by volumetric hydrophobization of the material.

The purpose of this research is to study the opportunity of increasing the water resistance of clay-slag autoclaved composite materials by using an organomineral sludge waste of oil-extracting industry as a water-repelling admixture.

2 Methods and Materials

As original raw components for carrying out the research the steelmaking slag of JSC «Oskolsky electrometallurgical works» (JSC «OEMW»), Stary Oskol, Russia, was used, the chemical composition of which is presented in Table 1. A distinctive feature of this slag is its unstable structure, i.e. the slag is prone to dicalcium silicate disintegration as a result of polymorphic transformation of $2CaO \cdot SiO_2$ from β- into γ-modification in the process of slag cooling.

Table 1 Chemical composition of raw materials, wt%

Material	SiO_2	Al_2O_3	Fe_2O_3	CaO	MgO	R_2O	MnO	Cr_2O_3	TiO_2
Gorodische clay	66.25	11.86	4.73	1.21	2.45	5.48	–	–	0.78
OEMW slag	23.90	3.00	12.00	46.30	7.50	0.23	1.8	0.9	–
Mineral part of sludge (diatomite)	86.54	2.40	0.89	5.85	0.54	0.36	3.26	–	0.14

According to the X-ray phase analysis findings (Fig. 2), the basic minerals of the slag include γ-dicalcium silicate (shannonite), okermanite, iron oxides—wustite and magnetite, calcium ferrites and some amount of free calcium hydroxide.

To obtain clay-slag autoclaved composite materials the clay from a deposit in the Gorodische settlement, Belgorod region, Russia, was used. The sample was presented with light-brown medium-density loose rock; its chemical composition is presented in Table 2.

The mineral composition of clay was evaluated on the basis of X-ray phase analysis findings (Fig. 2b). According to the obtained data, the Gorodische clay is characterized with polymineral composition, and contains two groups of clay minerals—kaolinite and the prevailing montmorillonite group minerals. The presence of some impurity minerals—calcite and free silica—should be also noted. The clay-slag mix of the following composition was used, wt%: Gorodische clay—40; hydraulic-cooled OEMW slag, fraction 0–5 mm—60; lime (CaO)—5, over 100%.

The weighed raw components were mixed and moistened with water to moisture content 28%. The cylindrical samples of clay-slag composite materials 3 cm high and 3 cm in diameter were shaped by semidry molding at specific pressure 20 MPa, and autoclaved under factory conditions at steam pressure 1 MPa.

As a modifying water-repelling admixture the application of oil-extracting industry waste kieselguhr sludge (WKS) from the «EFKO» plant, Alekseevka, Belgorod region,
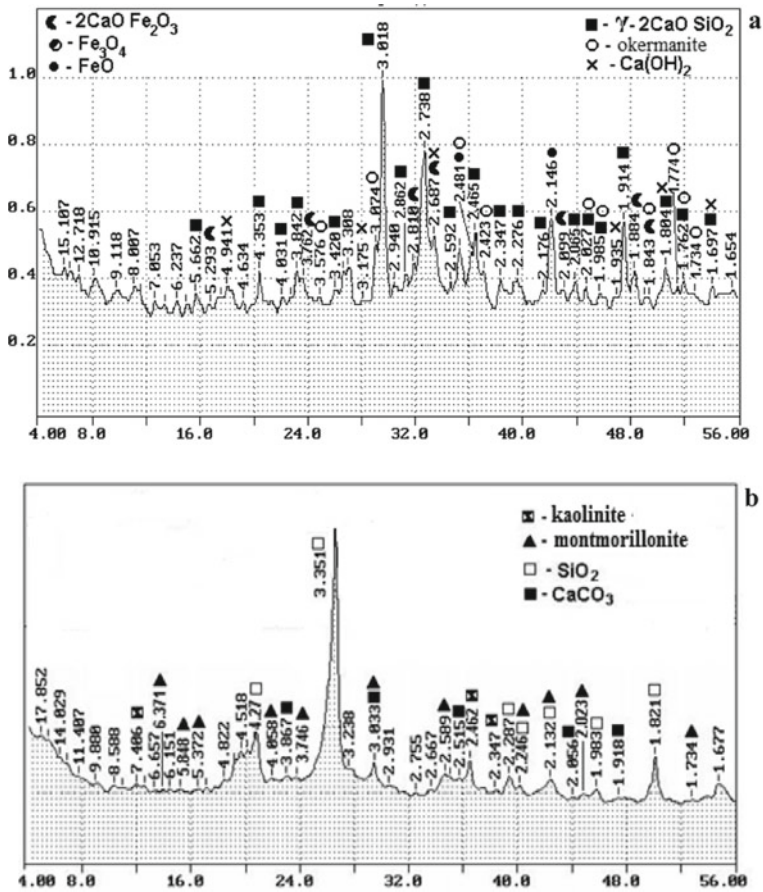
Fig. 2 X-ray phase analysis of raw materials: **a** hydraulic-cooled OEMW steelmaking slag, fraction 0–5 mm, **b** Gorodische clay

Table 2 Composition of the organic part of kieselguhr sludge, wt%

Component	Value
Phospholipids	3.9
Monoacylglycerides	5.3
Diglycerides	13.2
Polyatomic alcohols	6.0
Free fatty acids	3.2
Triglycerides	63.8
Waxes	3.8

Russia, was considered. Kieselguhr sludge is the waste, generated at winterization stage of oil refining during oil clarification from waxes and wax-like impurities.

WKS is a dingy-white slow stock with organic impurities content up to 65%. The mineral part of the sludge is represented with diatomite—sedimentary rock, formed by siliciferous frustules of microphytic diatomic algae—diatoms and radiolarians. The main component of the siliciferous frustule (skeleton) is presented with amorphous siliceous hydrates of various hydration degree—opal varieties of the type $mSiO_2 \cdot nH_2O$; the crystalline component is presented with quartz impurities. The chemical composition of mineral part—diatomite, is presented in Table 1.

The composition of organic part of kieselguhr sludge is presented in Table 2. The presence of vegetable waxes and wax-like substances in amount 3.8% in the organic part of kieselguhr sludge provides it with high hydrophobic properties—contact angle of wetting is 130º (Fig. 3).
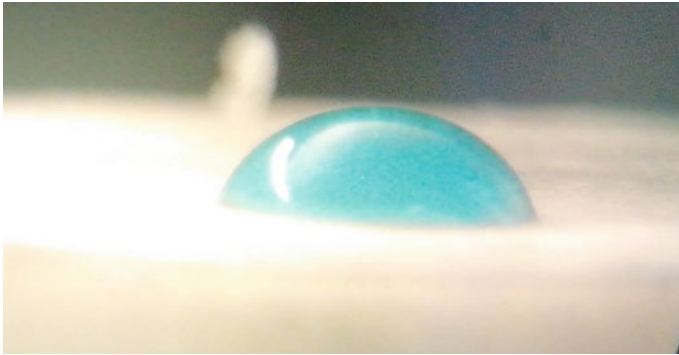
Fig. 3 Water drop on the surface of waste kieselguhr sludge

3   Results and Discussions

The sludge was added in amounts of 0.5; 0.8; 1; 1.2 and 1.5% of solid components weight. The results, presented in Fig. 4, have demonstrated that the optimal admixture content makes up 0.8%, which provides a slight increase of compression strength in comparison with the control sample.

In Fig. 5a, b the water sorption kinetics and capillary suction kinetics of a clay-slag autoclaved silicate concrete control sample and of a sample with the optimal amount of kieselguhr sludge are presented. The results have shown that adding the sludge reduces the water sorption and capillary suction of concrete samples almost by half in comparison with control samples of silicate concrete. This indicates the change of the material's structure and type of porosity.

As it is known, the drawbacks of volumetric hydrophobization include the adverse influence on setting processes as a result of mixture particles shielding, which can cause compression strength decrease [10, 12].
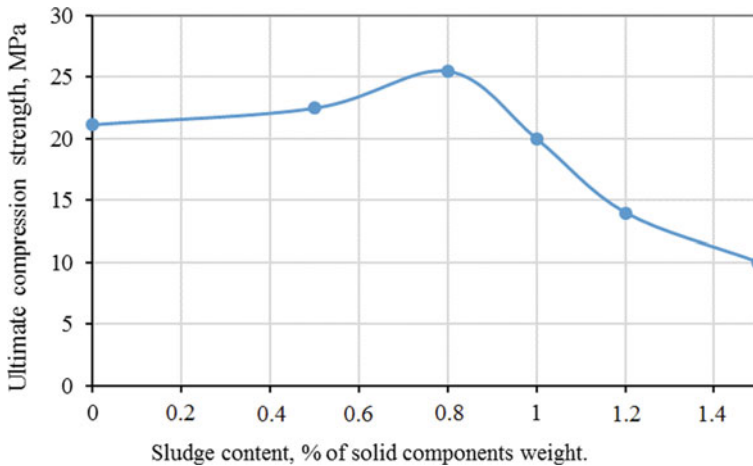
Fig. 4 The influence of kieselguhr sludge content on strength properties of clay-slag autoclaved composites

In this case the strength properties decrease takes place at sludge content over 1%. Adding sludge in amounts up to 1% results in stabilization and slight increase of strength properties. It may be assumed that this is due to peculiarities of sludge particles structure—waxes and wax-like substances are placed on diatomite surface.

The operating principle of sludge particles consists in leaching of amorphous silica, contained in diatomite, and its participation in low-basic hydrated calcium silicates synthesis in conditions of high temperatures and pressure with the subsequent impregnation of the silicate matrix with the released hydrophobic components of sludge, which contain, among other substances, vegetable waxes and wax-like components.

So, the obtained findings confirm the feasibility of using oil-extracting industry waste kieselguhr sludge as a water-repelling admixture for clay-slag autoclaved composite materials. It should be noted that the optimal sludge content makes up 0.8% of solid components weight, which provides high hydrophobic properties of composite materials and their stable strength properties.

The carried-out research confirms the possibility of increasing service life (durability) of the composite clay-slag autoclaved concrete and the structures, made of it, in actual operating conditions.

4 Conclusions

Based on the results of the research, the following conclusions can be drawn:

- oil-extracting industry waste kieselguhr sludge can be used as a water-repellent additive for clay-slag autoclavable composite materials;
- the optimal sludge content makes up 0.8% of solid components weight, which provides high hydrophobic properties of composite materials and their stable strength properties;
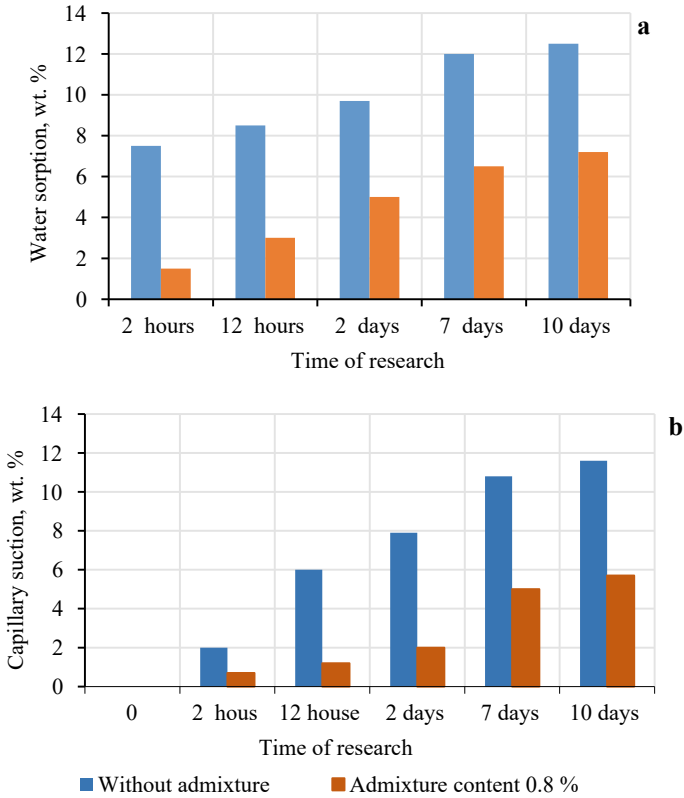
Fig. 5 Water sorption kinetics (**a**) and capillary suction kinetics (**b**) of clay-slag autoclaved composite material samples with the optimal kieselguhr sludge content

- adding the sludge reduces the water sorption and capillary suction of concrete samples almost by half in comparison with control samples of silicate concrete.

References

1. Tolstoy, A.D., Fomina, E.V., Milkina, A.S.: Durability of fine-grained high-strength concrete in corrosive environment. FarEastCon, 032036 (2020)
2. Kaklyugin, A.V., Stupen, N.S., Kastornykh, L.I., Kovalenko, V.V.: Dependence of air-setting binders-based pressed materials water resistance on open porosity value. News of Higher Educational Institutions. Investments. Construction. Real estate **10**(1), 68–75 (2020). https://doi.org/10.21285/2227-2917-2020-1-68-75

3. Lisichkin, G.V., Olenin, A.Y.: Hydrophobization of inorganic materials by surface chemical modification (review). J. Appl. Chem. **93**(1), 5–19 (2020). https://doi.org/10.31857/S0044461820010016

4. Lin, Y., Wang, L., Krumpfer, J.W., Watkins, J.J., McCarthy, T.J.: Hydrophobization of inorganic oxide surfaces using dimethylsilanediol. Langmuir **29**(5), 1329–1332 (2013)

5. Tokareva, E.V., Tkachev, I.V., Sansiev, G.V., Fedorchenko, G.D., Ivanova, A.A., Grishin, P.A., Markovic, S., Maryasev, I.G., Kuzmin, A.V.: Study of the process of hydrophobization of carbonate rock with organic acids. Oil Bus. **3**, 73–76 (2022). https://doi.org/10.24887/0028-2448-2022-3-73-76

6. Kiyko, P.I., Chernykh, T.N., Ulrikh, D.V., Kriushin, M.V.: Mechanisms for creation of self-cleaning surfaces of construction materials. News Higher Educ. Inst. Constr. **6**(750), 61–69 (2021). https://doi.org/10.32683/0536-1052-2021-750-6-61-69

7. Zorin, D.A., Ivaschenko, N.V., Dobrina, K.E.: Efficient complex waterproofing agents for self-cleaning façade materials. Bulletin of BSTU named after V.G. Shukhov, vol. 4, pp. 16–23 (2019). https://doi.org/10.34031/article_5cb1e6595c5ba2.05324270

8. Massalimov, B.I., Yanakhmetov, M.R., Chuykin, A.E., Urakaev, F.H., Uralbekov, B.M., Burkitbaev, M.M.: Hydrophobization of dense and fine concrete by polysulfide solutions. Nanotechnol. Constr. Sci. Online Mag. **8**(5), 85–99 (2016). https://doi.org/10.15828/2075-8545-2016-8-5-85-99

9. Fedosov, S.V., Rumyantseva, V.E., Konovalova, V.S., Karavaev, I.V.: On the issue of improving adhesion of composite reinforcement with cement concrete. Bulletin of the Volga State Technological University. Series: Materials. Constructions. Technologies, vol. 1, pp. 95–102 (2020). https://doi.org/10.25686/2542-114X.2020.1.95

10. Pshembayev, M.K.: Physical and chemical fundamentals of protection processes for surface layer of concrete road paving by impregnating compositions. Sci. Technol. **16**(2), 144–152 (2017). https://doi.org/10.21122/2227-1031-2017-16-2-144-152

11. Kosulina, T.I., Tsokur, O.S., Chernykh, V.F.: Application of heavy oil residues recycling products as water-repelling admixtures. Ecol. Ind. Russia **23**(4), 36–40 (2019). https://doi.org/10.18412/1816-0395-2019-4-36-40

12. Suleymanova, L.A., Malyukova, M.V., Slepukhin, A.S., Krushelnitskaya, E.A., Tolstoy, A.D.: Influence of a modifying additive with hydrophobic effect on vibropressed products' performance characteristics. Bulletin of BSTU named after V.G. Shukhov **9**, 8–13 (2019). https://doi.org/10.34031/article_5da44154d5e735.90950690

The Study of the Patterns of Soil Contact with a Solid Surface

V. V. Kocherzhenko ⓘ, L. A. Suleymanova$^{(\boxtimes)}$ ⓘ, and A. V. Kocherzhenko ⓘ

Belgorod State Technological University named after V.G. Shukhov, Belgorod, Russia
`ludmilasuleimanova@yandex.ru`

Abstract. The ability of some soil grains to move relative to others makes them look like liquids. At the same time, each particle of a granular medium, taken separately, has all the properties of a solid body. These particles form a granular body capable of absorbing external compressive loads, which makes granular bodies look like solids. In the article, considering soils as a dispersed, discretely isotropic medium (granular system), theoretically, by modeling the contact of soil particles with a solid smooth surface, the area of actual contact at various levels of convergence is established. At the same time, reference curves for the contact of various sands were established using their relative magnitude. For five types of sands, contact characteristics were determined depending on their density. For clay, loam and sandy loam, the dependence of the relative actual contact area on the plasticity number is determined. At the same time, in the range $0.25 \leq I_p \leq 0.75$, analytical dependences for sandy loam, loam and clay of the relative actual contact density on the plasticity number I_p were determined.

Keywords: Soil · Grainy media · Particle contact · Solid surface · Flow index

1 Introduction

Knowledge of the patterns of formation of the actual area of contact of soil particles with a solid surface is necessary for calculating the external friction of soils [1–3]. The doctrine of actual contact areas is an integral part of the fractional interaction of soil with a solid surface [4–6]. When a granular medium comes into contact with a solid surface, the contact will not be continuous, only at certain points on the surface will they perceive the load applied to the ground. The sum of such discrete contact areas forms the actual contact area (ACA). Thus, the ACA determines that area of the surface of the contacting bodies, where their force interaction is realized. The nature of the formation of areas of contact between a soil particle and a solid surface is shown in Fig. 1. The formation of the ACA under load occurs as a result of the introduction or collapse of individual microroughnesses, and when a tangential load is applied, plastic displacement of a softer material.

In this paper, the interaction of soils with a solid surface was considered based on the following assumptions:
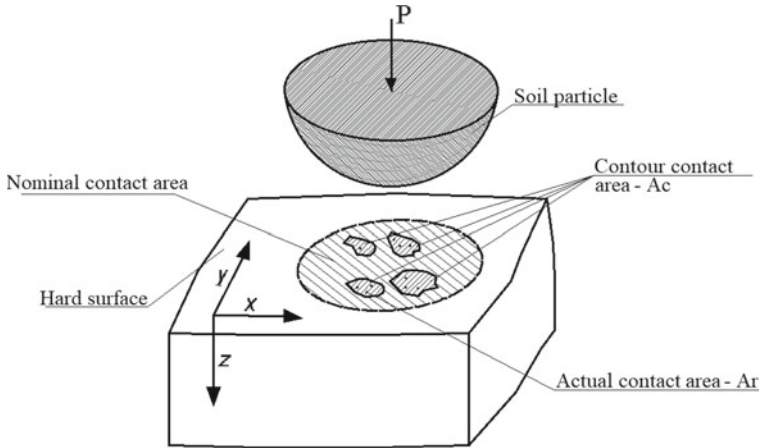
Fig. 1 The nature of the formation of areas of contact between a soil particle and a solid surface

- soil is considered as a dispersed, discretely isotropic medium (granular system), consisting of granular particles and pores;
- the formation of the friction force of soils occurs at the points of actual contact, while the nominal, contour and actual area of contacts differ;
- the roughness of a smooth solid surface is negligible compared to the roughness of sandy soils, so it can be neglected.

The most important characteristic of the microgeometry of a rough surface, including a dispersed medium in contact with a solid surface, is the support surface curve, which characterizes the distribution of material (soil particles) in contact with a solid surface [7–10].

Initially, the curves of the supporting surface were built on the basis of surface profilograms, while the sums of sections of microroughnesses of a straight line drawn at a certain distance from the base to the length of the taken profile were plotted along the abscissa axis, and the distances from the base of the profile to the selected section were plotted along the ordinate axis (Fig. 1).

2 Methods and Materials

The reference curve is expressed in relative terms [10]. In this case, the ratio of the cross-sectional area at a given level A_s to the contour area A_c is plotted along the abscissa axis, i.e. the area of the rough surface, and along the ordinate axis—the ratio of convergence a, equal to the difference between the maximum height of the irregularities and the height of the given level to the maximum height of the irregularities, i.e.:

- relative proximity:

$$\varepsilon = \frac{a}{H_{\max}}; \quad a = H_{\max} - \varepsilon_i. \tag{1}$$

- relative cross-sectional area at some level:

$$\eta_s = \frac{A_s}{A_c}. \tag{2}$$

Using the above method, reference curves were constructed for four types of sandy soil: coarse sand (well-rolled), medium-sized sand, and two types of fine sand with different granulometric composition.

Particles of four types of sandy soil with different granulometric composition were modeled as spheres of different diameters.

At the same time, they resorted to calculating the weighted average diameter for each type of soil according to the formula:

$$D_{s.v.} = \frac{D_1 \cdot q_1 + D_2 \cdot q_2 + \ldots + D_n \cdot q_n}{q_1 + q_2 + \ldots + q_n}, \tag{3}$$

where D_1, D_2,..., D_n are the diameters of sand particle fractions; q_1, q_2,..., q_n is the weight of each fraction of particles in a given type of sand.

Thus, coarse sand was modeled in the form of spheres with a diameter of 1.21 mm (according to the granulometric composition, they are 97.9%); sand of medium size was modeled in the form of spheres with a diameter of 0.375 mm (72%) and spheres with a diameter.

0.175 mm (15%); fine sand of the first type contained spheres 0.375 mm in diameter (22.7%) and 0.175 mm in diameter (61.3%); fine sand of the second type was modeled in the form of spheres with a diameter of 0.175 mm (32%) and spheres with a diameter of 0.1 mm (51%). At the same time, the weighted average diameter of the four types of soils studied was: coarse sand—$D_{s.v.} = 1.2$ mm, medium-sized sand, 0.34 mm, fine sand of the first type, 0.192 mm; fine sand of the second type—0.129 mm.

The calculation model of the interaction of sandy soil particles with a solid smooth surface is shown in Fig. 2a.
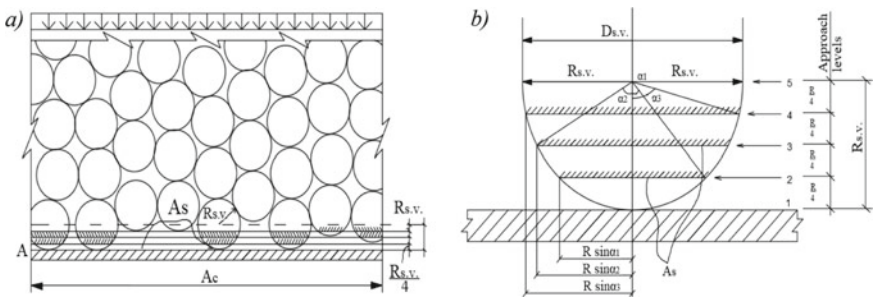
Fig. 2 Calculation model of contact of sandy soil particles with a hard-smooth surface (**a**); calculation scheme for determining the contact area of sand particles at different levels of approach (**b**)

The maximum height of the irregularities was divided into five levels. The calculation scheme for determining the contact area of sand particles at different levels of approach in a flat formulation of the problem-a is shown in Fig. 2b.

The formation of the contact area, in addition to the level of approach, is influenced by the packing density of sand particles, which is characterized by the porosity coefficient $e = n/m$. According to [11], the proportion of solid particles per unit volume of soil $m = \frac{1}{1+e}$.

It is natural to assume that the distribution law of soil particles in an arbitrary cross section (Fig. 2a) and in the contact zone is the same, then the number of particles at the contact (along the A-A line) corresponds to the proportion of solid particles in the soil volume.

Thus, for the types of sand under consideration, it is possible to construct reference curves in relative terms: $1 - \varepsilon$ and η.

Taking into account the classification of sands in construction according to the density of composition, the reference curves were calculated and plotted in relative values for the soils under consideration with a porosity coefficient of 0.5; 0.8 and 1.0.

To bring sand particles closer to a solid surface, five levels are taken according to Fig. 2b. With a known proportion of solid particles in contact with a solid surface at given porosities, the actual contact areas are calculated using the expression:

$$A_s = D_{s.v.} \cdot \sin \alpha \cdot \frac{1}{1+b}, \qquad (4)$$

in this case, the contour area on which the spots of actual contact are located is taken as $20\, D_{s.v.}$, then the relative cross-sectional area of sand particles at a certain level is determined by the ratio:

$$\eta = \frac{A_s}{20 D_{s.v.}}. \qquad (5)$$

3   Results and Discussion

On Fig. 3 shows the reference curves for the contact of sands with a hard smooth surface: coarse sand, medium size sand and fine sand of various densities.

Further studying the relationship between the volumetric and contact characteristics of sandy soils and based on the assumption, the number of contacts of particles of a granular medium, modeled by spheres with a diameter of $D_{s.v.}$, with a solid surface for maximum packing ($e = 0.258$) and maximum porosity ($e = 0.476$) was theoretically calculated.

Based on the geometric characteristics of the sandy soil model, the number of particles in the soil skeleton was determined. The number of sandy soil particles that will be in contact with a hard smooth surface depends on the normal pressure on the soil and the porosity (density) of the soil—e.

Taking into account the classification of sands by particle size and composition density, five types of sands were considered: gravelly ($D_{s.v.} = 2.3$ mm); large ($D_{s.v.} = 1.155$ mm); medium size ($D_{s.v.} = 0.375$ mm); fine ($D_{s.v.} = 0.172$ mm) and silty ($D_{s.v.} = 0.075$ mm), in dense, medium density, and loose composition with the corresponding porosity coefficients.
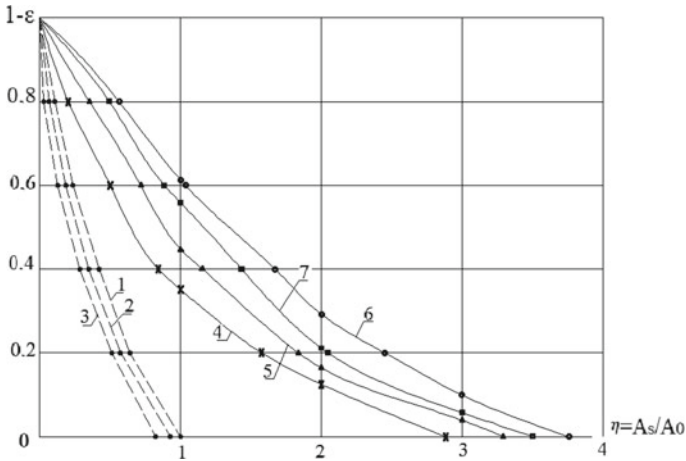
Fig. 3 Reference curves of contact of coarse sand ($D_{s.v.} = 1.25$ mm) with a hard smooth surface: 1—at porosity coefficient $e = 0.5$; 2—at $e = 0.8$; 3—at $e = 1.0$ (dashed lines) and sand of medium size ($D_{s.v.} = 0.34$ mm) and fine sand ($D_{s.v.} = 0.175$ mm): 4—for sand of medium size with $e = 0.5$; 5—for sand of medium size with $e = 1.0$; 6—for fine sand with $e = 0.5$; 7—for fine sand with $e = 1.0$ (solid lines).

Taking the unit of soil volume as $1.0 \times 1.0 \times 1.0$ cm, the number of soil particles in the skeleton was set equal to $m = 1/(1 + e)$, considering the volume of the particle with a diameter of $D_{s.v.}$ equal $\frac{1}{6}\pi D_{s.v.}^3$, тогда количество частиц $\frac{m}{\frac{1}{6}\pi D_{s.v.}^3}$.

Based on this, the number of particles in a volume of 1.0 cm^3 and the number of contacts of sand particles with a hard smooth surface were determined depending on their density. The results of the study of the contact characteristics of gravelly, coarse and medium-sized sand are shown in Fig. 4.
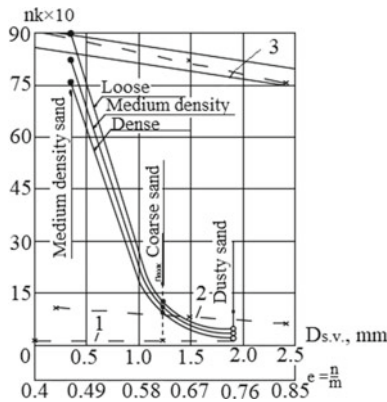
Fig. 4 Dependence of the number of contacts of sand particles (n_k) with a hard smooth surface on the particle diameter ($D_{s.v.}$) and soil density (e): 1—for gravelly soil $D_{s.v.} = 2.3$ mm; 2—for coarse sand $D_{s.v.} = 1.155$ mm; 3—for sand of medium size $D_{s.v.} = 0.375$ mm

The obtained results of theoretical studies of the dependence of the number of contacts of sand particles of different granulometric composition and density with a hard smooth surface are consistent with the reference contact curves for the same sands of different densities, obtained by modeling the contact of sandy soil at different levels of approach (Fig. 2).

Taking into account that cohesive soils, according to the classifications, are subdivided into sandy loam, loam and clay, the dependences of the fluidity index and the relative actual contact area on the plasticity number are considered for them (Fig. 5).
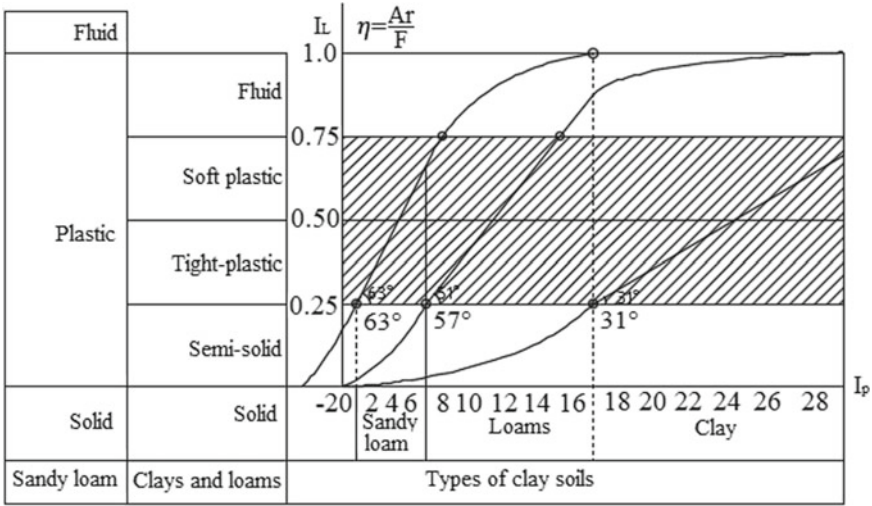
Fig. 5 Dependence of the flow index and the relative actual contact area on the plasticity number: 1—for sandy loam; 2—for loams; 3—for clays

According to the data obtained, at the second stage of compaction of clay soils during the period of plastic deformation, the straight section for sandy loam has an inclination to the abscissa axis of 63°, for loams, the angle of inclination is 51°, and for clay, 31°. This indicates that the stage of plastic deformations is minimal in sandy loams ($0 < I_p < 7$), somewhat larger in loams ($7 < I_p < 17$), and clays have a very large range of plastic deformations $I_p > 17$ (Fig. 5). On the presented dependences of the formation of the relative actual area of contact of clay soils with a solid surface on the plasticity number, it is traced how the physical state of clay soils: solid, semi-solid, hard-plastic, soft-plastic and fluid step by step affects the formation of the actual contact area with a smooth solid surface.

4 Conclusion

Thus, based on the assumptions made, studying the interaction of a granular medium with a smooth solid surface based on the developed computational model when approaching

under normal pressure, as well as studying the features of contacting clay soils with a solid surface, the authors made the following conclusions:

Having determined the weighted average particle diameter for four types of soils under study, they were modeled as a sphere with a diameter equal to the weighted average diameter with porosity coefficients e, and an expression was established for calculating the actual contact area.

Based on the geometric models of five types of sand (gravelly, coarse, medium-sized, fine and dusty) and their density (dense, medium-density and loose) with the corresponding porosity coefficients, the number of contacts of sand particles with a hard smooth surface was theoretically determined.

The obtained dependences of the flow index and the relative actual contact area on the plasticity number for three types of cohesive soils (sandy loam, loam and clay) showed that at the second stage of compaction (during the period of plastic deformations), the straight sections have a different slope: to the abscissa axis: for sandy loam—63°, for loams—51°, for clays—31°.

References

1. Wang, J., Hu, F., Xu, C., Zhao, S., Liu, J., Tu, K., Song, S.: Effects of soil bulk density and water content on the mechanical stability of soil structure using. Nongye Gongcheng Xuebao/Trans. Chin. Soc. Agric. Eng. **37**(19), 147–155 (2021). https://doi.org/10.11975/j.issn.1002-6819.2021.19.017

2. Leifer, D.: Advanced building technologies for sustainability. Constr. Econ. Buil. **12**(4), 91–92 (2015)

3. Kocherzhenko, V.V., Suleymanova, L.A., Kolesnikov, M.S.: Innovative structural and technological developments of pile foundation engineering. IOP Conf. Series Mater. Sci. Eng. **945**(1), 012035 (2020)

4. Ter-Martirosyan, Z.G., Ter-Martirosyan, A.Z., Dam, H.H.: Settlement and bearing capacity of rectangular footing in reliance on the pre-overburden pressure of soil foundation. Appl. Sci. (Switzerland) **11**(24), 12124 (2021). https://doi.org/10.3390/app112412124

5. Mo, P.-Q., Zhou, G., Gao, F., Li, R.: Bearing capacity of surface circular footings on granular material under low gravity fields. J. Rock Mech. Geotech. Eng. **13**(3), 612–625 (2021). https://doi.org/10.1016/j.jrmge.2020.11.009

6. Shi, F., Lu, K.-L., Yin, Z.-K.: Determination of three-dimensional passive slip surface of rigid retaining walls in translational failure mode and calculation of earth pressures. Yantu Lixue/Rock Soil Mech. **42**(3), 735–745 (2021). https://doi.org/10.16285/j.rsm.2020.1298

7. Nguyen, D.L., Ohtsuka, S., Hoshina, T., Isobe, K.: Discussion on size effect of footing in ultimate bearing capacity of sandy soil using rigid plastic finite element method. Soils Found. **56**(1), 93–103 (2016). https://doi.org/10.1016/j.sandf.2016.01.007

8. Du, N.L., Ohtsuka, S., Hoshina, T., Isobe, K., Kaneda, K.: Ultimate bearing capacity analysis of ground against inclined load by taking account of nonlinear property of shear strength. Int. J. GEOMATE **5**(2), 678–684 (2013)

9. Zheng, J., Hryciw, R.D.: Traditional soil particle sphericity, roundness and surface roughness by computational geometry. Geotechnique **65**(6), 494–506 (2015). https://doi.org/10.1680/geot.14.P.192

10. Kocherzhenko, V.V.: The study on soils external friction. IOP Conf. Series Mater. Sci. Eng. **698**(2), 022026 (2019). https://doi.org/10.1088/1757-899X/698/2/022026

11. Nikonorov, V.V., Nikonorova, D.O., Pikus, G.A.: Thermophysical properties of the soil massif. Mag. Civil Eng. **92**(8), 27–35 (2019). https://doi.org/10.18720/MCE.92.2

Stress–Strain State Simulation for the Eccentrically Compressed Reinforced Concrete Columns with Local Prestress at the Manufacturing Stage

A. A. Lipovich[1] , A. S. Chepurnenko[1,2] , E. A. A. Al-Wali[1] ,
and S. V. Klyuev[3(✉)]

[1] Don State Technical University, 1 Gagarin Sq., Rostov-On-Don 344000, Russia
[2] Kazan Federal University, Kazan, Russia
[3] Belgorod State Technological University named after V.G. Shukhov, Belgorod, Russia
klyuyev@yandex.ru

Abstract. The article is devoted to columns with local prestressing of tensile reinforcement. Such columns can be used with large eccentricities of the longitudinal force, for example, in industrial buildings. Prestressing of the reinforcement in the structures under consideration is created using tension couplings. The design of columns with local prestressing is described. The derivation of resolving equations for determining the stress–strain state at the manufacturing stage is given, taking into account the nonlinear properties of concrete. The calculation model is based on the hypothesis of plane sections. The problem is reduced to a system of two equations for axial deformation and element curvature. An algorithm for the numerical solution of the resulting system is described, which is implemented in the Matlab environment. A formula for the deflection of the element at the manufacturing stage is obtained. Verification was performed by comparison with the finite element software package LIRA in three-dimensional nonlinear formulation.

Keywords: Reinforced concrete · Prestressed columns · Manufacturing stage · Local prestress · Numerical modeling

1 Introduction

Reinforced concrete structures currently form the basis of industrial and civil construction and largely determine the level of its development. In recent years, there has been significant progress in the theory and practice of reinforced concrete structures, but the possibilities for their further improvement are not completely exhausted. This mainly applies to structures with prestressing, which makes it possible to efficiently use high-strength reinforcement, significantly reducing metal consumption and thereby significantly reducing construction costs [1–3].

Existing research and design developments on prestressed reinforced concrete structures are mostly devoted to structures in which the reinforcement is pre-tensioned, which can significantly improve the crack resistance of reinforced concrete elements [4–6].

Traditional methods of manufacturing prestressed reinforced concrete structures involve pulling prestressing reinforcement over the entire length of the element. This causes negative effects at the end sections—non-closing cracks appear on the upper faces of the elements, local fragmentation of concrete occurs due to the action of concentrated forces at the ends of the structure [7]. In addition, when the bending moment is variable along the length of the element, the reinforcement and the level of prestress determined by the maximum force for the end lightly loaded sections will be redundant [8].

In existing publications on prestressed concrete, elements with local prestressing of reinforcement are practically not given attention. There are only few works on reinforced concrete beams with local prestressing [9–12].

However, prestressing of tensile reinforcement may be required not only for beams, but also for eccentrically compressed columns with large longitudinal force eccentricities. In the case of flexible columns, due to the occurrence of additional eccentricity of the longitudinal force caused by the deflection of the element, the bending moment in such structures is not constant along the length, and the creation of prestresses along the entire length of the element is impractical [13].

We offer a new type of reinforced concrete columns with local pre-stressing. In the process of concreting the columns, sinuses are left in the areas that will be further subject to pre-tension (Fig. 1).

With a constant reinforcement class along the length of the column, the reinforcing bars of the tension zone consist of two sections connected by couplings. In couplings, a right-hand thread is cut in half of the length, and a left-hand thread is cut in the other half. Appropriate threads are cut at the ends of the joined reinforcing bars. Depending on the direction of rotation of the coupling, the ends of the rods approach or move away, and thus pre-tension or compression stresses are created. After creating prestresses, the sinuses are concreted.

The purpose of this work is to develop a model for the stress–strain state (SSS) calculation of such structures at the manufacturing stage.

2 Methods

When deriving the resolving equations for the calculation of stress–strain state, the following hypotheses are accepted:

1. Hypothesis of plane sections;
2. No influence of prestressing reinforcement on the stress–strain state of the support sections ($0 \leq x \leq (l - l_0)/2$ and $(l + l_0)/2 \leq x \leq l$) at the manufacturing stage, where l_0 is the length of the local prestress zone, l is the length of the column);
3. The stress concentration at the junction of the stressed and non-stressed sections of the column, associated with a change in the dimensions of the cross section, is neglected;
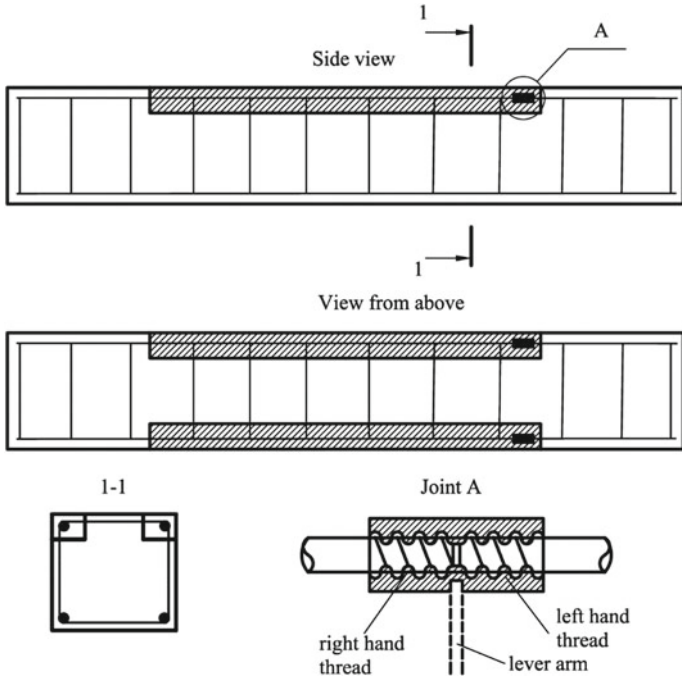
Fig. 1 Design of the column with local prestressing

Taking into account the hypotheses introduced, the bending moment in the pre-stressed zone is constant at the manufacturing stage, and there are no stresses in the concrete and reinforcement in the support sections. The calculation scheme for the first stage is shown in Fig. 2.

When deriving equations, in order to take into account the nonlinear work of concrete, we will assume that its modulus of elasticity changes along the height of the section, how it is done, for example, in [14–16]. We consider tensile stresses to be positive for concrete and reinforcement, which is shown in Fig. 3.

The deformation of the concrete in the prestressed zone, taking into account the hypothesis of plane sections, is written as:

$$\varepsilon_b = \varepsilon_0 - y\chi, \tag{1}$$

where ε_0 is the axial deformation, χ is the element curvature, y is the coordinate relative to the geometric center of gravity of the section (excluding sinuses).

The values ε_0 and χ are constant in the area l_0. Stresses in concrete are defined as follows:

$$\sigma_b(y) = E_b(y)\varepsilon_b = E_b(y)(\varepsilon_0 - y\chi). \tag{2}$$

The stresses in the reinforcement A_s' are found from the condition of its joint work with concrete:

$$\sigma_s' = E_s\left(\varepsilon_0 - y_s'\chi\right), \tag{3}$$
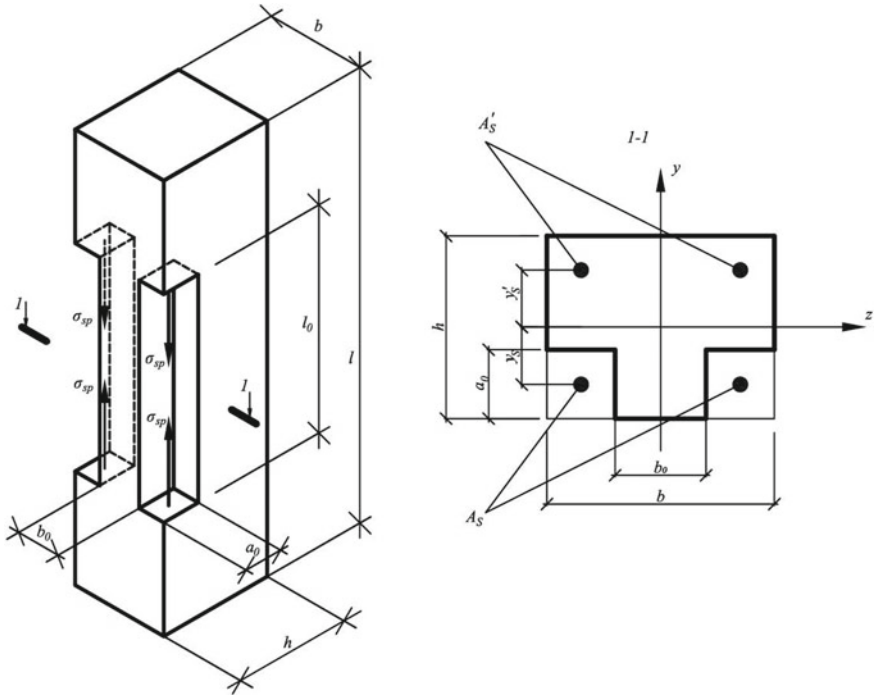
Fig. 2 Calculation scheme for determining the SSS at the manufacturing stage
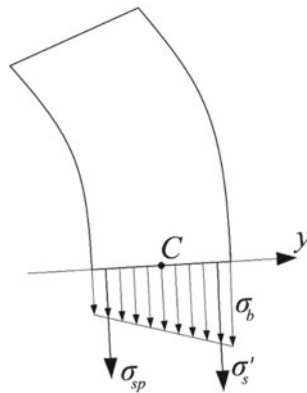
Fig. 3 Equilibrium of the cut-off part in the manufacturing stage

where E_s is the elasticity modulus of the reinforcement.

We compose the sum of the moments for the point C (according to Fig. 4), which divides the height of the section in half:

$$\sigma_{sp} A_s y_s = \int_A \sigma_b(y) y \mathrm{d}A + \sigma_s' A_s' y_s', \tag{4}$$
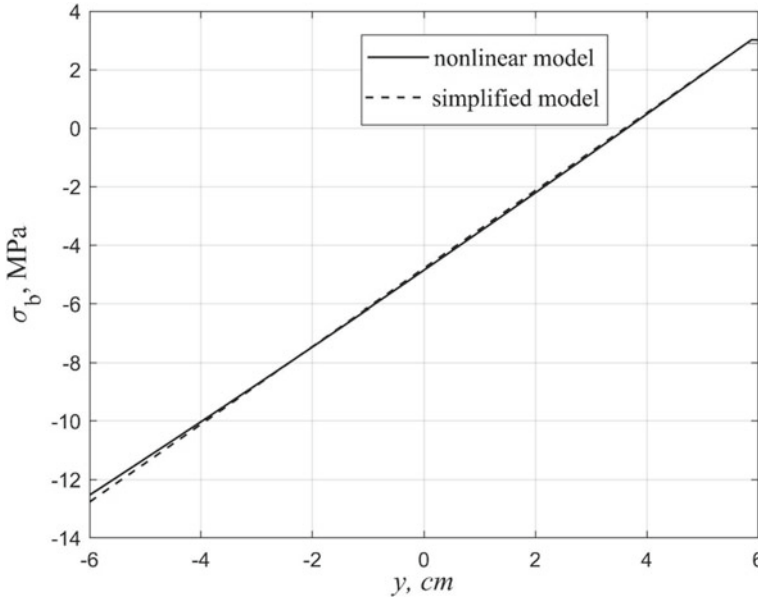
Fig. 4 Changes of stresses in concrete along the height of the section

where A is the area of the concrete section, $\sigma_s{'}$ are the stresses in the compressed (at the stage of loading with the compressive force F) reinforcement, σ_{sp} are the stresses in the pretensioned reinforcement, A_s and $A_s{'}$ are respectively the area of the pretensioned and compressed (at the stage of loading with the compressive force F) reinforcement, y_s and $y_s{'}$ are respectively the distances (in absolute value) from the geometric center of gravity of the section to the centers of gravity of the reinforcement A_s and $A_s{'}$.

The integral over the concrete area in (4) is written as:

$$\int_A \sigma_b(y)y\mathrm{d}A = b_0 \int_{-h/2}^{h/2} \sigma_b(y)y\mathrm{d}y + (b - b_0) \cdot \int_{-h/2+a_0}^{h/2} \sigma_b(y)y\mathrm{d}y, \tag{5}$$

where b_0 is the width of the section in the zone of local prestressing, h is the height of the section.

Next, we compose the sum of the projections on the longitudinal axis of the column:

$$\sigma_{sp}A_s + \sigma_s'A_s' + \int_A \sigma_b(y)\mathrm{d}A = 0. \tag{6}$$

The integral in (6) is calculated by analogy with (5).
Substituting (2) and (3) into (4), we obtain the following equation:

$$\varepsilon_0 \left(E_s A_s' y_s' + b_0 \int_{-h/2}^{h/2} E_b(y)y\mathrm{d}y + (b - b_0) \int_{-h/2+a_0}^{h/2} E_b(y)y\mathrm{d}y \right) -$$

$$-\chi\left(E_sA_s'\left(y_s'\right)^2 + b_0 \int\limits_{-h/2}^{h/2} E_b(y)y^2\mathrm{d}y + (b-b_0)\int\limits_{-h/2+a_0}^{h/2} E_b(y)y^2\mathrm{d}y\right) = \sigma_{sp}A_sy_s.$$

(7)

The second resolving equation for the manufacturing stage is obtained by substituting (2) and (3) into (6):

$$\varepsilon_0\left(b_0 \int\limits_{-h/2}^{h/2} E_b(y)\mathrm{d}y + (b-b_0)\int\limits_{-h/2+a_0}^{h/2} E_b(y)\mathrm{d}y + E_sA_s'\right) -$$

$$-\chi\left(b_0 \int\limits_{-h/2}^{h/2} E_b(y)y\mathrm{d}y + (b-b_0) + \int\limits_{-h/2+a_0}^{h/2} E_b(y)y\mathrm{d}y + E_sA_s'y_s\right) = -\sigma_{sp}A_s. \quad (8)$$

The system of Eqs. (7) and (8) can be written in the following form:

$$\begin{bmatrix} ES & -EI \\ EA & -ES \end{bmatrix}\begin{Bmatrix} \varepsilon_0 \\ \chi \end{Bmatrix} = \begin{Bmatrix} \sigma_{sp}A_sy_s \\ -\sigma_{sp}A_s \end{Bmatrix}.$$

(9)

The EI value is the bending stiffness in the section l0, EA is the cross-sectional stiffness in central tension or compression, the ES value with a constant modulus of elasticity of concrete along the section height is equivalent to the product of the modulus of elasticity of the reduced section and the static moment.

The problem of the SSS determining is solved by the method of successive approximations. The height section is divided into n_y parts Δy. The stress–strain diagram for the compressed zone can be given by the Sargin formula used in Eurocodes:

$$\frac{\sigma}{R} = \frac{k\eta - \eta^2}{1 + (k-2)\eta},$$

(10)

where $\eta = \varepsilon/\varepsilon_R$; ε_R is the strain value at the top of the diagram; R is the strength of concrete; coefficient k determines the curvature of the diagram $\sigma - \varepsilon$; $k = 1/\lambda_R$, where λ_R is the coefficient of the secant modulus change at the top of the diagram $\sigma - \varepsilon$.

The value of ε_R is determined by the empirical formula obtained by Nesvetaev et al. [17]:

$$\varepsilon_R = \alpha(R/E_0)^{0.5},$$

(11)

where $\alpha = 0.058$ for heavy concrete.

As a first approximation, we consider that the concrete modulus of elasticity is constant along the height of the section. Axial deformation and element curvature are determined from Eq. (9). Then stresses in concrete are determined by formula (2). Further, the secant modulus $\overline{E}(\varepsilon)$ is calculated from the total deformation ε_b.

After calculating the secant modulus, the modulus of elasticity of concrete at each point is corrected according to the formula:

$$E_{i+1} = \left(E_i + \overline{E}(\varepsilon)\right)/2,$$

(12)

where E_i is the concrete modulus of elasticity in the current approximation, E_{i+1} is the concrete modulus of elasticity in the next approximation.

The criterion for the end of the iterative process is the condition:

$$\frac{|\sigma_i - \sigma_{i-1}|}{\sigma_i} \cdot 100\% < \delta, \tag{13}$$

where σ_i and σ_{i-1} are, respectively, the maximum absolute value of the stresses in the current and previous approximations, δ is the specified calculation accuracy in percent, which we take equal to 0.1%.

The deflection in the middle of the column can be calculated by the formula:

$$f = \rho - \sqrt{\rho^2 - \left(\frac{l_0}{2}\right)^2} + \frac{l(l - l_0)}{4\rho}, \tag{14}$$

where $\rho = 1/\chi$.

3   Results and Discussion

Let us consider the example of calculation with the following initial data: $b = 25$ cm, $h = 12$ cm, $l = 180$ cm, $l_0 = 95$ cm, $b_0 = 14$ cm, $a_0 = 5.5$ cm, $E_{b0} = 3.47 \cdot 10^4$ MPa, compressive strength of concrete $R = 46.4$ MPa, tensile strength $R_t = 2.9$ MPa, $\sigma_{sp} = 400$ MPa, diameter of reinforcing bars $d = 12$ mm, reinforcing bars snap coordinates $y_s = y'_s = 3$ cm.

Figure 4 shows the theoretical graph of the stresses change in concrete along the height of the section at the stage of creating prestresses. The dashed line corresponds to the solution according to the simplified method, when the non-linearity of concrete in the compressed zone is not taken into account.

There is no noticeable difference between the calculation taking into account the nonlinear stress diagram in the compressed zone and the simplified approach at the stage of prestressing.

The theoretical deflection at the moment of prestresses creation was 1.23 mm.

Also, to control the reliability of the results, finite element modeling of the pre-stressing stage in the LIRA software package was done. The calculation was performed in a physically non-linear formulation, concrete was modeled by volumetric FE in the form of parallelepipeds, and reinforcement was modeled by bar FE. The law of concrete deformation was assigned exponential, and elastic work was taken for reinforcement. In order to save machine time, a quarter of the structure was considered. The prestress was modeled by a concentrated force $F = \sigma_{sp} A_s$. The maximum deflection value obtained in LIRA was 1.27 mm, which differs from the author's solution by 3.3%. Isofields of vertical displacements are shown in Fig. 5.

4   Conclusion

The resolving equations are obtained and the algorithm for calculating the stress–strain state of columns with local prestress at the manufacturing stage is developed. Verification
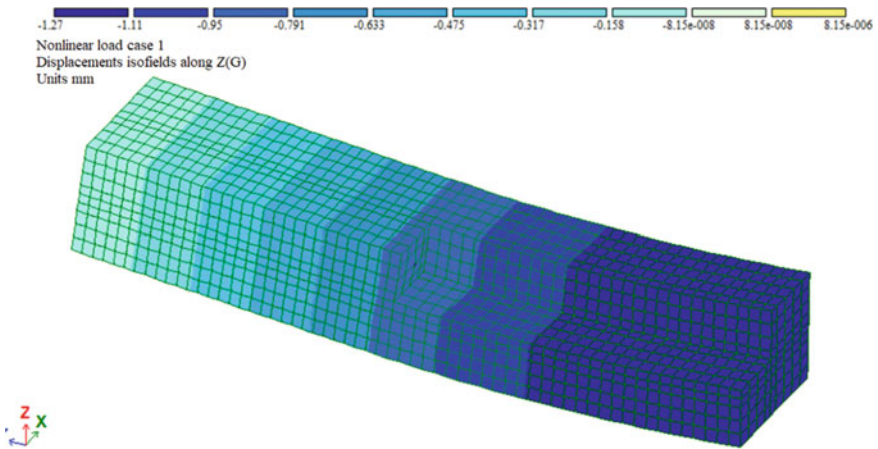
Fig. 5 Isofields of vertical displacements in LIRA

was performed by comparison with the calculation using the finite element method in the LIRA software package in a three-dimensional nonlinear formulation. The discrepancy of the results does not exceed 5%. It was also found that at the stage of prestresses creation, one can neglect the nonlinearity of the work of concrete in the compressed zone.

References

1. Xiong, X., Yao, G., Su, X.: Experimental and numerical studies on seismic behavior of bonded and unbonded prestressed steel reinforced concrete frame beam. Eng. Struct. **167**, 567–581 (2018)
2. Yang, Y., et al.: Protective effect of unbonded prestressed ultra-high performance reinforced concrete slab against gas explosion in buried utility tunnel. Process Saf. Environ. Prot. **149**, 370–384 (2021)
3. Bhanugoban, M., Yapa, H.D., Dirar, S.: Efficient shear retrofitting of reinforced concrete beams using prestressed deep embedded bars. Eng. Struct. **246**, 113053 (2021)
4. Pham, T.D., Hong, W.K.: Investigation of strain evolutions in prestressed reinforced concrete beams based on nonlinear finite element analyses considering concrete plasticity and concrete damaged plasticity. J. Asian Archit. Build. Eng. **21**(2), 448–468 (2022)
5. Kolchunov, V.I., Iliushchenko, T.A.: Crack resistance criterion of plane stress RC elements with prestressed reinforcement. J. Phys: Conf. Ser. **1425**(1), 012095 (2019)
6. Kolchunov, V.I., et al.: Failure simulation of a RC multi-storey building frame with prestressed girders. Mag. Civil Eng. **8**(92), 155–162 (2019)
7. Okumus, P., Oliva, M.G.: Evaluation of crack control methods for end zone cracking in prestressed concrete bridge girders. PCI J. **58**(2), 91–105 (2013)
8. Krivitskiy, P., et al.: Shear resistance of prestressed concrete beams with the constant and variable height. MATEC Web Conf. **350**, 00006 (2021)
9. Mailyan, D.R., Mailyan, L.D.: Conditions of maximum economic efficiency and environmental safety of reinforced concrete columns with precompressed reinforcement. Mater. Sci. Forum **931**, 269–274 (2018)

10. Taoum, A., Jiao, H., Holloway, D.: Flexural behaviour of locally post-tensioned reinforced concrete beams. Aust. J. Struct. Eng. **16**(3), 180–186 (2015)
11. Klyuev, S.V., Khezhev, T.A., Pukharenko, Y.V., Klyuev, A.V.: Fibers and their properties for concrete reinforcement. Mater. Sci. Forum MSF **945**, 125–130 (2018)
12. Klyuev, S.V., Bratanovskiy, S.N., Trukhanov, S.V., Manukyan, H.A.: Strengthening of concrete structures with composite based on carbon fiber. J. Comput. Theor. Nanosci. **16**(7), 2810–2814 (2019)
13. Mailyan, D.R., Del Socorro, V.A.L.: Effective reinforced concrete structures of monolithic frame buildings and structures. IOP Conf. Series Mater. Sci. Eng. **913**(3), 032049 (2020)
14. Chepurnenko, V. et al.: Calculation of eccentrically compressed reinforced concrete columns under various creep laws. E3S Web of Conferences, vol. 281, pp. 01050 (2021)
15. Chepurnenko, A. et al. Stress-strain state of the short eccentrically compressed reinforced concrete columns with nonlinear creep. E3S Web of Conferences, vol. 281, pp. 01049 (2021)
16. Ishchenko, A.V., Pogodin, D.A.: Calculation of reinforced concrete arches on stability when creeping. IOP Conf. Series Mater. Sci. Eng. **698**, 022086 (2019)
17. Nesvetaev, G., Koryanova, Y., Zhilnikova, T.: On effect of superplasticizers and mineral additives on shrinkage of hardened cement paste and concrete. MATEC Web Conf. **196**, 04018 (2018)

Filled Polyurethane Foam with Improved Quality Indicators

L. A. Suleymanova$^{(\boxtimes)}$ ⦿, A. V. Kocherzhenko ⦿, and I. S. Ryabchevskiy ⦿

Belgorod State Technological University named after V.G. Shukhov, Belgorod, Russia
`ludmilasuleimanova@yandex.ru`

Abstract. One of the most important advantages of polyurethane foams is the ability to produce products in one step. Foaming and curing of this insulation does not require heat supply due to the exothermic synthesis reaction that occurs when two or more liquid components are mixed, with simultaneous adhesion of polyurethane foam to various surfaces due to good adhesion to almost any materials. At the same time, having a low density, this foam polymer is able to withstand fairly large loads. Samples were taken from the tailings filtration field of the Stoilensky GOK (Gubkin, Russia) from various sites as the studied raw materials, their granulometric and chemical compositions were determined, and the harmonic diameters of the filler particles were determined. Based on the calculation results, the dependence of the foaming coefficient on the average harmonic diameter of the filler was determined. An experiment planning matrix has been developed, based on the results of which mathematical models of the dependence of the coefficient of foaming of laboratory samples of polyurethane foam filled with tailings were built. Three zones of tailings are considered based on the results of sampling. Analyzing the results obtained, a quantitative and qualitative assessment of the influence of each factor separately, as well as their combination, on the change in the "composition–properties" system was derived.

Keywords: Polyurethane foam · Mineral filler · Ferrous quartz wet magnetic separation waste · Foaming rate

1 Introduction

Due to its porous structure, polyurethane foam is one of the best thermal insulation materials. Due to low diffusion, the time for changing the initial thermal conductivity is not long enough [1–3].

Formation of polyurethane foams Polyurethane foams are formed by the interaction of isocyanates having more than one reactive group (–N=C=O) with polyols containing at least two reactive hydroxyl functional groups in the molecule [4–6].

During the foaming and curing of the polymer, bubbles form in the polymer solution, and the bubbles grow and stabilize. Therefore, regardless of the difference between foams and polyurethane foams in colloidal gas–liquid systems, the phenomena occurring in mobile systems are in full accordance with the laws of colloidal chemistry [7].

For example, the bubbles that form in a polyurethane foam system are similar to the bubbles in a water-soap system. At the same time, it is clear that such a comparison is impossible in terms of the duration of the existence of bubbles in the foam due to the rapid increase in the viscosity and elasticity of the polymer phase [8, 9].

According to Plateau's rules, the most probable form of gas structural elements are dodecahedral pentagonal dodecahedrons, in each edge of which three films converge, the angles between which are equal to 120°. The edges of the polyhedron are characterized by thickenings (Plateo-Gibbs channels), their shape in cross section is a spherical triangle, which is clearly shown in Fig. 1.
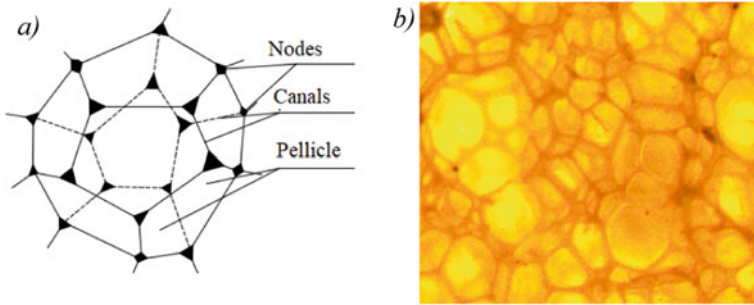
Fig. 1 Unit cell of polyurethane foam: **a** scheme; **b** microstructure (×50 magnification)

The fillers that make up polyurethane foams change the parameters of the foaming process, which, in turn, changes the macrostructure and properties of polyurethane foams. Since fillers are not always compatible with the polymer to a certain extent, it is not possible to unambiguously assess the effect of fillers as negative. Sometimes fillers act as emulsion stabilizers.

2 Methods and Materials

In this article, for the first time, a variant of filling polyurethane foam with industrial waste from mining and processing plants, and specifically, with waste from the wet separation of ferruginous quartzites (hereinafter referred to as tails) [1–3], is proposed. The scheme of the tailing's filtration field is shown in Fig. 2.

After selecting models from the tailings filtration fields, their chemical (Table 1) and granulometric (Table 2) compositions were determined.

The conducted studies showed that the samples do not differ significantly in their chemical composition (Table 1), but they differ in particle size distribution (Table 2).

Under the influence of the hydraulic energy of the water flow, fractionation of the tailings particles and their differentiation in size and specific gravity of various minerals occur [10–12]. The largest and heaviest particles fall out near the pulp outlet and form the so-called drain or pulp outlet zone at the tailings. The layout of the tailings sections depending on their granulometric composition is shown in Fig. 3.
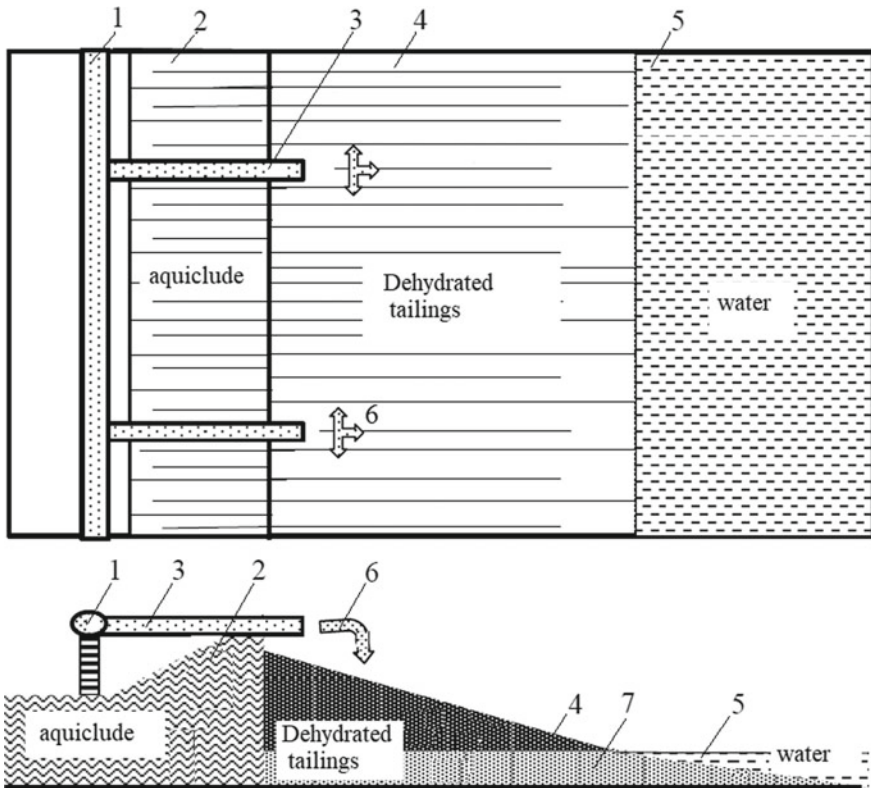
Fig. 2 Scheme of the tailings filtration field in the section: 1—main slurry pipeline; 2—dam from aquiclude; 3—distribution pipeline; 4—main filtration field; 5—site of deposition of silt residues of tailings; 6—pulp spreading directions; 7—tailings located in the water

This zone extends approximately 50 m from the exit point (zone 1). Areas of average and specific gravity form intermediate zones (zones 2 and 3) with a total width of 120–170 m. The smallest and lightest particles are carried away to the polar zone, where they are covered with water and form the so-called silt (zone 4). This tailings structure is preserved after the completion of the alluvial layer in the filtration zone.

3 Results and Discussion

When planning the experiment, the following factors were taken as variable factors: the consumption of tailings and the ratio between the components. For a more detailed explanation of the mathematical model of polyurethane foam, orthogonal central programming is used, which depends on variables in the form of second-order polynomials. Table 3 shows the planning conditions that show the natural values of the coding coefficients.

Let's say the average consumption of waste, clay and sand is 30% by weight of polyurethane with a variation of 20%. The average ratio of the levels of polyisocyanate

Table 1 Chemical composition of material samples

Model No.		Chemical composition, %							
		SiO_2	Fe	Fe_2O_3	FeO	CaO	MgO	Al_2O_3	The rest
Zone 1	1	66.3	12.2	9.1	5.6	2.3	2.5	0.8	1.2
	2	65.4	11.8	9.5	5.9	2.6	2.8	0.5	1.5
	3	66.8	12.6	9.7	4.8	2.1	2.1	0.48	1.42
	4	66.3	13.1	8.6	4.9	2.9	2.8	0.53	1.07
	5	65.8	12.8	9.4	5.2	2.5	2.3	0.59	1.4
Mean		66.12	12.5	9.26	5.28	2.48	2.5	0.58	1.318
Zone 2	6	67.7	10.8	10.3	5.3	1.8	1.6	0.9	1.6
	7	68.3	10.3	11.5	4.4	1.7	1.9	1.2	0.7
	8	66.9	11.1	10.8	5.6	2.1	1.7	0.7	1.1
	9	68.1	10.8	11.3	4.7	1.5	2.1	0.8	0.7
	10	66.8	11.2	10.9	5.1	1.9	1.8	1.1	1.2
Mean		67.56	10.84	10.96	5.02	1.8	1.82	0.94	1.06
Zone 3	11	68.7	9.6	12.2	5.1	1.3	1.2	1.2	0.7
	12	69.3	8.1	12.1	4.8	1.8	1.5	1.3	1.1
	13	67.8	9.3	12.8	4.5	1.5	1.3	0.9	1.9
	14	69.7	9.1	11.1	4.2	1.9	1.8	1.4	0.8
	15	68.7	8.8	12.1	4.8	1.7	1.7	1.1	1.1
Mean		68.84	8.98	12.06	4.68	1.64	1.5	1.18	1.12

and polyol components was taken as 1, since the recommended ratio for the polyurethane component without fillers is 100:100. The range of change is 0.1.

The essence of the method is to determine the mathematical relationship between the given properties and the use of materials, the properties of parts and process factors. Depending on the number of factors and the situation of the problem being solved, the number of tests is carried out according to a given corresponding plan. The planning matrix and experimental data are given in the Table 4.

The results of the experiment are processed using mathematical statistics to obtain algebraic equations that reflect the relationship between the studied properties and the initial factors, using regression equations, you can build graphs and nomograms that allow you to quickly adjust as each factor changes. The value of the output parameter. When using a nomogram, the output parameters can be kept at a given level by appropriately modifying the factors included in the regression equation.

Based on the equations obtained, a mathematical model was constructed for the dependence of the foaming coefficient of laboratory samples of polyurethane foam on the factors under study (Fig. 4).

Table 2 Granulometric composition of laboratory samples of the material

Model No.		Fraction content, %, with fraction size, mm				
		1–0.5	0.5–0.25	0.25–0.1	0.1–0.05	< 0.05
Zone 1	1	18.5	28.6	39.3	8.8	4.8
	2	21.3	28.7	36.2	10.5	3.3
	3	20.7	27.4	38.8	9.4	3.7
	4	22.4	29.3	37.2	8.3	2.8
	5	20.3	26.7	40.5	9.3	3.2
Mean			28.14	38.4	9.26	3.56
Zone 2	6	10.6	18.3	47.1	14.4	9.6
	7	8.1	19.6	47.8	13.7	10.8
	8	9.9	18.8	46.1	12.4	12.8
	9	9.2	20.1	48.2	13.3	9.2
	10	8.3	18.9	46.8	13.5	12.4
Mean			19.14	47.2	13.46	10.96
Zone 3	11	4.1	9.7	53.6	16.4	16.2
	12	3.8	8.6	56.1	15.2	16.3
	13	4.7	7.8	55.8	17.1	14.6
	14	5.1	8.4	56.2	18.2	12.1
	15	3.4	8.1	54.6	16.6	17.3
Mean			8.52	55.26	16.7	15.3

In the transition from coded factors to natural ones, the optimal ratio of components was found, which is 100:100.

4 Conclusions

Thus, the possibility of using waste from the processing of ferruginous quartzites of the Stoilensky GOK (Russia) as a mineral filler for polyurethane foam has been experimentally proven. The structure of the newly obtained composite insulation was studied. Mining industry wastes (tailings) are embedded in a polyurethane matrix and are intrastructural.
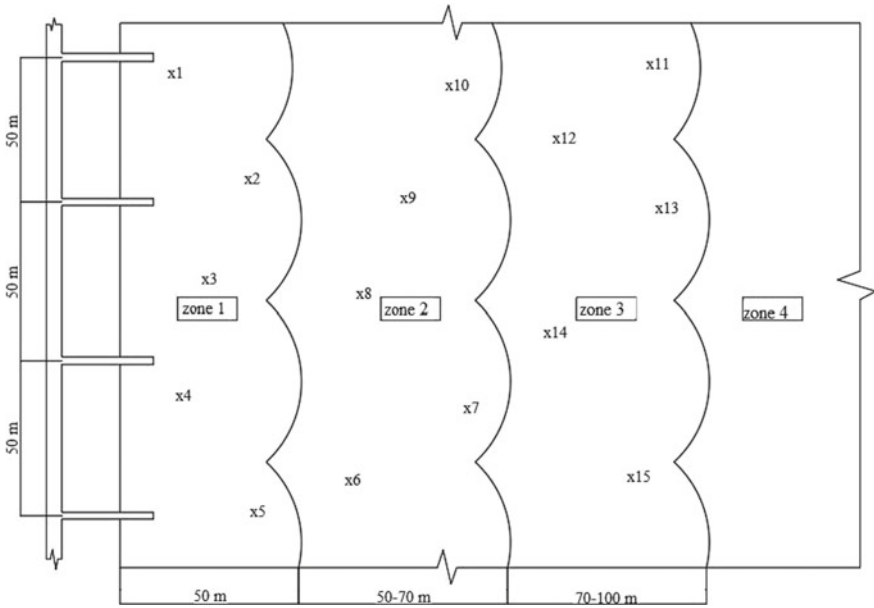
Fig. 3 Scheme of location of tailings sections depending on their granulometric composition (material sampling by zones)

Table 3 Experiment planning conditions

Factor		Level of variation			Interval of variation
Natural view	Coded view	+ 1	0	− 1	
Filler consumption, %	X_1	50	30	10	20
Component ratio	X_2	1.1	1.0	0.9	0.1

Table 4 Planning matrix and experimental data

No. of experience	Factors		K_{foam} models of polyurethane foam filled with tails		
	X1	X2	Tails of zone 1, × 1000	Tails of zone 2, × 1000	Tails of zone 3, × 1000
1	+ 1	+ 1	630	520	420
2	+ 1	− 1	610	510	410
3	− 1	+ 1	1070	680	480
4	− 1	− 1	1050	670	470
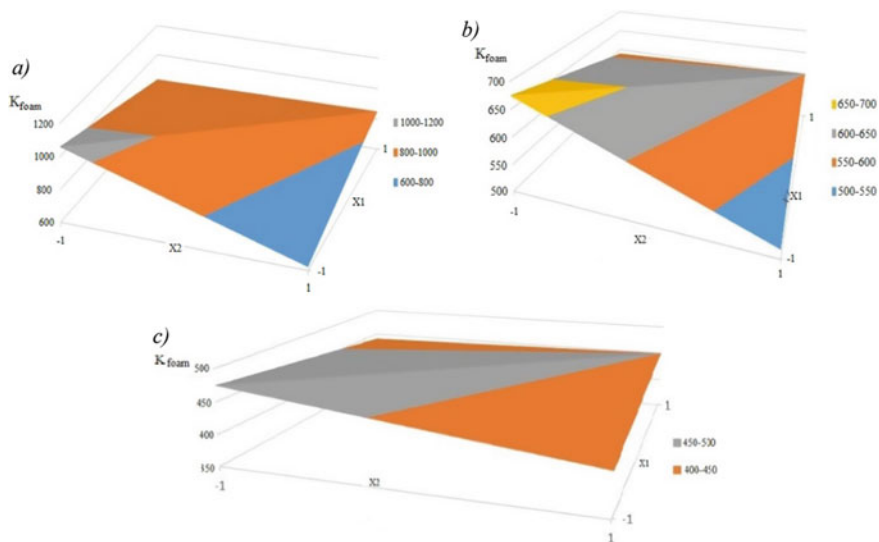
Fig. 4 Mathematical model of the dependence of the coefficient of foaming of laboratory samples of polyurethane foam filled with tailings: **a** zone1; **b** zone 2; **c** zone 3

References

1. Zhu, X., Li, X., Mi, H.-Y., Jing, X., Dong, B., He, P., Liu, C., Shen, C.: Graphene oxide/thermoplastic polyurethane wrinkled foams with enhanced compression performance fabricated by dynamic supercritical CO_2 foaming. J. Appl. Polym. Sci. **139**(27), e52485 (2022). https://doi.org/10.1002/app.52485

2. Suleimanova, L.A., Kocherzenko, A.V., Ryabchevsky, I.S.: Dependence of the performance coefficient on the average harmonic diameter of polyurethane foam. Bull. BSTU named after V.G. Shukhov **4**(5), 28–35 (2019). https://doi.org/10.34031/article_5ce292c9837090.54164650

3. Suleimanova, L.A., Pogorelova, I.A., Kocherzenko, A.V., Ryabchevsky, I.S.: Effect of mineral fillers on the polyurethane foam performance properties. Mater. Sci. Forum **974**, 267–272 (2020). https://doi.org/10.4028/www.scientific.net/MSF.974.267

4. Wang, C., Wu, Y., Li, Y., Shao, Q., Yan, X., Han, C., Wang, Z., Liu, Z., Guo, Z.: Flame-retardant rigid polyurethane foam with a phosphorus-nitrogen single intumescent flame retardant. Polym. Adv. Technol. **29**(1), 668–676 (2018). https://doi.org/10.1002/pat.4105

5. Saha, M.C., Kabir, Md.E., Jeelani, S.: Enhancement in thermal and mechanical properties of polyurethane foam infused with nanoparticles. Mater. Sci. Eng. A **479**(1–2), 213–222 (2008). https://doi.org/10.1016/j.msea.2007.06.060

6. Zhang, C., Shi, Z., Li, A., Zhang, Y.-F.: Rgo-coated polyurethane foam/segmented polyurethane composites as solid–solid phase change thermal interface material. Polymers **12**(12), 1–9 (2020). https://doi.org/10.3390/polym12123004

7. Pham, C.T., Nguyen, B.T., Nguyen, H.T.T., Kang, S.-J., Kim, J., Lee, P.-C., Hoang, D.: Comprehensive investigation of the behavior of polyurethane foams based on conventional polyol and oligo-ester-ether-diol from waste poly(ethylene terephthalate): fireproof performances, thermal stabilities, and physicomechanical properties. ACS Omega **5**(51), 33053–33063 (2020). https://doi.org/10.1021/acsomega.0c04555

8. Huang, Y., Zhou, J., Sun, P., Zhang, L., Qian, X., Jiang, S., Shi, C.: Green, tough and highly efficient flame-retardant rigid polyurethane foam enabled by double network hydrogel coatings. Soft Matter **17**(46), 10555–10565 (2021). https://doi.org/10.1039/d1sm01213d

9. Semenov, A., Smirnov, A., Stepanov, M., Kharaldin, N., Borovkov, A.: The simplified approach to numerical modeling of polyurethane foam shock absorbers of complex structure: determination of effective mechanical properties and preparation of mathematical models of a homogenized material. J. Phys: Conf. Ser. **2131**(4), 042056 (2021). https://doi.org/10.1088/1742-6596/2131/4/042056

10. Cui, Z., Fan, Y., Liu, X., Si, J., Wang, Q.: Fabrication and characteristic of 3-D porous thermoplastic polyurethane/deacetylated cellulose acetate composite foam with outstanding mechanical property and oil/water separation performance. J. Appl. Polym. Sci. **139**(22), 52268 (2022). https://doi.org/10.1002/app.52268

11. Abu-Jdayil, B., Mourad, A.-H., Hittini, W., Hassan, M., Hameedi, S.: Traditional, state-of-the-art and renewable thermal building insulation materials: an overview. Constr. Build. Mater. **214**, 709–735 (2019). https://doi.org/10.1016/j.conbuildmat.2019.04.102

12. Yang, H., Yu, B., Song, P., Maluk, C., Wang, H.: Surface-coating engineering for flame retardant flexible polyurethane foams: a critical review. Compos. B Eng. **176**, 107185 (2019). https://doi.org/10.1016/j.compositesb.2019.107185

Author Index